

Energy-harvesting characteristics of damped piezoelectric phononic crystals and locally resonant and inertially amplified elastic metamaterials



Swansea University
Prifysgol Abertawe

Ibrahim Patrick

Supervisors:

Prof. S. Adhikari

Prof. H. Haddad Khodaparast

Advisor: Prof. M.I. Hussein

Department of Aerospace Engineering
Swansea University

Submitted to Swansea University in fulfilment of
the requirements for the degree of
Doctor of Philosophy

Faculty of Science and Engineering

June 2023

Copyright: The Author, Ibrahim Patrick, 2023.

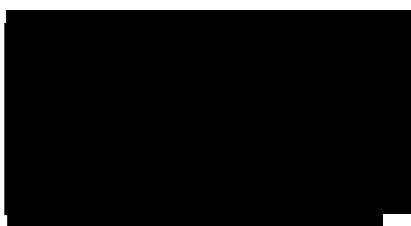
Distributed under the terms of a Creative Commons Attribution-NonCommercial-NoDerivatives 4.0 International License (CC BY-NC-ND 4.0).

To my parents

Declarations

This work has not previously been accepted in substance for any degree and is not being concurrently submitted in candidature for any degree.

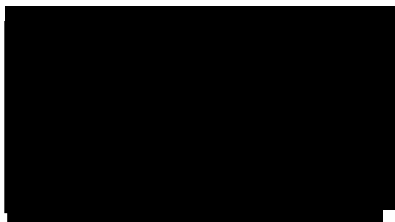
Signature:



Date: 12 June 2023

This thesis is the result of my own investigations, except where otherwise stated. Other sources are acknowledged by explicit references. A bibliography is appended.

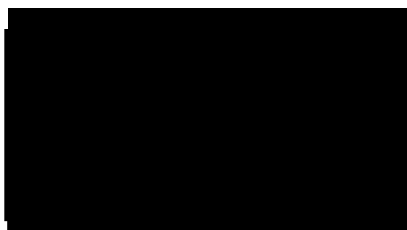
Signature:



Date: 12 June 2023

I hereby give consent for my thesis, if accepted, to be available for electronic sharing **after expiry of a bar-on-access approved by Swansea University.**

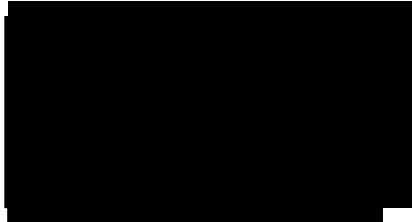
Signature:



Date: 12 June 2023

The University's ethical procedures have been followed and, where appropriate, that ethical approval has been granted.

Signature:



Date: 12 June 2023

Ibrahim Patrick
June 2023

Acknowledgements

First and foremost, I would like to praise and thank Allah, who is God Almighty, the Most Gracious, and the Most Merciful, with all my heart for blessing me in ways unmentionable, for bestowing upon me the ability to carry out the work included in this thesis and, consequently, realize its completion, for keeping me self-motivated, and for granting me the strength and courage to face all the hardships I encountered during my time as a PhD student. Although expressing gratitude towards a deity in the acknowledgement section of a thesis is uncommon, this section of my thesis will be pointless if I do not thank the God I worship. I strongly believe that one's faith can make them persevere and achieve things never before imagined, and my faith, without the shadow of a doubt, has helped me to overcome all the hardships in my life and emerge at the other end with immense peace, contentment, and gratitude.

I would like to profoundly thank my former supervisor, Professor Sondipon Adhikari, for taking me under his wing as a research student, offering me his expert research guidance, helping me to network with external collaborators, and being patient during the times when I faced long-term hardships, all the while inquiring about my wellbeing.

I am duty-bound to earnestly thank Professor Mahmoud I. Hussein at the University of Colorado, Boulder, whose technical expertise and research guidance and ideas were indispensable for the completion of this thesis. I would like to extend my sincere gratitude to him for collaborating in my first publication and for involving me in one of his own; these publications undoubtedly form the backbone of this thesis. I am immensely thankful to him for treating me as one of his own research students and acting as a committed inspirational external advisor.

I would like to extend my gratitude to my current supervisor, Professor Hamed Haddad Khodaparast, for taking me on as his research student for the last few crucial months of my candidature as a result of my former supervisor moving to a different university. I would like to thank him for motivating me at every step to give that final push towards completion.

I am where I am today because of everything that my mother Maria has done for me by God's blessings since the moment I was born. I would like to thank her for believing in me and showering me with her unwavering love, concern, support, optimism, and reassurances

while I faced many personal challenges during my time as a PhD student. I only wish that my father, John, was alive today to see me realize the remarkable feat of completing this thesis.

This acknowledgement section would be undeniably incomplete without thanking my loving wife, Abrar. I would like to thank her for consistently supporting me in every way she could throughout the process of writing my thesis, diligently offering kind words of encouragement, and, most importantly, showing admirable patience since getting married to me.

Abstract

Vibration energy harvesting is an emerging technology that enables electrical low-power generation using electromechanical structures or devices with piezoelectric elements. The prevailing approach for the characterization of the energy-harvesting performance in these devices is to consider a finite structure operating under forced vibration conditions. This thesis introduces an alternative framework whereby the intrinsic energy-harvesting characteristics are rigorously quantified independent of the forcing and the structure size, and by doing so, the notion of a piezoelectric material is considered rather than a finite piezoelectric electromechanical structure. To illustrate the intrinsic quantification termed as “intrinsic energy-harvesting availability,” suspended monoatomic and diatomic piezoelectric phononic crystals (MPPnCs and DPPnCs) are considered and treated with Bloch’s theorem; consequently, the representative energy-harvesting characteristics within the span of the unit cell’s Brillouin zone (BZ) are formally quantified. In the absence of shunted piezoelectric elements, the wavenumber-dependent dissipation (damping-ratio) of the phononic crystal (PnC) is computed and shown to increase, as expected, with the level of prescribed (raw) damping. With the inclusion of the piezoelectric elements, the wavenumber-dependent dissipation rises by an amount proportional to the energy intrinsically available for harvesting; upon summation of this increased amount over all the damping-ratio branches (acoustic and optical modes) and subsequent complete integration over the BZ, a quantity representative of the net, i.e., useful, dissipative energy intrinsically available for harvesting is obtained. Piezoelectric elements comprising purely resistive and inductor-equipped shunt circuits are investigated. A parametric design study yielding optimal piezoelectric-element properties in terms of the proposed intrinsic energy-harvesting availability measure is also presented.

Metadamping is the phenomenon of either enhanced or diminished intrinsic dissipation in a material emanating from the material’s internal structural dynamics. It has previously been demonstrated that an elastic locally resonant metamaterial (LRM) may be designed to exhibit higher or lower dissipation compared to a statically equivalent PnC with the same amount of prescribed damping. In this thesis, it is revealed that even further dissipation (positive metadamping) or, alternatively, further reduction of loss (negative metadamping) may be attained in an inertially amplified material (IAM) and an inertially amplified locally

resonant metamaterial (IALRM) compared to a statically equivalent PnC and LRM with the same amount of prescribed damping. This is demonstrated by a passive configuration whereby an attenuation peak is generated by the motion of an auxiliary mass connected to the main/baseline mass by an inclined rigid link. It is further illustrated that by coupling the inertially amplified attenuation peak with that of a local-resonance attenuation peak, a trade-off between the temporal- and spatial-attenuation intensities associated with the material properties is observed for a given range of the inertial-amplifier angle, i.e., angle between the inclined rigid links and the central axis of the metamaterial. As a result, design for desired performance is possible along this trade-off regime by adjustment of the inertial-amplifier angle, i.e., passive tuning. A region of monotonic increase in both attenuation types also exists for a different range of the inertial-amplifier angle. These results create a pathway for highly expanding the Ashby space for load-bearing and damping capacities or stiffness-damping capacities via design of a material's internal structure.

Building upon the work on characterizing the amount of useful dissipative energy intrinsically available for harvesting in a piezoelectric periodic media, the energy-harvesting availability is illustrated for a locally resonant piezoelectric metamaterial (LRPM) and an inertially amplified locally resonant piezoelectric metamaterial (IALRPM). It is also demonstrated that an LRPM with the same piezoelectric electrical parameters and the same amount of prescribed damping as for a statically equivalent reference piezoelectric phononic crystal (PPnC) exhibits an inherent emergence in the intrinsic energy-harvesting availability. This intrinsic phenomenon is termed as "metaharvesting." Furthermore, it is shown that an IALRPM with the same piezoelectric electrical parameters and the same amount of prescribed damping as for a statically equivalent LRPM and a statically equivalent reference PPnC exhibits a further emergence in the intrinsic energy-harvesting availability, i.e., enhanced metaharvesting.

Table of contents

List of figures	xiv
List of tables	xxviii
1 Introduction	1
1.1 Brief summary of pertinent topics	1
1.2 Problem statement and thesis objectives	6
1.3 Thesis outline	7
1.4 Thesis outcomes: journal articles, conference presentations, and posters . .	8
1.4.1 Journal publications	8
1.4.2 Conference presentations	9
1.4.3 Research posters	9
2 Literature Review	10
2.1 Introduction	10
2.2 Energy harvesting in electromechanical structures	10
2.3 Material dynamics of elastic periodic media	14
2.4 Energy harvesting in elastic periodic materials	25
2.5 Metadamping: Emergence of dissipation/damping in elastic metamaterials .	26
2.6 Summary and conclusions	30
3 Wave Propagation in One-Dimensional Phononic Crystals and Piezoelectric Phononic Crystals	33
3.1 Introduction	33
3.2 Overview of monoatomic phononic crystals	34
3.2.1 Without grounding	34
3.2.2 With grounding	37
3.3 Monoatomic piezoelectric phononic crystals	38

3.3.1	Without grounding	39
3.3.2	With grounding	42
3.4	Wave-propagation and dissipation characteristics of monoatomic phononic crystals and piezoelectric phononic crystals	46
3.4.1	Without grounding	46
3.4.2	With grounding	49
3.5	Overview of diatomic phononic crystals	50
3.5.1	Without grounding	52
3.5.2	With grounding	54
3.6	Diatomic piezoelectric phononic crystals	56
3.6.1	Without grounding	56
3.6.2	With grounding	61
3.7	Wave-propagation and dissipation characteristics of diatomic phononic crystals and piezoelectric phononic crystals	67
3.7.1	Without grounding	67
3.7.2	With grounding	70
3.8	Overview of locally resonant metamaterials	71
3.8.1	Without grounding	73
3.8.2	With grounding	74
3.9	Locally resonant piezoelectric metamaterials	76
3.9.1	Without grounding	76
3.9.2	With grounding	81
3.10	Wave-propagation and dissipation characteristics of locally resonant metamaterials and piezoelectric metamaterials	86
3.10.1	Without grounding	86
3.10.2	With grounding	88
3.11	Overview of inertially amplified locally resonant metamaterials	90
3.11.1	Without grounding	91
3.11.2	With grounding	93
3.12	Inertially amplified locally resonant piezoelectric metamaterials	95
3.12.1	Without grounding	95
3.12.2	With grounding	101
3.13	Wave-propagation and dissipation characteristics of inertially amplified locally resonant metamaterials and piezoelectric metamaterials	106
3.13.1	Without grounding	106
3.13.2	With grounding	108

3.14	Summary and conclusions	109
4	Wave Propagation in Two-Dimensional Phononic Crystals and Piezoelectric Phononic Crystals	112
4.1	Introduction	112
4.2	Monoatomic phononic crystal	113
4.3	Piezoelectric monoatomic phononic crystals	118
4.3.1	Shunt circuit without an inductor	120
4.3.2	Shunt circuit with an inductor	123
4.4	Wave-propagation and dissipation analysis of monoatomic phononic crystal and piezoelectric phononic crystals	127
4.5	Summary and conclusions	133
5	Brillouin-zone characterization of piezoelectric-material intrinsic energy-harvesting availability	135
5.1	Introduction	135
5.2	Examples of piezoelectric phononic crystals modelled as <i>materials</i> with intrinsic properties	136
5.3	Brief overview of phononic crystal models	138
5.3.1	Monoatomic phononic crystal	138
5.3.2	Diatomic phononic crystal	142
5.4	Piezoelectric phononic crystals	145
5.4.1	Monoatomic piezoelectric phononic crystals	145
5.4.2	Diatomic piezoelectric phononic crystals	150
5.5	Wave-propagation and dissipation characteristics of piezoelectric phononic crystals: damped frequencies, raw dissipation, and energy-harvesting availability	157
5.5.1	Monoatomic configurations	157
5.5.2	Diatomic configurations	161
5.6	Parametric analysis of the energy-harvesting-availability metric	165
5.6.1	Monoatomic piezoelectric phononic crystals	165
5.6.2	Diatomic piezoelectric phononic crystals	171
5.7	Summary and Conclusions	175
6	Metadamping in inertially amplified materials: Trade-off between spatial attenuation and temporal attenuation	179
6.1	Introduction	179

6.2	Inertially amplified chains: physical configurations and mathematical models	182
6.2.1	Physical configurations	182
6.2.2	Mathematical models	182
6.3	Extreme levels of positive and negative metadamping	186
6.4	Regime displaying trade-off between temporal attenuation and spatial attenuation	193
6.5	Summary and conclusions	194
7	Metaharvesting: Emergent intrinsic energy harvesting by piezoelectric metamaterials	198
7.1	Introduction	198
7.2	Bloch's theorem for non-piezoelectric and piezoelectric periodic media . .	201
7.2.1	Overview of phononic crystal, locally resonant metamaterial, and inertially amplified locally resonant metamaterial	202
7.2.2	Phononic crystal, locally resonant metamaterial, and inertially amplified locally resonant metamaterial with shunted piezoelectric elements	205
7.3	Wave-propagation and dissipation characteristics of non-piezoelectric and piezoelectric periodic media: metadamping, energy-harvesting availability, and metaharvesting	208
7.3.1	Mathematical definitions of metadamping, energy-harvesting availability and metaharvesting	208
7.3.2	Metadamping: an emergence in dissipation in locally resonant and inertially amplified locally resonant metamaterials	212
7.3.3	Energy-harvesting availability: intrinsic representation of useful dissipative energy available for harvesting	213
7.3.4	Metaharvesting: Locally resonant and inertially amplified locally resonant emergent energy-harvesting availability	218
7.4	Summary and conclusions	219
8	Summary and conclusions	224
8.1	Thesis summary	224
8.2	Directions for future research	226
	Bibliography	227
	Appendix A Coefficients of non-dimensional equations	236
A.1	Monoatomic phononic crystal	236

A.2	Diatomic phononic crystal	236
A.3	Monoatomic piezoelectric phononic crystal without inductor	237
A.4	Monoatomic piezoelectric phononic crystal with inductor	237
A.5	Diatomic piezoelectric phononic crystal without inductor	237
A.6	Diatomic piezoelectric phononic crystal with inductor	239

List of figures

2.1	[14] Power density vs. voltage comparison between common developmental and lithium/lithium-ion power supply schemes.	11
2.2	Some examples of electromechanical structures. (a) Experimental set-up of a cantilevered piezoelectric energy harvester under base excitation and the corresponding schematic on the right [2]. (b) Schematics of piezoelectric vibration-energy harvesters, comprising of two different types of shunt circuits, under base excitation [87]. (c) Schematics of vortex-induced piezoelectric vibration-energy harvesters comprising of two different types of shunt circuits [88]. (d) Illustration of stack-type piezoelectric vibration-energy harvesters, comprising of two different types of shunt circuits, under base excitation [89]. (e) Schematic of a non-linear inverted-beam used for piezoelectric vibration-energy harvesting (PVEH); piezoelectric elements placed along the beam are not shown [22].	12
2.3	[77] Schematics of inertially amplified piezoelectric vibration-energy harvesters comprising of two different types of shunt circuits.	13
2.4	[2] Schematic illustrating the working principle of a piezoelectric vibration-energy harvesting (PVEH) system.	14
2.5	[80] (a) Example of a layered medium (continuous model). (b) Equivalent mass-spring system (discretized lumped-parameter model). (c) Dispersion diagram of the continuous model obtained through analytical and numerical treatments. (d) Dispersion diagram of the discrete model determined analytically. (e) Displacement profile in the finite layered medium at different frequencies depicting the comparison of response between the (top) pass band and (bottom) stop band (band gap) cases.	16
2.6	[38] Cross-section of a binary composite system: square array of infinite cylinders A periodically arranged in an infinite matrix B.	18

- 2.7 Demonstration of the discretization of (a) an infinite bilayered continuum model into (b) a lumped-parameter diatomic discrete model. 19
- 2.8 [108] An overview of mechanical metamaterials in existing literature. The five rows illustrate (a) auxetic, (b) light-weight, (c) negative-parameter, i.e., negative mass density and/or moduli at a finite frequency $\omega \neq 0$, (d) pentamode, and (e) origami mechanical metamaterials. The left column illustrates a combination of the Milton map, bulk modulus B vs. shear modulus G , and the Ashby map, a particular modulus vs. mass density ρ . At the point of crossing of the three arrows, which point towards the positive directions, all the parameters are zero. In each entry in the first-column, ordinary solids (shown in black) are compared with the corresponding metamaterials (shown in red). The center column depicts blueprints of (extended) unit cells featuring characteristic structural elements, and the right column shows electron micrographs of fabricated structures. The metamaterials shown can (a) be easily compressible, yet not easily deformable; (b) be ultra-lightweight, yet ultrastrong; (c) exhibit complete band gaps or support back-propagating waves; (d) be easily deformable, yet not easily compressible; (e) be deployable, bistable, and reprogrammable. The potential applications could be as (a) shock absorbers, (b) support structures, (c) reflectors or concentrators, (d) mechanical cloaks, and (e) structures for space missions. Figures reproduced with permission: (a) © 1987 AAAS, (b) © 2014 PNAS, (c) © 2000 AAAS, (d) © 2012 AIP, and (e) © 2014 AAAS. 21
- 2.9 [52] (a) Inertially amplified infinite periodic lattice and (b) the associated irreducible unit cell. The thin lines with stiffness k and big dots with mass m form a triangular truss structure; the thick lines with stiffness k_a and the small dots with mass m_a constitute the amplification mechanisms. The angle θ dictates the amplification generated by the mechanisms. The numbers 1-7 denote the nodes within the unit cell. (c) Hexagonal first Brillouin zone of the reciprocal lattice. The shaded area represents the irreducible Brillouin zone (IBZ); γ_1 and γ_2 are components of the wavevector, and $\Gamma \rightarrow K \rightarrow M \rightarrow \Gamma$ is the wavevector path around the IBZ. (d) Detailed view of the amplification mechanism. 22

- 2.10 [53] (a) Inertially amplified infinite periodic lattice and (b) the associated irreducible unit cell. The vertical and horizontal thin lines have stiffness k and the big dots have mass m . Each central mass m_c is attached to the neighbouring masses m through lines with stiffness k_c . Consequently, k , k_c , m , and m_c constitute the structural backbone of the lattice; the thick lines with stiffness k_a and the small dots with mass m_a constitute the amplification mechanisms. The angle θ dictates the amplification generated by the mechanisms. (c) First Brillouin zone of the reciprocal lattice depicting the shaded irreducible Brillouin zone (IBZ); γ_1 and γ_2 are wavevector components, and $\Gamma \rightarrow X \rightarrow M \rightarrow \Gamma$ is the wavevector path around the IBZ. 23
- 2.11 [55] (a) Inertially amplified chain comprised of a levered (inertial-amplifier) mass and a local-resonance mass and (b) the associated unit cell. The thick green lines represent rigid links; M denotes the baseline mass; m_a denotes the inertial-amplifier mass; m denotes the local-resonance mass; K is the baseline stiffness; k is the local-resonance stiffness; k_a is the stiffness of the spring connecting the two inertial-amplifier masses. 24
- 2.12 [66] A general illustration of piezoelectric vibration energy-harvesting (PVEH) system using phononic crystals (PnCs) and locally resonant metamaterials (LRMs). The process of harvesting elastic-wave energy using mechanical elements such as local resonators and defect cavities is shown as a schematic at the top, where the piezoelectric material and electrical circuit converts the elastic-wave energy from vibrations and sound to electrical energy. 26
- 2.13 (a) Infinite version (left) of a rod (continuum) with periodic shunted piezoelectric patches and the finite version on the right [57]. (b) A piezoelectric phononic crystal (PnC) cantilever beam (left) and the corresponding unit cell [64]. (c) Multifunctional design of an electromechanical structure capable of simultaneous wave filtering and energy harvesting [60]. (d) Schematic of a piezoelectric vibration energy-harvesting system (PVEH) involving a base structure composed of two alternating media [65]. (e) Example of a one-dimensional phononic piezoelectric cantilever beam [62]. 27
- 2.14 (a) Schematic of a piezo-embedded negative-mass material [113]. (b) Unit cell of an acoustic/elastic locally resonant metamaterial (LRM) [73]. (c) Schematic of a piezo-embedded negative-stiffness metamaterial [114]. . . . 28
- 2.15 [80] Ashby chart depicting the stiffness and damping for common materials and illustrating the evident trade-off between the two. 29

2.16	[79] Lumped-parameter unit-cell models of (a) an acoustic metamaterial (AM) and (b) a phononic crystal (PnC). (c) Metadamping in dipolar AM: overall total damping capacity versus long-wave sonic speed; $\lim_{\kappa \rightarrow 0} C_{\text{stat}} = d\omega/d\kappa$, where ω is damped frequency and κ is wavenumber.	30
2.17	[115] Lumped-parameter unit-cell models of (a) viscoelastically and (b) viscously damped phononic crystal (PnC) (left) and dipolar acoustic metamaterial (AM) (right). (c) Metadamping in dipolar AM for the viscoelastic and viscous cases. (d) Lumped-parameter unit-cell model of a monopolar AM. (e) Metadamping in the monopolar and dipolar metamaterials only for the viscous case.	31
2.18	[80] Lumped-parameter unit-cell models of (a) phononic crystal (PnC), (b) dipolar acoustic metamaterial (AM), and (c) monopolar AM. (d) Metadamping in the monopolar and dipolar metamaterials.	32
2.19	[116, 117] (a) A linear oscillator consisting of a negative stiffness element and (b) a novel hybrid metamaterial configuration that integrates the attributes of phononic crystals (PnCs) and acoustic metamaterials (AMs).	32
3.1	Schematic of (a) a monoatomic phononic-crystal (MPnC) chain without grounding and (b) the associated unit cell.	35
3.2	Schematic of (a) a monoatomic-phononic-crystal (MPnC) chain with grounding and (b) the associated unit cell.	38
3.3	Schematic of (a) a monoatomic piezoelectric phononic-crystal (MPPnC) chain without grounding and (b) the associated unit cell.	39
3.4	Schematic of (a) a monoatomic piezoelectric phononic-crystal (MPPnC) chain with grounding and (b) the associated unit cell.	42
3.5	(a) Normalized-damped-frequency band structure, (b) damping-ratio diagrams, and (c) cumulative-damping-ratio diagrams for the monoatomic phononic crystal (MPnC) and monoatomic piezoelectric phononic crystals (MPPnCs) without grounding.	48
3.6	(a) Normalized-damped-frequency band structure, (b) damping-ratio diagrams, and (c) cumulative-damping-ratio diagrams for the monoatomic phononic crystal (MPnC) and monoatomic piezoelectric phononic crystals (MPPnCs) with grounding.	51
3.7	Schematic of (a) a diatomic phononic-crystal (DPnC) chain without grounding and (b) the associated unit cell.	52
3.8	Schematic of (a) a diatomic phononic-crystal (DPnC) chain with grounding and (b) the associated unit cell.	55

3.9	Schematic of (a) a diatomic piezoelectric phononic-crystal (DPPnC) chain without grounding and (b) the associated unit cell.	57
3.10	Schematic of (a) a diatomic piezoelectric phononic-crystal (DPPnC) chain with grounding and (b) the associated unit cell.	61
3.11	(a) Frequency band structure, (b) damping-ratio diagrams, and (c) cumulative-damping-ratio diagrams for the diatomic phononic crystal (DPnC) and diatomic piezoelectric phononic crystals (DPPnCs) without grounding.	69
3.12	(a) Frequency band structure, (b) damping-ratio diagrams, and (c) cumulative-damping-ratio diagrams for the diatomic phononic crystal (DPnC) and diatomic piezoelectric phononic crystals (DPPnCs) with grounding.	72
3.13	Schematic of (a) a locally resonant metamaterial (LRM) chain without grounding and (b) the associated unit cell.	73
3.14	Schematic of (a) a locally resonant metamaterial (LRM) chain with grounding and (b) the associated unit cell.	75
3.15	Schematic of (a) a locally resonant piezoelectric metamaterial (LRPM) chain without grounding and (b) the associated unit cell.	77
3.16	Schematic of (a) a locally resonant piezoelectric metamaterial (LRPM) chain with grounding and (b) the associated unit cell.	81
3.17	(a) Frequency band structure, (b) damping-ratio diagrams, and (c) cumulative-damping-ratio diagrams for the locally resonant metamaterial (LRM) and locally resonant piezoelectric metamaterials (LRPMs) without grounding.	87
3.18	(a) Frequency band structure, (b) damping-ratio diagrams, and (c) cumulative-damping-ratio diagrams for the locally resonant metamaterial (LRM) and locally resonant piezoelectric metamaterials (LRPMs) with grounding.	90
3.19	Schematic of (a) an inertially amplified locally resonant metamaterial (IALRM) chain without grounding and (b) the associated unit cell.	92
3.20	Schematic of (a) an inertially amplified-locally resonant-metamaterial (IALRM) chain with grounding and (b) the associated unit cell.	94
3.21	Schematic of (a) an inertially amplified locally resonant piezoelectric metamaterial (IALRPM) chain without grounding and (b) the associated unit cell.	96
3.22	Schematic of (a) an inertially amplified locally resonant piezoelectric metamaterial (IALRPM) chain with grounding and (b) the associated unit cell.	101

3.23	(a) Frequency band structure, (b) damping-ratio diagrams, and (c) cumulative-damping-ratio diagrams for the inertially amplified locally resonant meta-material (IALRM) and inertially amplified locally resonant piezoelectric metamaterials (IALRPMs) without grounding.	107
3.24	(a) Frequency band structure, (b) damping-ratio diagrams, and (c) cumulative-damping-ratio diagrams for the inertially amplified locally resonant meta-material (IALRM) and inertially amplified locally resonant piezoelectric metamaterials (IALRPMs) with grounding.	110
4.1	Schematic of (a) a monoatomic phononic-crystal (MPnC) lattice and (b) the associated unit cell.	114
4.2	Schematic of (a) a monoatomic piezoelectric phononic-crystal (MPPnC) lattice and (b) the associated unit cell.	119
4.3	Dimensionless-wavevector space (μ -space) including the First Brillouin Zone (FBZ) shown as green-shaded area, Irreducible Brillouin Zone (IBZ) shown as red-shaded area, dimensionless-wavevector path around the IBZ highlighted by the red-contoured right-angle triangle, and dimensionless-wavevectors shown by red lines with black arrows, which point towards the vector direction, for two-dimensional dispersion characteristics.	129
4.4	(a) Normalized-damped-frequency band structure, (b) damping-ratio diagrams, and (c) cumulative-damping-ratio diagrams for the monoatomic phononic crystal (MPnC) and monoatomic piezoelectric phononic crystals (MPPnCs).	130
4.5	Contour plots: (a) Transverse mode of normalized damped frequency, (b) Longitudinal mode of normalized damped frequency, (c) Transverse mode of damping ratio, and (d) Longitudinal mode of damping ratio for the monoatomic phononic crystal (MPnC) and monoatomic piezoelectric phononic crystals (MPPnCs).	132
4.6	Surface plots: (a) Transverse mode of normalized damped frequency, (b) Longitudinal mode of normalized damped frequency, (c) Transverse mode of damping ratio, and (d) Longitudinal mode of damping ratio for the monoatomic phononic crystal (MPnC) and monoatomic piezoelectric phononic crystals (MPPnCs).	133

5.1	(a) Physical conceptualization/configuration of a periodic chain of a monoatomic piezoelectric phononic crystal (MPPnC) with piezoelectric patches and (b) the corresponding monoatomic unit cell. (c) Physical conceptualization/configuration of a periodic chain of a diatomic piezoelectric phononic crystal (DPPnC) with piezoelectric patches and (d) the corresponding diatomic unit cell. Both configurations represent an infinite medium exhibiting intrinsic properties.	137
5.2	Schematic of (a) a monoatomic phononic-crystal (MPnC) chain with grounding and (b) the associated unit cell.	138
5.3	Schematic of (a) a diatomic phononic-crystal (DPnC) chain with grounding and (b) the associated unit cell.	143
5.4	Schematic of (a) a monoatomic piezoelectric phononic-crystal (MPPnC) chain comprising of energy harvesters with shunt circuits that are purely resistive and (b) the associated unit cell.	146
5.5	Schematic of (a) a monoatomic piezoelectric phononic-crystal (MPPnC) chain comprising of energy harvesters with shunt circuits that are purely resistive and (b) the associated unit cell.	148
5.6	Schematic of (a) a diatomic piezoelectric phononic-crystal (DPPnC) chain comprising of energy harvesters with shunt circuits that are purely resistive and (b) the associated unit cell.	151
5.7	Schematic of (a) a diatomic piezoelectric phononic-crystal (DPPnC) chain comprising of energy harvesters with shunt circuits that are purely resistive and (b) the associated unit cell.	154
5.8	Monoatomic models: Normalized damped-frequency band structures for the (a) monoatomic phononic crystal (MPnC), (b) monoatomic piezoelectric phononic crystal (MPPnC) without an inductor, and (c) monoatomic piezoelectric phononic crystal (MPPnC) with an inductor as a function of wavenumber for the prescribed damping levels $\eta = 0 \text{ Nsm}^{-1}$, $\eta = 0.218 \text{ Nsm}^{-1}$, and $\eta = 0.436 \text{ Nsm}^{-1}$	158
5.9	Monoatomic models: damping-ratio diagrams for the monoatomic phononic crystal (MPnC), monoatomic piezoelectric phononic crystal (MPPnC) without an inductor, and monoatomic piezoelectric phononic crystal (MPPnC) with an inductor as a function of wavenumber for the prescribed damping levels (a) $\eta = 0 \text{ Nsm}^{-1}$, (b) $\eta = 0.218 \text{ Nsm}^{-1}$, and (c) $\eta = 0.436 \text{ Nsm}^{-1}$	159

- 5.10 Monoatomic models: energy-harvesting availability metric $Z(\mu)$ and its cumulative value $Z^{\text{cum}}(\mu)$ for the prescribed damping levels (a) $\eta = 0 \text{ Nsm}^{-1}$, (b) $\eta = 0.218 \text{ Nsm}^{-1}$, and (c) $\eta = 0.436 \text{ Nsm}^{-1}$ 161
- 5.11 Diatomic models: Normalized damped-frequency band structures for the (a) diatomic phononic crystal (DPnC), (b) diatomic piezoelectric phononic crystal (DPPnC) without an inductor, and (c) diatomic piezoelectric phononic crystal (DPPnC) with an inductor as a function of wavenumber for the prescribed damping levels $\eta = 0 \text{ Nsm}^{-1}$, $\eta = 0.218 \text{ Nsm}^{-1}$, and $\eta = 0.436 \text{ Nsm}^{-1}$ 162
- 5.12 Diatomic models: Damping ratios ζ_1 (acoustic branch) and ζ_2 (optical branch) and summation of the two branches ζ_{sum} of the diatomic phononic crystal (DPnC), diatomic piezoelectric phononic crystal (DPPnC) without an inductor, and diatomic piezoelectric phononic crystal (DPPnC) with an inductor as a function of wavenumber for the prescribed damping levels $\eta = 0 \text{ Nsm}^{-1}$ (first column), $\eta = 0.218 \text{ Nsm}^{-1}$ (second column), and $\eta = 0.436 \text{ Nsm}^{-1}$ (third column). 164
- 5.13 Diatomic models: energy-harvesting availability metrics $Z_1(\mu)$, $Z_2(\mu)$, and $Z_{\text{sum}}(\mu)$ and the corresponding cumulative values $Z_1^{\text{cum}}(\mu)$, $Z_2^{\text{cum}}(\mu)$, and $Z_{\text{sum}}^{\text{cum}}(\mu)$ associated with the damping ratios ζ_1 (acoustic branch) and ζ_2 (optical branch) and summation of the two branches ζ_{sum} , respectively. The results are presented for prescribed damping levels (a) $\eta = 0 \text{ Nsm}^{-1}$, (b) $\eta = 0.218 \text{ Nsm}^{-1}$, and (c) $\eta = 0.436 \text{ Nsm}^{-1}$ 166
- 5.14 Monoatomic models: Variation of the total energy-harvesting-availability metric Z^{tot} with the prescribed damping level η ($\eta = C_1 = C_2$) for the monoatomic piezoelectric phononic crystal (MPPnC) without an inductor and the monoatomic piezoelectric phononic crystal (MPPnC) with an inductor. 167
- 5.15 Monoatomic models: variation of the total energy-harvesting-availability metric Z^{tot} with the non-dimensional resistor constant α for the monoatomic piezoelectric phononic crystal (MPPnC) without an inductor and the monoatomic piezoelectric phononic crystal (MPPnC) with an inductor at prescribed damping levels (a) $\eta = 0 \text{ Nsm}^{-1}$, (b) $\eta = 0.218 \text{ Nsm}^{-1}$, and (c) $\eta = 0.436 \text{ Nsm}^{-1}$. 168
- 5.16 Monoatomic models: variation of the total energy-harvesting-availability metric Z^{tot} with the non-dimensional inductor constant β for the monoatomic piezoelectric phononic crystal (MPPnC) with an inductor at prescribed damping levels (a) $\eta = 0 \text{ Nsm}^{-1}$, (b) $\eta = 0.218 \text{ Nsm}^{-1}$, and (c) $\eta = 0.436 \text{ Nsm}^{-1}$. 169

- 5.17 Monoatomic models: variation of the total energy-harvesting-availability metric Z^{tot} with the electromechanical coupling θ for the monoatomic piezoelectric phononic crystal (MPPnC) without an inductor and the monoatomic piezoelectric phononic crystal (MPPnC) with an inductor at prescribed damping levels (a) $\eta = 0 \text{ Nsm}^{-1}$, (b) $\eta = 0.218 \text{ Nsm}^{-1}$, and (c) $\eta = 0.436 \text{ Nsm}^{-1}$. 170
- 5.18 Diatomic models: Variation of the total energy-harvesting-availability metric $Z_{\text{sum}}^{\text{tot}}$ with the prescribed damping level η ($\eta = C_1 = C_2 = C_3 = C_4$) for the diatomic piezoelectric phononic crystal (DPPnC) without an inductor and the diatomic piezoelectric phononic crystal (DPPnC) with an inductor. . . . 171
- 5.19 Diatomic models: variation of the total energy-harvesting-availability metric $Z_{\text{sum}}^{\text{tot}}$ with the non-dimensional resistor constants α_1 and α_2 for the diatomic piezoelectric phononic crystal (DPPnC) without an inductor and the diatomic piezoelectric phononic crystal (DPPnC) with an inductor at prescribed damping levels (a) $\eta = 0 \text{ Nsm}^{-1}$, (b) $\eta = 0.218 \text{ Nsm}^{-1}$, and (c) $\eta = 0.436 \text{ Nsm}^{-1}$. 172
- 5.20 Diatomic models: variation of the total energy-harvesting-availability metric $Z_{\text{sum}}^{\text{tot}}$ with the non-dimensional inductor constants β_1 and β_2 for the diatomic piezoelectric phononic crystal (DPPnC) with an inductor at prescribed damping levels (a) $\eta = 0 \text{ Nsm}^{-1}$, (b) $\eta = 0.218 \text{ Nsm}^{-1}$, and (c) $\eta = 0.436 \text{ Nsm}^{-1}$. 174
- 5.21 Diatomic models: variation of the total energy-harvesting-availability metric $Z_{\text{sum}}^{\text{tot}}$ with the electromechanical coupling values θ_1 and θ_2 for the diatomic piezoelectric phononic crystal (DPPnC) without an inductor and the diatomic piezoelectric phononic crystal (DPPnC) with an inductor at prescribed damping levels (a) $\eta = 0 \text{ Nsm}^{-1}$, (b) $\eta = 0.218 \text{ Nsm}^{-1}$, and (c) $\eta = 0.436 \text{ Nsm}^{-1}$. 175
- 6.1 Unit-cell schematics of (a) a diatomic phononic crystal (PnC), (b) a locally resonant metamaterial (LRM), (c) an inertially amplified material (IAM), and (d) an inertially amplified locally resonant metamaterial (IALRM). . . . 180

- 6.2 Analysis of the inertially amplified material (IAM) with no resonating mass. (a) Unit-cell schematics of statically equivalent chains, including a phononic crystal (PnC), locally resonant metamaterial (LRM), and three variations of the IAM exhibiting $\phi = 13^\circ$, 24° , and 43° , respectively. All the inertial-amplifier masses are restricted to motion in only the vertical direction. (b) Frequency band structure for the undamped and damped unit cells; results for the damped unit cells are shown only for real wave numbers. (c) Damping-ratio diagrams for the damped unit cells. (d) Damping-emergence metric Z : for the LRM, the sum of the two damping-ratio branches of the PnC has been used as the reference quantity (ζ_{sum}), and for the IAMs, the average of the two damping-ratio branches of the PnC ($\zeta_{\text{sum}}/2$) has been used as the reference quantity as distinguished by the asterisk applied to the subscript 1. (e) Damping-emergence metric Z for the IAMs, where the damping ratio corresponding to the acoustic branch of the PnC is used as the reference quantity. In sub-figures (b) and (c), the subscripts “1”, “2”, and “sum” indicate the acoustic branch, optical branch, and sum of the two branches, respectively. 188
- 6.3 Analysis of the inertially amplified locally resonant metamaterial (IALRM), i.e., with a resonating mass. (a) Unit-cell schematics of statically equivalent chains, including a phononic crystal (PnC), locally resonant metamaterial (LRM), and three variations of the IALRM exhibiting $\phi = 13^\circ$, 24° , and 43° , respectively. All the inertial-amplifier masses are restricted to motion in only the vertical direction. (b) Frequency band structure for the undamped and damped unit cells; results for the damped unit cells are only shown for real wave numbers. (c) Damping-ratio diagrams for the damped unit cells. (d) Damping-emergence metric Z . In sub-figures (a) and (b), the subscripts “1”, “2”, and “sum” indicate the acoustic branch, optical branch, and sum of the two branches, respectively. The orange curves in the third column are the results for the special case IALRM- 13° *, which is statically equivalent to the PnC and obtained by only increasing the local-resonator stiffness of IALRM- 13° from $k_{\text{IALRM}} = 40 \text{ Nm}^{-1}$ to $k_{\text{IALRM}^*} = 500 \text{ Nm}^{-1}$, presented for the purpose of illustrating negative metadamping at $\phi = 13^\circ$ 190

- 6.4 Illustration of metadamping: total damping ratio based on the first branch, ζ_1^{tot} , versus long-wave speed of sound C_g in the periodic chains. (a) Positive or negative metadamping (depending on value of ϕ) exhibited in the case of inertially amplified material (IAM) with no resonating mass; blue- and green-shaded areas represent regions of positive and negative metadamping, respectively. Maximum positive and negative metadamping are reached at IAM-90° and IAM-10°, respectively. The intensity of positive metadamping increases as the color of the blue shaded areas gets darker. 191
- 6.5 Illustration of metadamping: total damping ratio based on the sum of the two damping-ratio branches, $\zeta_{\text{sum}}^{\text{tot}}$, i.e., overall total damping capacity. (b) Positive metadamping exhibited in the case of inertially amplified locally resonant metamaterial (IALRM); blue-shaded area represents the region of positive metadamping. Maximum positive metadamping is reached at IA-90°. The intensity of positive metadamping increases as the color of the blue shaded areas gets darker. The orange curves are the results for the special cases IALRM-10°*, IALRM-13°*, and IALRM-90°*, which are also statically equivalent to the PnC and obtained by only increasing the local-resonator stiffness of the IALRMs from $k_{\text{IALRM}} = 40 \text{ Nm}^{-1}$ to $k_{\text{IALRM}^*} = 500 \text{ Nm}^{-1}$, presented for the purpose of illustrating negative metadamping, which reaches its maximum at $\phi = 10^\circ$ 192
- 6.6 Performance characteristics for the inertially amplified locally resonant metamaterial (IALRM). (a) Temporal-attenuation intensity: total damping ratio $\zeta_{\text{sum}}^{\text{tot}}$ versus inertial-amplifier angle ϕ . (b) Spatial-attenuation intensity: minimum attenuation μ_{min} versus ϕ ; inset depicts a schematic that illustrates the μ_{min} quantity. (c) Minimum attenuation μ_{min} versus total damping ratio $\zeta_{\text{sum}}^{\text{tot}}$; inset in sub-figure (c) shows an enlarged version of the trade-off region. The points A-E, corresponding to five different values of ϕ , have been specifically chosen and used to illustrate the evolution of the temporal- and spatial-attenuation properties with ϕ whereby a region is identified that features a trade-off between the temporal and spatial attenuation intensities. 193
- 6.7 (a) Frequency band structure (first column), illustrating the spatial attenuation, and (b) damping-ratio diagrams (second column), illustrating the temporal attenuation, corresponding to the five chosen values of ϕ ; insets in column (a) show the corresponding plots with the y-axis reproduced in a log scale. Results for the damped IALRMs are shown only for real dimensionless wavenumbers. 195

6.8	Non-dimensional parameter δ as a function of inertial-amplifier mass ratio (ratio of the inertial-amplifier mass to the baseline mass) ε and the inertial-amplifier angle ϕ	196
7.1	An overview of the unit-cell comparisons addressed in this work in a wave-propagation and dissipation framework and at a material level. The unit cells addressed in this work are phononic crystal (PnC), locally resonant metamaterial (LRM), inertially amplified locally resonant metamaterial (IALRM), piezoelectric phononic crystal (PPnC), locally resonant piezoelectric metamaterial (LRPM), and inertially amplified locally resonant piezoelectric metamaterial (IALRPM), which are statically equivalent to each other.	200
7.2	Unit-cell schematics of statically equivalent (a) phononic crystal (PnC), (b) locally resonant metamaterial (LRM), (c) inertially amplified locally resonant metamaterial (IALRM), (d) piezoelectric phononic crystal (PPnC), (e) locally resonant piezoelectric metamaterial (LRPM), and (f) inertially amplified locally resonant piezoelectric metamaterial (IALRPM).	201
7.3	(a) Unit-cell schematics, (b) normalized damped-frequency band structures, and (c) damping-ratio diagrams for the statically equivalent phononic crystal (PnC), locally resonant metamaterial (LRM), and inertially amplified locally resonant metamaterial (IALRM), and (d) damping-emergence quantities for the LRM and IALRM relative to the PnC corresponding to the summation of the two damping-ratio branches ζ_{sum}	213
7.4	Damping-emergence quantities, shown as shaded regions, for the locally resonant metamaterial (LRM) and inertially amplified locally resonant metamaterial (IALRM) relative to the phononic crystal (PnC) corresponding to the (a) acoustic damping-ratio branch ζ_1 , (b) optical damping-ratio branch ζ_2 , and (c) summation of the two branches ζ_{sum}	214
7.5	(a) Unit-cell schematics, (b) normalized damped-frequency band structures, and (c) damping-ratio diagrams for the phononic crystal (PnC) and piezoelectric phononic crystal (PPnC), and (d) energy-harvesting availability in the PPnC relative to the PnC corresponding to the summation of the two damping-ratio branches ζ_{sum}	215
7.6	(a) Unit-cell schematics, (b) normalized damped-frequency band structures, and (c) damping-ratio diagrams for the locally resonant metamaterial (LRM) and locally resonant piezoelectric metamaterial (LRPM), and (d) energy-harvesting availability in the LRPM relative to the LRM corresponding to the summation of the two damping-ratio branches ζ_{sum}	216

- 7.7 (a) Unit-cell schematics, (b) normalized damped-frequency band structures, and (c) damping-ratio diagrams for the inertially amplified locally resonant metamaterial (IALRM) and inertially amplified locally resonant piezoelectric metamaterial (IALRPM), and (d) energy-harvesting availability in the IALRPM relative to the IALRM corresponding to the summation of the two damping-ratio branches ζ_{sum} 217
- 7.8 Energy-harvesting availability, shown as shaded regions, in the piezoelectric phononic crystal (PPnC), locally resonant piezoelectric metamaterial (LRPM), and inertially amplified locally resonant piezoelectric metamaterial (IALRPM) relative to the phononic crystal (PnC), locally resonant metamaterial (LRM), and inertially amplified locally resonant metamaterial (IALRM), respectively, corresponding to the (a) acoustic damping-ratio branch ζ_1 , (b) optical damping-ratio branch ζ_2 , and (c) summation of the two branches ζ_{sum} . 218
- 7.9 (a) Unit-cell schematics, (b) normalized damped-frequency band structures, and (c) damping-ratio diagrams for the statically equivalent piezoelectric phononic crystal (PPnC), locally resonant piezoelectric metamaterial (LRPM), and inertially amplified locally resonant piezoelectric metamaterial (IALRPM), and (d) emergent energy-harvesting availability (EHA)—metaharvesting—in the LRPM and IALRPM relative to the PPnC corresponding to the summation of the two damping-ratio branches ζ_{sum} 220
- 7.10 Emergent energy-harvesting availability or the phenomenon of metaharvesting, shown as shaded regions, in the locally resonant piezoelectric metamaterial (LRPM) and inertially amplified locally resonant piezoelectric metamaterial (IALRPM) relative to the PPnC corresponding to the (a) acoustic damping-ratio branch ζ_1 , (b) optical damping-ratio branch ζ_2 , and (c) summation of the two branches ζ_{sum} 221
- 7.11 Damping-ratio diagrams for the phononic crystal (PnC), piezoelectric phononic crystal (PPnC), locally resonant metamaterial (LRM), locally resonant piezoelectric metamaterial (LRPM), inertially amplified locally resonant metamaterial (IALRM), and inertially amplified locally resonant piezoelectric metamaterial (IALRPM); the figure above depicts the phenomenon of metadamping, the concept of energy-harvesting availability, and the newly introduced phenomenon of metaharvesting as per figures 7.1 and 7.2. Each damping-ratio diagram depicts the acoustic branch (ζ_1), optical branch (ζ_2), and the summation of the two aforementioned branches (ζ_{sum}). 222

- 7.12 Relation between non-dimensional damped frequencies and their corresponding damping ratios for the phononic crystal (PnC), piezoelectric phononic crystal (PPnC), locally resonant metamaterial (LRM), locally resonant piezoelectric metamaterial (LRPM), inertially amplified locally resonant metamaterial (IALRM), and inertially amplified locally resonant piezoelectric metamaterial (IALRPM). The dash-dot lines show the relation for the acoustic branch, and the dotted lines show the relation for the optical branch. . . . [223](#)

List of tables

3.1	Mechanical and dimensionless electrical parameters employed in the monoatomic phononic crystal (MPnC) and monoatomic piezoelectric phononic crystals (MPPnCs) without grounding.	46
3.2	Total values of damping ratios of the monoatomic PnC (MPnC) and monoatomic piezoelectric PnCs (MPPnCs) without grounding.	49
3.3	Mechanical and dimensionless electrical parameters employed in the monoatomic phononic crystal (MPnC) and monoatomic piezoelectric phononic crystals (MPPnCs) with grounding.	50
3.4	Total values of damping ratios of the monoatomic phononic crystal (MPnC) and monoatomic piezoelectric phononic crystals (MPPnCs) with grounding.	50
3.5	Mechanical and dimensionless electrical parameters employed in the diatomic phononic crystal (DPnC) and diatomic piezoelectric phononic crystals (DPPnCs) without grounding.	68
3.6	Total values of damping ratios of the diatomic phononic crystal (DPnC) and diatomic piezoelectric phononic crystals (DPPnCs) without grounding.	70
3.7	Mechanical and dimensionless electrical parameters employed in the diatomic phononic crystal (DPnC) and diatomic piezoelectric phononic crystals (DPPnCs) with grounding.	71
3.8	Total values of damping ratios of the diatomic phononic crystal (DPnC) and diatomic piezoelectric phononic crystals (DPPnCs) with grounding.	71
3.9	Mechanical and dimensionless electrical parameters employed in the locally resonant metamaterial (LRM) and locally resonant piezoelectric metamaterials (LRPMs) without grounding.	86
3.10	Total values of damping ratios of the locally resonant metamaterial (LRM) and locally resonant piezoelectric metamaterials (LRPMs) without grounding.	88

3.11	Mechanical and dimensionless electrical parameters employed in the locally resonant metamaterial (LRM) and locally resonant piezoelectric metamaterials (LRPMs) with grounding.	89
3.12	Total values of damping ratios of the locally resonant metamaterial (LRM) and locally resonant piezoelectric metamaterials (LRPMs) with grounding.	89
3.13	Mechanical and dimensionless electrical parameters employed in the inertially amplified locally resonant metamaterial (IALRM) and inertially amplified locally resonant piezoelectric metamaterials (IALRPMs) without grounding.	106
3.14	Total values of damping ratios of the inertially amplified locally resonant metamaterial (IALRM) and inertially amplified locally resonant piezoelectric metamaterials (IALRPMs) without grounding.	108
3.15	Mechanical and dimensionless electrical parameters employed in the inertially amplified locally resonant metamaterial (IALRM) and inertially amplified locally resonant piezoelectric metamaterials (IALRPMs) with grounding.	109
3.16	Total values of damping ratios of the inertially amplified locally resonant metamaterial (IALRM) and inertially amplified locally resonant piezoelectric metamaterials (IALRPMs) with grounding.	109
4.1	Position of, values of g_1 and g_2 for, and location of all the unit cells, shown in figure 4.1(a), in reference to the $(p, q)^{\text{th}}$ unit cell at the centre.	116
4.2	Mechanical and dimensionless electrical parameters employed in the monoatomic phononic crystal (MPnC) and monoatomic piezoelectric phononic crystals (MPPnCs).	128
4.3	Total values of damping ratios associated with the monoatomic phononic crystal (MPnC) and monoatomic piezoelectric phononic crystals (MPPnCs) with grounding.	131
5.1	Parameters employed in the monoatomic phononic crystal (MPnC) and monoatomic piezoelectric phononic crystals (MPPnCs).	157
5.2	Parameters employed in the diatomic phononic crystal (DPnC) and diatomic piezoelectric phononic crystals (DPPnCs).	162
5.3	Monoatomic models: optimal values of the non-dimensional resistor constant α for the monoatomic piezoelectric phononic crystal (MPPnC) without an inductor and the monoatomic piezoelectric phononic crystal (MPPnC) with an inductor at the three prescribed damping levels η	168

5.4	Monoatomic models: optimal values of the non-dimensional inductor constant β for the monoatomic piezoelectric phononic crystal (MPPnC) with an inductor at the three prescribed damping levels η	169
5.5	Monoatomic models: optimal values of the electromechanical coupling θ for the monoatomic piezoelectric phononic crystal (MPPnC) without an inductor and the monoatomic piezoelectric phononic crystal (MPPnC) with an inductor at the three prescribed damping levels η	170
5.6	Diatomic models: optimal values of the non-dimensional resistor constants α_1 and α_2 for the diatomic piezoelectric phononic crystal (DPPnC) without an inductor and the diatomic piezoelectric phononic crystal (DPPnC) with an inductor at the three prescribed damping levels η	173
5.7	Diatomic models: optimal values of the non-dimensional inductor constants β_1 and β_2 for the diatomic piezoelectric phononic crystal (DPPnC) with an inductor at the three prescribed damping levels η	173
5.8	Diatomic models: optimal values of the electromechanical coupling values θ_1 and θ_2 for the diatomic piezoelectric phononic crystal (DPPnC) without an inductor and the diatomic piezoelectric phononic crystal (DPPnC) with an inductor at the three prescribed damping levels η	175
6.1	Parameters employed for the unit-cell models examined in figures 6.2, 6.3, and 6.6.	187
7.1	Mechanical and non-dimensional electrical parameters employed in the piezoelectric unit cells, namely, piezoelectric phononic crystal (PPnC), locally resonant piezoelectric metamaterial (LRPM), and inertially amplified piezoelectric metamaterial (IAPM), considered in the present chapter; the mechanical parameters are the same for the non-piezoelectric and piezoelectric unit cells.	209

Chapter 1

Introduction

1.1 Brief summary of pertinent topics

Energy harvesting [1, 2] is the process of aggregating low-level ambient energy and converting it into useful electrical energy and has been a topic of intensive fruitful research for the past few decades. The notion of capturing or harvesting different types of energies, such as kinetic (waves and wind), thermal (solar), and electromagnetic, in nature or from man-made constructs has led to a variety of modern innovative techniques of power generation, and this venture continues to grow vibrantly among various research communities. The advent of low-power energy-harvesting systems that can be utilized to power devices that are usually battery operated has brought about new opportunities for the design of energy-efficient products. Among the diverse range of energy-harvesting techniques that currently exist, vibration-based energy harvesting has received substantial attention from researchers across a variety of disciplines [3]. Many artificial structures are susceptible to low-frequency structural vibrations; this naturally led to the promising avenue of harnessing the vibration (kinetic) energy, arising due to ambient, base-excited, or forced mechanical vibrations, that would, otherwise, simply dissipate as loss. Energy can be harvested from mechanical-vibration sources by employing piezoelectric material [2, 4, 5], shape memory alloys [6], ionic polymer metal composites [7, 8], magnetostrictive materials [9], and bistable systems [10]. Piezoelectric vibration-energy harvesting (PVEH) in particular has demonstrated practical promise for the generation of low-power electricity for a variety of applications including micro electrical devices [11], wireless sensors [12], transducers [13], micro-electromechanical-system (MEMS) portable devices [14], structural health monitoring devices [15–17], biomedical implants [18] among others. Sodano *et al.* [19] and Anton *et al.* [4] presented in-depth research reviews on vibration-energy harvesting using piezoelectric-material-based structures.

A considerable amount of theoretical and experimental research has been carried out on harvesting energy from the mechanical vibrations of cantilever beams with a tip mass and a piezoelectric substrate/patch bonded to its surface [2, 20, 21]. Energy harvesting in beams with a tip mass have also been examined in the non-linear vibrations regime [22]. In the last two decades, a significant amount of research has also been undertaken in the area of active vibration suppression using piezoelectric systems [23–27]. In the last decade, the area of active vibration suppression has been merged with that of PVEH, which has resulted in many insightful results with many possible practical applications [28]. The energy-harvesting electromechanical structures proposed and analysed in the existing literature have been analysed at the extrinsic level, i.e., with considerations pertaining to sizing, forcing, and boundary conditions (operational requirements).

Concurrent to energy-harvesting research, the study of elastic/plane-wave propagation in infinite periodic media, such as artificially structured periodic materials (waveguide) [29–31], has been an explosive area of research over the past three decades. In this domain, two key classes of engineered materials emerged: phononic crystals (PnCs) [32–38] and acoustic/elastic locally resonant metamaterials (LRMs) [39–42]. When the wavelength in a periodic array is of the order of the lattice spacing, PnCs undergo Bragg scattering, which results in a band structure¹, exhibiting band gaps (stop bands), shaped by scattering of waves due to periodic inclusions and/or interferences between transmitted and reflected waves at interfaces and/or boundaries within the medium. In acoustic/elastic LRMs, in addition to wave interferences, the band structure is also influenced by couplings, arising due to hybridizations, between resonance modes of the substructure, e.g., a local resonator, and elastic-wave modes in the hosting medium when the wavelength is much larger than the lattice constant [43]. The band-gap phenomenon, dissipation characterized by damping ratio, and other wave-propagation characteristics, such as group and phase velocities, in reciprocal lattice space [44, 45] have been among the key features of interest in both these classes of materials. Among the important characteristics are the spatial-attenuation (measure of decay in space) and temporal-attenuation (measure of decay in time) properties in particular. Regardless of the level of dissipation for both free and driven waves, spatial attenuation exists in phononic materials and is exhibited in and quantified by the imaginary part of the wavenumber² domain [46, 47]. More on free and driven waves can be found in section 2.3 of chapter 2. For free waves in a damped model, the temporal attenuation or level of

¹A band structure is a graphical representation of frequency regions within which waves are allowed to propagate (pass bands or transmission bands) and frequency regions within which waves are not allowed to propagate (stop bands or attenuation bands).

²A wave exhibits a temporal angular frequency (rad s^{-1}) and a spatial angular frequency (rad m^{-1}). The spatial angular frequency is referred to as the wavenumber. Wavenumbers are generally complex, i.e., $\kappa = \kappa_{\text{real}} + i\kappa_{\text{imag}}$ [46–48].

dissipation is quantified by the wavenumber-dependent damping ratio corresponding to each frequency dispersion branch [47]. While comparably wide Bragg band gaps may be realized by rigorous unit-cell-topology design and optimization [49, 50], the unit cell is essentially constrained to be of the order of the interference-waves wavelength, which indicates relatively high-frequency band gaps for a small unit cell. While locally resonant metamaterials boast an efficient realization of sub-wavelength low-frequency band gaps with small unit cells due to the independency of the local-resonance couplings from the wave interferences across the periodic host medium, they tend to be excessively narrow and require a relatively heavy resonator to exhibit significantly lower frequency band gaps [51]. In pursuit of addressing the aforementioned limitations, the mechanism/concept of inertial amplification has been introduced as an alternative for band-gap generation in periodic structured media [52–54]. An inertially amplified locally resonant metamaterial (IALRM) exhibits a subtle contrast to an LRM—in addition to a local resonator, it involves a mechanical mechanism which magnifies the “effective inertia” of the unit cell [55, 56]. The mechanism, generally, involves an auxiliary mass connected to the main masses within two adjacent unit cells via rigid links.

The merging of the research areas of PVEH and periodic media, PnCs and LRMs in general, has gained a lot of attention in the last decade. The amalgamation of piezoelectricity into PnCs for active tuning or energy harvesting has been the subject of various studies [57–65]. Furthermore, piezoelectric energy harvesting in elastic LRMs has received widespread attention in the energy harvesting community as evidenced in the reviews by Lee *et al.* [66], Hu *et al.* [67], and Chen *et al.* [68]. Piezoelectricity can be used for energy harvesting [69] and/or active tuning of the local-resonance characteristics for vibration attenuation [70] or waveguiding [71]. The latter two applications are also referred to as band-gap tuning or wave filtering. In a mass-in-mass elastic-metamaterial, i.e., an LRM, model statically equivalent to a PnC model, in a local-resonance state, the effective mass can become negative near the resonant frequency and the dynamic response results in an out-of-phase oscillation as opposed to the in-phase input force. Owing to the out-of-phase oscillations, the resultant force approaches zero at the resonant frequency; i.e., the net displacement is considerably suppressed, and the accumulated wave energy remains localized within the resonators. By installing an appropriate piezoelectric mechanism at the site of wave-energy localization, the harvesting efficiency achieved is higher than that of a conventional piezoelectric substrate [72]. Owing to the high Q-factor³ associated with the local-resonance mechanism and the relatively narrow range of the resonating frequency, elastic metamaterials with an augmented mass are well suited for efficient PVEH. For the aforementioned reasons, LRMs can portray

³Q-factor is defined as the ratio of the initial energy stored in the resonator to the energy lost in one oscillatory cycle.

simultaneous dual functionalities of vibration attenuation and energy harvesting and have been demonstrated to do so [73–76]. As the enhanced PVEH performance of an LRM stems from the local-resonance mechanism, amplifying the inertia of the local resonator could result in even further enhancement. Adhikari *et al.* [77] showed that a configuration comprising of a cantilever beam with bimorph piezoelectric layers and an inertially amplified tip mass resulted in enhanced low-frequency PVEH. Similar to aperiodic energy-harvesting structures, the energy-harvesting periodic electromechanical structures proposed and analysed in the existing literature have been analysed at the structural or extrinsic level, i.e., with considerations pertaining to sizing, forcing, and boundary conditions (operational requirements).

The study of dissipation in phononic materials is crucial because the intrinsic dissipation/damping performance of a material in dissipating kinetic/vibrational energy induced by elastic waves determines the energy-harvesting performance of an electromechanical structure made out of the same material. Different types of phononic materials exhibit different amounts of intrinsic dissipation, i.e., dissipation due to the internal design or microstructure. This amount of intrinsic dissipation is termed as “loss” and, naturally, will always be lost during the energy-harvesting process within a piezoelectric electromechanical structure designed using a particular phononic material, i.e., it will not be harvested. However, the higher the amount of intrinsic dissipation within the phononic material, the better will be the energy-harvesting performance because a higher amount of intrinsic dissipation indicates that the phononic material is also intrinsically geared towards dissipating or absorbing and potentially harvesting a large amount of vibrational energy, surpassing the amount that is represented by the intrinsic dissipation.

The phenomenon of dissipation is of significant importance in the area of structural dynamics and, hence, has been continually subjected to in-depth theoretical research, which has resulted in interesting and valuable findings, which have been exploited in many areas of engineering. In a finite structure, dissipation depends on the structural dimensions and forcing frequency. In an infinite periodic medium, such as an artificially structured periodic material (waveguide), dissipation also shows a wavenumber (or wavevector) dependency. Damping exhibited by materials is an intrinsic property which may play a critical role in determining the structural response when present in a structural configuration. The relation between damping capacity (dissipation) and stiffness of materials has been the focus of rigorous research over the past few decades. Materials such as crystalline diamond and ceramics that exhibit high stiffness, i.e., load-bearing capacity, are generally at a disadvantage when it comes to damping capacity which is quite low. Contrarily, materials that are highly dissipative, such as rubber- and foam-based materials, generally tend to possess low load-bearing capacities. When it comes to applications such as vibration attenuation, shock absorption, and acoustic

absorption, an increase in the damping intensity in the materials used, generally, ensues at the expense of stiffness or mechanical load-bearing capacity, i.e., the trade-off is quite prominent. Precisely engineering a material that possesses the capability of exhibiting damping and stiffness properties in just the right proportion for a specific operational requirement has been an active area of research within the domain of dynamics of materials, where one of the vital objectives is to overcome the trade-off between stiffness and damping.

Materials such as fibre-reinforced composites and metal alloys can be tuned to exhibit stiffness and damping capacities in nearly the right proportion but not quite accurately. A class of materials referred to as hierarchical composite materials [78] has been shown to overcome the trade-off in principle. Lattice or periodic materials, an emerging class of materials as discussed above, such as one- or two-dimensional PnCs, LRMs, or IALRMs offer promising results with regards to simultaneously maximizing damping and stiffness capacities. In an elastic waveguide, the representation of dissipation as an *intrinsic wavenumber-dependent quantity—damping ratio—provides a fundamental measure that is independent of global dimensions, boundary conditions, and nature of forcing*. A structure might be comprised of many constituent substructures, each with its own dimensions along the x-, y-, and z-directions. The term “global dimension” indicates the overall dimensions of the structure along the aforementioned three directions. Contrarily, a material has no associated dimensions. In the last decade, acoustic metamaterials with local-resonance properties [39] were proposed as a candidate for usage in materials designed to exhibit high levels of dissipation while maintaining high stiffness. This led to the introduction of the phenomenon of metadamping [79, 80] in which a locally resonant metamaterial exhibits high levels of dissipation throughout the Brillouin-Zone (BZ) spectrum as a result of an emergence of damping due to the presence of the local resonance. The phenomenon of metadamping has also been investigated in inerter-based metamaterials. Aladwani *et al.* [81], presented a detailed study on how the dispersion profiles, damping performance, and versatility of metamaterials can be shaped and augmented by reconfiguring different variations of hierarchical inertant mechanical networks. The research accentuates the vital roles played by different types of inertant mechanical networks and the damping placement within them in influencing the response, band-gap characteristics, and emergent dissipation. The choice of the inertant network and appropriate internal damping deployment can be adjusted to realize an efficient damped response suitable for specific applications in structural dynamics. The article presents a comprehensive comparative analysis of dissipation shown by various types of inertant mechanisms. However, it does not illustrate the enhanced emergence of dissipation, i.e., metadamping, due to the inertant mechanisms relative to a statically equivalent PnC

or an LRM for a wide range of long-wave sonic speeds, i.e., group velocities (measure of quasi-static stiffnesses) by mere passive tuning.

1.2 Problem statement and thesis objectives

While the research works mentioned above have examined the electromechanical dispersion characteristics, the focus has purely been on the energy-harvesting capacity of the aperiodic or periodic electromechanical structure; i.e., the analysis has been performed to quantify the amount of energy harvested in the form of electrical power and maximize it at the extrinsic or structural level, where the focus is on the structural-dynamics performance and the electromechanical structure is constrained by factors such as global dimensions, nature of forcing, and boundary conditions. Moreover, every energy-harvesting electromechanical periodic structure loses a certain amount of vibrational/kinetic energy, referred to as “loss,” due to raw damping and possibly due to environmental factors, and this loss goes unaccounted for during the performance analysis. With regards to the trade-off between dissipation and load-bearing (stiffness) capacities, up until now, the phenomenon of metadamping has only been illustrated in LRMs relative to a statically equivalent PnC for a wide range of long-wave sonic speeds. This thesis addresses the aforementioned issues and, in the process, lays out and accomplishes the following objectives:

1. A new formal approach, applicable to shunted piezoelectric periodic media, is presented for the characterization of the amount of useful dissipative energy available for harvesting—*energy-harvesting availability*—that is fundamentally at the intrinsic or material level in contrast to the extrinsic or structural/device level. The underlying rationale behind energy-harvesting availability is to take the “loss,” inevitable due to raw damping and environmental factors, into account and, consequently, give a formal wavenumber-dependent representation of the net dissipative energy intrinsically available for harvesting. The proposed concept of energy-harvesting availability aims to appreciate the quality and performance of a piezoelectric periodic media at an intrinsic unit-cell level and does not take anything away from or disagree in any way with energy-harvesting analysis for a finite piezoelectric periodic media. (chapter 5) [82].
2. It is revealed that even further dissipation (positive metadamping) or, alternatively, further reduction of loss (negative metadamping) may be attained in an inertially amplified material (IAM) and an inertially amplified locally resonant metamaterial

- (IALRM) compared to the improvements attained by a statically equivalent elastic LRM (chapter 6) [48].
3. By combining inertial amplification with local resonance, i.e., in the IALRM, and, consequently, coupling the inertially amplified attenuation peak with that of a local-resonance attenuation peak, the unique phenomenon of a trade-off between the temporal- and spatial-attenuation intensities associated with the material properties is observed for a given range of the inertial-amplifier angle, i.e., angle between the rigid links and the central axis of the metamaterial (chapter 6).
 4. It is demonstrated that the intrinsic energy-harvesting availability is enhanced by a local-resonance mechanism and even further enhanced by adding an inertial-amplification mechanism; this enhancement is, essentially, an emergence of intrinsic energy-harvesting availability and, hence, is termed as *metaharvesting* (chapter 7).

The concept/quantification of intrinsic (independent of forcing, structure size, and boundary conditions) energy-harvesting availability is demonstrated in suspended piezoelectric phononic crystals (PPnC) under free vibration and comprising of shunted circuits without and with an inductor by comparing its dissipation characteristics, obtained after Bloch analysis, to that of its non-piezoelectric counterpart with the same amount of prescribed (raw) damping. By considering the PPnC as a discretized (lumped-parameter model) material and solely investigating the effects of the piezoelectric parameters, it is demonstrated that it exhibits higher wavenumber-dependent damping-ratio in comparison to the statically equivalent PnC, where the difference in damping-ratio is a representation of the useful dissipative energy intrinsically available for harvesting. Positive and negative metadamping in the IAM and the IALRM is demonstrated by using a statically equivalent PnC and a statically equivalent LRM as references. The phenomenon of metaharvesting in a locally resonant piezoelectric metamaterial (LRPM) and enhanced metaharvesting in an inertially amplified locally resonant piezoelectric metamaterial (IALRPM) is demonstrated by employing a statically equivalent PPnC with the same piezoelectric material parameters and the same amount of prescribed damping as the reference.

1.3 Thesis outline

The outline of this thesis is as follows. In addition to introducing the topics relevant to this thesis by presenting a summarized literature review in section 1.1 of the current introductory chapter, chapter 2 further expounds on the pertinent topics in a brief literature review. Chapter 3 presents an overview of the dispersion and dissipation characteristics, in a

Bloch wave-propagation framework, of diverse types of one-dimensional non-piezoelectric and piezoelectric periodic media, namely, PnC, PPnC, LRM, LRPM, IALRM, and IALRPM, to illustrate the applicability of the analytical work presented in chapter 5 to the aforementioned piezoelectric periodic media. The dispersive and dissipative behaviours of the non-piezoelectric and piezoelectric periodic materials are presented in a comparative format. Chapter 4 presents the dispersion and dissipation characteristics, in a Bloch wave-propagation framework, of a two-dimensional PnC and PPnC to demonstrate that the analytical work presented in chapter 5 is also applicable to two-dimensional cases. For simplicity, only a monoatomic PnC and the corresponding piezoelectric version are considered. Chapter 5 illustrates the new intrinsic concept of energy-harvesting availability in suspended PPnCs and presents optimal values for the piezoelectric-element properties in terms of the proposed intrinsic quantity. Chapter 6 illustrates the phenomena of positive and negative metadamping in an IAM and an IALRM and the unique phenomenon of a trade-off between the temporal- and spatial-attenuation intensities associated with the material properties. Chapter 7 presents an overview of metadamping in an LRM and an IALRM and demonstrates energy-harvesting availability in an LRPM and an IALRPM and, consequently, an emergence of energy-harvesting availability, i.e., metaharvesting, in the LRPM and the IALRPM by comparing the quantity to that of the statically equivalent PPnC. Finally, chapter 8 summarizes the previous chapters and gives a few potential future works.

1.4 Thesis outcomes: journal articles, conference presentations, and posters

The research outcomes of this thesis are contained within the following literary works, namely peer-reviewed journal publications, conference presentations, and research posters:

1.4.1 Journal publications

- Hussein MI, **Patrick I**, Banerjee A, and Adhikari S. Metadamping in inertially amplified metamaterials: Trade-off between spatial attenuation and temporal attenuation. *Journal of Sound and Vibration*, page 116977, 2022, doi.org/10.1016/j.jsv.2022.116977. (contents of chapter 6) [48].
- **Patrick I**, Adhikari S, and Hussein MI. Brillouin-zone characterization of piezoelectric material intrinsic energy-harvesting availability. *Smart Materials and Structures*, 30(8):085022, 2021, doi.org/10.1088/1361-665X/ac0c2c. (contents of chapter 5) [82].

The most recent article is published as a “Rapid Communication” in the Journal of Sound and Vibration (JSV). Rapid Communications in the JSV are short papers focusing on fundamentally new and innovative ideas, new experimental observations, or definition of new arduous problems. The contents of chapter 7 will potentially form the journal article titled “Metaharvesting: Emergent energy harvesting by piezoelectric metamaterials,” which is being prepared for submission.

1.4.2 Conference presentations

- **Patrick I** and Adhikari S. Wave Propagation in mechanical metamaterial configurations with piezoelectric vibration-energy harvesters. Proceedings of the 10th International Conference on Metamaterials, Photonic Crystals, and Plasmonics (META 2019), July 23-26, 2019, Lisbon, Portugal, ISSN: 2429-1390.

1.4.3 Research posters

- **Patrick I** and Adhikari S. Wave propagation in energy-harvesting mechanical metamaterials. Zienkiewicz Centre for Computational Engineering (ZCCE) postgraduate workshop 2019, College of Engineering, Bay Campus, Swansea University, Swansea, 2019.
- **Patrick I** and Adhikari S. Wave propagation in energy-harvesting mechanical metamaterials. Zienkiewicz Centre for Computational Engineering (ZCCE) postgraduate workshop 2018, College of Engineering, Bay Campus, Swansea University, Swansea, 2018.

Chapter 2

Literature Review

2.1 Introduction

Considering the objectives of the thesis and that it is an amalgamation of the domains of elastic periodic materials (material dynamics or elastodynamics) and energy harvesting, investigating dispersion and dissipation characteristics, it would be effective to present a brief literature survey in the following four categories:

- Energy harvesting in electromechanical structures,
- Material dynamics of elastic periodic media,
- Energy harvesting in elastic periodic media,
- Metadamping: Emergence of dissipation/damping in elastic metamaterials.

The aforementioned topics are briefly surveyed in the existing literature and presented as reviews in the following sections.

2.2 Energy harvesting in electromechanical structures

The idea of scavenging useful energy effectively has been researched extensively, and this is manifested in many physical realizations, i.e., energy-harvesting systems, and numerous publications demonstrating new concepts and optimization studies. The term “useful” in the phrase “useful energy” is key as there is always some loss that dissipates into the environment. Endeavours have been made to capture or harvest different types of energies, e.g., kinetic (vibrational (wind/waves)), thermal, and electromagnetic, from ambient or artificial sources

using various types of contraptions; this has led to a variety of innovative and efficient methods of low-power generation, and this trend continues to grow actively in the energy-harvesting communities [3]. Low-power battery-operated devices can be potentially powered by low-power energy-harvesting systems. Generally, with regards to practical applications, low-power energy-harvesting systems are manifested in micro electromechanical system (MEMS) devices. Of the many energy-harvesting strategies, harvesting the kinetic energy from ambient or forced vibrations has been comprehensively studied under the combined areas of structural dynamics and energy harvesting. As mentioned by Williams and Yates in their work [83] on vibrational energy harvesting for microsystems, the three fundamental vibration-to-electric energy conversion techniques are piezoelectric [84], electrostatic [85], and electromagnetic [86] transductions. A significant amount of research has been conducted on the implementation of the aforementioned conversion mechanisms for low power yield using ambient vibrations. The experimental research concerning these mechanisms are summarized in the review articles by Beeby *et al.* [11] and Cook-Chennault *et al.* [14]. Among the three transduction mechanisms, piezoelectricity has been in the spotlight for the past two decades. Many review articles [4, 13, 14, 19] have laid a special emphasis on piezoelectricity.

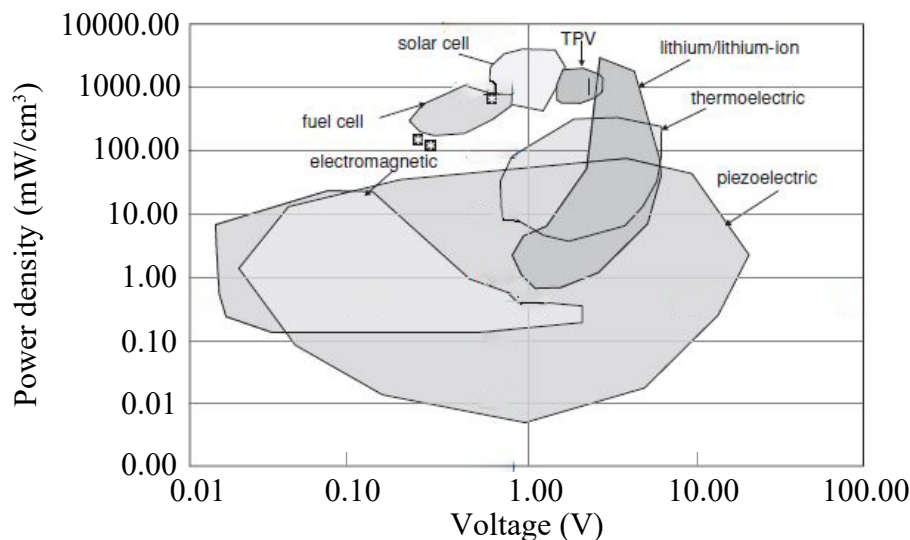


Figure 2.1: [14] Power density vs. voltage comparison between common developmental and lithium/lithium-ion power supply schemes.

The advantages that make piezoelectric materials the most sought-after in the field of vibration-based energy harvesting are their immense power densities¹ and easy applicability. Figure 2.1 depicts the power density versus voltage comparisons for a range of energy-

¹Power density of an energy harvester is the ratio of the output power to the device volume for a given input.

harvesting systems; as evident, piezoelectric covers the largest area in the plot; this type of figure is referred to as an Ashby plot. The advantages of piezoelectric energy harvesting over the electrostatic and electromagnetic avenues are that no external voltage input is required, i.e., the output voltage emerges from the constitutive behaviour of the piezoelectric material, and that piezoelectric devices can be manufactured at the macro scale as well as micro scale, owing to thick-film and thin-film fabrication techniques.

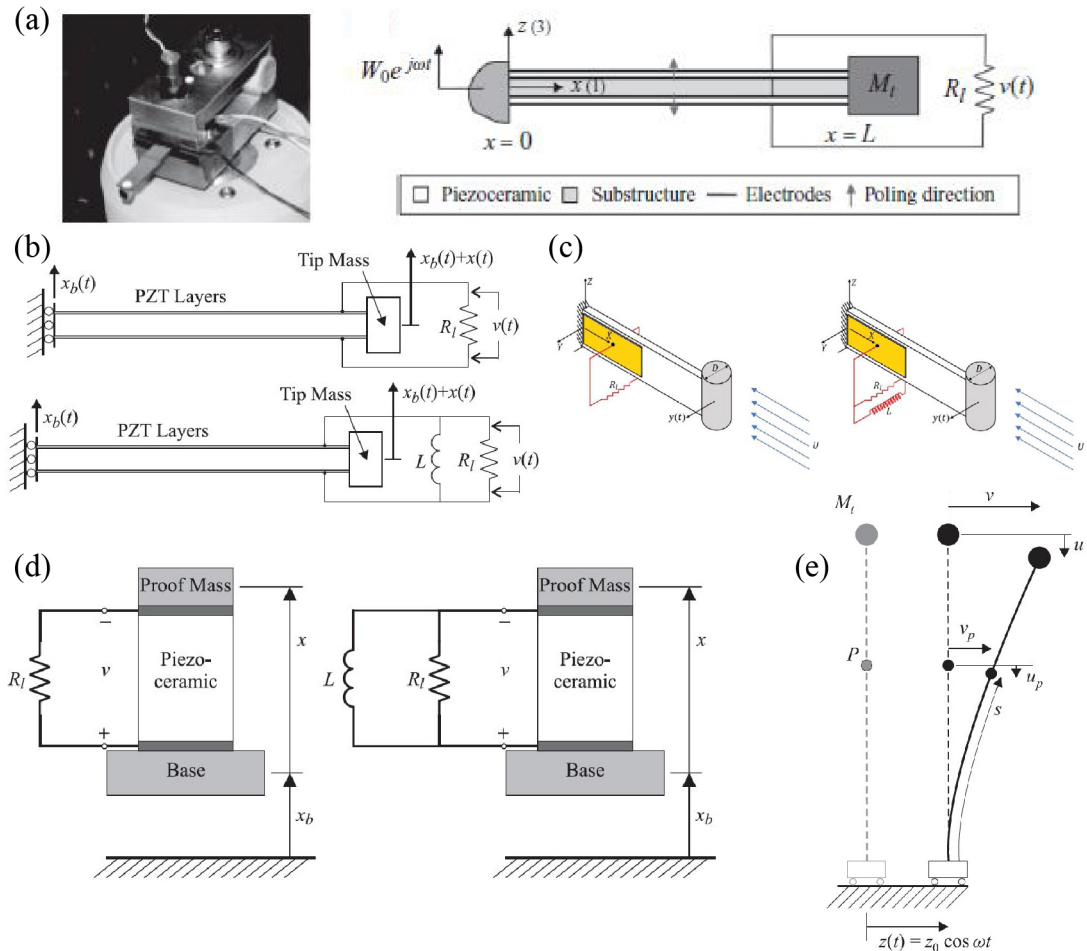


Figure 2.2: Some examples of electromechanical structures. (a) Experimental set-up of a cantilevered piezoelectric energy harvester under base excitation and the corresponding schematic on the right [2]. (b) Schematics of piezoelectric vibration-energy harvesters, comprising of two different types of shunt circuits, under base excitation [87]. (c) Schematics of vortex-induced piezoelectric vibration-energy harvesters comprising of two different types of shunt circuits [88]. (d) Illustration of stack-type piezoelectric vibration-energy harvesters, comprising of two different types of shunt circuits, under base excitation [89]. (e) Schematic of a non-linear inverted-beam used for piezoelectric vibration-energy harvesting (PVEH); piezoelectric elements placed along the beam are not shown [22].

The beginning of piezoelectric vibration-energy harvesting (PVEH) involved the analysis of simple, but bulk, finite electromechanical structures subject to limitations such as overall structural size and strength, boundary conditions, nature of forcing, and efficiency of piezoelectric elements. A majority of the piezoelectric vibration-energy harvesters appear in the form of cantilevered beams [1, 2, 20] with one or two piezoceramic layers, i.e., a unimorph or a bimorph configuration. The cantilever beam is situated on a vibrating host structure, and the dynamic strain induced in the piezoceramic layer(s), owing to base excitation or base harmonic forcing applied to the structure, yields an alternating voltage output across their electrodes. An example of such an arrangement is portrayed in figure 2.2(a). Figure 2.2 illustrates a few examples [2, 87–89], from the existing literature, of energy-harvesting electromechanical structures comprising of cantilevered beams. The piezoelectric stacks shown in figure 2.2(d) are an exception. In certain limited cases, stack- [90] and cymbal-type [91] transducers are used under direct force excitation. In stack- and cymbal-type transducers, polyvinylidene fluoride (PVDF) membranes may also be utilized for piezoelectric power generation; however, they exhibit very low electromechanical coupling as opposed to piezoceramics. In the theoretical and experimental research pertaining to piezoelectric energy harvesting, it is routine to consider a resistive load in the electrical domain, i.e., in the shunt circuit, in order to estimate the performance of a device for AC power generation. In addition to a purely resistive shunt mechanism, electronic load consisting of a resistor as well as an inductor has also been considered in the literature as evident in figures 2.2(b), 2.2(c), and 2.2(d). Recently, inertially amplified PVEH cantilevered beams with a tip mass and

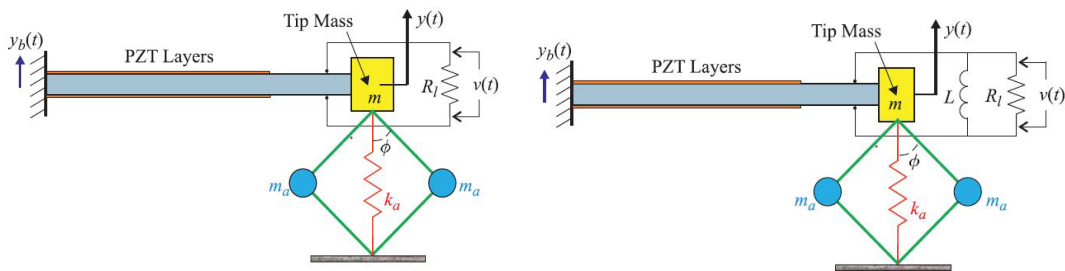


Figure 2.3: [77] Schematics of inertially amplified piezoelectric vibration-energy harvesters comprising of two different types of shunt circuits.

piezoelectric elements with shunt circuits that are purely resistive or consist of an inductor, shown in figure 2.3, have been shown to result in low-frequency enhanced PVEH with the enhancement attributed to the inertial amplifier mechanisms.

Considering the output from an electrical engineering perspective, in order to charge a lightweight battery or a capacitor via the harvested energy, the alternating output voltage should be converted to a stable rectified voltage by means of a rectifier bridge and a smoothing

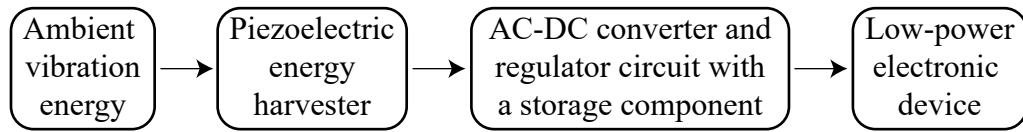


Figure 2.4: [2] Schematic illustrating the working principle of a piezoelectric vibration-energy harvesting (PVEH) system.

capacitor, which together comprise an AC-DC converter. Generally, a second stage DC-DC converter is implemented for output voltage regulation for the purpose of maximizing the power transfer to the storage device. The aforementioned process is crudely summarized in figure 2.4.

PVEH involving beams and masses has also been investigated in the non-linear vibrations regime [22] as evidenced by figure 2.2(e). The last two decades have witnessed an impressive amount of research in the area of active vibration suppression using piezoelectric systems [23–27], and in the last decade or so, the area of active vibration suppression has been fused with that of PVEH, which has significantly increased the potential for piezoelectric systems on account of many possible practical applications [28].

It is also worth mentioning an important application of PVEH: self-charging structures. Self-charging structures are constituted of elastic substructures, e.g., metallic or carbon fibre, flexible piezoceramics embedded in kapton² layers, and flexible thin-film battery layers [92, 93]. The objective of this particular application is to promote multifunctionality in scenarios involving low-power requirements, i.e., a self-charging structure is used as a load-bearing system and to power a wireless sensor in close proximity to the system utilizing the harvested and stored energy, e.g., a wing spar in a UAV [94, 95].

2.3 Material dynamics of elastic periodic media

The apparent properties of materials, such as mechanical, acoustic, etc., are the aggregated outcome of many interactions and processes occurring at a small-scale level within the microstructure of the material. As technology advances, the demand for exceptional materials to satisfy unprecedented operational requirements goes up. Hence, the capability to alter the microstructure in a custom manner and, subsequently, the behaviour of the material as a whole is extremely important. One might think that, logically, engineering the microstructure at the atomic or molecular level or at the grain scale in order to achieve the desired results falls under the broad umbrella of chemistry. An alternative route is the design and deployment of the internal structure at a “macroscopic” level in order to extract unique, perhaps even

²Kapton® is an unfilled polyimide thermoplastic material.

counterintuitive, behaviour/performance from the consequent structured/architected material; this could possibly lead to extending the boundary of the behaviour of materials; this route is especially realizable with the introduction of additive manufacturing technology. These architected materials may result in higher and more efficient energy harvesting due to their unique properties. In the current section, such architected materials, referred to as *phononic materials*, including phononic crystals (PnCs) [29–31] and acoustic/elastic metamaterials [39, 96, 97], are introduced and their dynamical features (material dynamics) are briefly discussed.

Phononic materials, typically, materialize from the periodic arrangement of small-scale fundamental blocks, much like molecules in crystalline materials, which, by means of scattering/interference and/or resonance phenomena, function to control the propagation of acoustic/elastic plane waves. At the fundamental level, across specific frequency ranges referred to as pass bands or transmission bands, a phononic material allows vibrational plane waves to propagate at different speeds as opposed to the constant sonic speeds of many conventional non-dispersive materials. Outside of these frequency ranges/bands, referred to as attenuation bands, stop bands, or band gaps, the internal structure of the material scatters and/or localizes the wave energy and, consequently, prohibits transmission in all or specific directions. Waveguides and acoustic filters are the two most common applications of the aforementioned characteristic. Nevertheless, through meticulous design of the building blocks constituting the material's internal structure, the unique dynamics of phononic materials may be exploited and implemented in a diverse range of applications, e.g., acoustic lenses [98], elastic/acoustic cloaks [99], phononic subsurfaces for the purpose of flow control [100]. Other types of applications can be found in [101]. As opposed to simple non-dispersive cantilevered beams, different types of periodic media, e.g., PnCs, locally resonant metamaterials (LRMs), and inertially amplified locally resonant metamaterials (IALRMs), may result in higher and more efficient energy harvesting due to their unique property of wave-energy localization, which can lead to simultaneous vibration attenuation and energy harvesting as discussed in section 2.4.

Figures 2.5(a) and (b) [80] illustrate one of the earliest and simplest examples of a phononic material, which is a one-dimensional medium constituted of periodically alternating layers of varying composition, mass-density and elasticity [102–104]. Figure 2.5(a) depicts a continuous model of the phononic material/medium whereas figure 2.5(b) depicts the discretized model of the same material. Within a homogeneous medium, an elastic (vibrational) wave of arbitrary frequency ω and wavenumber κ , i.e., spatial frequency, propagates at a constant velocity given by $C_{\text{ph}} = \frac{\omega}{\kappa}$, where C_{ph} is referred to as the phase velocity. As per figure 2.5(c), within a phononic material, waves with different frequencies propagate

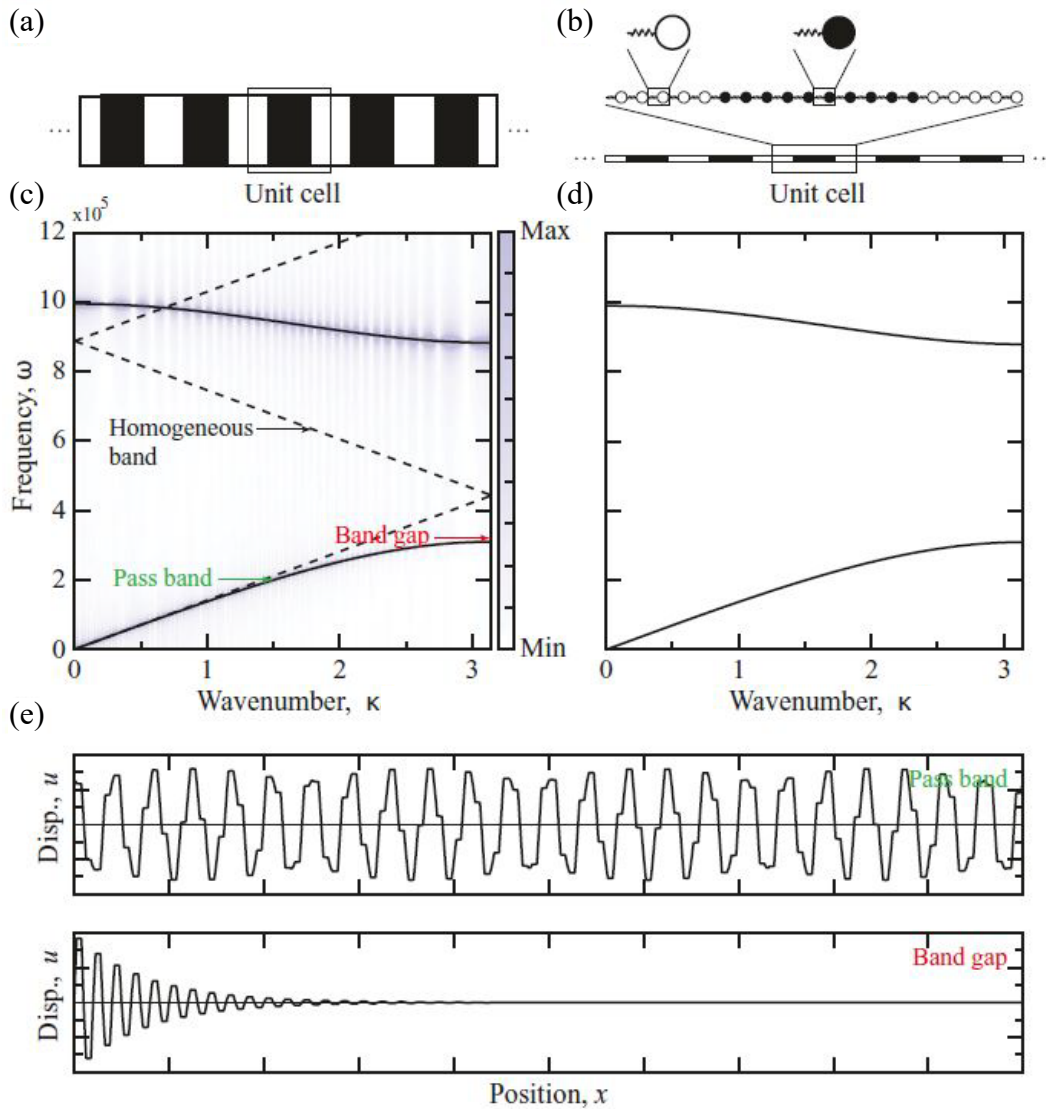


Figure 2.5: [80] (a) Example of a layered medium (continuous model). (b) Equivalent mass-spring system (discretized lumped-parameter model). (c) Dispersion diagram of the continuous model obtained through analytical and numerical treatments. (d) Dispersion diagram of the discrete model determined analytically. (e) Displacement profile in the finite layered medium at different frequencies depicting the comparison of response between the (top) pass band and (bottom) stop band (band gap) cases.

at different velocities—a phenomenon referred to as dispersion—indicating a non-linear relationship between ω and κ . In the case of the layered medium, this is achieved by the superposition of waves transmitted and reflected at the layer interfaces. Additionally, over specific frequency ranges, the scattering/interference is enough to prevent the waves associated with those ranges from propagating through the material. Figure 2.5(c) illustrates each

of the aforementioned scenarios where the displacement profiles are plotted for several unit cells; a unit cell is the fundamental block/structure that is periodic/repetitive. In the pass band, the wave propagates through the phononic material such that the displacement profile covers the entire domain, which is theoretically infinite. Contrastingly, in the stop band or band gap, the wave amplitude decays with distance, and the displacement nodes stay fixed in space for all time instants.

Figure 2.5(c), essentially, shows an example of analytical and numerical simulation results [80] for a layered medium composed of 100 unit cells. For the simulation, the layered medium is disturbed by an impulse at mid-span, which produces a wide spectrum of waves propagating away from the site of disturbance. The waves interact only with each other and the underlying material periodicity before reaching either end of the medium; hence, such an arrangement acts like an infinite medium. Under such conditions, a Fourier transform of the displacement in space, with $e^{i\kappa x}$, and time, with $e^{-i\omega t}$, yields the density plot shown in figure 2.5(c), where the narrow (along the horizontal) darker regions identify waves with spectral characteristics, i.e., ω and κ , suitable for transmission through the medium and the wider brighter regions represent incompatible characteristics, i.e., waves that are attenuated (not allowed to propagate). The colour map shown in figure 2.5(c) and similar type of diagrams obtained via numerical simulation are informative in revealing the dispersion characteristics of different types of phononic materials; although, they are computationally time-consuming and expensive, in particular for two- and three-dimensional models involving unit cells with a complex design. As an alternative, owing to the periodic arrangement of material constituents, similar to molecules in crystalline materials, the phononic material can be theoretically analysed via the Floquet-Bloch theorem, generally referred to as the Bloch theorem, arising from the field of solid-state physics. For one-dimensional elastodynamic cases, the theorem is expressed as [105, 106]

$$u(x, t) = \tilde{u}(x)e^{i(\kappa x - \omega t)}, \quad (2.1)$$

where u is displacement; \tilde{u} is the displacement amplitude; x is position, t is time; and $\sqrt{-1}$ is the imaginary unit. The amplitude function \tilde{u} exhibits the same periodicity at the underlying medium as the unit-cell length or the lattice spacing, a . Consequently, $u(x + na, t) = u(x, t)e^{i\kappa na}$ for any arbitrary integer $n \in [-\infty, \infty]$; this theoretically permits the solution for an infinite number of unit cells, $[x - \infty a, x + \infty a]$, to be obtained from the analysis of only a single unit cell of size a at position x , i.e., only a finite portion of material of size a . This concept also applies to two- and three-dimensional models. By considering and analysing only a single unit cell instead of a multitude of cells, Bloch's theorem substantially diminishes computational demands and produces a compact theoretical representation of

the wave propagation or dispersion characteristics. Figure 2.5(c) demonstrates excellent agreement when comparing the numerical (density plot) and analytical (smooth curves) results for the layered medium.

The last three decades, roughly, have witnessed a surge in research pertaining to investigations and applications of two-dimensional phononic crystals. The two-part review article [38] gives some interesting examples of two-dimensional bulk phononic crystals of different types based on the constituent materials, e.g., solid objects (inclusions) embedded in a solid background (matrix), solid objects embedded in a liquid, and liquid-liquid. Figure 2.6 provides

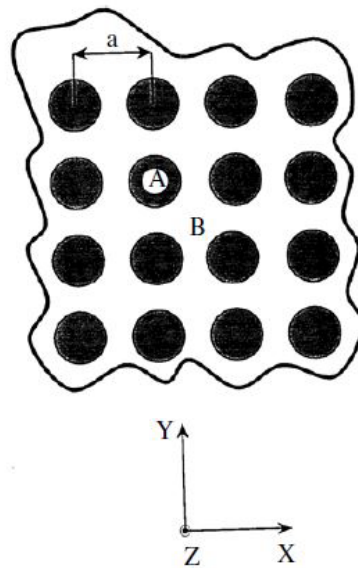


Figure 2.6: [38] Cross-section of a binary composite system: square array of infinite cylinders A periodically arranged in an infinite matrix B.

an example of the type of two-dimensional periodic media reviewed in the paper. The first part illustrates that the bandwidth of the stop band is strongly influenced by the nature of the constituent materials (solid or fluid), the disparity between the physical characteristics, e.g., density and elastic modulus, of the inclusions and the matrix, the geometry of the periodic arrangement of inclusions, and the shape and filling factor of the inclusions. The second part of the review paper presents some possible applications of two-dimensional composite materials. Specifically, it is shown that features such as cavities, waveguides, stubs, etc., known as defect modes, inserted within the two-dimensional periodic structure may lead to selective frequency filtering and efficient devices for wavelength demultiplexing. The possibility of sonic insulators, with comparatively small thicknesses of PnC samples, for frequencies of the magnitude of KHz is also presented. Finally, the vibration modes of a

two-dimensional crystal plate, i.e., a phononic crystal of finite thickness along the axis of inclusions, are presented.

A layered (continuous) medium is one of the most rudimentary practical representations of a phononic material and a simple demonstration. Generally, in phononic-media analysis, lumped-parameter models are considered, exploiting the theoretical benefit (periodicity) of Bloch's theorem, to capture all the essential physics; make the connection between unit-cell configuration and performance more accessible; and alleviate computational time and cost. Concerning the ability of a lumped-parameter model to capture the essential physics (dynamics), it can be observed that the dispersion diagram of the lumped-parameter (discrete) model, shown in figure 2.5(d), accurately resembles the dispersion diagram of its continuum version. The discretization portrayed in figures 2.5(a) and 2.5(b) can be better visualized in figure 2.7. The lumped-parameter model in figure 2.7(b) employs masses and springs to

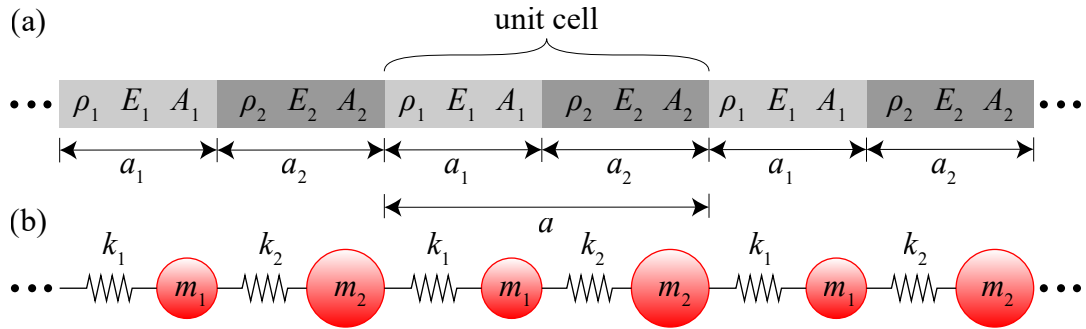


Figure 2.7: Demonstration of the discretization of (a) an infinite bilayered continuum model into (b) a lumped-parameter diatomic discrete model.

represent each layer of the bilayered continuum model shown in figure 2.7(a). The mass and spring, representative of each layer, are defined as $m_* = \rho_* A_* a_*$ and $k_* = \frac{E_* A_*}{a_*}$, respectively, where m_* is mass, k_* is the stiffness coefficient of the spring; ρ_* , E_* , A_* , and a_* denote the density, Young's modulus, cross-sectional area, and length of a layer, respectively; and the subscript $*$ denotes 1 or 2, corresponding to the two layers. The arrangement of two layers in the continuum model and of equivalent masses and springs in the lumped-parameter model constitutes a unit cell with length a .

The unit-cell of a PnC interacts with travelling elastic/plane waves to promote scattering/interferences and generate band gaps; this indicates a dependency on the unit-cell size to generate band gaps. Over the past two decades, metamaterials, whose exceptional mechanical and dynamical properties emanate from a uniquely customized internal architecture, have stimulated intensive research in the field of acoustics [39], electromagnetics [107], and, fairly recently, mechanics [108]. In acoustic/elastic LRMs, in addition to wave interferences, the band structure is also shaped by couplings, arising due to hybridizations, between resonance

modes of the substructure, e.g., a local resonator, and elastic-wave modes in the hosting medium when the wavelength is much larger than the lattice spacing [43]. With regards to dynamical aspects, many of the extraordinary properties of metamaterials, e.g., negative effective mass/density, negative elastic/bulk modulus, negative refractive index, are often the homogenized demonstration of sub-wavelength resonances engineered into every individual unit cell. Some additional advances in mechanical metamaterials include ultra-lightweight, pentamode, anisotropic mass density, origami, non-linear, bistable, and reprogrammable mechanical metamaterials (see figure 2.8 and reference [108] for a summary of these advances). Figure 2.8 [108] presents some examples of advanced metamaterials with diverse applications. The resonating bodies operate to localize, instead of scattering and/or reflecting, the wave energy to generate band gaps. They may take the form of localized oscillators distributed along the length of a rod [109], elastically coated heavy spheres in an epoxy matrix [39], cylindrical or square pillars in an epoxy matrix [38], pillars [40, 110, 111], voids in an epoxy matrix [112], among others.

With regards to phononic band gaps in phononic/periodic media, in a considerable portion of the existing literature, they are generated through two widely-known means, namely, Bragg scattering and local resonances. There are two approaches for wave-propagation or dispersion analysis of damped phononic media. In the first, the frequencies are assumed to be real, which allows damping effects to be exhibited only in the form of complex wavenumbers ($\kappa = \kappa_{\text{real}} + i\kappa_{\text{imag}}$). This is physically representative of a medium experiencing wave propagation as a result of continuous driving frequency and dissipation manifesting only in the form of spatial attenuation. This approach is referred to as the “driven-waves” approach and follows a $\kappa = \kappa(\omega)$ formulation ensuing from either a linear or a quadratic eigenvalue problem; i.e., a real frequency is supplied, and the underlying eigenvalue problem is solved for a corresponding pair of real and imaginary wavenumbers, describing propagation and attenuation constants, respectively. All wave modes are described by complex wavenumbers. In the second approach, the frequencies are allowed to be complex, which allows damping effects to be exhibited in the form of temporal attenuation. This is physically representative of a medium permitting free dissipative wave motion, e.g., free vibration due to impulse excitation. This approach is called the “free-waves” approach and follows a $\omega = \omega(\kappa)$ formulation resulting from a linear eigenvalue problem; i.e., a real wavenumber is supplied, and the underlying eigenvalue problem is solved for corresponding complex frequencies, where the real and imaginary parts provide the loss factor and the frequency for each wave mode, respectively. Often, it is thought that the two approaches discussed above are the only two available options, i.e., approach involving real frequencies and complex wavenumbers and approach involving real wavenumbers and complex frequencies. However, if a medium

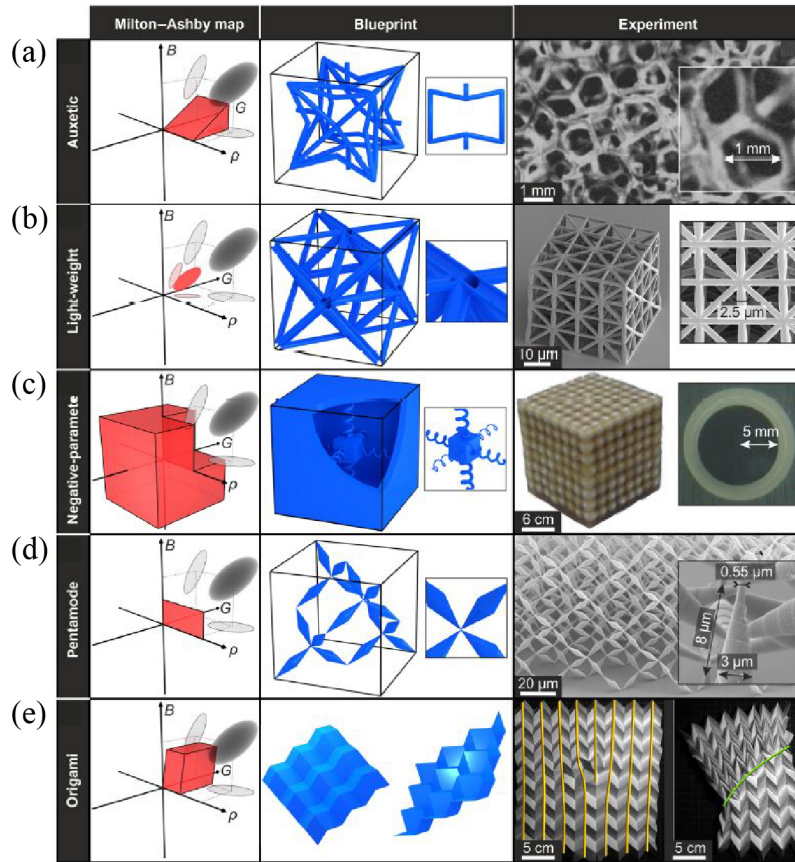


Figure 2.8: [108] An overview of mechanical metamaterials in existing literature. The five rows illustrate (a) auxetic, (b) light-weight, (c) negative-parameter, i.e., negative mass density and/or moduli at a finite frequency $\omega \neq 0$, (d) pentamode, and (e) origami mechanical metamaterials. The left column illustrates a combination of the Milton map, bulk modulus B vs. shear modulus G , and the Ashby map, a particular modulus vs. mass density ρ . At the point of crossing of the three arrows, which point towards the positive directions, all the parameters are zero. In each entry in the first-column, ordinary solids (shown in black) are compared with the corresponding metamaterials (shown in red). The center column depicts blueprints of (extended) unit cells featuring characteristic structural elements, and the right column shows electron micrographs of fabricated structures. The metamaterials shown can (a) be easily compressible, yet not easily deformable; (b) be ultra-lightweight, yet ultrastrong; (c) exhibit complete band gaps or support back-propagating waves; (d) be easily deformable, yet not easily compressible; (e) be deployable, bistable, and reprogrammable. The potential applications could be as (a) shock absorbers, (b) support structures, (c) reflectors or concentrators, (d) mechanical cloaks, and (e) structures for space missions. Figures reproduced with permission: (a) © 1987 AAAS, (b) © 2014 PNAS, (c) © 2000 AAAS, (d) © 2012 AIP, and (e) © 2014 AAAS.

exhibits spatial attenuation in an undamped state, which is true for phononic media within stop bands, then, theoretically, there must be an imaginary wavenumber component along

with the real wavenumber component even when the frequencies are complex. This is a more complete representation of the dispersion curves for damped free-wave motion in media that contain built-in mechanisms for spatial attenuation, e.g., Bragg scattering and local resonance. Reference [47] comprehensively gives an all-complex solution, i.e., complex wavenumbers and complex frequencies, for damped free vibration in one-dimensional systems by providing an algorithm, based on a quadratic eigenvalue problem, that provides dispersion curves and damping ratios for both spatially propagating and attenuating waves.

In the last decade, the field of material dynamics has witnessed the introduction and implementation of a new class of metamaterials referred to as inertially amplified metamaterials (IAMs). These metamaterials are unique in the way that the effective inertia of the wave-propagation medium (waveguide) is amplified by means of embedded amplification mechanisms. In reference [52], inertial amplification is utilized to generate band gaps in

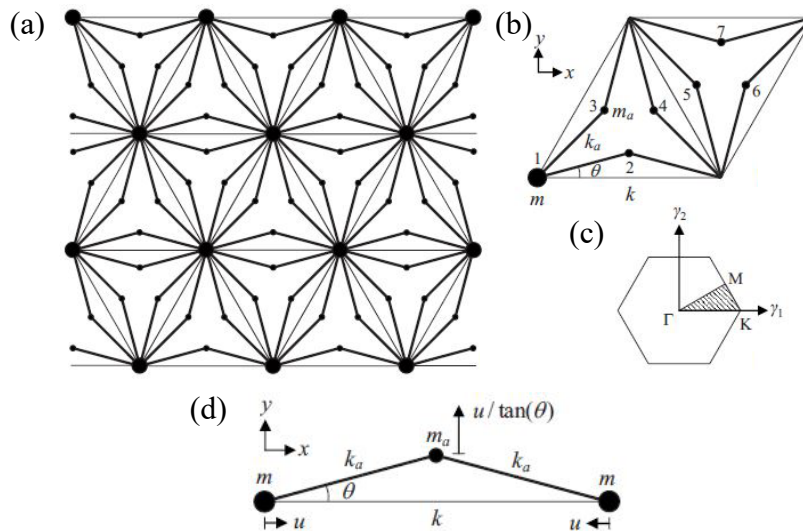


Figure 2.9: [52] (a) Inertially amplified infinite periodic lattice and (b) the associated irreducible unit cell. The thin lines with stiffness k and big dots with mass m form a triangular truss structure; the thick lines with stiffness k_a and the small dots with mass m_a constitute the amplification mechanisms. The angle θ dictates the amplification generated by the mechanisms. The numbers 1-7 denote the nodes within the unit cell. (c) Hexagonal first Brillouin zone of the reciprocal lattice. The shaded area represents the irreducible Brillouin zone (IBZ); γ_1 and γ_2 are components of the wavevector, and $\Gamma \rightarrow K \rightarrow M \rightarrow \Gamma$ is the wavevector path around the IBZ. (d) Detailed view of the amplification mechanism.

a two-dimensional mass-spring lattice shown in figure 2.9, and the sensitivity of the band gaps, induced by inertial amplification, to parametric variations is quantified. Figure 2.9(c) illustrates some key concepts used for presenting wave-propagation results: the first Brillouin

zone (FBZ) and the irreducible Brillouin Zone (IBZ). The FBZ is the smallest area or volume in reciprocal space that contains information about the infinitely repeating unit cell that makes up a crystal lattice. For a phononic media in one, two, or, three dimensions, the FBZ is contained within $[-\pi, \pi]$ along the x -, y -, and z -directions. The IBZ is a reduced portion of the FBZ that contains unique points providing all the necessary information about a unit cell. It is realized by simply eliminating equivalent points, in the FBZ, that exist due to symmetry. The dimensionless-wavevector ($\boldsymbol{\mu}$) path around the IBZ, e.g., $\Gamma \rightarrow K \rightarrow M \rightarrow \Gamma$, is the outline of the IBZ that consists of $\boldsymbol{\mu}$ -points comprising x -components $\mu_x = \kappa_x a_x$, y -components $\mu_y = \kappa_y a_y$, and z -components $\mu_z = \kappa_z a_z$; κ_x , κ_y , and κ_z are wavevector components and a_x , a_y , and a_z are unit-cell lengths or lattice spacings along the x -, y -, and z -directions, respectively. It is demonstrated that inertial amplification results in very wide band gaps at low frequencies. In reference [53], the characteristics of inertial-amplification-induced band gaps

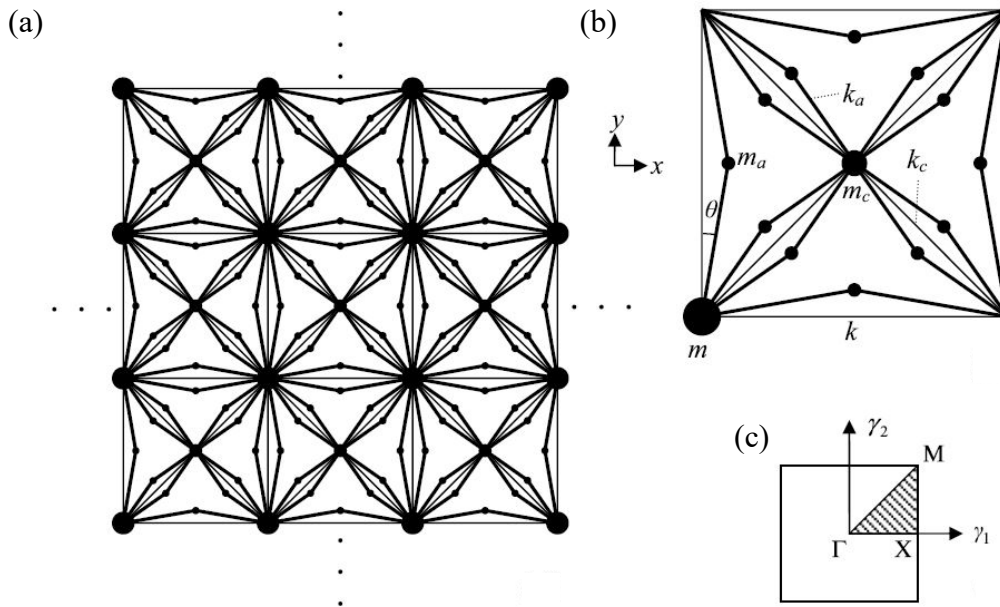


Figure 2.10: [53] (a) Inertially amplified infinite periodic lattice and (b) the associated irreducible unit cell. The vertical and horizontal thin lines have stiffness k and the big dots have mass m . Each central mass m_c is attached to the neighbouring masses m through lines with stiffness k_c . Consequently, k , k_c , m , and m_c constitute the structural backbone of the lattice; the thick lines with stiffness k_a and the small dots with mass m_a constitute the amplification mechanisms. The angle θ dictates the amplification generated by the mechanisms. (c) First Brillouin zone of the reciprocal lattice depicting the shaded irreducible Brillouin zone (IBZ); γ_1 and γ_2 are wavevector components, and $\Gamma \rightarrow X \rightarrow M \rightarrow \Gamma$ is the wavevector path around the IBZ.

are obtained for the lattice shown in figure 2.10 and compared with those of local-resonance and Bragg band gaps in finite lattices. Deep inertial-amplification gaps are obtained at low fre-

quencies without employing a myriad of unit cells; the gaps computed remain deep irrelevant of boundary conditions, excitation direction, or vibration mode. Similar to reference [53], in reference [54], it is shown that a two-dimensional solid structure embedded with inertial-amplification mechanisms can exhibit a wide and deep phononic band gap at low frequencies. The width and depth of the band gaps, induced by inertial amplification, are computed both analytically via a distributed parameter model and numerically via one-dimensional and two-dimensional finite element models. The inertial-amplification mechanisms are optimized to produce wide and deep band gaps at low frequencies. In reference [56], elastic/plane wave motion in a continuous elastic rod with a periodically attached inertial-amplification mechanism is investigated. The mechanism exhibits characteristics analogous to an “inertor” commonly used in vehicle suspension systems; however, it is constructed and implemented in a way that modifies the intrinsic properties of a continuous structure. The elastodynamic band structure of the hybrid model allows band gaps that are exceedingly wide and deep at low frequencies in comparison to what can be obtained by employing standard local resonators. Using the inertially amplified hybrid model, a large band gap may be realized with practically twenty times less added mass as opposed to what is needed in a configuration involving a standard local resonator. The hybrid model also features unique qualitative characteristics in its dispersion curves, e.g., a characteristic double-peak in the spatial attenuation profile within the band gaps and the possibility of combination of two neighbouring gaps resulting in a large gap, where the the two neighbouring gaps are contiguous to each other.

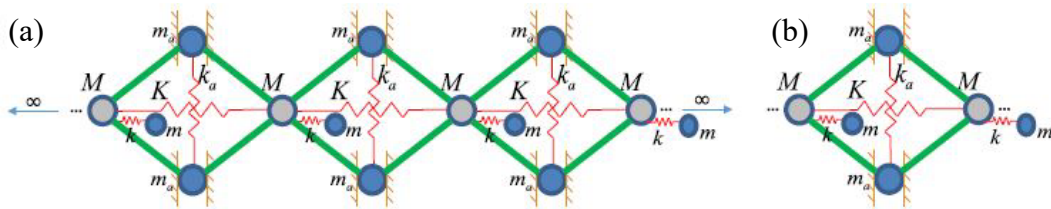


Figure 2.11: [55] (a) Inertially amplified chain comprised of a levered (inertial-amplifier) mass and a local-resonance mass and (b) the associated unit cell. The thick green lines represent rigid links; M denotes the baseline mass; m_a denotes the inertial-amplifier mass; m denotes the local-resonance mass; K is the baseline stiffness; k is the local-resonance stiffness; k_a is the stiffness of the spring connecting the two inertial-amplifier masses.

As mentioned earlier in the discussion pertaining to reference [56], a unique feature in an inertially amplified band gap is that it may exhibit two coupled peaks in the imaginary wavenumber spectrum of its dispersion band structure. In reference [55], a double-attenuation band gap is shown to emerge, in an inertially amplified chain depicted in figure 2.11, specifically from the modal coupling of a levered (inertial-amplifier) mass with a conventional local-resonance mass separately attached to the base. The periodic arrangement shown in

figure 2.11 presents a foundationally unique mechanical mechanism for the shaping of inertially-amplified phononic band gaps and yields an avenue for combining strength and breadth in the wave spatial-attenuation characteristics.

2.4 Energy harvesting in elastic periodic materials

Phononic materials or waveguides, namely, PnCs and metamaterials, enable the guiding, focusing, and localizing of elastic or acoustic waves in different ways. The physical mechanisms behind wave manipulation are briefly discussed in chapter 1 and section 2.3. The reader may also refer to comprehensive reviews by reviews by Lee *et al.* [66], Hu *et al.* [67], and Chen *et al.* [68]. From PVEH using conventional beam-based finite structures, naturally, the next step of progression was towards PVEH using periodic structures. The amalgamation of the broad domains of PVEH and periodic media have resulted in many multifunctional applications, e.g., simultaneous vibration suppression and energy harvesting as demonstrated by Hu *et al.* [73, 74] by using acoustic/elastic LRMs. Figure 2.12 illustrates the general principle of PVEH in PnCs, e.g., a PnC with defect cavities, and LRMs.

Thorp *et al.* [57] proposed the electromechanical structure, shown in figure 2.13(a), comprising of a rod with periodic shunted piezoelectric patches to control wave propagation in the longitudinal direction. The continuous periodic structure boasts the capability of filtering wave propagation, i.e., wave filtering, over certain frequency bands, i.e., stop bands. The structure also demonstrates band-gap tuning by employing the shunted piezoelectric elements. Cao *et al.* [64] proposed a piezoelectric PnC cantilever beam with a variable cross-section, shown in figure 2.13(b), for energy harvesting. Gonella *et al.* [60] proposed the multifunctional structural design, shown in figure 2.13(c), possessing the combined capabilities of wave filtering and energy harvesting. Shin *et al.* [65] presented a PVEH structure, shown in figure 2.13(d), consisting of a beam composed of two different alternating materials with a piezoelectric patch (PZT-5H) bonded to the surface; the PnC beam amplifies the input waves resulting in an improvement in energy harvesting. Chen *et al.* [62] also came forth with a design, shown in figure 2.13(e), constituted of a piezoelectric PnC cantilever beam and piezoelectric patches (PZT-5H) for energy harvesting as a result of the widening of the resonant bandwidth.

In the last decade, LRMs have spurred intensive research [66–68] in the PVEH community. Dwivedi *et al.* proposed the piezo-embedded negative-mass material, shown in figure 2.14(a), for simultaneous vibration attenuation and energy harvesting and, for a finite number of unit cells, computed the voltage and power produced by the piezoelectric elements along with the system transmissibility via the backward substitution method. Hu *et al.* also proposed

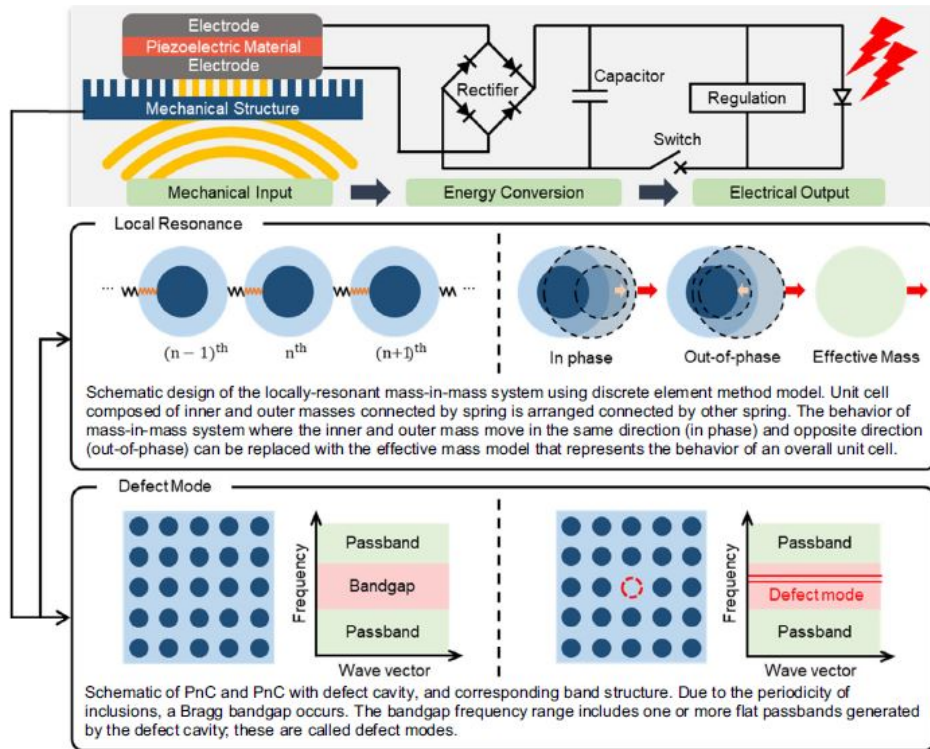


Figure 2.12: [66] A general illustration of piezoelectric vibration energy-harvesting (PVEH) system using phononic crystals (PnCs) and locally resonant metamaterials (LRMs). The process of harvesting elastic-wave energy using mechanical elements such as local resonators and defect cavities is shown as a schematic at the top, where the piezoelectric material and electrical circuit converts the elastic-wave energy from vibrations and sound to electrical energy.

a metastructure, shown in figure 2.14(b), capable of simultaneous vibration suppression and energy harvesting. Dwivedi *et al.* explored simultaneous vibration attenuation and energy harvesting in a piezo-embedded negative-stiffness metamaterial as well, which is portrayed in figure 2.14(c). The proposed metamaterial exhibited negative stiffness and consisted of an energy-harvesting material installed within the local-resonance mechanisms. The results included a parametric investigation, which suggested enhanced performance of the metamaterial in the context of simultaneous vibration attenuation and energy harvesting.

2.5 Metadamping: Emergence of dissipation/damping in elastic metamaterials

Numerous applications pertaining to structural dynamics, where strength of materials and vibration control must be given their due importance, require materials that simultaneously

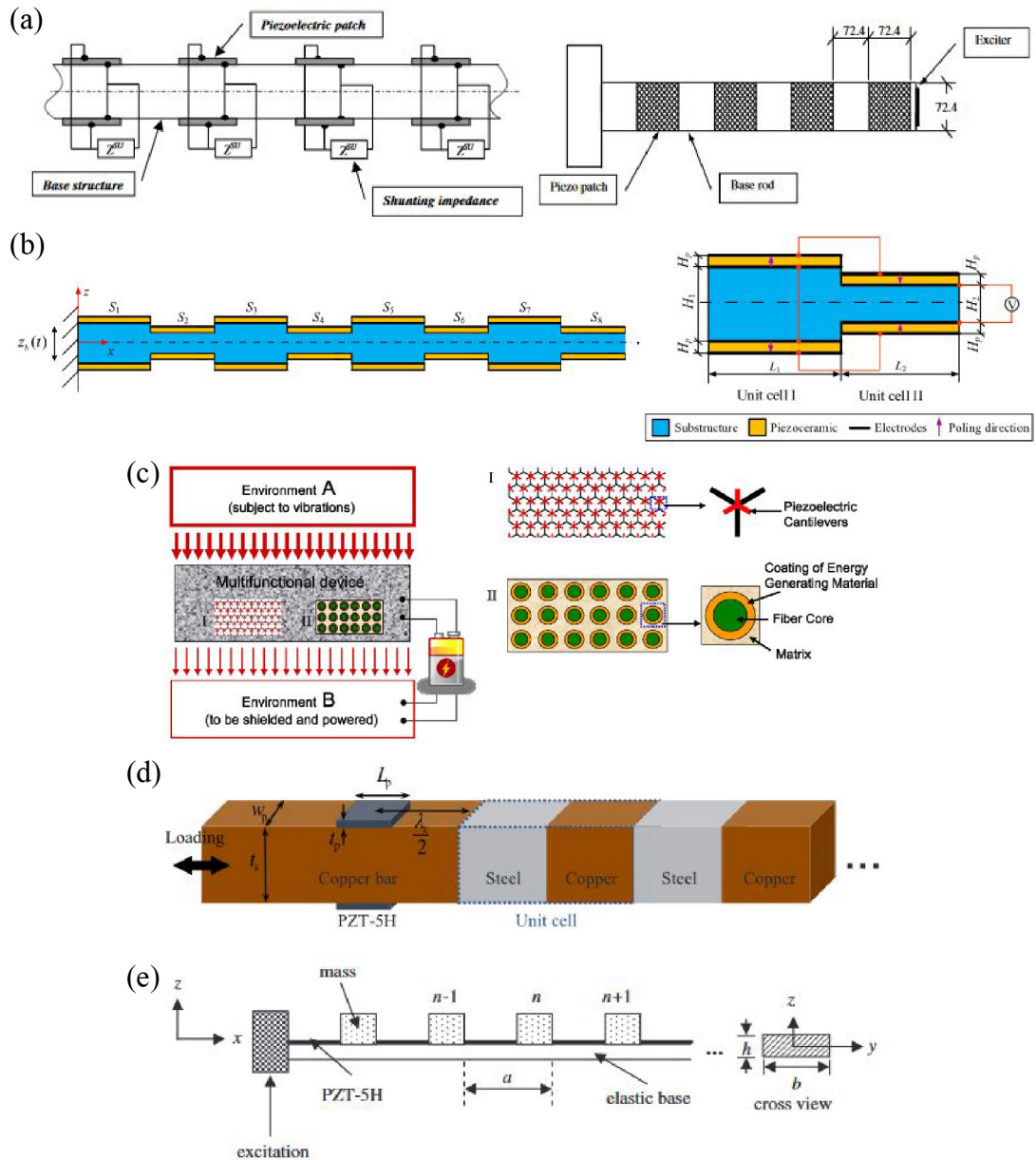


Figure 2.13: (a) Infinite version (left) of a rod (continuum) with periodic shunted piezoelectric patches and the finite version on the right [57]. (b) A piezoelectric phononic crystal (PnC) cantilever beam (left) and the corresponding unit cell [64]. (c) Multifunctional design of an electromechanical structure capable of simultaneous wave filtering and energy harvesting [60]. (d) Schematic of a piezoelectric vibration energy-harvesting system (PVEH) involving a base structure composed of two alternating media [65]. (e) Example of a one-dimensional phononic piezoelectric cantilever beam [62].

exhibit high damping, i.e., vibration or shock suppression, and mechanical stiffness, i.e., load-bearing capacity; nevertheless, for conventional materials, an increase in one of the

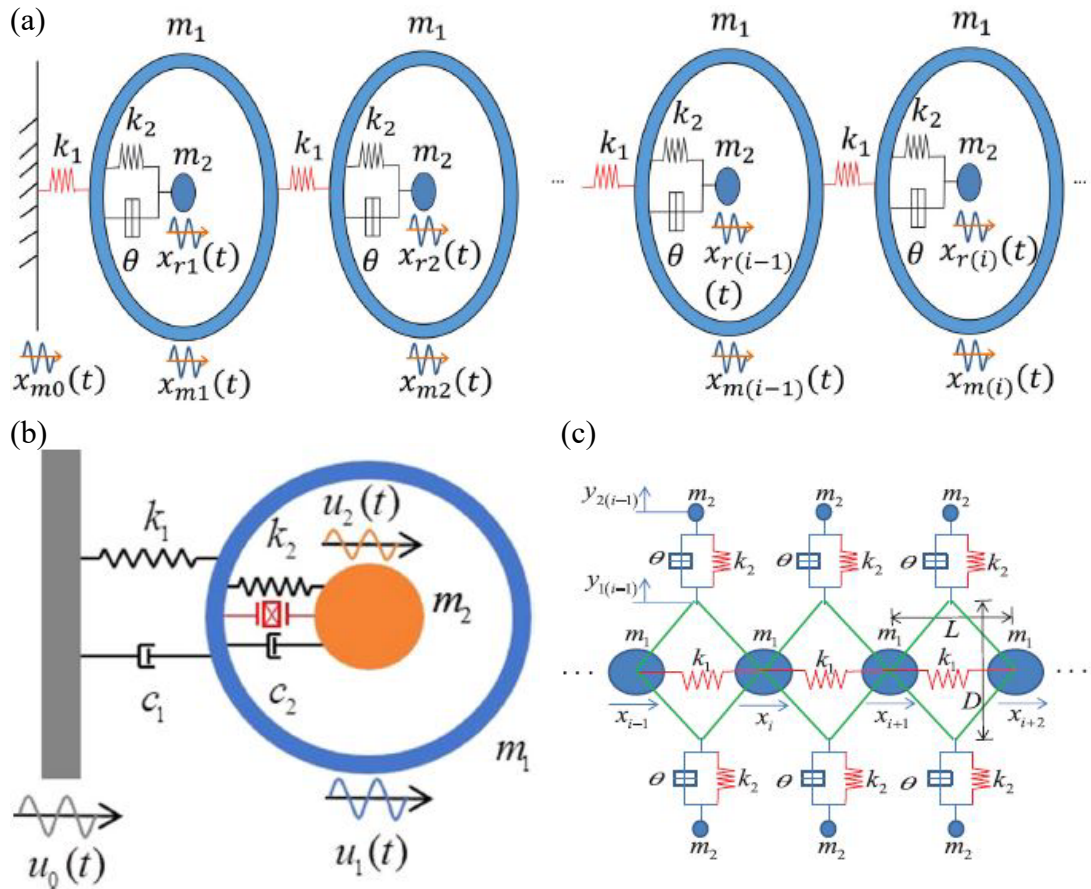


Figure 2.14: (a) Schematic of a piezo-embedded negative-mass material [113]. (b) Unit cell of an acoustic/elastic locally resonant metamaterial (LRM) [73]. (c) Schematic of a piezo-embedded negative-stiffness metamaterial [114].

aforementioned aspects comes at the expense of the other. Rubber and steel are good examples to understand the trade-off between the damping and load-bearing capacities; they exhibit the trade-off opposite to each other; i.e., rubber is highly dissipative but has a poor load-bearing capacity; whereas, steel has a high load-bearing capacity but a poor damping capacity. Figure 2.15 presents the stiffness and damping capacities of traditional materials and, consequently, illustrates the trade-off in an Ashby plot.

In addition to the unique characteristics and novel applications in the absence of damping, metamaterials may show an enhanced capacity to attenuate waves compared to equivalent traditional unstructured materials and PnCs under the influence of damping. This means that metamaterials can potentially exhibit high damping levels with unaltered load-bearing capacity. The phenomenon of this emergence of dissipation or damping capacity is termed as metadamping [79]. The phenomenon of metadamping can be observed across a wide spectrum rather than a narrow set of frequencies and has been demonstrated in locally

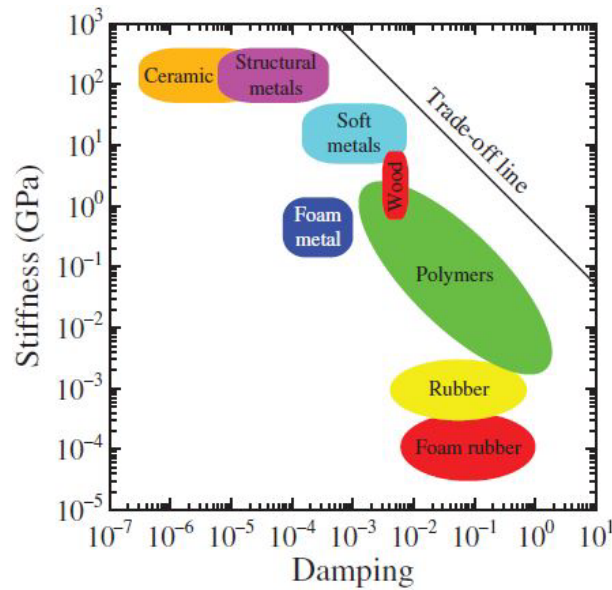


Figure 2.15: [80] Ashby chart depicting the stiffness and damping for common materials and illustrating the evident trade-off between the two.

resonant metamaterials consisting of monopolar [115] and dipolar [79, 115] local resonances and resonances in more complex configurations [116, 117]. Figure 2.16 depicts unit cells of locally resonant dipolar acoustic metamaterial (AM) and PnC and the phenomenon of metadamping in the AM relative to the statically equivalent PnC, by means of an Ashby diagram, as illustrated in the work by Hussein *et al.* [79]. Frazier *et al.* [115] extended metadamping analysis to viscoelastically damped models. Figure 2.17 presents schematics of viscoelastically and viscously damped PnC and dipolar AM and viscously damped monopolar AM and illustrates metadamping in the two metamaterials. Similar to figure 2.17, figure 2.18, obtained from the work by Bacquet *et al.* [80], also shows the unit cells for the PnC and the two metamaterials and illustrates metadamping by considering the average of the damping-ratio modes. Reference [80] also goes on to demonstrate metadamping in metamaterials with non-local resonances. Antoniadis *et al.* [116] presented a stiff and dynamically stable linear oscillator, depicted in figure 2.19(a) consisting of a negative stiffness element to provide a general theoretical basis for a novel damping and vibration-isolation concept. The oscillator is designed to use the same damping elements, overall static stiffness, and mass as a reference linear single-degree-of-freedom (SDoF) oscillator. An optimized version of the system with the negative-stiffness element is shown to present exceptional damping capacity, higher than that of the reference system by several orders of magnitude, particularly in cases where the prescribed damping of the reference system is exceedingly low. DePauw *et al.* [117] proposed a novel hybrid metamaterial configuration, figure 2.19(b), that integrates

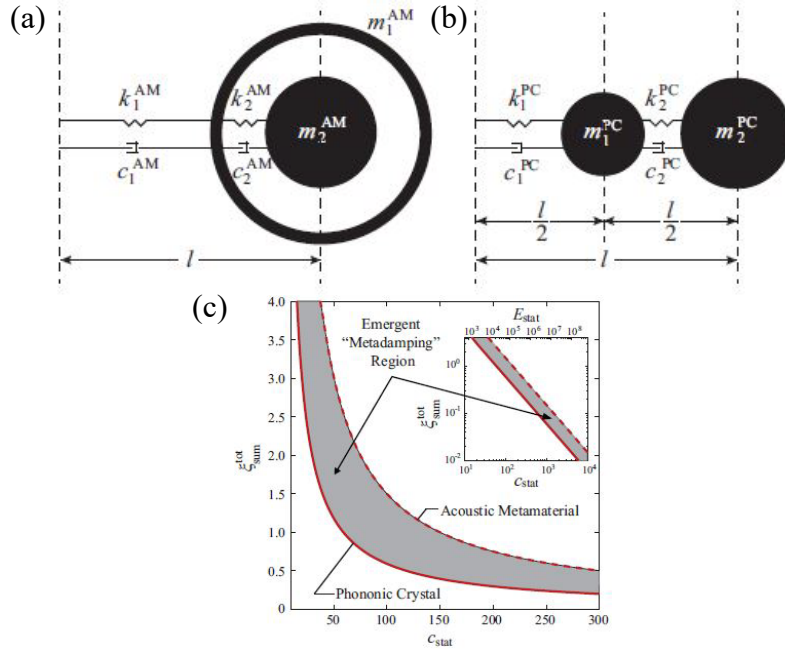


Figure 2.16: [79] Lumped-parameter unit-cell models of (a) an acoustic metamaterial (AM) and (b) a phononic crystal (PnC). (c) Metadamping in dipolar AM: overall total damping capacity versus long-wave sonic speed; $\lim_{\kappa \rightarrow 0} C_{\text{stat}} = d\omega/d\kappa$, where ω is damped frequency and κ is wavenumber.

the attributes of PnCs and AMs. The dispersion characteristics of the system, referred to as phononic resonator, is shown to change across a broad spectrum of behaviours that can, through optimal selection of inertial and stiffness parameters, be tuned to mimic a locally resonant mechanism, phononic crystal, and uniform homogeneous lattice as well. With the introduction of damping elements, the emergent dissipative effect, i.e., metadamping, in the phononic resonator is shown to surpass that of a statically equivalent AM under certain conditions specified in the paper. Recently, metadamping has also been explored in inertially amplified materials, where the inertial-amplification mechanism is actively tuned via a piezoelectric element [118]; however, the mechanism does not possess a local-resonance mechanism.

2.6 Summary and conclusions

This chapter serves the purpose of briefly familiarizing the reader on the topics of PVEH in aperiodic and periodic (phononic) electromechanical structures and damping capacities of phononic materials by presenting the basics of energy harvesting, dynamics of phononic materials, and dissipation augmentation, i.e., metadamping, by means of a brief literature

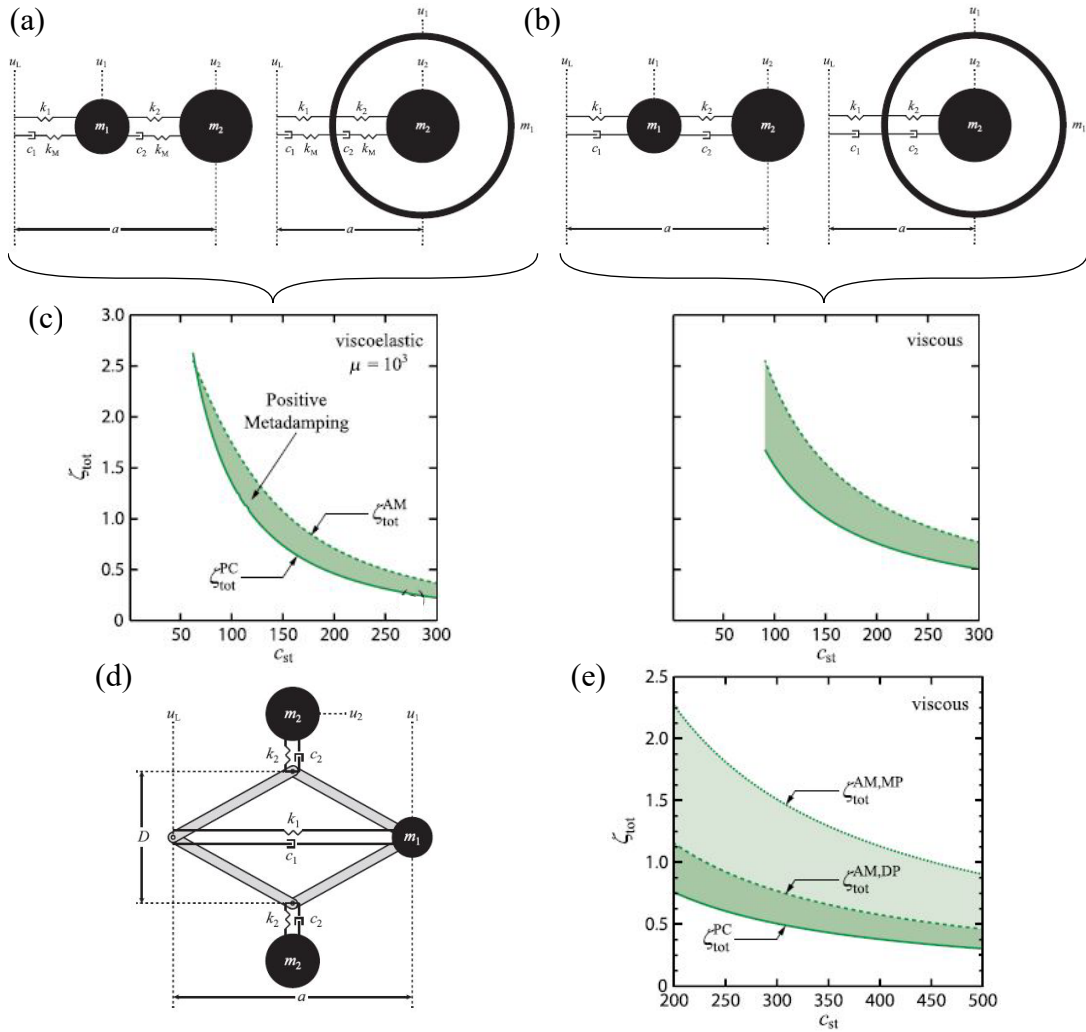


Figure 2.17: [115] Lumped-parameter unit-cell models of (a) viscoelastically and (b) viscously damped phononic crystal (PnC) (left) and dipolar acoustic metamaterial (AM) (right). (c) Metadamping in dipolar AM for the viscoelastic and viscous cases. (d) Lumped-parameter unit-cell model of a monopolar AM. (e) Metadamping in the monopolar and dipolar metamaterials only for the viscous case.

survey. Note that all the electromechanical PVEH structures presented in this survey are investigated at a structural level, i.e., subject to sizing, forcing, and relevant boundary conditions.

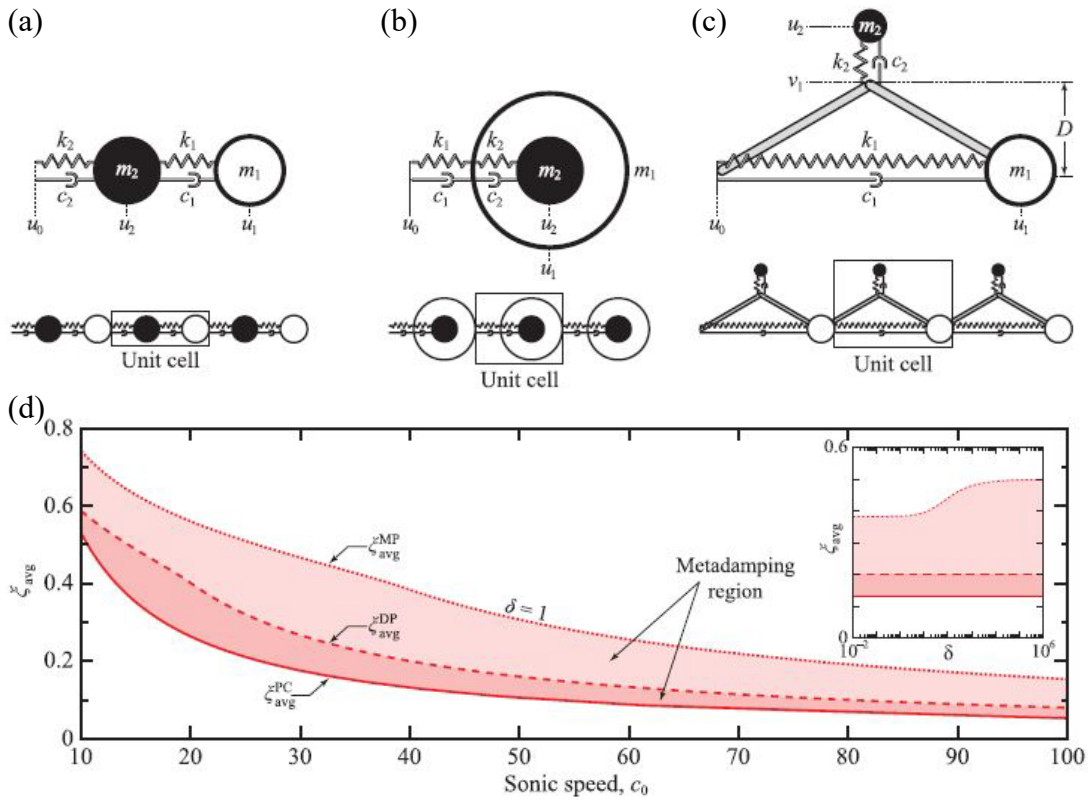


Figure 2.18: [80] Lumped-parameter unit-cell models of (a) phononic crystal (PnC), (b) dipolar acoustic metamaterial (AM), and (c) monopolar AM. (d) Metadamping in the monopolar and dipolar metamaterials.

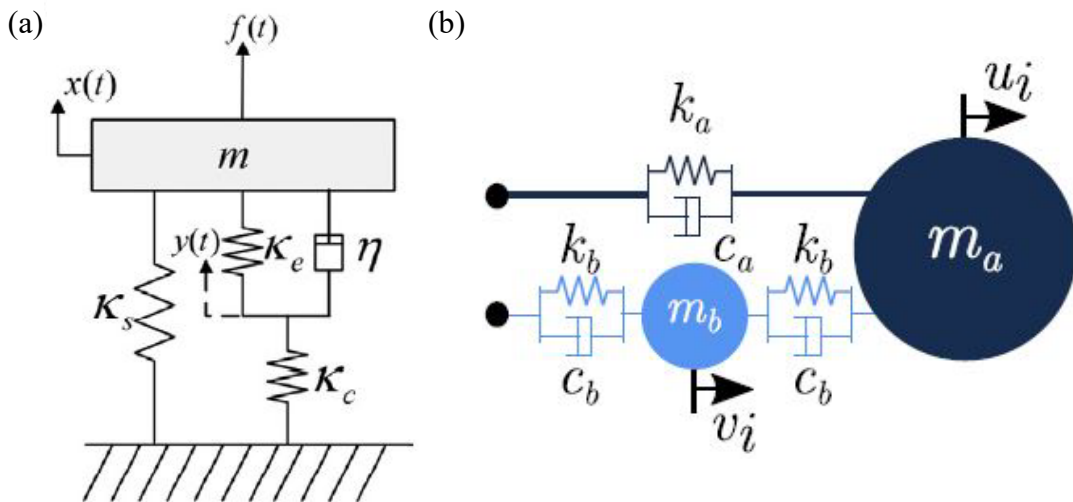


Figure 2.19: [116, 117] (a) A linear oscillator consisting of a negative stiffness element and (b) a novel hybrid metamaterial configuration that integrates the attributes of phononic crystals (PnCs) and acoustic metamaterials (AMs).

Chapter 3

Wave Propagation in One-Dimensional Phononic Crystals and Piezoelectric Phononic Crystals

3.1 Introduction

In order to present a better understanding of the wave-propagation and dissipation characteristics of one-dimensional non-piezoelectric and piezoelectric periodic media in a comprehensive comparative manner, distinctive configurations of diverse periodic media are considered and elaborated in this chapter. Each case/configuration is complimented with a detailed schematic shown in the figures. The introductory theoretical framework for the analysis of the propagation of elastic waves through different configurations of linear elastic periodic media under free vibration and with and without energy harvesters is laid out by employing a generalized Bloch's theorem for plane waves followed by a state-space transformation to set up an eigenvalue problem. In doing so, the dispersion relations are derived and the mathematical definition of the solution, i.e., the eigenvalues, is given. Consequently, the mathematical definition of the two most crucial characteristics, when it comes to behaviour of periodic media, are extracted: wave-propagation or dispersion characteristic of wavenumber-dependent damped frequencies and dissipation characteristic of damping ratios. By considering a particular periodic media and its piezoelectric variant under free vibration, independent of structural size, i.e., considering an infinite media, and independent of boundary conditions, the intrinsic characteristics of the media can be obtained/computed and comparatively analysed as stated in the introductory chapter. In the case of piezoelectric periodic media being analysed under the aforementioned conditions, any difference from the

normal version can only be attributed to the electrical parameters of the shunting mechanism incorporated in the energy harvesters such as piezoelectric patches.

The layout of the chapter is as follows. As phononic crystals (PnCs) are the most fundamental type of periodic media that have been considered intensively from a research perspective, monoatomic and diatomic PnCs with and without energy harvesters are discussed; each of the aforementioned cases are considered with and without grounding. With regards to the energy harvesters, cases of shunt circuit without inductor and with inductor are both considered. Locally resonant metamaterials (LRMs) and locally resonant piezoelectric metamaterials (LRPMs), in similar configurations as the PnCs and piezoelectric PnCs, respectively, are also considered. Finally, inertially amplified locally resonant metamaterials (IALRMs), that are gaining a lot of attention due to their exploitable peculiar properties, are examined at the end along with their piezoelectric counterparts (inertially amplified locally resonant piezoelectric metamaterials or IALRPMs) in similar configuration as the PnCs and piezoelectric PnCs. For all the configurations examined, the most general case of fully damped is considered as in real world applications, an undamped system is unrealistic to realize. For all the cases, the damped frequencies and damping ratios are presented in a comparative format in a custom results section.

3.2 Overview of monoatomic phononic crystals

In this section, the application of generalized Bloch's theorem to different configurations of monoatomic phononic crystals (MPnCs) is elaborated as an overview to familiarise the reader with the methodology of the application to monoatomic periodic media. A periodic media is basically a tessellation and arrangement of certain unique basic (unit) cells in a periodic fashion, and the resulting material is termed as a lattice. From the eigenvalue solution, the mathematical definitions of certain core parameters such as wavenumber-dependent damped frequency, resonant frequency, damping ratio, phase velocity, and group velocity are extracted.

3.2.1 Without grounding

Figure 3.1 presents the schematics of an MPnC chain under free vibration without any grounding and the associated unit cell as lumped-parameter models.

In figure 3.1, n is used to identify and refer to the central unit cell under consideration and can be any non-zero positive integer in a finite lattice; $(n + 1)$ and $(n - 1)$ are used to identify and refer to the unit cells on the right and left of the central (n^{th}) unit cell, respectively; m

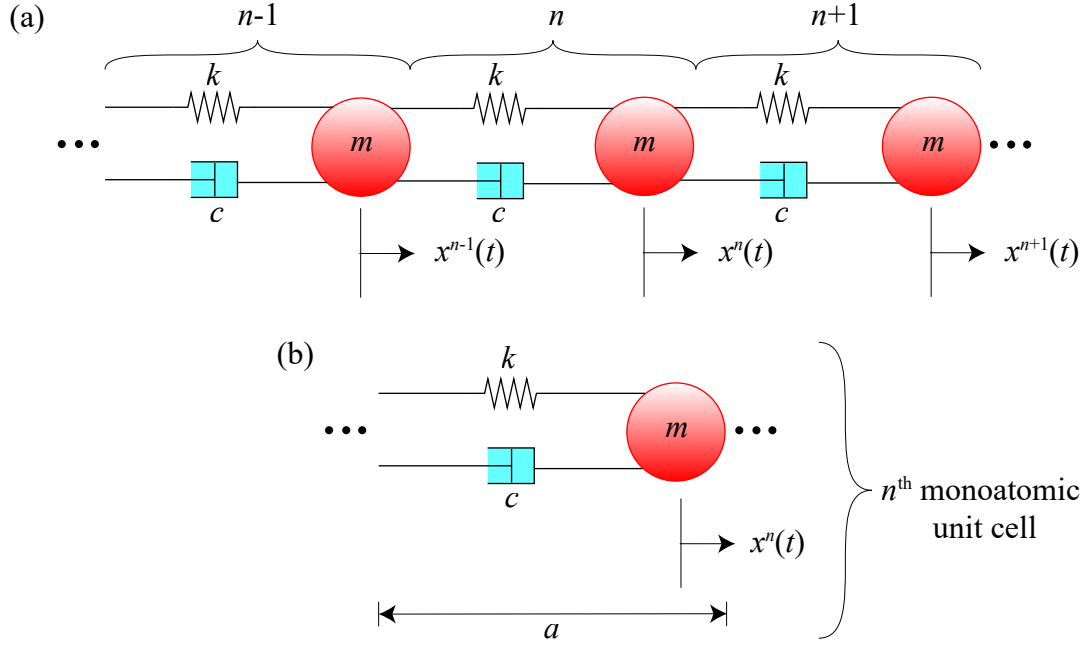


Figure 3.1: Schematic of (a) a monoatomic phononic-crystal (MPnC) chain without grounding and (b) the associated unit cell.

denotes the mass; k is the stiffness coefficient of the springs; c is the damping coefficient of the viscous damping dashpots; $x^n(t)$ and $x^{n\pm 1}(t)$ are the displacements of the masses, with respect to time t , in the n^{th} , $(n+1)^{\text{th}}$, and $(n-1)^{\text{th}}$ unit cells, respectively; and a is the length of a unit-cell or lattice spacing.

The forces on the mass in the central unit cell, i.e., the n^{th} unit cell shown in figure 3.1(b), under free vibration can be aggregated, and the governing equation pertaining to the central unit cell can be written as

$$m\ddot{x}^n + c(2\dot{x}^n - \dot{x}^{n-1} - \dot{x}^{n+1}) + k(2x^n - x^{n-1} - x^{n+1}) = 0, \quad (3.1)$$

where the number of overhead dots indicates the order of derivative with respect to time.

As per Bloch's theorem, the plane-wave solution [119] for the displacement of a mass in a periodic unit cell is given by

$$x^{n+g}(r, \kappa; t) = \tilde{x}(t)e^{i\kappa(n+g)a}, \quad (3.2)$$

where x is the displacement; $g \in [-\infty, \infty]$ is an integer used to locate and refer to any unit cell relative to the central unit cell under consideration, i.e., the n^{th} unit cell shown in figure 3.1; r is the one-dimensional position vector of the n^{th} unit cell given by $r = na$; κ is wavenumber; \tilde{x} is the displacement (complex-wave) amplitude in the wavenumber domain; and $i = \sqrt{-1}$

is the imaginary unit. For the central unit cell under consideration, $g = 0$ (n^{th} unit cell), and for the unit cells towards the left and right of the central unit cell, $g = -1$, and $g = +1$, respectively; i.e., they are the $(n-1)^{\text{th}}$ and $(n+1)^{\text{th}}$ unit cells. Substituting equation (3.2) in equation (3.1) yields a homogeneous equation for the displacement amplitude, \tilde{x} , which can be written as

$$m\ddot{\tilde{x}} + c(2 - e^{-i\kappa a} - e^{i\kappa a})\dot{\tilde{x}} + k(2 - e^{-i\kappa a} - e^{i\kappa a})\tilde{x} = 0. \quad (3.3)$$

Equation (3.3) can now be converted into a first order equation, through a state-space transformation [119–121] of the form

$$\mathbf{A}\dot{\mathbf{Y}} + \mathbf{B}\mathbf{Y} = \mathbf{0}, \quad (3.4)$$

where

$$\mathbf{A} = \begin{pmatrix} 0 & 1 \\ m & c(2 - e^{-i\kappa a} - e^{i\kappa a}) \end{pmatrix}; \quad \mathbf{B} = \begin{pmatrix} -1 & 0 \\ 0 & k(2 - e^{-i\kappa a} - e^{i\kappa a}) \end{pmatrix};$$

and $\mathbf{Y} = \begin{pmatrix} \dot{\tilde{x}} \\ \tilde{x} \end{pmatrix}$. (3.5)

For equation (3.4), a solution of the form $\mathbf{Y} = \tilde{\mathbf{Y}}_{\lambda} e^{\lambda t}$ is assumed, where $\tilde{\mathbf{Y}}_{\lambda}$ is a complex-amplitude state-space vector corresponding to eigenvalue λ . The dispersion relation and, consequently, the wave-propagation and dissipation characteristics can now be obtained by implementing the solution in equation (3.4) and solving the resulting eigenvalue problem given by

$$|\mathbf{A}^{-1}\mathbf{B} + \lambda\mathbf{I}| = 0. \quad (3.6)$$

Expanding equation (3.6) for this particular case yields a second-order equation in terms of λ , which, upon solving, gives two complex roots appearing as a complex-conjugate pair. The complex solution for the eigenvalue problem at a given value of κ can be expressed as [29]

$$\lambda(\kappa) = -\zeta(\kappa)\omega_r(\kappa) \pm i\omega_d(\kappa) = -\zeta(\kappa)\omega_r(\kappa) \pm i\omega_r(\kappa)\sqrt{1 - \zeta(\kappa)^2}. \quad (3.7)$$

In the expression above, ω_r is the wavenumber-dependent resonant frequency defined as

$$\omega_r(\kappa) = \text{Abs}[\lambda(\kappa)]; \quad (3.8)$$

ω_d is the wavenumber-dependent damped frequency defined as

$$\omega_d(\kappa) = \text{Im}[\lambda(\kappa)]; \quad (3.9)$$

and $\zeta(\kappa)$ is the wavenumber-dependent damping ratio defined as

$$\zeta(\kappa) = -\frac{\text{Re}[\lambda(\kappa)]}{\text{Abs}[\lambda(\kappa)]}. \quad (3.10)$$

The phase velocity and the group velocity can also be obtained by using the definitions

$$C_{\text{ph}} = \frac{\omega_{\text{d}}}{\kappa} \text{ and } C_{\text{g}} = \frac{\partial \omega_{\text{d}}}{\partial \kappa}, \quad (3.11)$$

respectively.

3.2.2 With grounding

Figure 3.2 presents the schematics of an MPnC chain under free vibration with grounding and the associated unit cell as lumped-parameter models. This case is representative of a scenario where the PnC chain is attached to bars; i.e., each unit cell is attached to a bar. For the sake of simplification, the bars are simply modelled as damped oscillators.

The forces on the mass in the central unit cell, i.e., the n^{th} unit cell shown in figure 3.2(b), under free vibration can be aggregated, and the governing equation pertaining to the central unit cell can be written as

$$m\ddot{x}^n + c_1(2\dot{x}^n - \dot{x}^{n-1} - \dot{x}^{n+1}) + c_2\dot{x}^n + k_1(2x^n - x^{n-1} - x^{n+1}) + k_2x^n = 0. \quad (3.12)$$

Substituting equation (3.2) in equation (3.12) yields a homogeneous equation for the displacement amplitude, \tilde{x} , which can be written as

$$m\ddot{\tilde{x}} + (c_1(2 - e^{-i\kappa a} - e^{i\kappa a}) + c_2)\dot{\tilde{x}} + (k_1(2 - e^{-i\kappa a} - e^{i\kappa a}) + k_2)\tilde{x} = 0. \quad (3.13)$$

The dispersion relation for this particular case can now be formulated by subjecting equation (3.13) to a state-space transformation of the form given in equation (3.4), where

$$\mathbf{A} = \begin{pmatrix} 0 & 1 \\ m & c_1(2 - e^{-i\kappa a} - e^{i\kappa a}) + c_2 \end{pmatrix};$$

$$\mathbf{B} = \begin{pmatrix} -1 & 0 \\ 0 & k_1(2 - e^{-i\kappa a} - e^{i\kappa a}) + k_2 \end{pmatrix}; \text{ and } \mathbf{Y} = \begin{pmatrix} \dot{\tilde{x}} \\ \tilde{x} \end{pmatrix}, \quad (3.14)$$

implementing a solution of the form $\mathbf{Y} = \tilde{\mathbf{Y}}_{\lambda} e^{\lambda t}$, and solving the resulting eigenvalue problem of the form given in equation (3.6). Expanding equation (3.6) for this particular case yields a

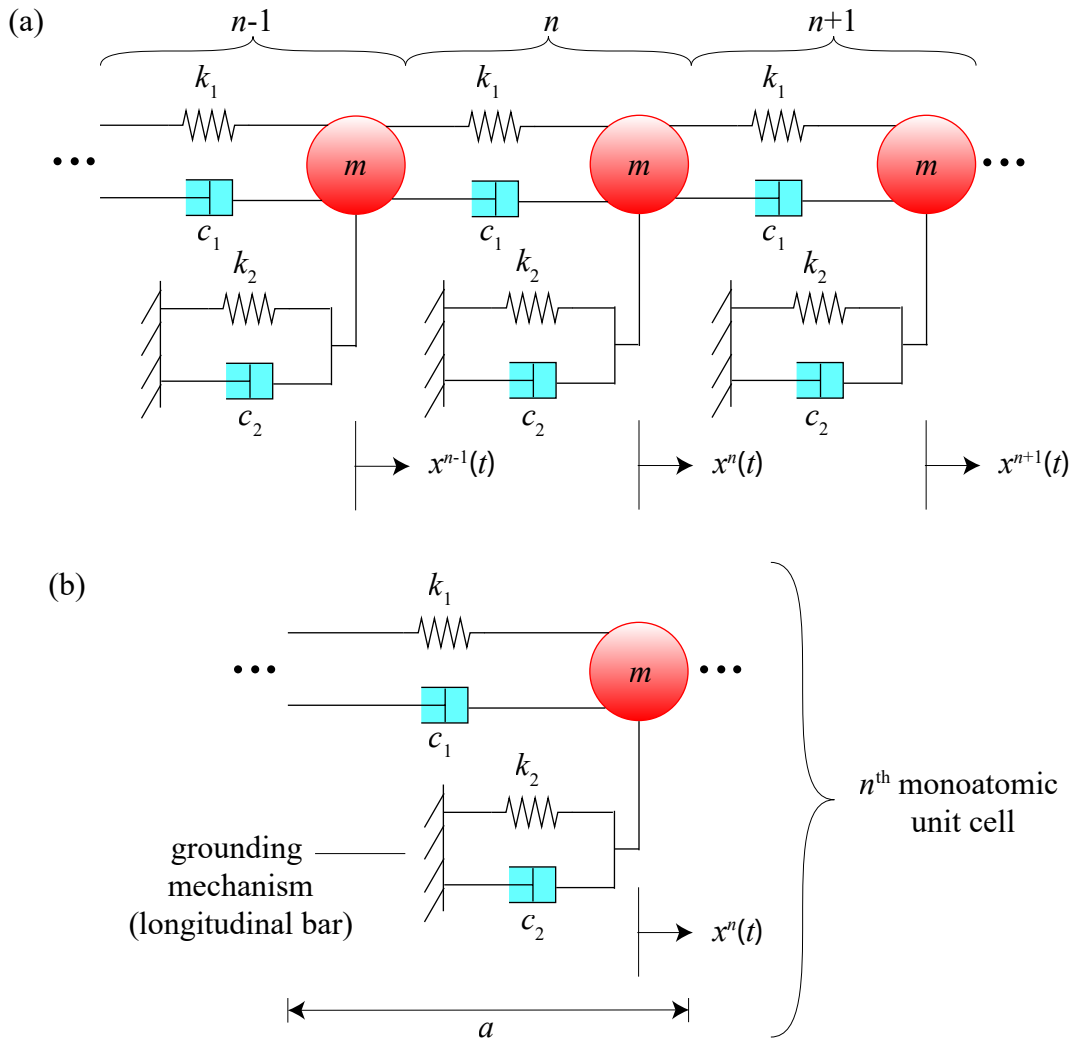


Figure 3.2: Schematic of (a) a monoatomic-phononic-crystal (MPnC) chain with grounding and (b) the associated unit cell.

second-order equation in terms of λ , which, upon solving, gives two complex roots appearing as a complex-conjugate pair.

3.3 Monoatomic piezoelectric phononic crystals

This section expounds upon the application of generalized Bloch’s theorem to different configurations of monoatomic piezoelectric phononic crystals (MPPnCs). The piezoelectric elements considered in the analysis are comprised of a shunt circuit which are either purely resistive or consist of an inductor. The configurations addressed in this section are, essentially, the piezoelectric counterparts of the configurations addressed in section 3.2.

3.3.1 Without grounding

Figure 3.3 presents the schematics of an MPPnC chain under free vibration without any grounding and the associated unit cell as lumped-parameter models. In figure 3.3, $v^n(t)$ and $v^{n\pm 1}(t)$ are the voltages, with respect to time, generated in the n^{th} , $(n+1)^{\text{th}}$, and $(n-1)^{\text{th}}$ unit cells, respectively, and θ is the electromechanical coupling of the shunted piezoelectric elements. The piezoelectric elements are placed between the masses.

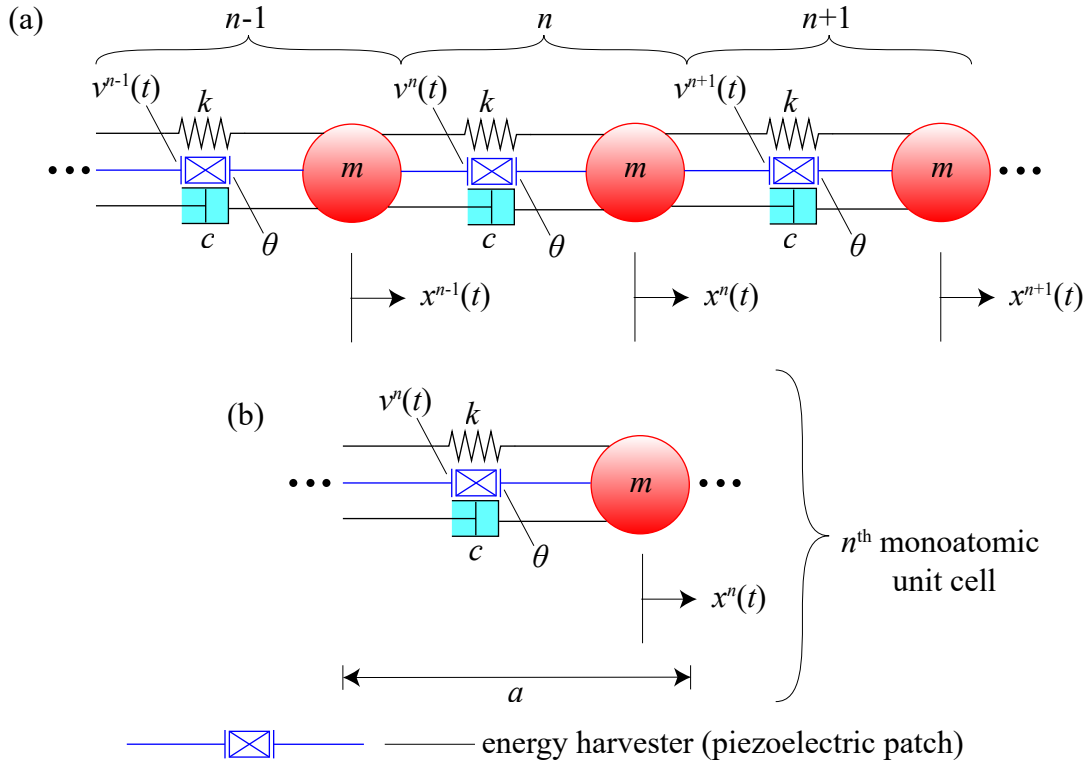


Figure 3.3: Schematic of (a) a monoatomic piezoelectric phononic-crystal (MPPnC) chain without grounding and (b) the associated unit cell.

Shunt circuit without an inductor

The governing electromechanical equations pertaining to the n^{th} unit cell under free vibration consisting of a piezoelectric element with a shunt circuit lacking an inductor [73] can be written as

$$m\ddot{x}^n + c(2\dot{x}^n - \dot{x}^{n-1} - \dot{x}^{n+1}) + k(2x^n - x^{n-1} - x^{n+1}) + \theta v^n - \theta v^{n+1} = 0, \quad (3.15)$$

$$-\theta(\dot{x}^n - \dot{x}^{n-1}) + C_p \dot{v}^n + \frac{1}{R} v^n = 0, \quad (3.16)$$

where C_p and R are the capacitance and resistance of the shunt circuit, respectively.

Similar to the displacement field (equation (3.2)), the voltage field can be mathematically treated with a plane-wave solution given by a generalized Bloch's theorem; hence, the plane-wave solution for the voltage generated in a piezoelectric element in a periodic unit cell can be written as

$$v^{n+g}(r, \kappa; t) = \tilde{v}(t)e^{i\kappa(n+g)a}, \quad (3.17)$$

where \tilde{v} is the voltage amplitude. Substituting equations (3.2) and (3.17) in equations (3.15) and (3.16) yields the following Bloch-transformed homogeneous equations for the displacement amplitude \tilde{x} and the voltage amplitude \tilde{v} :

$$m\ddot{\tilde{x}} + c(2 - e^{-i\kappa a} - e^{i\kappa a})\dot{\tilde{x}} + k(2 - e^{-i\kappa a} - e^{i\kappa a})\tilde{x} + (\theta - \theta e^{i\kappa a})\tilde{v} = 0, \quad (3.18)$$

$$(-\theta + \theta e^{-i\kappa a})\dot{\tilde{x}} + C_p\dot{\tilde{v}} + \frac{1}{R}\tilde{v} = 0. \quad (3.19)$$

The dispersion relation for this particular case can now be formulated by subjecting equations (3.18) and (3.19) to a state-space transformation of the form given in equation (3.4), where

$$\mathbf{A} = \begin{pmatrix} 0 & 1 & 0 \\ m & c(2 - e^{-i\kappa a} - e^{i\kappa a}) & 0 \\ 0 & -\theta + \theta e^{-i\kappa a} & C_p \end{pmatrix};$$

$$\mathbf{B} = \begin{pmatrix} -1 & 0 & 0 \\ 0 & k(2 - e^{-i\kappa a} - e^{i\kappa a}) & \theta - \theta e^{i\kappa a} \\ 0 & 0 & \frac{1}{R} \end{pmatrix}; \text{ and } \mathbf{Y} = \begin{pmatrix} \dot{\tilde{x}} \\ \tilde{x} \\ \tilde{v} \end{pmatrix}, \quad (3.20)$$

implementing a solution of the form $\mathbf{Y} = \tilde{\mathbf{Y}}_\lambda e^{\lambda t}$, and solving the resulting eigenvalue problem of the form given in equation (3.6). Expanding equation (3.6) for this particular case yields a third-order equation in terms of λ , which, upon solving, gives a real root and two complex roots appearing as a complex-conjugate pair.

Shunt circuit with an inductor

The governing electromechanical equations pertaining to the n^{th} unit cell under free vibration consisting of a piezoelectric element with a shunt circuit including an inductor can be written

as

$$m\ddot{x}^n + c(2\dot{x}^n - \dot{x}^{n-1} - \dot{x}^{n+1}) + k(2x^n - x^{n-1} - x^{n+1}) + \theta v^n - \theta v^{n+1} = 0, \quad (3.21)$$

$$-\theta(\dot{x}^n - \dot{x}^{n-1}) + C_p \dot{v}^n + \frac{1}{R} \dot{v}^n + \frac{1}{L} v^n = 0, \quad (3.22)$$

where L is the inductance of the shunt circuit.

Substituting equations (3.2) and (3.17) in equations (3.15) and (3.16) produces the following Bloch-transformed homogeneous equations for the displacement amplitude \tilde{x} and the voltage amplitude \tilde{v} :

$$m\ddot{\tilde{x}} + c(2 - e^{-i\kappa a} - e^{i\kappa a})\dot{\tilde{x}} + k(2 - e^{-i\kappa a} - e^{i\kappa a})\tilde{x} + (\theta - \theta e^{i\kappa a})\tilde{v} = 0, \quad (3.23)$$

$$(-\theta + \theta e^{-i\kappa a})\dot{\tilde{x}} + C_p \dot{\tilde{v}} + \frac{1}{R} \dot{\tilde{v}} + \frac{1}{L} \tilde{v} = 0. \quad (3.24)$$

Equations (3.23) and (3.24) can be written in matrix form as

$$\mathbf{Z}_1 \ddot{\tilde{\mathbf{E}}} + \mathbf{Z}_2 \dot{\tilde{\mathbf{E}}} + \mathbf{Z}_3 \tilde{\mathbf{E}} = \mathbf{0}, \quad (3.25)$$

where

$$\mathbf{Z}_1 = \begin{pmatrix} m & 0 \\ -\theta + \theta e^{-i\kappa a} & C_p \end{pmatrix}; \quad \mathbf{Z}_2 = \begin{pmatrix} c(2 - e^{i\kappa a} - e^{-i\kappa a}) & 0 \\ 0 & \frac{1}{R} \end{pmatrix};$$

$$\mathbf{Z}_3 = \begin{pmatrix} k(2 - e^{i\kappa a} - e^{-i\kappa a}) & \theta - \theta e^{i\kappa a} \\ 0 & \frac{1}{L} \end{pmatrix}; \quad \text{and } \tilde{\mathbf{E}} = \begin{pmatrix} \tilde{x} \\ \tilde{v} \end{pmatrix}. \quad (3.26)$$

The dispersion relation for this particular case can now be formulated by subjecting equation (3.25) to a state-space transformation of the form given in equation (3.4), where

$$\mathbf{A} = \begin{pmatrix} \mathbf{0} & \mathbf{I} \\ \mathbf{Z}_1 & \mathbf{Z}_2 \end{pmatrix}; \quad \mathbf{B} = \begin{pmatrix} -\mathbf{I} & \mathbf{0} \\ \mathbf{0} & \mathbf{Z}_3 \end{pmatrix}; \quad \text{and } \mathbf{Y} = \begin{pmatrix} \dot{\tilde{\mathbf{E}}} \\ \tilde{\mathbf{E}} \end{pmatrix}, \quad (3.27)$$

implementing a solution of the form $\mathbf{Y} = \tilde{\mathbf{Y}}_\lambda e^{\lambda t}$, and solving the resulting eigenvalue problem of the form given in equation (3.6). Expanding equation (3.6) for this particular case yields a fourth-order equation in terms of λ , which, upon solving, yields two real roots and two complex roots appearing as a complex-conjugate pair.

3.3.2 With grounding

Figure 3.4 presents the schematics of an MPPnC chain under free vibration with grounding and the associated unit cell as lumped-parameter models. In figure 3.4, the subscripts 1 and 2 distinguish between the parameters corresponding to the piezoelectric elements that are part of the baseline and the piezoelectric elements that are attached to the grounding mechanism simply modelled as a damped oscillator.

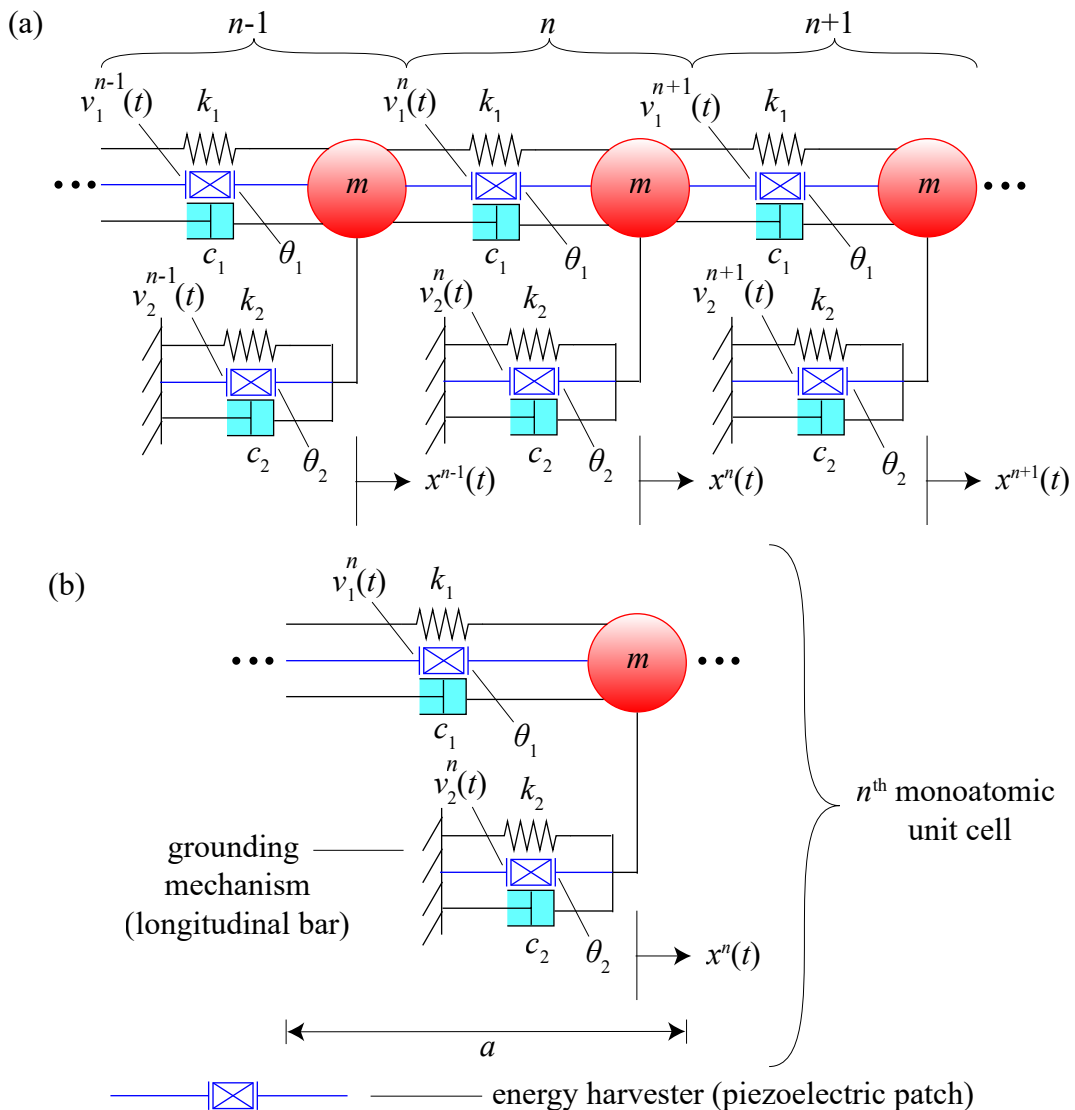


Figure 3.4: Schematic of (a) a monoatomic piezoelectric phononic-crystal (MPPnC) chain with grounding and (b) the associated unit cell.

Shunt circuit without an inductor

The governing electromechanical equations pertaining to the n^{th} unit cell under free vibration consisting of a piezoelectric element with a shunt circuit lacking an inductor can be written as

$$m\dot{x}^n + c_1(2\dot{x}^n - \dot{x}^{n-1} - \dot{x}^{n+1}) + c_2\dot{x}^n + k_1(2x^n - x^{n-1} - x^{n+1}) + k_2x^n + \theta_1 v_1^n + \theta_2 v_2^n - \theta_1 v_1^{n+1} = 0, \quad (3.28)$$

$$-\theta_1(\dot{x}^n - \dot{x}^{n-1}) + C_{p1}\dot{v}_1^n + \frac{1}{R_1}v_1^n = 0, \quad (3.29)$$

$$-\theta_2\dot{x}^n + C_{p2}\dot{v}_2^n + \frac{1}{R_2}v_2^n = 0. \quad (3.30)$$

The plane-wave solution for the voltages generated in a periodic unit cell with multiple voltage outputs can be written as

$$v_l^{n+g}(r, \kappa; t) = \hat{v}_l(t)e^{i\kappa(n+g)a}, \quad (3.31)$$

where $l = 1, 2$ is an index corresponding to the voltages generated in the two piezoelectric elements in the monoatomic unit cell. Substituting equations (3.2) and (3.31) in equations (3.28) and (3.29) yields the following Bloch-transformed homogeneous equations for the displacement amplitude \tilde{x} and the voltage amplitudes \tilde{v}_1 and \tilde{v}_2 :

$$m\ddot{\tilde{x}} + (c_1(2 - e^{-i\kappa a} - e^{i\kappa a}) + c_2)\dot{\tilde{x}} + (k_1(2 - e^{-i\kappa a} - e^{i\kappa a}) + k_2)\tilde{x} + (\theta_1 - \theta_1 e^{i\kappa a})\tilde{v}_1 + \theta_2\tilde{v}_2 = 0, \quad (3.32)$$

$$(-\theta_1 + \theta_1 e^{-i\kappa a})\dot{\tilde{x}} + C_{p1}\dot{\tilde{v}}_1 + \frac{1}{R_1}\tilde{v}_1 = 0, \quad (3.33)$$

$$-\theta_2\dot{\tilde{x}} + C_{p2}\dot{\tilde{v}}_2 + \frac{1}{R_2}\tilde{v}_2 = 0. \quad (3.34)$$

The dispersion relation for this particular case can now be formulated by subjecting equations (3.32), (3.33), and (3.34) to a state-space transformation of the form given in equation (3.4),

where

$$\mathbf{A} = \begin{pmatrix} 0 & 1 & 0 & 0 \\ m & c_1(2 - e^{-i\kappa a} - e^{i\kappa a}) + c_2 & 0 & 0 \\ 0 & -\theta_1 + \theta_1 e^{-i\kappa a} & C_{p1} & 0 \\ 0 & -\theta_2 & 0 & C_{p2} \end{pmatrix};$$

$$\mathbf{B} = \begin{pmatrix} -1 & 0 & 0 & 0 \\ 0 & k_1(2 - e^{-i\kappa a} - e^{i\kappa a}) + k_2 & \theta_1 - \theta_1 e^{i\kappa a} & \theta_2 \\ 0 & 0 & \frac{1}{R_1} & 0 \\ 0 & 0 & 0 & \frac{1}{R_2} \end{pmatrix}; \text{ and } \mathbf{Y} = \begin{pmatrix} \dot{\tilde{x}} \\ \tilde{x} \\ \tilde{v}_1 \\ \tilde{v}_2 \end{pmatrix}. \quad (3.35)$$

implementing a solution of the form $\mathbf{Y} = \tilde{\mathbf{Y}}_\lambda e^{\lambda t}$, and solving the resulting eigenvalue problem of the form given in equation (3.6). Expanding equation (3.6) for this particular case yields a fourth-order equation in terms of λ , which, upon solving, yields two real roots and two complex roots appearing as a complex-conjugate pair.

Shunt circuit with an inductor

The governing electromechanical equations pertaining to the n^{th} unit cell under free vibration consisting of a piezoelectric element with a shunt circuit including an inductor can be formulated as

$$m\dot{x}^n + c_1(2\dot{x}^n - \dot{x}^{n-1} - \dot{x}^{n+1}) + c_2\dot{x}^n + k_1(2x^n - x^{n-1} - x^{n+1}) + k_2x^n + \theta_1 v_1^n + \theta_2 v_2^n - \theta_1 v_1^{n+1} = 0, \quad (3.36)$$

$$-\theta_1(\dot{x}^n - \dot{x}^{n-1}) + C_{p1}\dot{v}_1^n + \frac{1}{R_1}v_1^n + \frac{1}{L_1}v_1^n = 0, \quad (3.37)$$

$$-\theta_2\dot{x}^n + C_{p2}\dot{v}_2^n + \frac{1}{R_2}v_2^n + \frac{1}{L_2}v_2^n = 0. \quad (3.38)$$

Substituting equations (3.2) and (3.31) in equations (3.28) and (3.29) yields the following Bloch-transformed homogeneous equations for the displacement amplitude \tilde{x} and the voltage

amplitudes \tilde{v}_1 and \tilde{v}_2 :

$$m\ddot{\tilde{x}} + (c_1(2 - e^{-i\kappa a} - e^{i\kappa a}) + c_2)\dot{\tilde{x}} + (k_1(2 - e^{-i\kappa a} - e^{i\kappa a}) + k_2)\tilde{x} + (\theta_1 - \theta_1 e^{i\kappa a})\tilde{v}_1 + \theta_2\tilde{v}_2 = 0, \quad (3.39)$$

$$(-\theta_1 + \theta_1 e^{-i\kappa a})\ddot{\tilde{x}} + C_{p1}\ddot{\tilde{v}}_1 + \frac{1}{R_1}\dot{\tilde{v}}_1 + \frac{1}{L_1}\tilde{v}_1 = 0, \quad (3.40)$$

$$-\theta_2\ddot{\tilde{x}} + C_{p2}\ddot{\tilde{v}}_2 + \frac{1}{R_2}\dot{\tilde{v}}_2 + \frac{1}{L_2}\tilde{v}_2 = 0. \quad (3.41)$$

Equations (3.39), (3.40), and (3.41) can be compactly written in a matrix form as

$$\mathbf{Z}_1\ddot{\tilde{\mathbf{E}}} + \mathbf{Z}_2\dot{\tilde{\mathbf{E}}} + \mathbf{Z}_3\tilde{\mathbf{E}} = \mathbf{0}, \quad (3.42)$$

where

$$\mathbf{Z}_1 = \begin{pmatrix} m & 0 & 0 \\ -\theta_1 + \theta_1 e^{-i\kappa a} & C_{p1} & 0 \\ -\theta_2 & 0 & C_{p2} \end{pmatrix};$$

$$\mathbf{Z}_2 = \begin{pmatrix} c_1(2 - e^{i\kappa a} - e^{-i\kappa a}) + c_2 & 0 & 0 \\ 0 & \frac{1}{R_1} & 0 \\ 0 & 0 & \frac{1}{R_2} \end{pmatrix};$$

$$\mathbf{Z}_3 = \begin{pmatrix} k_1(2 - e^{i\kappa a} - e^{-i\kappa a}) + k_2 & \theta_1 - \theta_1 e^{i\kappa a} & \theta_2 \\ 0 & \frac{1}{L_1} & 0 \\ 0 & 0 & \frac{1}{L_2} \end{pmatrix}; \text{ and } \tilde{\mathbf{E}} = \begin{pmatrix} \tilde{x} \\ \tilde{v}_1 \\ \tilde{v}_2 \end{pmatrix}. \quad (3.43)$$

The dispersion relation for this particular case can now be formulated by subjecting equation (3.42) to a state-space transformation of the form given in equation (3.4), where

$$\mathbf{A} = \begin{pmatrix} \mathbf{0} & \mathbf{I} \\ \mathbf{Z}_1 & \mathbf{Z}_2 \end{pmatrix}; \mathbf{B} = \begin{pmatrix} -\mathbf{I} & \mathbf{0} \\ \mathbf{0} & \mathbf{Z}_3 \end{pmatrix}; \text{ and } \mathbf{Y} = \begin{pmatrix} \dot{\tilde{\mathbf{E}}} \\ \tilde{\mathbf{E}} \end{pmatrix}, \quad (3.44)$$

implementing a solution of the form $\mathbf{Y} = \tilde{\mathbf{Y}}_\lambda e^{\lambda t}$, and solving the resulting eigenvalue problem of the form given in equation (3.6). Expanding equation (3.6) for this particular case yields a sixth-order equation in terms of λ , which, upon solving, yields four real roots and two complex roots appearing as a complex-conjugate pair.

3.4 Wave-propagation and dissipation characteristics of monoatomic phononic crystals and piezoelectric phononic crystals

This section presents the wave-propagation and dissipation characteristics of the different configurations of MPnCs and MPPnCs discussed so far in a graphical comparative format.

3.4.1 Without grounding

Table 3.1 details the parameters utilized in the computation of the dispersion (band structure) and damping-ratio characteristics of the MPnC and MPPnCs without grounding.

Table 3.1: Mechanical and dimensionless electrical parameters employed in the monoatomic phononic crystal (MPnC) and monoatomic piezoelectric phononic crystals (MPPnCs) without grounding.

Parameter	MPnC	MPPnC without an inductor	MPPnC with an inductor	Unit
a	1	1	1	m
m	0.0170	0.0170	0.0170	Kg
k	5×10^3	5×10^3	5×10^3	Nm^{-1}
c	2	2	2	Nsm^{-1}
α	—	0.1399	0.1399	—
β	—	—	0.3162	—
k_{coeff}^2	—	0.9714	0.9714	—

The unit-cell length or lattice spacing a is chosen to have the unit of metre to be consistent with S.I. units for all the parameters. As all the cases being solved are linear, the results will remain unchanged for any length scale as long as all the parameters have compatible units.

A large portion of the energy-harvesting community predominantly expresses certain electrical parameters in their non-dimensional form as evident in existing literature [87–89]. For consistency with the existing literature, the electrical parameters of the shunt circuits, namely, electromechanical coupling, resistance, capacitance, and inductance, are

non-dimensionalized and presented in table 3.1 as

$$\alpha = \bar{\omega} C_p R, \quad (3.45a)$$

$$\beta = \bar{\omega}^2 C_p L, \quad (3.45b)$$

$$k_{\text{coeff}}^2 = \frac{\theta^2}{k C_p}, \quad (3.45c)$$

where $\bar{\omega} = \sqrt{\frac{k}{m}}$.

Considering that the quantity that is of paramount interest and the subject of investigation in this work is the wavenumber-dependent (on account of propagation of elastic waves) damping ratio which is the rate of dissipation, it would be effective to quantify the damping ratio as a single value. This is realized, firstly, by cumulatively integrating the damping ratio over the irreducible Brillouin Zone (IBZ) as

$$\zeta^{\text{cum}}(\mu) = \int_0^\mu \zeta \, d\mu \quad (\mu \in [0, \pi]), \quad (3.46)$$

where μ is the dimensionless wavenumber defined as $\mu = \kappa a$, and, secondly, by obtaining the total value, upon complete integration over the BZ, defined as

$$\zeta^{\text{tot}} = \zeta^{\text{cum}}(\pi). \quad (3.47)$$

The quantity ζ^{tot} is the total area under the curve and represents an overall quantification of the damping capacity of a specific periodic unit cell.

Figure 3.5 depicts the normalized damped frequency, damping ratio, and cumulative damping ratio for the MPnC and MPPnCs without grounding in the irreducible Brillouin Zone (IBZ), i.e., for $\mu \in [0, \pi]$. The damped frequencies are normalized (non-dimensionalized) by using $\bar{\omega}$; i.e., the plots depict $\Omega = \frac{\omega_d}{\bar{\omega}}$. The shaded region in figure 3.5(a) illustrates the *transmission band* of the periodic media; i.e., waves can only propagate within this spectrum. The region above this is referred to as the *attenuation band*, which extends to ∞ ; i.e., waves cannot propagate within this spectrum. As the MPnC and MPPnCs give rise to only one complex-conjugate pair, they present only one mode/branch of frequency and damping ratio. The MPnC and MPPnCs are statically equivalent; i.e., they have the same long-wave speed¹,

¹Group velocity is given by the slope of frequency, ω (rad s⁻¹), vs. wavenumber, κ (rad m⁻¹); i.e., $C_g = \frac{\partial \omega}{\partial \kappa}$. As $\kappa = \frac{2\pi}{\lambda}$, where λ is wavelength, a small value of κ indicates a long/large wavelength; hence, the slope or the group velocity obtained at a very small value of κ is referred to as the long-wave speed; i.e., $C_g = \lim_{\kappa \rightarrow 0} \frac{\partial \omega}{\partial \kappa}$. While comparing the performance of different types of phononic media, it is crucial to ensure that they are statically equivalent to each other for a fair comparison. In the literature, the group velocity C_g is used as a

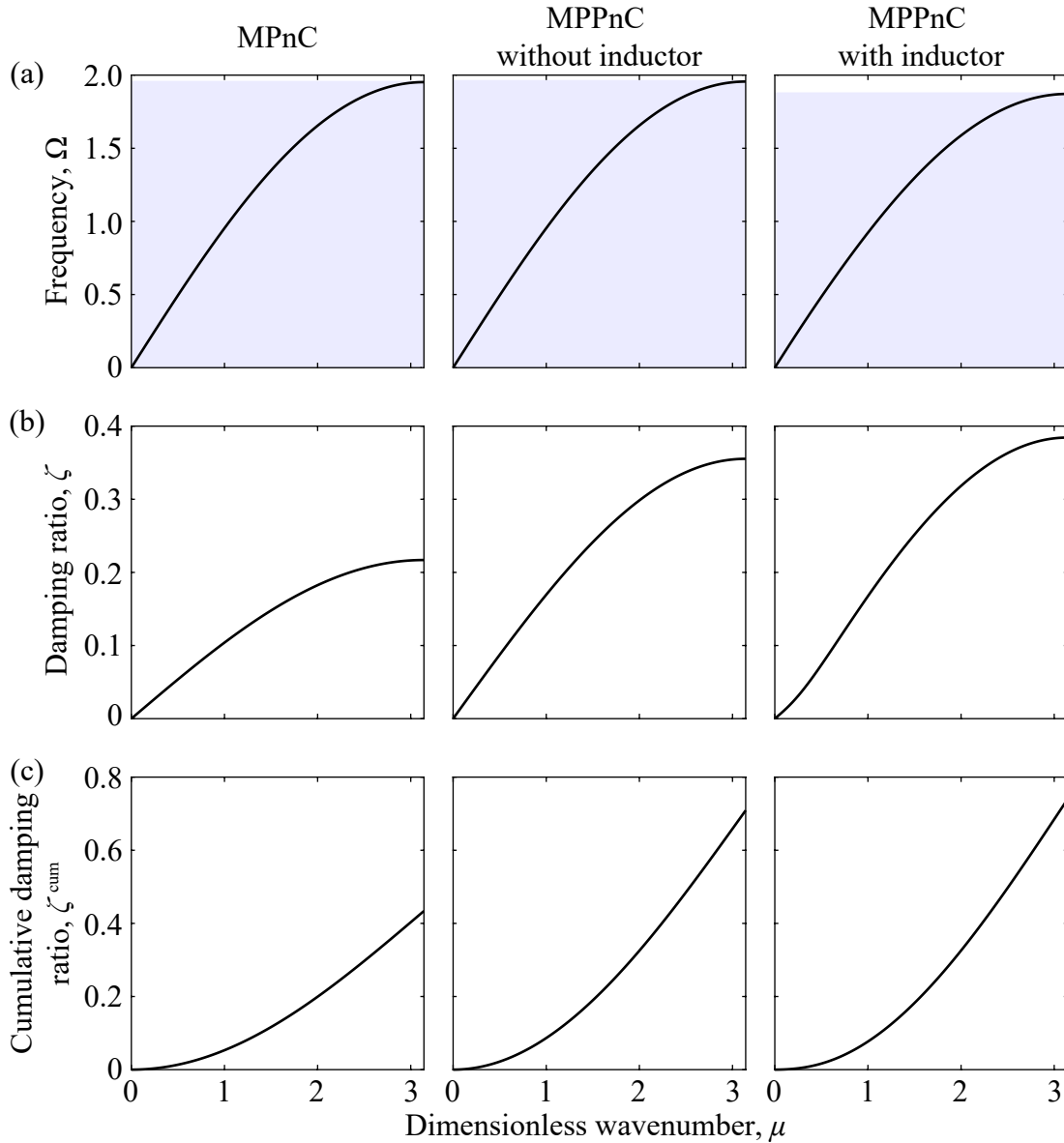


Figure 3.5: (a) Normalized-damped-frequency band structure, (b) damping-ratio diagrams, and (c) cumulative-damping-ratio diagrams for the monoatomic phononic crystal (MPnC) and monoatomic piezoelectric phononic crystals (MPPnCs) without grounding.

which is basically the group velocity or the slope of the ω_d vs. κ curve at a very small value of κ . This ensures a fair comparison to be made. Fabricating a periodic media with piezoelectric elements does not alter its static equivalency as evident from figure 3.5(a). The MPPnC with an inductor depicts a small decrease in the frequency, Ω , towards the end of representation of the effective quasi-static stiffness of a periodic media and, consequently, to ensure static equivalency with other periodic media. Static equivalency is ensured by making sure that the group velocities of all the periodic media in the comparative analysis are equal.

the BZ, but overall, the frequency plots do not exhibit a significant difference in their trend. Contrarily, the damping ratio curves shown in figure 3.5(b) show a remarkable difference for approximately similar band structures; the MPPnCs show a significant increase in dissipation compared to the MPnC, and the MPPnC with an inductor shows the highest dissipation. Note that the increase in dissipation can only be attributed to the piezoelectric elements as the three periodic media have the same amount of raw (prescribed) damping given in table 3.1. Figure 3.5(c) illustrates the integrated (cumulative) values, ζ^{cum} , of the damping ratios. The MPPnCs present a significantly increased rate of ζ^{cum} in comparison to the MPnC. The value of ζ^{cum} at $\mu = \pi$ gives the total integrated value ζ^{tot} , which is the highest for the MPPnC with an inductor. Table 3.2 details the ζ^{tot} values for the three periodic media.

Table 3.2: Total values of damping ratios of the monoatomic PnC (MPnC) and monoatomic piezoelectric PnCs (MPPnCs) without grounding.

Parameter	MPnC	MPPnC without an inductor	MPPnC with an inductor	Unit
ζ^{tot}	0.4339	0.7091	0.7391	—

3.4.2 With grounding

Table 3.3 details the parameters utilized in the computation of the dispersion (band structure) and damping-ratio characteristics of the MPnC and MPPnCs with grounding.

Considering that there are two piezoelectric elements in this particular case, the electrical parameters of the shunt circuit are non-dimensionalized as

$$\alpha_l = \bar{\omega}_l C_{p_l} R_l, \quad (3.48a)$$

$$\beta_l = \bar{\omega}_l^2 C_{p_l} L_l, \quad (3.48b)$$

$$k_{\text{coeff}_l}^2 = \frac{\theta_l^2}{k_l C_{p_l}}, \quad (3.48c)$$

where $l = 1, 2$ is an index corresponding to the parameters of the two piezoelectric elements and the frequencies obtained using the two springs: $\bar{\omega}_1 = \sqrt{\frac{k_1}{m}}$ and $\bar{\omega}_2 = \sqrt{\frac{k_2}{m}}$.

Figure 3.6 depicts the normalized damped frequency, damping ratio, and cumulative damping ratio for the MPnC and MPPnCs with grounding in the irreducible BZ, i.e., for $\mu \in [0, \pi]$. The damped frequencies are normalized with respect to $\bar{\omega}_1$; i.e., the plots depict $\Omega = \frac{\omega_d}{\bar{\omega}_1}$. As the periodic media are grounded, the frequency curves do not originate from

Table 3.3: Mechanical and dimensionless electrical parameters employed in the monoatomic phononic crystal (MPnC) and monoatomic piezoelectric phononic crystals (MPPnCs) with grounding.

Parameter	MPnC	MPPnC without an inductor	MPPnC with an inductor	Unit
a	1	1	1	m
m	0.0170	0.0170	0.0170	Kg
k_1	3×10^4	3×10^4	3×10^4	Nm ⁻¹
k_2	1.5000×10^4	1.5000×10^4	1.5000×10^4	Nm ⁻¹
c_1	0.2180	0.2180	0.2180	Nsm ⁻¹
c_2	0.2180	0.2180	0.2180	Nsm ⁻¹
α_1	—	0.3427	0.3427	—
α_2	—	0.2423	0.2423	—
β_1	—	—	0.5691	—
β_2	—	—	0.2846	—
$k_{\text{coeff}_1}^2$	—	0.1619	0.1619	—
$k_{\text{coeff}_2}^2$	—	0.3238	0.3238	—

zero unlike the previous case where the periodic media have no grounding. The frequency plots do not exhibit a significant difference, but for approximately similar band structures, the damping ratio curves shown in figure 3.6(b) show a remarkable difference. The MPPnCs show a significant increase in dissipation compared to the MPnC, and the MPPnC with an inductor shows the highest dissipation. In figure 3.6(c), the MPPnCs present a significantly increased rate of ζ^{cum} in comparison to the MPnC. The value of ζ^{tot} is the highest for the MPPnC with an inductor. Table 3.4 details the ζ^{tot} values for the three periodic media.

Table 3.4: Total values of damping ratios of the monoatomic phononic crystal (MPnC) and monoatomic piezoelectric phononic crystals (MPPnCs) with grounding.

Parameter	MPnC	MPPnC without an inductor	MPPnC with an inductor	Unit
ζ^{tot}	0.0286	0.1546	0.1812	—

3.5 Overview of diatomic phononic crystals

In this section, the application of generalized Bloch's theorem to different configurations of diatomic phononic crystals (DPnCs) is elaborated as an overview to familiarise the reader

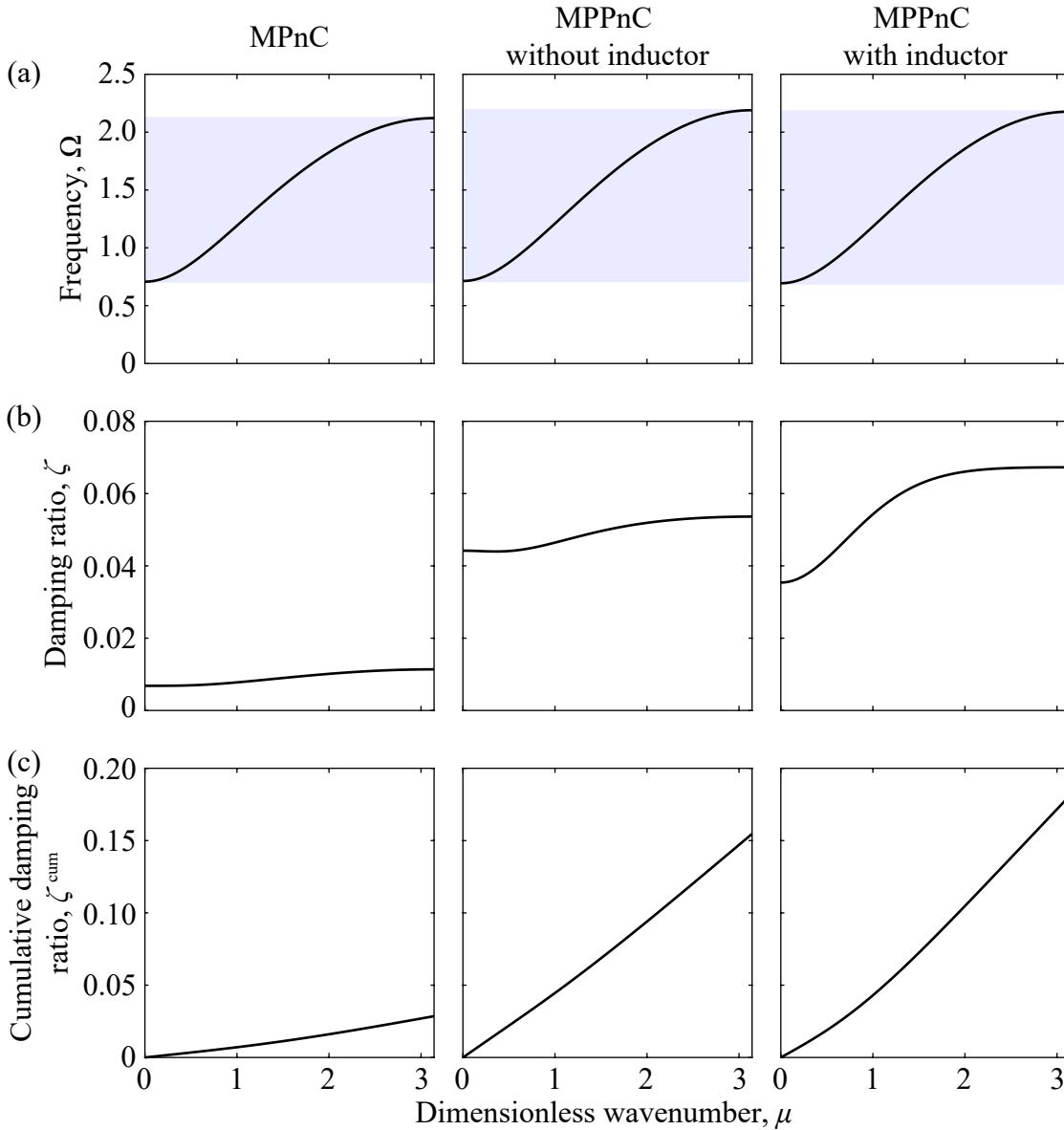


Figure 3.6: (a) Normalized-damped-frequency band structure, (b) damping-ratio diagrams, and (c) cumulative-damping-ratio diagrams for the monoatomic phononic crystal (MPnC) and monoatomic piezoelectric phononic crystals (MPPnCs) with grounding.

with the methodology of Bloch treatment of diatomic periodic media. From the eigenvalue solution for the diatomic case, the mathematical definitions of certain core parameters such as wavenumber-dependent damped frequency, resonant frequency, damping ratio, phase velocity, and group velocity are extracted.

3.5.1 Without grounding

Figure 3.7 presents the schematics of a DPnC chain under free vibration without any grounding and the associated unit cell as lumped-parameter models. A unit cell, depicted in figure 3.7(b), consists of two unequal masses: m_1 and m_2 .

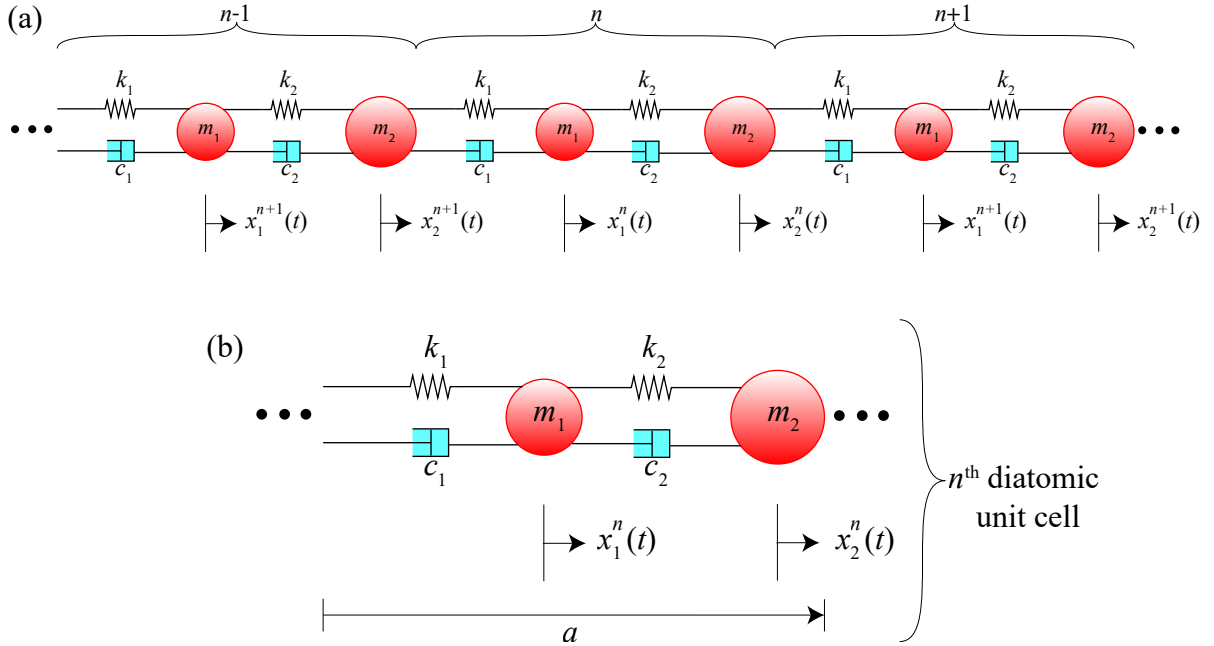


Figure 3.7: Schematic of (a) a diatomic phononic-crystal (DPnC) chain without grounding and (b) the associated unit cell.

The forces on the masses in the central unit cell, i.e., the n^{th} unit cell shown in figure 3.7(b), under free vibration can be aggregated, and the governing equations pertaining to the central unit cell can be written as

$$m_1 \ddot{x}_1^n + (c_1 + c_2) \dot{x}_1^n - c_2 \dot{x}_2^n - c_1 \dot{x}_2^{n-1} + (k_1 + k_2) x_1^n - k_2 x_2^n - k_1 x_2^{n-1} = 0, \quad (3.49)$$

$$m_2 \ddot{x}_2^n + (c_1 + c_2) \dot{x}_2^n - c_2 \dot{x}_1^n - c_1 \dot{x}_1^{n+1} + (k_1 + k_2) x_2^n - k_2 x_1^n - k_1 x_1^{n+1} = 0. \quad (3.50)$$

For the diatomic case, the Bloch theorem's plane-wave solution for the displacements of the masses in any periodic unit cell is given by

$$x_l^{n+g}(r, \kappa; t) = \tilde{x}_l(t) e^{i\kappa(n+g)a}, \quad (3.51)$$

where $l = 1, 2$ is an index corresponding to the two masses in a unit cell. Substituting equation (3.51) in equations (3.49) and (3.50) yields the following Bloch-transformed homogeneous

equations for the displacement amplitudes \tilde{x}_1 and \tilde{x}_2 :

$$m_1\ddot{\tilde{x}}_1 + (c_1 + c_2)\dot{\tilde{x}}_1 + (-c_2 - c_1e^{-i\kappa a})\dot{\tilde{x}}_2 + (k_1 + k_2)\tilde{x}_1 + (-k_2 - k_1e^{-i\kappa a})\tilde{x}_2 = 0, \quad (3.52)$$

$$m_2\ddot{\tilde{x}}_2 + (c_1 + c_2)\dot{\tilde{x}}_2 + (-c_2 - c_1e^{i\kappa a})\dot{\tilde{x}}_1 + (k_1 + k_2)\tilde{x}_2 + (-k_2 - k_1e^{i\kappa a})\tilde{x}_1 = 0. \quad (3.53)$$

Equations (3.52) and (3.53) can be assembled into a matrix form as

$$\mathbf{M}\ddot{\tilde{\mathbf{X}}} + \mathbf{C}(\kappa)\dot{\tilde{\mathbf{X}}} + \mathbf{K}(\kappa)\tilde{\mathbf{X}} = \mathbf{0}, \quad (3.54)$$

where

$$\tilde{\mathbf{X}} = \begin{pmatrix} \tilde{x}_1 \\ \tilde{x}_2 \end{pmatrix}; \mathbf{M} = \begin{pmatrix} m_1 & 0 \\ 0 & m_2 \end{pmatrix}; \mathbf{C}(\kappa) = \begin{pmatrix} c_1 + c_2 & -c_2 - c_1e^{-i\kappa a} \\ -c_2 - c_1e^{i\kappa a} & c_1 + c_2 \end{pmatrix};$$

$$\text{and } \mathbf{K}(\kappa) = \begin{pmatrix} k_1 + k_2 & -k_2 - k_1e^{-i\kappa a} \\ -k_2 - k_1e^{i\kappa a} & k_1 + k_2 \end{pmatrix}. \quad (3.55)$$

The dispersion relation can now be formulated by subjecting equation (3.54) to a state-space transformation of the form given in equation (3.4), where

$$\mathbf{A} = \begin{pmatrix} \mathbf{0} & \mathbf{I} \\ \mathbf{M} & \mathbf{C}(\kappa) \end{pmatrix}; \mathbf{B} = \begin{pmatrix} -\mathbf{I} & \mathbf{0} \\ \mathbf{0} & \mathbf{K}(\kappa) \end{pmatrix}; \text{ and } \mathbf{Y} = \begin{pmatrix} \dot{\tilde{\mathbf{X}}} \\ \tilde{\mathbf{X}} \end{pmatrix}. \quad (3.56)$$

For equation (3.4) corresponding to this case, a solution of the form $\mathbf{Y} = \tilde{\mathbf{Y}}_\lambda e^{\lambda t}$ is assumed, where $\tilde{\mathbf{Y}}_\lambda$ is a complex-amplitude state-space vector corresponding to eigenvalue λ . The dispersion relation and, consequently, the wave-propagation and dissipation characteristics can now be obtained by implementing the solution in equation (3.4) for this case and solving the resulting eigenvalue problem of the form given in equation (3.6). Expanding equation (3.6) for this particular case yields a fourth-order equation in terms of λ , which, upon solving, gives four complex roots appearing as two complex-conjugate pairs. The complex solution for the eigenvalue problem, for the diatomic case, at a given value of κ can be expressed as

$$\lambda_l(\kappa) = -\zeta_l(\kappa)\omega_{r_l}(\kappa) \pm i\omega_{d_l}(\kappa) = -\zeta_l(\kappa)\omega_{r_l}(\kappa) \pm i\omega_{r_l}(\kappa)\sqrt{1 - \zeta_l(\kappa)^2}, \quad (3.57)$$

where the subscript l identifies each complex-conjugate pair and, consequently, the mode or branch number. All diatomic cases, on account of the two complex-conjugate pairs, exhibit

two modes or branches: the acoustic (lower/first) branch given by $l = 1$ and the optical (higher/second) branch given by $l = 2$. In equation (3.57), ω_{r_l} is the wavenumber-dependent resonant frequency defined as

$$\omega_{r_l}(\kappa) = \text{Abs}[\lambda_l(\kappa)]; \quad (3.58)$$

ω_{d_l} is the wavenumber-dependent damped frequency defined as

$$\omega_{d_l}(\kappa) = \text{Im}[\lambda_l(\kappa)]; \quad (3.59)$$

and $\zeta_l(\kappa)$ is the wavenumber-dependent damping ratio defined as

$$\zeta_l(\kappa) = -\frac{\text{Re}[\lambda_l(\kappa)]}{\text{Abs}[\lambda_l(\kappa)]}. \quad (3.60)$$

The phase velocity and the group velocity can also be obtained by using the definitions

$$C_{\text{ph}_l} = \frac{\omega_{d_l}}{\kappa} \text{ and } C_{\text{g}_l} = \frac{\partial \omega_{d_l}}{\partial \kappa}, \quad (3.61)$$

respectively.

3.5.2 With grounding

Figure 3.8 presents the schematics of a DPnC chain under free vibration with grounding and the associated unit cell as lumped-parameter models. This case is representative of a scenario where the PnC chain is attached to bars; i.e., each mass in a unit cell is attached to a bar. For the sake of simplification, the bars are simply modelled as damped oscillators as shown in figure 3.8.

The forces on the masses in the central unit cell, i.e., the n^{th} unit cell shown in figure 3.8(b), under free vibration can be aggregated, and the governing equations pertaining to the central unit cell can be written as

$$m_1 \ddot{x}_1^n + (c_1 + c_2 + c_3) \dot{x}_1^n - c_2 \dot{x}_2^n - c_1 \dot{x}_2^{n-1} + (k_1 + k_2 + k_3) x_1^n - k_2 x_2^n - k_1 x_2^{n-1} = 0, \quad (3.62)$$

$$m_2 \ddot{x}_2^n + (c_1 + c_2 + c_4) \dot{x}_2^n - c_2 \dot{x}_1^n - c_1 \dot{x}_1^{n+1} + (k_1 + k_2 + k_4) x_2^n - k_2 x_1^n - k_1 x_1^{n+1} = 0. \quad (3.63)$$

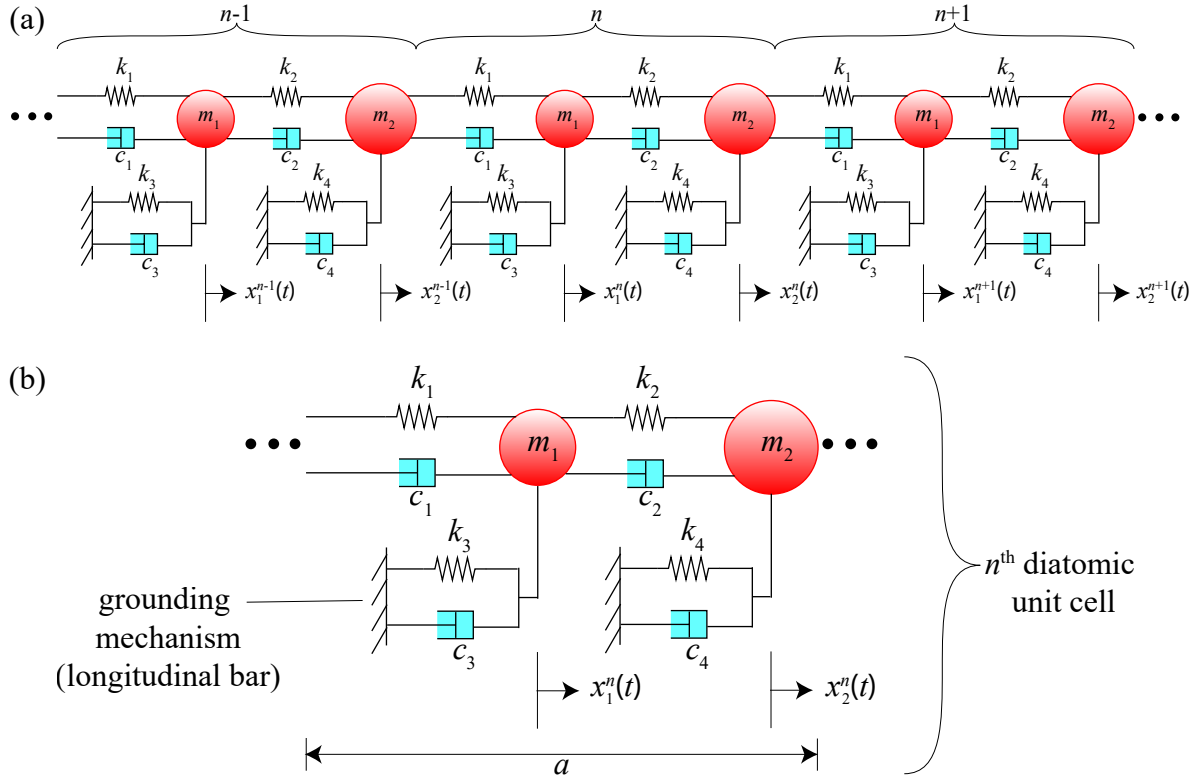


Figure 3.8: Schematic of (a) a diatomic phononic-crystal (DPnC) chain with grounding and (b) the associated unit cell.

Substituting equation (3.51) in equations (3.62) and (3.63) yields the following Bloch-transformed homogeneous equations for the displacement amplitudes \tilde{x}_1 and \tilde{x}_2 :

$$m_1 \ddot{\tilde{x}}_1 + (c_1 + c_2 + c_3) \dot{\tilde{x}}_1 + (-c_2 - c_1 e^{-i\kappa a}) \dot{\tilde{x}}_2 + (k_1 + k_2 + k_3) \tilde{x}_1 + (-k_2 - k_1 e^{-i\kappa a}) \tilde{x}_2 = 0, \quad (3.64)$$

$$m_2 \ddot{\tilde{x}}_2 + (c_1 + c_2 + c_4) \dot{\tilde{x}}_2 + (-c_2 - c_1 e^{i\kappa a}) \dot{\tilde{x}}_1 + (k_1 + k_2 + k_4) \tilde{x}_2 + (-k_2 - k_1 e^{i\kappa a}) \tilde{x}_1 = 0. \quad (3.65)$$

Equations (3.64) and (3.65) can be compacted into a matrix form as

$$\mathbf{M} \ddot{\tilde{\mathbf{X}}} + \mathbf{C}(\kappa) \dot{\tilde{\mathbf{X}}} + \mathbf{K}(\kappa) \tilde{\mathbf{X}} = \mathbf{0}, \quad (3.66)$$

where

$$\begin{aligned} \tilde{\mathbf{X}} &= \begin{pmatrix} \tilde{x}_1 \\ \tilde{x}_2 \end{pmatrix}; \mathbf{M} = \begin{pmatrix} m_1 & 0 \\ 0 & m_2 \end{pmatrix}; \mathbf{C}(\kappa) = \begin{pmatrix} c_1 + c_2 + c_3 & -c_2 - c_1 e^{-i\kappa a} \\ -c_2 - c_1 e^{i\kappa a} & c_1 + c_2 + c_4 \end{pmatrix}; \\ \text{and } \mathbf{K}(\kappa) &= \begin{pmatrix} k_1 + k_2 + k_3 & -k_2 - k_1 e^{-i\kappa a} \\ -k_2 - k_1 e^{i\kappa a} & k_1 + k_2 + k_4 \end{pmatrix}. \end{aligned} \quad (3.67)$$

The dispersion relation can now be formulated by subjecting equation (3.66) to a state-space transformation of the form given in equation (3.4), where

$$\mathbf{A} = \begin{pmatrix} \mathbf{0} & \mathbf{I} \\ \mathbf{M} & \mathbf{C}(\kappa) \end{pmatrix}; \mathbf{B} = \begin{pmatrix} -\mathbf{I} & \mathbf{0} \\ \mathbf{0} & \mathbf{K}(\kappa) \end{pmatrix}; \text{ and } \mathbf{Y} = \begin{pmatrix} \dot{\tilde{\mathbf{X}}} \\ \tilde{\mathbf{X}} \end{pmatrix}, \quad (3.68)$$

implementing a solution of the form $\mathbf{Y} = \tilde{\mathbf{Y}}_\lambda e^{\lambda t}$, and solving the resulting eigenvalue problem of the form given in equation (3.6). Expanding equation (3.6) for this particular case yields a fourth-order equation in terms of λ , which, upon solving, gives four complex roots appearing as two complex-conjugate pairs.

3.6 Diatomic piezoelectric phononic crystals

In this section, the application of generalized Bloch's theorem to different configurations of diatomic piezoelectric phononic crystals (DPPnCs) is elaborated. Similar to the monoatomic case, the piezoelectric elements considered in the analysis are comprised of a shunt circuit which are either purely resistive or consist of an inductor. The configurations addressed in this section are, essentially, the piezoelectric counterparts of the configurations addressed in section 3.5.

3.6.1 Without grounding

Figure 3.9 presents the schematics of a DPPnC chain under free vibration without any grounding and the associated unit cell as lumped-parameter models.

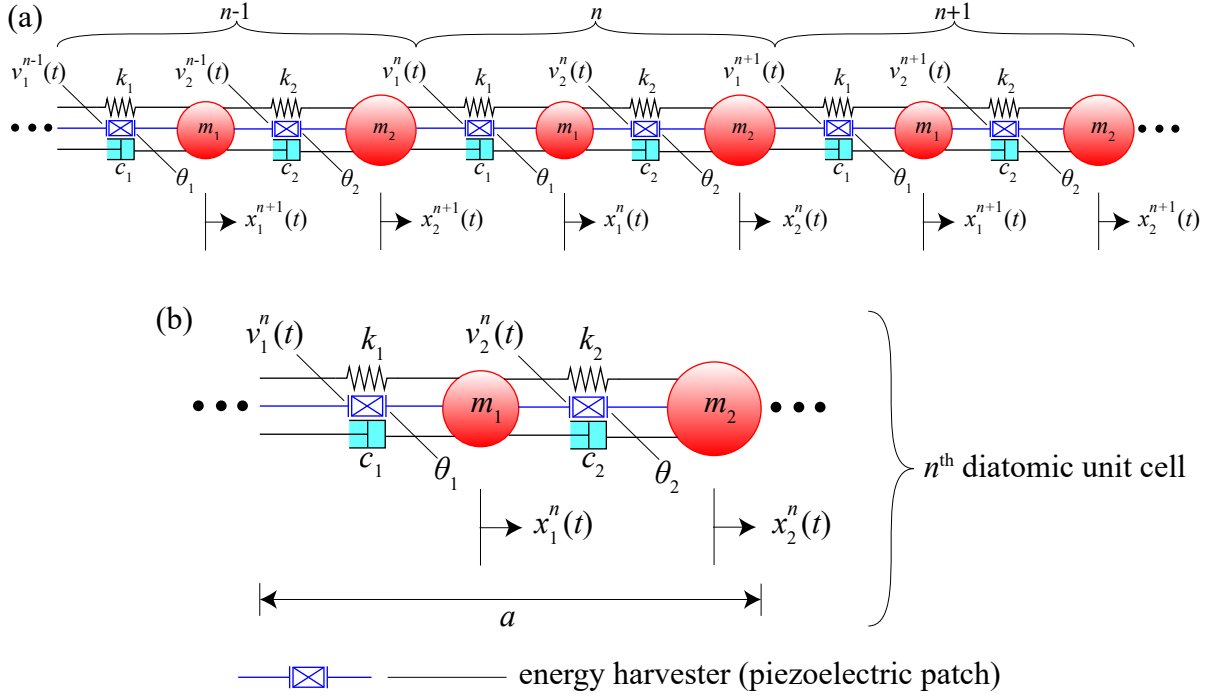


Figure 3.9: Schematic of (a) a diatomic piezoelectric phononic-crystal (DPPnC) chain without grounding and (b) the associated unit cell.

Shunt circuit without an inductor

The governing electromechanical equations pertaining to the n^{th} unit cell under free vibration consisting of piezoelectric elements with a shunt circuit lacking an inductor can be written as

$$m_1 \ddot{x}_1^n + (c_1 + c_2) \dot{x}_1^n - c_2 \dot{x}_2^n - c_1 \dot{x}_2^{n-1} + (k_1 + k_2) x_1^n - k_2 x_2^n - k_1 x_2^{n-1} + \theta_1 v_1^n - \theta_2 v_2^n = 0, \quad (3.69)$$

$$m_2 \ddot{x}_2^n + (c_1 + c_2) \dot{x}_2^n - c_2 \dot{x}_1^n - c_1 \dot{x}_1^{n+1} + (k_1 + k_2) x_2^n - k_2 x_1^n - k_1 x_1^{n+1} + \theta_2 v_2^n - \theta_1 v_1^{n+1} = 0, \quad (3.70)$$

$$-\theta_1 (\dot{x}_1^n - \dot{x}_2^{n-1}) + C_{p1} \dot{v}_1^n + \frac{1}{R_1} v_1^n = 0, \quad (3.71)$$

$$-\theta_2 (\dot{x}_2^n - \dot{x}_1^n) + C_{p2} \dot{v}_2^n + \frac{1}{R_2} v_2^n = 0. \quad (3.72)$$

The plane-wave solution for the voltage generated in the piezoelectric element of a periodic diatomic unit cell is similar to equation (3.31). Substituting equations (3.51) and (3.31) in equations (3.69)–(3.72) yields the following Bloch-transformed homogeneous

equations for the displacement amplitudes \tilde{x}_1 and \tilde{x}_2 and the voltage amplitudes \tilde{v}_1 and \tilde{v}_2 :

$$m_1\ddot{\tilde{x}}_1 + (c_1 + c_2)\dot{\tilde{x}}_1 + (-c_2 - c_1e^{-i\kappa a})\dot{\tilde{x}}_2 + (k_1 + k_2)\tilde{x}_1 + (-k_2 - k_1e^{-i\kappa a})\tilde{x}_2 + \theta_1\tilde{v}_1 + (-\theta_2)\tilde{v}_2 = 0, \quad (3.73)$$

$$m_2\ddot{\tilde{x}}_2 + (c_1 + c_2)\dot{\tilde{x}}_2 + (-c_2 - c_1e^{i\kappa a})\dot{\tilde{x}}_1 + (k_1 + k_2)\tilde{x}_2 + (-k_2 - k_1e^{i\kappa a})\tilde{x}_1 + (-\theta_1e^{i\kappa a})\tilde{v}_1 + \theta_2\tilde{v}_2 = 0, \quad (3.74)$$

$$-\theta_1\dot{\tilde{x}}_1 + \theta_1e^{-i\kappa a}\dot{\tilde{x}}_2 + C_{p1}\dot{\tilde{v}}_1 + \frac{1}{R_1}\tilde{v}_1 = 0, \quad (3.75)$$

$$-\theta_2\dot{\tilde{x}}_2 + \theta_2\dot{\tilde{x}}_1 + C_{p2}\dot{\tilde{v}}_2 + \frac{1}{R_2}\tilde{v}_2 = 0. \quad (3.76)$$

Equations (3.73)–(3.76) can be compacted into matrix equations as

$$\mathbf{M}\ddot{\tilde{\mathbf{X}}} + \mathbf{C}(\kappa)\dot{\tilde{\mathbf{X}}} + \mathbf{K}(\kappa)\tilde{\mathbf{X}} + \mathbf{T}_1(\kappa)\tilde{\mathbf{V}} = \mathbf{0}, \quad (3.77)$$

$$\mathbf{T}_2(\kappa)\dot{\tilde{\mathbf{X}}} + \mathbf{C}_p\dot{\tilde{\mathbf{V}}} + \mathbf{R}\tilde{\mathbf{V}} = \mathbf{0}, \quad (3.78)$$

where

$$\begin{aligned} \tilde{\mathbf{X}} &= \begin{pmatrix} \tilde{x}_1 \\ \tilde{x}_2 \end{pmatrix}; \quad \tilde{\mathbf{V}} = \begin{pmatrix} \tilde{v}_1 \\ \tilde{v}_2 \end{pmatrix}; \quad \mathbf{M} = \begin{pmatrix} m_1 & 0 \\ 0 & m_2 \end{pmatrix}; \\ \mathbf{C}(\kappa) &= \begin{pmatrix} c_1 + c_2 & -c_2 - c_1e^{-i\kappa a} \\ -c_2 - c_1e^{i\kappa a} & c_1 + c_2 \end{pmatrix}; \\ \mathbf{K}(\kappa) &= \begin{pmatrix} k_1 + k_2 & -k_2 - k_1e^{-i\kappa a} \\ -k_2 - k_1e^{i\kappa a} & k_1 + k_2 \end{pmatrix}; \\ \mathbf{T}_1(\kappa) &= \begin{pmatrix} \theta_1 & -\theta_2 \\ -\theta_1e^{i\kappa a} & \theta_2 \end{pmatrix}; \quad \mathbf{T}_2(\kappa) = \begin{pmatrix} -\theta_1 & \theta_1e^{-i\kappa a} \\ \theta_2 & -\theta_2 \end{pmatrix}; \\ \mathbf{C}_p &= \begin{pmatrix} C_{p1} & 0 \\ 0 & C_{p2} \end{pmatrix}; \quad \text{and } \mathbf{R} = \begin{pmatrix} \frac{1}{R_1} & 0 \\ 0 & \frac{1}{R_2} \end{pmatrix}. \end{aligned} \quad (3.79)$$

The dispersion relation can now be formulated by subjecting equations (3.77) and (3.78) to a state-space transformation of the form given in equation (3.4), where

$$\mathbf{A} = \begin{pmatrix} \mathbf{0} & \mathbf{I} & \mathbf{0} \\ \mathbf{M} & \mathbf{C}(\kappa) & \mathbf{0} \\ \mathbf{0} & \mathbf{T}_2(\kappa) & \mathbf{C}_p \end{pmatrix}; \quad \mathbf{B} = \begin{pmatrix} -\mathbf{I} & \mathbf{0} & \mathbf{0} \\ \mathbf{0} & \mathbf{K}(\kappa) & \mathbf{T}_1(\kappa) \\ \mathbf{0} & \mathbf{0} & \mathbf{R} \end{pmatrix}; \quad \text{and } \mathbf{Y} = \begin{pmatrix} \dot{\tilde{\mathbf{X}}} \\ \tilde{\mathbf{X}} \\ \dot{\tilde{\mathbf{V}}} \end{pmatrix}, \quad (3.80)$$

implementing a solution of the form $\mathbf{Y} = \tilde{\mathbf{Y}}_\lambda e^{\lambda t}$, and solving the resulting eigenvalue problem of the form given in equation (3.6). Expanding equation (3.6) for this particular case yields a sixth-order equation in terms of λ , which, upon solving, gives four complex roots appearing as two complex-conjugate pairs and two real roots.

Shunt circuit with an inductor

The governing electromechanical equations pertaining to the n^{th} unit cell under free vibration consisting of piezoelectric elements with a shunt circuit including an inductor can be written as

$$m_1 \ddot{x}_1^n + (c_1 + c_2) \dot{x}_1^n - c_2 \dot{x}_2^n - c_1 \dot{x}_2^{n-1} + (k_1 + k_2) x_1^n - k_2 x_2^n - k_1 x_2^{n-1} + \theta_1 v_1^n - \theta_2 v_2^n = 0, \quad (3.81)$$

$$m_2 \ddot{x}_2^n + (c_1 + c_2) \dot{x}_2^n - c_2 \dot{x}_1^n - c_1 \dot{x}_1^{n+1} + (k_1 + k_2) x_2^n - k_2 x_1^n - k_1 x_1^{n+1} + \theta_2 v_2^n - \theta_1 v_1^{n+1} = 0, \quad (3.82)$$

$$-\theta_1 (\dot{x}_1^n - \dot{x}_2^{n-1}) + C_{p1} \dot{v}_1^n + \frac{1}{R_1} \dot{v}_1^n + \frac{1}{L_1} v_1^n = 0, \quad (3.83)$$

$$-\theta_2 (\dot{x}_2^n - \dot{x}_1^n) + C_{p2} \dot{v}_2^n + \frac{1}{R_2} \dot{v}_2^n + \frac{1}{L_2} v_2^n = 0. \quad (3.84)$$

Substituting equations (3.51) and (3.31) in equations (3.81)–(3.84) yields the following Bloch-transformed homogeneous equations for the displacement amplitudes \tilde{x}_1 and \tilde{x}_2 and the voltage amplitudes \tilde{v}_1 and \tilde{v}_2 :

$$m_1 \ddot{\tilde{x}}_1 + (c_1 + c_2) \dot{\tilde{x}}_1 + (-c_2 - c_1 e^{-i\kappa a}) \dot{\tilde{x}}_2 + (k_1 + k_2) \tilde{x}_1 + (-k_2 - k_1 e^{-i\kappa a}) \tilde{x}_2 + \theta_1 \tilde{v}_1 + (-\theta_2) \tilde{v}_2 = 0, \quad (3.85)$$

$$m_2 \ddot{\tilde{x}}_2 + (c_1 + c_2) \dot{\tilde{x}}_2 + (-c_2 - c_1 e^{i\kappa a}) \dot{\tilde{x}}_1 + (k_1 + k_2) \tilde{x}_2 + (-k_2 - k_1 e^{i\kappa a}) \tilde{x}_1 + (-\theta_1 e^{i\kappa a}) \tilde{v}_1 + \theta_2 \tilde{v}_2 = 0, \quad (3.86)$$

$$-\theta_1 \dot{\tilde{x}}_1 + \theta_1 e^{-i\kappa a} \dot{\tilde{x}}_2 + C_{p1} \dot{\tilde{v}}_1 + \frac{1}{R_1} \dot{\tilde{v}}_1 + \frac{1}{L_1} \tilde{v}_1 = 0, \quad (3.87)$$

$$-\theta_2 \dot{\tilde{x}}_2 + \theta_2 \dot{\tilde{x}}_1 + C_{p2} \dot{\tilde{v}}_2 + \frac{1}{R_2} \dot{\tilde{v}}_2 + \frac{1}{L_2} \tilde{v}_2 = 0. \quad (3.88)$$

Equations (3.85)–(3.88) can be compactly written in a matrix format as

$$\mathbf{M}\ddot{\tilde{\mathbf{X}}} + \mathbf{C}(\kappa)\dot{\tilde{\mathbf{X}}} + \mathbf{K}(\kappa)\tilde{\mathbf{X}} + \mathbf{T}_1(\kappa)\tilde{\mathbf{V}} = \mathbf{0}, \quad (3.89)$$

$$\mathbf{T}_2(\kappa)\tilde{\mathbf{X}} + \mathbf{C}_p\dot{\tilde{\mathbf{V}}} + \mathbf{R}\tilde{\mathbf{V}} + \mathbf{L}\tilde{\mathbf{V}} = \mathbf{0}, \quad (3.90)$$

where

$$\begin{aligned}
\tilde{\mathbf{X}} &= \begin{pmatrix} \tilde{x}_1 \\ \tilde{x}_2 \end{pmatrix}; \quad \tilde{\mathbf{V}} = \begin{pmatrix} \tilde{v}_1 \\ \tilde{v}_2 \end{pmatrix}; \quad \mathbf{M} = \begin{pmatrix} m_1 & 0 \\ 0 & m_2 \end{pmatrix}; \\
\mathbf{C}(\kappa) &= \begin{pmatrix} c_1 + c_2 & -c_2 - c_1 e^{-i\kappa a} \\ -c_2 - c_1 e^{i\kappa a} & c_1 + c_2 \end{pmatrix}; \\
\mathbf{K}(\kappa) &= \begin{pmatrix} k_1 + k_2 & -k_2 - k_1 e^{-i\kappa a} \\ -k_2 - k_1 e^{i\kappa a} & k_1 + k_2 \end{pmatrix}; \\
\mathbf{T}_1(\kappa) &= \begin{pmatrix} \theta_1 & -\theta_2 \\ -\theta_1 e^{i\kappa a} & \theta_2 \end{pmatrix}; \quad \mathbf{T}_2(\kappa) = \begin{pmatrix} -\theta_1 & \theta_1 e^{-i\kappa a} \\ \theta_2 & -\theta_2 \end{pmatrix}; \\
\mathbf{C}_p &= \begin{pmatrix} C_{p1} & 0 \\ 0 & C_{p2} \end{pmatrix}; \quad \mathbf{R} = \begin{pmatrix} \frac{1}{R_1} & 0 \\ 0 & \frac{1}{R_2} \end{pmatrix}; \quad \text{and } \mathbf{L} = \begin{pmatrix} \frac{1}{L_1} & 0 \\ 0 & \frac{1}{L_2} \end{pmatrix}.
\end{aligned} \tag{3.91}$$

Equations (3.89) and (3.90) can be further compacted into a single matrix equation as

$$\mathbf{Z}_1 \ddot{\tilde{\mathbf{E}}} + \mathbf{Z}_2 \dot{\tilde{\mathbf{E}}} + \mathbf{Z}_3 \tilde{\mathbf{E}} = \mathbf{0}, \tag{3.92}$$

where

$$\begin{aligned}
\mathbf{Z}_1 &= \begin{pmatrix} \mathbf{M} & \mathbf{0} \\ \mathbf{T}_2(\kappa) & \mathbf{C}_p \end{pmatrix}; \quad \mathbf{Z}_2 = \begin{pmatrix} \mathbf{C}(\kappa) & \mathbf{0} \\ \mathbf{0} & \mathbf{R} \end{pmatrix}; \quad \mathbf{Z}_3 = \begin{pmatrix} \mathbf{K}(\kappa) & \mathbf{T}_1(\kappa) \\ \mathbf{0} & \mathbf{L} \end{pmatrix}; \\
&\quad \text{and } \tilde{\mathbf{E}} = \begin{pmatrix} \tilde{\mathbf{X}} \\ \tilde{\mathbf{V}} \end{pmatrix}.
\end{aligned} \tag{3.93}$$

The dispersion relation can now be formulated by subjecting equation (3.92) to a state-space transformation of the form given in equation (3.4), where

$$\mathbf{A} = \begin{pmatrix} \mathbf{0} & \mathbf{I} \\ \mathbf{Z}_1 & \mathbf{Z}_2 \end{pmatrix}; \quad \mathbf{B} = \begin{pmatrix} -\mathbf{I} & \mathbf{0} \\ \mathbf{0} & \mathbf{Z}_3 \end{pmatrix}; \quad \text{and } \mathbf{Y} = \begin{pmatrix} \dot{\tilde{\mathbf{E}}} \\ \tilde{\mathbf{E}} \end{pmatrix}, \tag{3.94}$$

implementing a solution of the form $\mathbf{Y} = \tilde{\mathbf{Y}}_\lambda e^{\lambda t}$, and solving the resulting eigenvalue problem of the form given in equation (3.6). Expanding equation (3.6) for this particular case yields an eight-order equation in terms of λ , which, upon solving, gives four complex roots appearing as two complex-conjugate pairs and four real roots.

3.6.2 With grounding

Figure 3.10 presents the schematics of a DPPnC chain under free vibration with grounding and the associated unit cell as lumped-parameter models.

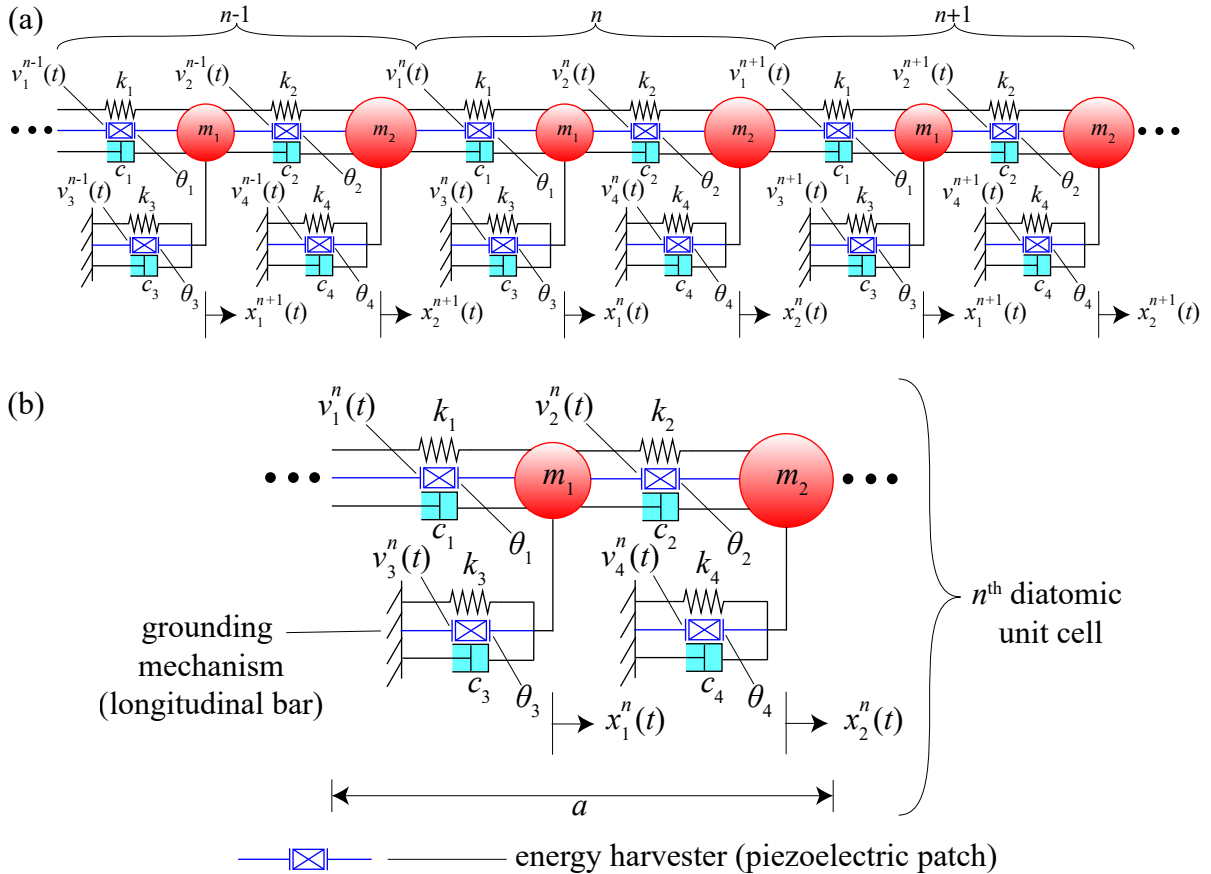


Figure 3.10: Schematic of (a) a diatomic piezoelectric phononic-crystal (DPPnC) chain with grounding and (b) the associated unit cell.

Shunt circuit without an inductor

The governing electromechanical equations pertaining to the n^{th} unit cell under free vibration consisting of piezoelectric elements with a purely resistive shunt circuit can be written as

$$m_1 \ddot{x}_1^n + (c_1 + c_2 + c_3) \dot{x}_1^n - c_2 \dot{x}_2^n - c_1 \dot{x}_2^{n-1} + (k_1 + k_2 + k_3) x_1^n - k_2 x_2^n - k_1 x_2^{n-1} + \theta_1 v_1^n - \theta_2 v_2^n + \theta_3 v_3^n = 0, \quad (3.95)$$

$$m_2 \ddot{x}_2^n + (c_1 + c_2 + c_4) \dot{x}_2^n - c_2 \dot{x}_1^n - c_1 \dot{x}_1^{n+1} + (k_1 + k_2 + k_4) x_2^n - k_2 x_1^n - k_1 x_1^{n+1} - \theta_1 v_1^{n+1} + \theta_2 v_2^n + \theta_4 v_4^n = 0, \quad (3.96)$$

$$-\theta_1 (\dot{x}_1^n - \dot{x}_2^{n-1}) + C_{p1} \dot{v}_1^n + \frac{1}{R_1} v_1^n = 0, \quad (3.97)$$

$$-\theta_2 (\dot{x}_2^n - \dot{x}_1^n) + C_{p2} \dot{v}_2^n + \frac{1}{R_2} v_2^n = 0, \quad (3.98)$$

$$-\theta_3 \dot{x}_1^n + C_{p3} \dot{v}_3^n + \frac{1}{R_3} v_3^n = 0, \quad (3.99)$$

$$-\theta_4 \dot{x}_2^n + C_{p4} \dot{v}_4^n + \frac{1}{R_4} v_4^n = 0. \quad (3.100)$$

Substituting equations (3.51) and (3.31) in equations (3.95)–(3.100) yields the following Bloch-transformed homogeneous equations for the displacement amplitudes \tilde{x}_1 and \tilde{x}_2 and the voltage amplitudes \tilde{v}_1 , \tilde{v}_2 , \tilde{v}_3 , and \tilde{v}_4 :

$$m_1 \ddot{\tilde{x}}_1 + (c_1 + c_2 + c_3) \dot{\tilde{x}}_1 + (-c_2 - c_1 e^{-i\kappa a}) \dot{\tilde{x}}_2 + (k_1 + k_2 + k_3) \tilde{x}_1 + (-k_2 - k_1 e^{-i\kappa a}) \tilde{x}_2 + \theta_1 \tilde{v}_1 + (-\theta_2) \tilde{v}_2 + \theta_3 \tilde{v}_3 = 0, \quad (3.101)$$

$$m_2 \ddot{\tilde{x}}_2 + (c_1 + c_2 + c_4) \dot{\tilde{x}}_2 + (-c_2 - c_1 e^{i\kappa a}) \dot{\tilde{x}}_1 + (k_1 + k_2 + k_4) \tilde{x}_2 + (-k_2 - k_1 e^{i\kappa a}) \tilde{x}_1 + (-\theta_1 e^{i\kappa a}) \tilde{v}_1 + \theta_2 \tilde{v}_2 + \theta_4 \tilde{v}_4 = 0, \quad (3.102)$$

$$-\theta_1 \dot{\tilde{x}}_1 + \theta_1 e^{-i\kappa a} \dot{\tilde{x}}_2 + C_{p1} \dot{\tilde{v}}_1 + \frac{1}{R_1} \tilde{v}_1 = 0, \quad (3.103)$$

$$-\theta_2 \dot{\tilde{x}}_2 + \theta_2 \dot{\tilde{x}}_1 + C_{p2} \dot{\tilde{v}}_2 + \frac{1}{R_2} \tilde{v}_2 = 0, \quad (3.104)$$

$$-\theta_3 \dot{\tilde{x}}_1 + C_{p3} \dot{\tilde{v}}_3 + \frac{1}{R_3} \tilde{v}_3 = 0, \quad (3.105)$$

$$-\theta_4 \dot{\tilde{x}}_2 + C_{p4} \dot{\tilde{v}}_4 + \frac{1}{R_4} \tilde{v}_4 = 0. \quad (3.106)$$

Equations (3.101)–(3.106) can be compacted into matrix equations as

$$\mathbf{M}\ddot{\tilde{\mathbf{X}}} + \mathbf{C}(\kappa)\dot{\tilde{\mathbf{X}}} + \mathbf{K}(\kappa)\tilde{\mathbf{X}} + \mathbf{T}_1^{\text{base}}(\kappa)\tilde{\mathbf{V}}^{\text{base}} + \mathbf{T}^{\text{bars}}\tilde{\mathbf{V}}^{\text{bars}} = \mathbf{0}, \quad (3.107)$$

$$\mathbf{T}_2^{\text{base}}(\kappa)\dot{\tilde{\mathbf{X}}} + \mathbf{C}_p^{\text{base}}\dot{\tilde{\mathbf{V}}}^{\text{base}} + \mathbf{R}^{\text{base}}\tilde{\mathbf{V}}^{\text{base}} = \mathbf{0}, \quad (3.108)$$

$$-\mathbf{T}^{\text{bars}}\dot{\tilde{\mathbf{X}}} + \mathbf{C}_p^{\text{bars}}\dot{\tilde{\mathbf{V}}}^{\text{bars}} + \mathbf{R}^{\text{bars}}\tilde{\mathbf{V}}^{\text{bars}} = \mathbf{0}, \quad (3.109)$$

where

$$\begin{aligned} \tilde{\mathbf{X}} &= \begin{pmatrix} \tilde{x}_1 \\ \tilde{x}_2 \end{pmatrix}; \quad \tilde{\mathbf{V}}^{\text{base}} = \begin{pmatrix} \tilde{v}_1 \\ \tilde{v}_2 \end{pmatrix}; \quad \tilde{\mathbf{V}}^{\text{bars}} = \begin{pmatrix} \tilde{v}_3 \\ \tilde{v}_4 \end{pmatrix}; \quad \mathbf{M} = \begin{pmatrix} m_1 & 0 \\ 0 & m_2 \end{pmatrix}; \\ \mathbf{C}(\kappa) &= \begin{pmatrix} c_1 + c_2 + c_3 & -c_2 - c_1 e^{-i\kappa a} \\ -c_2 - c_1 e^{i\kappa a} & c_1 + c_2 + c_4 \end{pmatrix}; \\ \mathbf{K}(\kappa) &= \begin{pmatrix} k_1 + k_2 + k_3 & -k_2 - k_1 e^{-i\kappa a} \\ -k_2 - k_1 e^{i\kappa a} & k_1 + k_2 + k_4 \end{pmatrix}; \\ \mathbf{T}_1^{\text{base}}(\kappa) &= \begin{pmatrix} \theta_1 & -\theta_2 \\ -\theta_1 e^{i\kappa a} & \theta_2 \end{pmatrix}; \quad \mathbf{T}_2^{\text{base}}(\kappa) = \begin{pmatrix} -\theta_1 & \theta_1 e^{-i\kappa a} \\ \theta_2 & -\theta_2 \end{pmatrix}; \\ \mathbf{T}^{\text{bars}} &= \begin{pmatrix} \theta_3 & 0 \\ 0 & \theta_4 \end{pmatrix}; \quad \mathbf{C}_p^{\text{base}} = \begin{pmatrix} C_{p1} & 0 \\ 0 & C_{p2} \end{pmatrix}; \quad \mathbf{C}_p^{\text{bars}} = \begin{pmatrix} C_{p3} & 0 \\ 0 & C_{p4} \end{pmatrix}; \\ \mathbf{R}^{\text{base}} &= \begin{pmatrix} \frac{1}{R_1} & 0 \\ 0 & \frac{1}{R_2} \end{pmatrix}; \quad \text{and } \mathbf{R}^{\text{bars}} = \begin{pmatrix} \frac{1}{R_3} & 0 \\ 0 & \frac{1}{R_4} \end{pmatrix}. \end{aligned} \quad (3.110)$$

Note that the superscripts "base" and "bars" are used to differentiate between the matrices consisting of electrical parameters of the piezoelectric elements on the base chain and the bars, respectively. The dispersion relation can now be formulated by subjecting equations (3.107)–(3.109) to a state-space transformation of the form given in equation (3.4), where

$$\begin{aligned} \mathbf{A} &= \begin{pmatrix} \mathbf{0} & \mathbf{I} & \mathbf{0} & \mathbf{0} \\ \mathbf{M} & \mathbf{C}(\kappa) & \mathbf{0} & \mathbf{0} \\ \mathbf{0} & \mathbf{T}_2^{\text{base}}(\kappa) & \mathbf{C}_p^{\text{base}} & \mathbf{0} \\ \mathbf{0} & -\mathbf{T}^{\text{bars}} & \mathbf{0} & \mathbf{C}_p^{\text{bars}} \end{pmatrix}; \\ \mathbf{B} &= \begin{pmatrix} -\mathbf{I} & \mathbf{0} & \mathbf{0} & \mathbf{0} \\ \mathbf{0} & \mathbf{K}(\kappa) & \mathbf{T}_1^{\text{base}}(\kappa) & \mathbf{T}^{\text{bars}} \\ \mathbf{0} & \mathbf{0} & \mathbf{R}^{\text{base}} & \mathbf{0} \\ \mathbf{0} & \mathbf{0} & \mathbf{0} & \mathbf{R}^{\text{bars}} \end{pmatrix}; \quad \text{and } \mathbf{Y} = \begin{pmatrix} \dot{\tilde{\mathbf{X}}} \\ \tilde{\mathbf{X}} \\ \tilde{\mathbf{V}}^{\text{base}} \\ \tilde{\mathbf{V}}^{\text{bars}} \end{pmatrix}, \end{aligned} \quad (3.111)$$

implementing a solution of the form $\mathbf{Y} = \tilde{\mathbf{Y}}_\lambda e^{\lambda t}$, and solving the resulting eigenvalue problem of the form given in equation (3.6). Expanding equation (3.6) for this particular case yields a eight-order equation in terms of λ , which, upon solving, gives four complex roots appearing as two complex-conjugate pairs and four real roots.

Shunt circuit with an inductor

The governing electromechanical equations pertinent to the n^{th} unit cell under free vibration consisting of piezoelectric elements with a shunt circuit including an inductor can be written as

$$m_1 \ddot{x}_1^n + (c_1 + c_2 + c_3) \dot{x}_1^n - c_2 \dot{x}_2^n - c_1 \dot{x}_2^{n-1} + (k_1 + k_2 + k_3) x_1^n - k_2 x_2^n - k_1 x_2^{n-1} + \theta_1 v_1^n - \theta_2 v_2^n + \theta_3 v_3^n = 0, \quad (3.112)$$

$$m_2 \ddot{x}_2^n + (c_1 + c_2 + c_4) \dot{x}_2^n - c_2 \dot{x}_1^n - c_1 \dot{x}_1^{n+1} + (k_1 + k_2 + k_4) x_2^n - k_2 x_1^n - k_1 x_1^{n+1} - \theta_1 v_1^{n+1} + \theta_2 v_2^n + \theta_4 v_4^n = 0, \quad (3.113)$$

$$-\theta_1 (\ddot{x}_1^n - \ddot{x}_2^{n-1}) + C_{p1} \ddot{v}_1^n + \frac{1}{R_1} \dot{v}_1^n + \frac{1}{L_1} v_1^n = 0, \quad (3.114)$$

$$-\theta_2 (\ddot{x}_2^n - \ddot{x}_1^n) + C_{p2} \ddot{v}_2^n + \frac{1}{R_2} \dot{v}_2^n + \frac{1}{L_2} v_2^n = 0, \quad (3.115)$$

$$-\theta_3 \ddot{x}_1^n + C_{p3} \ddot{v}_3^n + \frac{1}{R_3} \dot{v}_3^n + \frac{1}{L_3} v_3^n = 0, \quad (3.116)$$

$$-\theta_4 \ddot{x}_2^n + C_{p4} \ddot{v}_4^n + \frac{1}{R_4} \dot{v}_4^n + \frac{1}{L_4} v_4^n = 0. \quad (3.117)$$

Substituting equations (3.51) and (3.31) in equations (3.112)–(3.117) yields the following Bloch-transformed homogeneous equations for the displacement amplitudes \tilde{x}_1 and \tilde{x}_2 and

the voltage amplitudes \tilde{v}_1 , \tilde{v}_2 , \tilde{v}_3 , and \tilde{v}_4 :

$$m_1\ddot{\tilde{x}}_1 + (c_1 + c_2 + c_3)\dot{\tilde{x}}_1 + (-c_2 - c_1e^{-i\kappa a})\dot{\tilde{x}}_2 + (k_1 + k_2 + k_3)\tilde{x}_1 + (-k_2 - k_1e^{-i\kappa a})\tilde{x}_2 + \theta_1\tilde{v}_1 + (-\theta_2)\tilde{v}_2 + \theta_3\tilde{v}_3 = 0, \quad (3.118)$$

$$m_2\ddot{\tilde{x}}_2 + (c_1 + c_2 + c_4)\dot{\tilde{x}}_2 + (-c_2 - c_1e^{i\kappa a})\dot{\tilde{x}}_1 + (k_1 + k_2 + k_4)\tilde{x}_2 + (-k_2 - k_1e^{i\kappa a})\tilde{x}_1 + (-\theta_1e^{i\kappa a})\tilde{v}_1 + \theta_2\tilde{v}_2 + \theta_4\tilde{v}_4 = 0, \quad (3.119)$$

$$-\theta_1\ddot{\tilde{x}}_1 + \theta_1e^{-i\kappa a}\ddot{\tilde{x}}_2 + C_{p1}\dot{\tilde{v}}_1 + \frac{1}{R_1}\dot{\tilde{v}}_1 + \frac{1}{L_1}\tilde{v}_1 = 0, \quad (3.120)$$

$$-\theta_2\ddot{\tilde{x}}_2 + \theta_2\ddot{\tilde{x}}_1 + C_{p2}\dot{\tilde{v}}_2 + \frac{1}{R_2}\dot{\tilde{v}}_2 + \frac{1}{L_2}\tilde{v}_2 = 0, \quad (3.121)$$

$$-\theta_3\ddot{\tilde{x}}_1 + C_{p3}\dot{\tilde{v}}_3 + \frac{1}{R_3}\dot{\tilde{v}}_3 + \frac{1}{L_3}\tilde{v}_3 = 0, \quad (3.122)$$

$$-\theta_4\ddot{\tilde{x}}_2 + C_{p4}\dot{\tilde{v}}_4 + \frac{1}{R_4}\dot{\tilde{v}}_4 + \frac{1}{L_4}\tilde{v}_4 = 0. \quad (3.123)$$

Equations (3.118)–(3.123) can be fused into matrix equations as

$$\mathbf{M}\ddot{\tilde{\mathbf{X}}} + \mathbf{C}(\kappa)\dot{\tilde{\mathbf{X}}} + \mathbf{K}(\kappa)\tilde{\mathbf{X}} + \mathbf{T}_1^{\text{base}}(\kappa)\tilde{\mathbf{V}}^{\text{base}} + \mathbf{T}^{\text{bars}}\tilde{\mathbf{V}}^{\text{bars}} = \mathbf{0}, \quad (3.124)$$

$$\mathbf{T}_2^{\text{base}}(\kappa)\ddot{\tilde{\mathbf{X}}} + \mathbf{C}_p^{\text{base}}\dot{\tilde{\mathbf{V}}}^{\text{base}} + \mathbf{R}^{\text{base}}\dot{\tilde{\mathbf{V}}}^{\text{base}} + \mathbf{L}^{\text{base}}\tilde{\mathbf{V}}^{\text{base}} = \mathbf{0}, \quad (3.125)$$

$$-\mathbf{T}^{\text{bars}}\ddot{\tilde{\mathbf{X}}} + \mathbf{C}_p^{\text{bars}}\dot{\tilde{\mathbf{V}}}^{\text{bars}} + \mathbf{R}^{\text{bars}}\dot{\tilde{\mathbf{V}}}^{\text{bars}} + \mathbf{L}^{\text{bars}}\tilde{\mathbf{V}}^{\text{bars}} = \mathbf{0}, \quad (3.126)$$

where

$$\begin{aligned}
\tilde{\mathbf{X}} &= \begin{pmatrix} \tilde{x}_1 \\ \tilde{x}_2 \end{pmatrix}; \quad \tilde{\mathbf{V}}^{\text{base}} = \begin{pmatrix} \tilde{v}_1 \\ \tilde{v}_2 \end{pmatrix}; \quad \tilde{\mathbf{V}}^{\text{bars}} = \begin{pmatrix} \tilde{v}_3 \\ \tilde{v}_4 \end{pmatrix}; \quad \mathbf{M} = \begin{pmatrix} m_1 & 0 \\ 0 & m_2 \end{pmatrix}; \\
\mathbf{C}(\kappa) &= \begin{pmatrix} c_1 + c_2 + c_3 & -c_2 - c_1 e^{-i\kappa a} \\ -c_2 - c_1 e^{i\kappa a} & c_1 + c_2 + c_4 \end{pmatrix}; \\
\mathbf{K}(\kappa) &= \begin{pmatrix} k_1 + k_2 + k_3 & -k_2 - k_1 e^{-i\kappa a} \\ -k_2 - k_1 e^{i\kappa a} & k_1 + k_2 + k_4 \end{pmatrix}; \\
\mathbf{T}_1^{\text{base}}(\kappa) &= \begin{pmatrix} \theta_1 & -\theta_2 \\ -\theta_1 e^{i\kappa a} & \theta_2 \end{pmatrix}; \quad \mathbf{T}_2^{\text{base}}(\kappa) = \begin{pmatrix} -\theta_1 & \theta_1 e^{-i\kappa a} \\ \theta_2 & -\theta_2 \end{pmatrix}; \\
\mathbf{T}^{\text{bars}} &= \begin{pmatrix} \theta_3 & 0 \\ 0 & \theta_4 \end{pmatrix}; \quad \mathbf{C}_p^{\text{base}} = \begin{pmatrix} C_{p1} & 0 \\ 0 & C_{p2} \end{pmatrix}; \quad \mathbf{C}_p^{\text{bars}} = \begin{pmatrix} C_{p3} & 0 \\ 0 & C_{p4} \end{pmatrix}; \\
\mathbf{R}^{\text{base}} &= \begin{pmatrix} \frac{1}{R_1} & 0 \\ 0 & \frac{1}{R_2} \end{pmatrix}; \quad \mathbf{R}^{\text{bars}} = \begin{pmatrix} \frac{1}{R_3} & 0 \\ 0 & \frac{1}{R_4} \end{pmatrix}; \\
\mathbf{L}^{\text{base}} &= \begin{pmatrix} \frac{1}{L_1} & 0 \\ 0 & \frac{1}{L_2} \end{pmatrix}; \quad \text{and } \mathbf{L}^{\text{bars}} = \begin{pmatrix} \frac{1}{L_3} & 0 \\ 0 & \frac{1}{L_4} \end{pmatrix}. \tag{3.127}
\end{aligned}$$

Equations (3.124)–(3.126) can be further merged into a single matrix equation as

$$\mathbf{Z}_1 \ddot{\tilde{\mathbf{E}}} + \mathbf{Z}_2 \dot{\tilde{\mathbf{E}}} + \mathbf{Z}_3 \tilde{\mathbf{E}} = \mathbf{0}, \tag{3.128}$$

where

$$\begin{aligned}
\mathbf{Z}_1 &= \begin{pmatrix} \mathbf{M} & \mathbf{0} & \mathbf{0} \\ \mathbf{T}_2^{\text{base}}(\kappa) & \mathbf{C}_p^{\text{base}} & \mathbf{0} \\ -\mathbf{T}^{\text{bars}} & \mathbf{0} & \mathbf{C}_p^{\text{bars}} \end{pmatrix}; \quad \mathbf{Z}_2 = \begin{pmatrix} \mathbf{C}(\kappa) & \mathbf{0} & \mathbf{0} \\ \mathbf{0} & \mathbf{R}^{\text{base}} & \mathbf{0} \\ \mathbf{0} & \mathbf{0} & \mathbf{R}^{\text{bars}} \end{pmatrix}; \\
\mathbf{Z}_3 &= \begin{pmatrix} \mathbf{K}(\kappa) & \mathbf{T}_1^{\text{base}}(\kappa) & \mathbf{T}^{\text{bars}} \\ \mathbf{0} & \mathbf{L}^{\text{base}} & \mathbf{0} \\ \mathbf{0} & \mathbf{0} & \mathbf{L}^{\text{bars}} \end{pmatrix}; \quad \text{and } \tilde{\mathbf{E}} = \begin{pmatrix} \tilde{\mathbf{X}} \\ \tilde{\mathbf{V}}^{\text{base}} \\ \tilde{\mathbf{V}}^{\text{bars}} \end{pmatrix}. \tag{3.129}
\end{aligned}$$

The dispersion relation can now be formulated by subjecting equation (3.128) to a state-space transformation of the form given in equation (3.4), where

$$\mathbf{A} = \begin{pmatrix} \mathbf{0} & \mathbf{I} \\ \mathbf{Z}_1 & \mathbf{Z}_2 \end{pmatrix}; \mathbf{B} = \begin{pmatrix} -\mathbf{I} & \mathbf{0} \\ \mathbf{0} & \mathbf{Z}_3 \end{pmatrix}; \text{ and } \mathbf{Y} = \begin{pmatrix} \dot{\tilde{\mathbf{E}}} \\ \tilde{\mathbf{E}} \end{pmatrix}, \quad (3.130)$$

implementing a solution of the form $\mathbf{Y} = \tilde{\mathbf{Y}}_\lambda e^{\lambda t}$, and solving the resulting eigenvalue problem of the form given in equation (3.6). Expanding equation (3.6) for this particular case yields an twelfth-order equation in terms of λ , which, upon solving, gives four complex roots appearing as two complex-conjugate pairs and eight real roots.

3.7 Wave-propagation and dissipation characteristics of diatomic phononic crystals and piezoelectric phononic crystals

This section presents the wave-propagation and dissipation characteristics of the different configurations of DPnCs and DPPnCs discussed so far in a graphical comparative format.

3.7.1 Without grounding

Table 3.5 details the parameters utilized in the computation of the dispersion (band structure) and damping-ratio characteristics of the DPnC and DPPnCs without grounding.

The electrical parameters of the shunt circuit are non-dimensionalized as

$$\alpha_l = \bar{\omega}_l C_{p_l} R_l, \quad (3.131a)$$

$$\beta_l = \bar{\omega}_l^2 C_{p_l} L_l, \quad (3.131b)$$

$$k_{\text{coeff}_l}^2 = \frac{\theta_l^2}{k_l C_{p_l}}, \quad (3.131c)$$

where $l = 1, 2$ is an index corresponding to the parameters of the two piezoelectric elements and the frequencies obtained from the two mass-spring pairs: $\bar{\omega}_1 = \sqrt{\frac{k_1}{m_1}}$ and $\bar{\omega}_2 = \sqrt{\frac{k_2}{m_2}}$.

As a diatomic unit cell has two modes or branches, the integrated (cumulative) and total value of the damping ratios are defined as

$$\zeta_l^{\text{cum}}(\mu) = \int_0^\mu \zeta_l \, d\mu \quad (l = 1, 2, \text{ or sum}; \mu \in [0, \pi]), \quad (3.132)$$

Table 3.5: Mechanical and dimensionless electrical parameters employed in the diatomic phononic crystal (DPnC) and diatomic piezoelectric phononic crystals (DPPnCs) without grounding.

Parameter	DPnC	DPPnC without an inductor	DPPnC with an inductor	Unit
a	1	1	1	m
m_1	0.0170	0.0170	0.0170	Kg
m_2	0.0340	0.0340	0.0340	Kg
k_1	2×10^4	2×10^4	2×10^4	Nm^{-1}
k_2	1×10^4	1×10^4	1×10^4	Nm^{-1}
c_1	0.2180	0.2180	0.2180	Nsm^{-1}
c_2	0.2180	0.2180	0.2180	Nsm^{-1}
α_1	—	0.1302	0.1302	—
α_2	—	0.2603	0.2603	—
β_1	—	—	0.4706	—
β_2	—	—	0.4706	—
$k_{\text{coeff}_1}^2$	—	0.2000	0.2000	—
$k_{\text{coeff}_2}^2$	—	0.8000	0.8000	—

and

$$\zeta_l^{\text{tot}} = \zeta_l^{\text{cum}}(\pi) \quad (l = 1, 2, \text{ or sum}), \quad (3.133)$$

respectively, where $l = 1, 2$, or sum corresponds to the acoustic branch, optical branch, and the summation of the two branches, respectively.

Figure 3.11 depicts the normalized damped frequencies, damping ratios, and cumulative damping ratios for the DPnC and DPPnCs without grounding in the IBZ, i.e., for $\mu \in [0, \pi]$. The damped frequencies are normalized with respect to $\bar{\omega}_1$; i.e., the plots depict $\Omega_l = \frac{\omega_{dl}}{\bar{\omega}_1}$, where $l=1$ (acoustic branch), 2 (optical branch). Considering that the diatomic unit cell has two branches, figure 3.11(a) presents two transmission bands and two attenuation bands as indicated by the shaded and non-shaded regions, respectively. The DPnC and DPPnCs without grounding exhibit a wider first transmission band as opposed to the second transmission band. The DPnC and DPPnCs have roughly similar band structures except that the DPnC shows a lower and narrower second transmission band. For dispersion band structures that are approximately similar, figure 3.11(b) shows a significant difference in the damping ratio curves. It is observed that, in comparison to the DPnC, the DPPnCs portray relatively higher levels of damping ratios ζ_1 and ζ_2 . For a better comparison, the summation of the two damping ratio curves, ζ_{sum} , is also plotted to show the total wave-number dependent damping ratio in the IBZ. In figure 3.11(c), the DPPnCs present

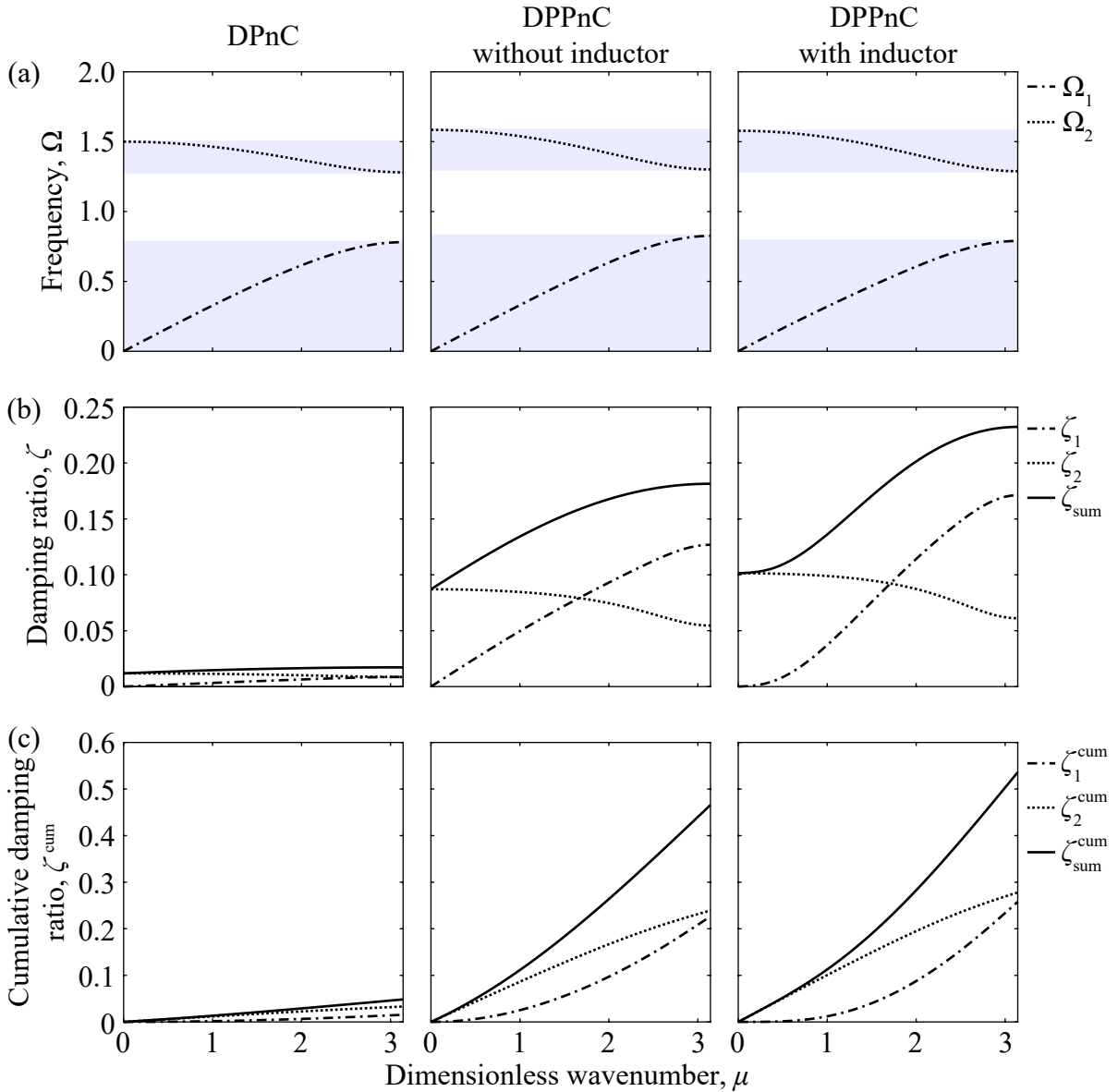


Figure 3.11: (a) Frequency band structure, (b) damping-ratio diagrams, and (c) cumulative-damping-ratio diagrams for the diatomic phononic crystal (DPnC) and diatomic piezoelectric phononic crystals (DPPnCs) without grounding.

a considerably higher rate of increase of ζ_l^{cum} ($l=1, 2$, or sum) in comparison to the DPnC. The value of ζ_l^{tot} ($l=1, 2$, or sum) is the highest for the DPPnC with an inductor. Table 3.6 details the ζ_l^{tot} values for the three periodic media.

Table 3.6: Total values of damping ratios of the diatomic phononic crystal (DPnC) and diatomic piezoelectric phononic crystals (DPPnCs) without grounding.

Parameter	DPnC	DPPnC without an inductor	DPPnC with an inductor	Unit
ζ_1^{tot}	0.0153	0.2265	0.2580	—
ζ_2^{tot}	0.0330	0.2393	0.2780	—
$\zeta_{\text{sum}}^{\text{tot}}$	0.0483	0.4658	0.5360	—

3.7.2 With grounding

Table 3.7 details the parameters utilized in the computation of the dispersion (band structure) and damping-ratio characteristics of the DPnC and DPPnCs with grounding.

Considering that there are four piezoelectric elements in a unit cell in this particular case, the electrical parameters of the shunt circuit are non-dimensionalized as

$$\alpha_l = \bar{\omega}_l C_{p_l} R_l, \quad (3.134a)$$

$$\beta_l = \bar{\omega}_l^2 C_{p_l} L_l, \quad (3.134b)$$

$$k_{\text{coeff}_l}^2 = \frac{\theta_l^2}{k_l C_{p_l}}, \quad (3.134c)$$

where $l = 1, 2, 3, 4$ is an index corresponding to the parameters of the four piezoelectric elements and the frequencies obtained from the four springs: $\bar{\omega}_1 = \sqrt{\frac{k_1}{m_1}}$, $\bar{\omega}_2 = \sqrt{\frac{k_2}{m_2}}$, $\bar{\omega}_3 = \sqrt{\frac{k_3}{m_1}}$, and $\bar{\omega}_4 = \sqrt{\frac{k_4}{m_2}}$.

Figure 3.12 depicts the normalized damped frequencies, damping ratios, and cumulative damping ratios for the DPnC and DPPnCs without grounding in the IBZ, i.e., for $\mu \in [0, \pi]$. The damped frequencies are normalized with respect to $\bar{\omega}_1$; i.e., the plots depict $\Omega_l = \frac{\omega_{d_l}}{\bar{\omega}_1}$, where $l=1$ (acoustic branch), 2 (optical branch). It is noticed in figure 3.12(a) that the transmission bands illustrated by the DPnC and DPPnCs with grounding are remarkably narrow and the three periodic media have approximately similar band structures except that the DPnC presents a slightly lower and narrower second transmission band. In figure 3.12(b), it is observed that the DPPnCs portray higher levels of ζ_1 , ζ_2 , and ζ_{sum} in comparison to the DPnC. In figure 3.12(c), the DPPnCs present a considerably higher rate of increase of ζ_l^{cum} ($l=1, 2$, or sum) in comparison to the DPnC. The DPPnC with an inductor demonstrates the highest values of ζ_1^{tot} , ζ_2^{tot} , and $\zeta_{\text{sum}}^{\text{tot}}$ as evidenced in table 3.8.

Table 3.7: Mechanical and dimensionless electrical parameters employed in the diatomic phononic crystal (DPnC) and diatomic piezoelectric phononic crystals (DPPnCs) with grounding.

Parameter	DPnC	DPPnC without an inductor	DPPnC with an inductor	Unit
a	1	1	1	m
m_1	0.0170	0.0170	0.0170	Kg
m_2	0.0340	0.0340	0.0340	Kg
k_1	2.0500×10^3	2.0500×10^3	2.0500×10^3	Nm^{-1}
k_2	1.0250×10^3	1.0250×10^3	1.0250×10^3	Nm^{-1}
k_3	4.1000×10^3	4.1000×10^3	4.1000×10^3	Nm^{-1}
k_4	4.1000×10^3	4.1000×10^3	4.1000×10^3	Nm^{-1}
c_1	0.2180	0.2180	0.2180	Nsm^{-1}
c_2	0.2180	0.2180	0.2180	Nsm^{-1}
c_3	0.2180	0.2180	0.2180	Nsm^{-1}
c_4	0.2180	0.2180	0.2180	Nsm^{-1}
α_1	—	0.4480	0.4480	—
α_2	—	0.2240	0.2240	—
α_3	—	0.6335	0.6335	—
α_4	—	0.4480	0.4480	—
β_1	—	—	0.4926	—
β_2	—	—	0.1232	—
β_3	—	—	0.9852	—
β_4	—	—	0.4926	—
$k_{\text{coeff}_1}^2$	—	0.2369	0.2369	—
$k_{\text{coeff}_2}^2$	—	0.4738	0.4738	—
$k_{\text{coeff}_3}^2$	—	0.1185	0.1185	—
$k_{\text{coeff}_4}^2$	—	0.1185	0.1185	—

Table 3.8: Total values of damping ratios of the diatomic phononic crystal (DPnC) and diatomic piezoelectric phononic crystals (DPPnCs) with grounding.

Parameter	DPnC	DPPnC without an inductor	DPPnC with an inductor	Unit
ζ_1^{tot}	0.0517	0.1659	0.2068	—
ζ_2^{tot}	0.1015	0.2613	0.3671	—
$\zeta_{\text{sum}}^{\text{tot}}$	0.1532	0.4272	0.5738	—

3.8 Overview of locally resonant metamaterials

In this section, the application of generalized Bloch's theorem to different configurations of locally resonant metamaterials (LRMs) is illustrated as an overview. LRMs are distinct to the

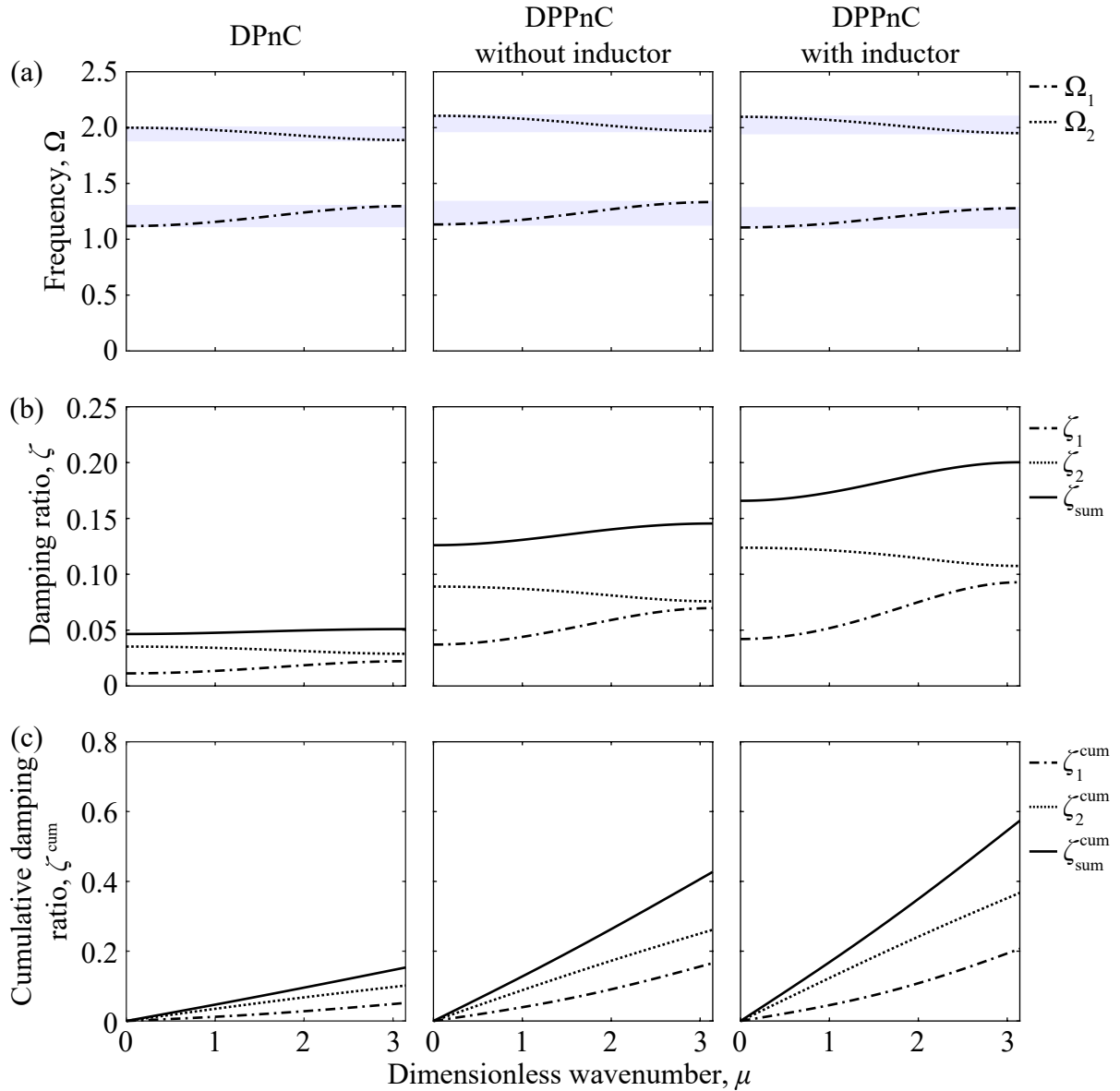


Figure 3.12: (a) Frequency band structure, (b) damping-ratio diagrams, and (c) cumulative-damping-ratio diagrams for the diatomic phononic crystal (DPnC) and diatomic piezoelectric phononic crystals (DPPnCs) with grounding.

PnCs in the way that they possess a locally resonant mechanism, usually, a mass, attached to the base mass via an oscillator.

3.8.1 Without grounding

Figure 3.13 presents the schematics of an LRM chain under free vibration without any grounding and the associated unit cell as lumped-parameter models. An LRM unit cell, depicted in figure 3.13(b), consists of a base mass m_1 and a locally resonant mass m_2 .

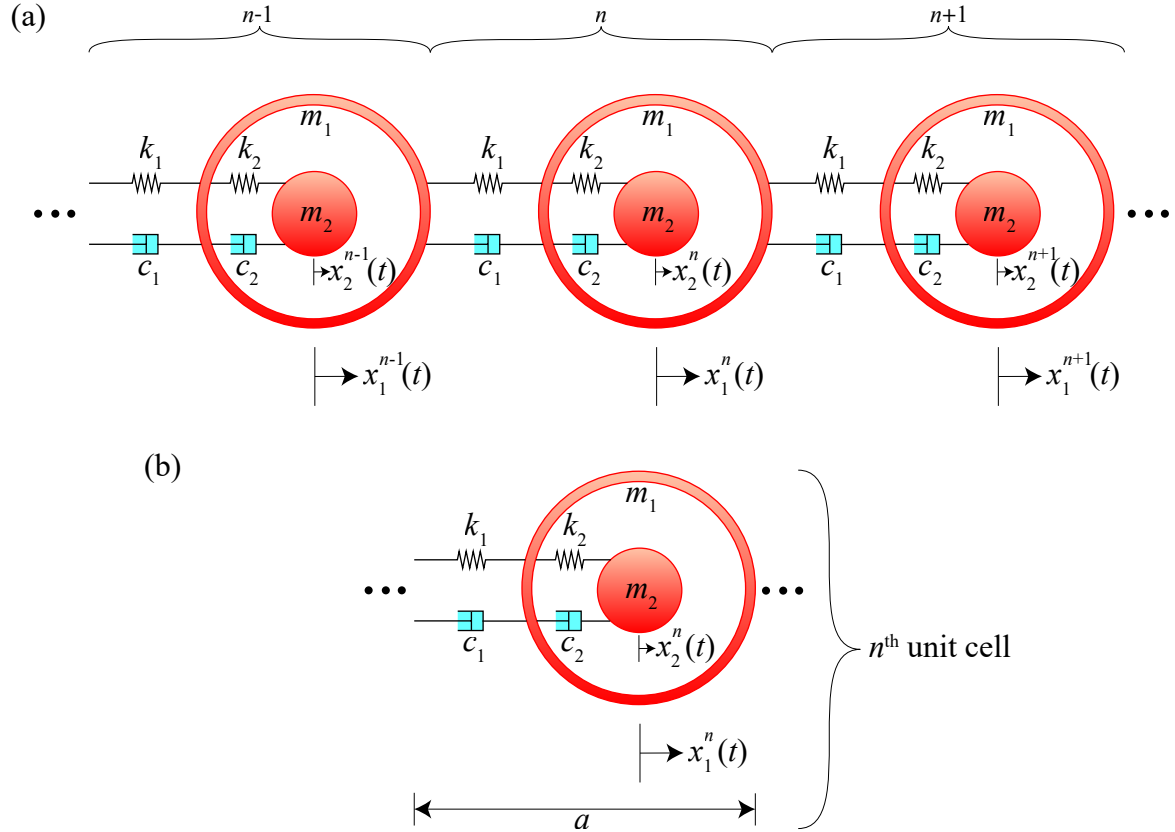


Figure 3.13: Schematic of (a) a locally resonant metamaterial (LRM) chain without grounding and (b) the associated unit cell.

The forces on the base mass and the locally resonant mass in the central unit cell, i.e., the n^{th} unit cell shown in figure 3.13(b), under free vibration can be aggregated, and the governing equations pertaining to the central unit cell can be written as

$$m_1 \ddot{x}_1^n + c_1(2\dot{x}_1^n - \dot{x}_1^{n-1} - \dot{x}_1^{n+1}) + c_2(\dot{x}_1^n - \dot{x}_2^n) + k_1(2x_1^n - x_1^{n-1} - x_1^{n+1}) + k_2(x_1^n - x_2^n) = 0, \quad (3.135)$$

$$m_2 \ddot{x}_2^n + c_2(\dot{x}_2^n - \dot{x}_1^n) + k_2(x_2^n - x_1^n) = 0. \quad (3.136)$$

Substituting equation (3.51) in equations (3.135) and (3.136) yields the following Bloch-transformed homogeneous equations for the displacement amplitudes \tilde{x}_1 and \tilde{x}_2 :

$$m_1\ddot{\tilde{x}}_1 + (c_1(2 - e^{-i\kappa a} - e^{i\kappa a}) + c_2)\dot{\tilde{x}}_1 + (-c_2)\dot{\tilde{x}}_2 + (k_1(2 - e^{-i\kappa a} - e^{i\kappa a}) + k_2)\tilde{x}_1 + (-k_2)\tilde{x}_2 = 0, \quad (3.137)$$

$$m_2\ddot{\tilde{x}}_2 + c_2\dot{\tilde{x}}_2 + (-c_2)\dot{\tilde{x}}_1 + k_2\tilde{x}_2 + (-k_2)\tilde{x}_1 = 0. \quad (3.138)$$

Equations (3.137) and (3.138) can be assembled into a matrix form as

$$\mathbf{M}\ddot{\tilde{\mathbf{X}}} + \mathbf{C}(\kappa)\dot{\tilde{\mathbf{X}}} + \mathbf{K}(\kappa)\tilde{\mathbf{X}} = \mathbf{0}, \quad (3.139)$$

where

$$\tilde{\mathbf{X}} = \begin{pmatrix} \tilde{x}_1 \\ \tilde{x}_2 \end{pmatrix}; \mathbf{M} = \begin{pmatrix} m_1 & 0 \\ 0 & m_2 \end{pmatrix}; \mathbf{C}(\kappa) = \begin{pmatrix} c_1(2 - e^{-i\kappa a} - e^{i\kappa a}) + c_2 & -c_2 \\ -c_2 & c_2 \end{pmatrix};$$

$$\text{and } \mathbf{K}(\kappa) = \begin{pmatrix} k_1(2 - e^{-i\kappa a} - e^{i\kappa a}) + k_2 & -k_2 \\ -k_2 & k_2 \end{pmatrix}. \quad (3.140)$$

The dispersion relation can now be formulated by subjecting equation (3.139) to a state-space transformation of the form given in equation (3.4), where

$$\mathbf{A} = \begin{pmatrix} \mathbf{0} & \mathbf{I} \\ \mathbf{M} & \mathbf{C}(\kappa) \end{pmatrix}; \mathbf{B} = \begin{pmatrix} -\mathbf{I} & \mathbf{0} \\ \mathbf{0} & \mathbf{K}(\kappa) \end{pmatrix}; \text{ and } \mathbf{Y} = \begin{pmatrix} \dot{\tilde{\mathbf{X}}} \\ \tilde{\mathbf{X}} \end{pmatrix}, \quad (3.141)$$

implementing a solution of the form $\mathbf{Y} = \tilde{\mathbf{Y}}_\lambda e^{\lambda t}$, and solving the resulting eigenvalue problem of the form given in equation (3.6). Expanding equation (3.6) for this particular case yields a fourth-order equation in terms of λ , which, upon solving, gives four complex roots appearing as two complex-conjugate pairs.

3.8.2 With grounding

Figure 3.14 presents the schematics of an LRM chain under free vibration with grounding and the associated unit cell as lumped-parameter models. This case is representative of a scenario where the LRM chain is attached to bars; i.e., the base mass m_1 in a unit cell is attached to a bar. For the sake of simplification, the bars are simply modelled as damped oscillators as shown in figure 3.14.

The forces on the base mass and the locally resonant mass in the central unit cell, i.e., the n^{th} unit cell shown in figure 3.14(b), under free vibration can be aggregated, and the

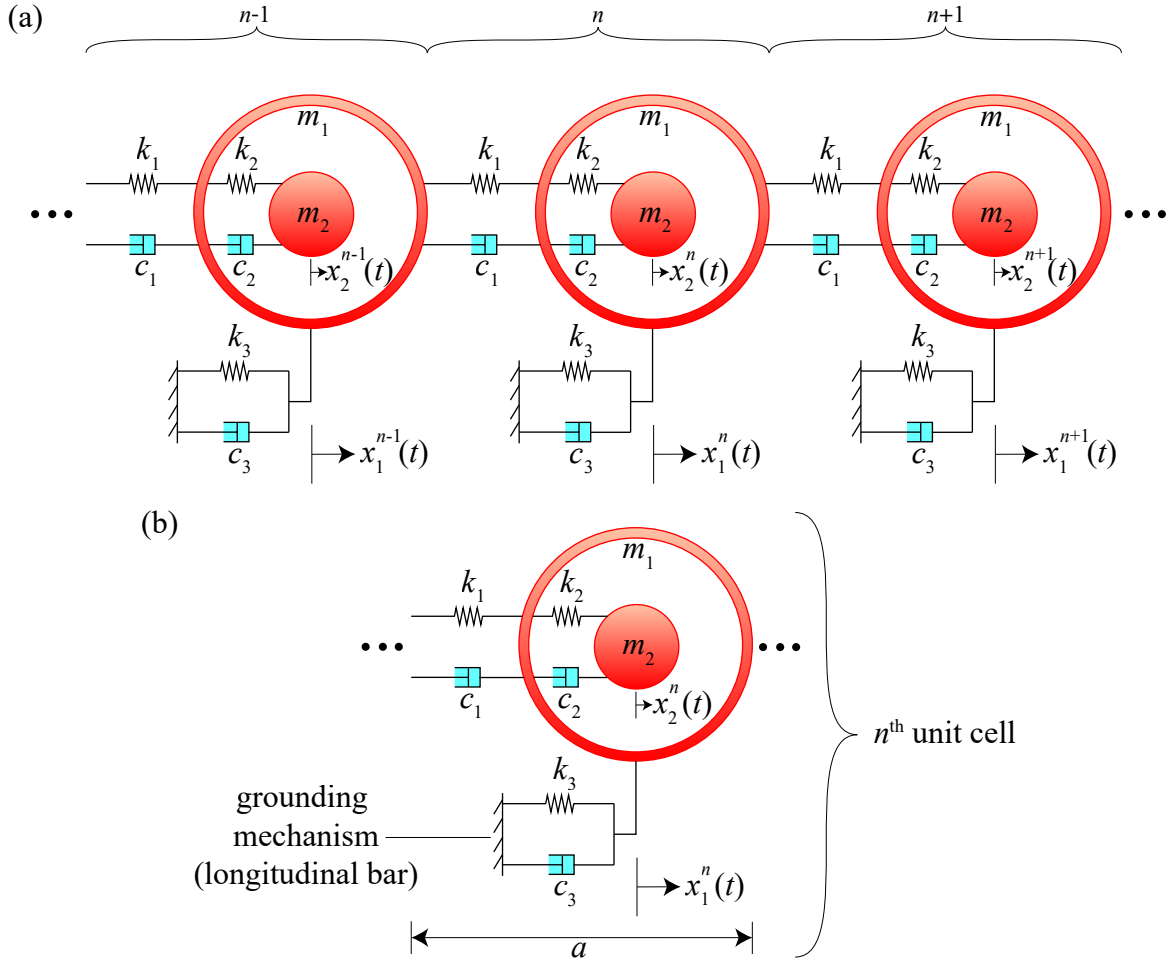


Figure 3.14: Schematic of (a) a locally resonant metamaterial (LRM) chain with grounding and (b) the associated unit cell.

governing equations pertaining to the central unit cell can be written as

$$m_1 \ddot{x}_1^n + c_1(2\dot{x}_1^n - \dot{x}_1^{n-1} - \dot{x}_1^{n+1}) + (c_2 + c_3)\dot{x}_1^n - c_2\dot{x}_2^n + k_1(2x_1^n - x_1^{n-1} - x_1^{n+1}) + (k_2 + k_3)x_1^n - k_2x_2^n = 0, \quad (3.142)$$

$$m_2 \ddot{x}_2^n + c_2(\dot{x}_2^n - \dot{x}_1^n) + k_2(x_2^n - x_1^n) = 0. \quad (3.143)$$

Substituting equation (3.51) in equations (3.142) and (3.143) yields the following Bloch-transformed homogeneous equations for the displacement amplitudes \tilde{x}_1 and \tilde{x}_2 :

$$m_1 \ddot{\tilde{x}}_1 + (c_1(2 - e^{-ika} - e^{ika}) + c_2 + c_3)\dot{\tilde{x}}_1 + (-c_2)\dot{\tilde{x}}_2 + (k_1(2 - e^{-ika} - e^{ika}) + k_2 + k_3)\tilde{x}_1 + (-k_2)\tilde{x}_2 = 0, \quad (3.144)$$

$$m_2 \ddot{\tilde{x}}_2 + c_2\dot{\tilde{x}}_2 + (-c_2)\dot{\tilde{x}}_1 + k_2\tilde{x}_2 + (-k_2)\tilde{x}_1 = 0. \quad (3.145)$$

Equations (3.144) and (3.145) can be compacted into a matrix form as

$$\mathbf{M}\ddot{\tilde{\mathbf{X}}} + \mathbf{C}(\kappa)\dot{\tilde{\mathbf{X}}} + \mathbf{K}(\kappa)\tilde{\mathbf{X}} = \mathbf{0}, \quad (3.146)$$

where

$$\tilde{\mathbf{X}} = \begin{pmatrix} \tilde{x}_1 \\ \tilde{x}_2 \end{pmatrix}; \mathbf{M} = \begin{pmatrix} m_1 & 0 \\ 0 & m_2 \end{pmatrix}; \mathbf{C}(\kappa) = \begin{pmatrix} c_1(2 - e^{-i\kappa a} - e^{i\kappa a}) + c_2 + c_3 & -c_2 \\ & -c_2 & c_2 \end{pmatrix};$$

$$\text{and } \mathbf{K}(\kappa) = \begin{pmatrix} k_1(2 - e^{-i\kappa a} - e^{i\kappa a}) + k_2 + k_3 & -k_2 \\ & -k_2 & k_2 \end{pmatrix}. \quad (3.147)$$

The dispersion relation can now be formulated by subjecting equation (3.146) to a state-space transformation of the form given in equation (3.4), where

$$\mathbf{A} = \begin{pmatrix} \mathbf{0} & \mathbf{I} \\ \mathbf{M} & \mathbf{C}(\kappa) \end{pmatrix}; \mathbf{B} = \begin{pmatrix} -\mathbf{I} & \mathbf{0} \\ \mathbf{0} & \mathbf{K}(\kappa) \end{pmatrix}; \text{ and } \mathbf{Y} = \begin{pmatrix} \dot{\tilde{\mathbf{X}}} \\ \tilde{\mathbf{X}} \end{pmatrix}, \quad (3.148)$$

implementing a solution of the form $\mathbf{Y} = \tilde{\mathbf{Y}}_\lambda e^{\lambda t}$, and solving the resulting eigenvalue problem of the form given in equation (3.6). Expanding equation (3.6) for this particular case yields a fourth-order equation in terms of λ , which, upon solving, gives four complex roots appearing as two complex-conjugate pairs.

3.9 Locally resonant piezoelectric metamaterials

This section delves into the application of generalized Bloch's theorem to different configurations of locally resonant piezoelectric metamaterials (LRPMs). The configurations addressed in this section are, essentially, the piezoelectric counterparts of the configurations addressed in section 3.8.

3.9.1 Without grounding

Figure 3.15 presents the schematics of an LRPM chain under free vibration without any grounding and the associated unit cell as lumped-parameter models.

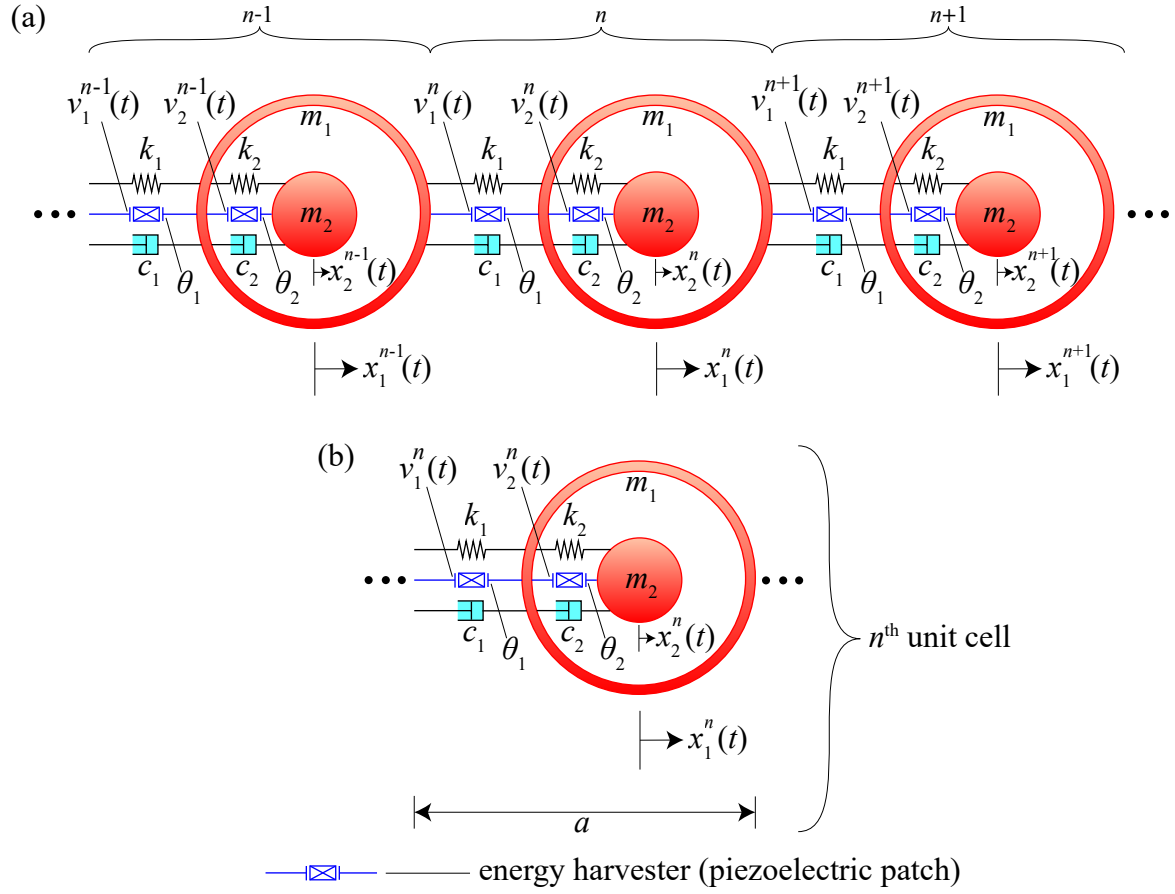


Figure 3.15: Schematic of (a) a locally resonant piezoelectric metamaterial (LRPM) chain without grounding and (b) the associated unit cell.

Shunt circuit without an inductor

The governing electromechanical equations pertaining to the n^{th} unit cell under free vibration consisting of piezoelectric elements with a shunt circuit lacking an inductor can be written as

$$m_1 \ddot{x}_1^n + c_1(2\dot{x}_1^n - \dot{x}_1^{n-1} - \dot{x}_1^{n+1}) + c_2(\dot{x}_1^n - \dot{x}_2^n) + k_1(2x_1^n - x_1^{n-1} - x_1^{n+1}) + k_2(x_1^n - x_2^n) + \theta_1 v_1^n - \theta_1 v_1^{n+1} - \theta_2 v_2^n = 0, \quad (3.149)$$

$$m_2 \ddot{x}_2^n + c_2(\dot{x}_2^n - \dot{x}_1^n) + k_2(x_2^n - x_1^n) + \theta_2 v_2^n = 0, \quad (3.150)$$

$$-\theta_1(\dot{x}_1^n - \dot{x}_1^{n-1}) + C_{p1} \dot{v}_1^n + \frac{1}{R_1} v_1^n = 0, \quad (3.151)$$

$$-\theta_2(\dot{x}_2^n - \dot{x}_1^n) + C_{p2} \dot{v}_2^n + \frac{1}{R_2} v_2^n = 0. \quad (3.152)$$

Substituting equations (3.51) and (3.31) in equations (3.149)–(3.152) yields the following Bloch-transformed homogeneous equations for the displacement amplitudes \tilde{x}_1 and \tilde{x}_2 and

the voltage amplitudes \tilde{v}_1 and \tilde{v}_2 :

$$m_1\ddot{\tilde{x}}_1 + (c_1(2 - e^{-i\kappa a} - e^{i\kappa a}) + c_2)\dot{\tilde{x}}_1 + (-c_2)\dot{\tilde{x}}_2 + (k_1(2 - e^{-i\kappa a} - e^{i\kappa a}) + k_2)\tilde{x}_1 + (-k_2)\tilde{x}_2 + (\theta_1 - \theta_1 e^{i\kappa a})\tilde{v}_1 + (-\theta_2)\tilde{v}_2 = 0, \quad (3.153)$$

$$m_2\ddot{\tilde{x}}_2 + c_2\dot{\tilde{x}}_2 + (-c_2)\dot{\tilde{x}}_1 + k_2\tilde{x}_2 + (-k_2)\tilde{x}_1 + \theta_2\tilde{v}_2 = 0, \quad (3.154)$$

$$(-\theta_1 + \theta_1 e^{-i\kappa a})\dot{\tilde{x}}_1 + C_{p1}\dot{\tilde{v}}_1 + \frac{1}{R_1}\tilde{v}_1 = 0, \quad (3.155)$$

$$-\theta_2\dot{\tilde{x}}_2 + \theta_2\dot{\tilde{x}}_1 + C_{p2}\dot{\tilde{v}}_2 + \frac{1}{R_2}\tilde{v}_2 = 0. \quad (3.156)$$

Equations (3.153)–(3.156) can be compacted into matrix equations as

$$\mathbf{M}\ddot{\tilde{\mathbf{X}}} + \mathbf{C}(\kappa)\dot{\tilde{\mathbf{X}}} + \mathbf{K}(\kappa)\tilde{\mathbf{X}} + \mathbf{T}_1(\kappa)\tilde{\mathbf{V}} = \mathbf{0}, \quad (3.157)$$

$$\mathbf{T}_2(\kappa)\dot{\tilde{\mathbf{X}}} + \mathbf{C}_p\dot{\tilde{\mathbf{V}}} + \mathbf{R}\tilde{\mathbf{V}} = \mathbf{0}, \quad (3.158)$$

where

$$\begin{aligned} \tilde{\mathbf{X}} &= \begin{pmatrix} \tilde{x}_1 \\ \tilde{x}_2 \end{pmatrix}; \quad \tilde{\mathbf{V}} = \begin{pmatrix} \tilde{v}_1 \\ \tilde{v}_2 \end{pmatrix}; \quad \mathbf{M} = \begin{pmatrix} m_1 & 0 \\ 0 & m_2 \end{pmatrix}; \\ \mathbf{C}(\kappa) &= \begin{pmatrix} c_1(2 - e^{-i\kappa a} - e^{i\kappa a}) + c_2 & -c_2 \\ -c_2 & c_2 \end{pmatrix}; \\ \mathbf{K}(\kappa) &= \begin{pmatrix} k_1(2 - e^{-i\kappa a} - e^{i\kappa a}) + k_2 & -k_2 \\ -k_2 & k_2 \end{pmatrix}; \\ \mathbf{T}_1(\kappa) &= \begin{pmatrix} \theta_1 - \theta_1 e^{i\kappa a} & -\theta_2 \\ 0 & \theta_2 \end{pmatrix}; \quad \mathbf{T}_2(\kappa) = \begin{pmatrix} -\theta_1 + \theta_1 e^{-i\kappa a} & 0 \\ \theta_2 & -\theta_2 \end{pmatrix}; \\ \mathbf{C}_p &= \begin{pmatrix} C_{p1} & 0 \\ 0 & C_{p2} \end{pmatrix}; \quad \text{and } \mathbf{R} = \begin{pmatrix} \frac{1}{R_1} & 0 \\ 0 & \frac{1}{R_2} \end{pmatrix}. \end{aligned} \quad (3.159)$$

The dispersion relation can now be derived by subjecting equations (3.157) and (3.158) to a state-space transformation of the form given in equation (3.4), where

$$\mathbf{A} = \begin{pmatrix} \mathbf{0} & \mathbf{I} & \mathbf{0} \\ \mathbf{M} & \mathbf{C}(\kappa) & \mathbf{0} \\ \mathbf{0} & \mathbf{T}_2(\kappa) & \mathbf{C}_p \end{pmatrix}; \quad \mathbf{B} = \begin{pmatrix} -\mathbf{I} & \mathbf{0} & \mathbf{0} \\ \mathbf{0} & \mathbf{K}(\kappa) & \mathbf{T}_1(\kappa) \\ \mathbf{0} & \mathbf{0} & \mathbf{R} \end{pmatrix}; \quad \text{and } \mathbf{Y} = \begin{pmatrix} \dot{\tilde{\mathbf{X}}} \\ \tilde{\mathbf{X}} \\ \tilde{\mathbf{V}} \end{pmatrix}, \quad (3.160)$$

implementing a solution of the form $\mathbf{Y} = \tilde{\mathbf{Y}}_\lambda e^{\lambda t}$, and solving the resulting eigenvalue problem of the form given in equation (3.6). Expanding equation (3.6) for this particular case yields a sixth-order equation in terms of λ , which, upon solving, gives four complex roots appearing as two complex-conjugate pairs and two real roots.

Shunt circuit with an inductor

The governing electromechanical equations pertaining to the n^{th} unit cell under free vibration consisting of piezoelectric elements with a shunt circuit equipped with an inductor can be written as

$$m_1 \ddot{x}_1^n + c_1(2\dot{x}_1^n - \dot{x}_1^{n-1} - \dot{x}_1^{n+1}) + c_2(\dot{x}_1^n - \dot{x}_2^n) + k_1(2x_1^n - x_1^{n-1} - x_1^{n+1}) + k_2(x_1^n - x_2^n) + \theta_1 v_1^n - \theta_1 v_1^{n+1} - \theta_2 v_2^n = 0, \quad (3.161)$$

$$m_2 \ddot{x}_2^n + c_2(\dot{x}_2^n - \dot{x}_1^n) + k_2(x_2^n - x_1^n) + \theta_2 v_2^n = 0, \quad (3.162)$$

$$-\theta_1(\dot{x}_1^n - \dot{x}_1^{n-1}) + C_{p1} \dot{v}_1^n + \frac{1}{R_1} v_1^n + \frac{1}{L_1} v_1^n = 0, \quad (3.163)$$

$$-\theta_2(\dot{x}_2^n - \dot{x}_1^n) + C_{p2} \dot{v}_2^n + \frac{1}{R_2} v_2^n + \frac{1}{L_2} v_2^n = 0. \quad (3.164)$$

Substituting equations (3.51) and (3.31) in equations (3.161)–(3.164) yields the following Bloch-transformed homogeneous equations for the displacement amplitudes \tilde{x}_1 and \tilde{x}_2 and the voltage amplitudes \tilde{v}_1 and \tilde{v}_2 :

$$m_1 \ddot{\tilde{x}}_1 + (c_1(2 - e^{-i\kappa a} - e^{i\kappa a}) + c_2)\dot{\tilde{x}}_1 + (-c_2)\dot{\tilde{x}}_2 + (k_1(2 - e^{-i\kappa a} - e^{i\kappa a}) + k_2)\tilde{x}_1 + (-k_2)\tilde{x}_2 + (\theta_1 - \theta_1 e^{i\kappa a})\tilde{v}_1 + (-\theta_2)\tilde{v}_2 = 0, \quad (3.165)$$

$$m_2 \ddot{\tilde{x}}_2 + c_2 \dot{\tilde{x}}_2 + (-c_2)\dot{\tilde{x}}_1 + k_2 \tilde{x}_2 + (-k_2)\tilde{x}_1 + \theta_2 \tilde{v}_2 = 0, \quad (3.166)$$

$$(-\theta_1 + \theta_1 e^{-i\kappa a})\dot{\tilde{x}}_1 + C_{p1} \dot{\tilde{v}}_1 + \frac{1}{R_1} \tilde{v}_1 + \frac{1}{L_1} \tilde{v}_1 = 0, \quad (3.167)$$

$$-\theta_2 \dot{\tilde{x}}_2 + \theta_2 \dot{\tilde{x}}_1 + C_{p2} \dot{\tilde{v}}_2 + \frac{1}{R_2} \tilde{v}_2 + \frac{1}{L_2} \tilde{v}_2 = 0. \quad (3.168)$$

Equations (3.165)–(3.168) can be assembled into matrix equations as

$$\mathbf{M}\ddot{\tilde{\mathbf{X}}} + \mathbf{C}(\kappa)\dot{\tilde{\mathbf{X}}} + \mathbf{K}(\kappa)\tilde{\mathbf{X}} + \mathbf{T}_1(\kappa)\tilde{\mathbf{V}} = \mathbf{0}, \quad (3.169)$$

$$\mathbf{T}_2(\kappa)\dot{\tilde{\mathbf{X}}} + \mathbf{C}_p\dot{\tilde{\mathbf{V}}} + \mathbf{R}\tilde{\mathbf{V}} + \mathbf{L}\tilde{\mathbf{V}} = \mathbf{0}, \quad (3.170)$$

where

$$\begin{aligned}
\tilde{\mathbf{X}} &= \begin{pmatrix} \tilde{x}_1 \\ \tilde{x}_2 \end{pmatrix}; \quad \tilde{\mathbf{V}} = \begin{pmatrix} \tilde{v}_1 \\ \tilde{v}_2 \end{pmatrix}; \quad \mathbf{M} = \begin{pmatrix} m_1 & 0 \\ 0 & m_2 \end{pmatrix}; \\
\mathbf{C}(\kappa) &= \begin{pmatrix} c_1(2 - e^{-i\kappa a} - e^{i\kappa a}) + c_2 & -c_2 \\ -c_2 & c_2 \end{pmatrix}; \\
\mathbf{K}(\kappa) &= \begin{pmatrix} k_1(2 - e^{-i\kappa a} - e^{i\kappa a}) + k_2 & -k_2 \\ -k_2 & k_2 \end{pmatrix}; \\
\mathbf{T}_1(\kappa) &= \begin{pmatrix} \theta_1 - \theta_1 e^{i\kappa a} & -\theta_2 \\ 0 & \theta_2 \end{pmatrix}; \quad \mathbf{T}_2(\kappa) = \begin{pmatrix} -\theta_1 + \theta_1 e^{-i\kappa a} & 0 \\ \theta_2 & -\theta_2 \end{pmatrix}; \\
\mathbf{C}_p &= \begin{pmatrix} C_{p1} & 0 \\ 0 & C_{p2} \end{pmatrix}; \quad \mathbf{R} = \begin{pmatrix} \frac{1}{R_1} & 0 \\ 0 & \frac{1}{R_2} \end{pmatrix}; \quad \text{and } \mathbf{L} = \begin{pmatrix} \frac{1}{L_1} & 0 \\ 0 & \frac{1}{L_2} \end{pmatrix}. \quad (3.171)
\end{aligned}$$

Equations (3.169) and (3.170) can be further compacted into a single matrix equation as

$$\mathbf{Z}_1 \ddot{\tilde{\mathbf{E}}} + \mathbf{Z}_2 \dot{\tilde{\mathbf{E}}} + \mathbf{Z}_3 \tilde{\mathbf{E}} = \mathbf{0}, \quad (3.172)$$

where

$$\begin{aligned}
\mathbf{Z}_1 &= \begin{pmatrix} \mathbf{M} & \mathbf{0} \\ \mathbf{T}_2(\kappa) & \mathbf{C}_p \end{pmatrix}; \quad \mathbf{Z}_2 = \begin{pmatrix} \mathbf{C}(\kappa) & \mathbf{0} \\ \mathbf{0} & \mathbf{R} \end{pmatrix}; \quad \mathbf{Z}_3 = \begin{pmatrix} \mathbf{K}(\kappa) & \mathbf{T}_1(\kappa) \\ \mathbf{0} & \mathbf{L} \end{pmatrix}; \\
&\quad \text{and } \tilde{\mathbf{E}} = \begin{pmatrix} \tilde{\mathbf{X}} \\ \tilde{\mathbf{V}} \end{pmatrix}. \quad (3.173)
\end{aligned}$$

The dispersion relation can now be formulated by subjecting equation (3.172) to a state-space transformation of the form given in equation (3.4), where

$$\mathbf{A} = \begin{pmatrix} \mathbf{0} & \mathbf{I} \\ \mathbf{Z}_1 & \mathbf{Z}_2 \end{pmatrix}; \quad \mathbf{B} = \begin{pmatrix} -\mathbf{I} & \mathbf{0} \\ \mathbf{0} & \mathbf{Z}_3 \end{pmatrix}; \quad \text{and } \mathbf{Y} = \begin{pmatrix} \dot{\tilde{\mathbf{E}}} \\ \tilde{\mathbf{E}} \end{pmatrix}, \quad (3.174)$$

implementing a solution of the form $\mathbf{Y} = \tilde{\mathbf{Y}}_\lambda e^{\lambda t}$, and solving the resulting eigenvalue problem of the form given in equation (3.6). Expanding equation (3.6) for this particular case yields an eight-order equation in terms of λ , which, upon solving, gives four complex roots appearing as two complex-conjugate pairs and four real roots.

3.9.2 With grounding

Figure 3.16 presents the schematics of an LRPM chain under free vibration with grounding and the associated unit cell as lumped-parameter models.

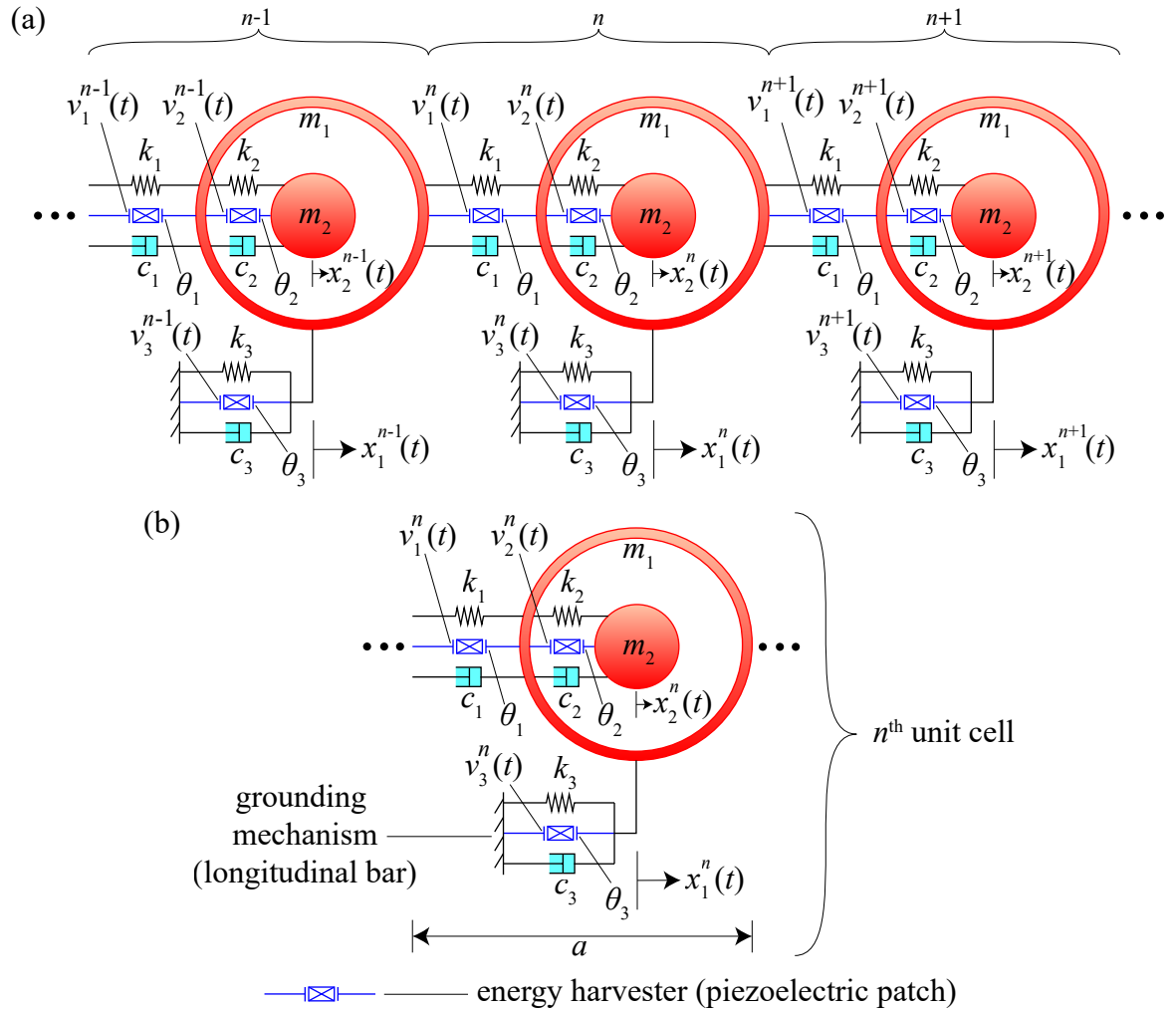


Figure 3.16: Schematic of (a) a locally resonant piezoelectric metamaterial (LRPM) chain with grounding and (b) the associated unit cell.

Shunt circuit without an inductor

The governing electromechanical equations pertaining to the n^{th} unit cell under free vibration consisting of piezoelectric elements with a purely resistive shunt circuit can be written as

$$m_1 \ddot{x}_1^n + c_1(2\dot{x}_1^n - \dot{x}_1^{n-1} - \dot{x}_1^{n+1}) + (c_2 + c_3)\dot{x}_1^n - c_2\dot{x}_2^n + k_1(2x_1^n - x_1^{n-1} - x_1^{n+1}) + (k_2 + k_3)x_1^n - k_2x_2^n + \theta_1 v_1^n - \theta_1 v_1^{n+1} - \theta_2 v_2^n + \theta_3 v_3^n = 0, \quad (3.175)$$

$$m_2 \ddot{x}_2^n + c_2(\dot{x}_2^n - \dot{x}_1^n) + k_2(x_2^n - x_1^n) + \theta_2 v_2^n = 0, \quad (3.176)$$

$$-\theta_1(\dot{x}_1^n - \dot{x}_1^{n-1}) + C_{p1}\dot{v}_1^n + \frac{1}{R_1}v_1^n = 0, \quad (3.177)$$

$$-\theta_2(\dot{x}_2^n - \dot{x}_1^n) + C_{p2}\dot{v}_2^n + \frac{1}{R_2}v_2^n = 0, \quad (3.178)$$

$$-\theta_3\dot{x}_1^n + C_{p3}\dot{v}_3^n + \frac{1}{R_3}v_3^n = 0. \quad (3.179)$$

Substituting equations (3.51) and (3.31) in equations (3.175)–(3.179) yields the following Bloch-transformed homogeneous equations for the displacement amplitudes \tilde{x}_1 and \tilde{x}_2 and the voltage amplitudes \tilde{v}_1 , \tilde{v}_2 , and \tilde{v}_3 :

$$m_1 \ddot{\tilde{x}}_1 + (c_1(2 - e^{-ika} - e^{ika}) + c_2 + c_3)\dot{\tilde{x}}_1 + (-c_2)\dot{\tilde{x}}_2 + (k_1(2 - e^{-ika} - e^{ika}) + k_2 + k_3)\tilde{x}_1 + (-k_2)\tilde{x}_2 + (\theta_1 - \theta_1 e^{ika})\tilde{v}_1 + (-\theta_2)\tilde{v}_2 + \theta_3\tilde{v}_3 = 0, \quad (3.180)$$

$$m_2 \ddot{\tilde{x}}_2 + c_2\dot{\tilde{x}}_2 + (-c_2)\dot{\tilde{x}}_1 + k_2\tilde{x}_2 + (-k_2)\tilde{x}_1 + \theta_2\tilde{v}_2 = 0, \quad (3.181)$$

$$(-\theta_1 + \theta_1 e^{-ika})\dot{\tilde{x}}_1 + C_{p1}\dot{\tilde{v}}_1 + \frac{1}{R_1}\tilde{v}_1 = 0, \quad (3.182)$$

$$-\theta_2\dot{\tilde{x}}_2 + \theta_2\dot{\tilde{x}}_1 + C_{p2}\dot{\tilde{v}}_2 + \frac{1}{R_2}\tilde{v}_2 = 0, \quad (3.183)$$

$$-\theta_3\dot{\tilde{x}}_1 + C_{p3}\dot{\tilde{v}}_3 + \frac{1}{R_3}\tilde{v}_3 = 0. \quad (3.184)$$

The dispersion relation can now be formulated by subjecting equations (3.180)–(3.184) to a state-space transformation of the form given in equation (3.4), where

$$\mathbf{A} = \begin{pmatrix} 0 & 1 & 0 & 0 & 0 & 0 & 0 \\ 0 & 0 & 0 & 1 & 0 & 0 & 0 \\ m_1 & c_1 b + c_2 + c_3 & 0 & -c_2 & 0 & 0 & 0 \\ 0 & -c_2 & m_2 & c_2 & 0 & 0 & 0 \\ 0 & -\theta_1 + \theta_1 e^{-ika} & 0 & 0 & C_{p1} & 0 & 0 \\ 0 & \theta_2 & 0 & -\theta_2 & 0 & C_{p2} & 0 \\ 0 & -\theta_3 & 0 & 0 & 0 & 0 & C_{p3} \end{pmatrix};$$

$$\mathbf{B} = \begin{pmatrix} -1 & 0 & 0 & 0 & 0 & 0 & 0 \\ 0 & 0 & -1 & 0 & 0 & 0 & 0 \\ 0 & k_1 b + k_2 + k_3 & 0 & -k_2 & \theta_1 - \theta_1 e^{ika} & -\theta_2 & \theta_3 \\ 0 & -k_2 & 0 & k_2 & 0 & \theta_2 & 0 \\ 0 & 0 & 0 & 0 & \frac{1}{R_1} & 0 & 0 \\ 0 & 0 & 0 & 0 & 0 & \frac{1}{R_2} & 0 \\ 0 & 0 & 0 & 0 & 0 & 0 & \frac{1}{R_3} \end{pmatrix};$$

$$\text{and } \mathbf{Y} = \begin{pmatrix} \dot{\tilde{x}}_1 \\ \tilde{x}_1 \\ \dot{\tilde{x}}_2 \\ \tilde{x}_2 \\ \tilde{v}_1 \\ \tilde{v}_2 \\ \tilde{v}_3 \end{pmatrix}, \quad (3.185)$$

implementing a solution of the form $\mathbf{Y} = \tilde{\mathbf{Y}}_\lambda e^{\lambda t}$, and solving the resulting eigenvalue problem of the form given in equation (3.6). Expanding equation (3.6) for this particular case yields a seventh-order equation in terms of λ , which, upon solving, gives four complex roots appearing as two complex-conjugate pairs and three real roots. In \mathbf{A} and \mathbf{B} in equation (3.185), the term $b = 2 - e^{-ika} - e^{ika}$.

Shunt circuit with an inductor

The governing electromechanical equations pertinent to the n^{th} unit cell under free vibration consisting of piezoelectric elements with a shunt circuit including an inductor can be written

as

$$m_1 \ddot{x}_1^n + c_1(2\dot{x}_1^n - \dot{x}_1^{n-1} - \dot{x}_1^{n+1}) + (c_2 + c_3)\dot{x}_1^n - c_2\dot{x}_2^n + k_1(2x_1^n - x_1^{n-1} - x_1^{n+1}) + (k_2 + k_3)x_1^n - k_2x_2^n + \theta_1 v_1^n - \theta_1 v_1^{n+1} - \theta_2 v_2^n + \theta_3 v_3^n = 0, \quad (3.186)$$

$$m_2 \ddot{x}_2^n + c_2(\dot{x}_2^n - \dot{x}_1^n) + k_2(x_2^n - x_1^n) + \theta_2 v_2^n = 0, \quad (3.187)$$

$$-\theta_1(\dot{x}_1^n - \dot{x}_1^{n-1}) + C_{p1}\ddot{v}_1^n + \frac{1}{R_1}\dot{v}_1^n + \frac{1}{L_1}v_1^n = 0, \quad (3.188)$$

$$-\theta_2(\dot{x}_2^n - \dot{x}_1^n) + C_{p2}\ddot{v}_2^n + \frac{1}{R_2}\dot{v}_2^n + \frac{1}{L_2}v_2^n = 0, \quad (3.189)$$

$$-\theta_3\dot{x}_1^n + C_{p3}\ddot{v}_3^n + \frac{1}{R_3}\dot{v}_3^n + \frac{1}{L_3}v_3^n = 0. \quad (3.190)$$

Substituting equations (3.51) and (3.31) in equations (3.186)–(3.190) yields the following Bloch-transformed homogeneous equations for the displacement amplitudes \tilde{x}_1 and \tilde{x}_2 and the voltage amplitudes \tilde{v}_1 , \tilde{v}_2 , and \tilde{v}_3 :

$$m_1 \ddot{\tilde{x}}_1 + (c_1(2 - e^{-ika} - e^{ika}) + c_2 + c_3)\dot{\tilde{x}}_1 + (-c_2)\dot{\tilde{x}}_2 + (k_1(2 - e^{-ika} - e^{ika}) + k_2 + k_3)\tilde{x}_1 + (-k_2)\tilde{x}_2 + (\theta_1 - \theta_1 e^{ika})\tilde{v}_1 + (-\theta_2)\tilde{v}_2 + \theta_3\tilde{v}_3 = 0, \quad (3.191)$$

$$m_2 \ddot{\tilde{x}}_2 + c_2\dot{\tilde{x}}_2 + (-c_2)\dot{\tilde{x}}_1 + k_2\tilde{x}_2 + (-k_2)\tilde{x}_1 + \theta_2\tilde{v}_2 = 0, \quad (3.192)$$

$$(-\theta_1 + \theta_1 e^{-ika})\dot{\tilde{x}}_1 + C_{p1}\ddot{\tilde{v}}_1 + \frac{1}{R_1}\dot{\tilde{v}}_1 + \frac{1}{L_1}\tilde{v}_1 = 0, \quad (3.193)$$

$$-\theta_2\dot{\tilde{x}}_2 + \theta_2\dot{\tilde{x}}_1 + C_{p2}\ddot{\tilde{v}}_2 + \frac{1}{R_2}\dot{\tilde{v}}_2 + \frac{1}{L_2}\tilde{v}_2 = 0, \quad (3.194)$$

$$-\theta_3\dot{\tilde{x}}_1 + C_{p3}\ddot{\tilde{v}}_3 + \frac{1}{R_3}\dot{\tilde{v}}_3 + \frac{1}{L_3}\tilde{v}_3 = 0. \quad (3.195)$$

Equations (3.191)–(3.195) can be fused into a matrix form as

$$\mathbf{Z}_1 \ddot{\tilde{\mathbf{E}}} + \mathbf{Z}_2 \dot{\tilde{\mathbf{E}}} + \mathbf{Z}_3 \tilde{\mathbf{E}} = \mathbf{0}, \quad (3.196)$$

where

$$\begin{aligned}
 \mathbf{Z}_1 &= \begin{pmatrix} m_1 & 0 & 0 & 0 & 0 \\ 0 & m_2 & 0 & 0 & 0 \\ -\theta_1 + \theta_1 e^{-i\kappa a} & 0 & C_{p1} & 0 & 0 \\ \theta_2 & -\theta_2 & 0 & C_{p2} & 0 \\ -\theta_3 & 0 & 0 & 0 & C_{p3} \end{pmatrix}; \\
 \mathbf{Z}_2 &= \begin{pmatrix} c_1 b + c_2 + c_3 & -c_2 & 0 & 0 & 0 \\ -c_2 & c_2 & 0 & 0 & 0 \\ 0 & 0 & \frac{1}{R_1} & 0 & 0 \\ 0 & 0 & 0 & \frac{1}{R_2} & 0 \\ 0 & 0 & 0 & 0 & \frac{1}{R_3} \end{pmatrix}; \\
 \mathbf{Z}_3 &= \begin{pmatrix} k_1 b + k_2 + k_3 & -k_2 & \theta_1 - \theta_1 e^{i\kappa a} & -\theta_2 & \theta_3 \\ -k_2 & k_2 & 0 & \theta_2 & 0 \\ 0 & 0 & \frac{1}{L_1} & 0 & 0 \\ 0 & 0 & 0 & \frac{1}{L_2} & 0 \\ 0 & 0 & 0 & 0 & \frac{1}{L_3} \end{pmatrix}; \text{ and } \tilde{\mathbf{E}} = \begin{pmatrix} \tilde{x}_1 \\ \tilde{x}_2 \\ \tilde{v}_1 \\ \tilde{v}_2 \\ \tilde{v}_3 \end{pmatrix}. \quad (3.197)
 \end{aligned}$$

In \mathbf{Z}_2 and \mathbf{Z}_3 , the term $b = 2 - e^{-i\kappa a} - e^{i\kappa a}$. The dispersion relation can now be formulated by subjecting equation (3.196) to a state-space transformation of the form given in equation (3.4), where

$$\mathbf{A} = \begin{pmatrix} \mathbf{0} & \mathbf{I} \\ \mathbf{Z}_1 & \mathbf{Z}_2 \end{pmatrix}; \mathbf{B} = \begin{pmatrix} -\mathbf{I} & \mathbf{0} \\ \mathbf{0} & \mathbf{Z}_3 \end{pmatrix}; \text{ and } \mathbf{Y} = \begin{pmatrix} \tilde{\mathbf{E}} \\ \tilde{\mathbf{E}} \end{pmatrix}, \quad (3.198)$$

implementing a solution of the form $\mathbf{Y} = \tilde{\mathbf{Y}}_\lambda e^{\lambda t}$, and solving the resulting eigenvalue problem of the form given in equation (3.6). Expanding equation (3.6) for this particular case yields a tenth-order equation in terms of λ , which, upon solving, gives four complex roots appearing as two complex-conjugate pairs and six real roots.

3.10 Wave-propagation and dissipation characteristics of locally resonant metamaterials and piezoelectric metamaterials

This section presents the wave-propagation and dissipation characteristics of the different configurations of LRMs and LRPMs discussed so far in a graphical comparative format.

3.10.1 Without grounding

Table 3.9 details the parameters utilized in the computation of the dispersion (band structure) and damping-ratio characteristics of the LRM and LRPMs without grounding. The electrical parameters of the shunt circuit are non-dimensionalized in a fashion similar to the case of DPPnC without grounding.

Table 3.9: Mechanical and dimensionless electrical parameters employed in the locally resonant metamaterial (LRM) and locally resonant piezoelectric metamaterials (LRPMs) without grounding.

Parameter	LRM	LRPM without an inductor	LRPM with an inductor	Unit
a	1	1	1	m
m_1	0.0170	0.0170	0.0170	Kg
m_2	0.0340	0.0340	0.0340	Kg
k_1	3×10^4	3×10^4	3×10^4	Nm ⁻¹
k_2	1.5000×10^4	1.5000×10^4	1.5000×10^4	Nm ⁻¹
c_1	2	2	2	Nsm ⁻¹
c_2	2	2	2	Nsm ⁻¹
α_1	—	0.1594	0.1594	—
α_2	—	0.3188	0.3188	—
β_1	—	—	0.7059	—
β_2	—	—	0.7059	—
$k_{\text{coeff}_1}^2$	—	0.1333	0.1333	—
$k_{\text{coeff}_2}^2$	—	0.5333	0.5333	—

Figure 3.17 depicts the normalized damped frequencies, damping ratios, and cumulative damping ratios for the LRM and LRPMs without grounding in the IBZ, i.e., for $\mu \in [0, \pi]$. The damped frequencies are normalized with respect to $\bar{\omega}_1 = \sqrt{\frac{k_1}{m_1}}$; i.e., the plots depict $\Omega_l = \frac{\omega_{d_l}}{\bar{\omega}_1}$, where $l=1$ (acoustic branch), 2 (optical branch). Considering that, similar to a DPPnC, a locally

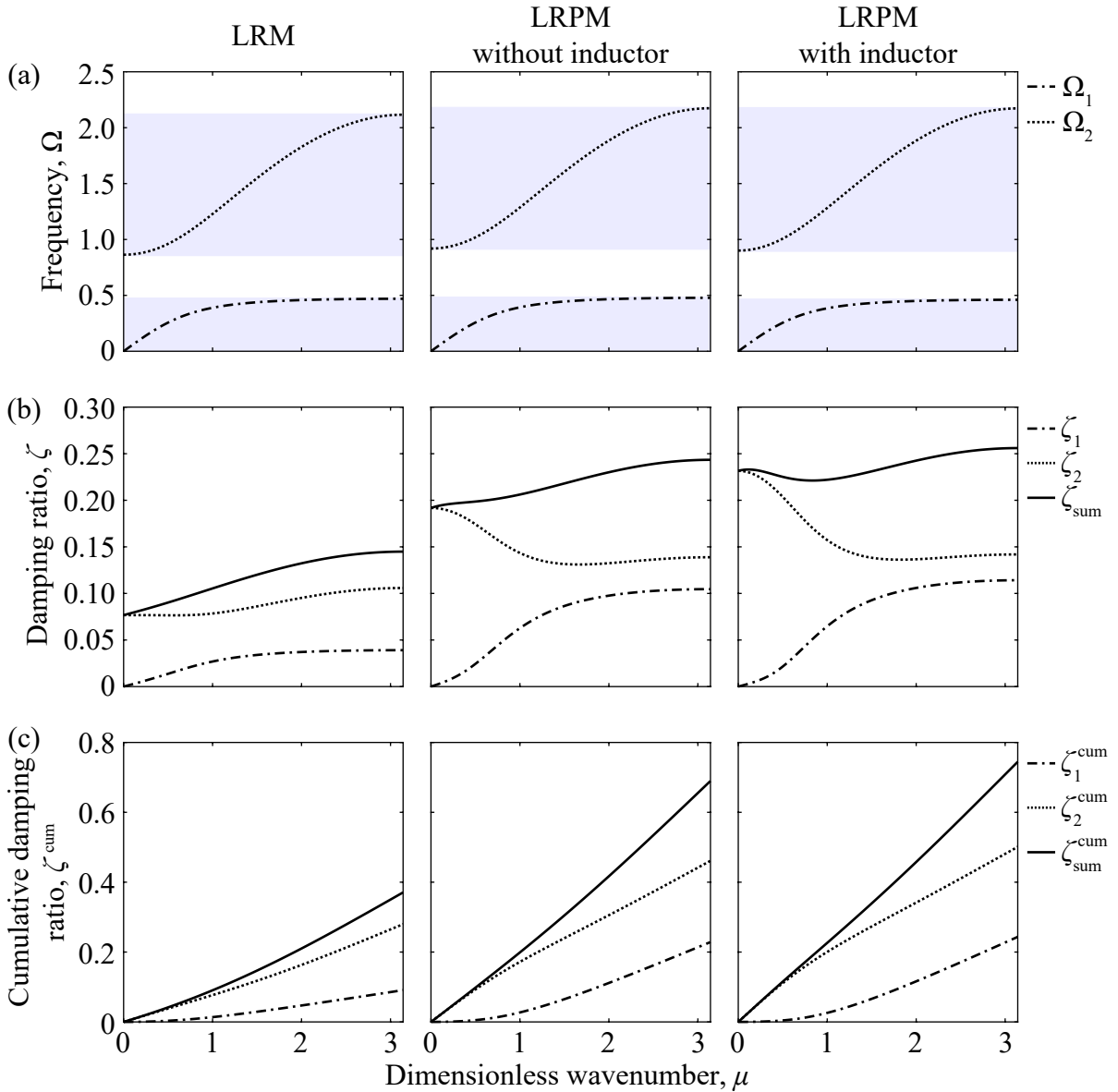


Figure 3.17: (a) Frequency band structure, (b) damping-ratio diagrams, and (c) cumulative-damping-ratio diagrams for the locally resonant metamaterial (LRM) and locally resonant piezoelectric metamaterials (LRPMs) without grounding.

resonant unit cell has two branches, figure 3.17(a) presents two transmission bands and two attenuation bands as indicated by the shaded and non-shaded regions, respectively. The LRM and LRPMs without grounding exhibit a wider second transmission band as opposed to the first transmission band. The three periodic media have a roughly similar band structure except that the LRM depicts a lower second transmission band. For dispersion band structures that are approximately similar, figure 3.17(b) shows a significant disparity in the damping ratio

curves. It is observed that, in comparison to the LRM, the LRPMS display higher levels of ζ_1 , ζ_2 , and ζ_{sum} . In figure 3.17(c), the LRPMS present a much higher rate of increase of ζ_l^{cum} ($l=1, 2$, or sum) in comparison to the LRM. The value of ζ_l^{tot} ($l=1, 2$, or sum) is the highest for the LRPM with an inductor. Table 3.10 details the ζ_l^{tot} values for the three periodic media.

Table 3.10: Total values of damping ratios of the locally resonant metamaterial (LRM) and locally resonant piezoelectric metamaterials (LRPMs) without grounding.

Parameter	LRM	LRPM without an inductor	LRPM with an inductor	Unit
ζ_1^{tot}	0.0909	0.2285	0.2436	—
ζ_2^{tot}	0.2798	0.4612	0.5012	—
$\zeta_{\text{sum}}^{\text{tot}}$	0.3707	0.6897	0.7447	—

3.10.2 With grounding

Table 3.11 details the parameters utilized in the computation of the dispersion (band structure) and damping-ratio characteristics of the LRM and LRPMS with grounding.

Considering that there are three piezoelectric elements in a unit cell in this particular case, the electrical parameters of the shunt circuit are non-dimensionalized as

$$\alpha_l = \bar{\omega}_l C_{p_l} R_l, \quad (3.199a)$$

$$\beta_l = \bar{\omega}_l^2 C_{p_l} L_l, \quad (3.199b)$$

$$k_{\text{coeff}_l}^2 = \frac{\theta_l^2}{k_l C_{p_l}}, \quad (3.199c)$$

where $l = 1, 2, 3$ is an index corresponding to the parameters of the three piezoelectric elements and the frequencies obtained from the three springs: $\bar{\omega}_1 = \sqrt{\frac{k_1}{m_1}}$, $\bar{\omega}_2 = \sqrt{\frac{k_2}{m_2}}$, and $\bar{\omega}_3 = \sqrt{\frac{k_3}{m_1}}$.

Figure 3.18 depicts the normalized damped frequencies, damping ratios, and cumulative damping ratios for the LRM and LRPMS without grounding in the IBZ, i.e., for $\mu \in [0, \pi]$. The damped frequencies are normalized with respect to $\bar{\omega}_1$; i.e., the plots depict $\Omega_l = \frac{\omega_{d_l}}{\bar{\omega}_1}$, where $l=1$ (acoustic branch), 2 (optical branch). It is noticed in figure 3.18(a) that the LRM and LRPMS with grounding exhibit a wider second transmission band as opposed to the first transmission band. The periodic media have an approximately similar band structure

Table 3.11: Mechanical and dimensionless electrical parameters employed in the locally resonant metamaterial (LRM) and locally resonant piezoelectric metamaterials (LRPMs) with grounding.

Parameter	LRM	LRPM without an inductor	LRPM with an inductor	Unit
a	1	1	1	m
m_1	0.0170	0.0170	0.0170	Kg
m_2	0.0340	0.0340	0.0340	Kg
k_1	5×10^3	5×10^3	5×10^3	Nm^{-1}
k_2	10×10^3	10×10^3	10×10^3	Nm^{-1}
k_3	5×10^3	5×10^3	5×10^3	Nm^{-1}
c_1	2	2	2	Nsm^{-1}
c_2	2	2	2	Nsm^{-1}
c_3	2	2	2	Nsm^{-1}
α_1	—	0.0651	0.0651	—
α_2	—	0.2603	0.2603	—
α_3	—	0.0651	0.0651	—
β_1	—	—	0.2353	—
β_2	—	—	0.9412	—
β_3	—	—	0.2353	—
$k_{\text{coeff}_1}^2$	—	0.8000	0.8000	—
$k_{\text{coeff}_2}^2$	—	0.8000	0.8000	—
$k_{\text{coeff}_3}^2$	—	0.8000	0.8000	—

except that the LRM presents a slightly lower second transmission band. In figure 3.18(b), it is noticed that the LRPMs portray higher levels of ζ_l ($l=1, 2$, or sum) in comparison to the LRM. In figure 3.18(c), the LRPMs present a considerably higher rate of increase of ζ_l^{cum} ($l=1, 2$, or sum) in comparison to the LRM. The LRPM with an inductor demonstrates the highest values of ζ_l^{tot} ($l=1, 2$, or sum) as evidenced in table 3.12.

Table 3.12: Total values of damping ratios of the locally resonant metamaterial (LRM) and locally resonant piezoelectric metamaterials (LRPMs) with grounding.

Parameter	LRM	LRPM without an inductor	LRPM with an inductor	Unit
ζ_1^{tot}	0.1824	0.3229	0.3264	—
ζ_2^{tot}	0.5885	0.9857	1.0442	—
$\zeta_{\text{sum}}^{\text{tot}}$	0.7709	1.3086	1.3706	—

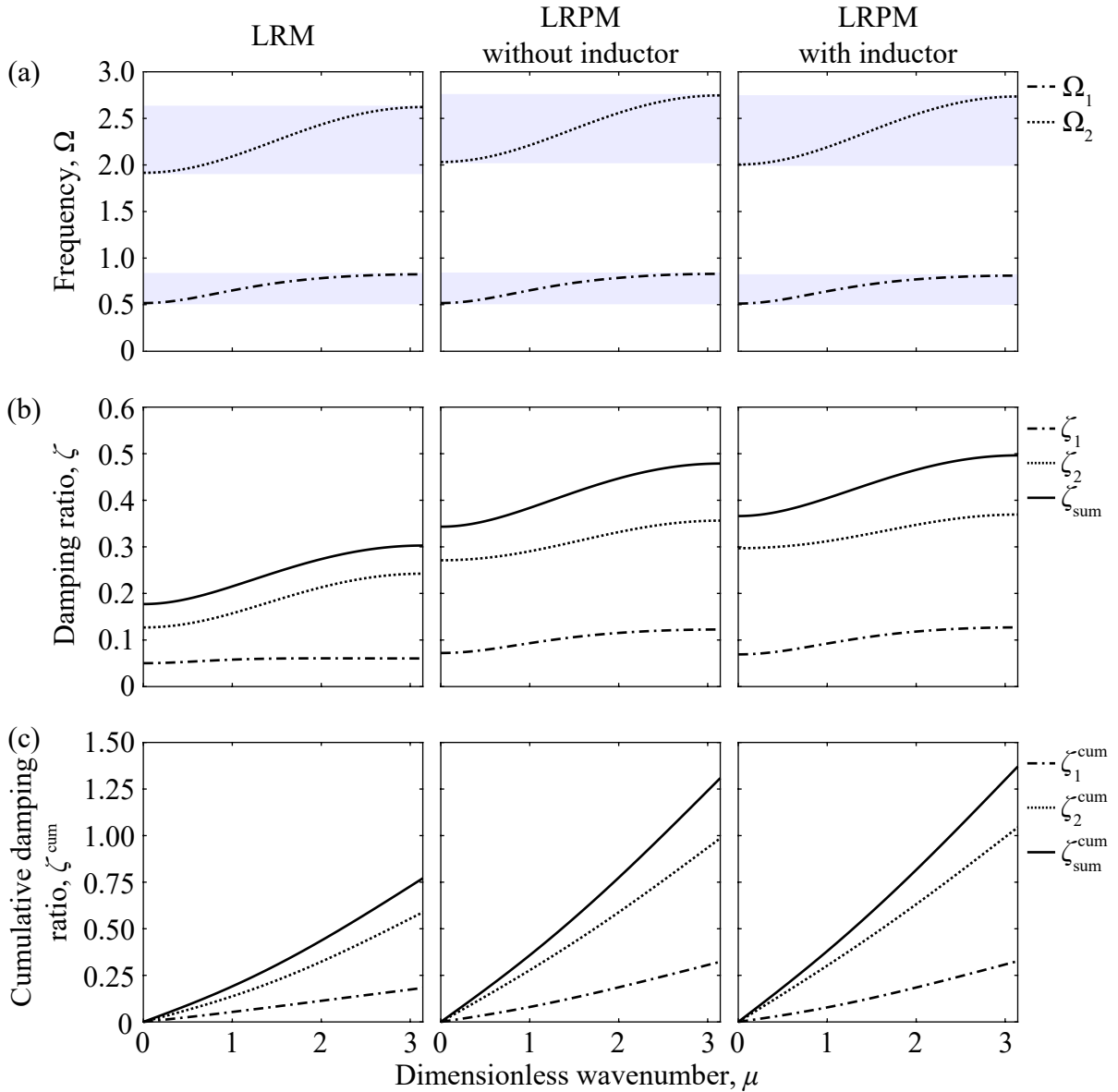


Figure 3.18: (a) Frequency band structure, (b) damping-ratio diagrams, and (c) cumulative-damping-ratio diagrams for the locally resonant metamaterial (LRM) and locally resonant piezoelectric metamaterials (LRPMs) with grounding.

3.11 Overview of inertially amplified locally resonant metamaterials

In this section, the application of generalized Bloch's theorem to different configurations of inertially amplified locally resonant metamaterials (IALRMs) is described as an overview. IALRMs are akin to LRMs, but in addition to containing a locally resonant mechanism,

usually, a mass, attached to the base mass via an oscillator, they are equipped with an inertial-amplifier mechanism, usually, a mass, attached to the baseline mass via rigid rods. The purpose of the inertial-amplifier mechanism is to increase the effective inertia of a unit cell.

3.11.1 Without grounding

Figure 3.19 presents the schematics of an IALRM chain under free vibration without any grounding and the associated unit cell as lumped-parameter models. In addition to each baseline mass in an IALRM chain connected to a locally resonant mass, each baseline mass is connected to the neighbouring baseline masses on the left and right by inertial-amplifier attachments, each of which is comprised of an auxiliary mass and two rigid links—one for each of the baseline masses—as shown in figure 3.19(a). Hence, an IALRM unit cell, depicted in figure 3.19(b), consists of a base mass m_1 , a locally resonant mass m_2 , and an inertial-amplifier mass m_3 . As the auxiliary or inertial-amplifier mass, m_3 , is connected to the baseline mass, m_1 , by a rigid link, the inertial rigid coupling does not alter the total degrees of freedom of a unit cell; hence, an IALRM unit cell will only have two degrees of freedom similar to the DPnC and LRM. In figure 3.19, ϕ is the inertial-amplifier angle, which is the angle between the rigid links and the baseline.

The forces on the base mass and the locally resonant mass in the central unit cell, i.e., the n^{th} unit cell shown in figure 3.19(b), under free vibration can be aggregated, and the governing equations pertaining to the central unit cell can be written as

$$m_1 \ddot{x}_1^n + \chi(m_3(\ddot{x}_1^n - \ddot{x}_1^{n-1})) - \chi(m_3(\ddot{x}_1^{n+1} - \ddot{x}_1^n)) + c_1(2\dot{x}_1^n - \dot{x}_1^{n-1} - \dot{x}_1^{n+1}) + c_2(\dot{x}_1^n - \dot{x}_2^n) + k_1(2x_1^n - x_1^{n-1} - x_1^{n+1}) + k_2(x_1^n - x_2^n) = 0, \quad (3.200)$$

$$m_2 \ddot{x}_2^n + c_2(\dot{x}_2^n - \dot{x}_1^n) + k_2(x_2^n - x_1^n) = 0, \quad (3.201)$$

where, from system kinematics [48], $\chi = \frac{1}{4 \tan^2 \phi}$. The detailed derivation of equation (3.200) is presented in section 6.2.2 of chapter 6.

Substituting equation (3.51) in equations (3.200) and (3.201) yields the following Bloch-transformed homogeneous equations for the displacement amplitudes \tilde{x}_1 and \tilde{x}_2 :

$$(m_1 + \chi m_3(2 - e^{-i\kappa a} - e^{i\kappa a}))\ddot{\tilde{x}}_1 + (c_1(2 - e^{-i\kappa a} - e^{i\kappa a}) + c_2)\dot{\tilde{x}}_1 + (-c_2)\dot{\tilde{x}}_2 + (k_1(2 - e^{-i\kappa a} - e^{i\kappa a}) + k_2)\tilde{x}_1 + (-k_2)\tilde{x}_2 = 0, \quad (3.202)$$

$$m_2 \ddot{\tilde{x}}_2 + c_2 \dot{\tilde{x}}_2 + (-c_2)\dot{\tilde{x}}_1 + k_2 \tilde{x}_2 + (-k_2)\tilde{x}_1 = 0. \quad (3.203)$$

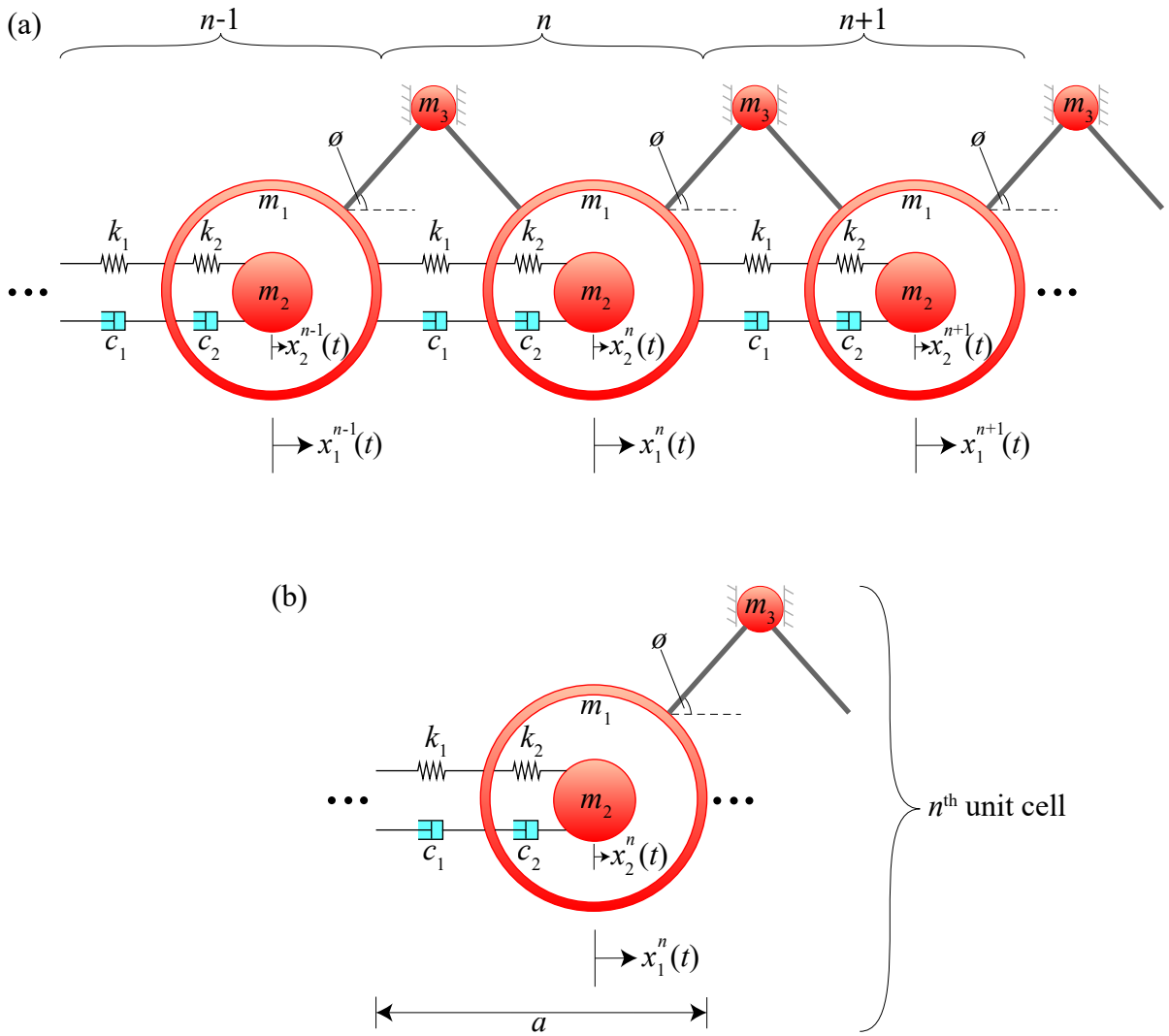


Figure 3.19: Schematic of (a) an inertially amplified locally resonant metamaterial (IALRM) chain without grounding and (b) the associated unit cell.

Equations (3.202) and (3.203) can be assembled into a matrix form as

$$\mathbf{M}\ddot{\mathbf{X}} + \mathbf{C}(\kappa)\dot{\mathbf{X}} + \mathbf{K}(\kappa)\mathbf{X} = \mathbf{0}, \quad (3.204)$$

where

$$\begin{aligned}\tilde{\mathbf{X}} &= \begin{pmatrix} \tilde{x}_1 \\ \tilde{x}_2 \end{pmatrix}; \mathbf{M} = \begin{pmatrix} m_1 + \frac{m_3}{4}(2 - e^{-ika} - e^{ika}) \cot^2 \phi & 0 \\ 0 & m_2 \end{pmatrix}; \\ \mathbf{C}(\kappa) &= \begin{pmatrix} c_1(2 - e^{-ika} - e^{ika}) + c_2 & -c_2 \\ -c_2 & c_2 \end{pmatrix}; \\ \text{and } \mathbf{K}(\kappa) &= \begin{pmatrix} k_1(2 - e^{-ika} - e^{ika}) + k_2 & -k_2 \\ -k_2 & k_2 \end{pmatrix}.\end{aligned}\quad (3.205)$$

The dispersion relation can now be formulated by subjecting equation (3.204) to a state-space transformation of the form given in equation (3.4), where

$$\mathbf{A} = \begin{pmatrix} \mathbf{0} & \mathbf{I} \\ \mathbf{M} & \mathbf{C}(\kappa) \end{pmatrix}; \mathbf{B} = \begin{pmatrix} -\mathbf{I} & \mathbf{0} \\ \mathbf{0} & \mathbf{K}(\kappa) \end{pmatrix}; \text{ and } \mathbf{Y} = \begin{pmatrix} \dot{\tilde{\mathbf{X}}} \\ \tilde{\mathbf{X}} \end{pmatrix}, \quad (3.206)$$

implementing a solution of the form $\mathbf{Y} = \tilde{\mathbf{Y}}_\lambda e^{\lambda t}$, and solving the resulting eigenvalue problem of the form given in equation (3.6). Expanding equation (3.6) for this particular case yields a fourth-order equation in terms of λ , which, upon solving, gives four complex roots appearing as two complex-conjugate pairs.

3.11.2 With grounding

Figure 3.20 presents the schematics of an IALRM chain under free vibration with grounding and the associated unit cell as lumped-parameter models. This case is representative of a scenario where the IALRM chain is attached to bars; i.e., the base mass m_1 in a unit cell is attached to a bar. For the sake of simplification, the bars are simply modelled as damped oscillators as shown in figure 3.20.

The forces on the base mass and the locally resonant mass in the central unit cell, i.e., the n^{th} unit cell shown in figure 3.20(b), under free vibration can be aggregated, and the governing equations pertaining to the central unit cell can be written as

$$\begin{aligned}m_1 \ddot{x}_1^n + \chi(m_3(\dot{x}_1^n - \dot{x}_1^{n-1})) - \chi(m_3(\dot{x}_1^{n+1} - \dot{x}_1^n)) + c_1(2x_1^n - x_1^{n-1} - x_1^{n+1}) \\ + (c_2 + c_3)\dot{x}_1^n - c_2\dot{x}_2^n + k_1(2x_1^n - x_1^{n-1} - x_1^{n+1}) + (k_2 + k_3)x_1^n - k_2x_2^n = 0,\end{aligned}\quad (3.207)$$

$$m_2 \ddot{x}_2^n + c_2(\dot{x}_2^n - \dot{x}_1^n) + k_2(x_2^n - x_1^n) = 0.\quad (3.208)$$

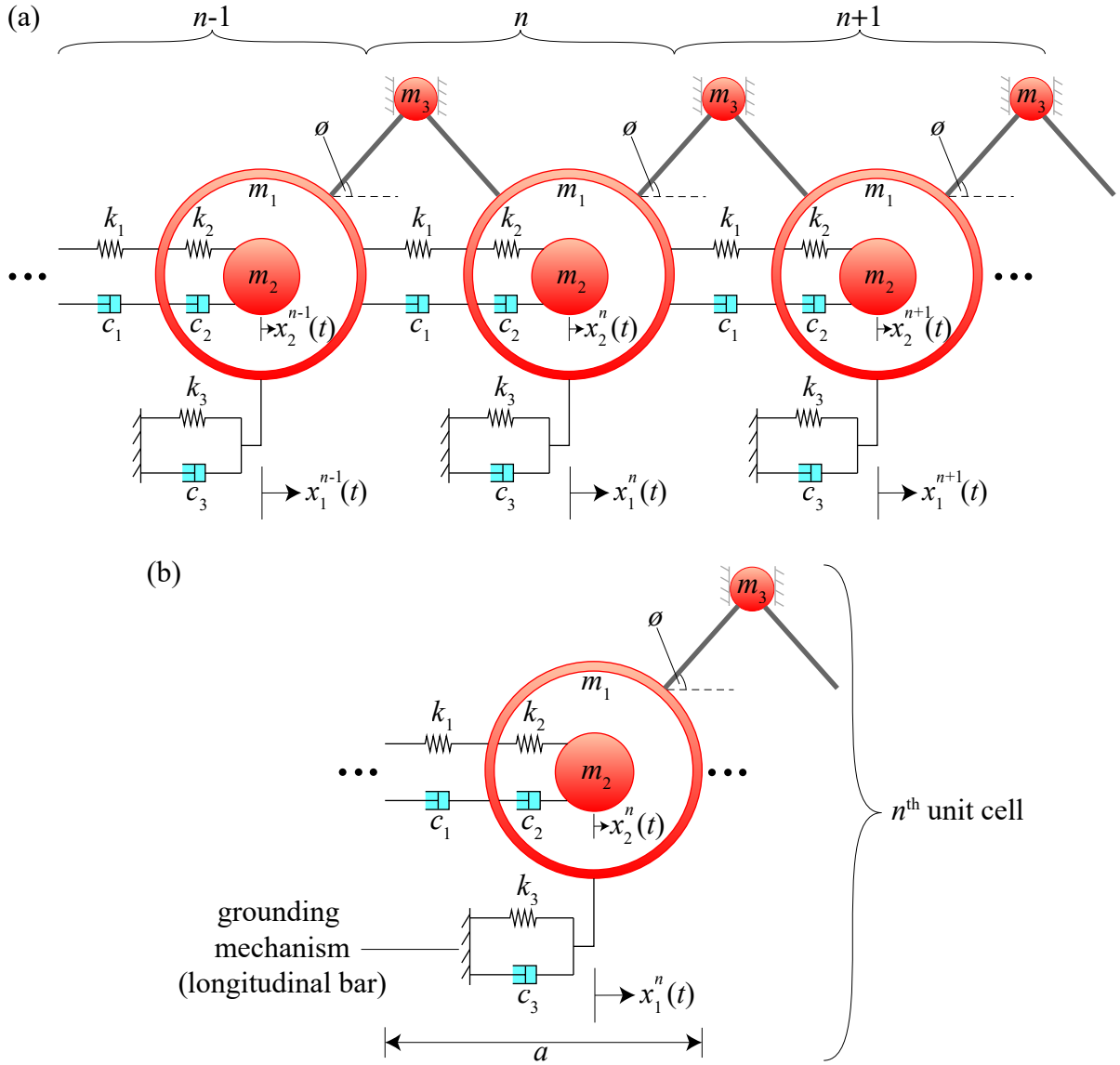


Figure 3.20: Schematic of (a) an inertially amplified-locally resonant-metamaterial (IALRM) chain with grounding and (b) the associated unit cell.

Substituting equation (3.51) in equations (3.207) and (3.208) yields the following Bloch-transformed homogeneous equations for the displacement amplitudes \tilde{x}_1 and \tilde{x}_2 :

$$(m_1 + \chi m_3(2 - e^{-ika} - e^{ika}))\ddot{\tilde{x}}_1 + (c_1(2 - e^{-ika} - e^{ika}) + c_2 + c_3)\dot{\tilde{x}}_1 + (-c_2)\dot{\tilde{x}}_2 + (k_1(2 - e^{-ika} - e^{ika}) + k_2 + k_3)\tilde{x}_1 + (-k_2)\tilde{x}_2 = 0, \quad (3.209)$$

$$m_2\ddot{\tilde{x}}_2 + c_2\dot{\tilde{x}}_2 + (-c_2)\dot{\tilde{x}}_1 + k_2\tilde{x}_2 + (-k_2)\tilde{x}_1 = 0. \quad (3.210)$$

Equations (3.209) and (3.210) can be compacted into a matrix form as

$$\mathbf{M}\ddot{\tilde{\mathbf{X}}} + \mathbf{C}(\kappa)\dot{\tilde{\mathbf{X}}} + \mathbf{K}(\kappa)\tilde{\mathbf{X}} = \mathbf{0}, \quad (3.211)$$

where

$$\begin{aligned} \tilde{\mathbf{X}} &= \begin{pmatrix} \tilde{x}_1 \\ \tilde{x}_2 \end{pmatrix}; \quad \mathbf{M} = \begin{pmatrix} m_1 + \frac{m_3}{4}(2 - e^{-i\kappa a} - e^{i\kappa a}) \cot^2 \phi & 0 \\ 0 & m_2 \end{pmatrix}; \\ \mathbf{C}(\kappa) &= \begin{pmatrix} c_1(2 - e^{-i\kappa a} - e^{i\kappa a}) + c_2 + c_3 & -c_2 \\ -c_2 & c_2 \end{pmatrix}; \\ \text{and } \mathbf{K}(\kappa) &= \begin{pmatrix} k_1(2 - e^{-i\kappa a} - e^{i\kappa a}) + k_2 + k_3 & -k_2 \\ -k_2 & k_2 \end{pmatrix}. \end{aligned} \quad (3.212)$$

The dispersion relation can now be formulated by subjecting equation (3.211) to a state-space transformation of the form given in equation (3.4), where

$$\mathbf{A} = \begin{pmatrix} \mathbf{0} & \mathbf{I} \\ \mathbf{M} & \mathbf{C}(\kappa) \end{pmatrix}; \quad \mathbf{B} = \begin{pmatrix} -\mathbf{I} & \mathbf{0} \\ \mathbf{0} & \mathbf{K}(\kappa) \end{pmatrix}; \quad \text{and } \mathbf{Y} = \begin{pmatrix} \dot{\tilde{\mathbf{X}}} \\ \tilde{\mathbf{X}} \end{pmatrix}, \quad (3.213)$$

implementing a solution of the form $\mathbf{Y} = \tilde{\mathbf{Y}}_\lambda e^{\lambda t}$, and solving the resulting eigenvalue problem of the form given in equation (3.6). Expanding equation (3.6) for this particular case yields a fourth-order equation in terms of λ , which, upon solving, gives four complex roots appearing as two complex-conjugate pairs.

3.12 Inertially amplified locally resonant piezoelectric metamaterials

This section delves into the application of generalized Bloch's theorem to different configurations of inertially amplified locally resonant piezoelectric metamaterials (IALRPMs). The configurations addressed in this section are, essentially, the piezoelectric counterparts of the configurations addressed in section 3.11.

3.12.1 Without grounding

Figure 3.21 presents the schematics of an IALRPM chain under free vibration without any grounding and the associated unit cell as lumped-parameter models.

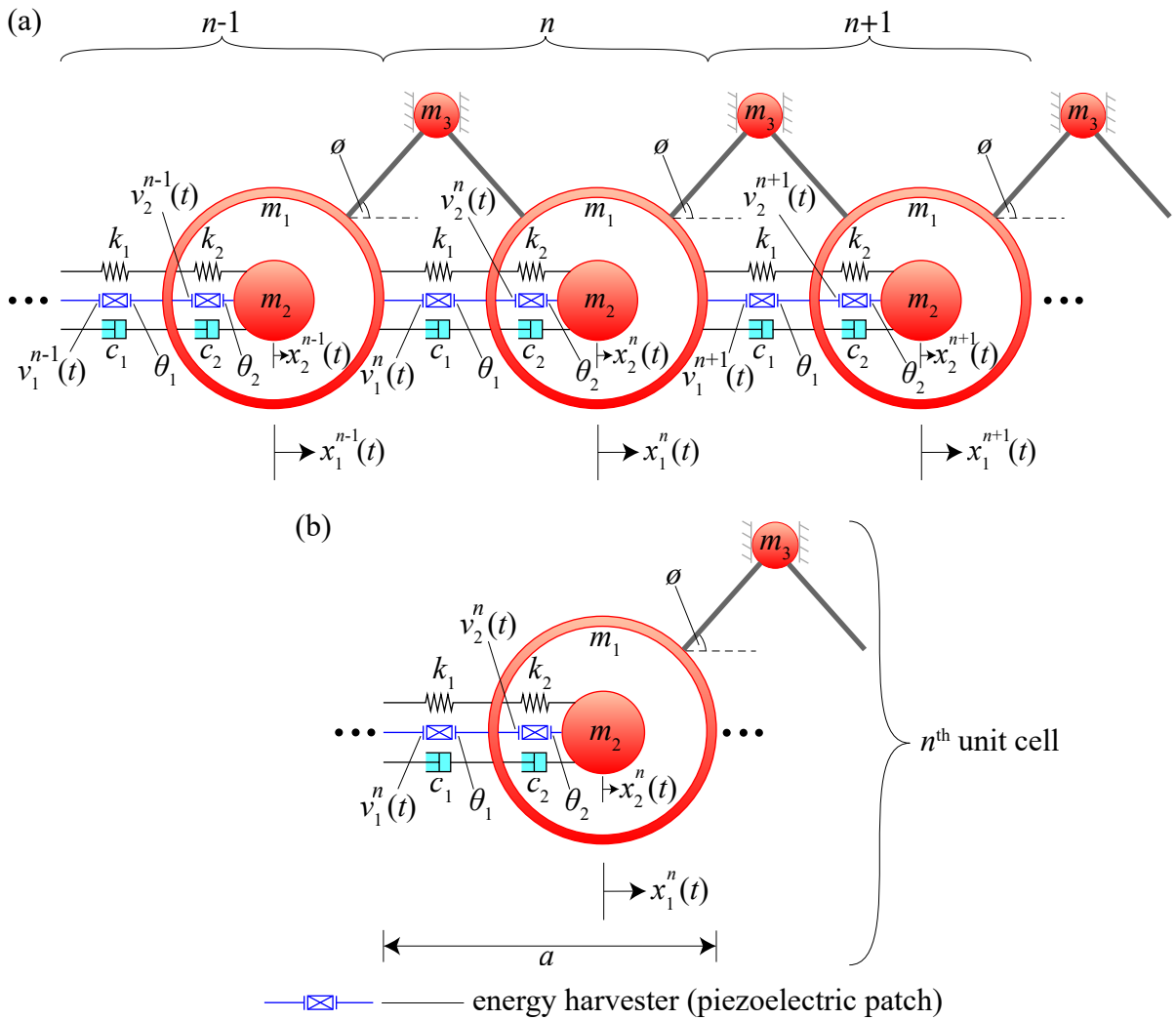


Figure 3.21: Schematic of (a) an inertially amplified locally resonant piezoelectric metamaterial (IALRPM) chain without grounding and (b) the associated unit cell.

Shunt circuit without an inductor

The governing electromechanical equations pertaining to the n^{th} unit cell under free vibration consisting of piezoelectric elements with a shunt circuit devoid of an inductor can be written

as

$$m_1 \ddot{x}_1^n + \chi(m_3(\dot{x}_1^n - \dot{x}_1^{n-1})) - \chi(m_3(\dot{x}_1^{n+1} - \dot{x}_1^n)) + c_1(2\dot{x}_1^n - \dot{x}_1^{n-1} - \dot{x}_1^{n+1}) + c_2(\dot{x}_1^n - \dot{x}_2^n) + k_1(2x_1^n - x_1^{n-1} - x_1^{n+1}) + k_2(x_1^n - x_2^n) + \theta_1 v_1^n - \theta_1 v_1^{n+1} - \theta_2 v_2^n = 0, \quad (3.214)$$

$$m_2 \ddot{x}_2^n + c_2(\dot{x}_2^n - \dot{x}_1^n) + k_2(x_2^n - x_1^n) + \theta_2 v_2^n = 0, \quad (3.215)$$

$$-\theta_1(\dot{x}_1^n - \dot{x}_1^{n-1}) + C_{p1} \dot{v}_1^n + \frac{1}{R_1} v_1^n = 0, \quad (3.216)$$

$$-\theta_2(\dot{x}_2^n - \dot{x}_1^n) + C_{p2} \dot{v}_2^n + \frac{1}{R_2} v_2^n = 0. \quad (3.217)$$

Substituting equations (3.51) and (3.31) in equations (3.214)–(3.217) yields the following Bloch-transformed homogeneous equations for the displacement amplitudes \tilde{x}_1 and \tilde{x}_2 and the voltage amplitudes \tilde{v}_1 and \tilde{v}_2 :

$$(m_1 + \chi m_3(2 - e^{-i\kappa a} - e^{i\kappa a}))\ddot{\tilde{x}}_1 + (c_1(2 - e^{-i\kappa a} - e^{i\kappa a}) + c_2)\dot{\tilde{x}}_1 + (-c_2)\dot{\tilde{x}}_2 + (k_1(2 - e^{-i\kappa a} - e^{i\kappa a}) + k_2)\tilde{x}_1 + (-k_2)\tilde{x}_2 + (\theta_1 - \theta_1 e^{i\kappa a})\tilde{v}_1 + (-\theta_2)\tilde{v}_2 = 0, \quad (3.218)$$

$$m_2 \ddot{\tilde{x}}_2 + c_2 \dot{\tilde{x}}_2 + (-c_2)\dot{\tilde{x}}_1 + k_2 \tilde{x}_2 + (-k_2)\tilde{x}_1 + \theta_2 \tilde{v}_2 = 0, \quad (3.219)$$

$$(-\theta_1 + \theta_1 e^{-i\kappa a})\dot{\tilde{x}}_1 + C_{p1} \dot{\tilde{v}}_1 + \frac{1}{R_1} \tilde{v}_1 = 0, \quad (3.220)$$

$$-\theta_2 \dot{\tilde{x}}_2 + \theta_2 \dot{\tilde{x}}_1 + C_{p2} \dot{\tilde{v}}_2 + \frac{1}{R_2} \tilde{v}_2 = 0. \quad (3.221)$$

Equations (3.218)–(3.221) can be compacted into matrix equations as

$$\mathbf{M}\ddot{\tilde{\mathbf{X}}} + \mathbf{C}(\kappa)\dot{\tilde{\mathbf{X}}} + \mathbf{K}(\kappa)\tilde{\mathbf{X}} + \mathbf{T}_1(\kappa)\tilde{\mathbf{V}} = \mathbf{0}, \quad (3.222)$$

$$\mathbf{T}_2(\kappa)\dot{\tilde{\mathbf{X}}} + \mathbf{C}_p\dot{\tilde{\mathbf{V}}} + \mathbf{R}\tilde{\mathbf{V}} = \mathbf{0}, \quad (3.223)$$

where

$$\begin{aligned}
\tilde{\mathbf{X}} &= \begin{pmatrix} \tilde{x}_1 \\ \tilde{x}_2 \end{pmatrix}; \quad \tilde{\mathbf{V}} = \begin{pmatrix} \tilde{v}_1 \\ \tilde{v}_2 \end{pmatrix}; \quad \mathbf{M} = \begin{pmatrix} m_1 + \frac{m_3}{4}(2 - e^{-i\kappa a} - e^{i\kappa a}) \cot^2 \phi & 0 \\ 0 & m_2 \end{pmatrix}; \\
\mathbf{C}(\kappa) &= \begin{pmatrix} c_1(2 - e^{-i\kappa a} - e^{i\kappa a}) + c_2 & -c_2 \\ -c_2 & c_2 \end{pmatrix}; \\
\mathbf{K}(\kappa) &= \begin{pmatrix} k_1(2 - e^{-i\kappa a} - e^{i\kappa a}) + k_2 & -k_2 \\ -k_2 & k_2 \end{pmatrix}; \\
\mathbf{T}_1(\kappa) &= \begin{pmatrix} \theta_1 - \theta_1 e^{i\kappa a} & -\theta_2 \\ 0 & \theta_2 \end{pmatrix}; \quad \mathbf{T}_2(\kappa) = \begin{pmatrix} -\theta_1 + \theta_1 e^{-i\kappa a} & 0 \\ \theta_2 & -\theta_2 \end{pmatrix}; \\
\mathbf{C}_p &= \begin{pmatrix} C_{p1} & 0 \\ 0 & C_{p2} \end{pmatrix}; \quad \text{and } \mathbf{R} = \begin{pmatrix} \frac{1}{R_1} & 0 \\ 0 & \frac{1}{R_2} \end{pmatrix}. \quad (3.224)
\end{aligned}$$

The dispersion relation can now be derived by subjecting equations (3.222) and (3.223) to a state-space transformation of the form given in equation (3.4), where

$$\mathbf{A} = \begin{pmatrix} \mathbf{0} & \mathbf{I} & \mathbf{0} \\ \mathbf{M} & \mathbf{C}(\kappa) & \mathbf{0} \\ \mathbf{0} & \mathbf{T}_2(\kappa) & \mathbf{C}_p \end{pmatrix}; \quad \mathbf{B} = \begin{pmatrix} -\mathbf{I} & \mathbf{0} & \mathbf{0} \\ \mathbf{0} & \mathbf{K}(\kappa) & \mathbf{T}_1(\kappa) \\ \mathbf{0} & \mathbf{0} & \mathbf{R} \end{pmatrix}; \quad \text{and } \mathbf{Y} = \begin{pmatrix} \dot{\tilde{\mathbf{X}}} \\ \tilde{\mathbf{X}} \\ \tilde{\mathbf{V}} \end{pmatrix}, \quad (3.225)$$

implementing a solution of the form $\mathbf{Y} = \tilde{\mathbf{Y}}_\lambda e^{\lambda t}$, and solving the resulting eigenvalue problem of the form given in equation (3.6). Expanding equation (3.6) for this particular case yields a sixth-order equation in terms of λ , which, upon solving, gives four complex roots appearing as two complex-conjugate pairs and two real roots.

Shunt circuit with an inductor

The governing electromechanical equations pertaining to the n^{th} unit cell under free vibration consisting of piezoelectric elements with a shunt circuit equipped with an inductor can be

written as

$$m_1 \ddot{x}_1^n + \chi(m_3(\dot{x}_1^n - \dot{x}_1^{n-1})) - \chi(m_3(\dot{x}_1^{n+1} - \dot{x}_1^n)) + c_1(2\dot{x}_1^n - \dot{x}_1^{n-1} - \dot{x}_1^{n+1}) + c_2(\dot{x}_1^n - \dot{x}_2^n) + k_1(2x_1^n - x_1^{n-1} - x_1^{n+1}) + k_2(x_1^n - x_2^n) + \theta_1 v_1^n - \theta_1 v_1^{n+1} - \theta_2 v_2^n = 0, \quad (3.226)$$

$$m_2 \ddot{x}_2^n + c_2(\dot{x}_2^n - \dot{x}_1^n) + k_2(x_2^n - x_1^n) + \theta_2 v_2^n = 0, \quad (3.227)$$

$$-\theta_1(\dot{x}_1^n - \dot{x}_1^{n-1}) + C_{p1} \dot{v}_1^n + \frac{1}{R_1} v_1^n + \frac{1}{L_1} v_1^n = 0, \quad (3.228)$$

$$-\theta_2(\dot{x}_2^n - \dot{x}_1^n) + C_{p2} \dot{v}_2^n + \frac{1}{R_2} v_2^n + \frac{1}{L_2} v_2^n = 0. \quad (3.229)$$

Substituting equations (3.51) and (3.31) in equations (3.226)–(3.229) yields the following Bloch-transformed homogeneous equations for the displacement amplitudes \tilde{x}_1 and \tilde{x}_2 and the voltage amplitudes \tilde{v}_1 and \tilde{v}_2 :

$$(m_1 + \chi m_3(2 - e^{-i\kappa a} - e^{i\kappa a}))\ddot{\tilde{x}}_1 + (c_1(2 - e^{-i\kappa a} - e^{i\kappa a}) + c_2)\dot{\tilde{x}}_1 + (-c_2)\dot{\tilde{x}}_2 + (k_1(2 - e^{-i\kappa a} - e^{i\kappa a}) + k_2)\tilde{x}_1 + (-k_2)\tilde{x}_2 + (\theta_1 - \theta_1 e^{i\kappa a})\tilde{v}_1 + (-\theta_2)\tilde{v}_2 = 0, \quad (3.230)$$

$$m_2 \ddot{\tilde{x}}_2 + c_2 \dot{\tilde{x}}_2 + (-c_2)\dot{\tilde{x}}_1 + k_2 \tilde{x}_2 + (-k_2)\tilde{x}_1 + \theta_2 \tilde{v}_2 = 0, \quad (3.231)$$

$$(-\theta_1 + \theta_1 e^{-i\kappa a})\ddot{\tilde{x}}_1 + C_{p1} \dot{\tilde{v}}_1 + \frac{1}{R_1} \tilde{v}_1 + \frac{1}{L_1} \tilde{v}_1 = 0, \quad (3.232)$$

$$-\theta_2 \ddot{\tilde{x}}_2 + \theta_2 \ddot{\tilde{x}}_1 + C_{p2} \dot{\tilde{v}}_2 + \frac{1}{R_2} \tilde{v}_2 + \frac{1}{L_2} \tilde{v}_2 = 0. \quad (3.233)$$

Equations (3.230)–(3.233) can be compactly written in a matrix format as

$$\mathbf{M}\ddot{\tilde{\mathbf{X}}} + \mathbf{C}(\kappa)\dot{\tilde{\mathbf{X}}} + \mathbf{K}(\kappa)\tilde{\mathbf{X}} + \mathbf{T}_1(\kappa)\tilde{\mathbf{V}} = \mathbf{0}, \quad (3.234)$$

$$\mathbf{T}_2(\kappa)\ddot{\tilde{\mathbf{X}}} + \mathbf{C}_p\dot{\tilde{\mathbf{V}}} + \mathbf{R}\tilde{\mathbf{V}} + \mathbf{L}\tilde{\mathbf{V}} = \mathbf{0}, \quad (3.235)$$

where

$$\begin{aligned}
\tilde{\mathbf{X}} &= \begin{pmatrix} \tilde{x}_1 \\ \tilde{x}_2 \end{pmatrix}; \quad \tilde{\mathbf{V}} = \begin{pmatrix} \tilde{v}_1 \\ \tilde{v}_2 \end{pmatrix}; \quad \mathbf{M} = \begin{pmatrix} m_1 + \frac{m_3}{4}(2 - e^{-i\kappa a} - e^{i\kappa a}) \cot^2 \phi & 0 \\ 0 & m_2 \end{pmatrix}; \\
\mathbf{C}(\kappa) &= \begin{pmatrix} c_1(2 - e^{-i\kappa a} - e^{i\kappa a}) + c_2 & -c_2 \\ -c_2 & c_2 \end{pmatrix}; \\
\mathbf{K}(\kappa) &= \begin{pmatrix} k_1(2 - e^{-i\kappa a} - e^{i\kappa a}) + k_2 & -k_2 \\ -k_2 & k_2 \end{pmatrix}; \\
\mathbf{T}_1(\kappa) &= \begin{pmatrix} \theta_1 - \theta_1 e^{i\kappa a} & -\theta_2 \\ 0 & \theta_2 \end{pmatrix}; \quad \mathbf{T}_2(\kappa) = \begin{pmatrix} -\theta_1 + \theta_1 e^{-i\kappa a} & 0 \\ \theta_2 & -\theta_2 \end{pmatrix}; \\
\mathbf{C}_p &= \begin{pmatrix} C_{p1} & 0 \\ 0 & C_{p2} \end{pmatrix}; \quad \mathbf{R} = \begin{pmatrix} \frac{1}{R_1} & 0 \\ 0 & \frac{1}{R_2} \end{pmatrix}; \quad \text{and } \mathbf{L} = \begin{pmatrix} \frac{1}{L_1} & 0 \\ 0 & \frac{1}{L_2} \end{pmatrix}. \quad (3.236)
\end{aligned}$$

Equations (3.234) and (3.235) can be further compacted into a single matrix equation as

$$\mathbf{Z}_1 \ddot{\tilde{\mathbf{E}}} + \mathbf{Z}_2 \dot{\tilde{\mathbf{E}}} + \mathbf{Z}_3 \tilde{\mathbf{E}} = \mathbf{0}, \quad (3.237)$$

where

$$\begin{aligned}
\mathbf{Z}_1 &= \begin{pmatrix} \mathbf{M} & \mathbf{0} \\ \mathbf{T}_2(\kappa) & \mathbf{C}_p \end{pmatrix}; \quad \mathbf{Z}_2 = \begin{pmatrix} \mathbf{C}(\kappa) & \mathbf{0} \\ \mathbf{0} & \mathbf{R} \end{pmatrix}; \quad \mathbf{Z}_3 = \begin{pmatrix} \mathbf{K}(\kappa) & \mathbf{T}_1(\kappa) \\ \mathbf{0} & \mathbf{L} \end{pmatrix}; \\
&\quad \text{and } \tilde{\mathbf{E}} = \begin{pmatrix} \tilde{\mathbf{X}} \\ \tilde{\mathbf{V}} \end{pmatrix}. \quad (3.238)
\end{aligned}$$

The dispersion relation can now be formulated by subjecting equation (3.237) to a state-space transformation of the form given in equation (3.4), where

$$\mathbf{A} = \begin{pmatrix} \mathbf{0} & \mathbf{I} \\ \mathbf{Z}_1 & \mathbf{Z}_2 \end{pmatrix}; \quad \mathbf{B} = \begin{pmatrix} -\mathbf{I} & \mathbf{0} \\ \mathbf{0} & \mathbf{Z}_3 \end{pmatrix}; \quad \text{and } \mathbf{Y} = \begin{pmatrix} \dot{\tilde{\mathbf{E}}} \\ \tilde{\mathbf{E}} \end{pmatrix}, \quad (3.239)$$

implementing a solution of the form $\mathbf{Y} = \tilde{\mathbf{Y}}_\lambda e^{\lambda t}$, and solving the resulting eigenvalue problem of the form given in equation (3.6). Expanding equation (3.6) for this particular case yields an eight-order equation in terms of λ , which, upon solving, gives four complex roots appearing as two complex-conjugate pairs and four real roots.

3.12.2 With grounding

Figure 3.22 presents the schematics of an IALRPM chain under free vibration with grounding and the associated unit cell as lumped-parameter models.

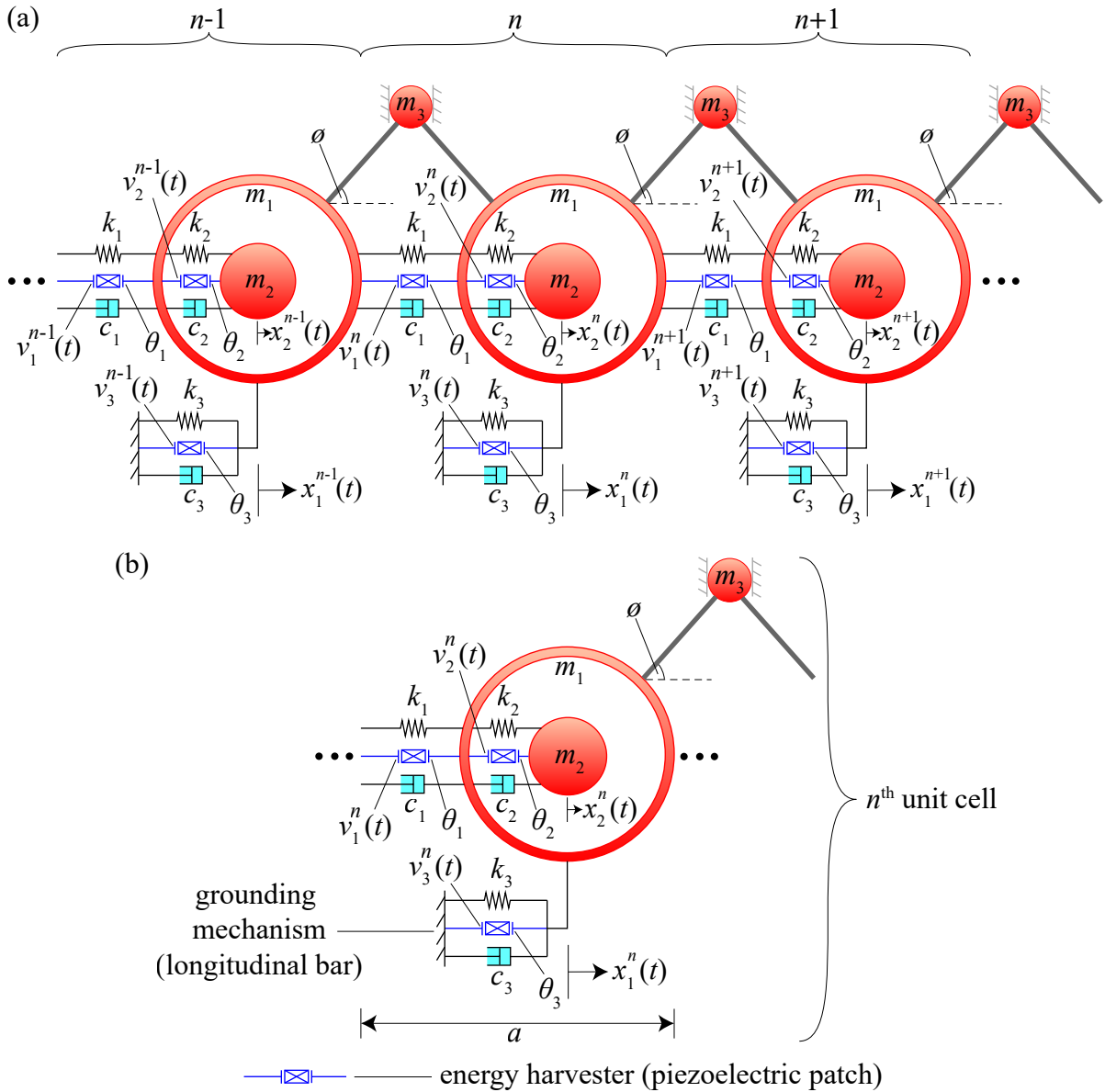


Figure 3.22: Schematic of (a) an inertially amplified locally resonant piezoelectric metamaterial (IALRPM) chain with grounding and (b) the associated unit cell.

Shunt circuit without an inductor

The governing electromechanical equations pertaining to the n^{th} unit cell under free vibration consisting of piezoelectric elements with a purely resistive shunt circuit can be written as

$$m_1 \ddot{x}_1^n + \chi(m_3(\dot{x}_1^n - \dot{x}_1^{n-1})) - \chi(m_3(\dot{x}_1^{n+1} - \dot{x}_1^n)) + c_1(2x_1^n - x_1^{n-1} - x_1^{n+1}) \\ + (c_2 + c_3)\dot{x}_1^n - c_2\dot{x}_2^n + k_1(2x_1^n - x_1^{n-1} - x_1^{n+1}) + (k_2 + k_3)x_1^n - k_2x_2^n \\ + \theta_1 v_1^n - \theta_1 v_1^{n+1} - \theta_2 v_2^n + \theta_3 v_3^n = 0, \quad (3.240)$$

$$m_2 \ddot{x}_2^n + c_2(\dot{x}_2^n - \dot{x}_1^n) + k_2(x_2^n - x_1^n) + \theta_2 v_2^n = 0, \quad (3.241)$$

$$-\theta_1(\dot{x}_1^n - \dot{x}_1^{n-1}) + C_{p1}\dot{v}_1^n + \frac{1}{R_1}v_1^n = 0, \quad (3.242)$$

$$-\theta_2(\dot{x}_2^n - \dot{x}_1^n) + C_{p2}\dot{v}_2^n + \frac{1}{R_2}v_2^n = 0, \quad (3.243)$$

$$-\theta_3\dot{x}_1^n + C_{p3}\dot{v}_3^n + \frac{1}{R_3}v_3^n = 0. \quad (3.244)$$

Substituting equations (3.51) and (3.31) in equations (3.240)–(3.244) yields the following Bloch-transformed homogeneous equations for the displacement amplitudes \tilde{x}_1 and \tilde{x}_2 and the voltage amplitudes \tilde{v}_1 , \tilde{v}_2 , and \tilde{v}_3 :

$$(m_1 + \chi m_3(2 - e^{-i\kappa a} - e^{i\kappa a}))\ddot{\tilde{x}}_1 + (c_1(2 - e^{-i\kappa a} - e^{i\kappa a}) + c_2 + c_3)\dot{\tilde{x}}_1 \\ + (-c_2)\dot{\tilde{x}}_2 + (k_1(2 - e^{-i\kappa a} - e^{i\kappa a}) + k_2 + k_3)\tilde{x}_1 + (-k_2)\tilde{x}_2 \\ + (\theta_1 - \theta_1 e^{i\kappa a})\tilde{v}_1 + (-\theta_2)\tilde{v}_2 + \theta_3\tilde{v}_3 = 0, \quad (3.245)$$

$$m_2\ddot{\tilde{x}}_2 + c_2\dot{\tilde{x}}_2 + (-c_2)\dot{\tilde{x}}_1 + k_2\tilde{x}_2 + (-k_2)\tilde{x}_1 + \theta_2\tilde{v}_2 = 0, \quad (3.246)$$

$$(-\theta_1 + \theta_1 e^{-i\kappa a})\dot{\tilde{x}}_1 + C_{p1}\dot{\tilde{v}}_1 + \frac{1}{R_1}\tilde{v}_1 = 0, \quad (3.247)$$

$$-\theta_2\dot{\tilde{x}}_2 + \theta_2\dot{\tilde{x}}_1 + C_{p2}\dot{\tilde{v}}_2 + \frac{1}{R_2}\tilde{v}_2 = 0, \quad (3.248)$$

$$-\theta_3\dot{\tilde{x}}_1 + C_{p3}\dot{\tilde{v}}_3 + \frac{1}{R_3}\tilde{v}_3 = 0. \quad (3.249)$$

The dispersion relation can now be formulated by subjecting equations (3.245)–(3.249) to a state-space transformation of the form given in equation (3.4), where

$$\mathbf{A} = \begin{pmatrix} 0 & 1 & 0 & 0 & 0 & 0 & 0 \\ 0 & 0 & 0 & 1 & 0 & 0 & 0 \\ m_1 + \frac{m_3}{4}b \cot^2 \phi & c_1 b + c_2 + c_3 & 0 & -c_2 & 0 & 0 & 0 \\ 0 & -c_2 & m_2 & c_2 & 0 & 0 & 0 \\ 0 & -\theta_1 + \theta_1 e^{-i\kappa a} & 0 & 0 & C_{p1} & 0 & 0 \\ 0 & \theta_2 & 0 & -\theta_2 & 0 & C_{p2} & 0 \\ 0 & -\theta_3 & 0 & 0 & 0 & 0 & C_{p3} \end{pmatrix};$$

$$\mathbf{B} = \begin{pmatrix} -1 & 0 & 0 & 0 & 0 & 0 & 0 \\ 0 & 0 & -1 & 0 & 0 & 0 & 0 \\ 0 & k_1 b + k_2 + k_3 & 0 & -k_2 & \theta_1 - \theta_1 e^{i\kappa a} & -\theta_2 & \theta_3 \\ 0 & -k_2 & 0 & k_2 & 0 & \theta_2 & 0 \\ 0 & 0 & 0 & 0 & \frac{1}{R_1} & 0 & 0 \\ 0 & 0 & 0 & 0 & 0 & \frac{1}{R_2} & 0 \\ 0 & 0 & 0 & 0 & 0 & 0 & \frac{1}{R_3} \end{pmatrix};$$

$$\text{and } \mathbf{Y} = \begin{pmatrix} \dot{\tilde{x}}_1 \\ \tilde{x}_1 \\ \dot{\tilde{x}}_2 \\ \tilde{x}_2 \\ \tilde{v}_1 \\ \tilde{v}_2 \\ \tilde{v}_3 \end{pmatrix}, \quad (3.250)$$

implementing a solution of the form $\mathbf{Y} = \tilde{\mathbf{Y}}_\lambda e^{\lambda t}$, and solving the resulting eigenvalue problem of the form given in equation (3.6). Expanding equation (3.6) for this particular case yields a seventh-order equation in terms of λ , which, upon solving, gives four complex roots appearing as two complex-conjugate pairs and three real roots. In \mathbf{A} and \mathbf{B} in equation (3.250), the term $b = 2 - e^{-i\kappa a} - e^{i\kappa a}$.

Shunt circuit with an inductor

The governing electromechanical equations pertinent to the n^{th} unit cell under free vibration consisting of piezoelectric elements with a shunt circuit including an inductor can be written

as

$$\begin{aligned}
& m_1 \ddot{x}_1^n + \chi(m_3(\dot{x}_1^n - \dot{x}_1^{n-1})) - \chi(m_3(\dot{x}_1^{n+1} - \dot{x}_1^n)) + c_1(2x_1^n - x_1^{n-1} - x_1^{n+1}) \\
& + (c_2 + c_3)\dot{x}_1^n - c_2\dot{x}_2^n + k_1(2x_1^n - x_1^{n-1} - x_1^{n+1}) + (k_2 + k_3)x_1^n - k_2x_2^n \\
& + \theta_1 v_1^n - \theta_1 v_1^{n+1} - \theta_2 v_2^n + \theta_3 v_3^n = 0, \quad (3.251)
\end{aligned}$$

$$m_2 \ddot{x}_2^n + c_2(\dot{x}_2^n - \dot{x}_1^n) + k_2(x_2^n - x_1^n) + \theta_2 v_2^n = 0, \quad (3.252)$$

$$-\theta_1(\dot{x}_1^n - \dot{x}_1^{n-1}) + C_{p1} \dot{v}_1^n + \frac{1}{R_1} \dot{v}_1^n + \frac{1}{L_1} v_1^n = 0, \quad (3.253)$$

$$-\theta_2(\dot{x}_2^n - \dot{x}_1^n) + C_{p2} \dot{v}_2^n + \frac{1}{R_2} \dot{v}_2^n + \frac{1}{L_2} v_2^n = 0, \quad (3.254)$$

$$-\theta_3 \dot{x}_1^n + C_{p3} \dot{v}_3^n + \frac{1}{R_3} \dot{v}_3^n + \frac{1}{L_3} v_3^n = 0. \quad (3.255)$$

Substituting equations (3.51) and (3.31) in equations (3.251)–(3.255) yields the following Bloch-transformed homogeneous equations for the displacement amplitudes \tilde{x}_1 and \tilde{x}_2 and the voltage amplitudes \tilde{v}_1 , \tilde{v}_2 , and \tilde{v}_3 :

$$\begin{aligned}
& (m_1 + \chi m_3(2 - e^{-i\kappa a} - e^{i\kappa a}))\ddot{\tilde{x}}_1 + (c_1(2 - e^{-i\kappa a} - e^{i\kappa a}) + c_2 + c_3)\dot{\tilde{x}}_1 \\
& + (-c_2)\dot{\tilde{x}}_2 + (k_1(2 - e^{-i\kappa a} - e^{i\kappa a}) + k_2 + k_3)\tilde{x}_1 + (-k_2)\tilde{x}_2 \\
& + (\theta_1 - \theta_1 e^{i\kappa a})\tilde{v}_1 + (-\theta_2)\tilde{v}_2 + \theta_3 \tilde{v}_3 = 0, \quad (3.256)
\end{aligned}$$

$$m_2 \ddot{\tilde{x}}_2 + c_2 \dot{\tilde{x}}_2 + (-c_2)\dot{\tilde{x}}_1 + k_2 \tilde{x}_2 + (-k_2)\tilde{x}_1 + \theta_2 \tilde{v}_2 = 0, \quad (3.257)$$

$$(-\theta_1 + \theta_1 e^{-i\kappa a})\ddot{\tilde{x}}_1 + C_{p1} \dot{\tilde{v}}_1 + \frac{1}{R_1} \dot{\tilde{v}}_1 + \frac{1}{L_1} \tilde{v}_1 = 0, \quad (3.258)$$

$$-\theta_2 \ddot{\tilde{x}}_2 + \theta_2 \ddot{\tilde{x}}_1 + C_{p2} \dot{\tilde{v}}_2 + \frac{1}{R_2} \dot{\tilde{v}}_2 + \frac{1}{L_2} \tilde{v}_2 = 0, \quad (3.259)$$

$$-\theta_3 \ddot{\tilde{x}}_1 + C_{p3} \dot{\tilde{v}}_3 + \frac{1}{R_3} \dot{\tilde{v}}_3 + \frac{1}{L_3} \tilde{v}_3 = 0. \quad (3.260)$$

Equations (3.256)–(3.260) can be fused into a matrix form as

$$\mathbf{Z}_1 \ddot{\mathbf{E}} + \mathbf{Z}_2 \dot{\mathbf{E}} + \mathbf{Z}_3 \mathbf{E} = \mathbf{0}, \quad (3.261)$$

where

$$\mathbf{Z}_1 = \begin{pmatrix} m_1 + \frac{m_3}{4}b \cot^2 \phi & 0 & 0 & 0 & 0 \\ 0 & m_2 & 0 & 0 & 0 \\ -\theta_1 + \theta_1 e^{-i\kappa a} & 0 & C_{p1} & 0 & 0 \\ \theta_2 & -\theta_2 & 0 & C_{p2} & 0 \\ -\theta_3 & 0 & 0 & 0 & C_{p3} \end{pmatrix};$$

$$\mathbf{Z}_2 = \begin{pmatrix} c_1 b + c_2 + c_3 & -c_2 & 0 & 0 & 0 \\ -c_2 & c_2 & 0 & 0 & 0 \\ 0 & 0 & \frac{1}{R_1} & 0 & 0 \\ 0 & 0 & 0 & \frac{1}{R_2} & 0 \\ 0 & 0 & 0 & 0 & \frac{1}{R_3} \end{pmatrix};$$

$$\mathbf{Z}_3 = \begin{pmatrix} k_1 b + k_2 + k_3 & -k_2 & \theta_1 - \theta_1 e^{i\kappa a} & -\theta_2 & \theta_3 \\ -k_2 & k_2 & 0 & \theta_2 & 0 \\ 0 & 0 & \frac{1}{L_1} & 0 & 0 \\ 0 & 0 & 0 & \frac{1}{L_2} & 0 \\ 0 & 0 & 0 & 0 & \frac{1}{L_3} \end{pmatrix}; \text{ and } \tilde{\mathbf{E}} = \begin{pmatrix} \tilde{x}_1 \\ \tilde{x}_2 \\ \tilde{v}_1 \\ \tilde{v}_2 \\ \tilde{v}_3 \end{pmatrix}. \quad (3.262)$$

In \mathbf{Z}_1 , \mathbf{Z}_2 , and \mathbf{Z}_3 , the term $b = 2 - e^{-i\kappa a} - e^{i\kappa a}$. The dispersion relation can now be formulated by subjecting equation (3.261) to a state-space transformation of the form given in equation (3.4), where

$$\mathbf{A} = \begin{pmatrix} \mathbf{0} & \mathbf{I} \\ \mathbf{Z}_1 & \mathbf{Z}_2 \end{pmatrix}; \mathbf{B} = \begin{pmatrix} -\mathbf{I} & \mathbf{0} \\ \mathbf{0} & \mathbf{Z}_3 \end{pmatrix}; \text{ and } \mathbf{Y} = \begin{pmatrix} \tilde{\mathbf{E}} \\ \tilde{\mathbf{E}} \end{pmatrix}, \quad (3.263)$$

implementing a solution of the form $\mathbf{Y} = \tilde{\mathbf{Y}}_\lambda e^{\lambda t}$, and solving the resulting eigenvalue problem of the form given in equation (3.6). Expanding equation (3.6) for this particular case yields a tenth-order equation in terms of λ , which, upon solving, gives four complex roots appearing as two complex-conjugate pairs and six real roots.

3.13 Wave-propagation and dissipation characteristics of inertially amplified locally resonant metamaterials and piezoelectric metamaterials

This section presents the wave-propagation and dissipation characteristics of the different configurations of IALRMs and IALRPMs discussed so far in a graphical comparative format.

3.13.1 Without grounding

Table 3.13 details the parameters utilized in the computation of the dispersion (band structure) and damping-ratio characteristics of the IALRM and IALRPMs without grounding. The electrical parameters of the shunt circuit are non-dimensionalized in a fashion similar to the case of DPPnC without grounding.

Table 3.13: Mechanical and dimensionless electrical parameters employed in the inertially amplified locally resonant metamaterial (IALRM) and inertially amplified locally resonant piezoelectric metamaterials (IALRPMs) without grounding.

Parameter	IALRM	IALRPM without an inductor	IALRPM with an inductor	Unit
a	1	1	1	m
m_1	0.0080	0.0080	0.0080	Kg
m_2	0.0340	0.0340	0.0340	Kg
m_3	0.0090	0.0090	0.0090	Kg
k_1	3×10^4	3×10^4	3×10^4	Nm^{-1}
k_2	1.5000×10^4	1.5000×10^4	1.5000×10^4	Nm^{-1}
c_1	2	2	2	Nsm^{-1}
c_2	2	2	2	Nsm^{-1}
ϕ	70	70	70	degree
α_1	—	0.2324	0.2324	—
α_2	—	0.3188	0.3188	—
β_1	—	—	1.2750	—
β_2	—	—	0.6000	—
$k_{\text{coeff}_1}^2$	—	0.1333	0.1333	—
$k_{\text{coeff}_2}^2$	—	0.5333	0.5333	—

Figure 3.23 depicts the normalized damped frequencies, damping ratios, and cumulative damping ratios for the IALRM and IALRPMs without grounding in the IBZ, i.e., for $\mu \in [0, \pi]$. The damped frequencies are normalized with respect to $\bar{\omega}_1 = \sqrt{\frac{k_1}{m_1}}$; i.e., the

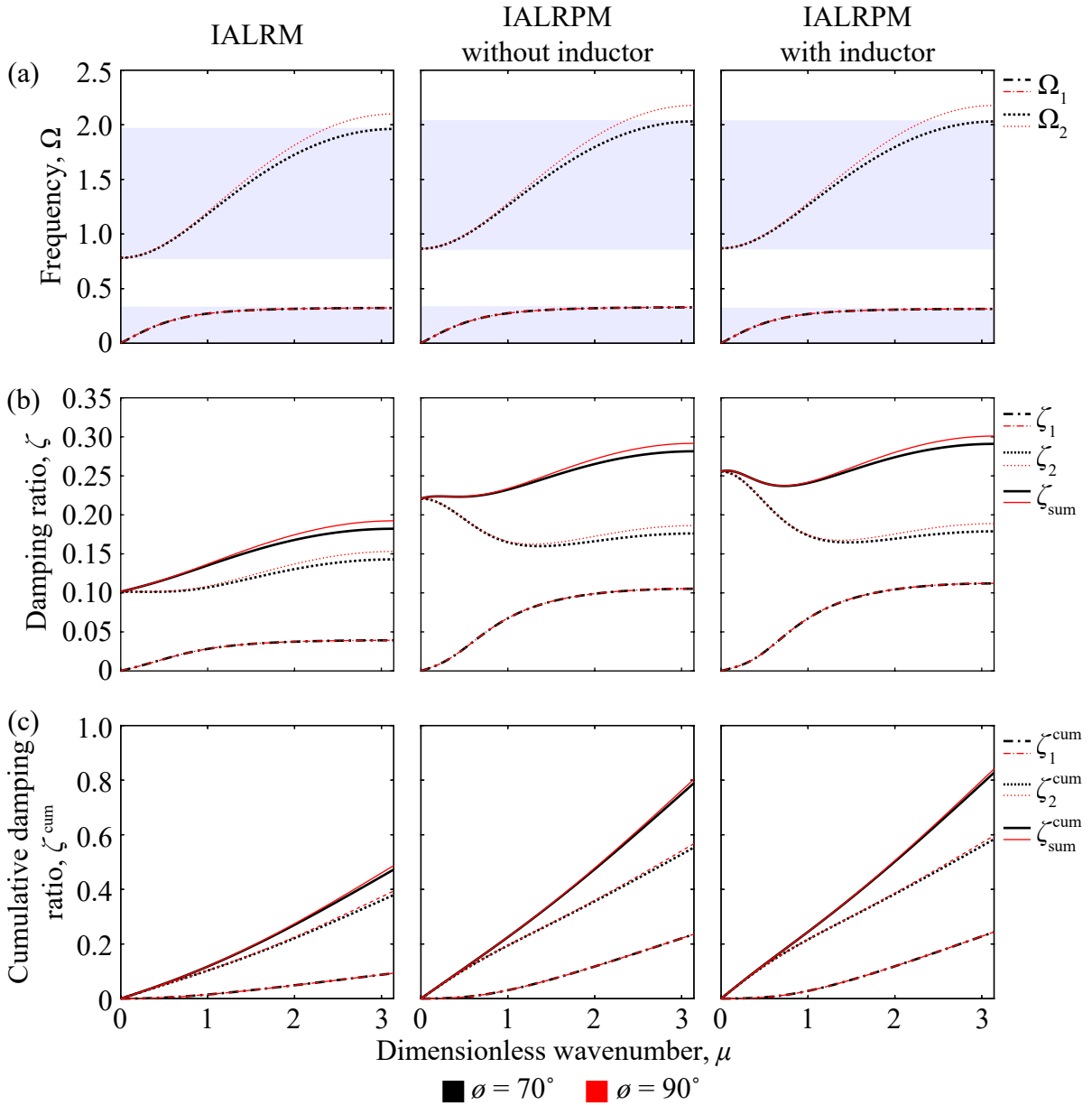


Figure 3.23: (a) Frequency band structure, (b) damping-ratio diagrams, and (c) cumulative-damping-ratio diagrams for the inertially amplified locally resonant metamaterial (IALRM) and inertially amplified locally resonant piezoelectric metamaterials (IALRPMs) without grounding.

plots depict $\Omega_l = \frac{\omega_{d_l}}{\bar{\omega}_1}$, where $l=1$ (acoustic branch), 2 (optical branch). The IALRM and IALRPMs without grounding exhibit a wider second transmission band as opposed to the first transmission band. The three periodic media have a roughly similar band structure except that the IALRM depicts a marginally lower second transmission band. For dispersion band structures that are approximately similar, figure 3.23(b) shows a significant distinction

in the damping ratio curves. It is observed that, in comparison to the IALRM, the IALRPMs show higher levels of ζ_l ($l=1, 2$, or sum). In figure 3.23(c), the IALRPMs indicate a much higher rate of increase of ζ_l^{cum} ($l=1, 2$, or sum) in comparison to the IALRM. The value of ζ_l^{tot} ($l=1, 2$, or sum) is the highest for the IALRPM with an inductor. Table 3.14 details the ζ_l^{tot} values for the three periodic media.

Table 3.14: Total values of damping ratios of the inertially amplified locally resonant metamaterial (IALRM) and inertially amplified locally resonant piezoelectric metamaterials (IALRPMs) without grounding.

Parameter	IALRM	IALRPM without an inductor	IALRPM with an inductor	Unit
ζ_1^{tot}	0.0930	0.2356	0.2437	—
ζ_2^{tot}	0.3795	0.5534	0.5836	—
$\zeta_{\text{sum}}^{\text{tot}}$	0.4725	0.7890	0.8273	—

3.13.2 With grounding

Table 3.15 details the parameters utilized in the computation of the dispersion (band structure) and damping-ratio characteristics of the IALRM and IALRPMs with grounding. The electrical parameters of the shunt circuit are non-dimensionalized in a fashion similar to the case of LRPM with grounding.

Figure 3.24 depicts the normalized damped frequencies, damping ratios, and cumulative damping ratios for the IALRM and IALRPMs without grounding in the IBZ, i.e., for $\mu \in [0, \pi]$. The damped frequencies are normalized with respect to $\bar{\omega}_1$; i.e., the plots depict $\Omega_l = \frac{\omega_{d_l}}{\bar{\omega}_1}$, where $l=1$ (acoustic branch), 2 (optical branch). It is noticed in figure 3.24(a) that the IALRM and IALRPMs with grounding exhibit a wider second transmission band as opposed to the first transmission band. The periodic media have approximately similar band structures except that the IALRM presents a lower second transmission band. In figure 3.24(b), the IALRPMs portray higher levels of ζ_l ($l=1, 2$, or sum) in comparison to the IALRM. In figure 3.24(c), the IALRPMs present a considerably higher rate of increase of ζ_l^{cum} ($l=1, 2$, or sum) in comparison to the IALRM. The IALRPM with an inductor demonstrates the highest values of ζ_l^{tot} ($l=1, 2$, or sum) as evidenced in table 3.16.

Table 3.15: Mechanical and dimensionless electrical parameters employed in the inertially amplified locally resonant metamaterial (IALRM) and inertially amplified locally resonant piezoelectric metamaterials (IALRPMs) with grounding.

Parameter	IALRM	IALRPM without inductor	IALRPM with inductor	Unit
a	1	1	1	m
m_1	0.0080	0.0080	0.0080	Kg
m_2	0.0340	0.0340	0.0340	Kg
m_3	0.0090	0.0090	0.0090	Kg
k_1	5×10^3	5×10^3	5×10^3	Nm^{-1}
k_2	10×10^3	10×10^3	10×10^3	Nm^{-1}
k_3	5×10^3	5×10^3	5×10^3	Nm^{-1}
c_1	2	2	2	Nsm^{-1}
c_2	2	2	2	Nsm^{-1}
c_3	2	2	2	Nsm^{-1}
ϕ	70	70	70	degree
α_1	—	0.0949	0.0949	—
α_2	—	0.2603	0.2603	—
α_3	—	0.0949	0.0949	—
β_1	—	—	0.5000	—
β_2	—	—	0.9412	—
β_3	—	—	0.5000	—
$k_{\text{coeff}_1}^2$	—	0.8000	0.8000	—
$k_{\text{coeff}_2}^2$	—	0.8000	0.8000	—
$k_{\text{coeff}_3}^2$	—	0.8000	0.8000	—

Table 3.16: Total values of damping ratios of the inertially amplified locally resonant metamaterial (IALRM) and inertially amplified locally resonant piezoelectric metamaterials (IALRPMs) with grounding.

Parameter	IALRM	IALRPM without inductor	IALRPM with inductor	Unit
ζ_1^{tot}	0.1816	0.3334	0.3385	—
ζ_2^{tot}	0.8293	1.2288	1.2615	—
$\zeta_{\text{sum}}^{\text{tot}}$	1.0109	1.5622	1.6000	—

3.14 Summary and conclusions

In this chapter, three classes of one-dimensional periodic media, namely, phononic crystals, locally resonant elastic metamaterials, and inertially amplified metamaterials with local

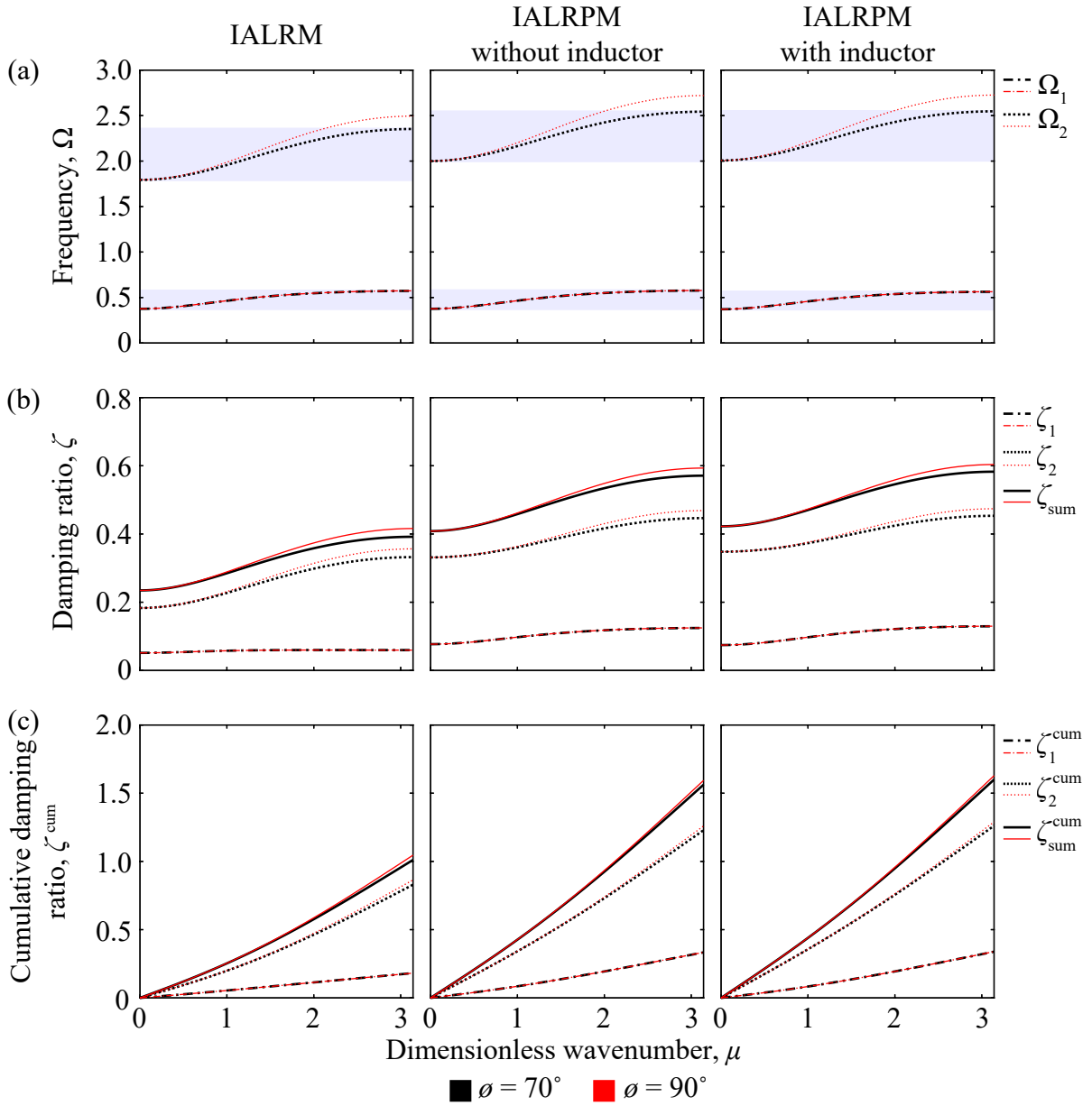


Figure 3.24: (a) Frequency band structure, (b) damping-ratio diagrams, and (c) cumulative-damping-ratio diagrams for the inertially amplified locally resonant metamaterial (IALRM) and inertially amplified locally resonant piezoelectric metamaterials (IALRPMs) with grounding.

resonance, are studied within a Bloch framework for the propagation of elastic waves as an introductory overview. Subsequently, the piezoelectric counterparts of the aforementioned periodic media are analysed. After applying the plane-wave Bloch solution to the governing equations, the resulting Bloch-transformed equation/s is/are cast as a first-order equation via a state-space formulation, and consequently, an eigenvalue problem is established, which is

solved in MATLAB to obtain the eigenvalues. From the complex eigenvalue solution, the wavenumber dependent damped frequencies and damping ratios are extracted and presented for the periodic media and piezoelectric media for a quantitative comparison. By performing Bloch analysis of an infinite piezoelectric periodic media, in the absence of forcing and boundary conditions, with shunted energy harvesters, the piezoelectric periodic media can be analysed as a material rather than a finite structure; i.e., the wave-propagation and dissipation characteristics obtained are *intrinsic* in nature. This chapter essentially serves the purpose of familiarizing the reader with the Bloch analysis of different types of one-dimensional piezoelectric periodic media and the type of relevant results to be expected in chapters 5, 6, and 7, where they are employed to develop conceptual metrics.

Chapter 4

Wave Propagation in Two-Dimensional Phononic Crystals and Piezoelectric Phononic Crystals

4.1 Introduction

As a premise, chapter 3 delved into the free-vibration analysis of the propagation of elastic waves through various configurations of one-dimensional periodic media, namely, monoatomic and diatomic phononic crystals, locally resonant metamaterial, and inertially amplified locally resonant metamaterial, and their piezoelectric counterparts. In this chapter, the application of the generalized Bloch's theorem is extended to two-dimensional monoatomic phononic-crystal (MPnC) and monoatomic piezoelectric phononic-crystal (MPPnC) lattices in order to gain an insight into their *intrinsic* wave-propagation and dissipation characteristics as the lattices are assumed to be under free vibration, independent of structural size (infinite in the x- and y-directions), and independent of boundary conditions. Unlike the one-dimensional cases, which were subjected to wavenumbers only along the x-direction, a two-dimensional lattice must be subjected to wavenumbers in the x- and y-directions; hence the lattice is analysed in a wavevector space ($\boldsymbol{\kappa}$ -space or reciprocal space) comprised of wavevectors with x-components κ_x and y-components κ_y . Propagation of plane waves in an elastic lattice material follows periodic patterns which are dictated by the type of lattice symmetry and the mechanical configuration of the unit cell, which is dictated by the number of masses, stiffness elements (springs), and damping elements (viscous dashpots) in a unit cell and their values. The lattices are presented as lumped-parameter models in detailed schematics shown in the figures. The theoretical framework adopted in this chapter is akin to

the one used in chapter 3; i.e., the analysis of the propagation of elastic waves through infinite linear elastic periodic lattice under free vibration and with and without energy harvesters is investigated by employing a generalized Bloch's theorem for two-dimensional plane waves followed by a state-space transformation to solve the governing system of equations. In doing so, the dispersion relations are derived and the mathematical definition of the solution, eigenvalues, is given. Consequently, the mathematical definitions of the wave-propagation and dissipation characteristics are extracted; i.e., the definitions of the wavenumber-dependent damped frequencies and damping ratios are extracted.

The layout of the chapter is as follows. Unlike chapter 3, this chapter only delves into two-dimensional MPnC and MPPnCs for simplicity. With regards to the energy harvesters, cases of shunt circuit without an inductor and with an inductor are both considered. For the MPnC, MPPnC without an inductor, and MPPnC with an inductor lattices, the most general case of fully damped is considered as in real world applications an undamped system is unrealistic to realize. For the three configurations, the damped frequencies and damping ratios are presented in the irreducible Brillouin Zone and the first Brillouin zone in a comparative format.

4.2 Monoatomic phononic crystal

In this section, the application of generalized Bloch's theorem to a two-dimensional monoatomic phononic-crystal (MPnC) lattice [122] is presented as a review in order to study the propagation of plane waves through the lattice.

Figure 4.1, presents the schematics of a MPnC lattice under free vibration and the associated unit cell as lumped-parameter models. The mass in each unit cell is connected to its neighbouring masses in all directions via springs and viscous dashpots. In figure 4.1(b), p and q are used to identify and refer to the central unit cell under consideration along the x - and y -directions, respectively, and can be any non-zero positive integer in a finite lattice; m denotes the mass; $k_{...}$ and $c_{...}$ denote the stiffness coefficients of the linear springs and the damping coefficients of the viscous dashpots, respectively, $x^{(p,q)}(t)$ and $y^{(p,q)}(t)$ are the displacements, with respect to time t , of a mass in the x - and y -directions, respectively; and a_x and a_y are the unit-cell dimensions or lattice spacings in the x - and y -directions, respectively. Moving in the anti-clockwise direction with respect to the horizontal direction, the elastic springs and viscous dashpots are placed at 0° , 45° , 90° , and 135° , which correspond to the subscripts 1, 2, 3, and 4, respectively, of the spring stiffness and damping coefficients.

The forces on the mass in the central unit cell, i.e., the $(p, q)^{\text{th}}$ unit cell shown in figure 4.1(b), under free vibration can be aggregated in the x - and y -directions, and the governing

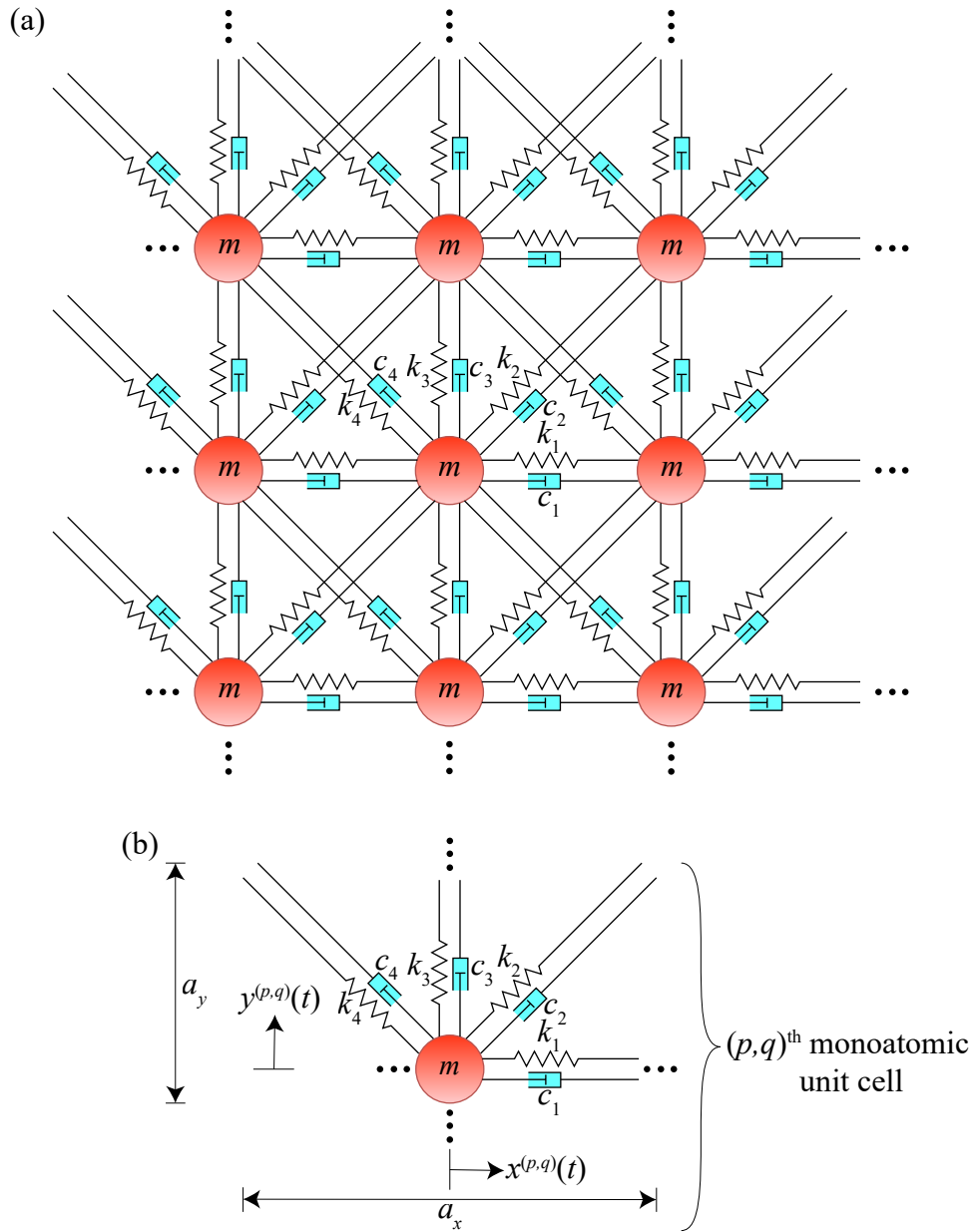


Figure 4.1: Schematic of (a) a monoatomic phononic-crystal (MPnC) lattice and (b) the associated unit cell.

equations pertaining to the two-dimensional motion of the mass in the central unit cell can be written as

$$\begin{aligned}
& m\ddot{x}^{(p,q)} + c_1 \left(\dot{x}^{(p,q)} - \dot{x}^{(p+1,q)} + \dot{x}^{(p,q)} - \dot{x}^{(p-1,q)} \right) \\
& + \frac{1}{2}c_2 \left(\dot{x}^{(p,q)} - \dot{x}^{(p+1,q+1)} + \dot{x}^{(p,q)} - \dot{x}^{(p-1,q-1)} + \dot{y}^{(p,q)} - \dot{y}^{(p+1,q+1)} + \dot{y}^{(p,q)} - \dot{y}^{(p-1,q-1)} \right) \\
& + \frac{1}{2}c_4 \left(\dot{x}^{(p,q)} - \dot{x}^{(p-1,q+1)} + \dot{x}^{(p,q)} - \dot{x}^{(p+1,q-1)} - \dot{y}^{(p,q)} + \dot{y}^{(p-1,q+1)} - \dot{y}^{(p,q)} + \dot{y}^{(p+1,q-1)} \right) \\
& \quad + k_1 \left(x^{(p,q)} - x^{(p+1,q)} + x^{(p,q)} - x^{(p-1,q)} \right) \\
& + \frac{1}{2}k_2 \left(x^{(p,q)} - x^{(p+1,q+1)} + x^{(p,q)} - x^{(p-1,q-1)} + y^{(p,q)} - y^{(p+1,q+1)} + y^{(p,q)} - y^{(p-1,q-1)} \right) \\
& + \frac{1}{2}k_4 \left(x^{(p,q)} - x^{(p-1,q+1)} + x^{(p,q)} - x^{(p+1,q-1)} - y^{(p,q)} + y^{(p-1,q+1)} - y^{(p,q)} + y^{(p+1,q-1)} \right) = 0,
\end{aligned} \tag{4.1}$$

$$\begin{aligned}
& m\ddot{y}^{(p,q)} + c_3 \left(\dot{y}^{(p,q)} - \dot{y}^{(p,q+1)} + \dot{y}^{(p,q)} - \dot{y}^{(p,q-1)} \right) \\
& + \frac{1}{2}c_2 \left(\dot{y}^{(p,q)} - \dot{y}^{(p+1,q+1)} + \dot{y}^{(p,q)} - \dot{y}^{(p-1,q-1)} + \dot{x}^{(p,q)} - \dot{x}^{(p+1,q+1)} + \dot{x}^{(p,q)} - \dot{x}^{(p-1,q-1)} \right) \\
& + \frac{1}{2}c_4 \left(\dot{y}^{(p,q)} - \dot{y}^{(p-1,q+1)} + \dot{y}^{(p,q)} - \dot{y}^{(p+1,q-1)} - \dot{x}^{(p,q)} + \dot{x}^{(p-1,q+1)} - \dot{x}^{(p,q)} + \dot{x}^{(p+1,q-1)} \right) \\
& \quad + k_3 \left(y^{(p,q)} - y^{(p,q+1)} + y^{(p,q)} - y^{(p,q-1)} \right) \\
& + \frac{1}{2}k_2 \left(y^{(p,q)} - y^{(p+1,q+1)} + y^{(p,q)} - y^{(p-1,q-1)} + x^{(p,q)} - x^{(p+1,q+1)} + x^{(p,q)} - x^{(p-1,q-1)} \right) \\
& + \frac{1}{2}k_4 \left(y^{(p,q)} - y^{(p-1,q+1)} + y^{(p,q)} - y^{(p+1,q-1)} - x^{(p,q)} + x^{(p-1,q+1)} - x^{(p,q)} + x^{(p+1,q-1)} \right) = 0,
\end{aligned} \tag{4.2}$$

where $(p+1, q)$, $(p-1, q)$, $(p, q+1)$, $(p, q-1)$, $(p+1, q+1)$, $(p-1, q+1)$, $(p-1, q-1)$, and $(p+1, q-1)$ refer to the unit cells to the right, left, top, bottom, top-right, top-left, bottom-left, and bottom-right, respectively, of the $(p, q)^{\text{th}}$ unit cell (central unit cell under consideration) and the number of overhead dots indicates the order of derivative with respect to time.

Considering that a two-dimensional lattice or grid must be subjected to wavenumbers in the x- and y-directions, i.e., the lattice must be analysed in a wavevector space ($\mathbf{\kappa}$ -space or reciprocal space) comprised of wavevectors with x- and y-components, the plane-wave solution for the displacements of a mass in a periodic unit cell is given by

$$\mathbf{U}^{(p+g_1, q+g_2)}(\mathbf{r}, \mathbf{\kappa}; t) = \tilde{\mathbf{U}}(t) e^{i[\kappa_x(p+g_1)a_x + \kappa_y(q+g_2)a_y]}, \tag{4.3}$$

where $\mathbf{U}^{(p+g_1, q+g_2)} = \left(x^{(p+g_1, q+g_2)}, y^{(p+g_1, q+g_2)} \right)^T$ is the displacement vector; $g_1 \in [-\infty, \infty]$ and $g_2 \in [-\infty, \infty]$ are integers used to locate a particular unit cell, relative to the $(p, q)^{\text{th}}$ unit cell, in the x- and y-directions, respectively;

$$\mathbf{r} = pa_x \mathbf{i} + qa_y \mathbf{j} \quad (4.4)$$

is the two-dimensional position vector of the $(p, q)^{\text{th}}$ unit cell with the x- and y-components given by pa_x and qa_y , respectively;

$$\boldsymbol{\kappa} = \kappa_x \mathbf{i} + \kappa_y \mathbf{j} \quad (4.5)$$

is the wavevector; $\tilde{\mathbf{U}} = (\tilde{x}, \tilde{y})^T$ is the displacement-amplitude vector; and $i = \sqrt{-1}$ is the imaginary unit. For the central unit cell under consideration, i.e., the $(p, q)^{\text{th}}$ unit cell, $g_1 = g_2 = 0$, and table 4.1 details the position of, values of g_1 and g_2 for, and location of all the neighbouring unit cells, shown in figure 4.1(a), relative to the $(p, q)^{\text{th}}$ unit cell.

Table 4.1: Position of, values of g_1 and g_2 for, and location of all the unit cells, shown in figure 4.1(a), in reference to the $(p, q)^{\text{th}}$ unit cell at the centre.

Position	g_1	g_2	Location relative to the $(p, q)^{\text{th}}$ unit cell
$(p+1, q)$	1	0	right
$(p-1, q)$	-1	0	left
$(p, q+1)$	0	1	top
$(p, q-1)$	0	-1	bottom
$(p+1, q+1)$	1	1	top-right
$(p-1, q+1)$	-1	1	top-left
$(p-1, q-1)$	-1	-1	bottom-left
$(p+1, q-1)$	1	-1	bottom-right

Substituting equation (4.3) in equations (4.1) and (4.2) yields the following Bloch-transformed homogeneous equations for the displacement amplitudes \tilde{x} and \tilde{y} :

$$m\ddot{\tilde{x}} + \hat{\tilde{x}}(c_1 b_1 + c_2 b_2 + c_4 b_3) + \hat{\tilde{y}}(c_2 b_2 - c_4 b_3) + \tilde{x}(k_1 b_1 + k_2 b_2 + k_4 b_3) + \tilde{y}(k_2 b_2 - k_4 b_3) = 0, \quad (4.6)$$

$$m\ddot{\tilde{y}} + \hat{\tilde{y}}(c_3 b_4 + c_2 b_2 + c_4 b_3) + \hat{\tilde{x}}(c_2 b_2 - c_4 b_3) + \tilde{y}(k_3 b_4 + k_2 b_2 + k_4 b_3) + \tilde{x}(k_2 b_2 - k_4 b_3) = 0. \quad (4.7)$$

In the aforementioned Bloch-transformed equations,

$$b_1 = 2 - e^{-i\kappa_x a_x} - e^{i\kappa_x a_x}, \quad (4.8)$$

$$b_2 = 1 - \frac{1}{2}e^{-i(\kappa_x a_x + \kappa_y a_y)} - \frac{1}{2}e^{i(\kappa_x a_x + \kappa_y a_y)}, \quad (4.9)$$

$$b_3 = 1 - \frac{1}{2}e^{-i(\kappa_x a_x - \kappa_y a_y)} - \frac{1}{2}e^{i(\kappa_x a_x - \kappa_y a_y)}, \quad (4.10)$$

$$b_4 = 2 - e^{-i\kappa_y a_y} - e^{i\kappa_y a_y}. \quad (4.11)$$

Equations (4.6) and (4.7) can be assembled into the matrix form

$$\mathbf{M}\ddot{\mathbf{U}} + \mathbf{C}(\boldsymbol{\kappa})\dot{\mathbf{U}} + \mathbf{K}(\boldsymbol{\kappa})\mathbf{U} = \mathbf{0}, \quad (4.12)$$

where

$$\mathbf{M} = \begin{pmatrix} m & 0 \\ 0 & m \end{pmatrix}; \quad \mathbf{C}(\boldsymbol{\kappa}) = \begin{pmatrix} c_1 b_1 + c_2 b_2 + c_4 b_3 & c_2 b_2 - c_4 b_3 \\ c_2 b_2 - c_4 b_3 & c_3 b_4 + c_2 b_2 + c_4 b_3 \end{pmatrix};$$

$$\text{and } \mathbf{K}(\boldsymbol{\kappa}) = \begin{pmatrix} k_1 b_1 + k_2 b_2 + k_4 b_3 & k_2 b_2 - k_4 b_3 \\ k_2 b_2 - k_4 b_3 & k_3 b_4 + k_2 b_2 + k_4 b_3 \end{pmatrix}. \quad (4.13)$$

Equation (4.12) can now be converted into a first order problem, through a state-space transformation [119–121] of the form

$$\mathbf{A}\dot{\mathbf{Y}} + \mathbf{B}\mathbf{Y} = \mathbf{0}, \quad (4.14)$$

where

$$\mathbf{A} = \begin{pmatrix} \mathbf{0} & \mathbf{I} \\ \mathbf{M} & \mathbf{C}(\boldsymbol{\kappa}) \end{pmatrix}; \quad \mathbf{B} = \begin{pmatrix} -\mathbf{I} & \mathbf{0} \\ \mathbf{0} & \mathbf{K}(\boldsymbol{\kappa}) \end{pmatrix}; \quad \text{and } \mathbf{Y} = \begin{pmatrix} \dot{\mathbf{U}} \\ \mathbf{U} \end{pmatrix}. \quad (4.15)$$

For equation (4.14), a solution of the form $\mathbf{Y} = \tilde{\mathbf{Y}}_\lambda e^{\lambda t}$ is assumed, where $\tilde{\mathbf{Y}}_\lambda$ is a complex-amplitude state-space vector corresponding to eigenvalue λ . The dispersion relation and, consequently, the wave-propagation and dissipation characteristics can now be obtained by implementing the solution in equation (4.14) and solving the resulting eigenvalue problem given by

$$|\mathbf{A}^{-1}\mathbf{B} + \lambda\mathbf{I}| = 0. \quad (4.16)$$

Expanding equation (4.16) for this particular case yields a fourth-order equation in terms of λ , which, upon solving, gives four complex roots appearing as two complex-conjugate pairs. The complex solution for the eigenvalue problem, in this case, at a given value of $\boldsymbol{\kappa}$ can be

expressed as

$$\lambda_l(\kappa) = -\zeta_s(\kappa)\omega_{r_l}(\kappa) \pm i\omega_{d_l}(\kappa) = -\zeta_l(\kappa)\omega_{r_l}(\kappa) \pm i\omega_{r_l}(\kappa)\sqrt{1 - \zeta_l(\kappa)^2}, \quad (4.17)$$

where the subscript l identifies the complex-conjugate pairs and, consequently, the mode or branch number. All two-dimensional monoatomic cases, on account of the two complex-conjugate pairs, exhibit two modes or branches: the transverse ($l = 1$) branch and the longitudinal ($l = 2$) branch. In the expression above, ω_{r_l} is the wavenumber-dependent resonant frequency which is defined as

$$\omega_{r_l}(\kappa) = \text{Abs}[\lambda_l(\kappa)]; \quad (4.18)$$

ω_{d_l} is the wavenumber-dependent damped frequency which is defined as

$$\omega_{d_l}(\kappa) = \text{Im}[\lambda_l(\kappa)]; \quad (4.19)$$

and $\zeta_l(\kappa)$ is the wavenumber-dependent damping ratio which is defined as

$$\zeta_l(\kappa) = -\frac{\text{Re}[\lambda_l(\kappa)]}{\text{Abs}[\lambda_l(\kappa)]}. \quad (4.20)$$

The phase and group velocities can also be obtained by using the definitions

$$C_{\text{ph}_l} = \frac{\omega_{d_l}}{\kappa} \text{ and } C_{\text{g}_l} = \frac{\partial \omega_{d_l}}{\partial \kappa}, \quad (4.21)$$

respectively.

4.3 Piezoelectric monoatomic phononic crystals

This section delves into the study of the propagation of plane waves through a two-dimensional MPPnC lattice with energy harvesters comprising of shunt circuits that are either purely resistive or are equipped with an inductor by means of the application of generalized Bloch's theorem to a two-dimensional MPPnC lattice with energy harvesters comprising of shunt circuits that are either purely resistive or equipped with an inductor.

Figure 4.2, presents the schematics of a MPPnC lattice under free vibration and the associated unit cell as lumped-parameter models. In figure 4.2, θ_{\dots} are the electromechanical coupling values and $v_{\dots}^{(p,q)}(t)$ are the voltages generated in a unit cell. An energy harvester, e.g., a piezoelectric patch, is placed between the mass in each unit cell and each of the

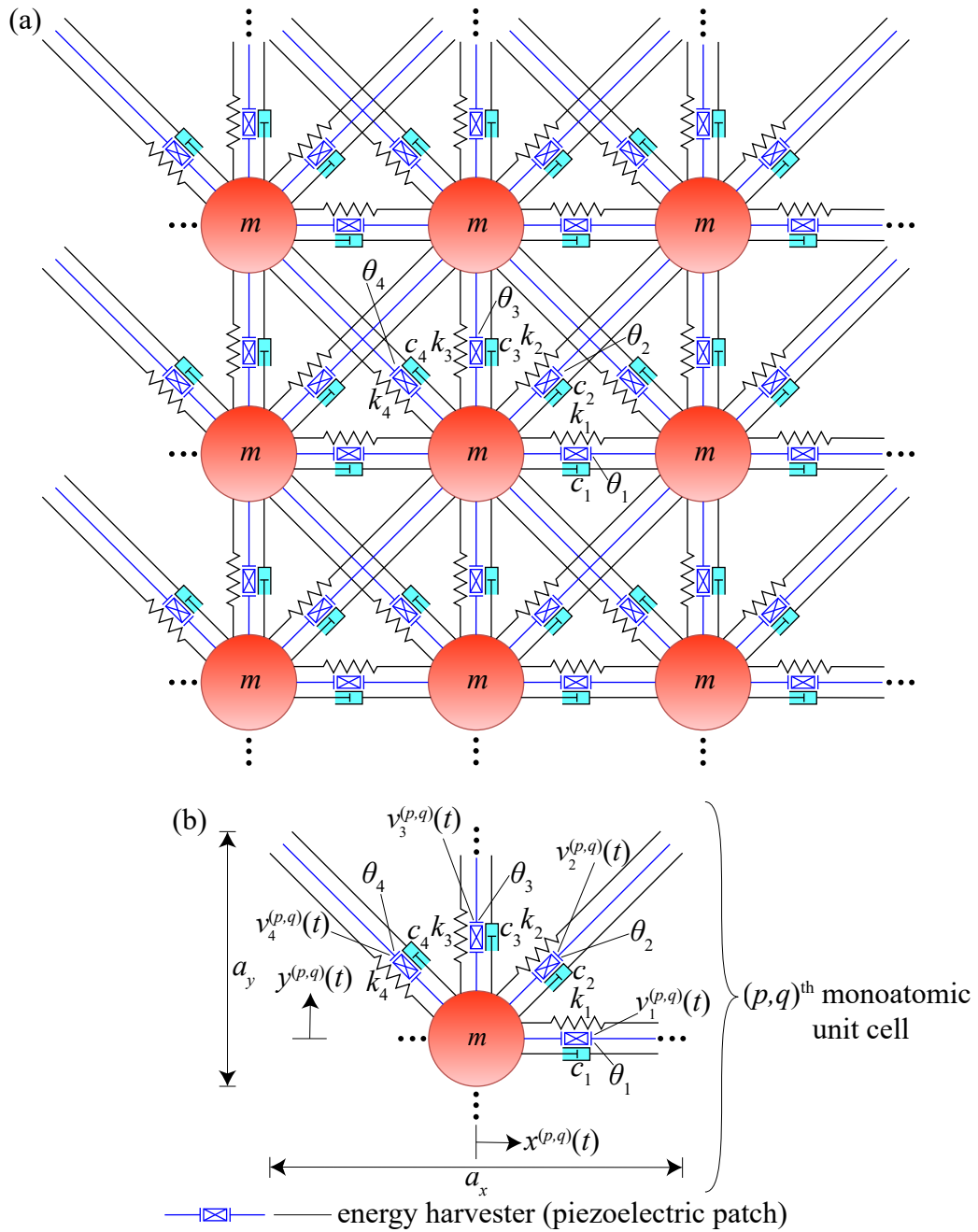


Figure 4.2: Schematic of (a) a monoatomic piezoelectric phononic-crystal (MPPnC) lattice and (b) the associated unit cell.

masses in the adjacent unit cells in all directions for the sake of considering a full-fledged piezoelectric lattice.

4.3.1 Shunt circuit without an inductor

In the set comprising of the governing electromechanical equations pertaining to the $(p, q)^{\text{th}}$ unit cell, the governing mechanical equations can be formulated by aggregating all the forces on the mass, due to the springs and dashpots in the unit cell, in the x- and y-directions. The governing mechanical equations, including the effects of the piezoelectric elements, pertaining to the $(p, q)^{\text{th}}$ unit cell under free vibration consisting of piezoelectric elements with shunt circuits lacking an inductor can be written as

$$\begin{aligned}
& m\ddot{x}^{(p,q)} + c_1 \left(\dot{x}^{(p,q)} - \dot{x}^{(p+1,q)} + \dot{x}^{(p,q)} - \dot{x}^{(p-1,q)} \right) \\
& + \frac{1}{2}c_2 \left(\dot{x}^{(p,q)} - \dot{x}^{(p+1,q+1)} + \dot{x}^{(p,q)} - \dot{x}^{(p-1,q-1)} + \dot{y}^{(p,q)} - \dot{y}^{(p+1,q+1)} + \dot{y}^{(p,q)} - \dot{y}^{(p-1,q-1)} \right) \\
& + \frac{1}{2}c_4 \left(\dot{x}^{(p,q)} - \dot{x}^{(p-1,q+1)} + \dot{x}^{(p,q)} - \dot{x}^{(p+1,q-1)} - \dot{y}^{(p,q)} + \dot{y}^{(p-1,q+1)} - \dot{y}^{(p,q)} + \dot{y}^{(p+1,q-1)} \right) \\
& \quad + k_1 \left(x^{(p,q)} - x^{(p+1,q)} + x^{(p,q)} - x^{(p-1,q)} \right) \\
& + \frac{1}{2}k_2 \left(x^{(p,q)} - x^{(p+1,q+1)} + x^{(p,q)} - x^{(p-1,q-1)} + y^{(p,q)} - y^{(p+1,q+1)} + y^{(p,q)} - y^{(p-1,q-1)} \right) \\
& + \frac{1}{2}k_4 \left(x^{(p,q)} - x^{(p-1,q+1)} + x^{(p,q)} - x^{(p+1,q-1)} - y^{(p,q)} + y^{(p-1,q+1)} - y^{(p,q)} + y^{(p+1,q-1)} \right) \\
& \quad + \theta_1 v_1^{(p-1,q)} - \theta_1 v_1^{(p,q)} + \frac{\theta_2}{2} v_2^{(p-1,q-1)} - \frac{\theta_2}{2} v_2^{(p,q)} - \frac{\theta_4}{2} v_4^{(p+1,q-1)} + \frac{\theta_4}{2} v_4^{(p,q)} = 0,
\end{aligned} \tag{4.22}$$

$$\begin{aligned}
& m\ddot{y}^{(p,q)} + c_3 \left(\dot{y}^{(p,q)} - \dot{y}^{(p,q+1)} + \dot{y}^{(p,q)} - \dot{y}^{(p,q-1)} \right) \\
& + \frac{1}{2}c_2 \left(\dot{y}^{(p,q)} - \dot{y}^{(p+1,q+1)} + \dot{y}^{(p,q)} - \dot{y}^{(p-1,q-1)} + \dot{x}^{(p,q)} - \dot{x}^{(p+1,q+1)} + \dot{x}^{(p,q)} - \dot{x}^{(p-1,q-1)} \right) \\
& + \frac{1}{2}c_4 \left(\dot{y}^{(p,q)} - \dot{y}^{(p-1,q+1)} + \dot{y}^{(p,q)} - \dot{y}^{(p+1,q-1)} - \dot{x}^{(p,q)} + \dot{x}^{(p-1,q+1)} - \dot{x}^{(p,q)} + \dot{x}^{(p+1,q-1)} \right) \\
& \quad + k_3 \left(y^{(p,q)} - y^{(p,q+1)} + y^{(p,q)} - y^{(p,q-1)} \right) \\
& + \frac{1}{2}k_2 \left(y^{(p,q)} - y^{(p+1,q+1)} + y^{(p,q)} - y^{(p-1,q-1)} + x^{(p,q)} - x^{(p+1,q+1)} + x^{(p,q)} - x^{(p-1,q-1)} \right) \\
& + \frac{1}{2}k_4 \left(y^{(p,q)} - y^{(p-1,q+1)} + y^{(p,q)} - y^{(p+1,q-1)} - x^{(p,q)} + x^{(p-1,q+1)} - x^{(p,q)} + x^{(p+1,q-1)} \right) \\
& \quad + \theta_3 v_3^{(p,q-1)} - \theta_3 v_3^{(p,q)} + \frac{\theta_2}{2} v_2^{(p-1,q-1)} - \frac{\theta_2}{2} v_2^{(p,q)} - \frac{\theta_4}{2} v_4^{(p+1,q-1)} + \frac{\theta_4}{2} v_4^{(p,q)} = 0.
\end{aligned} \tag{4.23}$$

The governing electrical equations pertaining to the $(p, q)^{\text{th}}$ unit cell under free vibration consisting of piezoelectric elements with shunt circuits lacking an inductor [73] can be

written as

$$-\theta_1 \left(\dot{x}^{(p+1,q)} - \dot{x}^{(p,q)} \right) + C_{p1} \dot{v}_1^{(p,q)} + \frac{1}{R_1} v_1^{(p,q)} = 0, \quad (4.24)$$

$$\frac{-\theta_2}{2} \left(\dot{x}^{(p+1,q+1)} - \dot{x}^{(p,q)} \right) - \frac{\theta_2}{2} \left(\dot{y}^{(p+1,q+1)} - \dot{y}^{(p,q)} \right) + C_{p2} \dot{v}_2^{(p,q)} + \frac{1}{R_2} v_2^{(p,q)} = 0, \quad (4.25)$$

$$-\theta_3 \left(\dot{y}^{(p,q+1)} - \dot{y}^{(p,q)} \right) + C_{p3} \dot{v}_3^{(p,q)} + \frac{1}{R_3} v_3^{(p,q)} = 0, \quad (4.26)$$

$$\frac{-\theta_4}{2} \left(\dot{x}^{(p,q)} - \dot{x}^{(p-1,q+1)} \right) - \frac{\theta_4}{2} \left(\dot{y}^{(p,q)} - \dot{y}^{(p-1,q+1)} \right) + C_{p4} \dot{v}_4^{(p,q)} + \frac{1}{R_4} v_4^{(p,q)} = 0. \quad (4.27)$$

Analogous to equation (4.3), the plane-wave solution for the voltages generated in a periodic unit-cell can be written as

$$v_l^{(p+g_1, q+g_2)}(\mathbf{r}, \boldsymbol{\kappa}; t) = \tilde{v}_l(t) e^{i[\kappa_x(p+g_1)a_x + \kappa_y(q+g_2)a_y]}, \quad (4.28)$$

where $l=1,2,3,4$ is an index corresponding to the voltages generated by the four piezoelectric elements in a unit cell. Substituting equations (4.3) and (4.28) in equations (4.22)–(4.27) yields the following Bloch-transformed homogeneous equations for the displacement amplitudes \tilde{x} and \tilde{y} and the voltage amplitudes \tilde{v}_1 , \tilde{v}_2 , \tilde{v}_3 , and \tilde{v}_4 :

$$\begin{aligned} m\ddot{\tilde{x}} + \dot{\tilde{x}}(c_1b_1 + c_2b_2 + c_4b_3) + \dot{\tilde{y}}(c_2b_2 - c_4b_3) + \tilde{x}(k_1b_1 + k_2b_2 + k_4b_3) \\ + \tilde{y}(k_2b_2 - k_4b_3) + \tilde{v}_1 \left(\theta_1 e^{-i\kappa_x a_x} - \theta_1 \right) + \tilde{v}_2 \left(\frac{\theta_2}{2} e^{-i(\kappa_x a_x + \kappa_y a_y)} - \frac{\theta_2}{2} \right) \\ + \tilde{v}_4 \left(\frac{\theta_4}{2} - \frac{\theta_4}{2} e^{i(\kappa_x a_x - \kappa_y a_y)} \right) = 0, \end{aligned} \quad (4.29)$$

$$\begin{aligned} m\ddot{\tilde{y}} + \dot{\tilde{y}}(c_3b_4 + c_2b_2 + c_4b_3) + \dot{\tilde{x}}(c_2b_2 - c_4b_3) + \tilde{y}(k_3b_4 + k_2b_2 + k_4b_3) \\ + \tilde{x}(k_2b_2 - k_4b_3) + \tilde{v}_3 \left(\theta_3 e^{-i\kappa_y a_y} - \theta_3 \right) + \tilde{v}_2 \left(\frac{\theta_2}{2} e^{-i(\kappa_x a_x + \kappa_y a_y)} - \frac{\theta_2}{2} \right) \\ + \tilde{v}_4 \left(\frac{\theta_4}{2} - \frac{\theta_4}{2} e^{i(\kappa_x a_x - \kappa_y a_y)} \right) = 0, \end{aligned} \quad (4.30)$$

$$\dot{\tilde{x}} \left(\theta_1 - \theta_1 e^{i\kappa_x a_x} \right) + C_{p1} \dot{\tilde{v}}_1 + \frac{1}{R_1} \tilde{v}_1 = 0, \quad (4.31)$$

$$\dot{\tilde{x}} \left(\frac{\theta_2}{2} - \frac{\theta_2}{2} e^{i(\kappa_x a_x + \kappa_y a_y)} \right) + \dot{\tilde{y}} \left(\frac{\theta_2}{2} - \frac{\theta_2}{2} e^{i(\kappa_x a_x + \kappa_y a_y)} \right) + C_{p2} \dot{\tilde{v}}_2 + \frac{1}{R_2} \tilde{v}_2 = 0, \quad (4.32)$$

$$\dot{\tilde{y}} \left(\theta_3 - \theta_3 e^{i\kappa_y a_y} \right) + C_{p3} \dot{\tilde{v}}_3 + \frac{1}{R_3} \tilde{v}_3 = 0, \quad (4.33)$$

$$\dot{\tilde{x}} \left(\frac{\theta_4}{2} e^{-i(\kappa_x a_x - \kappa_y a_y)} - \frac{\theta_4}{2} \right) + \dot{\tilde{y}} \left(\frac{\theta_4}{2} e^{-i(\kappa_x a_x - \kappa_y a_y)} - \frac{\theta_4}{2} \right) + C_{p4} \dot{\tilde{v}}_4 + \frac{1}{R_4} \tilde{v}_4 = 0. \quad (4.34)$$

The coefficients b_1 , b_2 , b_3 , and b_4 used in the aforementioned Bloch-transformed equations are stated in equations (4.8)–(4.11). Equations (4.29)–(4.34) can be compacted into a matrix form as

$$\mathbf{M}\ddot{\mathbf{U}} + \mathbf{C}(\boldsymbol{\kappa})\dot{\mathbf{U}} + \mathbf{K}(\boldsymbol{\kappa})\mathbf{U} + \mathbf{T}_1^{\text{perpd}}(\boldsymbol{\kappa})\tilde{\mathbf{V}}^{\text{perpd}} + \mathbf{T}_1^{\text{diag}}(\boldsymbol{\kappa})\tilde{\mathbf{V}}^{\text{diag}} = \mathbf{0}, \quad (4.35)$$

$$\mathbf{T}_2^{\text{perpd}}(\boldsymbol{\kappa})\dot{\mathbf{U}} + \mathbf{C}_p^{\text{perpd}}\dot{\tilde{\mathbf{V}}}^{\text{perpd}} + \mathbf{R}^{\text{perpd}}\tilde{\mathbf{V}}^{\text{perpd}} = \mathbf{0}, \quad (4.36)$$

$$\mathbf{T}_2^{\text{diag}}(\boldsymbol{\kappa})\dot{\mathbf{U}} + \mathbf{C}_p^{\text{diag}}\dot{\tilde{\mathbf{V}}}^{\text{diag}} + \mathbf{R}^{\text{diag}}\tilde{\mathbf{V}}^{\text{diag}} = \mathbf{0}, \quad (4.37)$$

where

$$\begin{aligned} \tilde{\mathbf{V}}^{\text{perpd}} &= \begin{pmatrix} \tilde{v}_1 \\ \tilde{v}_3 \end{pmatrix}; \quad \tilde{\mathbf{V}}^{\text{diag}} = \begin{pmatrix} \tilde{v}_2 \\ \tilde{v}_4 \end{pmatrix}; \quad \mathbf{M} = \begin{pmatrix} m & 0 \\ 0 & m \end{pmatrix}; \\ \mathbf{C}(\boldsymbol{\kappa}) &= \begin{pmatrix} c_1b_1 + c_2b_2 + c_4b_3 & c_2b_2 - c_4b_3 \\ c_2b_2 - c_4b_3 & c_3b_4 + c_2b_2 + c_4b_3 \end{pmatrix}; \\ \mathbf{K}(\boldsymbol{\kappa}) &= \begin{pmatrix} k_1b_1 + k_2b_2 + k_4b_3 & k_2b_2 - k_4b_3 \\ k_2b_2 - k_4b_3 & k_3b_4 + k_2b_2 + k_4b_3 \end{pmatrix}; \\ \mathbf{T}_1^{\text{perpd}}(\boldsymbol{\kappa}) &= \begin{pmatrix} \theta_1 e^{-i\kappa_x a_x} - \theta_1 & 0 \\ 0 & \theta_3 e^{-i\kappa_y a_y} - \theta_3 \end{pmatrix}; \\ \mathbf{T}_2^{\text{perpd}}(\boldsymbol{\kappa}) &= \begin{pmatrix} \theta_1 - \theta_1 e^{i\kappa_x a_x} & 0 \\ 0 & \theta_3 - \theta_3 e^{i\kappa_y a_y} \end{pmatrix}; \\ \mathbf{T}_1^{\text{diag}}(\boldsymbol{\kappa}) &= \begin{pmatrix} \frac{\theta_2}{2} e^{-i(\kappa_x a_x + \kappa_y a_y)} - \frac{\theta_2}{2} & \frac{\theta_4}{2} - \frac{\theta_4}{2} e^{i(\kappa_x a_x - \kappa_y a_y)} \\ \frac{\theta_2}{2} e^{-i(\kappa_x a_x + \kappa_y a_y)} - \frac{\theta_2}{2} & \frac{\theta_4}{2} - \frac{\theta_4}{2} e^{i(\kappa_x a_x - \kappa_y a_y)} \end{pmatrix}; \\ \mathbf{T}_2^{\text{diag}}(\boldsymbol{\kappa}) &= \begin{pmatrix} \frac{\theta_2}{2} - \frac{\theta_2}{2} e^{i(\kappa_x a_x + \kappa_y a_y)} & \frac{\theta_2}{2} - \frac{\theta_2}{2} e^{i(\kappa_x a_x + \kappa_y a_y)} \\ \frac{\theta_4}{2} e^{-i(\kappa_x a_x - \kappa_y a_y)} - \frac{\theta_4}{2} & \frac{\theta_4}{2} e^{-i(\kappa_x a_x - \kappa_y a_y)} - \frac{\theta_4}{2} \end{pmatrix}; \\ \mathbf{C}_p^{\text{perpd}} &= \begin{pmatrix} C_{p1} & 0 \\ 0 & C_{p3} \end{pmatrix}; \quad \mathbf{C}_p^{\text{diag}} = \begin{pmatrix} C_{p2} & 0 \\ 0 & C_{p4} \end{pmatrix}; \\ \mathbf{R}^{\text{perpd}} &= \begin{pmatrix} \frac{1}{R_1} & 0 \\ 0 & \frac{1}{R_3} \end{pmatrix}; \quad \text{and } \mathbf{R}^{\text{diag}} = \begin{pmatrix} \frac{1}{R_2} & 0 \\ 0 & \frac{1}{R_4} \end{pmatrix}. \end{aligned} \quad (4.38)$$

Note that the superscript “perpd” is used to refer to the matrices consisting of electrical parameters of the piezoelectric elements in the horizontal and vertical directions and the

superscript “diag” is used to refer to the matrices consisting of electrical parameters of the piezoelectric elements diagonal to the mass. The dispersion relation can now be formulated by subjecting equations (4.35)–(4.37) to a state-space transformation of the form given in equation (4.14), where

$$\mathbf{A} = \begin{pmatrix} \mathbf{0} & \mathbf{I} & \mathbf{0} & \mathbf{0} \\ \mathbf{M} & \mathbf{C}(\boldsymbol{\kappa}) & \mathbf{0} & \mathbf{0} \\ \mathbf{0} & \mathbf{T}_2^{\text{perpd}}(\boldsymbol{\kappa}) & \mathbf{C}_p^{\text{perpd}} & \mathbf{0} \\ \mathbf{0} & \mathbf{T}_2^{\text{diag}}(\boldsymbol{\kappa}) & \mathbf{0} & \mathbf{C}_p^{\text{diag}} \end{pmatrix};$$

$$\mathbf{B} = \begin{pmatrix} -\mathbf{I} & \mathbf{0} & \mathbf{0} & \mathbf{0} \\ \mathbf{0} & \mathbf{K}(\boldsymbol{\kappa}) & \mathbf{T}_1^{\text{perpd}}(\boldsymbol{\kappa}) & \mathbf{T}_1^{\text{diag}}(\boldsymbol{\kappa}) \\ \mathbf{0} & \mathbf{0} & \mathbf{R}^{\text{perpd}} & \mathbf{0} \\ \mathbf{0} & \mathbf{0} & \mathbf{0} & \mathbf{R}^{\text{diag}} \end{pmatrix}; \text{ and } \mathbf{Y} = \begin{pmatrix} \dot{\tilde{\mathbf{U}}} \\ \tilde{\mathbf{U}} \\ \tilde{\mathbf{v}}^{\text{perpd}} \\ \tilde{\mathbf{v}}^{\text{diag}} \end{pmatrix}, \quad (4.39)$$

implementing a solution of the form $\mathbf{Y} = \tilde{\mathbf{Y}}_\lambda e^{\lambda t}$, and solving the resulting eigenvalue problem of the form given in equation (4.16). Expanding equation (4.16) for this particular case yields an eight-order equation in terms of λ , which, upon solving, gives four complex roots appearing as two complex-conjugate pairs and four real roots.

4.3.2 Shunt circuit with an inductor

The governing mechanical equations, including the effects of the piezoelectric elements, pertaining to the $(p, q)^{\text{th}}$ unit cell under free vibration consisting of piezoelectric elements

with shunt circuits consisting of an inductor can be written as

$$\begin{aligned}
& m\ddot{x}^{(p,q)} + c_1 \left(\dot{x}^{(p,q)} - \dot{x}^{(p+1,q)} + \dot{x}^{(p,q)} - \dot{x}^{(p-1,q)} \right) \\
& + \frac{1}{2}c_2 \left(\dot{x}^{(p,q)} - \dot{x}^{(p+1,q+1)} + \dot{x}^{(p,q)} - \dot{x}^{(p-1,q-1)} + \dot{y}^{(p,q)} - \dot{y}^{(p+1,q+1)} + \dot{y}^{(p,q)} - \dot{y}^{(p-1,q-1)} \right) \\
& + \frac{1}{2}c_4 \left(\dot{x}^{(p,q)} - \dot{x}^{(p-1,q+1)} + \dot{x}^{(p,q)} - \dot{x}^{(p+1,q-1)} - \dot{y}^{(p,q)} + \dot{y}^{(p-1,q+1)} - \dot{y}^{(p,q)} + \dot{y}^{(p+1,q-1)} \right) \\
& \quad + k_1 \left(x^{(p,q)} - x^{(p+1,q)} + x^{(p,q)} - x^{(p-1,q)} \right) \\
& + \frac{1}{2}k_2 \left(x^{(p,q)} - x^{(p+1,q+1)} + x^{(p,q)} - x^{(p-1,q-1)} + y^{(p,q)} - y^{(p+1,q+1)} + y^{(p,q)} - y^{(p-1,q-1)} \right) \\
& + \frac{1}{2}k_4 \left(x^{(p,q)} - x^{(p-1,q+1)} + x^{(p,q)} - x^{(p+1,q-1)} - y^{(p,q)} + y^{(p-1,q+1)} - y^{(p,q)} + y^{(p+1,q-1)} \right) \\
& \quad + \theta_1 v_1^{(p-1,q)} - \theta_1 v_1^{(p,q)} + \frac{\theta_2}{2} v_2^{(p-1,q-1)} - \frac{\theta_2}{2} v_2^{(p,q)} - \frac{\theta_4}{2} v_4^{(p+1,q-1)} + \frac{\theta_4}{2} v_4^{(p,q)} = 0,
\end{aligned} \tag{4.40}$$

$$\begin{aligned}
& m\ddot{y}^{(p,q)} + c_3 \left(\dot{y}^{(p,q)} - \dot{y}^{(p,q+1)} + \dot{y}^{(p,q)} - \dot{y}^{(p,q-1)} \right) \\
& + \frac{1}{2}c_2 \left(\dot{y}^{(p,q)} - \dot{y}^{(p+1,q+1)} + \dot{y}^{(p,q)} - \dot{y}^{(p-1,q-1)} + \dot{x}^{(p,q)} - \dot{x}^{(p+1,q+1)} + \dot{x}^{(p,q)} - \dot{x}^{(p-1,q-1)} \right) \\
& + \frac{1}{2}c_4 \left(\dot{y}^{(p,q)} - \dot{y}^{(p-1,q+1)} + \dot{y}^{(p,q)} - \dot{y}^{(p+1,q-1)} - \dot{x}^{(p,q)} + \dot{x}^{(p-1,q+1)} - \dot{x}^{(p,q)} + \dot{x}^{(p+1,q-1)} \right) \\
& \quad + k_3 \left(y^{(p,q)} - y^{(p,q+1)} + y^{(p,q)} - y^{(p,q-1)} \right) \\
& + \frac{1}{2}k_2 \left(y^{(p,q)} - y^{(p+1,q+1)} + y^{(p,q)} - y^{(p-1,q-1)} + x^{(p,q)} - x^{(p+1,q+1)} + x^{(p,q)} - x^{(p-1,q-1)} \right) \\
& + \frac{1}{2}k_4 \left(y^{(p,q)} - y^{(p-1,q+1)} + y^{(p,q)} - y^{(p+1,q-1)} - x^{(p,q)} + x^{(p-1,q+1)} - x^{(p,q)} + x^{(p+1,q-1)} \right) \\
& \quad + \theta_3 v_3^{(p,q-1)} - \theta_3 v_3^{(p,q)} + \frac{\theta_2}{2} v_2^{(p-1,q-1)} - \frac{\theta_2}{2} v_2^{(p,q)} - \frac{\theta_4}{2} v_4^{(p+1,q-1)} + \frac{\theta_4}{2} v_4^{(p,q)} = 0.
\end{aligned} \tag{4.41}$$

The governing electrical equations pertaining to the $(p, q)^{\text{th}}$ unit cell under free vibration consisting of piezoelectric elements with shunt circuits including an inductor [73] can be

written as

$$-\theta_1 \left(\ddot{x}^{(p+1,q)} - \ddot{x}^{(p,q)} \right) + C_{p1} \ddot{v}_1^{(p,q)} + \frac{1}{R_1} \dot{v}_1^{(p,q)} + \frac{1}{L_1} v_1^{(p,q)} = 0, \quad (4.42)$$

$$\begin{aligned} -\frac{\theta_2}{2} \left(\ddot{x}^{(p+1,q+1)} - \ddot{x}^{(p,q)} \right) - \frac{\theta_2}{2} \left(\ddot{y}^{(p+1,q+1)} - \ddot{y}^{(p,q)} \right) + C_{p2} \ddot{v}_2^{(p,q)} + \frac{1}{R_2} \dot{v}_2^{(p,q)} \\ + \frac{1}{L_2} v_2^{(p,q)} = 0, \end{aligned} \quad (4.43)$$

$$-\theta_3 \left(\ddot{y}^{(p,q+1)} - \ddot{y}^{(p,q)} \right) + C_{p3} \ddot{v}_3^{(p,q)} + \frac{1}{R_3} \dot{v}_3^{(p,q)} + \frac{1}{L_3} v_3^{(p,q)} = 0, \quad (4.44)$$

$$\begin{aligned} -\frac{\theta_4}{2} \left(\ddot{x}^{(p,q)} - \ddot{x}^{(p-1,q+1)} \right) - \frac{\theta_4}{2} \left(\ddot{y}^{(p,q)} - \ddot{y}^{(p-1,q+1)} \right) + C_{p4} \ddot{v}_4^{(p,q)} + \frac{1}{R_4} \dot{v}_4^{(p,q)} \\ + \frac{1}{L_4} v_4^{(p,q)} = 0. \end{aligned} \quad (4.45)$$

Substituting equations (4.3) and (4.28) in equations (4.40)–(4.45) yields the following Bloch-transformed homogeneous equations for the displacement amplitudes \tilde{x} and \tilde{y} and the voltage amplitudes \tilde{v}_1 , \tilde{v}_2 , \tilde{v}_3 , and \tilde{v}_4 :

$$\begin{aligned} m\ddot{\tilde{x}} + \dot{\tilde{x}}(c_1b_1 + c_2b_2 + c_4b_3) + \dot{\tilde{y}}(c_2b_2 - c_4b_3) + \tilde{x}(k_1b_1 + k_2b_2 + k_4b_3) \\ + \tilde{y}(k_2b_2 - k_4b_3) + \tilde{v}_1 \left(\theta_1 e^{-i\kappa_x a_x} - \theta_1 \right) + \tilde{v}_2 \left(\frac{\theta_2}{2} e^{-i(\kappa_x a_x + \kappa_y a_y)} - \frac{\theta_2}{2} \right) \\ + \tilde{v}_4 \left(\frac{\theta_4}{2} - \frac{\theta_4}{2} e^{i(\kappa_x a_x - \kappa_y a_y)} \right) = 0, \end{aligned} \quad (4.46)$$

$$\begin{aligned} m\ddot{\tilde{y}} + \dot{\tilde{y}}(c_3b_4 + c_2b_2 + c_4b_3) + \dot{\tilde{x}}(c_2b_2 - c_4b_3) + \tilde{y}(k_3b_4 + k_2b_2 + k_4b_3) \\ + \tilde{x}(k_2b_2 - k_4b_3) + \tilde{v}_3 \left(\theta_3 e^{-i\kappa_y a_y} - \theta_3 \right) + \tilde{v}_2 \left(\frac{\theta_2}{2} e^{-i(\kappa_x a_x + \kappa_y a_y)} - \frac{\theta_2}{2} \right) \\ + \tilde{v}_4 \left(\frac{\theta_4}{2} - \frac{\theta_4}{2} e^{i(\kappa_x a_x - \kappa_y a_y)} \right) = 0, \end{aligned} \quad (4.47)$$

$$\ddot{\tilde{x}} \left(\theta_1 - \theta_1 e^{i\kappa_x a_x} \right) + C_{p1} \ddot{\tilde{v}}_1 + \frac{1}{R_1} \dot{\tilde{v}}_1 + \frac{1}{L_1} \tilde{v}_1 = 0, \quad (4.48)$$

$$\ddot{\tilde{x}} \left(\frac{\theta_2}{2} - \frac{\theta_2}{2} e^{i(\kappa_x a_x + \kappa_y a_y)} \right) + \ddot{\tilde{y}} \left(\frac{\theta_2}{2} - \frac{\theta_2}{2} e^{i(\kappa_x a_x + \kappa_y a_y)} \right) + C_{p2} \ddot{\tilde{v}}_2 + \frac{1}{R_2} \dot{\tilde{v}}_2 + \frac{1}{L_2} \tilde{v}_2 = 0, \quad (4.49)$$

$$\ddot{\tilde{y}} \left(\theta_3 - \theta_3 e^{i\kappa_y a_y} \right) + C_{p3} \ddot{\tilde{v}}_3 + \frac{1}{R_3} \dot{\tilde{v}}_3 + \frac{1}{L_3} \tilde{v}_3 = 0, \quad (4.50)$$

$$\begin{aligned} \ddot{\tilde{x}} \left(\frac{\theta_4}{2} e^{-i(\kappa_x a_x - \kappa_y a_y)} - \frac{\theta_4}{2} \right) + \ddot{\tilde{y}} \left(\frac{\theta_4}{2} e^{-i(\kappa_x a_x - \kappa_y a_y)} - \frac{\theta_4}{2} \right) + C_{p4} \ddot{\tilde{v}}_4 + \frac{1}{R_4} \dot{\tilde{v}}_4 \\ + \frac{1}{L_4} \tilde{v}_4 = 0. \end{aligned} \quad (4.51)$$

The coefficients b_1 , b_2 , b_3 , and b_4 used in the aforementioned Bloch-transformed equations are stated in equations (4.8)–(4.11). Equations (4.46)–(4.51) can be fused into a matrix form as

$$\mathbf{M}\ddot{\mathbf{U}} + \mathbf{C}(\boldsymbol{\kappa})\dot{\mathbf{U}} + \mathbf{K}(\boldsymbol{\kappa})\mathbf{U} + \mathbf{T}_1^{\text{perpd}}(\boldsymbol{\kappa})\tilde{\mathbf{V}}^{\text{perpd}} + \mathbf{T}_1^{\text{diag}}(\boldsymbol{\kappa})\tilde{\mathbf{V}}^{\text{diag}} = \mathbf{0}, \quad (4.52)$$

$$\mathbf{T}_2^{\text{perpd}}(\boldsymbol{\kappa})\ddot{\mathbf{U}} + \mathbf{C}_p^{\text{perpd}}\ddot{\mathbf{V}}^{\text{perpd}} + \mathbf{R}^{\text{perpd}}\dot{\mathbf{V}}^{\text{perpd}} + \mathbf{L}^{\text{perpd}}\tilde{\mathbf{V}}^{\text{perpd}} = \mathbf{0}, \quad (4.53)$$

$$\mathbf{T}_2^{\text{diag}}(\boldsymbol{\kappa})\ddot{\mathbf{U}} + \mathbf{C}_p^{\text{diag}}\ddot{\mathbf{V}}^{\text{diag}} + \mathbf{R}^{\text{diag}}\dot{\mathbf{V}}^{\text{diag}} + \mathbf{L}^{\text{diag}}\tilde{\mathbf{V}}^{\text{diag}} = \mathbf{0}, \quad (4.54)$$

where

$$\begin{aligned} \tilde{\mathbf{V}}^{\text{perpd}} &= \begin{pmatrix} \tilde{v}_1 \\ \tilde{v}_3 \end{pmatrix}; \quad \tilde{\mathbf{V}}^{\text{diag}} = \begin{pmatrix} \tilde{v}_2 \\ \tilde{v}_4 \end{pmatrix}; \quad \mathbf{M} = \begin{pmatrix} m & 0 \\ 0 & m \end{pmatrix}; \\ \mathbf{C}(\boldsymbol{\kappa}) &= \begin{pmatrix} c_1b_1 + c_2b_2 + c_4b_3 & c_2b_2 - c_4b_3 \\ c_2b_2 - c_4b_3 & c_3b_4 + c_2b_2 + c_4b_3 \end{pmatrix}; \\ \mathbf{K}(\boldsymbol{\kappa}) &= \begin{pmatrix} k_1b_1 + k_2b_2 + k_4b_3 & k_2b_2 - k_4b_3 \\ k_2b_2 - k_4b_3 & k_3b_4 + k_2b_2 + k_4b_3 \end{pmatrix}; \\ \mathbf{T}_1^{\text{perpd}}(\boldsymbol{\kappa}) &= \begin{pmatrix} \theta_1 e^{-i\kappa_x a_x} - \theta_1 & 0 \\ 0 & \theta_3 e^{-i\kappa_y a_y} - \theta_3 \end{pmatrix}; \\ \mathbf{T}_2^{\text{perpd}}(\boldsymbol{\kappa}) &= \begin{pmatrix} \theta_1 - \theta_1 e^{i\kappa_x a_x} & 0 \\ 0 & \theta_3 - \theta_3 e^{i\kappa_y a_y} \end{pmatrix}; \\ \mathbf{T}_1^{\text{diag}}(\boldsymbol{\kappa}) &= \begin{pmatrix} \frac{\theta_2}{2} e^{-i(\kappa_x a_x + \kappa_y a_y)} - \frac{\theta_2}{2} & \frac{\theta_4}{2} - \frac{\theta_4}{2} e^{i(\kappa_x a_x - \kappa_y a_y)} \\ \frac{\theta_2}{2} e^{-i(\kappa_x a_x + \kappa_y a_y)} - \frac{\theta_2}{2} & \frac{\theta_4}{2} - \frac{\theta_4}{2} e^{i(\kappa_x a_x - \kappa_y a_y)} \end{pmatrix}; \\ \mathbf{T}_2^{\text{diag}}(\boldsymbol{\kappa}) &= \begin{pmatrix} \frac{\theta_2}{2} - \frac{\theta_2}{2} e^{i(\kappa_x a_x + \kappa_y a_y)} & \frac{\theta_2}{2} - \frac{\theta_2}{2} e^{i(\kappa_x a_x + \kappa_y a_y)} \\ \frac{\theta_4}{2} e^{-i(\kappa_x a_x - \kappa_y a_y)} - \frac{\theta_4}{2} & \frac{\theta_4}{2} e^{-i(\kappa_x a_x - \kappa_y a_y)} - \frac{\theta_4}{2} \end{pmatrix}; \\ \mathbf{C}_p^{\text{perpd}} &= \begin{pmatrix} C_{p1} & 0 \\ 0 & C_{p3} \end{pmatrix}; \quad \mathbf{C}_p^{\text{diag}} = \begin{pmatrix} C_{p2} & 0 \\ 0 & C_{p4} \end{pmatrix}; \\ \mathbf{R}^{\text{perpd}} &= \begin{pmatrix} \frac{1}{R_1} & 0 \\ 0 & \frac{1}{R_3} \end{pmatrix}; \quad \mathbf{R}^{\text{diag}} = \begin{pmatrix} \frac{1}{R_2} & 0 \\ 0 & \frac{1}{R_4} \end{pmatrix}; \end{aligned}$$

$$\mathbf{L}^{\text{perpd}} = \begin{pmatrix} \frac{1}{L_1} & 0 \\ 0 & \frac{1}{L_3} \end{pmatrix}; \text{ and } \mathbf{L}^{\text{diag}} = \begin{pmatrix} \frac{1}{L_2} & 0 \\ 0 & \frac{1}{L_4} \end{pmatrix}. \quad (4.55)$$

Equations (4.52)–(4.54) can be further merged into a single matrix equation as

$$\mathbf{Z}_1 \ddot{\tilde{\mathbf{E}}} + \mathbf{Z}_2 \dot{\tilde{\mathbf{E}}} + \mathbf{Z}_3 \tilde{\mathbf{E}} = \mathbf{0}, \quad (4.56)$$

where

$$\begin{aligned} \mathbf{Z}_1 &= \begin{pmatrix} \mathbf{M} & \mathbf{0} & \mathbf{0} \\ \mathbf{T}_2^{\text{perpd}}(\boldsymbol{\kappa}) & \mathbf{C}_p^{\text{perpd}} & \mathbf{0} \\ \mathbf{T}_2^{\text{diag}}(\boldsymbol{\kappa}) & \mathbf{0} & \mathbf{C}_p^{\text{diag}} \end{pmatrix}; \mathbf{Z}_2 = \begin{pmatrix} \mathbf{C}(\boldsymbol{\kappa}) & \mathbf{0} & \mathbf{0} \\ \mathbf{0} & \mathbf{R}^{\text{perpd}} & \mathbf{0} \\ \mathbf{0} & \mathbf{0} & \mathbf{R}^{\text{diag}} \end{pmatrix}; \\ \mathbf{Z}_3 &= \begin{pmatrix} \mathbf{K}(\boldsymbol{\kappa}) & \mathbf{T}_1^{\text{perpd}}(\boldsymbol{\kappa}) & \mathbf{T}_1^{\text{diag}}(\boldsymbol{\kappa}) \\ \mathbf{0} & \mathbf{L}^{\text{perpd}} & \mathbf{0} \\ \mathbf{0} & \mathbf{0} & \mathbf{L}^{\text{perpd}} \end{pmatrix}; \text{ and } \tilde{\mathbf{E}} = \begin{pmatrix} \tilde{\mathbf{U}} \\ \tilde{\mathbf{V}}^{\text{perpd}} \\ \tilde{\mathbf{V}}^{\text{diag}} \end{pmatrix}. \end{aligned} \quad (4.57)$$

The dispersion relation can now be formulated by subjecting equation (4.56) to a state-space transformation of the form given in equation (4.14), where

$$\mathbf{A} = \begin{pmatrix} \mathbf{0} & \mathbf{I} \\ \mathbf{Z}_1 & \mathbf{Z}_2 \end{pmatrix}; \mathbf{B} = \begin{pmatrix} -\mathbf{I} & \mathbf{0} \\ \mathbf{0} & \mathbf{Z}_3 \end{pmatrix}; \text{ and } \mathbf{Y} = \begin{pmatrix} \dot{\tilde{\mathbf{E}}} \\ \tilde{\mathbf{E}} \end{pmatrix}, \quad (4.58)$$

implementing a solution of the form $\mathbf{Y} = \tilde{\mathbf{Y}}_\lambda e^{\lambda t}$, and solving the resulting eigenvalue problem of the form given in equation (4.16). Expanding equation (4.16) for this particular case yields a twelfth-order equation in terms of λ , which, upon solving, gives four complex roots appearing as two complex-conjugate pairs and eight real roots.

4.4 Wave-propagation and dissipation analysis of monoatomic phononic crystal and piezoelectric phononic crystals

This section presents the wave-propagation and dissipation characteristics of MPnC and MPPnCs, discussed above, in a graphical comparative format. All the results are shown in a dimensionless-wavevector space ($\boldsymbol{\mu}$ -space) comprised of dimensionless wavevectors with x-components $\mu_x = \kappa_x a_x$ and y-components $\mu_y = \kappa_y a_y$. Table 3.7 details the parameters utilized

in the computation of the dispersion (band structure) and damping-ratio characteristics of the MPnC and MPPnCs.

Table 4.2: Mechanical and dimensionless electrical parameters employed in the monoatomic phononic crystal (MPnC) and monoatomic piezoelectric phononic crystals (MPPnCs).

Parameter	MPnC	MPPnC without an inductor	MPPnC with an inductor	Unit
a_x	1	1	1	m
a_y	1	1	1	m
m_1	0.0170	0.0170	0.0170	Kg
k_1	5×10^3	5×10^3	5×10^3	Nm^{-1}
k_2	5×10^3	5×10^3	5×10^3	Nm^{-1}
k_3	5×10^3	5×10^3	5×10^3	Nm^{-1}
k_4	5×10^3	5×10^3	5×10^3	Nm^{-1}
c_1	0.2180	0.2180	0.2180	Nsm^{-1}
c_2	0.2180	0.2180	0.2180	Nsm^{-1}
c_3	0.2180	0.2180	0.2180	Nsm^{-1}
c_4	0.2180	0.2180	0.2180	Nsm^{-1}
α_1	—	0.1302	0.1302	—
α_2	—	0.1302	0.1302	—
α_3	—	0.1302	0.1302	—
α_4	—	0.1302	0.1302	—
β_1	—	—	0.2353	—
β_2	—	—	0.2353	—
β_3	—	—	0.2353	—
β_4	—	—	0.2353	—
$k_{\text{coeff}_1}^2$	—	0.6250	0.6250	—
$k_{\text{coeff}_2}^2$	—	0.6250	0.6250	—
$k_{\text{coeff}_3}^2$	—	0.6250	0.6250	—
$k_{\text{coeff}_4}^2$	—	0.6250	0.6250	—

The electrical parameters of the shunting mechanism associated with a piezoelectric element (piezoelectric patch), namely, electromechanical coupling, resistance, capacitance, and inductance, are non-dimensionalized and presented in table 4.2, in accordance with the existing literature [87–89], as

$$\alpha_l = \bar{\omega}_l C_{p_l} R_l, \quad (4.59a)$$

$$\beta_l = \bar{\omega}_l^2 C_{p_l} L_l, \quad (4.59b)$$

$$k_{\text{coeff}_l}^2 = \frac{\theta_l^2}{k_l C_{p_l}}, \quad (4.59c)$$

where $l = 1, 2, 3, 4$ is an index corresponding to the parameters of the four piezoelectric elements and the frequencies obtained from the four springs: $\bar{\omega}_1 = \sqrt{\frac{k_1}{m}}$, $\bar{\omega}_2 = \sqrt{\frac{k_2}{m}}$, $\bar{\omega}_3 = \sqrt{\frac{k_3}{m}}$, and $\bar{\omega}_4 = \sqrt{\frac{k_4}{m}}$.

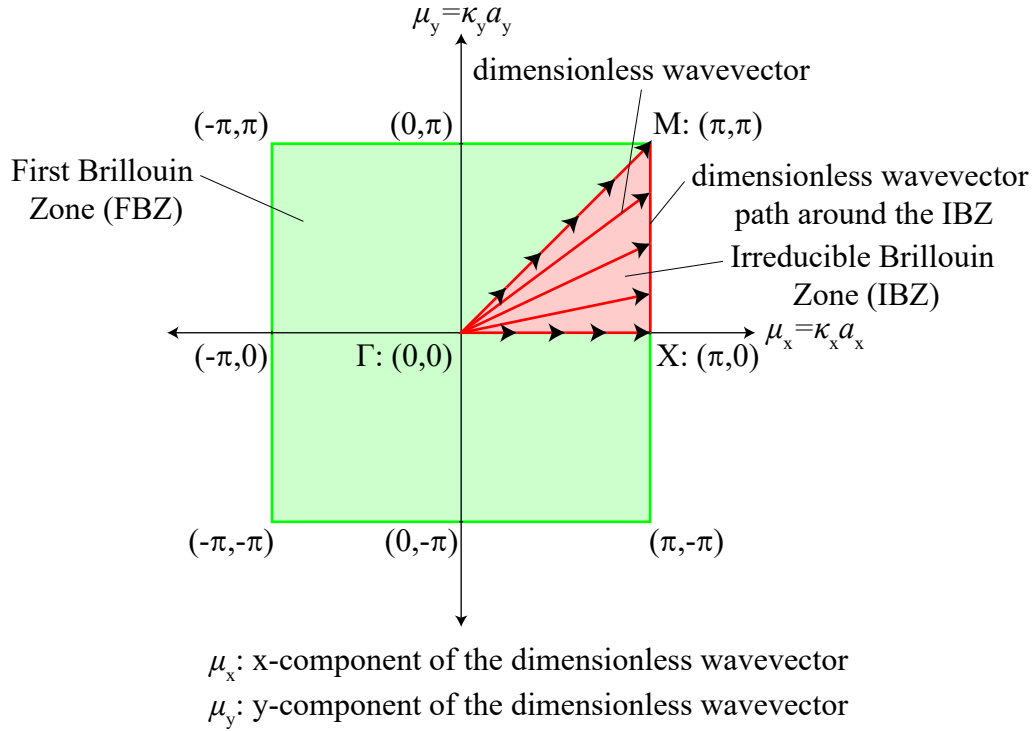


Figure 4.3: Dimensionless-wavevector space (μ -space) including the First Brillouin Zone (FBZ) shown as green-shaded area, Irreducible Brillouin Zone (IBZ) shown as red-shaded area, dimensionless-wavevector path around the IBZ highlighted by the red-contoured right-angle triangle, and dimensionless-wavevectors shown by red lines with black arrows, which point towards the vector direction, for two-dimensional dispersion characteristics.

Figure 4.3 depicts the dimensionless-wavevector space (μ -space) comprising of relevant zones which are used to present two-dimensional wave-propagation and dissipation characteristics. For two-dimensional lattices of the type addressed in this chapter, there exists only one Brillouin zone, the First Brillouin Zone (FBZ) shown as green-shaded area, which is periodic in the x- and y-directions. For the FBZ, $\mu_x = [-\pi, \pi]$, and $\mu_y = [-\pi, \pi]$. The FBZ can be reduced to a zone which is symmetric about the origin and cannot be reduced any further; this zone is referred to as the Irreducible Brillouin Zone (IBZ), which is illustrated as the red-shaded area in figure 4.3. The damped-frequencies (dispersion diagram) and damping ratios for two-dimensional lattices can be easily presented as contour and surface plots in the FBZ, but in order to illustrate them as curves on a plot, the dimensionless-wavevector path

around the IBZ is chosen; as shown in figure 4.3, this path is highlighted by the red-contoured right-angle triangle and consists of μ -points comprising of $\mu_x = \kappa_x a_x$ and $\mu_y = \kappa_y a_y$ values.

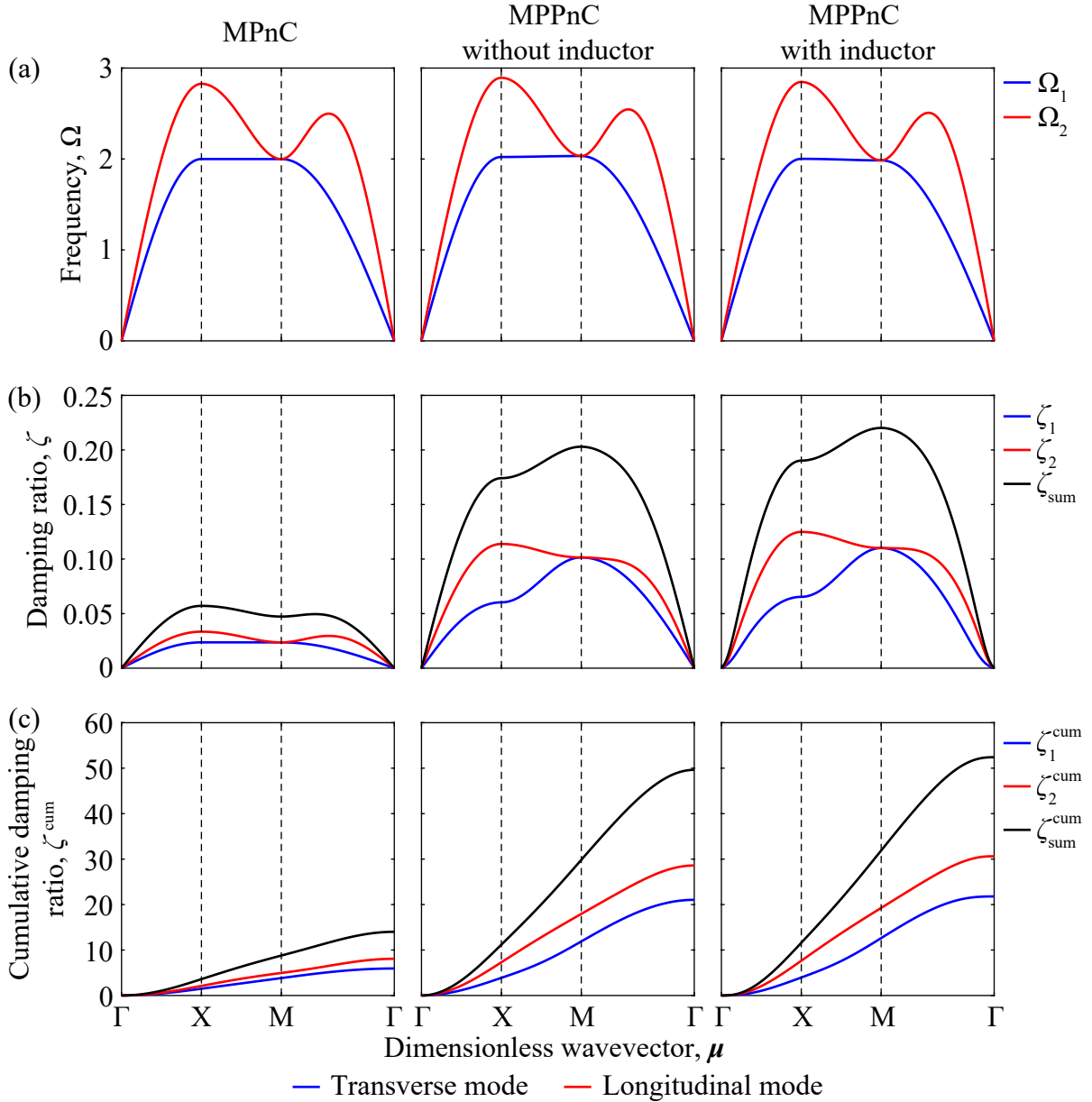


Figure 4.4: (a) Normalized-damped-frequency band structure, (b) damping-ratio diagrams, and (c) cumulative-damping-ratio diagrams for the monoatomic phononic crystal (MPnC) and monoatomic piezoelectric phononic crystals (MPPnCs).

Figure 4.4 illustrates the normalized (non-dimensional) damped frequencies and damping ratios corresponding to the transverse and longitudinal modes associated with the MPnC and MPPnCs along the wavevector path $\Gamma \rightarrow X \rightarrow M \rightarrow \Gamma$. Transverse mode corresponds to unit-cell motion that is along the xy -plane and perpendicular to the direction of wave

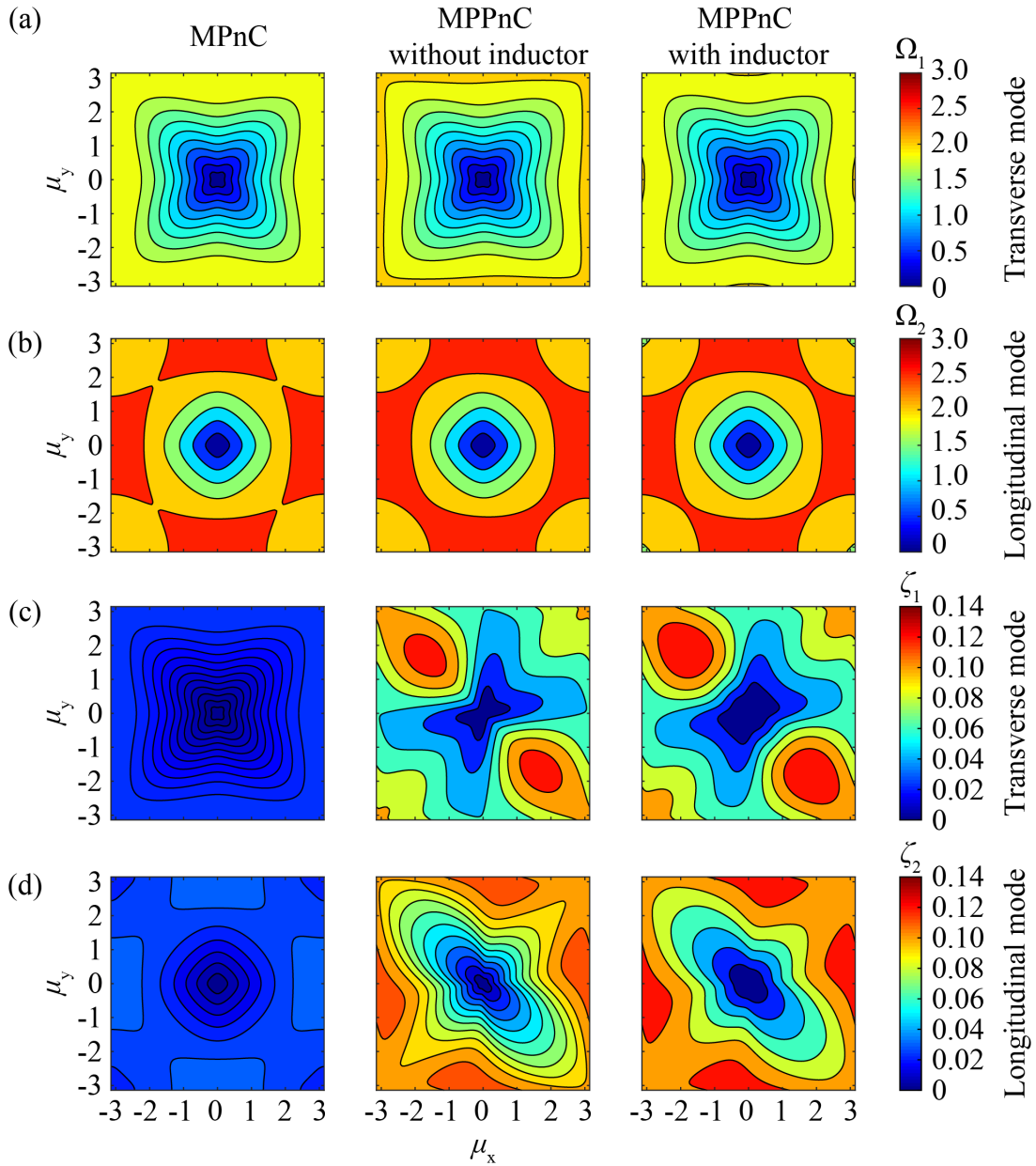
propagation along the xy -plane, and longitudinal mode corresponds to unit-cell motion that is along the xy -plane and collinear to the direction of wave propagation along the xy -plane. For both modes, the unit-cell motion and direction of wave propagation are restricted to the xy -plane. Transverse and longitudinal modes are identified by plotting the eigenvectors, i.e., mode shapes, and observing the direction of motion of the unit-cell mass. A total of 339 points are chosen along the dimensionless-wavevector path to produce the results depicted in figure 4.4. The damped frequencies are normalized with respect to $\bar{\omega}_1$; i.e., the plots depict $\Omega_l = \frac{\omega_{d_l}}{\bar{\omega}_1}$, where $l=1$ (transverse mode), 2 (longitudinal mode). Figure 4.4(a) presents almost similar dispersion band structures for the three periodic media. For dispersion band structures that are approximately similar, figure 4.4(b) contrarily shows a huge disparity between the damping ratios associated with the MPnC and MPPnCs. It is observed that, in comparison to the MPnC, the MPPnCs portray significantly higher levels of dissipation; i.e., significantly higher levels of damping ratios ζ_1 and ζ_2 . For a better comparison, the summation of the two damping ratio curves, ζ_{sum} , is also plotted to show the total dimensionless-wavevector-dependent damping ratio in the IBZ. As the intrinsic quantity that is of paramount interest and the subject of investigation in this work is the dimensionless-wavevector-dependent damping ratio which is the rate of dissipation, the damping-ratio modes are effectively quantified as a single value as done in chapter 3. This is realized, firstly, by cumulatively integrating the damping ratio and, secondly, by obtaining the total value upon complete integration along the dimensionless-wavevector path $\Gamma \rightarrow X \rightarrow M \rightarrow \Gamma$. As two-dimensional wave-propagation and dissipation analysis involves wavevectors (dimensional or dimensionless), the cumulative and complete integration is performed with unit spacing. In figure 4.4(c), the MPPnCs present a considerably higher rate of increase of ζ_l^{cum} ($l=1, 2$, or sum) in comparison to the MPnC.

Table 4.3: Total values of damping ratios associated with the monoatomic phononic crystal (MPnC) and monoatomic piezoelectric phononic crystals (MPPnCs) with grounding.

Parameter	MPnC	MPPnC without an inductor	MPPnC with an inductor	Unit
ζ_1^{tot}	5.9385	21.0378	21.7867	—
ζ_2^{tot}	8.7078	28.5923	30.6229	—
$\zeta_{\text{sum}}^{\text{tot}}$	14.0093	49.6301	52.4096	—

Table 4.3 details the ζ^{tot} values for the three periodic media. The MPPnC with an inductor demonstrates the highest values of ζ_1^{tot} , ζ_2^{tot} , and $\zeta_{\text{sum}}^{\text{tot}}$ as evidenced in table 4.3.

Figures 4.5 and 4.6 illustrate the contour and surface plots, respectively, in the FBZ for the two normalized-damped-frequency and damping-ratio modes associated with the MPnC and MPPnCs. Figures 4.5(c), 4.5(d), 4.6(c), and 4.6(d) show a significant difference in the



$\Omega_{1,2}$: Dimensionless frequency μ_x : x-component of the dimensionless wavevector
 $\zeta_{1,2}$: Damping ratio μ_y : y-component of the dimensionless wavevector

Figure 4.5: Contour plots: (a) Transverse mode of normalized damped frequency, (b) Longitudinal mode of normalized damped frequency, (c) Transverse mode of damping ratio, and (d) Longitudinal mode of damping ratio for the monoatomic phononic crystal (MPnC) and monoatomic piezoelectric phononic crystals (MPPnCs).

damping-ratio modes associated with the MPnC and MPPnCs, which is in agreement with figures 4.4(c) and 4.4(d).

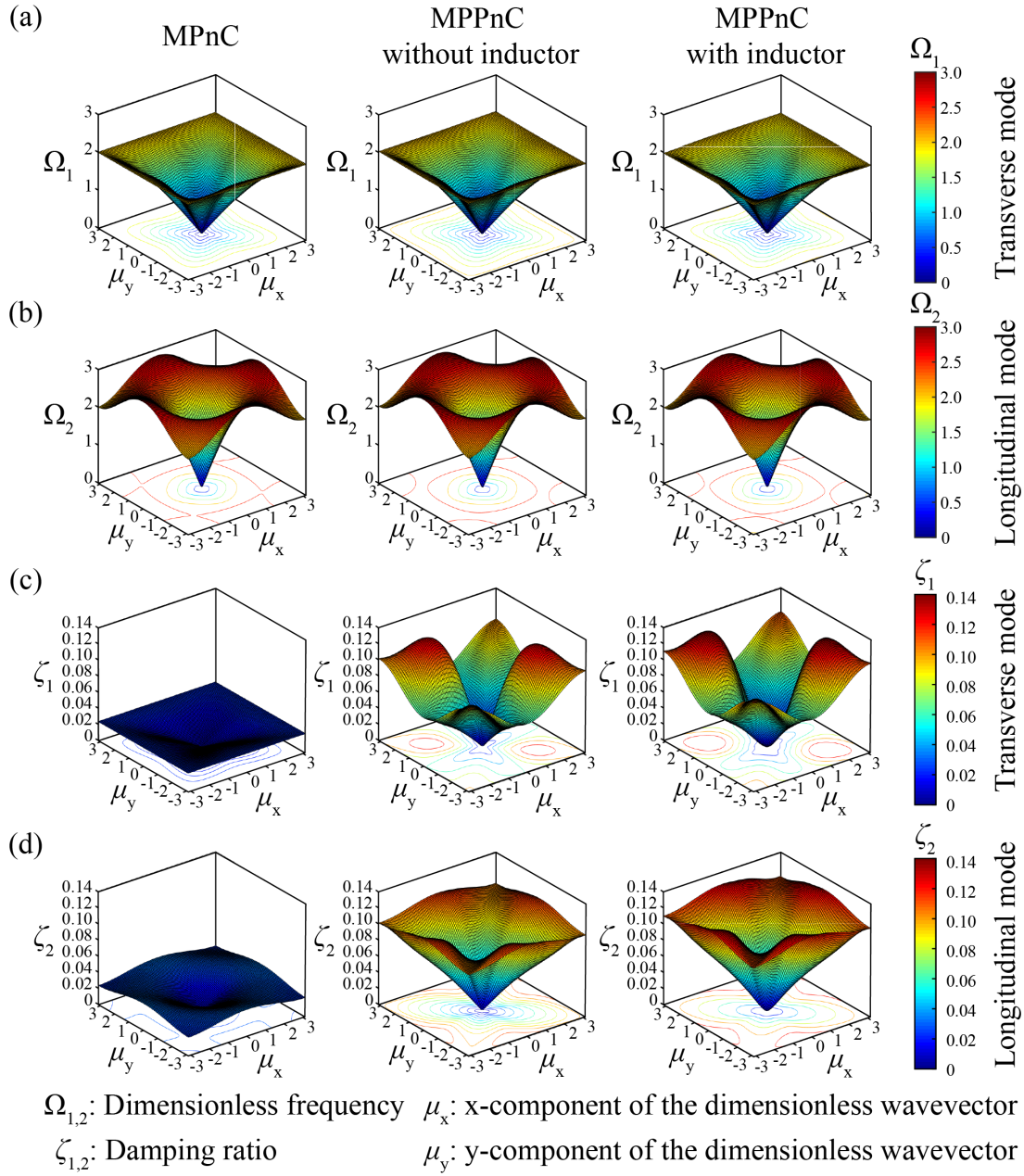


Figure 4.6: Surface plots: (a) Transverse mode of normalized damped frequency, (b) Longitudinal mode of normalized damped frequency, (c) Transverse mode of damping ratio, and (d) Longitudinal mode of damping ratio for the monoatomic phononic crystal (MPnC) and monoatomic piezoelectric phononic crystals (MPPnCs).

4.5 Summary and conclusions

In this chapter, two-dimensional MPnC and MPPnCs with and without inductor are investigated within a Bloch framework for free waves. The governing mechanical equations, for

the MPnC, and electromechanical equations, for the MPPnC, are derived and treated with two-dimensional plane-wave Bloch solution. The resulting Bloch-transformed equation/s is/are cast into a first-order equation via a state-space formulation, and consequently, an eigenvalue problem is established, which is solved in MATLAB to obtain the eigenvalues. From the complex eigenvalue solution, the wavevector-dependent damped frequencies and damping ratios are extracted and presented for the periodic media and piezoelectric media for a quantitative comparison in dimensionless-wavevector space. By performing Bloch analysis of a two-dimensional infinite piezoelectric periodic media, in the absence of forcing and boundary conditions, with shunted energy harvesters, the piezoelectric periodic media can be treated as a material rather than a finite structure; i.e., the wave-propagation and dissipation characteristics obtained are *intrinsic* in nature, which allows for effective analysis, comparative study, and physical-modelling decisions at the most fundamental level. This chapter, essentially, is an extension of one-dimensional Bloch analysis and serves the purpose of establishing the fact that any quantitative or qualitative study involving the utilization of one-dimensional results, of the type discussed in chapter 3, can also be replicated for two-dimensional cases.

Chapter 5

Brillouin-zone characterization of piezoelectric-material intrinsic energy-harvesting availability

5.1 Introduction

-The merger of the research-intensive fields of artificially structured materials such as phononic crystals (PnCs), locally resonant metamaterials (LRMs), and inertially amplified locally resonant metamaterials (IALRMs) and energy harvesting—periodic-media-based energy harvesting—has recently emerged as a promising research area within the broader domain of dynamics of materials. Incorporation of piezoelectricity into phononic crystals for active tuning or energy harvesting has been the focus of numerous studies [57–65, 123, 124]. Similarly, elastic metamaterials have been linked with energy harvesting as surveyed in the review by Chen *et al* [68]. An attractive feature in this context is the ability to use piezoelectricity to actively tune the local resonance properties for attenuation [70], waveguiding [71], or energy harvesting [69]. Simultaneous vibration suppression and energy harvesting may also be realized, as demonstrated by Hu *et al* [73, 74]. The theoretical and experimental studies of harnessing energy and generating power efficiently from artificial structures based on phononic crystals and acoustic/elastic metamaterials continue to receive significant attention and carry an immense amount of scope and future potential.

While some of the research mentioned above has examined the dispersion characteristics considering a combination of elastic and piezoelectric properties [1, 2, 4, 19], when it comes to analysis of the actual energy-harvesting capacity/availability, this has been done at the *structural* level where the focus is on the structural dynamics of the systems presented. In

this chapter, a new formal approach is presented for the characterization of energy-harvesting availability that is fundamentally at the *material* level rather than the structural or device level. Monoatomic and diatomic PnCs with integrated piezoelectric elements are considered and modelled as damped media within a Bloch wave-propagation analysis framework [46, 47]. The wavenumber-dependent damping ratio—which is a rigorous measure of dissipation capacity—is obtained within the irreducible Brillouin zone (IBZ) and compared directly with that of the same PnC without the piezoelectric elements. The dissipation curves for the latter, the non-piezoelectric medium, give a direct indication of the “raw” dissipation which represents unexploited/lost energy. On the other hand, the difference in the dissipation curves between the two systems—the PnC with piezoelectric elements versus the PnC without piezoelectric elements—provides a formal intrinsic wavenumber-dependent representation of the amount of energy available for harvesting. This Brillouin-zone-based approach for energy-harvesting-availability characterization directly follows the characterization framework for the concept of “metadamping” [79], where the wavenumber-dependent dissipation of two statically equivalent waveguides are directly compared to produce a formal measure of either enhanced [79, 125] or reduced [125] dissipation (or damping capacity).

The layout of the chapter is divided as follows. In section 5.2, an example of a piezoelectric phononic crystal modelled from a materials perspective is presented conceptually, considering both monoatomic and diatomic configurations. In section 5.3, the application of Bloch’s theorem to a monoatomic PnC and a diatomic PnC is presented. The application of Bloch’s theorem to piezoelectric PnCs (PPnCs) is then followed in section 5.4. Wave propagation and dissipation characteristics and the calculation of the representative energy-harvesting availability is detailed in section 5.5. A parametric study is provided in section 5.6, followed by concluding remarks in section 5.7.

5.2 Examples of piezoelectric phononic crystals modelled as *materials* with intrinsic properties

In this section, physical conceptualizations of two configurations of piezoelectric PnCs featuring monoatomic and diatomic periodicities are introduced.

Figure 5.1 depicts concept designs for monoatomic (figure 5.1(a)) and diatomic (figure 5.1(b)) PnC periodic media and the corresponding unit cells (figures 5.1(c) and 5.1(d)). These configurations are selected for their suitability for future experimental realization; however, they serve only as example configurations. The monoatomic piezoelectric phononic crystal (MPPnC) configuration comprises of a periodic arrangement of equally sized masses,

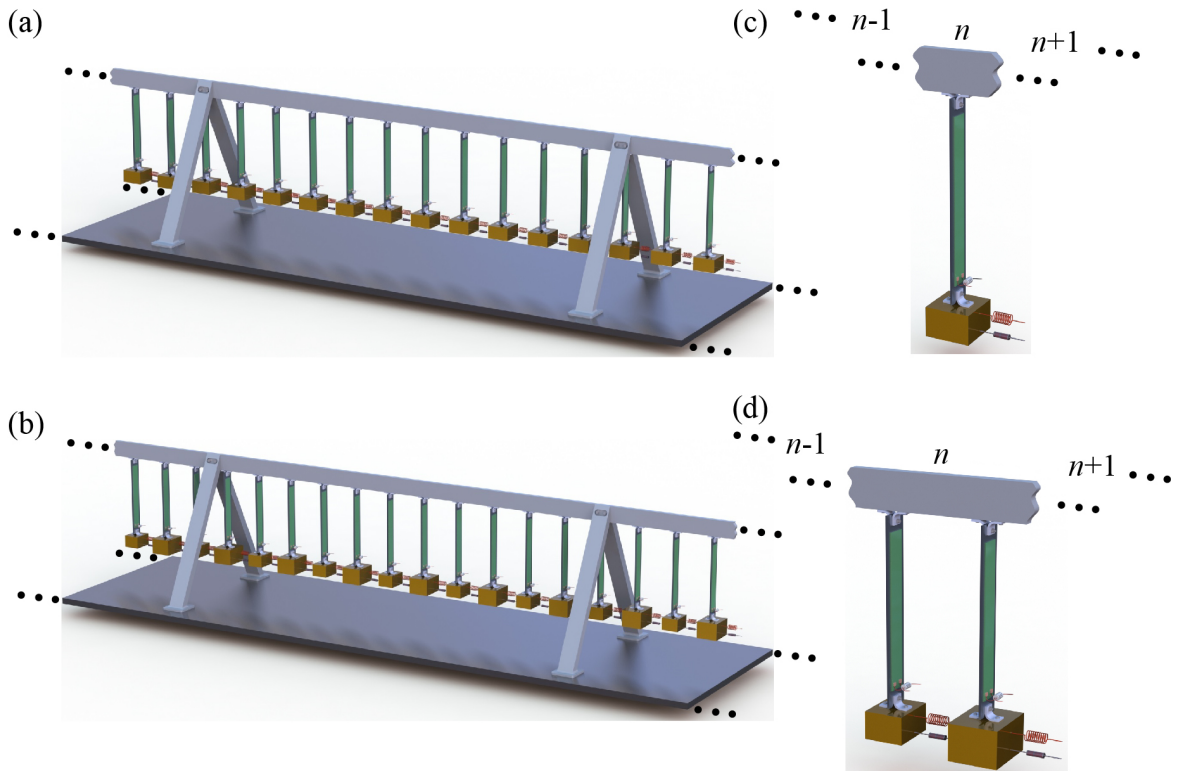


Figure 5.1: (a) Physical conceptualization/configuration of a periodic chain of a monoatomic piezoelectric phononic crystal (MPPnC) with piezoelectric patches and (b) the corresponding monoatomic unit cell. (c) Physical conceptualization/configuration of a periodic chain of a diatomic piezoelectric phononic crystal (DPPnC) with piezoelectric patches and (d) the corresponding diatomic unit cell. Both configurations represent an infinite medium exhibiting intrinsic properties.

each suspended by a longitudinal bar. Each of the bars is equipped with a unimorph piezoelectric patch consisting of a shunt circuit that is either purely resistive or equipped with an inductor; this patch performs the energy-harvesting function. The piezoelectric patch shown in figure 1 can use polyvinylidene fluoride (PVDF) films, which are known to have a high d_{31} coefficient [1]. Each mass has one degree of freedom; i.e., motion of the masses is restricted only to the x -direction. The masses are interconnected by springs and viscous damping elements (dashpots). The diatomic piezoelectric phononic crystal (DPPnC) configuration comprises of a periodic arrangement of alternating small and large masses each also suspended by a longitudinal bar. The rest of the set-up is similar to the monoatomic configuration. In analysing each case, a generalized form of Bloch's theorem is applied on a single representative unit cell to accommodate complex frequencies [46, 47] and then obtain the wavenumber-dependent dispersion and damping-ratio diagrams for a specific set of parameters. For simplicity, lumped-parameter mass-spring-dashpot models have been

utilized in this investigation; see section 5.3 for details on the models and the application of Bloch's theorem.

5.3 Brief overview of phononic crystal models

5.3.1 Monoatomic phononic crystal

The grounded MPnC chain without energy harvesters (piezoelectric patches) and the corresponding unit cell are represented as lumped-model parameters by the schematics shown in figures 5.2(a) and 5.2(b), respectively. This case is representative of a scenario where the PnC chain is attached to grounding mechanisms, which could be longitudinal bars, comprising of springs and viscous dashpots; i.e., each unit cell is attached to the grounding mechanism.

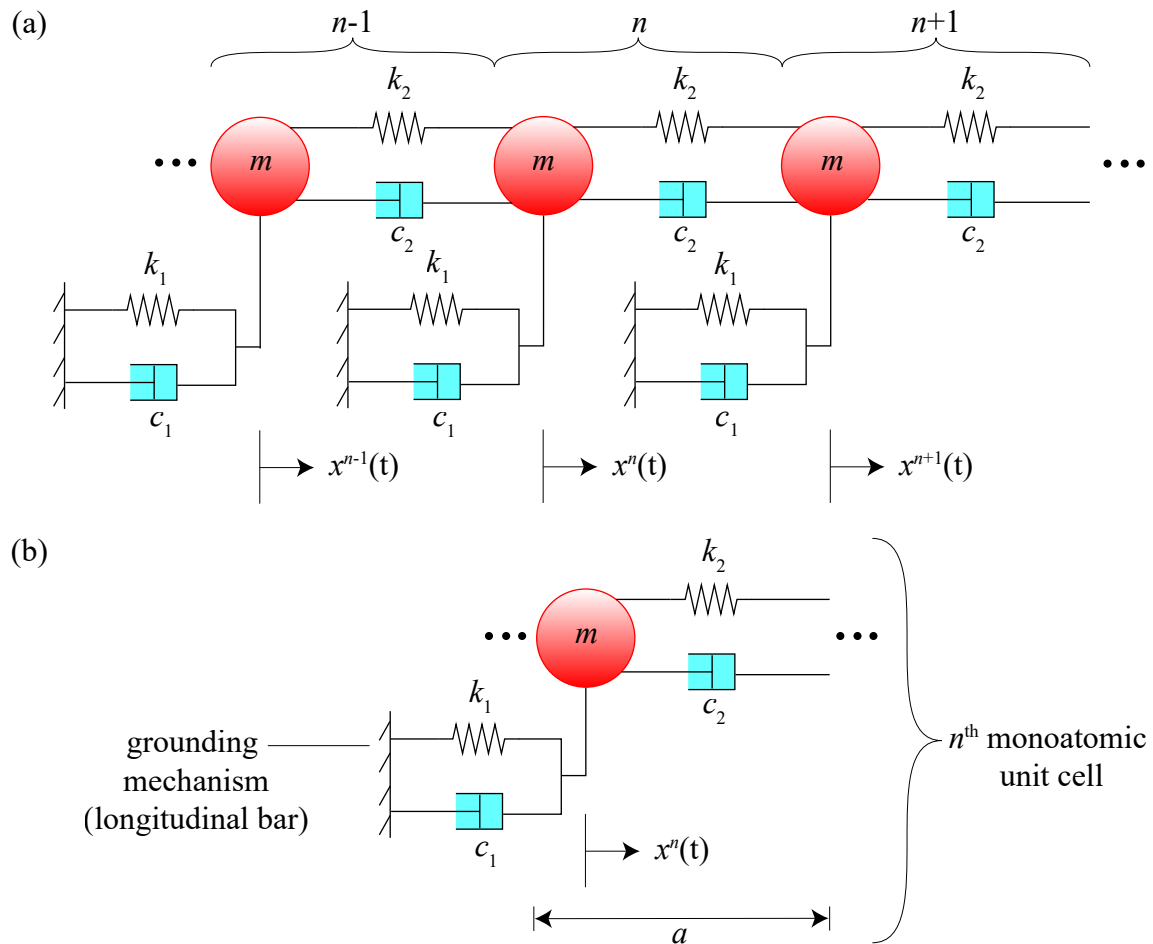


Figure 5.2: Schematic of (a) a monoatomic phononic-crystal (MPnC) chain with grounding and (b) the associated unit cell.

In figure 5.2(a), n is used to identify and refer to the central unit cell under consideration and can be any non-zero positive integer in a finite lattice; $(n + 1)$ and $(n - 1)$ are used to identify and refer to the unit cells to the right and left of the central (n^{th}) unit cell, respectively; m denotes the mass; k_{\dots} and c_{\dots} denote the stiffness coefficients of the linear springs and the damping coefficients of the viscous dashpots, respectively; $x^n(t)$ and $x^{n\pm 1}(t)$ are the displacements of the masses, with respect to time t , in the n^{th} , $(n + 1)^{\text{th}}$, and $(n - 1)^{\text{th}}$ unit cells, respectively; and a is the length of a unit-cell or lattice spacing.

The governing equation of motion for mass m in the n^{th} unit cell is written as

$$m\ddot{x}^n + c_2(2\dot{x}^n - \dot{x}^{n-1} - \dot{x}^{n+1}) + c_1\dot{x}^n + k_2(2x^n - x^{n-1} - x^{n+1}) + k_1x^n = 0, \quad (5.1)$$

where the number of overhead dots indicates the order of derivative with respect to time.

A plane-wave Bloch solution [119] of the form

$$x^{n+g}(r, \kappa; t) = \tilde{x}(t)e^{i\kappa(n+g)a} \quad (5.2)$$

is imposed, where x is the displacement; $g \in [-\infty, \infty]$ is an integer used to locate and refer to any unit cell relative to the central unit cell under consideration, i.e., the n^{th} unit cell shown in figure 5.2(b); r is the one-dimensional position vector of the n^{th} unit cell given by $r = na$; κ is the wavenumber; \tilde{x} is the displacement amplitude in the wavenumber domain; and $i = \sqrt{-1}$ is the imaginary unit. For the central unit cell under consideration, $g = 0$ (n^{th} unit cell), and for the unit cells towards the left and right of the central unit cell, $g = -1$, and $g = +1$, respectively; i.e., they are the $(n - 1)^{\text{th}}$ and $(n + 1)^{\text{th}}$ unit cells. Substituting equation (5.2) in equation (5.1) yields a homogeneous equation for the displacement amplitude, \tilde{x} , which can be written as

$$m\ddot{\tilde{x}} + (c_2(2 - e^{-i\kappa a} - e^{i\kappa a}) + c_1)\dot{\tilde{x}} + (k_2(2 - e^{-i\kappa a} - e^{i\kappa a}) + k_1)\tilde{x} = 0. \quad (5.3)$$

Equation (5.3) can now be converted into a first order problem through a state-space transformation [119–121] of the form

$$\mathbf{A}\dot{\mathbf{Y}} + \mathbf{B}\mathbf{Y} = \mathbf{0}, \quad (5.4)$$

where the system matrices and the state vector are

$$\mathbf{A} = \begin{pmatrix} 0 & 1 \\ m & c_2(2 - e^{-i\kappa a} - e^{i\kappa a}) + c_1 \end{pmatrix};$$

$$\mathbf{B} = \begin{pmatrix} -1 & 0 \\ 0 & k_2(2 - e^{-i\kappa a} - e^{i\kappa a}) + k_1 \end{pmatrix}; \text{ and } \mathbf{Y} = \begin{pmatrix} \dot{\tilde{x}} \\ \tilde{x} \end{pmatrix}. \quad (5.5)$$

For equation (5.4), a solution of the form $\mathbf{Y} = \tilde{\mathbf{Y}}_\lambda e^{\lambda t}$ is assumed, where $\tilde{\mathbf{Y}}_\lambda$ is a complex-amplitude state-space vector corresponding to eigenvalue λ . The dispersion relation and, consequently, the wave-propagation and dissipation characteristics can now be obtained by substituting the solution in equation (5.4) and solving the resulting eigenvalue problem given by

$$|\mathbf{A}^{-1}\mathbf{B} + \lambda \mathbf{I}| = 0. \quad (5.6)$$

Expanding equation (5.6) for this particular case yields a second-order equation in terms of λ (shown in equation (5.12)), which, upon solving, gives two complex roots appearing as a complex-conjugate pair. The complex solution for the eigenvalue problem at a given value of κ can be expressed as [29]

$$\lambda_l(\kappa) = -\zeta_l(\kappa)\omega_{r_l}(\kappa) \pm i\omega_{d_l}(\kappa) = -\zeta_l(\kappa)\omega_{r_l}(\kappa) \pm i\omega_{r_l}(\kappa)\sqrt{1 - \zeta_l(\kappa)^2}, \quad (5.7)$$

where the subscript l identifies the complex-conjugate pairs and, consequently, the mode or branch number; for all monoatomic models, $l=1$ as they give rise to only one complex-conjugate pair. In equation (5.7), the wavenumber-dependent resonant frequency ω_{r_l} defined as

$$\omega_{r_l}(\kappa) = \text{Abs}[\lambda_l(\kappa)], \quad (5.8)$$

the wavenumber-dependent damped frequency ω_{d_l} defined as

$$\omega_{d_l}(\kappa) = \text{Im}[\lambda_l(\kappa)], \quad (5.9)$$

and the wavenumber-dependent damping ratio $\zeta_l(\kappa)$ defined as

$$\zeta_l(\kappa) = -\frac{\text{Re}[\lambda_l(\kappa)]}{\text{Abs}[\lambda_l(\kappa)]} \quad (5.10)$$

can be extracted. The phase and group velocities corresponding to a particular mode or branch can also be obtained by using the definitions

$$C_{\text{ph}_l} = \frac{\omega_{d_l}}{\kappa} \text{ and } C_{\text{g}_l} = \frac{\partial \omega_{d_l}}{\partial \kappa}, \quad (5.11)$$

respectively.

The second-order equation for the MPnC model obtained in terms of λ by solving equation (5.6) can be non-dimensionalized by some parametric manipulation. Solving equation (5.6) and using the identities $e^{i\kappa a} + e^{-i\kappa a} = 2 \cos \kappa a$ and $1 - \cos \kappa a = 2 \sin^2 \frac{\kappa a}{2}$ yields

$$\lambda^2 + \left(\frac{4c_2 \sin^2 \left(\frac{\kappa a}{2} \right) + c_1}{m} \right) \lambda + \frac{4k_2 \sin^2 \left(\frac{\kappa a}{2} \right) + k_1}{m} = 0. \quad (5.12)$$

The lumped-model parameters of the MPnC are used to facilitate the non-dimensionalization, and the following definitions are introduced:

$$\begin{aligned} k_1 &= k, \\ k_2 &= \gamma_1 k, \\ c_1 &= c, \\ c_2 &= \gamma_2 c, \\ \lambda &= i\omega. \end{aligned} \quad (5.13)$$

In the definition $\lambda = i\omega$, the branch index l has been dropped for brevity, and ω is introduced to denote a complex frequency as the general solution of a characteristic equation derived from the state-space eigenvalue problem of the form specified in equation (5.6). The following quantities are also defined to aid the non-dimensionalization process:

$$\Omega = \frac{\omega}{\bar{\omega}}, \quad (5.14a)$$

$$\bar{\omega} = \sqrt{\frac{k}{m}}, \quad (5.14b)$$

$$\text{and } \bar{\zeta} = \frac{c}{2m\bar{\omega}}. \quad (5.14c)$$

In the aforementioned definitions, Ω denotes non-dimensional damped frequency; $\bar{\omega}$ is a characteristic frequency defined in terms of k and m ; and $\bar{\zeta}$ is a damping factor. Substituting

equation (5.13) in equation (5.12) gives

$$(i\omega)^2 + \frac{c}{m}4\gamma_2 \sin^2\left(\frac{\kappa a}{2}\right) (i\omega) + \frac{k}{m}4\gamma_1 \sin^2\left(\frac{\kappa a}{2}\right) = 0. \quad (5.15)$$

Dividing equation (5.15) by $\bar{\omega}^2$ and using equation (5.14) produces

$$(i\Omega)^2 + a_1(i\Omega) + a_2 = 0. \quad (5.16)$$

Equation (5.16) has two complex roots appearing as a complex conjugate pair. The non-dimensional damped frequency and the damping ratio, same as obtained using equation (5.10), can be obtained by using the definitions $\Omega_l = \text{Im}[(i\Omega)_l(\kappa)]$ and $\zeta_l(\kappa) = -\frac{\text{Re}[(i\Omega)_l(\kappa)]}{\text{Abs}[(i\Omega)_l(\kappa)]}$, respectively. The coefficients of non-dimensional equation (5.16) are given in appendix A.1. In section 5.5, the main results are presented while defining all the parameters in their dimensional form in the MATLAB code written to compute the roots/eigenvalues; however, the non-dimensional version provides a more general presentation of the characteristic equation. This interchangeable approach of use of either dimensional or non-dimensional notation will be used where appropriate in this chapter.

5.3.2 Diatomic phononic crystal

The grounded DPnC chain without energy harvesters (piezoelectric patches) and the corresponding unit cell are represented as lumped-model parameters using the schematics shown in figures 5.3(a) and 5.3(b), respectively.

The governing equations of motion for masses m_1 and m_2 in the n^{th} unit cell can be written as

$$m_1\ddot{x}_1^n + (c_1 + c_2 + c_4)\dot{x}_1^n - c_4\dot{x}_2^{n-1} - c_2\dot{x}_2^n + (k_1 + k_2 + k_4)x_1^n - k_4x_2^{n-1} - k_2x_2^n = 0, \quad (5.17)$$

$$m_2\ddot{x}_2^n + (c_2 + c_3 + c_4)\dot{x}_2^n - c_4\dot{x}_1^{n+1} - c_2\dot{x}_1^n + (k_2 + k_3 + k_4)x_2^n - k_4x_1^{n+1} - k_2x_1^n = 0. \quad (5.18)$$

The plane-wave Bloch solution for the displacements in the diatomic case can be written with a slight modification to the solution in the monoatomic case as

$$x_l^{n+g}(r, \kappa; t) = \tilde{x}_l(t)e^{i\kappa(n+g)a}, \quad (5.19)$$

where $l = 1, 2$ is an index corresponding to the two masses in a unit cell. Substituting equation (5.19) in equations (5.17) and (5.18) yields the following Bloch-transformed homogeneous

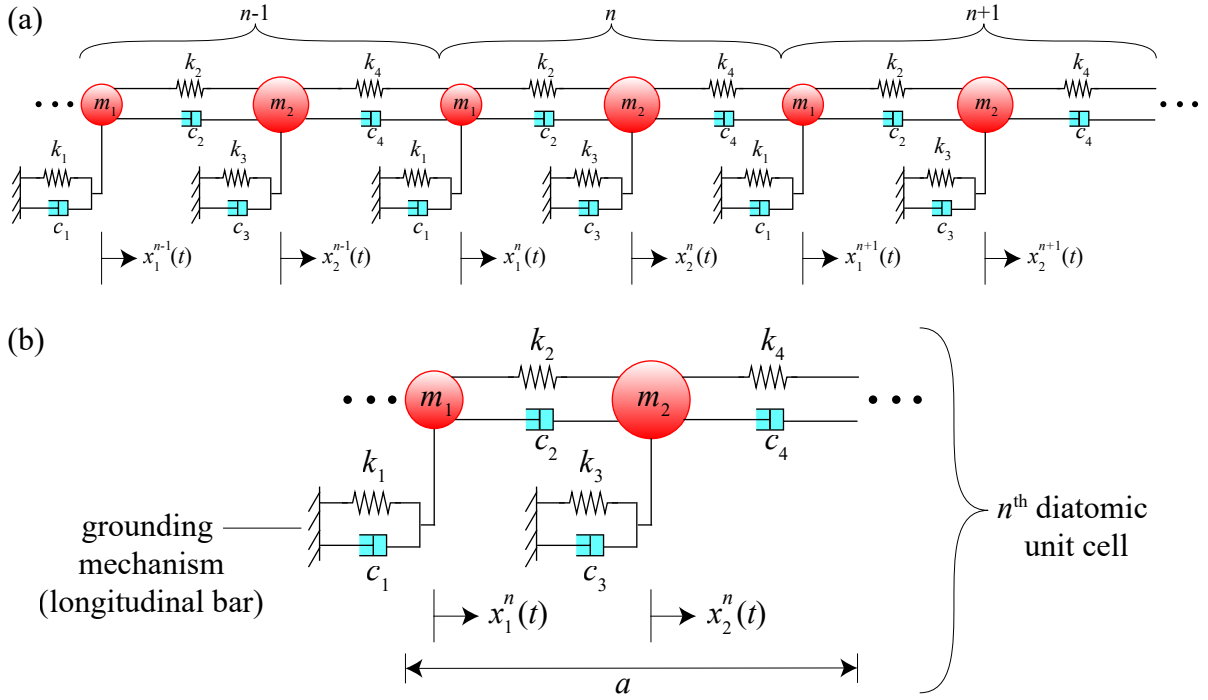


Figure 5.3: Schematic of (a) a diatomic phononic-crystal (DPnC) chain with grounding and (b) the associated unit cell.

equations for the displacement amplitudes \tilde{x}_1 and \tilde{x}_2 :

$$m_1 \ddot{\tilde{x}}_1 + (c_1 + c_2 + c_4) \dot{\tilde{x}}_1 + (-c_2 - c_4 e^{-i\kappa a}) \dot{\tilde{x}}_2 + (k_1 + k_2 + k_4) \tilde{x}_1 + (-k_2 - k_4 e^{-i\kappa a}) \tilde{x}_2 = 0, \quad (5.20)$$

$$m_2 \ddot{\tilde{x}}_2 + (c_2 + c_3 + c_4) \dot{\tilde{x}}_2 + (-c_2 - c_4 e^{i\kappa a}) \dot{\tilde{x}}_1 + (k_2 + k_3 + k_4) \tilde{x}_2 + (-k_2 - k_4 e^{i\kappa a}) \tilde{x}_1 = 0. \quad (5.21)$$

Equations (5.20) and (5.21) can be compacted into a matrix form as

$$\mathbf{M} \ddot{\tilde{\mathbf{X}}} + \mathbf{C}(\kappa) \dot{\tilde{\mathbf{X}}} + \mathbf{K}(\kappa) \tilde{\mathbf{X}} = \mathbf{0}, \quad (5.22)$$

where

$$\tilde{\mathbf{X}} = \begin{pmatrix} \tilde{x}_1 \\ \tilde{x}_2 \end{pmatrix}; \quad \mathbf{M} = \begin{pmatrix} m_1 & 0 \\ 0 & m_2 \end{pmatrix}; \quad \mathbf{C}(\kappa) = \begin{pmatrix} c_1 + c_2 + c_4 & -c_2 - c_4 e^{-i\kappa a} \\ -c_2 - c_4 e^{i\kappa a} & c_2 + c_3 + c_4 \end{pmatrix};$$

$$\text{and } \mathbf{K}(\kappa) = \begin{pmatrix} k_1 + k_2 + k_4 & -k_2 - k_4 e^{-i\kappa a} \\ -k_2 - k_4 e^{i\kappa a} & k_2 + k_3 + k_4 \end{pmatrix}. \quad (5.23)$$

The dispersion relation can now be formulated by subjecting equation (5.22) to a state-space transformation of the form given in equation (5.4), where

$$\mathbf{A} = \begin{pmatrix} \mathbf{0} & \mathbf{I} \\ \mathbf{M} & \mathbf{C}(\kappa) \end{pmatrix}; \mathbf{B} = \begin{pmatrix} -\mathbf{I} & \mathbf{0} \\ \mathbf{0} & \mathbf{K}(\kappa) \end{pmatrix}; \text{ and } \mathbf{Y} = \begin{pmatrix} \dot{\tilde{\mathbf{X}}} \\ \tilde{\mathbf{X}} \end{pmatrix}. \quad (5.24)$$

For equation (5.4) corresponding to this case, a solution of the form $\mathbf{Y} = \tilde{\mathbf{Y}}_\lambda e^{\lambda t}$ is assumed, where $\tilde{\mathbf{Y}}_\lambda$ is a complex-amplitude state-space vector corresponding to eigenvalue λ . The dispersion relation and, consequently, the wave-propagation and dissipation characteristics can now be obtained by employing the solution in equation (5.4) for this case and solving the resulting eigenvalue problem of the form given in equation (5.6). Expanding equation (5.6) for this particular case yields a fourth-order equation in terms of λ , which, upon solving, gives four complex roots appearing as two complex-conjugate pairs. Given that the unit cell is diatomic, a physical root corresponding to the acoustic branch ($l = 1$), which is the lower/first branch, and a physical root corresponding to the optical branch ($l = 2$), which is the higher/second branch, is obtained using equation (5.7).

In order to non-dimensionalize the diatomic model's fourth-order equation, in terms of λ , in a manner similar to the monoatomic case, m_1 and the lumped-model parameters representing the longitudinal bar attached to it are utilized, and the following definitions are introduced:

$$\begin{aligned} m_1 &= m, \\ m_2 &= \gamma_1 m, \\ k_1 &= k, \\ k_2 &= \gamma_2 k, \\ k_3 &= \gamma_3 k, \\ k_4 &= \gamma_4 k, \\ c_1 &= c, \\ c_2 &= \gamma_5 c, \\ c_3 &= \gamma_6 c, \\ c_4 &= \gamma_7 c, \\ \lambda &= i\omega. \end{aligned} \quad (5.25)$$

Substituting equation (5.25), dividing the resulting equation by $\bar{\omega}^4$, and using equation (5.14) yields the characteristic equation

$$(i\Omega)^4 + a_1(i\Omega)^3 + a_2(i\Omega)^2 + a_3(i\Omega) + a_4 = 0. \quad (5.26)$$

Equation (5.26) has four complex roots appearing as two complex conjugate pairs. The coefficients of the non-dimensional equation (5.26) can be found in appendix A.2.

5.4 Piezoelectric phononic crystals

In this section, purely resistive and inductor-equipped MPPnCs and DPPnCs are introduced and subjected to Bloch analysis to treat the displacement and voltage fields. The piezoelectric elements (patches) are attached on the grounding mechanisms, which are modelled as damped oscillators.

5.4.1 Monoatomic piezoelectric phononic crystals

This section expands on the MPPnC configurations.

Shunt circuit without an inductor

Figure 5.4 presents the schematics of an MPPnC chain under free vibration comprising of energy harvesters with shunt circuits that are purely resistive and the associated unit cell as lumped-parameter models.

In figure 5.4, $v^n(t)$ and $v^{n\pm 1}(t)$ are the voltages, with respect to time t , generated by the shunted piezoelectric elements, and R and θ are the resistance and electromechanical coupling of the shunt circuits, respectively.

The coupled governing electromechanical equations [87] pertaining to the n^{th} unit cell under free vibration and consisting of a piezoelectric element with a purely resistive shunt circuit are written as

$$m\ddot{x}^n + c_2(2\dot{x}^n - \dot{x}^{n-1} - \dot{x}^{n+1}) + c_1\dot{x}^n + k_2(2x^n - x^{n-1} - x^{n+1}) + k_1x^n - \theta v^n = 0, \quad (5.27)$$

$$\theta\dot{x}^n + C_p\dot{v}^n + \frac{1}{R}v^n = 0, \quad (5.28)$$

where C_p is the capacitance of the shunt circuit.

Analogous to the displacement (equation (5.2)), the voltage generated in a periodic monoatomic unit cell can be mathematically treated with a plane-wave solution given by a

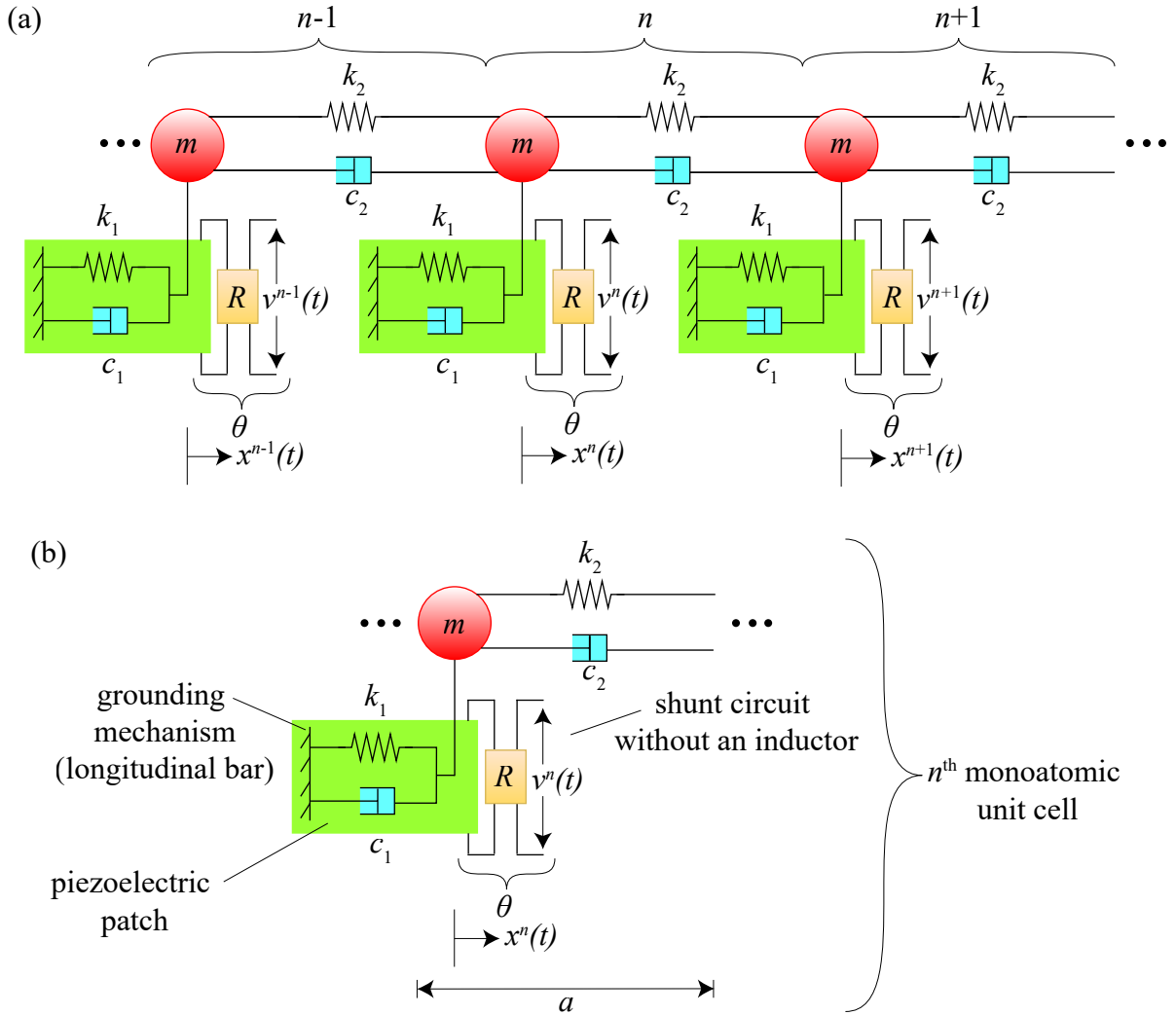


Figure 5.4: Schematic of (a) a monoatomic piezoelectric phononic-crystal (MPPnC) chain comprising of energy harvesters with shunt circuits that are purely resistive and (b) the associated unit cell.

generalized Bloch's theorem, which can be written as

$$v^{n+g}(r, \kappa; t) = \tilde{v}(t)e^{i\kappa(n+g)a}, \quad (5.29)$$

where \tilde{v} is the voltage amplitude in the wavenumber domain. Substituting equations (5.2) and (5.29) in equations (5.27) and (5.28) yields the following Bloch-transformed homogeneous

equations for the displacement and voltage amplitudes \tilde{x} and \tilde{v} , respectively:

$$m\ddot{\tilde{x}} + (c_2(2 - e^{-i\kappa a} - e^{i\kappa a}) + c_1)\dot{\tilde{x}} + (k_2(2 - e^{-i\kappa a} - e^{i\kappa a}) + k_1)\tilde{x} - \theta\tilde{v} = 0, \quad (5.30)$$

$$\theta\dot{\tilde{x}} + C_p\dot{\tilde{v}} + \frac{1}{R}\tilde{v} = 0. \quad (5.31)$$

Converting equations (5.30) and (5.31) to a first-order equation via a state-space transformation results in equation (5.4), for which the system matrices and the state vector are

$$\mathbf{A} = \begin{pmatrix} 0 & 1 & 0 \\ m & c_1 + c_2(2 - e^{i\kappa a} - e^{-i\kappa a}) & 0 \\ 0 & \theta & C_p \end{pmatrix};$$

$$\mathbf{B} = \begin{pmatrix} -1 & 0 & 0 \\ 0 & k_1 + k_2(2 - e^{i\kappa a} - e^{-i\kappa a}) & -\theta \\ 0 & 0 & \frac{1}{R} \end{pmatrix}; \text{ and } \hat{\mathbf{Y}} = \begin{pmatrix} \dot{\tilde{x}} \\ \tilde{x} \\ \tilde{v} \end{pmatrix}. \quad (5.32)$$

Similar to the MPnC model, the damped-frequency and damping-ratio band structures are obtained by applying a solution of the form $\mathbf{Y} = \tilde{\mathbf{Y}}_\lambda e^{\lambda t}$ and solving the associated eigenvalue problem of the form given in equation (5.6). From equation (5.6) for the current MPPnC model, a third-order equation in terms of λ is obtained, which has a real root and two complex roots appearing as a complex conjugate pair; hence, this particular case exhibits only one branch.

In order to non-dimensionalize the present MPPnC model's third-order equation in terms of λ , the lumped-model parameters of the longitudinal bar are chosen in the manner described in equation (5.13). The following non-dimensional electrical parameters, incorporating and simultaneously non-dimensionalizing the electrical parameters of the shunt circuit, are also introduced for the purpose of non-dimensionalization:

$$\alpha = \bar{\omega}C_pR, \quad (5.33a)$$

$$k_{\text{coeff}}^2 = \frac{\theta^2}{m\bar{\omega}^2C_p} = \frac{\theta^2}{kC_p}. \quad (5.33b)$$

In equation (5.33), α can be referred to as the non-dimensional resistor constant, and k_{coeff}^2 can be referred to as the electromechanical coupling coefficient. The non-dimensional resistor constant, α , is also referred to as dimensionless time constant in some literature [87]. Substituting equation (5.13) in the MPPnC model's third-order equation in terms of λ , dividing the resulting equation by $\bar{\omega}^3$, and using equations (5.14) and (5.33) yields the

characteristic equation

$$(i\Omega)^3 + a_1(i\Omega)^2 + a_2(i\Omega) + a_3 = 0. \quad (5.34)$$

Equation (5.34) has a real root and two complex roots appearing as a complex conjugate pair. The coefficients of the non-dimensional equation (5.34) can be found in appendix A.3.

Shunt circuit with an inductor

Figure 5.5 presents the schematics of an MPPnC chain under free vibration comprising of energy harvesters with shunt circuits that are equipped with an inductor and the associated unit cell as lumped-parameter models. In figure 5.5, L denotes the inductance of the shunt circuit.

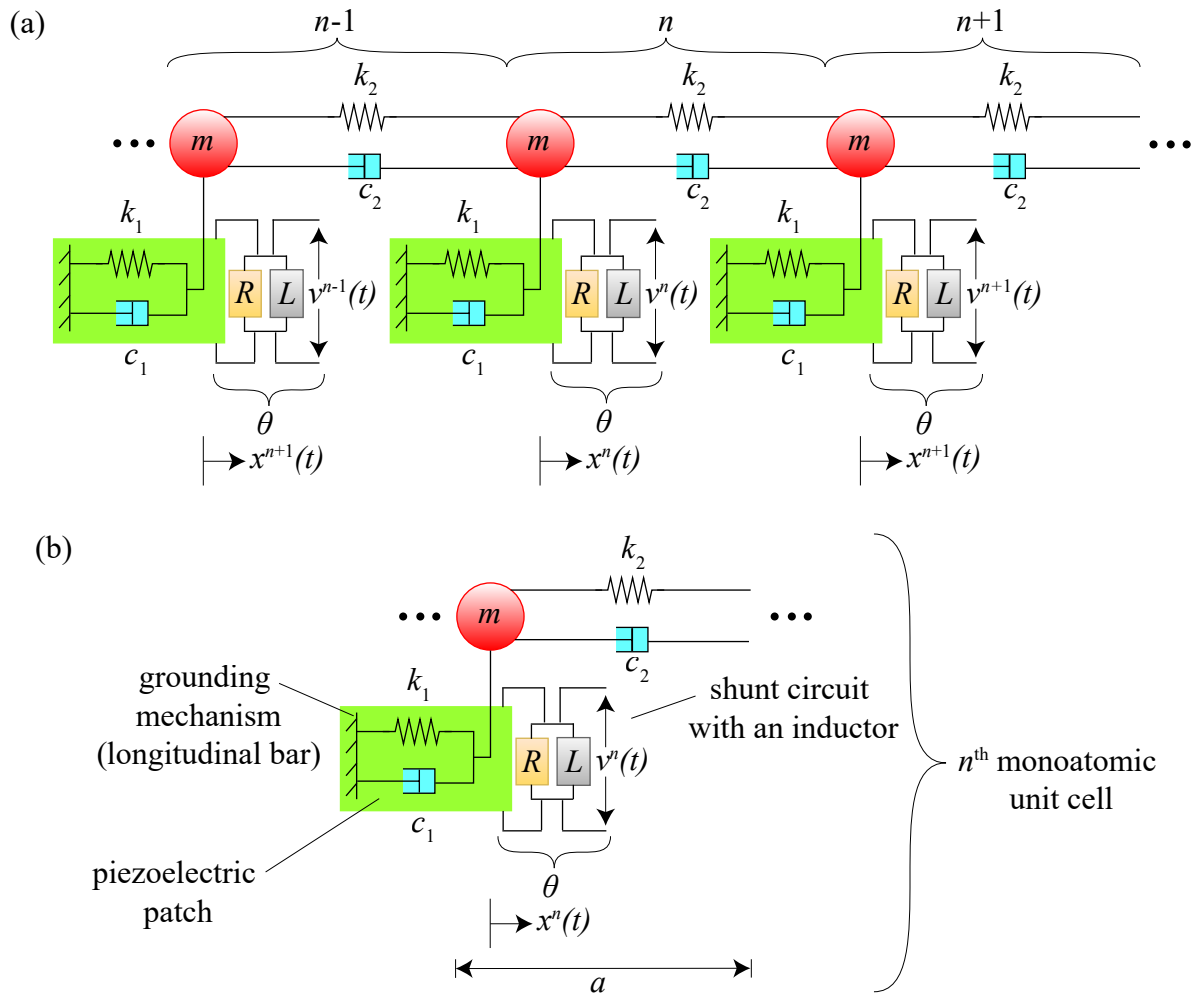


Figure 5.5: Schematic of (a) a monoatomic piezoelectric phononic-crystal (MPPnC) chain comprising of energy harvesters with shunt circuits that are purely resistive and (b) the associated unit cell.

The coupled governing electromechanical equations [87] pertaining to the n^{th} unit cell under free vibration and consisting of a piezoelectric element with an inductor-equipped shunt circuit are written as

$$m\ddot{x}^n + c_2(2\dot{x}^n - \dot{x}^{n-1} - \dot{x}^{n+1}) + c_1\dot{x}^n + k_2(2x^n - x^{n-1} - x^{n+1}) + k_1x^n - \theta v^n = 0, \quad (5.35)$$

$$\theta\ddot{x}^n + C_p\ddot{v}^n + \frac{1}{R_l}\dot{v}^n + \frac{1}{L}v^n = 0. \quad (5.36)$$

Substituting equations (5.2) and (5.29) in equations (5.35) and (5.36) yields the following Bloch-transformed homogeneous equations for the displacement and voltage amplitudes \tilde{x} and \tilde{v} , respectively:

$$m\ddot{\tilde{x}} + (c_2(2 - e^{-ika} - e^{ika}) + c_1)\dot{\tilde{x}} + (k_2(2 - e^{-ika} - e^{ika}) + k_1)\tilde{x} - \theta\tilde{v} = 0, \quad (5.37)$$

$$\theta\ddot{\tilde{x}} + C_p\ddot{\tilde{v}} + \frac{1}{R}\dot{\tilde{v}} + \frac{1}{L}\tilde{v} = 0. \quad (5.38)$$

Equations (5.37) and (5.38) can be compactly written in a matrix form as

$$\mathbf{Z}_1\ddot{\tilde{\mathbf{E}}} + \mathbf{Z}_2\dot{\tilde{\mathbf{E}}} + \mathbf{Z}_3\tilde{\mathbf{E}} = \mathbf{0}, \quad (5.39)$$

where

$$\mathbf{Z}_1 = \begin{pmatrix} m & 0 \\ \theta & C_p \end{pmatrix}; \quad \mathbf{Z}_2 = \begin{pmatrix} c_1 + c_2(2 - e^{ika} - e^{-ika}) & 0 \\ 0 & \frac{1}{R} \end{pmatrix};$$

$$\mathbf{Z}_3 = \begin{pmatrix} k_1 + k_2(2 - e^{ika} - e^{-ika}) & -\theta \\ 0 & \frac{1}{L} \end{pmatrix}; \quad \text{and } \tilde{\mathbf{E}} = \begin{pmatrix} \tilde{x} \\ \tilde{v} \end{pmatrix}. \quad (5.40)$$

Converting equations (5.39) to a first-order equation via a state-space transformation results in equation (5.4), for which the system matrices and the state vector are

$$\mathbf{A} = \begin{pmatrix} \mathbf{0} & \mathbf{I} \\ \mathbf{Z}_1 & \mathbf{Z}_2 \end{pmatrix}; \quad \mathbf{B} = \begin{pmatrix} -\mathbf{I} & \mathbf{0} \\ \mathbf{0} & \mathbf{Z}_3 \end{pmatrix}; \quad \text{and } \mathbf{Y} = \begin{pmatrix} \dot{\tilde{\mathbf{E}}} \\ \tilde{\mathbf{E}} \end{pmatrix}. \quad (5.41)$$

The damped-frequency and damping-ratio band structures are now obtained by applying a solution of the form $\mathbf{Y} = \tilde{\mathbf{Y}}_\lambda e^{\lambda t}$ and solving the associated eigenvalue problem of the form given in equation (5.6). From equation (5.6) for the current MPPnC model, a fourth-order equation in terms of λ is obtained, which, depending on the choice of parameters, either has two complex roots appearing as a complex-conjugate pair and two real roots or four

complex roots appearing as two complex conjugate pairs. For the purpose of obtaining wave-propagation and dissipation characteristics, the set of electrical parameters must be carefully selected in order to obtain two complex roots appearing as a complex-conjugate pair and two real roots.

Non-dimensionalization of the present MPPnC model's fourth-order equation in terms of λ is carried out by using an approach similar to the previous case. In addition to equation (5.33), another non-dimensional electrical parameter defined as

$$\beta = \bar{\omega}^2 C_p L \quad (5.42)$$

is introduced to realize the non-dimensionalization process. In the definition given in equation (5.42), β can be referred to as a non-dimensional inductor constant. Substituting equation (5.13) in the current MPPnC model's fourth-order equation in terms of λ , dividing the resulting equation by $\bar{\omega}^4$, and using equations (5.14), (5.33), and (5.42) yields the characteristic equation

$$(i\Omega)^4 + a_1(i\Omega)^3 + a_2(i\Omega)^2 + a_3(i\Omega) + a_4 = 0. \quad (5.43)$$

Equation (5.43), for an appropriately selected set of non-dimensional electrical parameters, has two real roots and two complex roots appearing as a complex conjugate pair. The coefficients of the non-dimensional equation (5.43) can be found in appendix A.4.

5.4.2 Diatomic piezoelectric phononic crystals

This section expands on the DPPnC configurations.

Shunt circuit without an inductor

The diatomic configuration consisting of shunted piezoelectric elements (patches) where the shunt circuits do not consist of an inductor is represented using the schematic shown in figure 5.6.

The coupled governing electromechanical equations pertaining to the n^{th} unit cell under free vibration consisting of piezoelectric elements with shunt circuits lacking an inductor are

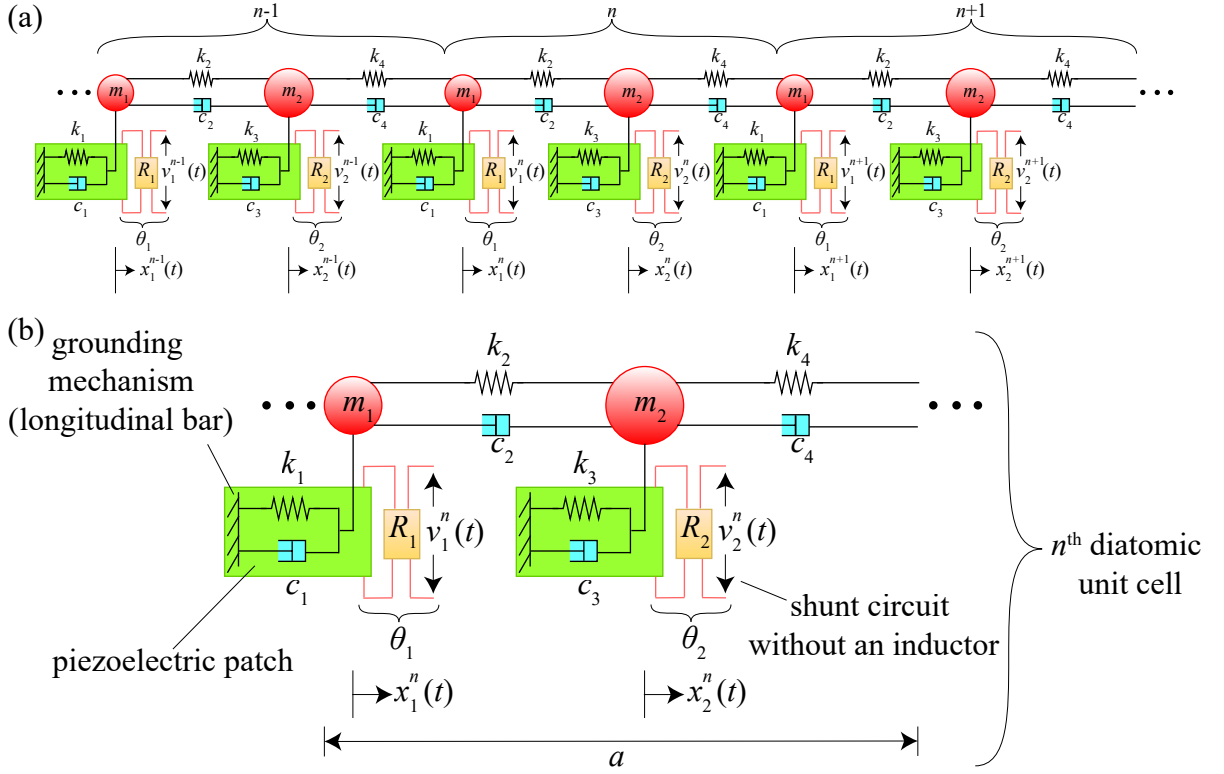


Figure 5.6: Schematic of (a) a diatomic piezoelectric phononic-crystal (DPPnC) chain comprising of energy harvesters with shunt circuits that are purely resistive and (b) the associated unit cell.

written as

$$m_1 \ddot{x}_1^n + (c_1 + c_2 + c_4) \dot{x}_1^n - c_4 \dot{x}_2^{n-1} - c_2 \dot{x}_2^n + (k_1 + k_2 + k_4) x_1^n - k_4 x_2^{n-1} - k_2 x_2^n - \theta_1 v_1^n = 0, \quad (5.44)$$

$$m_2 \ddot{x}_2^n + (c_2 + c_3 + c_4) \dot{x}_2^n - c_4 \dot{x}_1^{n+1} - c_2 \dot{x}_1^n + (k_2 + k_3 + k_4) x_2^n - k_4 x_1^{n+1} - k_2 x_1^n - \theta_2 v_2^n = 0, \quad (5.45)$$

$$\theta_1 \dot{x}_1^n + C_{p1} \dot{v}_1^n + \frac{1}{R_1} v_1^n = 0, \quad (5.46)$$

$$\theta_2 \dot{x}_2^n + C_{p2} \dot{v}_2^n + \frac{1}{R_2} v_2^n = 0. \quad (5.47)$$

The plane-wave Bloch solution for the voltages in the diatomic case can be written with a slight modification to the solution in the monoatomic case in the following manner:

$$v_l^{n+g}(r, \kappa; t) = \hat{v}_l(t) e^{i\kappa(n+g)a}, \quad (5.48)$$

where $l = 1, 2$ is an index corresponding to the voltages generated in the two piezoelectric elements in a unit cell. Substituting equations (5.19) and (5.48) in equations (5.44)–(5.47) yields the following Bloch-transformed homogeneous equations for the displacement amplitudes \tilde{x}_1 and \tilde{x}_2 and the voltage amplitudes \tilde{v}_1 and \tilde{v}_2 :

$$m_1 \ddot{\tilde{x}}_1 + (c_1 + c_2 + c_4) \dot{\tilde{x}}_1 + (-c_2 - c_4 e^{-i\kappa a}) \dot{\tilde{x}}_2 + (k_1 + k_2 + k_4) \tilde{x}_1 + (-k_2 - k_4 e^{-i\kappa a}) \tilde{x}_2 - \theta_1 \tilde{v}_1 = 0, \quad (5.49)$$

$$m_2 \ddot{\tilde{x}}_2 + (c_2 + c_3 + c_4) \dot{\tilde{x}}_2 + (-c_2 - c_4 e^{i\kappa a}) \dot{\tilde{x}}_1 + (k_2 + k_3 + k_4) \tilde{x}_2 + (-k_2 - k_4 e^{i\kappa a}) \tilde{x}_1 - \theta_2 \tilde{v}_2 = 0, \quad (5.50)$$

$$\theta_1 \dot{\tilde{x}}_1 + C_{p1} \dot{\tilde{v}}_1 + \frac{1}{R_1} \tilde{v}_1 = 0, \quad (5.51)$$

$$\theta_2 \dot{\tilde{x}}_2 + C_{p2} \dot{\tilde{v}}_2 + \frac{1}{R_2} \tilde{v}_2 = 0. \quad (5.52)$$

Equations (5.49)–(5.52) can be compacted into matrix equations as

$$\mathbf{M}\ddot{\tilde{\mathbf{X}}} + \mathbf{C}(\kappa)\dot{\tilde{\mathbf{X}}} + \mathbf{K}(\kappa)\tilde{\mathbf{X}} - \mathbf{T}\tilde{\mathbf{V}} = \mathbf{0}, \quad (5.53)$$

$$\mathbf{T}\dot{\tilde{\mathbf{X}}} + \mathbf{C}_p\dot{\tilde{\mathbf{V}}} + \mathbf{R}\tilde{\mathbf{V}} = \mathbf{0}, \quad (5.54)$$

where

$$\begin{aligned} \tilde{\mathbf{X}} &= \begin{pmatrix} \tilde{x}_1 \\ \tilde{x}_2 \end{pmatrix}; \quad \tilde{\mathbf{V}} = \begin{pmatrix} \tilde{v}_1 \\ \tilde{v}_2 \end{pmatrix}; \quad \mathbf{M} = \begin{pmatrix} m_1 & 0 \\ 0 & m_2 \end{pmatrix}; \\ \mathbf{C}(\kappa) &= \begin{pmatrix} c_1 + c_2 + c_4 & -c_4 e^{-i\kappa a} - c_2 \\ -c_4 e^{i\kappa a} - c_2 & c_2 + c_3 + c_4 \end{pmatrix}; \\ \mathbf{K}(\kappa) &= \begin{pmatrix} k_1 + k_2 + k_4 & -k_4 e^{-i\kappa a} - k_2 \\ -k_4 e^{i\kappa a} - k_2 & k_2 + k_3 + k_4 \end{pmatrix}; \\ \mathbf{T} &= \begin{pmatrix} \theta_1 & 0 \\ 0 & \theta_2 \end{pmatrix}; \quad \mathbf{C}_p = \begin{pmatrix} C_{p1} & 0 \\ 0 & C_{p2} \end{pmatrix}; \quad \text{and } \mathbf{R} = \begin{pmatrix} \frac{1}{R_1} & 0 \\ 0 & \frac{1}{R_2} \end{pmatrix}. \end{aligned} \quad (5.55)$$

The dispersion relation can now be formulated by subjecting equations (5.53) and (5.54) to a state-space transformation of the form given in equation (5.4), where

$$\mathbf{A} = \begin{pmatrix} \mathbf{0} & \mathbf{I} & \mathbf{0} \\ \mathbf{M} & \mathbf{C}(\kappa) & \mathbf{0} \\ \mathbf{0} & \mathbf{T} & \mathbf{C}_p \end{pmatrix}, \quad \mathbf{B} = \begin{pmatrix} -\mathbf{I} & \mathbf{0} & \mathbf{0} \\ \mathbf{0} & \mathbf{K}(\kappa) & -\mathbf{T} \\ \mathbf{0} & \mathbf{0} & \mathbf{R} \end{pmatrix}, \quad \text{and } \mathbf{Y} = \begin{pmatrix} \dot{\tilde{\mathbf{X}}} \\ \tilde{\mathbf{X}} \\ \dot{\tilde{\mathbf{V}}} \end{pmatrix}. \quad (5.56)$$

The damped-frequency band structure and damping-ratio diagrams are then obtained by applying a solution of the form $\mathbf{Y} = \tilde{\mathbf{Y}}_\lambda e^{\lambda t}$ and solving the associated eigenvalue problem of the form given in equation (5.6). Solving equation (5.6) for this particular case yields a sixth-order equation in terms of λ , which has two real roots and four complex roots appearing as two complex conjugate pairs.

In order to non-dimensionalize the sixth-order equation of the present DPPnC model in terms of λ , m_1 , the lumped-model parameters of the longitudinal bar attached to it, and the electrical parameters of the shunted piezoelectric patch bonded to that bar are selected in the manner described in equation (5.25). In addition to the definitions given in equation (5.25), the following definitions are introduced:

$$\begin{aligned}\theta_1 &= \theta, \\ \theta_2 &= \gamma_8 \theta, \\ C_{p1} &= C_p, \\ C_{p2} &= \gamma_9 C_p, \\ R_1 &= R, \\ R_2 &= \gamma_{10} R.\end{aligned}\tag{5.57}$$

Substituting equations (5.25) and (5.57) in the present DPPnC model's sixth-order equation in terms of λ , dividing the resulting equation by $\bar{\omega}^6$, and using equations (5.14) and (5.33) yields the characteristic equation

$$(i\Omega)^6 + a_1(i\Omega)^5 + a_2(i\Omega)^4 + a_3(i\Omega)^3 + a_4(i\Omega)^2 + a_5(i\Omega) + a_6 = 0.\tag{5.58}$$

Equation (5.58) has two real roots and four complex roots appearing as two complex-conjugate pairs. The coefficients of the non-dimensional equation (5.58) are available in appendix A.5.

Shunt circuit with an inductor

Finally, the diatomic configuration consisting of shunted piezoelectric elements (patches) where the shunt circuits are equipped with an inductor is represented using the schematic shown in figure 5.7.

The coupled governing electromechanical equations pertaining to the n^{th} unit cell under free vibration consisting of piezoelectric elements with shunt circuits equipped with an

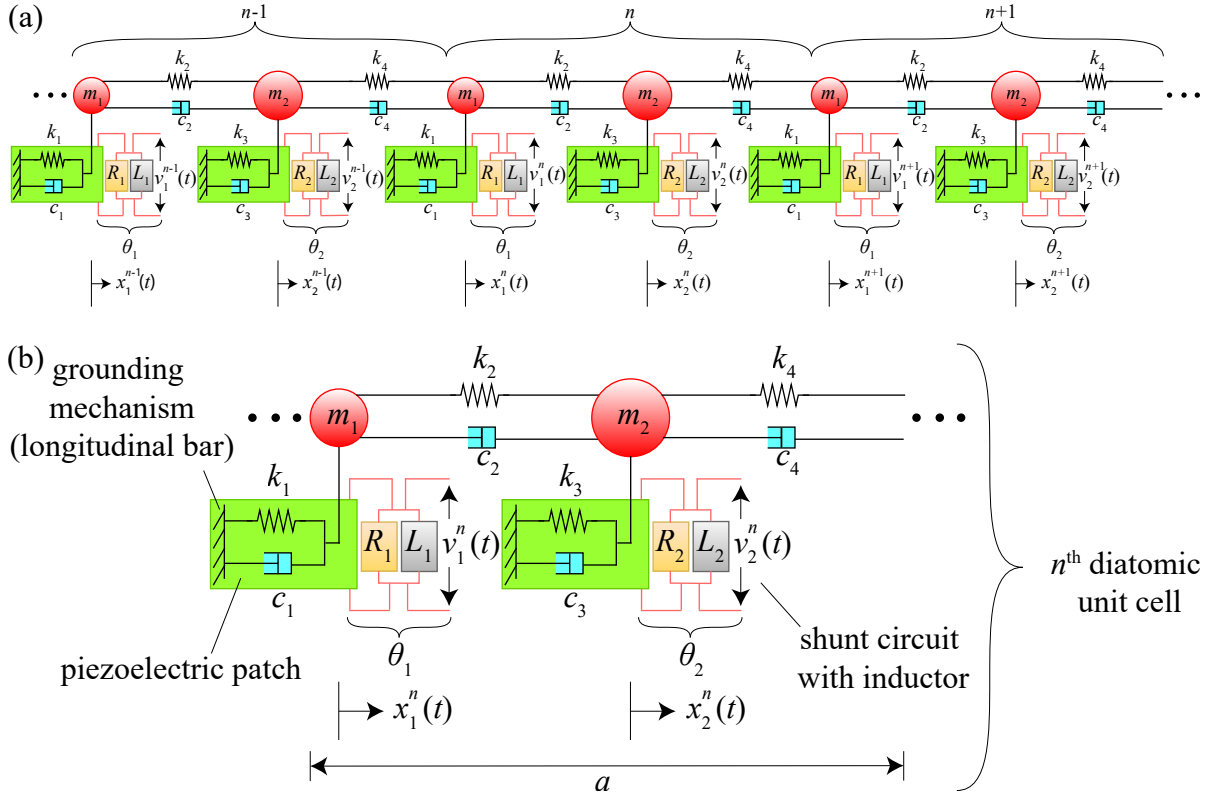


Figure 5.7: Schematic of (a) a diatomic piezoelectric phononic-crystal (DPPnC) chain comprising of energy harvesters with shunt circuits that are purely resistive and (b) the associated unit cell.

inductor are written as

$$m_1 \ddot{x}_1^n + (c_1 + c_2 + c_4) \dot{x}_1^n - c_4 \dot{x}_2^{n-1} - c_2 \dot{x}_2^n + (k_1 + k_2 + k_4) x_1^n - k_4 x_2^{n-1} - k_2 x_2^n - \theta_1 v_1^n = 0, \quad (5.59)$$

$$m_2 \ddot{x}_2^n + (c_2 + c_3 + c_4) \dot{x}_2^n - c_4 \dot{x}_1^{n+1} - c_2 \dot{x}_1^n + (k_2 + k_3 + k_4) x_2^n - k_4 x_1^{n+1} - k_2 x_1^n - \theta_2 v_2^n = 0, \quad (5.60)$$

$$\theta_1 \dot{x}_1^n + C_{p1} \dot{v}_1^n + \frac{1}{R_1} v_1^n + \frac{1}{L_1} v_1^n = 0, \quad (5.61)$$

$$\theta_2 \dot{x}_2^n + C_{p2} \dot{v}_2^n + \frac{1}{R_2} v_2^n + \frac{1}{L_2} v_2^n = 0. \quad (5.62)$$

Substituting equations (5.19) and (5.48) in equations (5.59)–(5.62) yields the following Bloch-transformed homogeneous equations for the displacement amplitudes \tilde{x}_1 and \tilde{x}_2 and

the voltage amplitudes \tilde{v}_1 and \tilde{v}_2 :

$$m_1\ddot{\tilde{x}}_1 + (c_1 + c_2 + c_4)\dot{\tilde{x}}_1 + (-c_2 - c_4e^{-i\kappa a})\dot{\tilde{x}}_2 + (k_1 + k_2 + k_4)\tilde{x}_1 + (-k_2 - k_4e^{-i\kappa a})\tilde{x}_2 - \theta_1\tilde{v}_1 = 0 \quad (5.63)$$

$$m_2\ddot{\tilde{x}}_2 + (c_2 + c_3 + c_4)\dot{\tilde{x}}_2 + (-c_2 - c_4e^{i\kappa a})\dot{\tilde{x}}_1 + (k_2 + k_3 + k_4)\tilde{x}_2 + (-k_2 - k_4e^{i\kappa a})\tilde{x}_1 - \theta_2\tilde{v}_2 = 0 \quad (5.64)$$

$$\theta_1\ddot{\tilde{x}}_1 + C_{p1}\ddot{\tilde{v}}_1 + \frac{1}{R_1}\dot{\tilde{v}}_1 + \frac{1}{L_1}\tilde{v}_1 = 0 \quad (5.65)$$

$$\theta_2\ddot{\tilde{x}}_2 + C_{p2}\ddot{\tilde{v}}_2 + \frac{1}{R_2}\dot{\tilde{v}}_2 + \frac{1}{L_2}\tilde{v}_2 = 0. \quad (5.66)$$

Equations (5.63)–(5.66) can be compacted into matrix equations as

$$\mathbf{M}\ddot{\tilde{\mathbf{X}}} + \mathbf{C}(\kappa)\dot{\tilde{\mathbf{X}}} + \mathbf{K}(\kappa)\tilde{\mathbf{X}} - \mathbf{T}\tilde{\mathbf{V}} = \mathbf{0}, \quad (5.67)$$

$$\mathbf{T}\ddot{\tilde{\mathbf{X}}} + \mathbf{C}_p\ddot{\tilde{\mathbf{V}}} + \mathbf{R}\dot{\tilde{\mathbf{V}}} + \mathbf{L}\tilde{\mathbf{V}} = \mathbf{0}, \quad (5.68)$$

where

$$\begin{aligned} \tilde{\mathbf{X}} &= \begin{pmatrix} \tilde{x}_1 \\ \tilde{x}_2 \end{pmatrix}; \quad \tilde{\mathbf{V}} = \begin{pmatrix} \tilde{v}_1 \\ \tilde{v}_2 \end{pmatrix}; \quad \mathbf{M} = \begin{pmatrix} m_1 & 0 \\ 0 & m_2 \end{pmatrix}; \\ \mathbf{C}(\kappa) &= \begin{pmatrix} c_1 + c_2 + c_4 & -c_4e^{-i\kappa a} - c_2 \\ -c_4e^{i\kappa a} - c_2 & c_2 + c_3 + c_4 \end{pmatrix}; \\ \mathbf{K}(\kappa) &= \begin{pmatrix} k_1 + k_2 + k_4 & -k_4e^{-i\kappa a} - k_2 \\ -k_4e^{i\kappa a} - k_2 & k_2 + k_3 + k_4 \end{pmatrix}; \\ \mathbf{T} &= \begin{pmatrix} \theta_1 & 0 \\ 0 & \theta_2 \end{pmatrix}; \quad \mathbf{C}_p = \begin{pmatrix} C_{p1} & 0 \\ 0 & C_{p2} \end{pmatrix}; \quad \mathbf{R} = \begin{pmatrix} \frac{1}{R_1} & 0 \\ 0 & \frac{1}{R_2} \end{pmatrix}; \quad \text{and } \mathbf{L} = \begin{pmatrix} \frac{1}{L_1} & 0 \\ 0 & \frac{1}{L_2} \end{pmatrix}. \end{aligned} \quad (5.69)$$

Equations (5.67) and (5.68) can be further compacted into a single matrix equation as

$$\mathbf{Z}_1\ddot{\tilde{\mathbf{E}}} + \mathbf{Z}_2\dot{\tilde{\mathbf{E}}} + \mathbf{Z}_3\tilde{\mathbf{E}} = \mathbf{0}, \quad (5.70)$$

where

$$\mathbf{Z}_1 = \begin{pmatrix} \mathbf{M} & \mathbf{0} \\ \mathbf{T} & \mathbf{C}_p \end{pmatrix}; \quad \mathbf{Z}_2 = \begin{pmatrix} \mathbf{C}(\kappa) & \mathbf{0} \\ \mathbf{0} & \mathbf{R} \end{pmatrix}; \quad \mathbf{Z}_3 = \begin{pmatrix} \mathbf{K}(\kappa) & -\mathbf{T} \\ \mathbf{0} & \mathbf{L} \end{pmatrix}; \quad \text{and } \tilde{\mathbf{E}} = \begin{pmatrix} \tilde{\mathbf{X}} \\ \tilde{\mathbf{V}} \end{pmatrix}. \quad (5.71)$$

The dispersion relation can now be formulated by subjecting equation (5.70) to a state-space transformation of the form given in equation (5.4), implementing a solution of the form $\mathbf{Y} = \tilde{\mathbf{Y}}_\lambda e^{\lambda t}$, and solving the resulting eigenvalue problem of the form given in equation (5.6). The state-space matrices and the state vector in equation (5.4) for the current DPPnC model are

$$\mathbf{A} = \begin{pmatrix} \mathbf{0} & \mathbf{I} \\ \mathbf{Z}_1 & \mathbf{Z}_2 \end{pmatrix}; \mathbf{B} = \begin{pmatrix} -\mathbf{I} & \mathbf{0} \\ \mathbf{0} & \mathbf{Z}_3 \end{pmatrix}; \text{ and } \mathbf{Y} = \begin{pmatrix} \dot{\tilde{\mathbf{E}}} \\ \tilde{\mathbf{E}} \end{pmatrix}. \quad (5.72)$$

Upon solving equation (5.6) for the current DPPnC model, an eight-order equation in terms of λ is obtained, which, depending on the choice of parameters, either has four complex roots appearing as two complex-conjugate pairs and four real roots or eight complex roots appearing as four complex-conjugate pairs. For the purpose of obtaining wave-propagation and dissipation characteristics, the set of electrical parameters must be carefully selected in order to obtain four complex roots appearing as a complex-conjugate pair and four real roots.

Non-dimensionalization of the present DPPnC model's eight-order equation in terms of λ is carried out in a fashion similar to the previous DPPnC model without an inductor. As the present model incorporates an inductor, the following definitions are added:

$$\begin{aligned} L_1 &= L, \\ L_2 &= \gamma_{11}L. \end{aligned} \quad (5.73)$$

Substituting equations (5.25), (5.57) and (5.73) in the present DPPnC model's eight-order equation in terms of λ , dividing the resulting equation by $\bar{\omega}^8$, and using equations (5.14), (5.33), and (5.42) yields the characteristic equation

$$\begin{aligned} (i\Omega)^8 + a_1(i\Omega)^7 + a_2(i\Omega)^6 + a_3(i\Omega)^5 + a_4(i\Omega)^4 + a_5(i\Omega)^3 + a_6(i\Omega)^2 + a_7(i\Omega) \\ + a_8 = 0. \end{aligned} \quad (5.74)$$

Equation (5.74), for an appropriately selected set of non-dimensional electrical parameters, has four real roots and four complex roots appearing as two complex-conjugate pairs. The coefficients of the non-dimensional equation (5.74) can be found in appendix A.6.

5.5 Wave-propagation and dissipation characteristics of piezoelectric phononic crystals: damped frequencies, raw dissipation, and energy-harvesting availability

In this section, the wave-propagation and dissipation characteristics of the monoatomic and diatomic configurations with and without energy harvesters are examined: namely, MPnC, MPPnC without an inductor, MPPnC with an inductor, DPnC, DPPnC without an inductor, and DPPnC with an inductor. For each case, the damped-dispersion and damping-ratio diagrams are computed first. The wavenumber-dependent damping ratios of the non-piezo PnCs are then subtracted from those of the corresponding piezo PnCs to quantify the energy-harvesting availability for each model. The analysis is performed for both the monoatomic and diatomic models.

5.5.1 Monoatomic configurations

This section sets forth the investigation of the characteristics of all the monoatomic models by comparing the frequency and damping-ratio band structures of the MPnC, MPPnC without an inductor, and MPPnC with an inductor across the irreducible Brillouin Zone (IBZ). All the results in this section are generated for $\mu \in [0, \pi]$, i.e., the IBZ, where μ is the dimensionless wavenumber defined as $\mu = \kappa a$. The parameters used to generate the plots are given in table 5.1.

Table 5.1: Parameters employed in the monoatomic phononic crystal (MPnC) and monoatomic piezoelectric phononic crystals (MPPnCs).

Parameter	MPnC	MPPnC without an inductor	MPPnC with an inductor	Unit
a	1	1	1	m
m	0.0170	0.0170	0.0170	Kg
k_1	4.1000×10^3	4.1000×10^3	4.1000×10^3	Nm^{-1}
k_2	2.0500×10^3	2.0500×10^3	2.0500×10^3	Nm^{-1}
α	—	0.2323	0.2323	—
β	—	—	0.8296	—
θ	—	-8.5700×10^{-3}	-8.5700×10^{-3}	NV^{-1}

The parameters have been taken from a previous study [88] which investigates vibrational energy harvesting using a cantilever beam with a tip mass submerged in a vortex flow field. Concerning the damping prescription for the three monoatomic systems, only the special

case where the two dashpots in each system have the same prescribed damping-coefficient value is considered, i.e., $\eta = c_1 = c_2$. Three levels of damping are analysed, namely, no damping ($\eta = 0 \text{ Nsm}^{-1}$), a low damping level ($\eta = 0.218 \text{ Nsm}^{-1}$), and a high damping level ($\eta = 0.436 \text{ Nsm}^{-1}$). The damping levels, i.e., damping coefficients, $\eta = 0.218 \text{ Nsm}^{-1}$ and $\eta = 0.436 \text{ Nsm}^{-1}$ are loosely termed as low and high, respectively, as simply doubling the lower value gives a good estimation of a high value in order to avoid overestimation and the system becoming overdamped. The aim here is to investigate the effect of increasing the damping level in the three systems on their damping ratios obtained after Bloch analysis. Later on in section 5.6.1, the maximum value that the damping levels in the MPPnCs can take before making them overdamped are shown in figure 5.14. In table 5.1, $\alpha = \bar{\omega}_1 C_p R$, and $\beta = \bar{\omega}_1^2 C_p L$. As the piezoelectric element is attached to the longitudinal bar modelled by the damped oscillator with spring stiffness k_1 and $\bar{\omega}_1 = \sqrt{\frac{k_1}{m}}$, $\bar{\omega}_1$ is used to compute α and β .

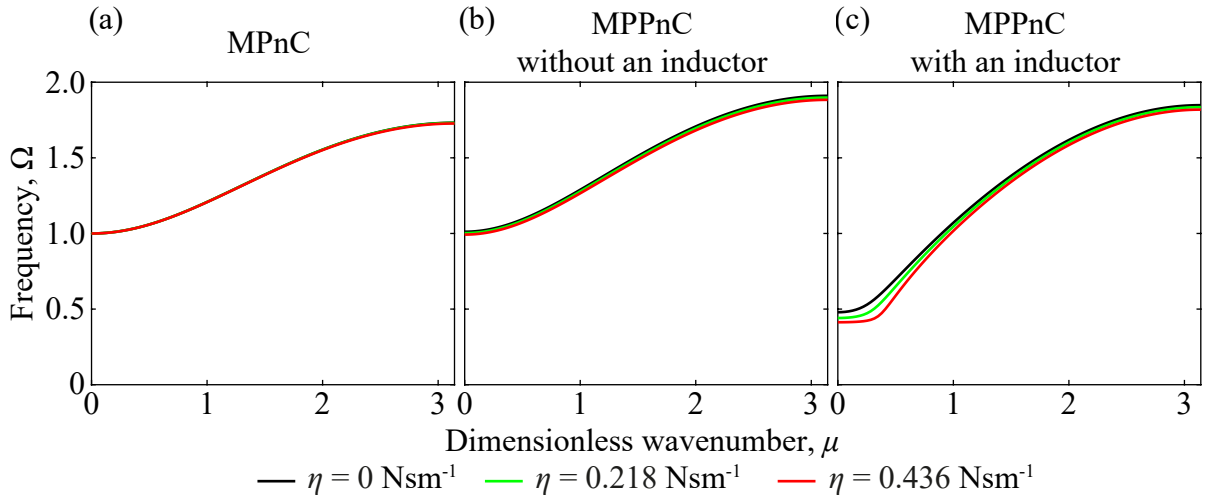


Figure 5.8: Monoatomic models: Normalized damped-frequency band structures for the (a) monoatomic phononic crystal (MPnC), (b) monoatomic piezoelectric phononic crystal (MPPnC) without an inductor, and (c) monoatomic piezoelectric phononic crystal (MPPnC) with an inductor as a function of wavenumber for the prescribed damping levels $\eta = 0 \text{ Nsm}^{-1}$, $\eta = 0.218 \text{ Nsm}^{-1}$, and $\eta = 0.436 \text{ Nsm}^{-1}$.

Figure 5.8 depicts a comparison of the wavenumber-dependent normalized damped-frequency (dispersion) curves for the three monoatomic configurations at the three selected damping levels. The damped frequency of each monoatomic model, at each of the three prescribed damping levels, is normalized (non-dimensionalized) with respect to $\bar{\omega}_1$ (stated above); i.e., the plots depict $\Omega = \frac{\omega_d}{\bar{\omega}_1}$, where ω_d is the dimensional (rad/sec) wavenumber-dependent damped frequency. Note that the frequency obtained for the MPnC at $\eta = 0 \text{ Nsm}^{-1}$ is undamped. Figure 5.8(a) illustrates a near overlap of the frequencies across the

IBZ as η varies for the MPnC. In figure 5.8(b), a modest drop in the frequencies is noticed for the MPPnC without an inductor across the entire IBZ as η increases. In figure 5.8(c), a more noticeable drop in the frequencies across the entire IBZ is observed for the MPPnC with an inductor, particularly in the interval $\mu = [0, 1]$, as η increases. Since the mechanical parameters are the same, the three systems are statically equivalent; i.e., the slope of their dispersion curves (group velocity C_g) in the long-wave limit is the same. Since the three monoatomic chains developed for this study are grounded (i.e., attached to a frame as depicted in figures 5.2, 5.4, and 5.5), the frequencies in the long-wave limit $\lim_{\mu \rightarrow 0}$ are non-zero.

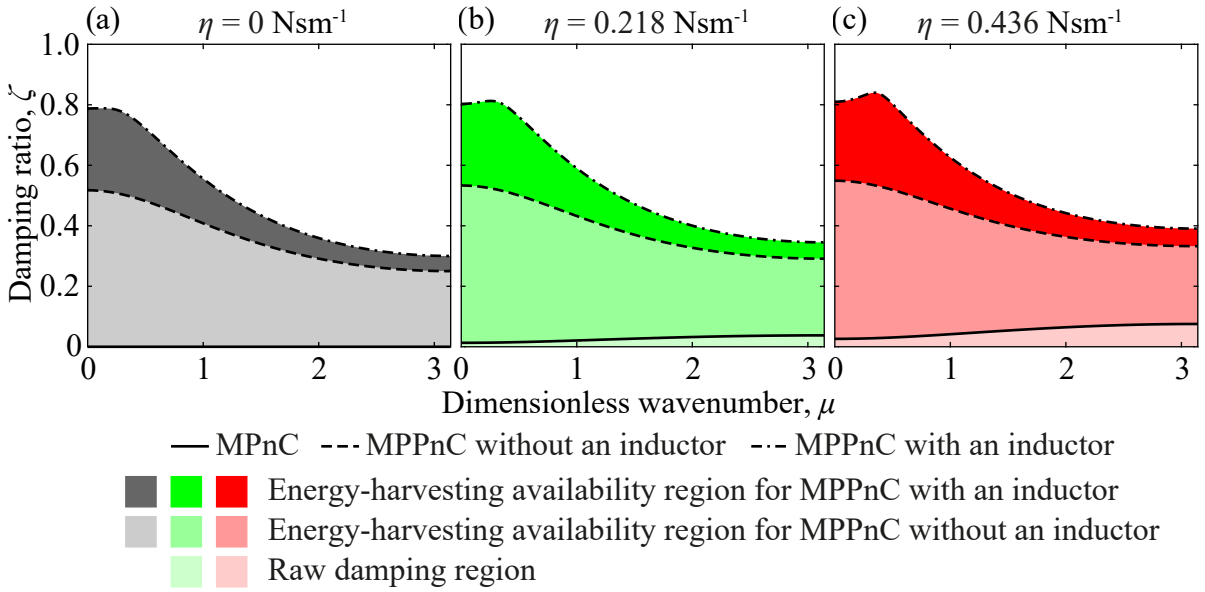


Figure 5.9: Monoatomic models: damping-ratio diagrams for the monoatomic phononic crystal (MPnC), monoatomic piezoelectric phononic crystal (MPPnC) without an inductor, and monoatomic piezoelectric phononic crystal (MPPnC) with an inductor as a function of wavenumber for the prescribed damping levels (a) $\eta = 0 \text{ Nsm}^{-1}$, (b) $\eta = 0.218 \text{ Nsm}^{-1}$, and (c) $\eta = 0.436 \text{ Nsm}^{-1}$.

Figure 5.9 illustrates a comparison of damping ratio ζ between the MPnC, MPPnC without an inductor, and MPPnC with an inductor at the three prescribed damping levels. When $\eta = 0 \text{ Nsm}^{-1}$, $\zeta = 0$ for the MPnC for all dimensionless wavenumbers ($\mu \in [0, \pi]$), but figure 5.9(a) shows non-zero dissipation in the other systems. This directly demonstrates that adding piezoelectric elements introduces dissipation into a system, which is in fact consistent with the very nature of the energy-harvesting aspect since it is the dissipated energy that provides the source for harvesting. For the three prescribed damping levels, a significantly higher damping ratio is exhibited by the MPPnC without an inductor and more so by the MPPnC with an inductor when compared to the non-piezo MPnC. As η increases, the damping ratio of all three models increase as expected. For the MPPnC with an inductor,

a discernible change can be seen in the interval $\mu = [0, 0.5]$. For the three prescribed damping levels, the areas under the curves have been shaded with colours of varying intensities in order to distinguish between the regions of different damping-ratio intensities. The bottom shaded regions for the damped ($\eta \neq 0 \text{ Nsm}^{-1}$) cases are directly attributed to the "raw system damping" since these regions are not associated with the presence of piezoelectric elements. The darker coloured regions above are, therefore, attributed to the dissipation made "available" for harvesting by the addition of the piezoelectric elements (without or with an inductor); i.e., the darker coloured regions are intrinsically representative of the energy "available" for harvesting. These dissipation regions associated with the piezoelectric PnCs are intrinsic in nature; i.e., they are dependent only on the unit-cell properties including the electromechanical coupling, θ , and the electrical parameters of the piezoelectric-element shunt circuit and not on the dimensions and boundary conditions of a finite structure or any external forcing.

To provide a compact numerical quantification of the useful dissipation (level of energy-harvesting availability) added to the MPnC due to the utilization of piezoelectric elements, the following wavenumber-dependent metric referred to as the *energy-harvesting-availability* metric is defined:

$$Z|_*(\mu) = \zeta|_*(\mu) - \zeta|_{\text{MPnC}}(\mu) \quad (\mu \in [0, \pi]). \quad (5.75)$$

In equation (5.75), the subscript "*" indicates MPPnC without an inductor or MPPnC with an inductor. The cumulative and total value of $Z(\mu)|_*$ are also defined as

$$Z^{\text{cum}}|_*(\mu) = \int_0^\mu Z|_* \, d\mu \quad (\mu \in [0, \pi]), \quad (5.76)$$

and

$$Z^{\text{tot}}|_* = Z^{\text{cum}}|_*(\pi), \quad (5.77)$$

respectively. The total value is computed to quantify the overall difference in the damping ratio ζ and, hence, arrive at a single number to represent the total energy-harvesting availability for a given model.

Figure 5.10 displays the energy-harvesting availability metrics $Z(\mu)|_*$ (subscript "*" indicating MPPnC without an inductor or MPPnC with an inductor) and their cumulative values $Z^{\text{cum}}|_*(\mu)$ and also gives their total values $Z^{\text{tot}}|_*$ (a single total representative quantity) across the IBZ at the three damping levels. Higher values of Z^{tot} are observed for the MPPnC with an inductor compared to the MPPnC without an inductor at all damping levels; this quantifies the inductor's role in improving the energy-harvesting availability. A small increase

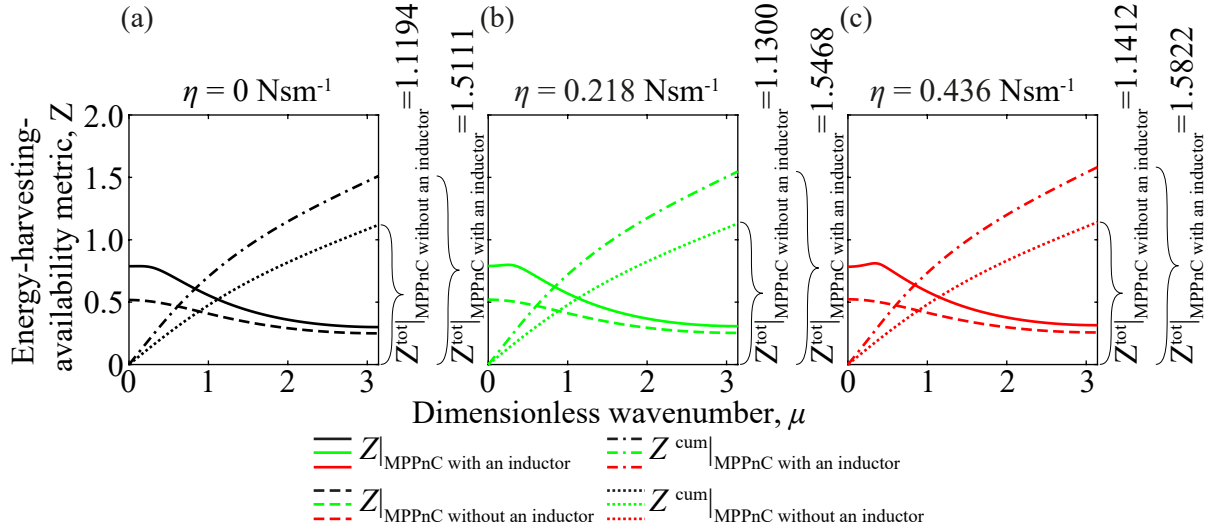


Figure 5.10: Monoatomic models: energy-harvesting availability metric $Z(\mu)$ and its cumulative value $Z^{\text{cum}}(\mu)$ for the prescribed damping levels (a) $\eta = 0 \text{ Nsm}^{-1}$, (b) $\eta = 0.218 \text{ Nsm}^{-1}$, and (c) $\eta = 0.436 \text{ Nsm}^{-1}$.

in Z^{tot} is noticed for the MPPnCs as the damping level increases. This, in turn, indicates that the prescribed damping level in a piezoelectric PnC affects the energy-harvesting availability.

5.5.2 Diatomic configurations

In this section, similar calculations as in the monoatomic case are performed for the diatomic configurations: DPnC, DPPnC without an inductor, and DPPnC with an inductor. All the results in this section are generated for $\mu \in [0, \pi]$, i.e., the IBZ. The parameters used for the diatomic models are given in table 5.2. Similar to the investigation carried out for the monoatomic models, only the special case where the four dashpots in each system have the same prescribed damping value is considered; i.e., $\eta = c_1 = c_2 = c_3 = c_4$. The same three levels of damping as for the monoatomic case are used for the diatomic case.

The non-dimensional electrical parameters stated in table 5.2 are defined as

$$\alpha_l = \bar{\omega}_l C_{p_l} R_l, \quad (5.78a)$$

$$\beta_l = \bar{\omega}_l^2 C_{p_l} L_l, \quad (5.78b)$$

where $l = 1, 2$ is an index corresponding to the parameters of the two piezoelectric elements and the frequencies obtained from the two bar-mass pairs: $\bar{\omega}_1 = \sqrt{\frac{k_1}{m_1}}$ and $\bar{\omega}_2 = \sqrt{\frac{k_3}{m_2}}$.

Figure 5.11 depicts a comparison of the damped-dispersion curves for the three diatomic configurations at the three prescribed damping levels. Both the damped frequencies of

Table 5.2: Parameters employed in the diatomic phononic crystal (DPnC) and diatomic piezoelectric phononic crystals (DPPnCs).

Parameter	DPnC	DPPnC without an inductor	DPPnC with an inductor	Unit
a	1	1	1	m
m_1	0.0170	0.0170	0.0170	Kg
m_2	0.0255	0.0255	0.0255	Kg
k_1	4.1000×10^3	4.1000×10^3	4.1000×10^3	Nm^{-1}
k_2	1.0250×10^3	1.0250×10^3	1.0250×10^3	Nm^{-1}
k_3	4.1000×10^3	4.1000×10^3	4.1000×10^3	Nm^{-1}
k_4	2.0500×10^3	2.0500×10^3	2.0500×10^3	Nm^{-1}
α_1	—	0.2534	0.2534	—
α_2	—	0.2069	0.2069	—
β_1	—	—	1.0371	—
β_2	—	—	0.6914	—
θ_1	—	-8.5700×10^{-3}	-8.5700×10^{-3}	NV^{-1}
θ_2	—	-8.5700×10^{-3}	-8.5700×10^{-3}	NV^{-1}

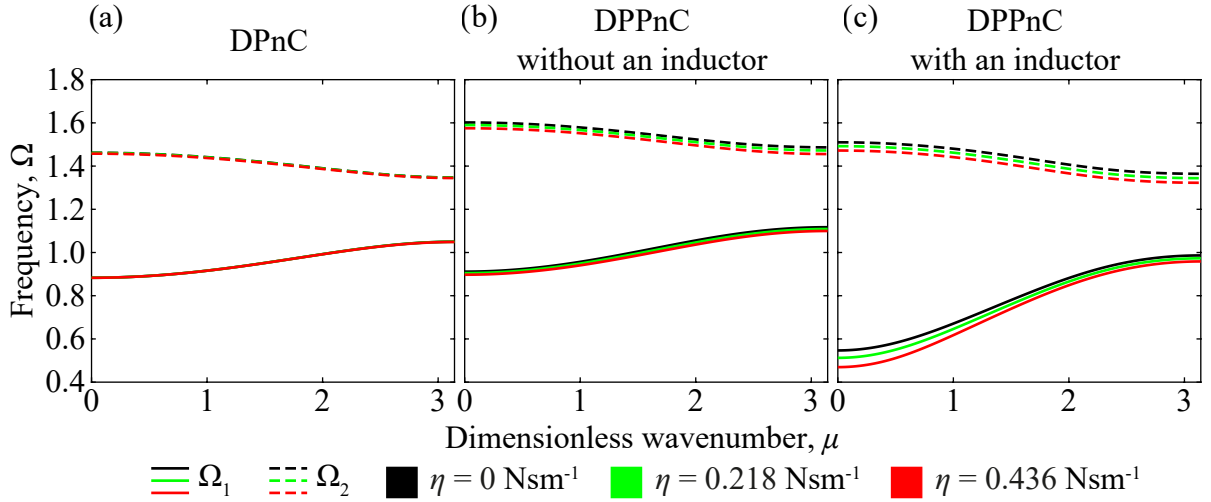


Figure 5.11: Diatomic models: Normalized damped-frequency band structures for the (a) diatomic phononic crystal (DPnC), (b) diatomic piezoelectric phononic crystal (DPPnC) without an inductor, and (c) diatomic piezoelectric phononic crystal (DPPnC) with an inductor as a function of wavenumber for the prescribed damping levels $\eta = 0 \text{ Nsm}^{-1}$, $\eta = 0.218 \text{ Nsm}^{-1}$, and $\eta = 0.436 \text{ Nsm}^{-1}$.

each diatomic model, at each of the three prescribed damping levels, are normalized (non-dimensionalized) with respect to $\bar{\omega}_1$ (stated above); i.e., the plots depict $\Omega_l = \frac{\omega_{dl}}{\bar{\omega}_1}$, where ω_{dl} is the dimensional (rad/sec) wavenumber-dependent damped frequency and $l=1$ (acoustic

branch), 2 (optical branch). Note that the frequencies obtained for the DPnC at $\eta = 0$ Nsm^{-1} are undamped. Similar to the monoatomic case, it is seen in figure 5.11(a) that for the DPnC the frequencies associated with the acoustic and the optical branches nearly overlap at the three damping levels. In figure 5.11(b) for the MPPnC without an inductor, a noticeable uniform drop in both branches is observed as η increases. For the MPPnC with an inductor, figure 5.11(c) depicts even stronger drops, especially, for the acoustic branch at lower wavenumbers. Since the mechanical parameters are the same across the three systems, they are statically equivalent, which again provides an appropriate comparison between the three cases. Similar to the monoatomic models, the acoustic-branch frequencies of the three diatomic models in the long-wave limit ($\lim \mu \rightarrow 0$) are non-zero due to the periodic media being grounded as depicted in figures 5.3, 5.6, and 5.7.

Figure 5.9 provides a comparison of the damping ratios ζ_1 (acoustic branch) and ζ_2 (optical branch) and their summation ζ_{sum} between the DPnC, DPPnC without an inductor, and DPPnC with an inductor at the three prescribed damping levels. When $\eta = 0$ Nsm^{-1} , ζ_1 , ζ_2 , and ζ_{sum} are equal to zero for the DPnC since it is not damped. In contrast, the DPPnC models exhibit dissipation even in the absence of prescribed damping. As previously explained for the monoatomic models, this is a direct indication of the energy-harvesting character of the piezoelectric models as this dissipation stems exclusively from the electromechanical couplings and electrical parameters of the shunt circuits attached to the piezoelectric elements. For the three prescribed damping levels, significantly higher damping ratios are exhibited by the DPPnC without an inductor and more so by the DPPnC with an inductor when compared to the non-piezo DPnC. For the three configurations, a significant increase in ζ_1 , ζ_2 , and ζ_{sum} is seen as η increases. Analogous to the monoatomic results, the bottom shaded region for the damped ($\eta \neq 0$ Nsm^{-1}) cases are directly attributed to the "raw system damping" since this region is not associated with the presence of piezoelectric elements. The darker coloured regions above, on the other hand, are representative of the intrinsic energy-harvesting availability.

For the diatomic models, the wavenumber-dependent energy-harvesting-availability metric is slightly modified from that for the monoatomic models to account for the presence of two branches; it is therefore written as

$$Z_l|_*(\mu) = \zeta_l|_*(\mu) - \zeta_l|_{\text{DPnC}}(\mu) \quad (l = 1, 2, \text{ or sum}; \mu \in [0, \pi]). \quad (5.79)$$

In equation (5.79), the subscript “*” indicates DPPnC without an inductor or DPPnC with an inductor; $l = 1$ indicates the acoustic branch; and $l = 2$ indicates the optical branch. An alternative representation (not adopted here) is to replace the “sum” by an average; i.e.,

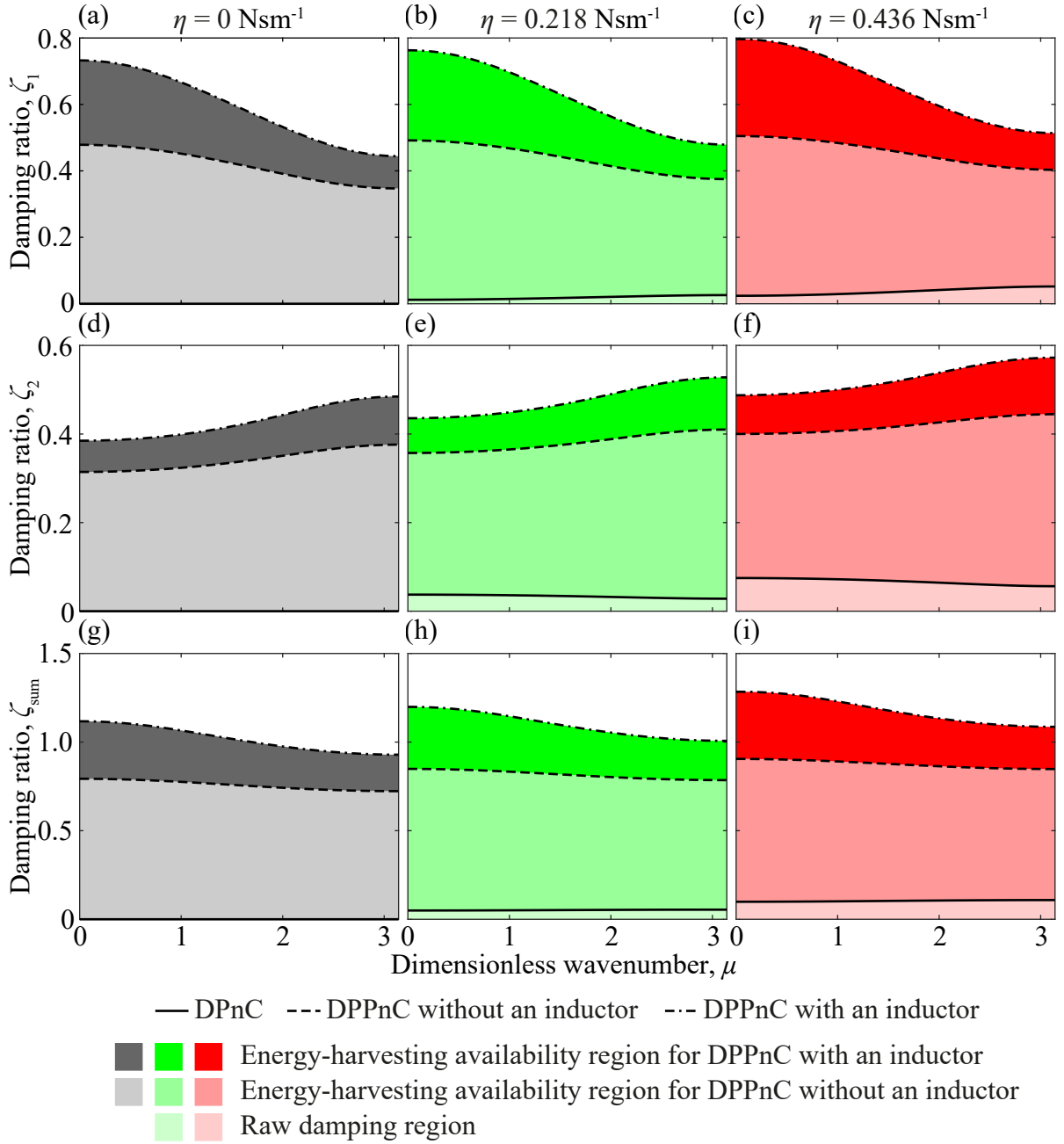


Figure 5.12: Diatomic models: Damping ratios ζ_1 (acoustic branch) and ζ_2 (optical branch) and summation of the two branches ζ_{sum} of the diatomic phononic crystal (DPnC), diatomic piezoelectric phononic crystal (DPPnC) without an inductor, and diatomic piezoelectric phononic crystal (DPPnC) with an inductor as a function of wavenumber for the prescribed damping levels $\eta = 0 \text{ Nsm}^{-1}$ (first column), $\eta = 0.218 \text{ Nsm}^{-1}$ (second column), and $\eta = 0.436 \text{ Nsm}^{-1}$ (third column).

$Z_{\text{avg}}|_*(\mu) = \frac{\sum_{l=1}^2 Z_l|_*(\mu)}{2}$. The cumulative and total value of $Z_l(\mu)|_*$ are also defined as

$$Z_l^{\text{cum}}|_*(\mu) = \int_0^\mu Z_l|_* d\mu \quad (\mu \in [0, \pi]), \quad (5.80)$$

and

$$Z_l^{\text{tot}}|_* = Z_l^{\text{cum}}|_*(\pi), \quad (5.81)$$

respectively.

Figures 5.9 depicts the wavenumber-dependent energy-harvesting-availability metrics, their cumulative values, and their total values corresponding to the acoustic-branch damping ratio ζ_1 , optical-branch damping ratio ζ_2 , and their summation ζ_{sum} . Similar to the monoatomic models, higher values of Z_l^{tot} ($l = 1, 2$, or sum) are noticed for the DPPnC with an inductor compared to the DPPnC without an inductor at the three prescribed damping levels. A relatively small increase is seen in $Z_l^{\text{tot}}|_*$ ($l = 1, 2$, or sum) for both the DPPnCs as the damping level increases, again, indicating that the level of prescribed damping has a relatively modest but noticeable effect on the performance of the piezoelectric elements. Upon comparing between Z_1 and Z_2 for the two DPPnCs, it is observed that Z_1 , corresponding to the acoustic-branch damping ratio, decreases slightly with the dimensionless wavenumber μ as in the monoatomic case, but, in contrast, Z_2 , corresponding to the optical-branch damping ratio, increases slightly with μ . This behaviour has implications for frequency-dependent energy harvesting since the optical branch corresponds to higher frequencies.

5.6 Parametric analysis of the energy-harvesting-availability metric

The energy-harvesting-availability metric introduced in this chapter represents a novel intrinsic characterization method. In this section, the effects of the various piezoelectric design parameters on this metric are examined. The behaviour of the total energy-harvesting-availability metric, Z^{tot} (monoatomic) and $Z_{\text{sum}}^{\text{tot}}$ (diatomic), for varying values of the non-dimensional electrical parameters is investigated. This enables one to undertake methodical exploration of the design space associated to periodic energy-harvesting media and gain insights on parameter-based optimal performance.

5.6.1 Monoatomic piezoelectric phononic crystals

In this section, a parametric analysis of the MPPnC models, purely resistive and inductor-equipped, is elaborated at the three selected prescribed damping levels, namely, $\eta = 0 \text{ Nsm}^{-1}$, $\eta = 0.218 \text{ Nsm}^{-1}$, and $\eta = 0.436 \text{ Nsm}^{-1}$. The analysis is performed for variation in the non-dimensional resistor constant α , the non-dimensional inductor constant β , and the electromechanical coupling θ . The two constants are chosen as the resistor and the

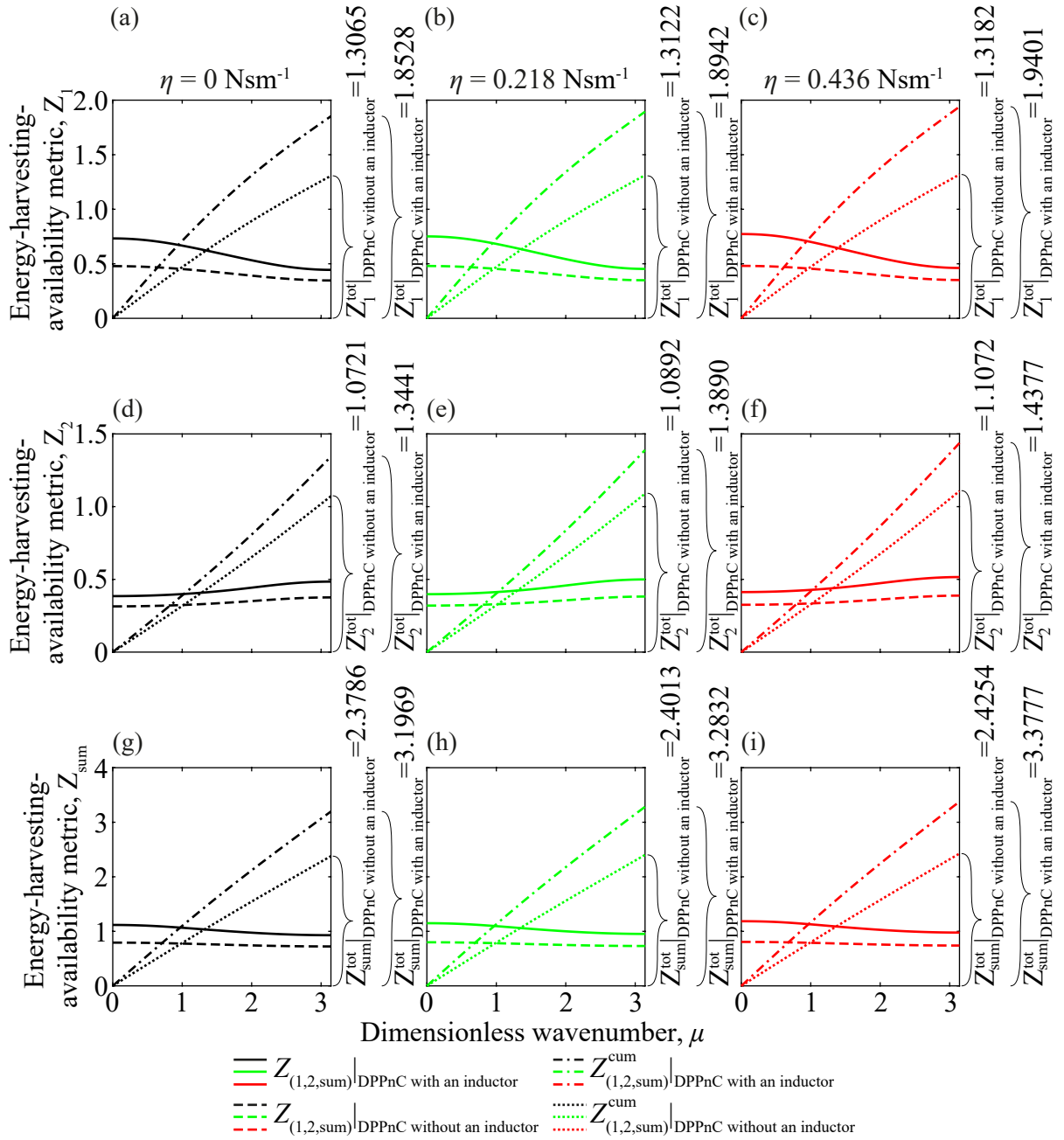


Figure 5.13: Diatomic models: energy-harvesting availability metrics $Z_1(\mu)$, $Z_2(\mu)$, and $Z_{\text{sum}}(\mu)$ and the corresponding cumulative values $Z_1^{\text{cum}}(\mu)$, $Z_2^{\text{cum}}(\mu)$, and $Z_{\text{sum}}^{\text{cum}}(\mu)$ associated with the damping ratios ζ_1 (acoustic branch) and ζ_2 (optical branch) and summation of the two branches ζ_{sum} , respectively. The results are presented for prescribed damping levels (a) $\eta = 0 \text{ Nsm}^{-1}$, (b) $\eta = 0.218 \text{ Nsm}^{-1}$, and (c) $\eta = 0.436 \text{ Nsm}^{-1}$.

inductor are key components within a shunt circuit, and the electromechanical coupling is

chosen as it influences the conversion efficiency of the useful dissipative energy, i.e., the mechanical/vibrational energy, into electrical energy.

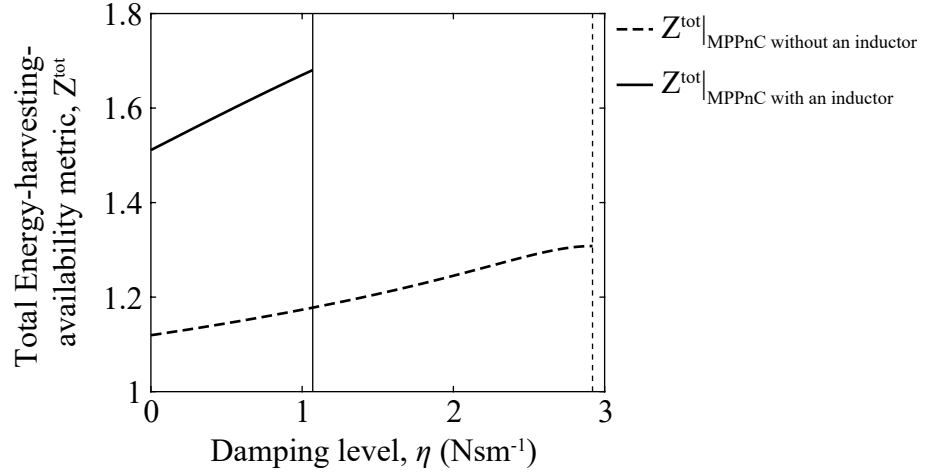


Figure 5.14: Monoatomic models: Variation of the total energy-harvesting-availability metric Z^{tot} with the prescribed damping level η ($\eta = C_1 = C_2$) for the monoatomic piezoelectric phononic crystal (MPPnC) without an inductor and the monoatomic piezoelectric phononic crystal (MPPnC) with an inductor.

Figure 5.14 shows the variation of Z^{tot} with changes in the prescribed damping level η while keeping fixed all the other parameters given in table 5.1. As observed in figure 5.10, it is evident that increasing the level of prescribed damping improves the energy-harvesting availability and the rate of this improvement is higher when the MPPnC incorporates an inductor. The prescribed damping levels have been carefully chosen for the analysis such that the MPPnCs do not become overdamped and remain in the regime of oscillatory free vibrations. An η value that renders the MPPnCs overdamped is considered as the cut-off prescribed damping threshold. It is observed that this threshold is $\eta = 2.92 \text{ Nsm}^{-1}$ for the MPPnC without an inductor and $\eta = 1.07 \text{ Nsm}^{-1}$ for the MPPnC with an inductor. This points to the ability of the MPPnC chain consisting of piezoelectric elements with purely resistive shunt circuits to endure more prescribed damping than the MPPnC chain consisting of piezoelectric elements with inductor-equipped shunt circuits while still sustaining a vibratory response character. However, as noted earlier, the presence of an inductor significantly increases the energy-harvesting availability.

Figure 5.15 shows the variation of Z^{tot} as a function of the non-dimensional resistor constant α for the MPPnCs. Since this quantity is defined as $\alpha = \bar{\omega}C_pR$, its value is varied by altering the value of the resistance R while keeping the rest of the parameters in table 5.1 constant. The value of R is varied between 10000 Ohms to 500000 Ohms in steps of 1000. Table 5.3 presents the optimal values of α and the corresponding maximum Z^{tot} values

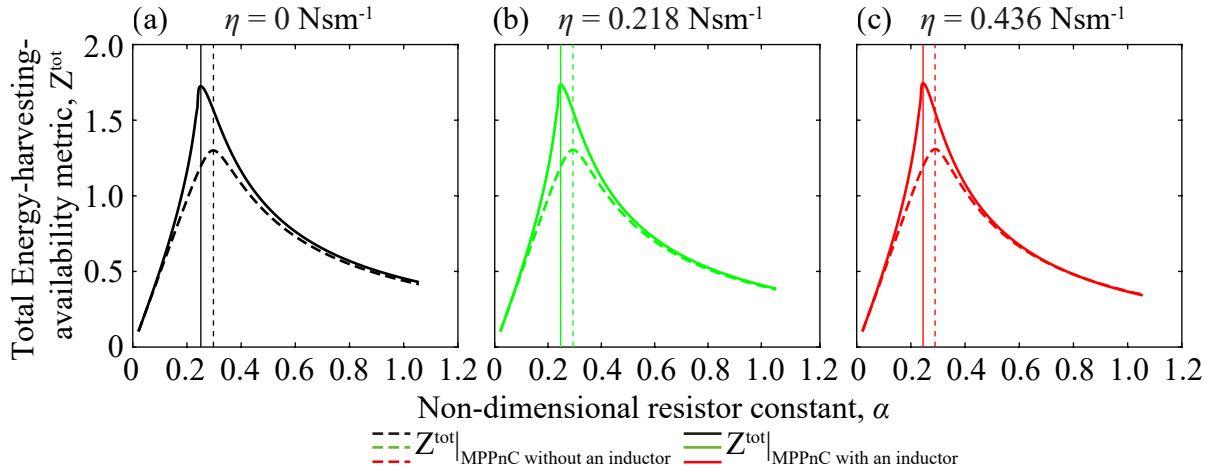


Figure 5.15: Monoatomic models: variation of the total energy-harvesting-availability metric Z^{tot} with the non-dimensional resistor constant α for the monoatomic piezoelectric phononic crystal (MPPnC) without an inductor and the monoatomic piezoelectric phononic crystal (MPPnC) with an inductor at prescribed damping levels (a) $\eta = 0 \text{ Nsm}^{-1}$, (b) $\eta = 0.218 \text{ Nsm}^{-1}$, and (c) $\eta = 0.436 \text{ Nsm}^{-1}$.

Table 5.3: Monoatomic models: optimal values of the non-dimensional resistor constant α for the monoatomic piezoelectric phononic crystal (MPPnC) without an inductor and the monoatomic piezoelectric phononic crystal (MPPnC) with an inductor at the three prescribed damping levels η .

MPPnC	η (Nsm^{-1})	optimal α	maximum Z^{tot}
without an inductor	0	0.2978	1.2999
	0.218	0.2935	1.3041
	0.436	0.2893	1.3084
with an inductor	0	0.2513	1.7249
	0.218	0.2471	1.7345
	0.436	0.2450	1.7446

for the two MPPnCs at the three chosen prescribed damping levels. It is noticed that for all three levels, the optimal value of α for the MPPnC with an inductor is lower compared to the MPPnC without an inductor, and as η increases, the optimal value of α decreases slightly for the two MPPnC models. As for the maximum Z^{tot} value for the two MPPnC models, its value appears to increase but fairly modestly with increase in η . From $\alpha \approx 0.6$ onwards, it can be noticed in figure 5.15 that $Z^{\text{tot}}|_{\text{MPPnC without an inductor}}$ begins to increase as η increases and appears to be on a trajectory to surpass $Z^{\text{tot}}|_{\text{MPPnC with an inductor}}$ at higher prescribed damping levels.

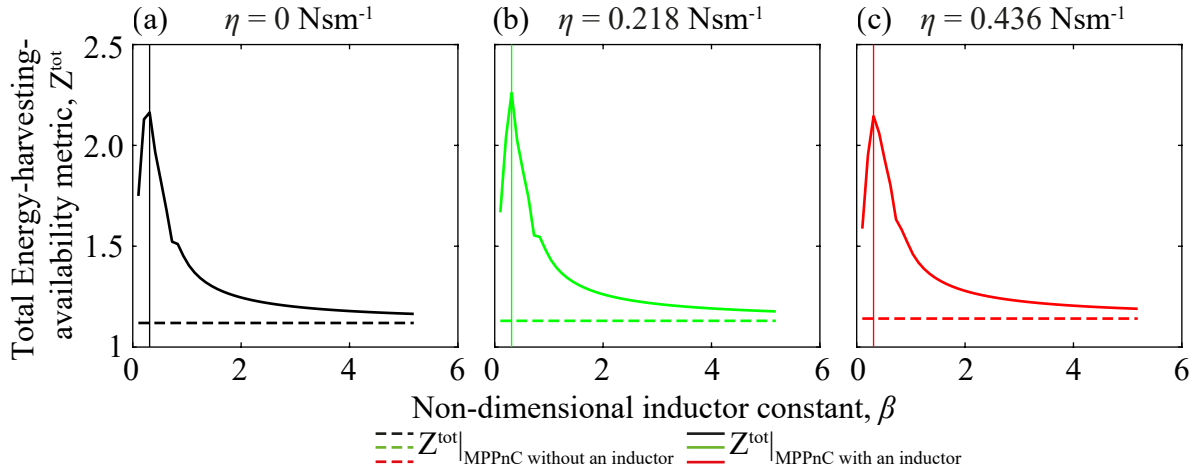


Figure 5.16: Monoatomic models: variation of the total energy-harvesting-availability metric Z^{tot} with the non-dimensional inductor constant β for the monoatomic piezoelectric phononic crystal (MPPnC) with an inductor at prescribed damping levels (a) $\eta = 0 \text{ Nsm}^{-1}$, (b) $\eta = 0.218 \text{ Nsm}^{-1}$, and (c) $\eta = 0.436 \text{ Nsm}^{-1}$.

Table 5.4: Monoatomic models: optimal values of the non-dimensional inductor constant β for the monoatomic piezoelectric phononic crystal (MPPnC) with an inductor at the three prescribed damping levels η .

MPPnC	η (Nsm^{-1})	optimal β	maximum Z^{tot}
with an inductor	0	0.3111	2.1631
	0.218	0.3111	2.2604
	0.436	0.3111	2.1451

Figure 5.16 shows the variation of Z^{tot} as the dimensionless inductor constant β varies for the MPPnCs. Since $\beta = \bar{\omega}^2 C_p L$, the value of β is varied by changing the value of the inductance L while keeping the rest of the parameters in table 5.1 constant. The value of L is varied between 100 H to 5000 H in steps of 100. Table 5.4 presents the optimal values of β and the corresponding maximum Z^{tot} values for the MPPnC with an inductor at the three chosen prescribed damping levels. It is seen that, for the chosen parameter set, the optimal value of β is 0.3111 for the three selected prescribed damping levels. As η increases, there is no unique trend in the maximum values of $Z^{\text{tot}}|_{\text{MPPnC with an inductor}}$. The relationship between L and η is important due to the fact that coupling any inductance with a high damping level has a tendency to push the system towards critical damping and eventually make the system overdamped. The figures broach that, for the case of MPPnC with an inductor, favourable energy-harvesting availability can be achieved at lower β values and low to moderate prescribed damping levels.

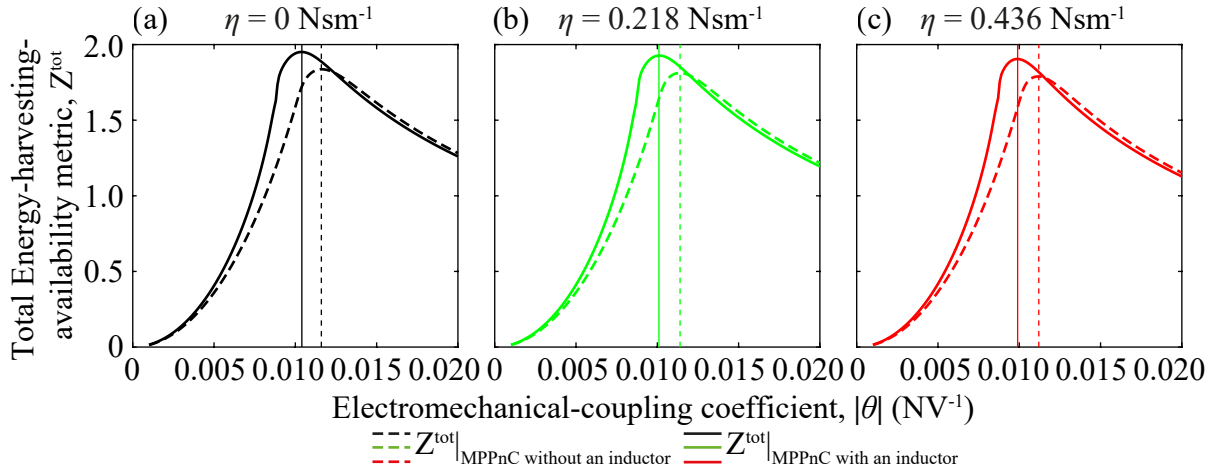


Figure 5.17: Monoatomic models: variation of the total energy-harvesting-availability metric Z^{tot} with the electromechanical coupling θ for the monoatomic piezoelectric phononic crystal (MPPnC) without an inductor and the monoatomic piezoelectric phononic crystal (MPPnC) with an inductor at prescribed damping levels (a) $\eta = 0 \text{ Nsm}^{-1}$, (b) $\eta = 0.218 \text{ Nsm}^{-1}$, and (c) $\eta = 0.436 \text{ Nsm}^{-1}$.

Table 5.5: Monoatomic models: optimal values of the electromechanical coupling θ for the monoatomic piezoelectric phononic crystal (MPPnC) without an inductor and the monoatomic piezoelectric phononic crystal (MPPnC) with an inductor at the three prescribed damping levels η .

MPPnC	η (Nsm^{-1})	optimal θ (NV^{-1})	maximum Z^{tot}
without an inductor	0	0.0116	1.8365
	0.218	0.0114	1.8123
	0.436	0.0112	1.7888
with an inductor	0	0.0104	1.9509
	0.218	0.0101	1.9271
	0.436	0.0099	1.9044

Figure 5.17 shows the variation of Z^{tot} as the electromechanical coupling θ varies for the MPPnCs. The value of θ , while keeping constant the rest of the parameters in table 5.1, is varied from $-1 \times 10^{-3} \text{ NV}^{-1}$ to $-20 \times 10^{-3} \text{ NV}^{-1}$ in steps of -0.1×10^{-3} . Table 5.5 shows the optimal values of θ and the corresponding maximum Z^{tot} values for the two MPPnCs at the three selected prescribed damping levels. For both the MPPnCs, it is observed that, as η increases, the optimal θ decreases but insignificantly and the maximum Z^{tot} decreases slightly. For all the three prescribed damping levels, optimal θ is lower for the MPPnC with an inductor than the MPPnC without an inductor. Beyond the optimal value of θ for the

MPPnC without an inductor, the maximum Z^{tot} is higher for the MPPnC without an inductor compared to the MPPnC with an inductor indicating higher energy-harvesting availability. From these results, it can be deduced that it is favourable to use an MPPnC with an inductor at lower values of θ ; although, the decrease in performance at higher values of θ , in comparison to an MPPnC without an inductor, is only relatively small.

5.6.2 Diatomic piezoelectric phononic crystals

In this section, the behaviour of $Z_{\text{sum}}^{\text{tot}}$ associated to the DPPnC models, purely resistive and inductor-equipped, is elaborated at the three selected prescribed damping levels, namely, $\eta = 0 \text{ Nsm}^{-1}$, $\eta = 0.218 \text{ Nsm}^{-1}$, and $\eta = 0.436 \text{ Nsm}^{-1}$. The parametric analysis is performed for variation in the non-dimensional resistor constants α_1 and α_2 , the non-dimensional inductor constants β_1 and β_2 , and the electromechanical coupling values θ_1 and θ_2 .

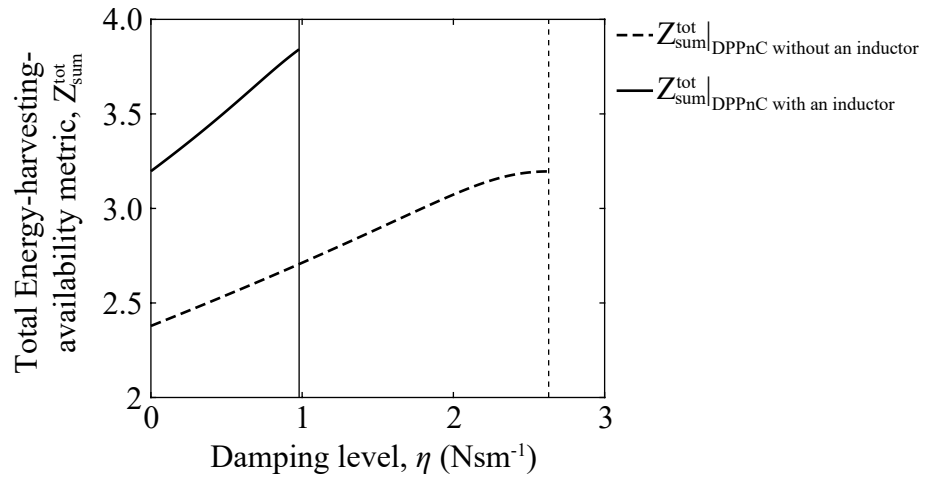


Figure 5.18: Diatomic models: Variation of the total energy-harvesting-availability metric $Z_{\text{sum}}^{\text{tot}}$ with the prescribed damping level η ($\eta = C_1 = C_2 = C_3 = C_4$) for the diatomic piezoelectric phononic crystal (DPPnC) without an inductor and the diatomic piezoelectric phononic crystal (DPPnC) with an inductor.

Figure 5.18 shows the variation of $Z_{\text{sum}}^{\text{tot}}$, as η changes, while the other parameters given in table 5.2 remain unaltered. It is discerned that the cut-off value for the prescribed damping level is 2.63 Nsm^{-1} for the DPPnC without an inductor and 0.98 Nsm^{-1} for the DPPnC with an inductor. It is again shown that higher useful dissipation is achieved by using a shunt circuit with an inductor at a relatively lower damping level (half of that required for the DPPnC without an inductor).

Figure 5.19 shows the variation of $Z_{\text{sum}}^{\text{tot}}$ as α_1 and α_2 varies for the DPPnCs. Procedure similar to the monoatomic case is employed to obtain the optimal values; i.e., R_1 and

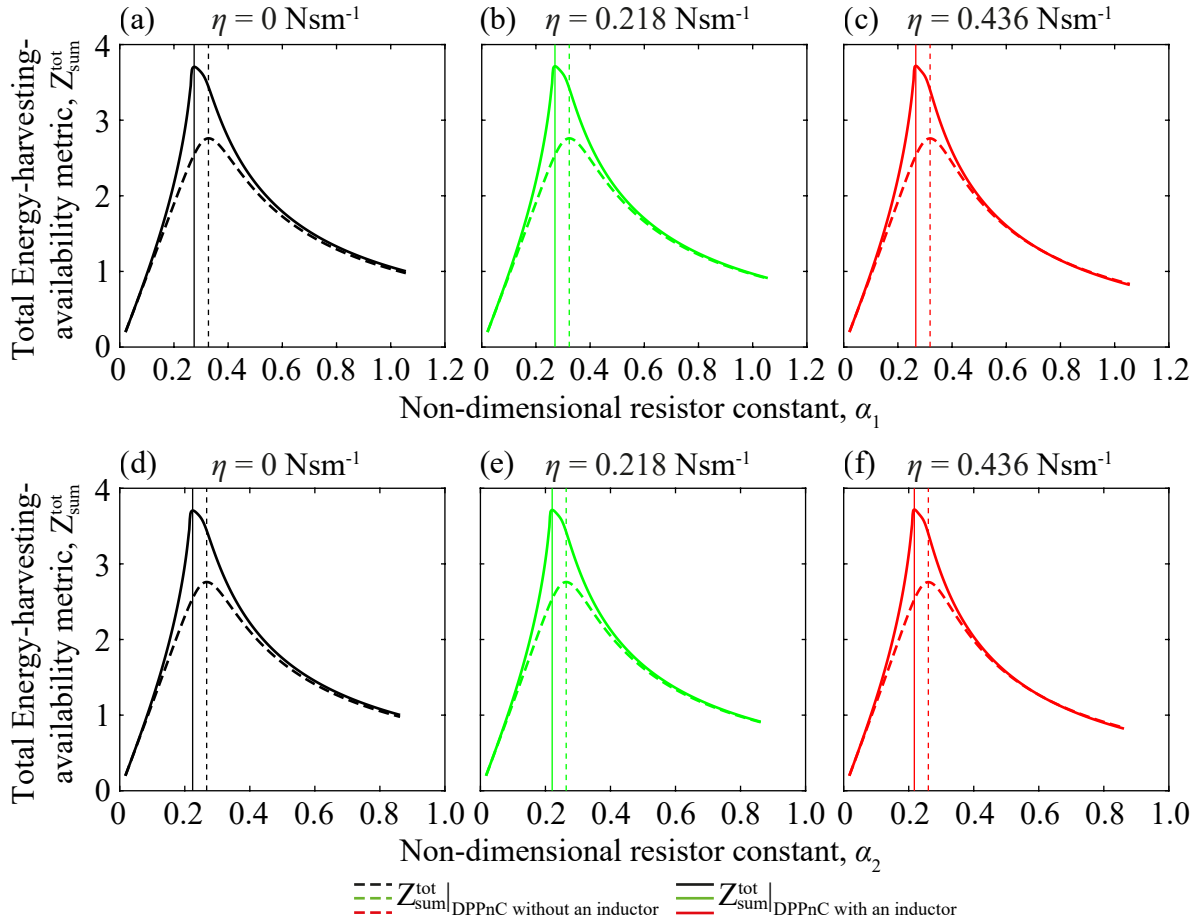


Figure 5.19: Diatomic models: variation of the total energy-harvesting-availability metric $Z_{\text{sum}}^{\text{tot}}$ with the non-dimensional resistor constants α_1 and α_2 for the diatomic piezoelectric phononic crystal (DPPnC) without an inductor and the diatomic piezoelectric phononic crystal (DPPnC) with an inductor at prescribed damping levels (a) $\eta = 0 \text{ Nsm}^{-1}$, (b) $\eta = 0.218 \text{ Nsm}^{-1}$, and (c) $\eta = 0.436 \text{ Nsm}^{-1}$.

R_2 are simultaneously and equally varied from 10000 Ohms to 500000 Ohms in steps of 1000. Table 5.5 displays the optimal values of α_1 and α_2 and the corresponding maximum $Z_{\text{sum}}^{\text{tot}}$ values for the two DPPnCs at the three damping levels. A trend similar to the monoatomic case is observed. For the three damping levels, the optimal values of α_1 and α_2 for the DPPnC with an inductor are lower compared to the DPPnC without an inductor. As η increases, the optimal values of α_1 and α_2 slightly decrease; the maximum values of $Z_{\text{sum}}^{\text{tot}}|_{\text{DPPnC without an inductor}}$ slightly decrease; and the maximum values of $Z_{\text{sum}}^{\text{tot}}|_{\text{DPPnC with an inductor}}$ marginally increase. However, it can be noticed in figure 5.19 that from $\alpha \approx 0.6$ onwards, $Z_{\text{sum}}^{\text{tot}}|_{\text{DPPnC without an inductor}}$ begins to increase and appears to be on a trajectory to surpass $Z_{\text{sum}}^{\text{tot}}|_{\text{DPPnC with an inductor}}$ at higher η values.

Table 5.6: Diatomic models: optimal values of the non-dimensional resistor constants α_1 and α_2 for the diatomic piezoelectric phononic crystal (DPPnC) without an inductor and the diatomic piezoelectric phononic crystal (DPPnC) with an inductor at the three prescribed damping levels η .

DPPnC	η (Nsm ⁻¹)	optimal α_1	optimal α_2	maximum $Z_{\text{sum}}^{\text{tot}}$
without an inductor	0	0.3273	0.2673	2.7599
	0.218	0.3231	0.2638	2.7598
	0.436	0.3189	0.2604	2.7587
with an inductor	0	0.2745	0.2241	3.7051
	0.218	0.2703	0.2207	3.7132
	0.436	0.2661	0.2173	3.7184

Table 5.7: Diatomic models: optimal values of the non-dimensional inductor constants β_1 and β_2 for the diatomic piezoelectric phononic crystal (DPPnC) with an inductor at the three prescribed damping levels η .

DPPnC	η (Nsm ⁻¹)	optimal β_1	optimal β_2	maximum $Z_{\text{sum}}^{\text{tot}}$
with an inductor	0	0.3111	0.2074	4.5976
	0.218	0.3111	0.2074	4.4154
	0.436	0.4148	0.2765	4.5744

Figure 5.20 shows the variation of $Z_{\text{sum}}^{\text{tot}}$ as β_1 and β_2 vary for the diatomic piezoelectric PnCs. An exercise similar to the monoatomic case is carried out to obtain the optimal values; i.e, L_1 and L_2 are simultaneously and equally varied from 100 H to 5000 H in steps of 100. Table 5.7 shows the optimal values of β_1 and β_2 and the corresponding maximum $Z_{\text{sum}}^{\text{tot}}$ values for the DPPnC with an inductor at the three prescribed damping levels. The optimal β_1 and β_2 are the same for $\eta = 0$ Nsm⁻¹ and $\eta = 0.218$ Nsm⁻¹ but increase for $\eta = 0.436$ Nsm⁻¹, which shows that as the prescribed raw damping level increases considerably, the optimal values of β_1 and β_2 will also increase. As η increases, there is no consistent trend in the maximum values of $Z_{\text{sum}}^{\text{tot}}|_{\text{DPPnC with an inductor}}$. The figures indicate that favourable energy-harvesting availability can be achieved at lower β values and prescribed damping levels.

Finally, figure 5.21 presents the variation of $Z_{\text{sum}}^{\text{tot}}$ as a function of θ for the two DPPnC models. An exercise similar to the monoatomic case is carried out to obtain the optimal values; i.e, θ_1 and θ_2 are simultaneously and equally varied from -1×10^{-3} NV⁻¹ to -20×10^{-3} NV⁻¹ in steps of -0.1×10^{-3} . Table 5.8 lists the optimal values of θ_1 and θ_2 and the corresponding maximum $Z_{\text{sum}}^{\text{tot}}$ values for the two DPPnCs at the three prescribed

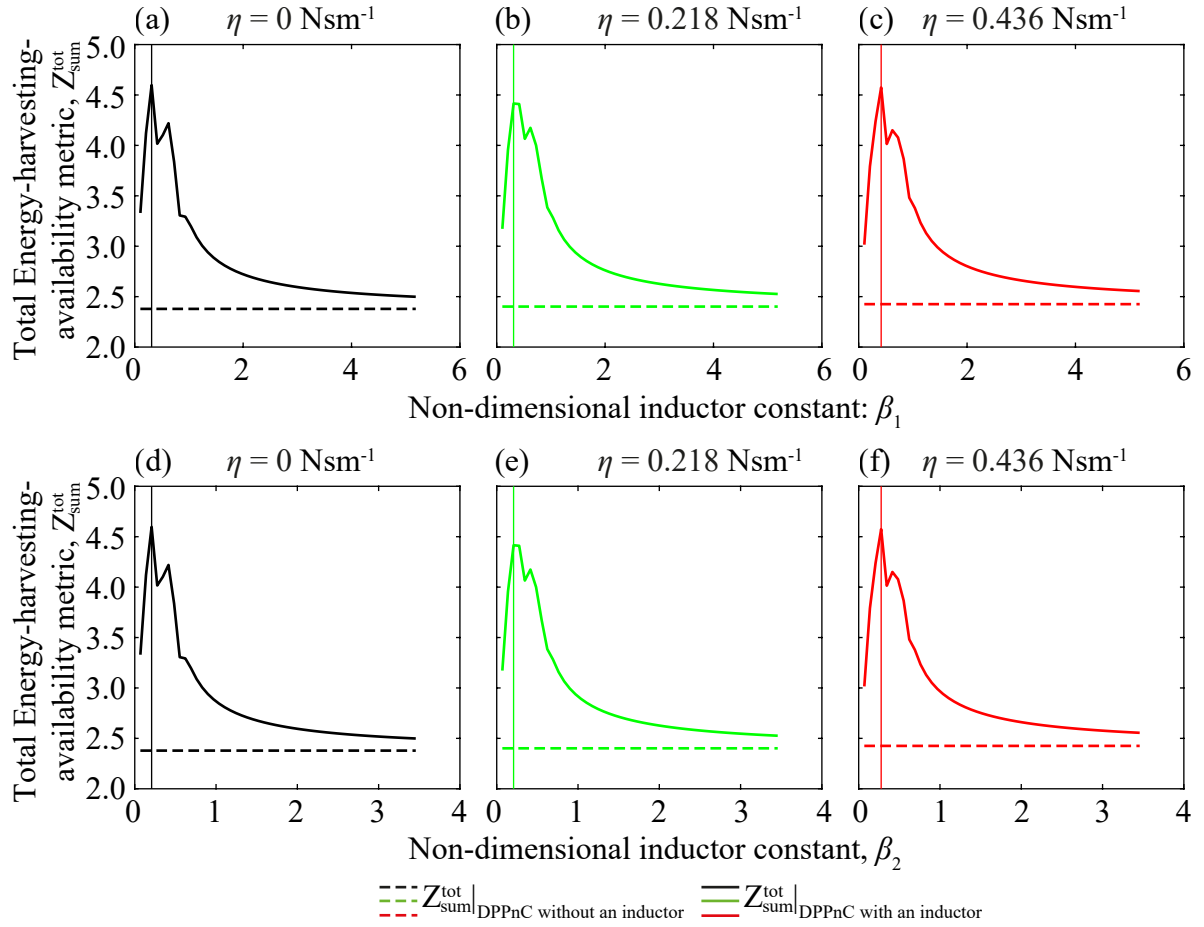


Figure 5.20: Diatomic models: variation of the total energy-harvesting-availability metric $Z_{\text{sum}}^{\text{tot}}$ with the non-dimensional inductor constants β_1 and β_2 for the diatomic piezoelectric phononic crystal (DPPnC) with an inductor at prescribed damping levels (a) $\eta = 0 \text{ Nsm}^{-1}$, (b) $\eta = 0.218 \text{ Nsm}^{-1}$, and (c) $\eta = 0.436 \text{ Nsm}^{-1}$.

damping levels. For both the DPPnCs, it is observed that, as η increases, the optimal values of θ_1 and θ_2 and the maximum $Z_{\text{sum}}^{\text{tot}}$ values decrease, although, insignificantly. At all the three prescribed damping levels, the optimal θ_1 and θ_2 values are insignificantly lower for the DPPnC with an inductor compared to the DPPnC without an inductor. Beyond the optimal values of θ_1 and θ_2 for the DPPnC without an inductor, $Z_{\text{sum}}^{\text{tot}}$ is higher for the DPPnC without an inductor, indicating higher energy-harvesting availability compared to the DPPnC with an inductor. From the plots, it can be inferred that it is favourable to use a DPPnC with an inductor at lower values of θ_1 and θ_2 with very modest comparative gains; nonetheless, the decrease in performance at higher values of θ_1 and θ_2 , in comparison to a DPPnC without an inductor, is only relatively small.

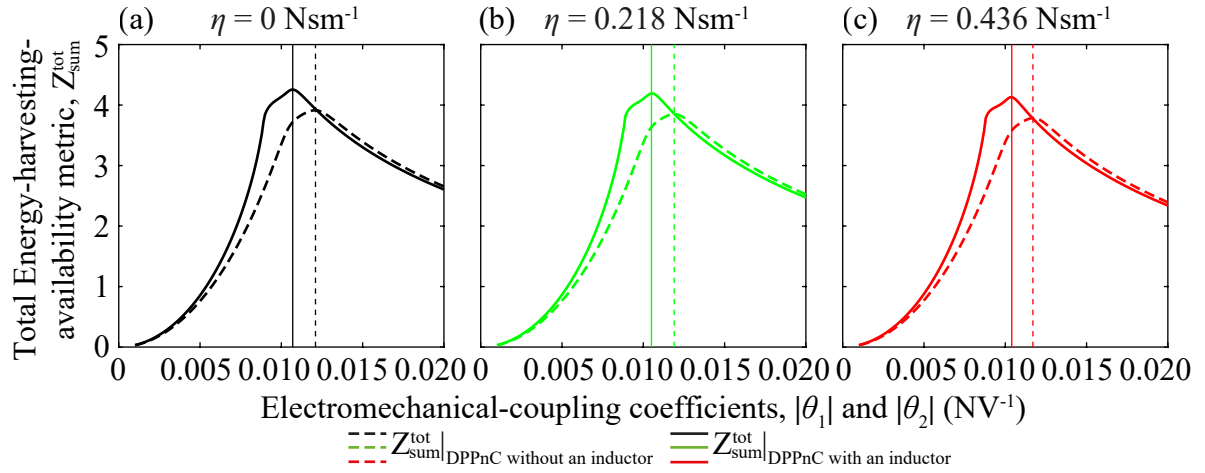


Figure 5.21: Diatomic models: variation of the total energy-harvesting-availability metric $Z_{\text{sum}}^{\text{tot}}$ with the electromechanical coupling values θ_1 and θ_2 for the diatomic piezoelectric phononic crystal (DPPnC) without an inductor and the diatomic piezoelectric phononic crystal (DPPnC) with an inductor at prescribed damping levels (a) $\eta = 0 \text{ Nsm}^{-1}$, (b) $\eta = 0.218 \text{ Nsm}^{-1}$, and (c) $\eta = 0.436 \text{ Nsm}^{-1}$.

Table 5.8: Diatomic models: optimal values of the electromechanical coupling values θ_1 and θ_2 for the diatomic piezoelectric phononic crystal (DPPnC) without an inductor and the diatomic piezoelectric phononic crystal (DPPnC) with an inductor at the three prescribed damping levels η .

DPPnC	η (Nsm^{-1})	optimal θ_1 (NV^{-1})	optimal θ_2 (NV^{-1})	maximum $Z_{\text{sum}}^{\text{tot}}$
without an inductor	0	0.0121	0.0121	3.9136
	0.218	0.0119	0.0119	3.8053
	0.436	0.0117	0.0117	3.7863
with an inductor	0	0.0107	0.0107	4.2564
	0.218	0.0105	0.0105	4.1938
	0.436	0.0104	0.0104	4.1309

5.7 Summary and Conclusions

Phononic crystals (PnCs) with piezoelectric patches are capable of harvesting energy from natural and artificial vibrations. In this chapter, an original approach is proposed for quantifying the intrinsic energy-harvesting availability—a new measure—for a given phononic crystal unit-cell configuration with shunted piezoelectric-elements. This is done by analytically evaluating the difference between the wavenumber-dependent damping ratio for a piezoelectric PnC and a corresponding statically equivalent non-piezoelectric PnC. This represents a rigor-

ous BZ characterization approach. The intrinsic energy-harvesting availability is a quantity representative of the intrinsic energy available for harvesting in the form of useful dissipation introduced by the shunted piezoelectric elements. Unlike the prevailing approach that examines the extrinsic piezoelectric energy-harvesting capacity—performance—of forced finite structures, the proposed approach is based on a material’s perspective; i.e., no forcing is considered nor are the overall structure size and global boundary conditions.

Four unique cases have been investigated by way of demonstration of the new measure, namely, monoatomic piezoelectric PnC (MPPnC) without an inductor, monoatomic piezoelectric PnC (MPPnC) with an inductor, diatomic piezoelectric PnC (DPPnC) without an inductor, and diatomic piezoelectric PnC (DPPnC) with an inductor. All PnC models are suspended, but the analysis is not restricted to suspended systems. The intrinsic analysis described in the present chapter can be imposed upon other well-known types of periodic media with and without a grounding or suspension mechanism, for example, locally resonant metamaterial (LRM) and inertially amplified locally resonant metamaterial (IALRM), introduced in chapter 3. The characteristic equation corresponding to each of the cases has been obtained in closed form. It is shown that the addition of piezoelectric elements (piezo patches) to the monoatomic and diatomic PnCs admitting free wave motion introduces “useful” dissipation, which is essentially the measure mentioned above as a representation of the amount of energy intrinsically available for harvesting (i.e., the energy that otherwise would be dissipated into the environment). The amount of raw dissipation introduced by means of prescribed damping has also been quantified (i.e., the energy that gets dissipated into the environment in any case). The specific technical contributions in this chapter are summarized as follows:

- Using Bloch’s theorem, a formal characterization of the intrinsic energy-harvesting availability—expressed using the $Z(\mu)$ metric—of piezoelectric PnCs under free wave motion has been presented.
- Cut-off prescribed damping levels for the piezoelectric PnCs to maintain vibration oscillations have been quantified for a given set of parameters.
- Introduction of an inductor in the shunt circuits of the piezoelectric elements attached to the PnCs is demonstrated to substantially increase the energy-harvesting availability.
- For maximum energy-harvesting availability, optimal values of key non-dimensional electrical design parameters, widely employed in the piezoelectric energy-harvesting literature, and the electromechanical coupling have been computed. This parameter search was driven by the new measure of energy-harvesting availability.

- For the parameters chosen, the DPPnC generally exhibits higher intrinsic energy-harvesting availability than the MPPnC when comparing the first damping-ratio branch of the former with the sole damping-ratio branch of the latter, particularly at high dimensionless wavenumbers.

The proposed theory provides a fundamental intrinsic characterization method for the design and/or selection of piezoelectric energy-harvesting materials from which structures/devices may be formed. The underlying approach for quantifying intrinsic energy-harvesting availability will be useful in formally and generally comparing, categorising, and designing future energy-harvesting phononic materials, including other novel types of phononic crystals and elastic metamaterials.

Different configurations from among the vast body of research investigating phononic crystals and elastic metamaterials [29–31, 126] may be investigated for intrinsic energy-harvesting availability. Chapter 7 delves into quantifying this intrinsic quantity for a locally resonant piezoelectric metamaterial (LRPM) and an inertially amplified locally resonant piezoelectric metamaterial (IALRPM) and comparing it with that of a statically equivalent DPPnC in order to assess the inherent superiority of a specific piezoelectric periodic material/media; this process can significantly influence the design process of energy-harvesting electromechanical structures. The proposed concept of energy-harvesting availability may also be investigated in various types of piezoelectric periodic media with other types of raw damping, e.g., viscoelastic damping in polymers and hysteretic materials. For viscoelastic analysis, the governing equations pertaining to the piezoelectric periodic media can be treated with the state-space formulation in the manner described in the work by Frazier *et al.* [115] to obtain an eigenvalue problem and, consequently, create dispersion and damping-ratio diagrams. However, given the inferior dissipation performance of viscoelastic damping compared to viscous damping, as shown by Frazier *et al.*, it can be deduced that piezoelectric periodic media with raw damping of the former type will exhibit a higher energy-harvesting availability compared to the same piezoelectric periodic media with raw damping of the latter type.

While the concept configurations presented appear large-scale and bulky and only lumped-parameter models are investigated, future research will easily adapt this new characterization method to (1) small-scale miniaturized piezoelectric-material systems and (2) more complex models. The existing literature on energy harvesting generally involves a finite structure that is exposed to either a harmonic or impulse excitation and perhaps subject to boundary conditions. In this chapter, the investigation has been carried out and the results have been presented from a theoretical perspective instead of an experimental perspective; i.e., the piezoelectric phononic crystals are considered to be independent of sizing, forcing, and

boundary conditions. All the piezoelectric models discussed in this chapter are linear, so scaling the electrical parameters, within reasonable limits, in any direction would lead to a linear variation in the results. The objective of the present chapter has been to visually elaborate a new criterion for analysing energy harvesting by looking at the problem from a periodic material's perspective (with no defined boundaries) rather than from a finite periodic structure's perspective; hence, the system parameters have been carefully chosen to demonstrate a marked difference between the results for the piezoelectric PnCs without an inductor and the piezoelectric PnCs with an inductor. The contents of the present chapter are contained within the following peer-reviewed publication:

- **Patrick I**, Adhikari S, and Hussein MI. Brillouin-zone characterization of piezoelectric material intrinsic energy-harvesting availability. *Smart Materials and Structures*, **30**(8):085022, 2021, doi.org/10.1088/1361-665X/ac0c2c.

Chapter 6

Metadamping in inertially amplified materials: Trade-off between spatial attenuation and temporal attenuation

6.1 Introduction

In structural dynamics, dissipation control and its means of implementation are key design factors. Dissipation is a measure of loss of energy as a function of time. In a finite structure, the dissipation characteristics have a spatial and frequency, i.e., spatio-temporal, dependency. In an infinite medium, such as a waveguide or a structured material, dissipation also exhibits a wavenumber (reader may refer to chapter 3) or wavevector (reader may refer to chapter 4) dependency [46, 119, 127, 128]. Representation of dissipation as an *intrinsic wavenumber-dependent quantity* provides a fundamental measure independent of global dimensions, boundary conditions, and nature of forcing. This measure is obtained by considering a representative unit cell of the medium of interest, applying Bloch's theorem to the governing equations of motion, and calculating the wavenumber-dependent damping ratio alongside the wavenumber-dependent damped frequency. Upon complete integration of each damping ratio branch over the irreducible Brillouin zone (IBZ), a cumulatively computed total measure of dissipation is obtained, which provides a measure of the branch-specific total damping capacity of the medium or material under consideration [79]. Upon performing the aforementioned exercise after summing over all the damping-ratio branches, the overall damping capacity of the medium or material under consideration is obtained.

The investigation of dissipation in periodic (phononic) materials carries significant importance with regards to energy harvesting as the inherent (intrinsic) dissipation characteristics

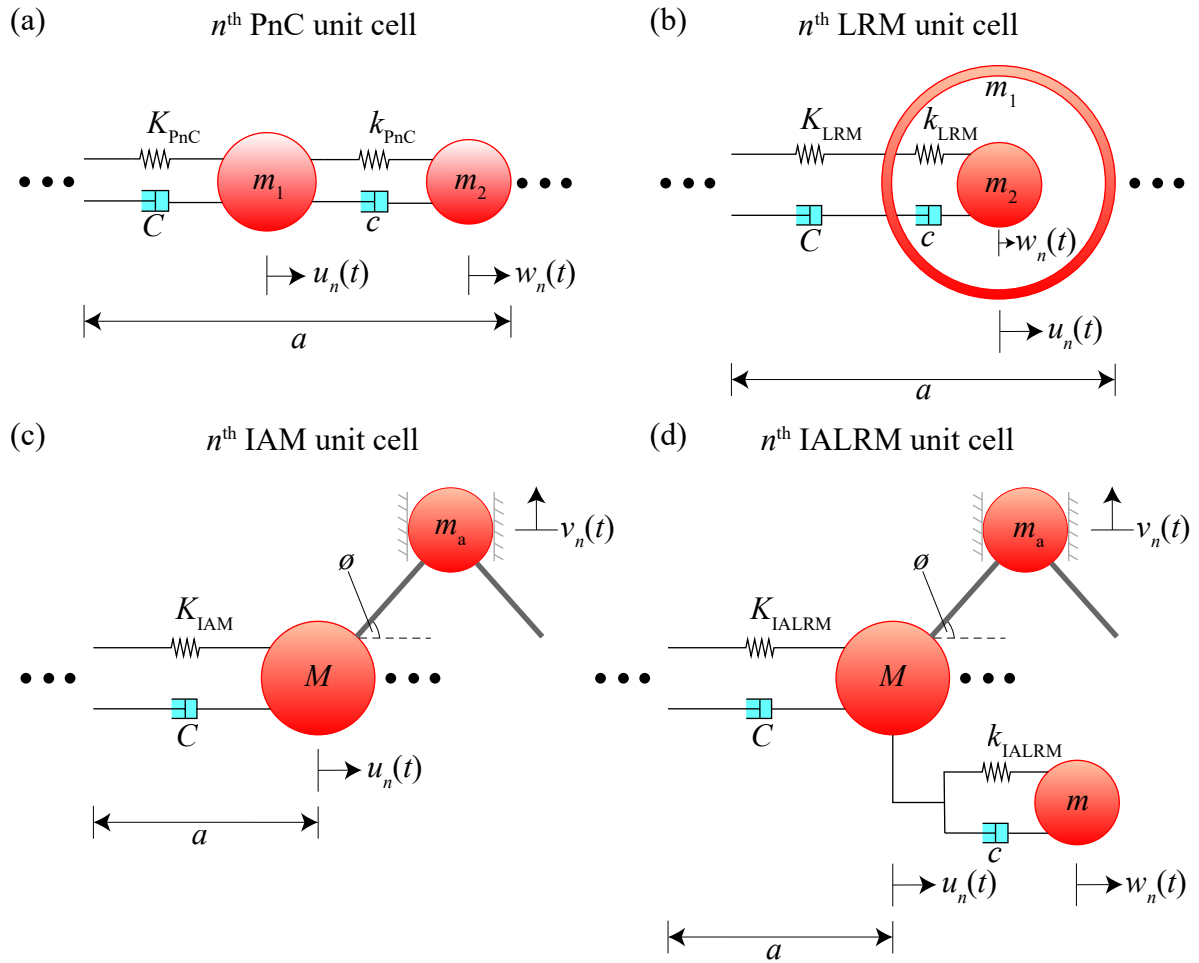


Figure 6.1: Unit-cell schematics of (a) a diatomic phononic crystal (PnC), (b) a locally resonant metamaterial (LRM), (c) an inertially amplified material (IAM), and (d) an inertially amplified locally resonant metamaterial (IALRM).

of a material determine the energy-harvesting capabilities of an electromechanical structure constructed from the same material. Diverse categories of phononic materials exhibit distinct levels of inherent dissipation, which is dependent upon the material's internal configuration or microstructure. This quantity of intrinsic dissipation is referred to as "loss" and inevitably dissipates during the energy-harvesting process within a piezoelectric electromechanical structure designed using a particular phononic material, thereby remaining unharnessed. Nonetheless, a higher degree of intrinsic dissipation within the phononic material corresponds to enhanced energy-harvesting performance. This elevated level of intrinsic dissipation implies that the phononic material possesses an inherent disposition to effectively absorb and conceivably harvest a significant amount of vibrational energy, beyond the amount that is represented by the inherent dissipation. Consequently, this chapter serves

as a comprehensive review, demonstrating an emergence of intrinsic dissipation, known as metadamping, in a locally resonant metamaterial (LRM). Additionally, it highlights the phenomenon of an augmented emergence of intrinsic dissipation, i.e., enhanced metadamping, observed in an inertially amplified material (IAM) and inertially amplified locally resonant metamaterial (IALRM). Metadamping is the phenomenon of either enhanced or diminished intrinsic dissipation in a material stemming from the material's internal structural dynamics. It has previously been shown that an LRM, of the type depicted in figure 6.1(b), may be designed to exhibit higher or lower dissipation compared to a statically equivalent phononic crystal (PnC), of the type depicted in figure 6.1(a), with the same amount of prescribed damping. In the present chapter, it is revealed that even further dissipation, or alternatively further reduction of loss, may be achieved in an IAM and IALRM, of the types depicted in figures 6.1(c) and 6.1(d), respectively, compared to a statically equivalent PnC and LRM with the same amount of prescribed damping.

In the lumped-parameter models depicted in figure 6.1, n is used to identify the central unit cell under consideration and can be any non-zero positive integer in a finite lattice; M and m_{\dots} denote masses; K_{\dots} and k_{\dots} are the spring stiffness constants of the linear springs; C and c are the damping coefficients of the viscous dashpots; $u_n(t)$, $w_n(t)$, and $v_n(t)$ are displacements; ϕ is the angle between the rigid links and the central axis of the inertially amplified metamaterial; and a is the length of the unit-cells or the lattice spacing.

The current chapter investigates metadamping in an IAM [52–54, 56] and an IALRM. Inertial amplification contrasts with local resonance in that it involves a mechanical mechanism to provide a magnification of the “effective inertia” of the massive portions or components of the system. Unlike local resonance, an IALRM will exhibit a band gap also affected by an inertial coupling. This concept may be manifested using a lever-arm effect that allows the inertia of a given mass to be magnified to a degree proportional to the arm length. It is shown that an IALRM may be passively tuned to exhibit a significant further boost in the damping capacity (positive metadamping) or in the reduction of loss (negative metadamping) compared to the improvements attained by a statically equivalent locally resonant elastic metamaterial. This behaviour is examined in a one-dimensional chain model that encompasses both an inertial-amplifier mass and a local-resonance mass separately attached to the baseline mass [55]. This configuration yields a two degrees-of-freedom system with a bounded band gap that features two coupled resonances. In addition to the extreme metadamping behaviour, this configuration yields a novel regime whereby a trade-off between the intensities of temporal attenuation (dissipation) and spatial attenuation (band-gap behaviour) manifests. These findings have potentially far-reaching implications on the design of future phononic materials with tailored spatio-temporal attenuation characteristics.

6.2 Inertially amplified chains: physical configurations and mathematical models

6.2.1 Physical configurations

A one-dimensional infinite IAM, periodic chain, is considered, where the unit cell consists of a baseline mass M connected to the adjacent baseline masses by springs with stiffness K_{IAM} and viscous damping dashpots with damping constant C ; the spring and dashpot act in parallel. Each baseline mass is also connected to its neighbour by an inertial-amplifier attachment, which comprises of an auxiliary mass m_a , referred to as the inertial-amplifier mass, and rigid links; thus, the inertial-amplifier mass is connected to a pair of baseline masses by the rigid links. This inertial-amplifier mass plays the key role of inducing inertial amplification as its acceleration is amplified owing to the lever-based connecting mechanism.

In the one-dimensional infinite IALRM, the unit cell consists of a baseline mass M connected to the adjacent baseline masses by springs with stiffness K_{IALRM} and viscous damping dashpots with damping constant C . Each baseline mass has the same inertial-amplifier attachment described above. In addition, a single-degree-of-freedom linear mass resonator, comprising of a spring and viscous damping dashpot arranged in parallel, is attached to the baseline mass in a unit cell. The mass, spring stiffness, and damping coefficient associated with the resonator are m , k_{IALRM} , and c , respectively. The resonator's modal degree-of-freedom couples with the modal degree-of-freedom associated with the inertially amplified baseline mass; this creates a band gap with a double-attenuation peak in the imaginary part of the complex dispersion diagram; this aspect is discussed and analysed in the results sections.

6.2.2 Mathematical models

Forces on the baseline mass from the inertial-amplifier mass

For the n^{th} unit cell, the kinematic relationship between the acceleration of the auxiliary mass, main mass, and mass in the preceding unit cell, i.e., \ddot{v}_n (shown in figures 6.1(c) and 6.1(d)), \ddot{u}_n , and \ddot{u}_{n-1} , respectively, is expressed as

$$\ddot{v}_n = \frac{(\ddot{u}_n - \ddot{u}_{n-1})}{2} \cot \phi, \quad (6.1)$$

where ϕ is the angle between the central axis of the inertially amplified chains and the rigid links of the inertial-amplifier attachment. In equation (6.1), the number of overhead dots

indicates the order of derivative with respect to time. If $F_{(n,n-1)}$ is the force in the rigid links due to the net movement of the baseline masses in the n^{th} and $(n-1)^{\text{th}}$ unit cells then the net force on the rigid links is calculated by balancing the forces on the inertial-amplifier mass in the following manner:

$$2F_{(n,n-1)} \sin \phi = m_a \ddot{v}_n = m_a (\ddot{u}_n - \ddot{u}_{n-1}) \frac{\cot \phi}{2}. \quad (6.2)$$

Isolating $F_{(n,n-1)}$ in equation (6.2) yields

$$F_{(n,n-1)} = \frac{m_a (\ddot{u}_n - \ddot{u}_{n-1})}{4 \sin \phi \tan \phi}. \quad (6.3)$$

The component of the force acting from the inertial-amplifier mass onto the baseline mass stemming from the net movement of the baseline masses in the n^{th} and $(n-1)^{\text{th}}$ unit cells along the direction of the wave propagation is

$$\tilde{F}_{(n,n-1)} = F_{(n,n-1)} \cos \phi = \frac{m_a (\ddot{u}_n - \ddot{u}_{n-1}) \cos \phi}{4 \sin \phi \tan \phi} = \chi m_a (\ddot{u}_n - \ddot{u}_{n-1}), \quad (6.4)$$

where $\chi = \frac{1}{4 \tan^2 \phi}$. Similar to equation (6.4), by following the steps above, the component of the force acting from the inertial-amplifier mass onto the baseline mass owing to the net movement of the baseline masses in the n^{th} and $(n+1)^{\text{th}}$ unit cells along the direction of the wave propagation is

$$\tilde{F}_{(n+1,n)} = F_{(n+1,n)} \cos \phi = \frac{m_a (\ddot{u}_{n+1} - \ddot{u}_n) \cos \phi}{4 \sin \phi \tan \phi} = \chi m_a (\ddot{u}_{n+1} - \ddot{u}_n). \quad (6.5)$$

Equations of motion for the unit cells

The governing equation of motion for the baseline mass in the n^{th} unit cell of the IALRM is

$$M\ddot{u}_n + C(2\dot{u}_n - \dot{u}_{n-1} - \dot{u}_{n+1}) + c(\dot{u}_n - \dot{w}_n) + K_{\text{IALRM}}(2u_n - u_{n-1} - u_{n+1}) + k_{\text{IALRM}}(u_n - w_n) + \tilde{F}_{(n,n-1)} - \tilde{F}_{(n+1,n)} = 0. \quad (6.6)$$

Substituting equations (6.4) and (6.5) in equation (6.6) produces

$$M\ddot{u}_n + C(2\dot{u}_n - \dot{u}_{n-1} - \dot{u}_{n+1}) + c(\dot{u}_n - \dot{w}_n) + K_{\text{IALRM}}(2u_n - u_{n-1} - u_{n+1}) + k_{\text{IALRM}}(u_n - w_n) + \chi(m_a(\ddot{u}_n - \ddot{u}_{n-1})) - \chi(m_a(\ddot{u}_{n+1} - \ddot{u}_n)) = 0. \quad (6.7)$$

The governing equation of motion for the resonating mass in the n^{th} unit cell of the IALRM is

$$m\ddot{w}_n + c(\dot{w}_n - \dot{u}_n) + k_{IALRM}(w_n - u_n) = 0. \quad (6.8)$$

Equations (6.7) and (6.8) together constitute the governing equations for the n^{th} unit cell, depicted in figure 6.1(d), of the IALRM. By slightly modifying equation (6.7), the governing equation of motion for the baseline mass in the n^{th} unit cell, depicted in figure 6.1(c), of the IAM can be written as

$$M\ddot{u}_n + C(2\dot{u}_n - \dot{u}_{n-1} - \dot{u}_{n+1}) + K_{IALRM}(2u_n - u_{n-1} - u_{n+1}) + \chi(m_a(\ddot{u}_n - \ddot{u}_{n-1})) - \chi(m_a(\ddot{u}_{n+1} - \ddot{u}_n)) = 0. \quad (6.9)$$

To characterize the metadamping performance of the IAM and IALRM, a statically equivalent PnC and a statically equivalent LRM are considered. The governing equations for the n^{th} unit cell of the PnC depicted in figure 6.1(a) can be written as

$$m_1\ddot{u}_n + (C + c)\dot{u}_n - c\dot{w}_n - C\dot{w}_{n-1} + (K_{PnC} + k_{PnC})u_n - k_{PnC}w_n - K_{PnC}w_{n-1} = 0, \quad (6.10)$$

$$m_2\ddot{w}_n + (C + c)\dot{w}_n - c\dot{u}_n - C\dot{u}_{n+1} + (K_{PnC} + k_{PnC})w_n - k_{PnC}u_n - K_{PnC}u_{n+1} = 0. \quad (6.11)$$

The governing equations for the n^{th} unit cell of the LRM depicted in figure 6.1(b) can be written as

$$m_1\ddot{u}_n + C(2\dot{u}_n - \dot{u}_{n-1} - \dot{u}_{n+1}) + c(\dot{u}_n - \dot{w}_n) + K_{LRM}(2u_n - u_{n-1} - u_{n+1}) + k_{LRM}(u_n - w_n) = 0, \quad (6.12)$$

$$m_2\ddot{w}_n + c(\dot{w}_n - \dot{u}_n) + k_{LRM}(w_n - u_n) = 0. \quad (6.13)$$

As per Bloch's theorem, the plane-wave solution for the displacements of masses in a periodic unit cell can be written as

$$u_{n+g}(r, \mathbf{\kappa}; t) = \tilde{u}(t)e^{i\mu(n+g)}, \quad (6.14)$$

$$w_{n+g}(r, \mathbf{\kappa}; t) = \tilde{w}(t)e^{i\mu(n+g)}, \quad (6.15)$$

where $g \in [-\infty, \infty]$ is an integer used to locate and refer to any unit cell relative to the central unit cell under consideration, i.e., the n^{th} unit cell shown in figure 6.1; r is the one-dimensional position vector of the n^{th} unit cell; $i = \sqrt{-1}$ is the imaginary unit; and μ is the dimensionless wavenumber, which can be written as $\mu = \kappa a$, where κ (rad m⁻¹) is the wavenumber, and a (m) is the length of the lattice unit cell as described in figure 6.1. For

the central unit cell under consideration, $g = 0$ (n^{th} unit cell), and for the unit cells towards the left and right of the central unit cell, $g = -1$, and $g = +1$, respectively; i.e., they are the $(n-1)^{\text{th}}$ and $(n+1)^{\text{th}}$ unit cells.

Substituting equations (6.14) and (6.15) in equations (6.7) and (6.8), i.e., the governing equations for the n^{th} unit cell of the IALRM, yields the following Bloch-transformed homogeneous matrix equation for the displacement amplitudes \tilde{u} and \tilde{w} :

$$\begin{aligned} \begin{pmatrix} M + \frac{1}{2}m_a(1 - \cos\mu)\cot^2\phi & 0 \\ 0 & m \end{pmatrix} \begin{pmatrix} \ddot{\tilde{u}}_n \\ \ddot{\tilde{w}}_n \end{pmatrix} + \begin{pmatrix} c + 2C(1 - \cos\mu) & -c \\ -c & c \end{pmatrix} \begin{pmatrix} \dot{\tilde{u}}_n \\ \dot{\tilde{w}}_n \end{pmatrix} \\ + \begin{pmatrix} k_{IA} + 2K_{IA}(1 - \cos\mu) & -k_{IA} \\ -k_{IA} & k_{IA} \end{pmatrix} \begin{pmatrix} \tilde{u}_n \\ \tilde{w}_n \end{pmatrix} = \begin{pmatrix} 0 \\ 0 \end{pmatrix}. \end{aligned} \quad (6.16)$$

Substituting equations (6.14) and (6.15) in equations (6.10) and (6.11), i.e., the governing equations for the n^{th} unit cell of the PnC, yields the following Bloch-transformed homogeneous matrix equation for the displacement amplitudes \tilde{u} and \tilde{w} :

$$\begin{aligned} \begin{pmatrix} m_1 & 0 \\ 0 & m_2 \end{pmatrix} \begin{pmatrix} \ddot{\tilde{u}}_n \\ \ddot{\tilde{w}}_n \end{pmatrix} + \begin{pmatrix} C + c & -c - Ce^{-i\mu} \\ -c - Ce^{i\mu} & C + c \end{pmatrix} \begin{pmatrix} \dot{\tilde{u}}_n \\ \dot{\tilde{w}}_n \end{pmatrix} \\ + \begin{pmatrix} K_{\text{PnC}} + k_{\text{PnC}} & -k_{\text{PnC}} - K_{\text{PnC}}e^{-i\mu} \\ -k_{\text{PnC}} - K_{\text{PnC}}e^{i\mu} & K_{\text{PnC}} + k_{\text{PnC}} \end{pmatrix} \begin{pmatrix} \tilde{u}_n \\ \tilde{w}_n \end{pmatrix} = \begin{pmatrix} 0 \\ 0 \end{pmatrix}. \end{aligned} \quad (6.17)$$

Substituting equations (6.14) and (6.15) in equations (6.12) and (6.13), i.e., the governing equations for the n^{th} unit cell of the LRM, yields the following Bloch-transformed homogeneous matrix equation for the displacement amplitudes \tilde{u} and \tilde{w} :

$$\begin{aligned} \begin{pmatrix} m_1 & 0 \\ 0 & m_2 \end{pmatrix} \begin{pmatrix} \ddot{\tilde{u}}_n \\ \ddot{\tilde{w}}_n \end{pmatrix} + \begin{pmatrix} c + 2C(1 - \cos\mu) & -c \\ -c & c \end{pmatrix} \begin{pmatrix} \dot{\tilde{u}}_n \\ \dot{\tilde{w}}_n \end{pmatrix} \\ + \begin{pmatrix} k_{\text{LRM}} + 2K_{\text{LRM}}(1 - \cos\mu) & -k_{\text{LRM}} \\ -k_{\text{LRM}} & k_{\text{LRM}} \end{pmatrix} \begin{pmatrix} \tilde{u}_n \\ \tilde{w}_n \end{pmatrix} = \begin{pmatrix} 0 \\ 0 \end{pmatrix}. \end{aligned} \quad (6.18)$$

Each of the matrix equations (6.16), (6.17) and (6.18) can be compactly written as

$$\mathbf{M}\ddot{\tilde{\mathbf{U}}} + \mathbf{C}(\mu)\dot{\tilde{\mathbf{U}}} + \mathbf{K}(\mu)\tilde{\mathbf{U}} = \mathbf{0}, \quad (6.19)$$

where $\tilde{\mathbf{U}} = (\tilde{u}_n \ \tilde{w}_n)^{\text{T}}$ (superscript ‘‘T’’ indicates a transpose operation), and the \mathbf{M} , $\mathbf{C}(\mu)$, and $\mathbf{K}(\mu)$ matrices are evident. Note that for the IALRM unit cell, the \mathbf{M} matrix is also a function of μ . Equation (6.19) for the three cases can now be converted into a first-order problem,

through a state-space transformation [119–121] of the form

$$\mathbf{A}\dot{\mathbf{Y}} + \mathbf{B}\mathbf{Y} = \mathbf{0}, \quad (6.20)$$

where

$$\mathbf{A} = \begin{pmatrix} \mathbf{0} & \mathbf{I} \\ \mathbf{M} & \mathbf{C}(\kappa) \end{pmatrix}; \mathbf{B} = \begin{pmatrix} -\mathbf{I} & \mathbf{0} \\ \mathbf{0} & \mathbf{K}(\kappa) \end{pmatrix}; \text{ and } \mathbf{Y} = \begin{pmatrix} \dot{\tilde{\mathbf{X}}} \\ \tilde{\mathbf{X}} \end{pmatrix}. \quad (6.21)$$

For equation (6.20), a solution of the form $\mathbf{Y} = \tilde{\mathbf{Y}}_\lambda e^{\lambda t}$ is assumed, where $\tilde{\mathbf{Y}}_\lambda$ is a complex-amplitude state-space vector corresponding to eigenvalue λ . The dispersion relation and, consequently, the wave-propagation and dissipation characteristics can now be obtained by implementing the solution in equation (6.20) and solving the resulting eigenvalue problem given by

$$|\mathbf{A}^{-1}\mathbf{B} + \lambda\mathbf{I}| = 0. \quad (6.22)$$

The dispersion relations of all the models are computed from the corresponding Bloch-transformed system of equations for values of the dimensionless wavenumber ranging from $\mu = 0 \rightarrow \pi$. The solution for the eigenvalue problem for a given μ is written as

$$\lambda_l(\mu) = -\zeta_l(\mu)\omega_{r_l}(\mu) \pm i\omega_{d_l}(\mu), \quad (6.23)$$

where ω_{r_l} and ω_{d_l} are the resonant and damped frequencies, respectively, and ζ_l is the wavenumber-dependent damping ratio. The subscript $l = 1, 2$ refers to the acoustic and optical branches, respectively.

6.3 Extreme levels of positive and negative metadamping

The qualitative analysis carried out in this chapter can be broadly divided into two parts: the first part involving the IAM, PnC, and LRM and the second part involving the IALRM, PnC, and LRM. The parameters used for all the models in the two parts are given in table 6.1.

The IAM, similar to the one in the analysis presented in [118], is investigated in the first part, and the dispersion and dissipation characteristics are detailed in figure 6.2. The unit cell for this model is depicted in the third, fourth, and fifth columns of figure 6.2 for, three different inertial-amplifier angles, $\phi = 13^\circ$, 24° , and 43° , respectively. These angles are chosen arbitrarily to represent qualitatively varying behaviours. For comparison, a standard diatomic PnC model and a mass-in-mass LRM model, each with the same long-wave speed of sound as the IAM, $C_g = 0.99$, are considered. This set up yields five distinct chains that are all statically equivalent. In this first part of the investigation involving the IAM, PnC,

Table 6.1: Parameters employed for the unit-cell models examined in figures 6.2, 6.3, and 6.6.

Parameter	Figure 6.2	Figure 6.3	Unit
a	1	1	m
M	1	1	Kg
m	—	0.1	Kg
m_a	0.1	0.1	Kg
K_{PnC}	120	120	Nm ⁻¹
k_{PnC}	1320	1200	Nm ⁻¹
K_{LRM}	110	109	Nm ⁻¹
k_{LRM}	179	179	Nm ⁻¹
K_{IAM}	100	—	Nm ⁻¹
K_{IALRM}	—	100	Nm ⁻¹
k_{IALRM}	—	40	Nm ⁻¹
k_{IALRM^*}	—	500	Nm ⁻¹
C	2	2	Nsm ⁻¹
c	0	2	Nsm ⁻¹

and LRM, for the PnC and LRM, $m_1 = M$, and $m_2 = m_a$. The damped-frequency dispersion diagrams and corresponding damping-ratio diagrams for each of the five systems are given in figures 6.2(b) and 6.2(c), respectively. In all the damped-frequency band-structure figures, the non-dimensional quantity $\Omega = \frac{\omega_d}{\omega_b}$ is plotted, where $\omega_b = \sqrt{\frac{K_{\text{PnC}}}{M}}$ is defined as the base frequency. The complex dispersion curves for the undamped version of all the models are also provided to show the frequency-dependent profile of spatial attenuation for each chain [55]. In figures 6.2(d) and 6.2(e), the wavenumber-dependent damping-emergence metric Z , which is a measure of metadamping, is plotted; this metric is defined as [79]

$$Z_l(\mu)|_* = \zeta_l(\mu)|_* - \zeta_l(\mu)|_{\text{PnC}} \quad (l = 1, 2, \text{ or sum}; \mu \in [0, \pi]), \quad (6.24)$$

where the subscript“*” indicates LRM or IAMs. It represents the difference between the damping ratio of the LRM or each of the IAMs and that of the reference PnC case. The index l indicates the acoustic branch ($l = 1$), optical branch ($l = 2$), and summation ($l = \text{sum}$) of the two branches. Any rise in $Z(\mu)$ above zero is indicative of positive metadamping, and in contrast, a drop in $Z(\mu)$ below zero is indicative of negative metadamping. The cumulative and total value of $Z(\mu)$ defined as

$$Z_l^{\text{cum}}|_*(\mu) = \int_0^\mu Z_l|_* d\mu \quad (l = 1, 2, \text{ or sum}; \mu \in [0, \pi]), \quad (6.25)$$

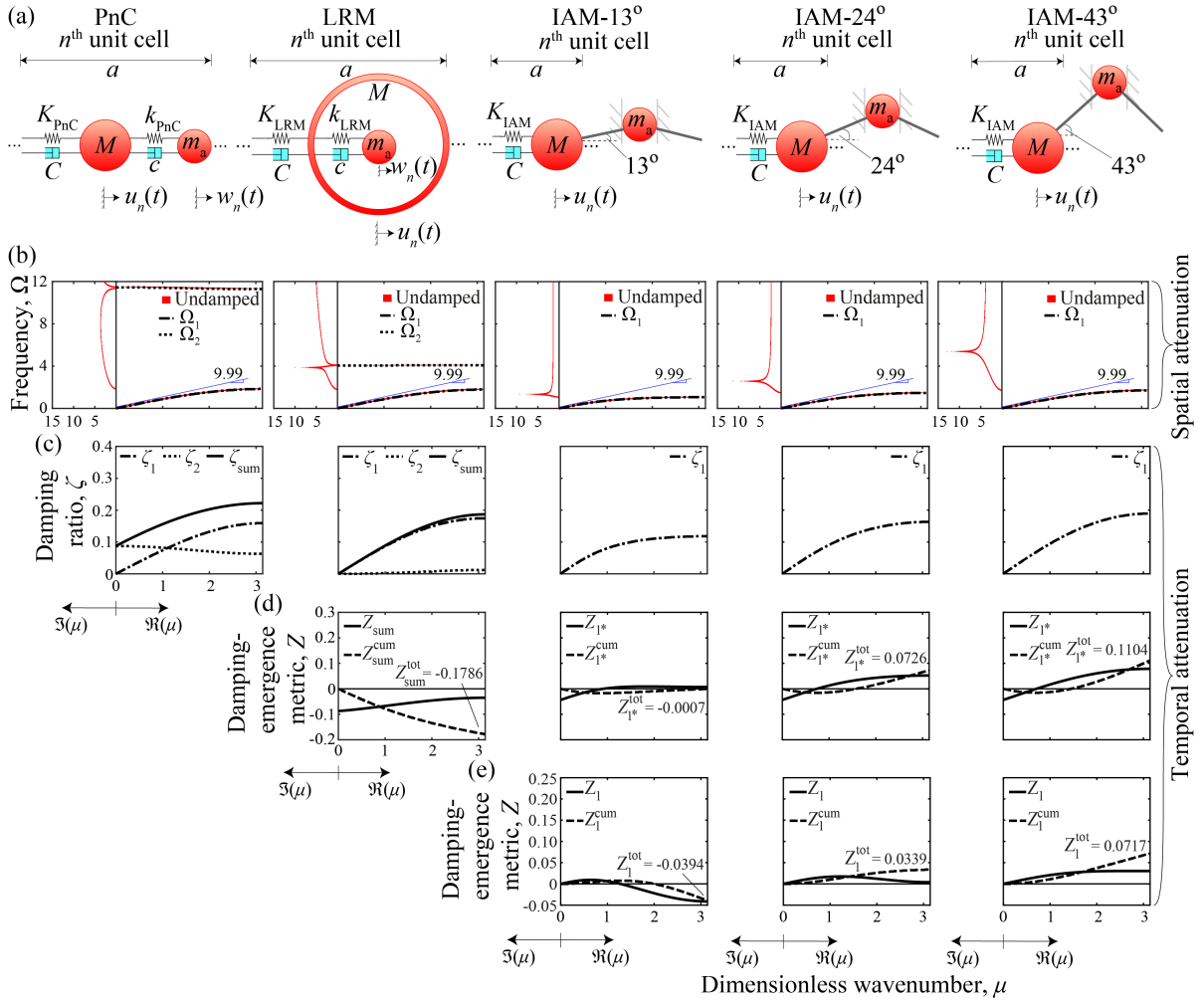


Figure 6.2: Analysis of the inertially amplified material (IAM) with no resonating mass. (a) Unit-cell schematics of statically equivalent chains, including a phononic crystal (PnC), locally resonant metamaterial (LRM), and three variations of the IAM exhibiting $\phi = 13^\circ$, 24° , and 43° , respectively. All the inertial-amplifier masses are restricted to motion in only the vertical direction. (b) Frequency band structure for the undamped and damped unit cells; results for the damped unit cells are shown only for real wave numbers. (c) Damping-ratio diagrams for the damped unit cells. (d) Damping-emergence metric Z : for the LRM, the sum of the two damping-ratio branches of the PnC has been used as the reference quantity (ζ_{sum}), and for the IAMs, the average of the two damping-ratio branches of the PnC ($\zeta_{\text{sum}}/2$) has been used as the reference quantity as distinguished by the asterisk applied to the subscript 1. (e) Damping-emergence metric Z for the IAMs, where the damping ratio corresponding to the acoustic branch of the PnC is used as the reference quantity. In sub-figures (b) and (c), the subscripts “1”, “2”, and “sum” indicate the acoustic branch, optical branch, and sum of the two branches, respectively.

and

$$Z_l^{\text{tot}}|_* = Z_l^{\text{cum}}|_*(\pi) \quad (l = 1, 2, \text{ or sum}), \quad (6.26)$$

respectively, are also utilized to further quantify the difference in the damping ratio. The quantity Z_l^{cum} represents the integrated value of Z_l over the irreducible Brillouin zone (IBZ), and upon complete integration over the IBZ, the total value of Z_l , which is Z_l^{tot} , is calculated to give an overall quantification of the positive or negative damping capacity with respect to the reference PnC. Since the IAM has only one branch, the Z quantity indicated as Z_{1*} in figure 6.2(d) is obtained by comparing the damping ratio of that branch with the average of the two damping-ratio branches, $\frac{\zeta_{\text{sum}}}{2}$, of the PnC. Alternatively, in figure 6.2(e), the comparison is made with the damping ratio of the first branch of the PnC. From the results, it is observed that for the parameters selected, as listed in table 6.1, the IAM exhibits positive metadamping with increasing levels of the inertial-amplifier angle ϕ .

The IALRM is investigated next in the second part, and the dispersion and dissipation characteristics are detailed in figure 6.3. In the second part of the investigation involving the IALRM, PnC, and LRM, for the PnC and LRM, $m_1 = M + m_a$, and $m_2 = m$. This allows the consideration of models with the same number of dispersion branches, and, importantly, generates an IALRM configuration that may exhibit a bounded band gap, as would an experimentally realizable material that is modelled as a continuum. An undamped version of this model has been recently investigated for spatial attenuation characteristics [55]. A monotonic increase is observed in positive metadamping, as expressed by the quantity $Z_{\text{sum}}^{\text{tot}}$, while progressing from LRM to IALRM with increasing values of the inertial-amplifier angle ϕ . This demonstrates an extreme level of positive metadamping significantly exceeding what is realized by an LRM. A special case is considered where IALRM-13° to IA-13°* by only increasing the local-resonator stiffness from $k_{\text{IALRM}} = 40 \text{ Nm}^{-1}$ to $k_{\text{IALRM}} = 500 \text{ Nm}^{-1}$; by doing so, the IALRM, which remains statically equivalent to the PnC, shows a significant reduction in the total dissipation at $\phi = 13^\circ$ to the point where it starts to exhibit negative metadamping as evidenced by the orange curves in figure 6.3. By considering this special case, it is illustrated that the level of metadamping for a given inertial-amplifier angle in an IALRM can be controlled and significantly altered by varying the value of the local-resonator stiffness while keeping the long-wave speed of sound unaltered.

Figure 6.4 extends the analysis of the IAM to a broad range of quasi-static speeds extending well beyond the values considered in figure 6.2; this provides an Ashby-like map for the damping capacity versus the long-wave speed, which is representative of the effective quasi-static stiffness of the chain. The damping capacity is presented for different periodic media at different values of the effective quasi-static stiffness, i.e., group velocities, to give a comprehensive picture of their dissipative performances. The damping capacity is obtained

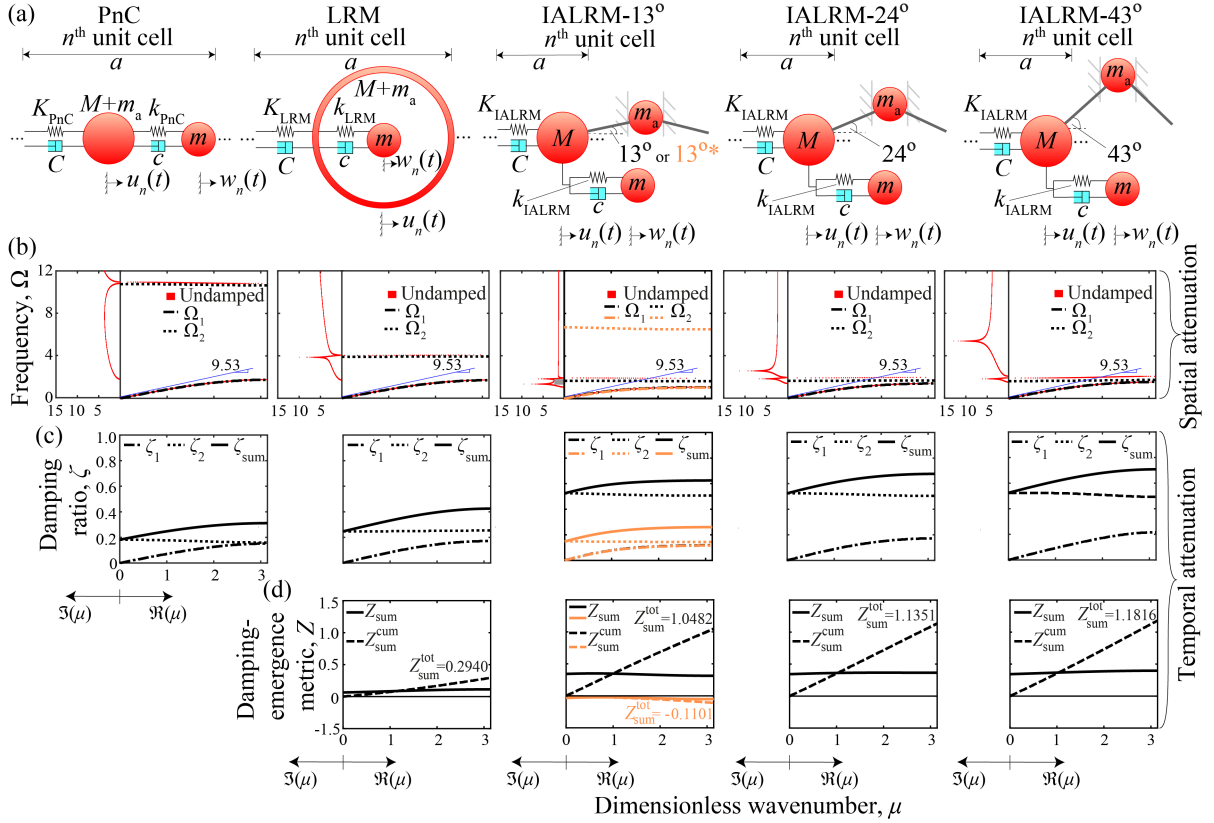


Figure 6.3: Analysis of the inertially amplified locally resonant metamaterial (IALRM), i.e., with a resonating mass. (a) Unit-cell schematics of statically equivalent chains, including a phononic crystal (PnC), locally resonant metamaterial (LRM), and three variations of the IALRM exhibiting $\phi = 13^\circ$, 24° , and 43° , respectively. All the inertial-amplifier masses are restricted to motion in only the vertical direction. (b) Frequency band structure for the undamped and damped unit cells; results for the damped unit cells are only shown for real wave numbers. (c) Damping-ratio diagrams for the damped unit cells. (d) Damping-emergence metric Z . In sub-figures (a) and (b), the subscripts “1”, “2”, and “sum” indicate the acoustic branch, optical branch, and sum of the two branches, respectively. The orange curves in the third column are the results for the special case IALRM- $13^{\circ*}$, which is statically equivalent to the PnC and obtained by only increasing the local-resonator stiffness of IALRM- 13° from $k_{\text{IALRM}} = 40 \text{ Nm}^{-1}$ to $k_{\text{IALRM}^*} = 500 \text{ Nm}^{-1}$, presented for the purpose of illustrating negative metadamping at $\phi = 13^\circ$.

by integrating the damping ratio over the IBZ and calculating its total value in the following manner:

$$\zeta_l^{\text{cum}}(\mu) = \int_0^\mu \zeta_l \, d\mu \quad (l = 1 \text{ or } \text{sum}; \mu \in [0, \pi]), \quad (6.27)$$

$$\zeta_l^{\text{tot}} = \zeta_l^{\text{cum}}(\pi) \quad (l = 1 \text{ or } \text{sum}). \quad (6.28)$$

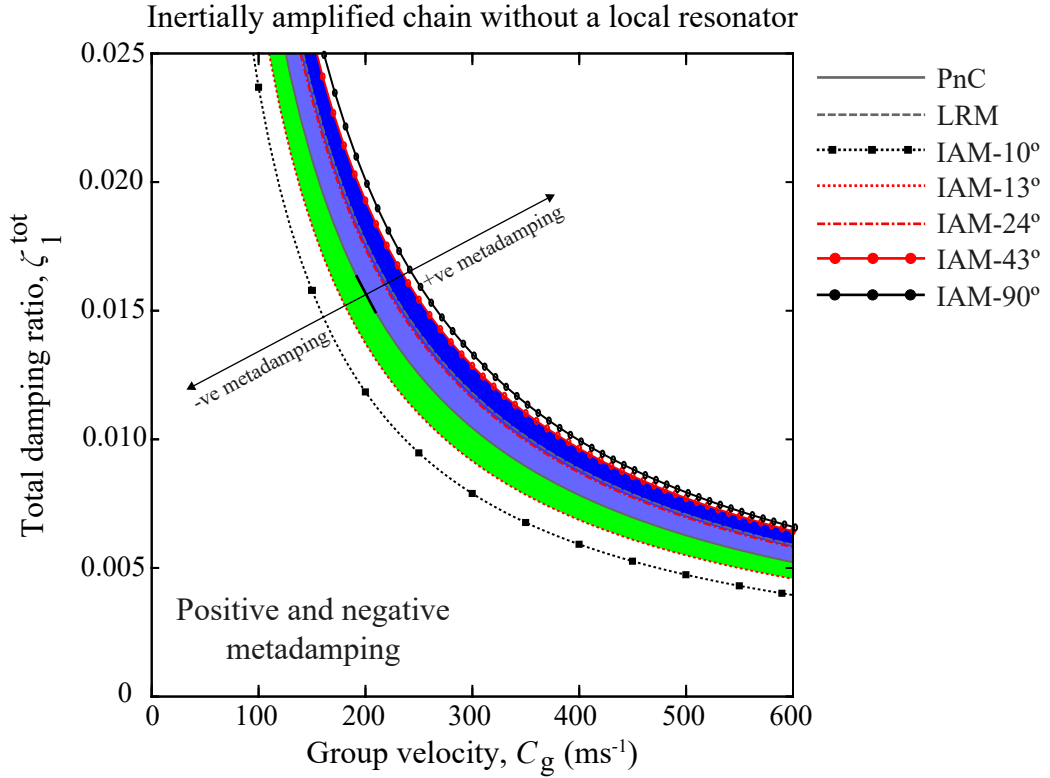


Figure 6.4: Illustration of metadamping: total damping ratio based on the first branch, ζ_1^{tot} , versus long-wave speed of sound C_g in the periodic chains. (a) Positive or negative metadamping (depending on value of ϕ) exhibited in the case of inertially amplified material (IAM) with no resonating mass; blue- and green-shaded areas represent regions of positive and negative metadamping, respectively. Maximum positive and negative metadamping are reached at IAM-90° and IAM-10°, respectively. The intensity of positive metadamping increases as the color of the blue shaded areas gets darker.

As the IAMs considered in figure 6.2 have only one damping-ratio branch, for a fair comparative analysis, only the first damping-ratio branch of the PnC and LRM are considered in figure 6.4. It is noticed in figure 6.4 that the LRM exhibits positive metadamping throughout the parameter range shown. It is also observed that the IAM exhibits even more positive metadamping for $\phi = 43^\circ$; however, the level of metadamping decreases as ϕ decreases. Eventually, for $\phi = 13^\circ$, the metadamping is illustrated to be strongly negative, i.e., the IAM exhibits less total loss compared to the statically equivalent PnC. A maximum value of negative metadamping is reached at $\phi = 10^\circ$; at angles below 10° , the static equivalence is no longer maintained.

Figure 6.5 extends the analysis of the IALRM to a broad range of quasi-static speeds extending well beyond the values considered in figure 6.3. In figure 6.5, positive metadamping is observed with increasing intensity as the inertial-amplifier angle ϕ increases. In figures 6.4

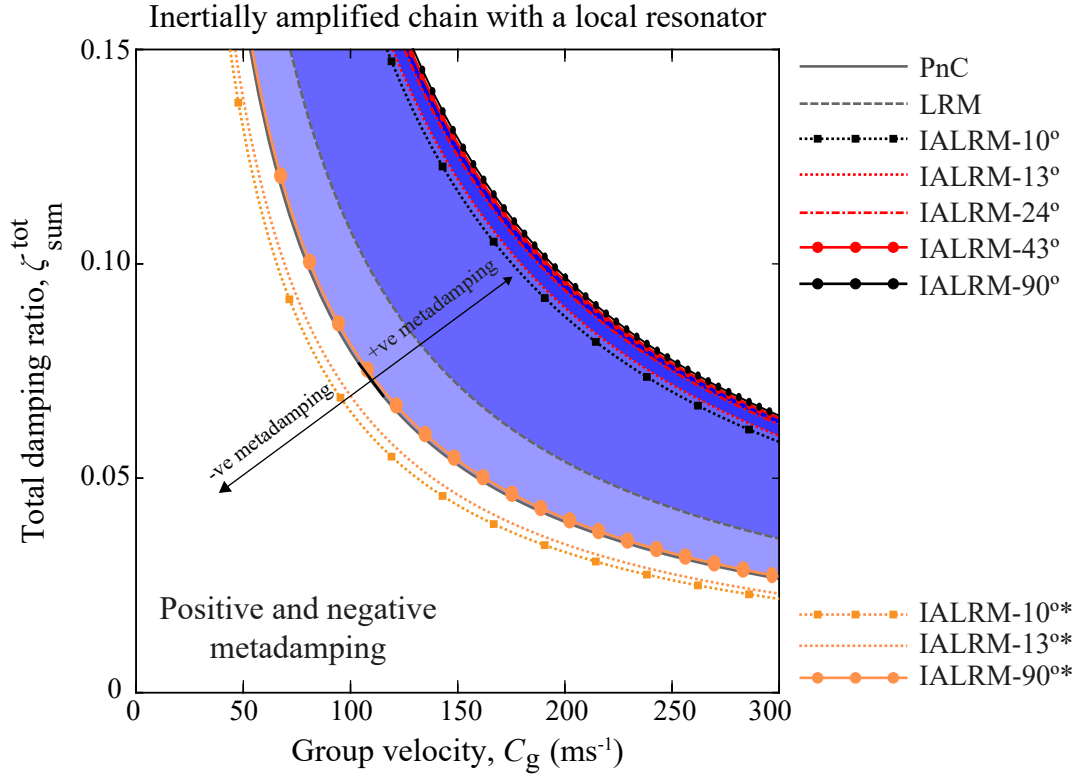


Figure 6.5: Illustration of metadamping: total damping ratio based on the sum of the two damping-ratio branches, $\zeta_{\text{sum}}^{\text{tot}}$, i.e., overall total damping capacity. (b) Positive metadamping exhibited in the case of inertially amplified locally resonant metamaterial (IALRM); blue-shaded area represents the region of positive metadamping. Maximum positive metadamping is reached at IA-90°. The intensity of positive metadamping increases as the color of the blue shaded areas gets darker. The orange curves are the results for the special cases IALRM-10°*, IALRM-13°*, and IALRM-90°*, which are also statically equivalent to the PnC and obtained by only increasing the local-resonator stiffness of the IALRMs from $k_{\text{IALRM}} = 40 \text{ Nm}^{-1}$ to $k_{\text{IALRM}^*} = 500 \text{ Nm}^{-1}$, presented for the purpose of illustrating negative metadamping, which reaches its maximum at $\phi = 10^\circ$.

and 6.5, the performance of the IAM and IALRM is also shown at $\phi = 90^\circ$; such an angle is practically unrealizable, but it gives the maximum theoretical limit for the metadamping level shown by the IAM and IALRM. The special case IA-13°* considered in figure 6.2 is also extended and shown in 6.5 along with two more special cases for IA-10° and IA-90° similarly represented by IA-10°* and IA-90°*, respectively.

6.4 Regime displaying trade-off between temporal attenuation and spatial attenuation

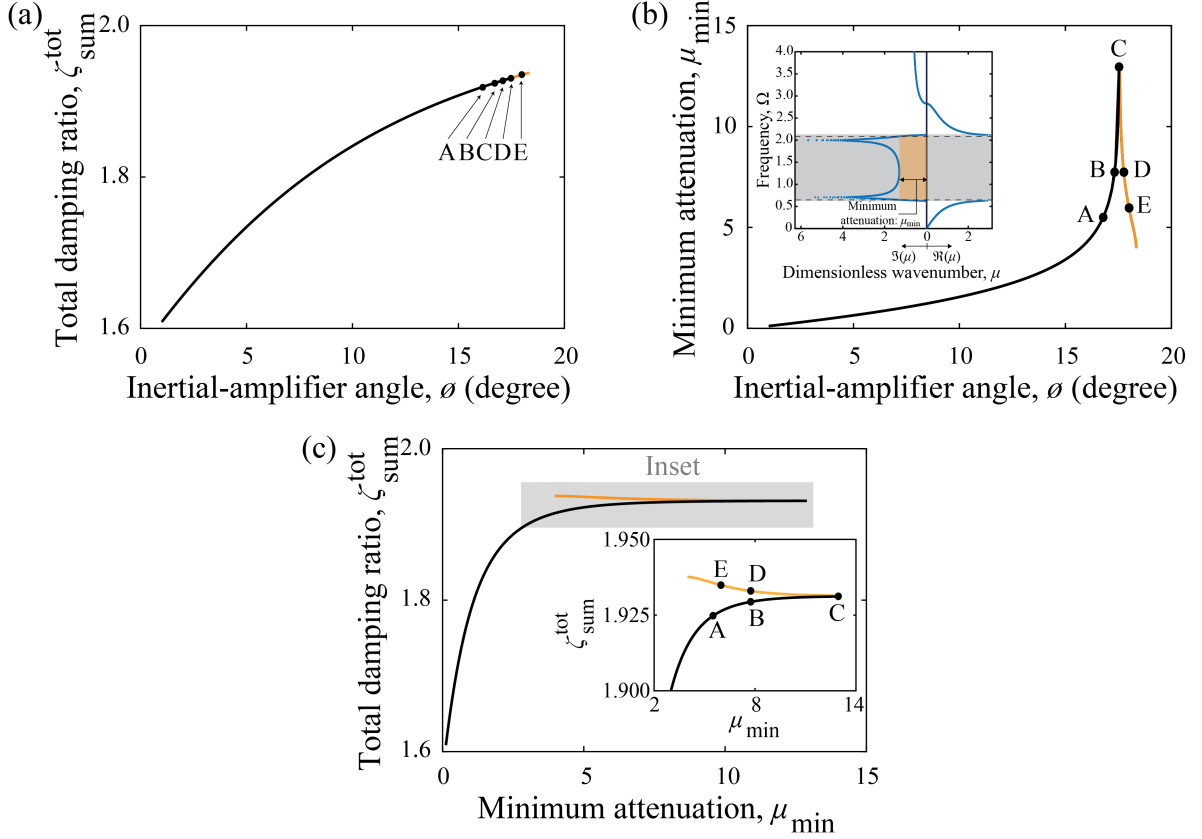


Figure 6.6: Performance characteristics for the inertially amplified locally resonant meta-material (IALRM). (a) Temporal-attenuation intensity: total damping ratio $\zeta_{\text{sum}}^{\text{tot}}$ versus inertial-amplifier angle ϕ . (b) Spatial-attenuation intensity: minimum attenuation μ_{min} versus ϕ ; inset depicts a schematic that illustrates the μ_{min} quantity. (c) Minimum attenuation μ_{min} versus total damping ratio $\zeta_{\text{sum}}^{\text{tot}}$; inset in sub-figure (c) shows an enlarged version of the trade-off region. The points A-E, corresponding to five different values of ϕ , have been specifically chosen and used to illustrate the evolution of the temporal- and spatial-attenuation properties with ϕ whereby a region is identified that features a trade-off between the temporal and spatial attenuation intensities.

In figure 6.6, the examination of IALRM, using the same parameters listed in table 6.1, is extended to examine the effects of the inertial-amplifier angle ϕ on the total damping ratio; i.e., on the intensity of the temporal attenuation, which is a measure of the total dissipation. However, its effect is also examined on the imaginary-wave-propagation-constant part of the spectrum, which represents the spatial attenuation. As shown in [55], for a certain range

of ϕ , the attenuation peak associated with the inertial-amplifier mechanism couples with the attenuation peak associated with the local-resonance mechanism. This yields a coupled double-attenuation peak, within a bounded band gap, in the imaginary-wavenumber part of the dispersion diagram. The strength of this spatial attenuation can be quantified by evaluating the minimum value of the imaginary dimensionless wavenumber bounded by the two peaks; this quantity is represented by μ_{\min} (see inset of figure 6.6(b) [55]).

Using $\zeta_{\text{sum}}^{\text{tot}}$ and μ_{\min} , figures 6.6(a) and 6.6(b), respectively, show the variation of the temporal- and spatial- attenuation intensities with the inertial-amplifier angle ϕ . Figure 6.6(c) combines these two relations in one plot, showing the temporal attenuation versus the spatial attenuation. It is observed that $\zeta_{\text{sum}}^{\text{tot}}$ increases monotonically with ϕ ; however, μ_{\min} increases monotonically up to a specific angle, $\phi = 17.532^\circ$; as the angle increases further, a trade-off is observed between the temporal- and spatial-attenuation intensities. This represents an unprecedented spatio-temporal attenuation trade-off phenomenon for an elastodynamic medium. This tradeoff is observed until $\phi = 18.348^\circ$ beyond which the coupled double-peak feature in the spatial-attenuation spectrum no longer exists; hence, the μ_{\min} measure is no longer valid. Figures 6.7(a) and 6.7(b) show, respectively, the frequency and damping-ratio diagrams for a selection of points in the parameter space, as marked in figures 6.6(a) and 6.6(b).

The dispersion and attenuation characteristics of the IALRM is intricately dependent on the unit cell's various design parameters. Using figure 6.8, certain non-dimensional parameters associated with an IALRM unit cell is introduced. The parameter $\varepsilon = \frac{m_a}{M}$ is the ratio of the inertial-amplifier mass to the baseline mass, and $\delta = \frac{\varepsilon}{4 \tan^2 \phi} = \frac{m_a}{4M \tan^2 \phi}$ represents the same ratio with the influence of the inertial-amplifier angle ϕ . Thus, the parameter δ directly represents the level of the effective inertial amplification by the inertial-amplifier mass due to a variation of the inertial-amplifier angle. It can be seen that the value of δ drastically increases as ϕ decreases and nearly linearly increases with ε . In the unamplified static state, the effective value of m_a is equal to the given value of m_a . The factor $4 \tan^2 \phi$ in the definition of δ indicates the level of inertial amplification; the higher this level, the higher the effective value of m_a and the stronger the impact on the dispersion and attenuation characteristics.

6.5 Summary and conclusions

In the present chapter, the dissipation characteristics of conventional elastic materials, namely, PnC and LRM are analysed and compared with two types of inertially amplified materials,

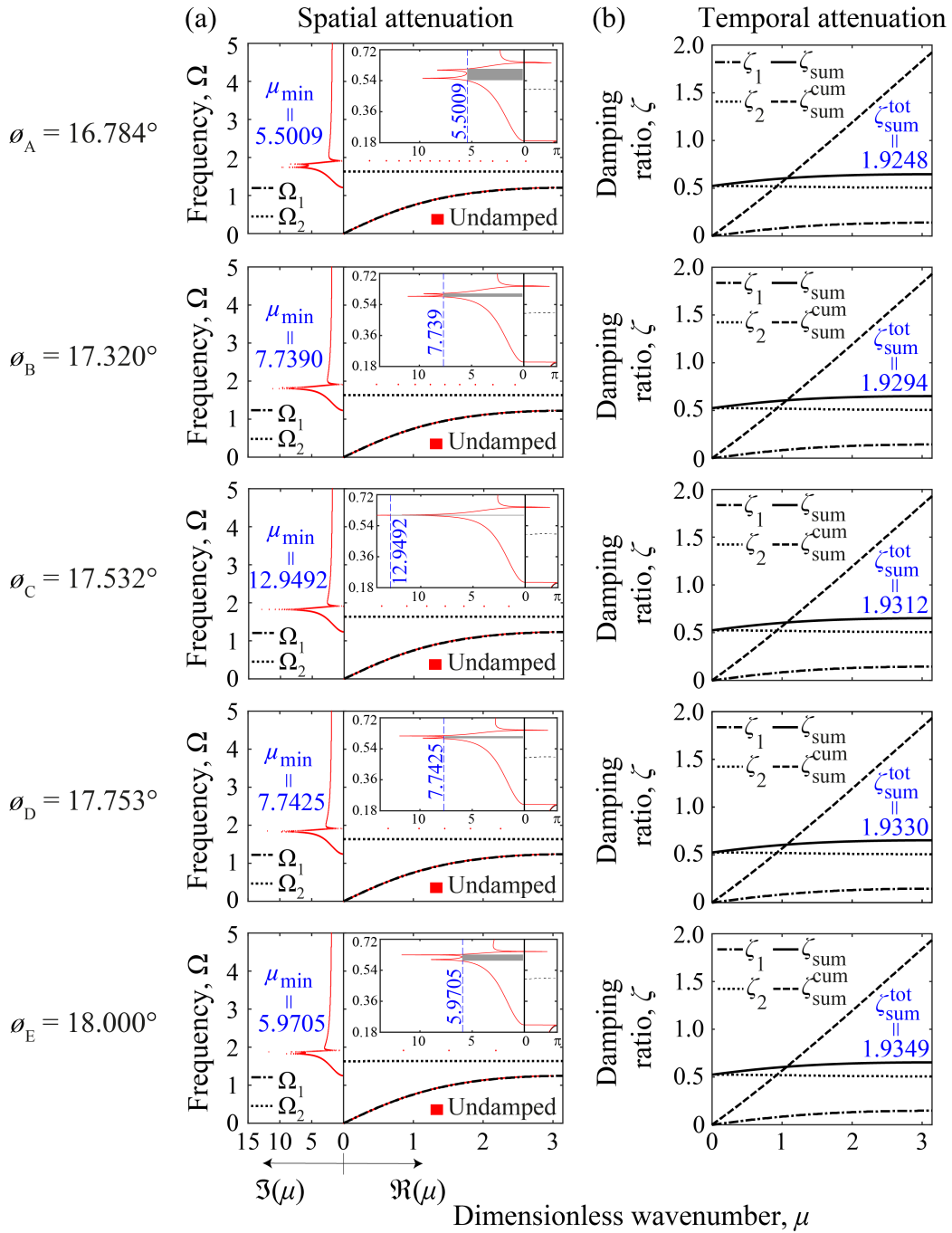


Figure 6.7: (a) Frequency band structure (first column), illustrating the spatial attenuation, and (b) damping-ratio diagrams (second column), illustrating the temporal attenuation, corresponding to the five chosen values of ϕ ; insets in column (a) show the corresponding plots with the y-axis reproduced in a log scale. Results for the damped IALRMs are shown only for real dimensionless wavenumbers.

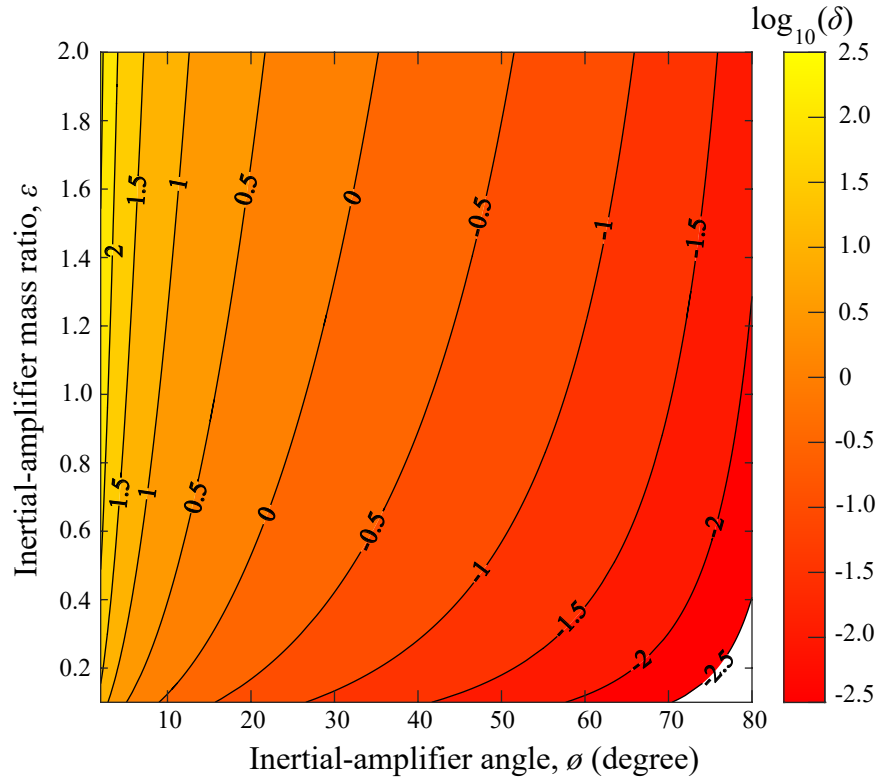


Figure 6.8: Non-dimensional parameter δ as a function of inertial-amplifier mass ratio (ratio of the inertial-amplifier mass to the baseline mass) ε and the inertial-amplifier angle ϕ .

i.e., without (IAM) and with a local resonator (IALRM). The governing equations for all the periodic media are presented and treated with Bloch's theorem in order to set up an eigenvalue problem which yields the damped frequencies and damping-ratios, which are presented as a function of non-dimensional dimensionless wavenumber in the real-number spectrum. The undamped frequencies for all the periodic media are also shown for real as well as imaginary non-dimensional wave-propagation constants. The dissipation in the LRM, IAM, and IALRM is compared with that in the PnC, and the difference in dissipation, its cumulative integration, and its total integration as a single-valued quantity are presented in the IBZ. The overall total damping ratio, which is a single-valued quantity obtained after total integration of the summation of all the damping-ratio branches, is computed for all the periodic media at a range of quasi-static speeds.

In this chapter, it is demonstrated that inertial amplification provides a route to effectively designing a structured material with simultaneously high stiffness and high damping capacity (positive metadamping) or low stiffness and low loss (negative metadamping). The levels of positive or negative metadamping attained are elevated and well exceed the performance of conventional elastic metamaterials. These attributes extend the boundaries of viscoelastic

dynamical properties of state-of-the-art structured-material systems. Furthermore, when combining inertial amplification with local resonance, i.e., in the IALRM, the unique phenomenon of a trade-off between the temporal- and spatial-attenuation intensities associated with the material properties is observed for a given range of the inertial-amplifier angle, ϕ . This is accomplished by only changing the inertial-amplifier angle in the IALRM, i.e., via passive tuning. By suitable adjustment of this angle, another regime is also realized that exhibits monotonic increase in both the attenuation types. These traits open the way for the design of future phononic materials with tailored spatio-temporal attenuation characteristics and could have significant implications on topological phononics and other currently existing areas within phononic engineering. The contents of the present chapter are contained within the following peer-reviewed “Rapid Communication” publication:

- Hussein MI, **Patrick I**, Banerjee A, and Adhikari S. Metadamping in inertially amplified metamaterials: Trade-off between spatial attenuation and temporal attenuation. *Journal of Sound and Vibration*, page 116977, 2022, doi.org/10.1016/j.jsv.2022.116977.

Chapter 7

Metaharvesting: Emergent intrinsic energy harvesting by piezoelectric metamaterials

7.1 Introduction

The harvesting of useful dissipative energy, arising due to structural vibrations that a wide range of mechanical systems encounter, using diverse types of shunted piezoelectric systems such as patches and stacks has continued to receive widespread attention since the past few decades, which has resulted in significant advancements in the specialized areas of piezoelectricity, energy-harvesting electromechanical design and piezoelectric vibration-energy harvesting (PVEH). A fairly new class of material, locally resonant (elastic) metamaterial (LRM), has proved to be quite effective in low-frequency energy harvesting as suggested in the reviews by Chen *et al.* [68] and Lee *et al.* [66]. In a mass-in-mass elastic-metamaterial, i.e., an LRM, model statically equivalent to a PnC model, in a local-resonance state, the effective mass can become negative near the resonant frequency; and the dynamic response results in an out-of-phase oscillation. As the resultant force approaches zero at the resonant frequency as a result of out-of-phase oscillations, the net displacement is considerably suppressed; and the accumulated wave energy localizes within the resonators. By installing an appropriate piezoelectric element at the site of wave-energy localization, the harvesting efficiency achieved is higher than that of a conventional piezoelectric substrate [72]. LRMs, with an augmented mass, are better equipped for efficient PVEH as a result of the high Q-factor associated with the local-resonance mechanism and the relatively narrow range of the resonating frequency. As a consequence of the aforementioned reasons, LRMs can

portray simultaneous dual functionalities of vibration attenuation and energy harvesting and have been demonstrated to do so [73–76]. Considering that the enhanced PVEH performance of an LRM stems from the local-resonance mechanism, inertial amplification of the main mass and the local-resonator mass could result in even further enhancement. Adhikari *et al.* [77] showed that a configuration comprising of a cantilever beam with bimorph piezoelectric layers and an inertially amplified tip mass resulted in enhanced low-frequency PVEH.

Similar to the premise of chapter 5, while the research works mentioned above have examined the electromechanical dispersion characteristics, the focus has purely been on energy-harvesting capacity of the electromechanical structure; i.e., the analysis is performed at the structural level, where the focus is on the structural dynamics/performance, and the electromechanical structure is constrained by factors such as global dimensions, boundary conditions, and nature of forcing. Chapter 6 [82] expounded upon the intrinsic—*independent of forcing, structure size, and boundary conditions*—characterization of the amount of dissipative energy available for harvesting in suspended piezoelectric phononic crystals (PPnCs) under free vibration and comprising of either purely resistive or inductor-equipped shunt circuits by comparing their dissipation characteristics to that of their non-piezoelectric versions, PnCs, with the same amount of prescribed (raw) damping and, thus, introduced the concept of *intrinsic energy-harvesting availability* in a piezoelectric material. This concept is a new formal approach for the characterization of the amount of useful energy available for harvesting that is fundamentally at the material level rather than the structural or device level. By considering the PPnCs as a material and solely studying the effects of the piezoelectric parameters, it was demonstrated that the PPnCs exhibited higher wavenumber-dependent dissipation, where the difference in dissipation is a representation of the useful dissipative energy intrinsically available for harvesting. In doing so, a formal wavenumber-dependent intrinsic representation of the amount of useful dissipative energy available for harvesting was presented. The current chapter presents a comprehensive analysis of the dissipation characteristics of non-piezoelectric and piezoelectric periodic media at a material level, i.e., an in-depth intrinsic analysis. The format of the detailed analysis is laid out in figure 7.1.

In the present chapter:

1. an overview of metadamping in LRM and inertially amplified locally resonant (elastic) metamaterial (IALRM) is presented by comparing them to a statically equivalent—same long-wave speed of sound—PnC as indicated by the horizontal arrow at the top of the intrinsic energetics schematics in figure 7.1;
2. an overview of the energy-harvesting availability in a piezoelectric phononic crystal (PPnC) is presented as indicated by the vertical arrow on the left side of the intrinsic energetics schematics in figure 7.1;

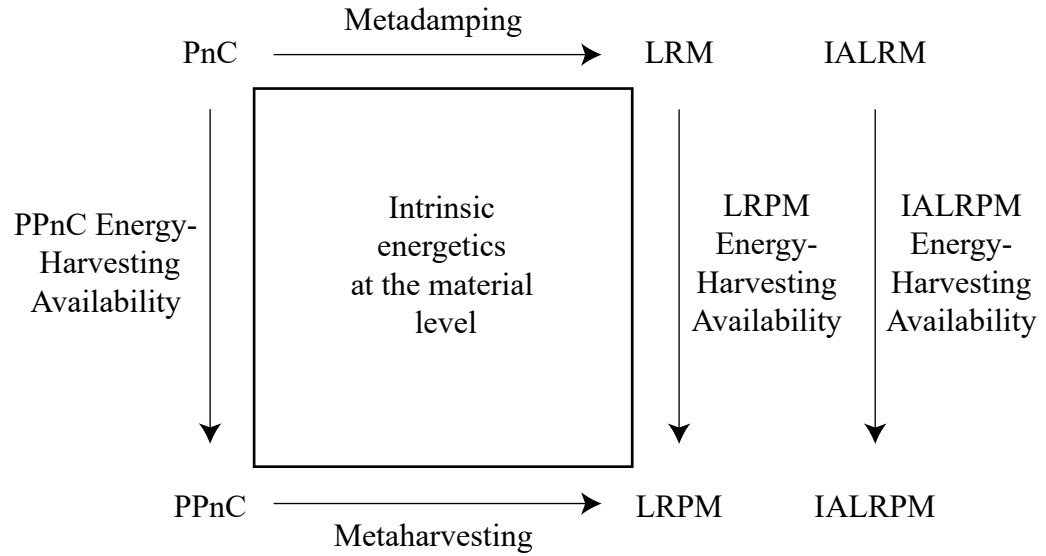


Figure 7.1: An overview of the unit-cell comparisons addressed in this work in a wave-propagation and dissipation framework and at a material level. The unit cells addressed in this work are phononic crystal (PnC), locally resonant metamaterial (LRM), inertially amplified locally resonant metamaterial (IALRM), piezoelectric phononic crystal (PPnC), locally resonant piezoelectric metamaterial (LRPM), and inertially amplified locally resonant piezoelectric metamaterial (IALRPM), which are statically equivalent to each other.

3. the energy-harvesting availability in a locally resonant piezoelectric metamaterial (LRPM) and an inertially amplified locally resonant piezoelectric metamaterial (IALRPM) is quantified as indicated by the two vertical arrows on the right side of the intrinsic energetics schematics in figure 7.1; and
4. upon comparing the intrinsic energy-harvesting availability of the LRPM and IALRPM with that of the statically equivalent PPnC, an emergence of intrinsic energy-harvesting availability, a phenomenon referred to as “metaharvesting,” is introduced as indicated by the horizontal arrow at the bottom of the intrinsic energetics schematics in figure 7.1.

The phenomenon of metaharvesting is analogous to the concept of metadamping except the quantity evaluated is associated with intrinsic piezoelectric energy harvesting rather than total dissipation. In the present work, only shunted circuits with an inductor are considered for the piezoelectric elements in the piezoelectric periodic media.

The layout of the chapter is as follows. Section 7.2 details the governing equations and their Bloch transformations for the non-piezoelectric and piezoelectric periodic media. In section 7.3, a comparative analysis, in the form of graphical results, of the dispersion and dissipation characteristics of the non-piezoelectric and piezoelectric periodic media is given,

addressing each of the arrows in figure 7.1. In section 7.4, as a summary, the damping ratios of all the periodic media addressed in this work and the relationship of their dispersion branches with the corresponding damping-ratio branches are presented along with concluding remarks.

7.2 Bloch's theorem for non-piezoelectric and piezoelectric periodic media

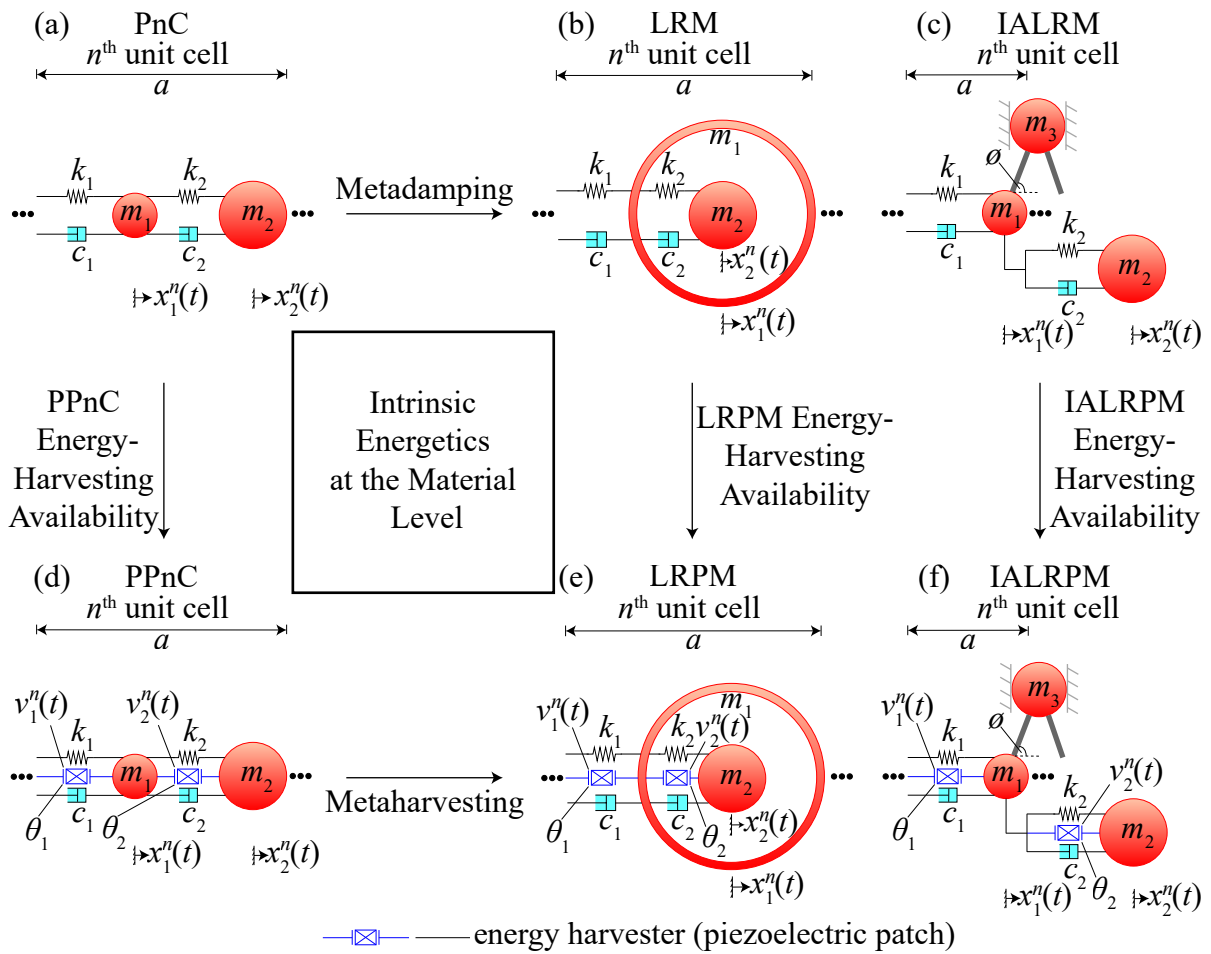


Figure 7.2: Unit-cell schematics of statically equivalent (a) phononic crystal (PnC), (b) locally resonant metamaterial (LRM), (c) inertially amplified locally resonant metamaterial (IALRM), (d) piezoelectric phononic crystal (PPnC), (e) locally resonant piezoelectric metamaterial (LRPM), and (f) inertially amplified locally resonant piezoelectric metamaterial (IALRPM).

Figure 7.2 illustrates the schematics of the unit cells of the non-piezoelectric and piezoelectric periodic media, as lumped-parameter models, discussed in the present chapter. In figure 7.2, a is the length of the lattice unit cell; ϕ is the angle between the central axis of the inertially amplified metamaterial and the rigid links of the inertial-amplifier attachment; m_{\dots} denote the masses; k_{\dots} and c_{\dots} denote the stiffness coefficients of the linear springs and the damping coefficients of the viscous dashpots, respectively, θ_{\dots} are the electromechanical couplings of the energy harvesters; n is used to identify the central unit cell under consideration and can be any non-zero positive integer in a finite lattice; $x_{\dots}^n(t)$ are the displacements of the masses, with respect to time t , in the n^{th} unit cell; and $v_{\dots}^n(t)$ are the voltages, with respect to time t , generated in the n^{th} unit cell. Note that the inertially amplified locally resonant metamaterials are similar to the locally resonant metamaterials except that, in addition to each baseline mass connected to a local resonator, each baseline mass is connected to the neighbouring baseline masses by inertial-amplifier attachments, each of which comprises of an auxiliary mass m_3 and two rigid links: one for each of the neighbouring baseline masses.

7.2.1 Overview of phononic crystal, locally resonant metamaterial, and inertially amplified locally resonant metamaterial

Phononic crystal

By collating the forces on the masses, the governing equations pertaining to the n^{th} unit cell of the diatomic PnC shown in figure 7.2(a) can be written as

$$m_1 \ddot{x}_1^n + (c_1 + c_2) \dot{x}_1^n - c_2 \dot{x}_2^n - c_1 \dot{x}_2^{n-1} + (k_1 + k_2) x_1^n - k_2 x_2^n - k_1 x_2^{n-1} = 0, \quad (7.1)$$

$$m_2 \ddot{x}_2^n + (c_1 + c_2) \dot{x}_2^n - c_2 \dot{x}_1^n - c_1 \dot{x}_1^{n+1} + (k_1 + k_2) x_2^n - k_2 x_1^n - k_1 x_1^{n+1} = 0, \quad (7.2)$$

where the number of overhead dots indicates the order of derivative with respect to time, and $(n+1)$ and $(n-1)$ are used to refer to the unit cells to the right and left of the central (n^{th}) unit cell, respectively.

As per Bloch's theorem, the plane-wave solution [119] for the displacements of the masses in a unit cell is given by

$$x_l^{n+g}(r, \mathbf{k}; t) = \tilde{x}_l(t) e^{i\mathbf{k}(n+g)a}, \quad (7.3)$$

where x is the displacement; $l = 1, 2$ is an index corresponding to the two masses in a unit cell; $g \in [-\infty, \infty]$ is an integer used to locate and refer to any unit cell relative to the central unit cell under consideration, i.e., the n^{th} unit cell shown in figure 7.2; r is the

one-dimensional position vector of the n^{th} unit cell given by $r = na$; κ is the wavenumber; \tilde{x}_l is the displacement wave amplitude; and $i = \sqrt{-1}$ is the imaginary unit. For the central unit cell under consideration, $g = 0$ (n^{th} unit cell), and for the unit cells towards the left and right of the central unit cell, $g = -1$, and $g = +1$, respectively; i.e., they are the $(n-1)^{\text{th}}$ and $(n+1)^{\text{th}}$ unit cells, respectively. Substituting equation (7.3) in equations (7.1) and (7.2), i.e., Bloch-transformation, yields two homogeneous equations for the displacement amplitudes, \tilde{x}_1 and \tilde{x}_2 , which can be written in a matrix form as

$$\mathbf{M}\ddot{\tilde{\mathbf{X}}} + \mathbf{C}(\kappa)\dot{\tilde{\mathbf{X}}} + \mathbf{K}(\kappa)\tilde{\mathbf{X}} = \mathbf{0}, \quad (7.4)$$

where

$$\tilde{\mathbf{X}} = \begin{pmatrix} \tilde{x}_1 \\ \tilde{x}_2 \end{pmatrix}; \mathbf{M} = \begin{pmatrix} m_1 & 0 \\ 0 & m_2 \end{pmatrix}; \mathbf{C}(\kappa) = \begin{pmatrix} c_1 + c_2 & -c_2 - c_1 e^{-i\kappa a} \\ -c_2 - c_1 e^{i\kappa a} & c_1 + c_2 \end{pmatrix};$$

$$\text{and } \mathbf{K}(\kappa) = \begin{pmatrix} k_1 + k_2 & -k_2 - k_1 e^{-i\kappa a} \\ -k_2 - k_1 e^{i\kappa a} & k_1 + k_2 \end{pmatrix}. \quad (7.5)$$

By means of state-space transformation, equation (7.4) is converted into a first-order state-space equation of the form

$$\mathbf{A}\dot{\mathbf{Y}} + \mathbf{B}\mathbf{Y} = \mathbf{0}, \quad (7.6)$$

where

$$\mathbf{A} = \begin{pmatrix} \mathbf{0} & \mathbf{I} \\ \mathbf{M} & \mathbf{C}(\kappa) \end{pmatrix}; \mathbf{B} = \begin{pmatrix} -\mathbf{I} & \mathbf{0} \\ \mathbf{0} & \mathbf{K}(\kappa) \end{pmatrix}; \text{ and } \mathbf{Y} = \begin{pmatrix} \dot{\tilde{\mathbf{X}}} \\ \tilde{\mathbf{X}} \end{pmatrix}. \quad (7.7)$$

For equation (7.6), a solution of the form $\mathbf{Y} = \tilde{\mathbf{Y}}_\lambda e^{\lambda t}$ is assumed, where $\tilde{\mathbf{Y}}_\lambda$ is a complex-amplitude state-space vector corresponding to eigenvalue λ . The dispersion relation is obtained by implementing the solution in equation (7.6) and solving the resulting eigenvalue problem given by

$$|\mathbf{A}^{-1}\mathbf{B} + \lambda\mathbf{I}| = 0. \quad (7.8)$$

Expanding equation (7.8) yields a fourth-order equation in terms of λ , which, upon solving, gives four complex roots appearing as two complex-conjugate pairs. The complex solution for the eigenvalue problem at a given value of κ is expressed as

$$\lambda_l(\kappa) = -\zeta_l(\kappa)\omega_{r_l}(\kappa) \pm i\omega_{d_l}(\kappa) = -\zeta_l(\kappa)\omega_{r_l}(\kappa) \pm i\omega_{r_l}(\kappa)\sqrt{1 - \zeta_l(\kappa)^2}, \quad (7.9)$$

where the subscript l refers to each complex-conjugate pair and, consequently, the mode or branch number. Considering that all the unit cells shown in figure 7.2 have two degrees

of freedom and their complex eigen solution comprises of two complex-conjugate pairs, they exhibit two modes or branches: the acoustic (lower/first) branch given by $l = 1$ and the optical (higher/second) branch given by $l = 2$. The definitions for the wavenumber-dependent resonant frequency ω_{r_l} , damped frequency ω_{d_l} , and damping ratio ζ_l can be extracted from equation (7.9) in the following manner:

$$\omega_{r_l}(\kappa) = \text{Abs}[\lambda_l(\kappa)], \quad (7.10)$$

$$\omega_{d_l}(\kappa) = \text{Im}[\lambda_l(\kappa)], \quad (7.11)$$

$$\zeta_l(\kappa) = -\frac{\text{Re}[\lambda_l(\kappa)]}{\text{Abs}[\lambda_l(\kappa)]}. \quad (7.12)$$

Locally resonant metamaterial

By aggregating the forces on the masses, the governing equations pertaining to the n^{th} unit cell of the LRM shown in figure 7.2(b) are written as

$$m_1 \ddot{x}_1^n + c_1(2\dot{x}_1^n - \dot{x}_1^{n-1} - \dot{x}_1^{n+1}) + c_2(\dot{x}_1^n - \dot{x}_2^n) + k_1(2x_1^n - x_1^{n-1} - x_1^{n+1}) + k_2(x_1^n - x_2^n) = 0, \quad (7.13)$$

$$m_2 \ddot{x}_2^n + c_2(\dot{x}_2^n - \dot{x}_1^n) + k_2(x_2^n - x_1^n) = 0. \quad (7.14)$$

Following a Bloch transformation of equations (7.13) and (7.14), the dispersion relation of the LRM is obtained in a similar manner as for the PnC in section 7.2.1. In equation (7.4) for the LRM, $\tilde{\mathbf{X}}$ and \mathbf{M} are the same as in equation (7.5);

$$\mathbf{C}(\kappa) = \begin{pmatrix} c_1(2 - e^{-i\kappa a} - e^{i\kappa a}) + c_2 & -c_2 \\ -c_2 & c_2 \end{pmatrix};$$

$$\text{and } \mathbf{K}(\kappa) = \begin{pmatrix} k_1(2 - e^{-i\kappa a} - e^{i\kappa a}) + k_2 & -k_2 \\ -k_2 & k_2 \end{pmatrix}. \quad (7.15)$$

Inertially amplified locally resonant metamaterial

In an IALRM unit cell shown in figure 7.2(c), as the auxiliary or inertial-amplifier mass, m_3 , is connected to the baseline mass, m_1 , by a rigid link, the inertial rigid coupling does not alter the total degrees of freedom of a unit cell; hence, an IALRM unit cell will only exhibit two degrees of freedom similar to the PnC and LRM. The governing equations pertaining to

the n^{th} unit cell of the IALRM are

$$m_1 \ddot{x}_1^n + c_1(2\dot{x}_1^n - \dot{x}_1^{n-1} - \dot{x}_1^{n+1}) + c_2(\dot{x}_1^n - \dot{x}_2^n) + k_1(2x_1^n - x_1^{n-1} - x_1^{n+1}) + k_2(x_1^n - x_2^n) + \chi(m_3(\dot{x}_1^n - \dot{x}_1^{n-1})) - \chi(m_3(\dot{x}_1^{n+1} - \dot{x}_1^n)) = 0, \quad (7.16)$$

$$m_2 \ddot{x}_2^n + c_2(\dot{x}_2^n - \dot{x}_1^n) + k_2(x_2^n - x_1^n) = 0, \quad (7.17)$$

where, from system kinematics, $\chi = \frac{1}{4 \tan^2 \phi}$.

Following a Bloch transformation of equations (7.16) and (7.17), the dispersion relation of the IALRM is obtained in a manner similar as for the PnC in section 7.2.1. In equation (7.4) for the IALRM, $\tilde{\mathbf{X}}$ is the same as in equation (7.5); $\mathbf{C}(\kappa)$ and $\mathbf{K}(\kappa)$ are the same as in equation (7.15); and

$$\mathbf{M} = \begin{pmatrix} m_1 + \frac{m_3}{4}(2 - e^{-i\kappa a} - e^{i\kappa a}) \cot^2 \phi & 0 \\ 0 & m_2 \end{pmatrix}. \quad (7.18)$$

7.2.2 Phononic crystal, locally resonant metamaterial, and inertially amplified locally resonant metamaterial with shunted piezoelectric elements

Piezoelectric phononic crystal

The governing electromechanical equations pertaining to the n^{th} unit cell of the PPnC shown in figure 7.2(c) can be written as

$$m_1 \ddot{x}_1^n + (c_1 + c_2)\dot{x}_1^n - c_2\dot{x}_2^n - c_1\dot{x}_2^{n-1} + (k_1 + k_2)x_1^n - k_2x_2^n - k_1x_2^{n-1} + \theta_1 v_1^n - \theta_2 v_2^n = 0, \quad (7.19)$$

$$m_2 \ddot{x}_2^n + (c_1 + c_2)\dot{x}_2^n - c_2\dot{x}_1^n - c_1\dot{x}_1^{n+1} + (k_1 + k_2)x_2^n - k_2x_1^n - k_1x_1^{n+1} + \theta_2 v_2^n - \theta_1 v_1^{n+1} = 0, \quad (7.20)$$

$$-\theta_1(\dot{x}_1^n - \dot{x}_2^{n-1}) + C_{p1} \dot{v}_1^n + \frac{1}{R_1} \dot{v}_1^n + \frac{1}{L_1} v_1^n = 0, \quad (7.21)$$

$$-\theta_2(\dot{x}_2^n - \dot{x}_1^n) + C_{p2} \dot{v}_2^n + \frac{1}{R_2} \dot{v}_2^n + \frac{1}{L_2} v_2^n = 0. \quad (7.22)$$

In equations (7.21) and (7.22), $C_{p\dots}$, R_{\dots} , and L_{\dots} are the capacitance, resistance, and inductance associated with the shunt circuits of the piezoelectric elements, respectively.

As per Bloch's theorem, the plane-wave solution for the voltages generated in piezoelectric elements in a periodic unit cell can be written as

$$v_l^{n+g}(r, \kappa; t) = \tilde{v}_l(t) e^{i\kappa(n+g)a}, \quad (7.23)$$

where \tilde{v} is the voltage amplitude. Substituting equations (7.3) and (7.23) in equations (7.19)–(7.22) yields four homogeneous equations, two for the displacement amplitudes \tilde{x}_1 and \tilde{x}_2 and two for the voltage amplitudes \tilde{v}_1 and \tilde{v}_2 , which can be written in matrix form as

$$\mathbf{M}\ddot{\tilde{\mathbf{X}}} + \mathbf{C}(\kappa)\dot{\tilde{\mathbf{X}}} + \mathbf{K}(\kappa)\tilde{\mathbf{X}} + \mathbf{T}_1(\kappa)\tilde{\mathbf{V}} = \mathbf{0}, \quad (7.24)$$

$$\mathbf{T}_2(\kappa)\ddot{\tilde{\mathbf{X}}} + \mathbf{C}_p\ddot{\tilde{\mathbf{V}}} + \mathbf{R}\dot{\tilde{\mathbf{V}}} + \mathbf{L}\tilde{\mathbf{V}} = \mathbf{0}. \quad (7.25)$$

In equations (7.24) and (7.25), $\tilde{\mathbf{X}}$, \mathbf{M} , $\mathbf{C}(\kappa)$, and $\mathbf{K}(\kappa)$ are the same as in equation (7.5);

$$\begin{aligned} \tilde{\mathbf{V}} &= \begin{pmatrix} \tilde{v}_1 \\ \tilde{v}_2 \end{pmatrix}; \quad \mathbf{T}_1(\kappa) = \begin{pmatrix} \theta_1 & -\theta_2 \\ -\theta_1 e^{i\kappa a} & \theta_2 \end{pmatrix}; \quad \mathbf{T}_2(\kappa) = \begin{pmatrix} -\theta_1 & \theta_1 e^{-i\kappa a} \\ \theta_2 & -\theta_2 \end{pmatrix}; \\ \mathbf{C}_p &= \begin{pmatrix} C_{p1} & 0 \\ 0 & C_{p2} \end{pmatrix}; \quad \mathbf{R} = \begin{pmatrix} \frac{1}{R_1} & 0 \\ 0 & \frac{1}{R_2} \end{pmatrix}; \quad \text{and } \mathbf{L} = \begin{pmatrix} \frac{1}{L_1} & 0 \\ 0 & \frac{1}{L_2} \end{pmatrix}. \end{aligned} \quad (7.26)$$

Equations (7.24) and (7.25) can be compacted into a single matrix equation as

$$\mathbf{Z}_1\ddot{\tilde{\mathbf{E}}} + \mathbf{Z}_2\dot{\tilde{\mathbf{E}}} + \mathbf{Z}_3\tilde{\mathbf{E}} = \mathbf{0}, \quad (7.27)$$

where

$$\begin{aligned} \mathbf{Z}_1 &= \begin{pmatrix} \mathbf{M} & \mathbf{0} \\ \mathbf{T}_2(\kappa) & \mathbf{C}_p \end{pmatrix}; \quad \mathbf{Z}_2 = \begin{pmatrix} \mathbf{C}(\kappa) & \mathbf{0} \\ \mathbf{0} & \mathbf{R} \end{pmatrix}; \quad \mathbf{Z}_3 = \begin{pmatrix} \mathbf{K}(\kappa) & \mathbf{T}_1(\kappa) \\ \mathbf{0} & \mathbf{L} \end{pmatrix}; \\ &\quad \text{and } \tilde{\mathbf{E}} = \begin{pmatrix} \tilde{\mathbf{X}} \\ \tilde{\mathbf{V}} \end{pmatrix}. \end{aligned} \quad (7.28)$$

The dispersion relation can now be formulated by subjecting equation (7.27) to a state-space transformation of the form given in equation (7.6), where

$$\mathbf{A} = \begin{pmatrix} \mathbf{0} & \mathbf{I} \\ \mathbf{Z}_1 & \mathbf{Z}_2 \end{pmatrix}; \quad \mathbf{B} = \begin{pmatrix} -\mathbf{I} & \mathbf{0} \\ \mathbf{0} & \mathbf{Z}_3 \end{pmatrix}; \quad \text{and } \mathbf{Y} = \begin{pmatrix} \tilde{\mathbf{E}} \\ \tilde{\mathbf{E}} \end{pmatrix}, \quad (7.29)$$

implementing a solution of the form $\mathbf{Y} = \tilde{\mathbf{Y}}_\lambda e^{\lambda t}$, and solving the resulting eigenvalue problem of the form given in equation (7.8). Expanding equation (7.8) for this particular case yields an eight-order equation in terms of λ , which, upon solving, gives four complex roots appearing as two complex-conjugate pairs and four real roots.

Locally resonant piezoelectric metamaterial

The governing electromechanical equations pertaining to the n^{th} unit cell of the LRPM shown in figure 7.2(e) can be written as

$$m_1 \ddot{x}_1^n + c_1(2\dot{x}_1^n - \dot{x}_1^{n-1} - \dot{x}_1^{n+1}) + c_2(\dot{x}_1^n - \dot{x}_2^n) + k_1(2x_1^n - x_1^{n-1} - x_1^{n+1}) + k_2(x_1^n - x_2^n) + \theta_1 v_1^n - \theta_1 v_1^{n+1} - \theta_2 v_2^n = 0, \quad (7.30)$$

$$m_2 \ddot{x}_2^n + c_2(\dot{x}_2^n - \dot{x}_1^n) + k_2(x_2^n - x_1^n) + \theta_2 v_2^n = 0, \quad (7.31)$$

$$-\theta_1(\dot{x}_1^n - \dot{x}_1^{n-1}) + C_{p1} \dot{v}_1^n + \frac{1}{R_1} \dot{v}_1^n + \frac{1}{L_1} v_1^n = 0, \quad (7.32)$$

$$-\theta_2(\dot{x}_2^n - \dot{x}_1^n) + C_{p2} \dot{v}_2^n + \frac{1}{R_2} \dot{v}_2^n + \frac{1}{L_2} v_2^n = 0. \quad (7.33)$$

Following a Bloch transformation of equations (7.30)–(7.33), the dispersion relation for the LRPM is obtained in a similar manner as for the PPnC in section 7.2.2. In equations (7.24) and (7.25) for the LRPM, $\tilde{\mathbf{X}}$ and \mathbf{M} are the same as in equation (7.5); $\mathbf{C}(\kappa)$ and $\mathbf{K}(\kappa)$ are the same as in equation (7.15); $\tilde{\mathbf{V}}$, \mathbf{C}_p , \mathbf{R} , and \mathbf{L} are the same as in equation (7.26);

$$\mathbf{T}_1(\kappa) = \begin{pmatrix} \theta_1 - \theta_1 e^{i\kappa a} & -\theta_2 \\ 0 & \theta_2 \end{pmatrix}; \text{ and } \mathbf{T}_2(\kappa) = \begin{pmatrix} -\theta_1 + \theta_1 e^{-i\kappa a} & 0 \\ \theta_2 & -\theta_2 \end{pmatrix}. \quad (7.34)$$

Inertially amplified locally resonant piezoelectric metamaterial

The governing electromechanical equations pertaining to the n^{th} unit cell of the IALRPM shown in figure 7.2(f) are

$$m_1 \ddot{x}_1^n + \chi(m_3(\dot{x}_1^n - \dot{x}_1^{n-1})) - \chi(m_3(\dot{x}_1^{n+1} - \dot{x}_1^n)) + c_1(2\dot{x}_1^n - \dot{x}_1^{n-1} - \dot{x}_1^{n+1}) + c_2(\dot{x}_1^n - \dot{x}_2^n) + k_1(2x_1^n - x_1^{n-1} - x_1^{n+1}) + k_2(x_1^n - x_2^n) + \theta_1 v_1^n - \theta_1 v_1^{n+1} - \theta_2 v_2^n = 0, \quad (7.35)$$

$$m_2 \ddot{x}_2^n + c_2(\dot{x}_2^n - \dot{x}_1^n) + k_2(x_2^n - x_1^n) + \theta_2 v_2^n = 0, \quad (7.36)$$

$$-\theta_1(\dot{x}_1^n - \dot{x}_1^{n-1}) + C_{p1} \dot{v}_1^n + \frac{1}{R_1} \dot{v}_1^n + \frac{1}{L_1} v_1^n = 0, \quad (7.37)$$

$$-\theta_2(\dot{x}_2^n - \dot{x}_1^n) + C_{p2} \dot{v}_2^n + \frac{1}{R_2} \dot{v}_2^n + \frac{1}{L_2} v_2^n = 0. \quad (7.38)$$

Following a Bloch transformation of equations (7.35)–(7.38), the dispersion relation for the IALRPM is obtained in a manner similar as for the PPnC in section 7.2.2. In equations (7.24) and (7.25) for the IALRPM, $\tilde{\mathbf{X}}$ is the same as in (7.5); \mathbf{M} is the same as in equation (7.18); $\mathbf{C}(\kappa)$ and $\mathbf{K}(\kappa)$ are the same as in equation (7.15); $\mathbf{T}_1(\kappa)$ and $\mathbf{T}_2(\kappa)$ are the same as in equation (7.34); and $\tilde{\mathbf{V}}$, \mathbf{C}_p , \mathbf{R} , and \mathbf{L} are the same as in equation (7.26).

7.3 Wave-propagation and dissipation characteristics of non-piezoelectric and piezoelectric periodic media: metadamping, energy-harvesting availability, and metaharvesting

In this section, the mathematical realizations of metadamping and energy-harvesting availability are presented as an overview; the mathematical definition of metaharvesting is presented; and consequently, each of the arrows shown in figure 7.2 are addressed by comparing the dissipation characteristics of the periodic media, with the parameters detailed in table 7.1, on either side of the arrows.

The electrical parameters of the shunt circuits of the piezoelectric elements are presented in table 7.1 after non-dimensionalizing them in the following manner:

$$\alpha_l = \bar{\omega}_l C_{p_l} R_l, \quad (7.39a)$$

$$\beta_l = \bar{\omega}_l^2 C_{p_l} L_l, \quad (7.39b)$$

$$k_{\text{coeff}_l}^2 = \frac{\theta_l^2}{k_l C_{p_l}}, \quad (7.39c)$$

In the equations above, $l = 1, 2$ is an index corresponding to the parameters of the two piezoelectric elements and the frequencies obtained from the two spring-mass pairs: $\bar{\omega}_1 = \sqrt{\frac{k_1}{m_1}}$ and $\bar{\omega}_2 = \sqrt{\frac{k_2}{m_2}}$.

7.3.1 Mathematical definitions of metadamping, energy-harvesting availability and metaharvesting

To quantify the increase in dissipation in the LRM and IALRM compared to the statically equivalent PnC, an intrinsic wavenumber-dependent quantity Z_{emerg_l} [79] is employed, which

Table 7.1: Mechanical and non-dimensional electrical parameters employed in the piezoelectric unit cells, namely, piezoelectric phononic crystal (PPnC), locally resonant piezoelectric metamaterial (LRPM), and inertially amplified piezoelectric metamaterial (IALPM), considered in the present chapter; the mechanical parameters are the same for the non-piezoelectric and piezoelectric unit cells.

Parameter	PPnC	LRPM	IALRPM	Unit
a	1	1	1	m
ϕ	—	—	70	degree
m_1	0.1	0.1	0.01	Kg
m_2	0.3	0.3	0.3	Kg
m_3	—	—	0.09	Kg
k_1	4.7130×10^5	1.1844×10^5	0.9131×10^5	Nm^{-1}
k_2	1.5710×10^5	0.3948×10^5	3.0437×10^4	Nm^{-1}
c_1	3	3	3	Nsm^{-1}
c_2	3	3	3	Nsm^{-1}
α_1	0.2605	0.1306	0.3626	—
α_2	0.3474	0.1741	0.1529	—
β_1	3.7704	0.9475	7.3048	—
β_2	1.6757	0.4211	0.3247	—
$k_{\text{coeff}_1}^2$	0.0430	0.1710	0.2218	—
$k_{\text{coeff}_2}^2$	0.0644	0.2565	0.3327	—

is defined as

$$Z_{\text{emerg}_l|*}(\mu) = \zeta_{l|*}(\mu) - \zeta_{l|\text{PnC}}(\mu) \quad \left(\begin{array}{l} l = 1, 2, \text{ or sum}; \\ * = \text{LRM or IALRM}; \\ \mu \in [0, \pi] \end{array} \right), \quad (7.40)$$

where the subscript “emerg” stands for emergence; l is an index referring to the acoustic branch ($l = 1$), optical branch ($l = 2$), or the summation ($l = \text{sum}$) of the two branches; the subscript $*$ is used to distinguish between the LRM and IALRM; and μ is the dimensionless wavenumber defined as $\mu = \kappa a$. The quantity Z_{emerg_l} represents the difference between the damping ratio of the LRM or IALRM and that of the statically equivalent reference PnC and, hence, is the *intrinsic wavenumber-dependent measure of the emergence of dissipation or damping* in an LRM or IALRM, which illustrates the *phenomenon of metadamping*. The

wavenumber-dependent cumulative and total value of Z_{emerg_l} defined as

$$Z_{\text{emerg}_l}^{\text{cum}}|_*(\mu) = \int_0^\mu Z_{\text{emerg}_l}|_* d\mu \quad \left(\begin{array}{l} l = 1, 2, \text{ or sum;} \\ * = \text{LRM or IALRM;} \\ \mu \in [0, \pi] \end{array} \right), \quad (7.41)$$

and

$$Z_{\text{emerg}_l}^{\text{tot}}|_* = Z_{\text{emerg}_l}^{\text{cum}}|_*(\pi) \quad (l = 1, 2, \text{ or sum}; * = \text{LRM or IALRM}), \quad (7.42)$$

respectively, are also used to further quantify the emergence in dissipation. The quantity $Z_{\text{emerg}_l}^{\text{cum}}$ represents the cumulatively integrated value of Z_{emerg_l} over the irreducible Brillouin zone (IBZ), and upon complete integration over the IBZ, the total value of Z_{emerg_l} , which is $Z_{\text{emerg}_l}^{\text{tot}}$ ($Z_{\text{emerg}_l}^{\text{cum}}$ evaluated at $\mu = \pi$), is calculated to give a single-valued total quantification of the differential dissipation capacity or metadamping pertaining to the acoustic branch, optical branch, or their summation for the LRM and IALRM with respect to the reference PnC. Note that, depending on the choice of the mechanical parameters, Z_{emerg_l} , $Z_{\text{emerg}_l}^{\text{cum}}$, and $Z_{\text{emerg}_l}^{\text{tot}}$ could be in the positive [79] or negative [48] regime.

To quantify the increase in dissipation, due to shunted piezoelectric elements, in the piezoelectric periodic media compared to their corresponding non-piezoelectric counterparts, an intrinsic wavenumber-dependent quantity Z_{EHA_l} [82] is employed, which is defined as

$$Z_{\text{EHA}_l}|_\otimes(\mu) = \zeta_l|_\otimes(\mu) - \zeta_l|_*(\mu) \quad \left(\begin{array}{l} l = 1, 2, \text{ or sum;} \\ \otimes = \text{PPnC, LRPM, or IALRPM;} \\ * = \text{PnC, LRM, or IALRM;} \\ \mu \in [0, \pi] \end{array} \right), \quad (7.43)$$

where the subscript EHA is an abbreviation for energy-harvesting availability, and the subscripts \otimes and $*$ are used to distinguish among the three piezoelectric periodic media and the corresponding three non-piezoelectric periodic media, respectively. The quantity Z_{EHA_l} represents the difference between the damping ratio of the piezoelectric periodic media and that of the corresponding reference non-piezoelectric periodic media; i.e., it is a measure of the useful dissipation arising purely due to the shunted piezoelectric elements and that is intrinsically available for harvesting by the same shunted piezoelectric elements considering that the raw dissipation, termed as “loss,” is lost in the viscous damping dashpots with a prescribed damping. Hence, the measure Z_{EHA_l} is defined as the *intrinsic wavenumber-dependent representation or characterization of the amount of useful dissipative energy available for harvesting* in a piezoelectric periodic media and illustrates the *concept of*

energy-harvesting availability. The wavenumber-dependent cumulative and total value of Z_{EHA_l} defined as

$$Z_{\text{EHA}_l}^{\text{cum}}|_{\otimes}(\mu) = \int_0^{\mu} Z_{\text{EHA}_l}|_{\otimes} d\mu \quad \left(\begin{array}{l} l = 1, 2, \text{ or sum;} \\ \otimes = \text{PPnC, LRPM, or IALRPM;} \\ \mu \in [0, \pi] \end{array} \right), \quad (7.44)$$

and

$$Z_{\text{EHA}_l}^{\text{tot}}|_{\otimes} = Z_{\text{EHA}_l}^{\text{cum}}|_{\otimes}(\pi) \quad \left(\begin{array}{l} l = 1, 2, \text{ or sum;} \\ \otimes = \text{PPnC, LRPM, or IALRPM} \end{array} \right), \quad (7.45)$$

respectively, are also used to further quantify the energy-harvesting availability in the three piezoelectric periodic media. The quantity $Z_{\text{EHA}_l}^{\text{cum}}$ represents the cumulatively integrated value of Z_{EHA_l} over the IBZ, and upon complete integration over the IBZ, the total value of Z_{EHA_l} , which is $Z_{\text{EHA}_l}^{\text{tot}}$ ($Z_{\text{EHA}_l}^{\text{cum}}$ evaluated at $\mu = \pi$), is calculated to give a single-valued total quantification of the energy-harvesting availability pertaining to the acoustic branch, optical branch, or their summation for the piezoelectric periodic media.

To quantify the increase in the “useful dissipation” in the LRPM and IALRPM relative to the statically equivalent PPnC, an intrinsic wavenumber-dependent quantity $Z_{\text{EHA}_l}^{\text{emerg}}$ is employed, which is defined as

$$Z_{\text{EHA}_l}^{\text{emerg}}|_{\otimes}(\mu) = Z_{\text{EHA}_l}|_{\otimes}(\mu) - Z_{\text{EHA}_l}|_{\text{PPnC}}(\mu) \quad \left(\begin{array}{l} l = 1, 2, \text{ or sum;} \\ \otimes = \text{LRPM, or IALRPM;} \\ \mu \in [0, \pi] \end{array} \right), \quad (7.46)$$

where the subscript \otimes is used to distinguish between the LRPM and IALRPM. Note that on the right-hand side in equation (7.46), the energy-harvesting availability Z_{EHA_l} is used instead of the damping ratio ζ_l as Z_{EHA_l} excludes the dissipation or loss arising due to the prescribed/raw damping whereas ζ_l includes it. The quantity $Z_{\text{EHA}_l}^{\text{emerg}}$ represents the difference between the energy-harvesting availability associated to the LRPM or IALRPM and that associated to the statically equivalent reference PPnC; hence, it is defined as the *intrinsic wavenumber-dependent measure of the emergence of the representative energy-harvesting availability* in an LRPM or IALRPM, which illustrates the *phenomenon of metaharvesting*. The cumulative and total value of $Z_{\text{EHA}_l}^{\text{emerg}}$ defined as

$$Z_{\text{EHA}_l}^{\text{emerg cum}}|_{\otimes}(\mu) = \int_0^{\mu} Z_{\text{EHA}_l}^{\text{emerg}}|_{\otimes} d\mu \quad \left(\begin{array}{l} l = 1, 2, \text{ or sum;} \\ \otimes = \text{PPnC, LRPM, or IALRPM;} \\ \mu \in [0, \pi] \end{array} \right), \quad (7.47)$$

and

$$Z_{\text{EHA}_l}^{\text{emerg}^{\text{tot}}} |_{\otimes} = Z_{\text{EHA}_l}^{\text{emerg}^{\text{cum}}} |_{\otimes}(\pi) \quad \left(\begin{array}{l} l = 1, 2, \text{ or sum;} \\ \otimes = \text{PPnC, LRPM, or IALRPM} \end{array} \right), \quad (7.48)$$

respectively, are also used to further quantify the emergence in the energy-harvesting availability. The quantity $Z_{\text{EHA}_l}^{\text{emerg}^{\text{cum}}}$ represents the cumulatively integrated value of $Z_{\text{EHA}_l}^{\text{emerg}}$ over the IBZ, and upon complete integration over the IBZ, the total value of $Z_{\text{EHA}_l}^{\text{emerg}}$, which is $Z_{\text{EHA}_l}^{\text{emerg}^{\text{tot}}}$ ($Z_{\text{EHA}_l}^{\text{emerg}^{\text{cum}}}$ evaluated at $\mu = \pi$), is calculated to give a single-valued total quantification of the emergent energy-harvesting availability or metaharvesting pertaining to the acoustic branch, optical branch, or their summation for the LRPM and IALRPM with respect to the reference PPnC.

7.3.2 Metadamping: an emergence in dissipation in locally resonant and inertially amplified locally resonant metamaterials

In this section, the top horizontal arrow, assigned to metadamping in the LRM and IALRM, in figure 7.2 is addressed through graphical results. Figure 7.3 depicts the unit-cell schematics of the PnC, LRM, and IALRM, their non-dimensional damped-frequency band structures, their damping-ratio diagrams, and the quantity Z_{emerg_l} ($l = \text{sum}$) for the LRM and IALRM. In all the dispersion diagrams presented in this chapter, the damped-frequencies associated with the acoustic and optical branches are plotted after non-dimensionalizing them with respect to $\bar{\omega}_1|_{\text{PnC}}$; i.e., $\Omega_l = \frac{\omega_{d_l}}{\bar{\omega}_1|_{\text{PnC}}}$ is plotted, where $l = 1$ (acoustic), 2 (optical) and $\bar{\omega}_1|_{\text{PnC}} = \sqrt{\frac{k_1|_{\text{PnC}}}{m_1|_{\text{PnC}}}}$. All the non-dimensional damped-frequency band structures and damping-ratio diagrams in this chapter are generated for $\mu \in [0, \pi]$, i.e., the IBZ. In figure 7.3(a), the LRM and IALRM exhibit a narrower first (acoustic) transmission band and a wider second (optical) transmission band compared to the PnC. In figure 7.3(c), the LRM exhibits higher damping ratios compared to the PnC; and the IALRM exhibits a further significant increase in the damping ratios; the increase is remarkable in the optical branch. Figure 7.3(d) shows an emergence in damping in the LRM and an even higher emergence, i.e., enhanced emergence, in the IALRM. Figure 7.4 displays metadamping corresponding to the acoustic damping-ratio branch ζ_1 , optical damping-ratio branch ζ_2 , and the summation of the two branches ζ_{sum} as shaded regions to highlight the contrast between the LRM and IALRM. The increase in the size of the shaded regions, Z_{emerg_l} ($l = 1, 2, \text{ and sum}$), while progressing from the LRM to the IALRM indicates a significant enhancement in metadamping in the IALRM.

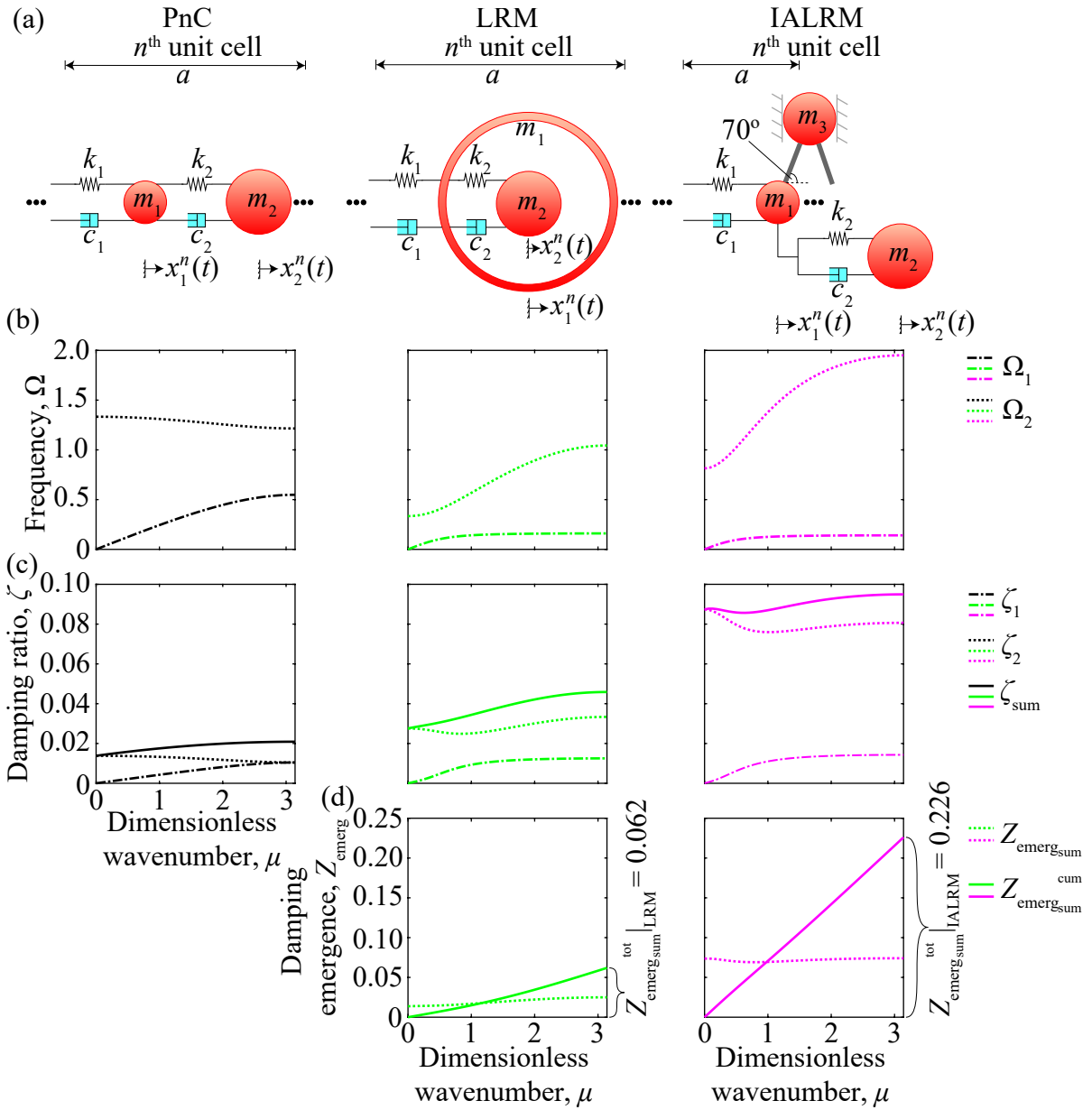


Figure 7.3: (a) Unit-cell schematics, (b) normalized damped-frequency band structures, and (c) damping-ratio diagrams for the statically equivalent phononic crystal (PnC), locally resonant metamaterial (LRM), and inertially amplified locally resonant metamaterial (IALRM), and (d) damping-emergence quantities for the LRM and IALRM relative to the PnC corresponding to the summation of the two damping-ratio branches ζ_{sum} .

7.3.3 Energy-harvesting availability: intrinsic representation of useful dissipative energy available for harvesting

In this section, the vertical arrows, assigned to energy-harvesting availability in the three piezoelectric periodic media, in figure 7.2 are graphically illustrated. Figures 7.5, 7.6, and

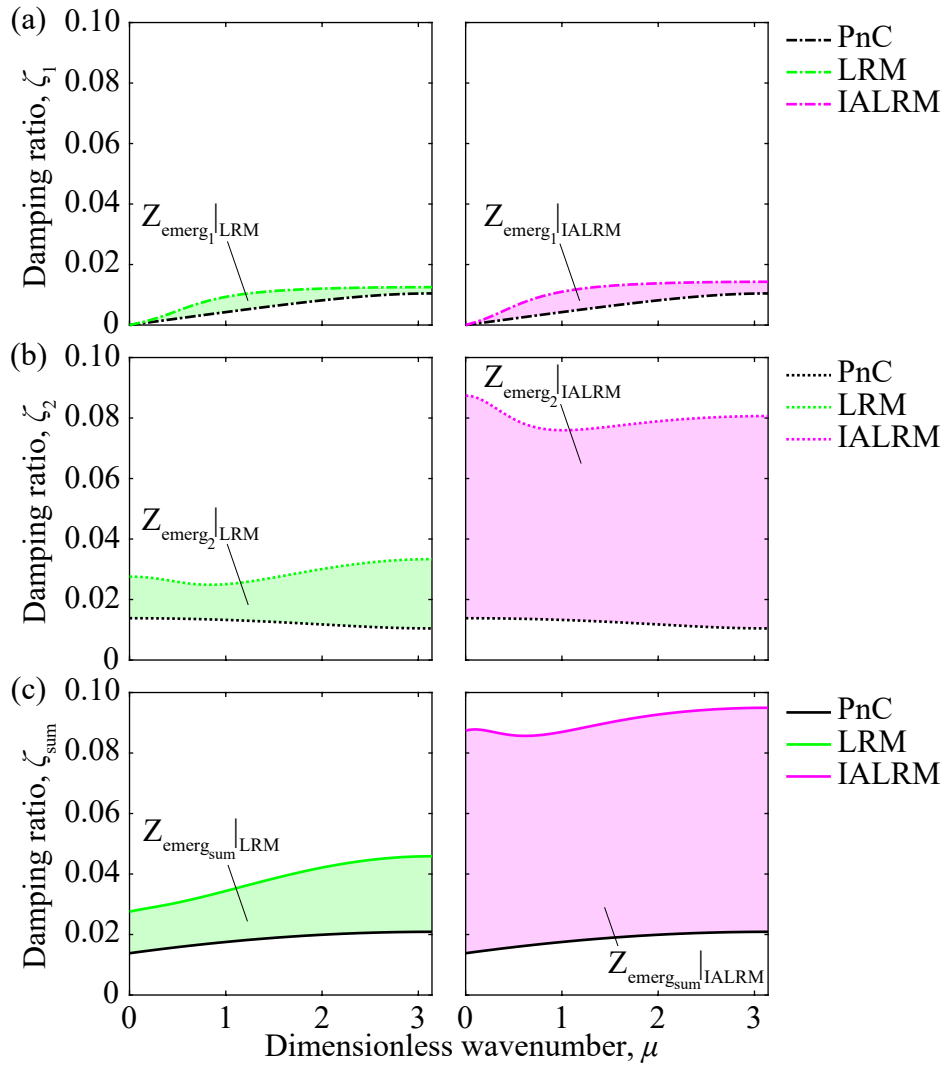


Figure 7.4: Damping-emergence quantities, shown as shaded regions, for the locally resonant metamaterial (LRM) and inertially amplified locally resonant metamaterial (IALRM) relative to the phononic crystal (PnC) corresponding to the (a) acoustic damping-ratio branch ζ_1 , (b) optical damping-ratio branch ζ_2 , and (c) summation of the two branches ζ_{sum} .

7.7 depict the non-dimensional damped-frequency band structure, damping-ratio diagram, and energy-harvesting availability $Z_{\text{EHA}_l}(l = \text{sum})$ for the PPnC, LRPM, and IALRPM, respectively, in comparison to their non-piezoelectric versions. The results In figures 7.5-7.7, subfigures (b) depict that the non-dimensional damped frequency band structures for the non-piezoelectric and piezoelectric periodic media are approximately similar. In figures 7.5-7.7, subfigures (c) show that the piezoelectric periodic media exhibit significantly higher damping ratios relative to their non-piezoelectric counterpart; in subfigures (d) for the three piezoelectric periodic media, it can be observed that the total value of the energy-harvesting

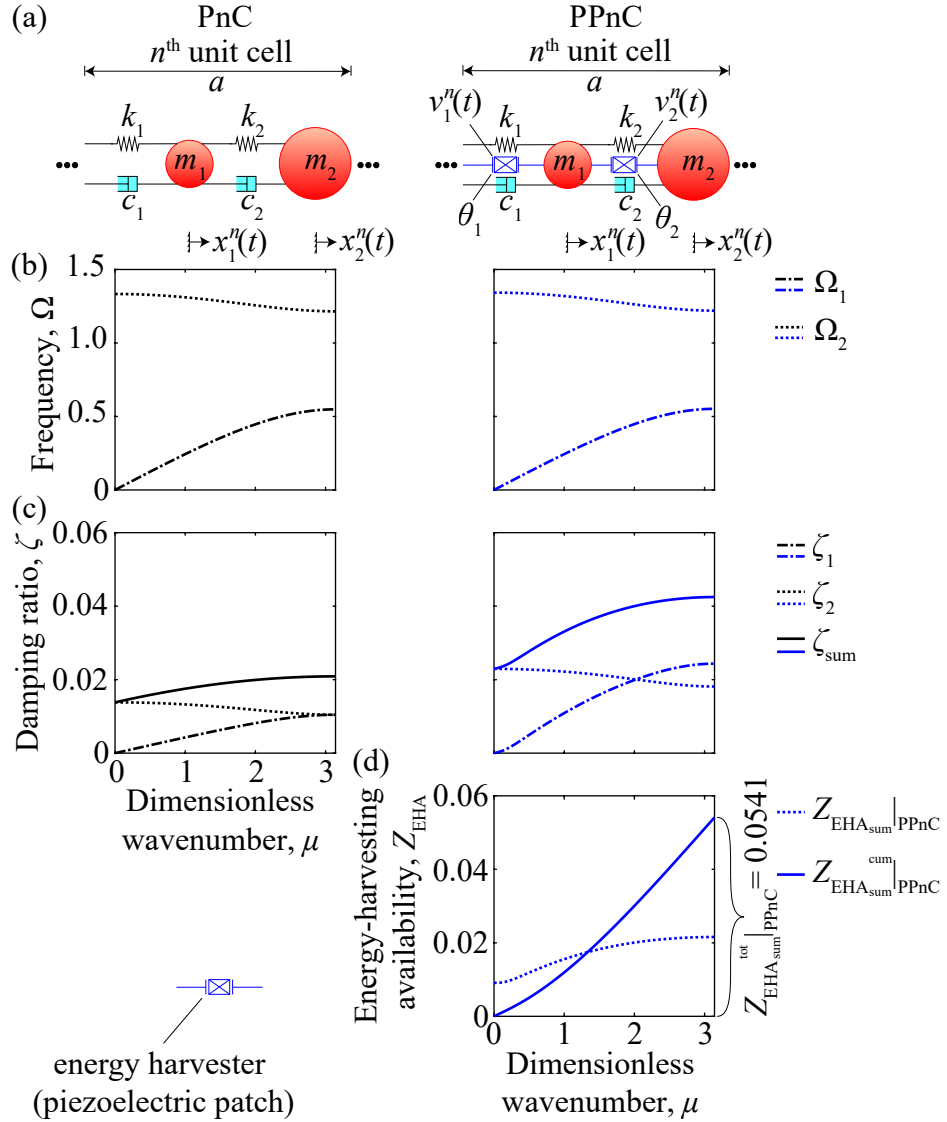


Figure 7.5: (a) Unit-cell schematics, (b) normalized damped-frequency band structures, and (c) damping-ratio diagrams for the phononic crystal (PnC) and piezoelectric phononic crystal (PPnC), and (d) energy-harvesting availability in the PPnC relative to the PnC corresponding to the summation of the two damping-ratio branches ζ_{sum} .

availability corresponding to the summation of the two damping-ratio branches (ζ_{sum}), $Z_{\text{EHA}_{\text{sum}}}^{\text{tot}}$, increases significantly while progressing from the PPnC to LRPM to IALRPM. Figure 7.8 displays the energy-harvesting availability corresponding to the acoustic damping-ratio branch ζ_1 , optical damping-ratio branch ζ_2 , and the summation of the two branches ζ_{sum} as shaded regions to highlight the contrast among the three piezoelectric periodic media. The increase in the size of the shaded regions, Z_{EHA_l} ($l = 1, 2,$ and sum), while progressing from the PPnC to LRPM indicates a significant enhancement in the energy-harvesting

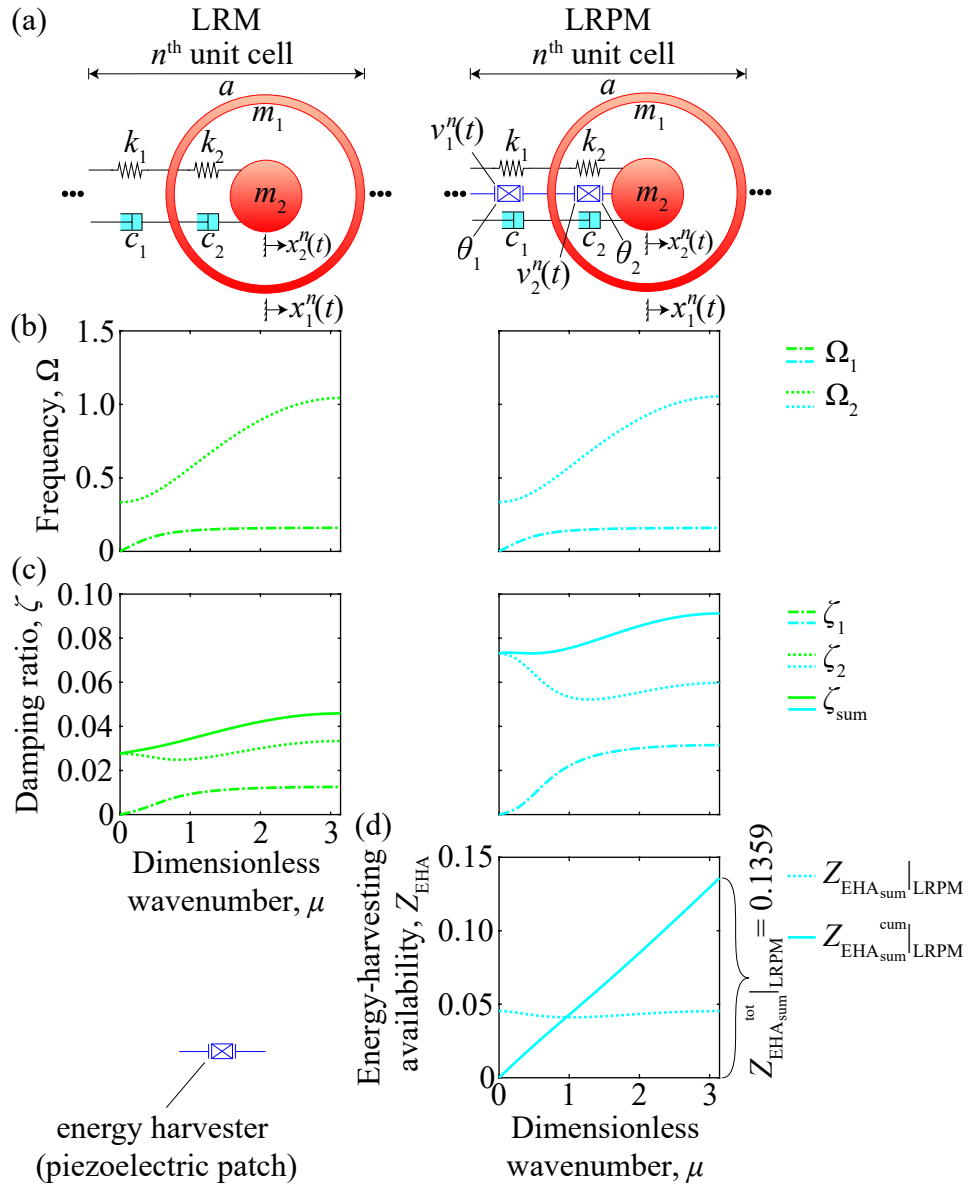


Figure 7.6: (a) Unit-cell schematics, (b) normalized damped-frequency band structures, and (c) damping-ratio diagrams for the locally resonant metamaterial (LRM) and locally resonant piezoelectric metamaterial (LRPM), and (d) energy-harvesting availability in the LRPM relative to the LRM corresponding to the summation of the two damping-ratio branches ζ_{sum} .

availability and indicates an even greater enhancement while progressing from the PPnC to IALRPM. When comparing the intrinsic energy-harvesting availability in the statically equivalent LRPM and IALRPM, it is evident that inertial amplification results in a significant improvement. For the IALRPM, results are shown at two different inertial-amplifier angles: $\phi = 70^\circ$ and $\phi = 90^\circ$. An angle of 90° is experimentally unrealizable but illustrates the maximum theoretical limit for quantities associated with an inertially amplified metamaterial.

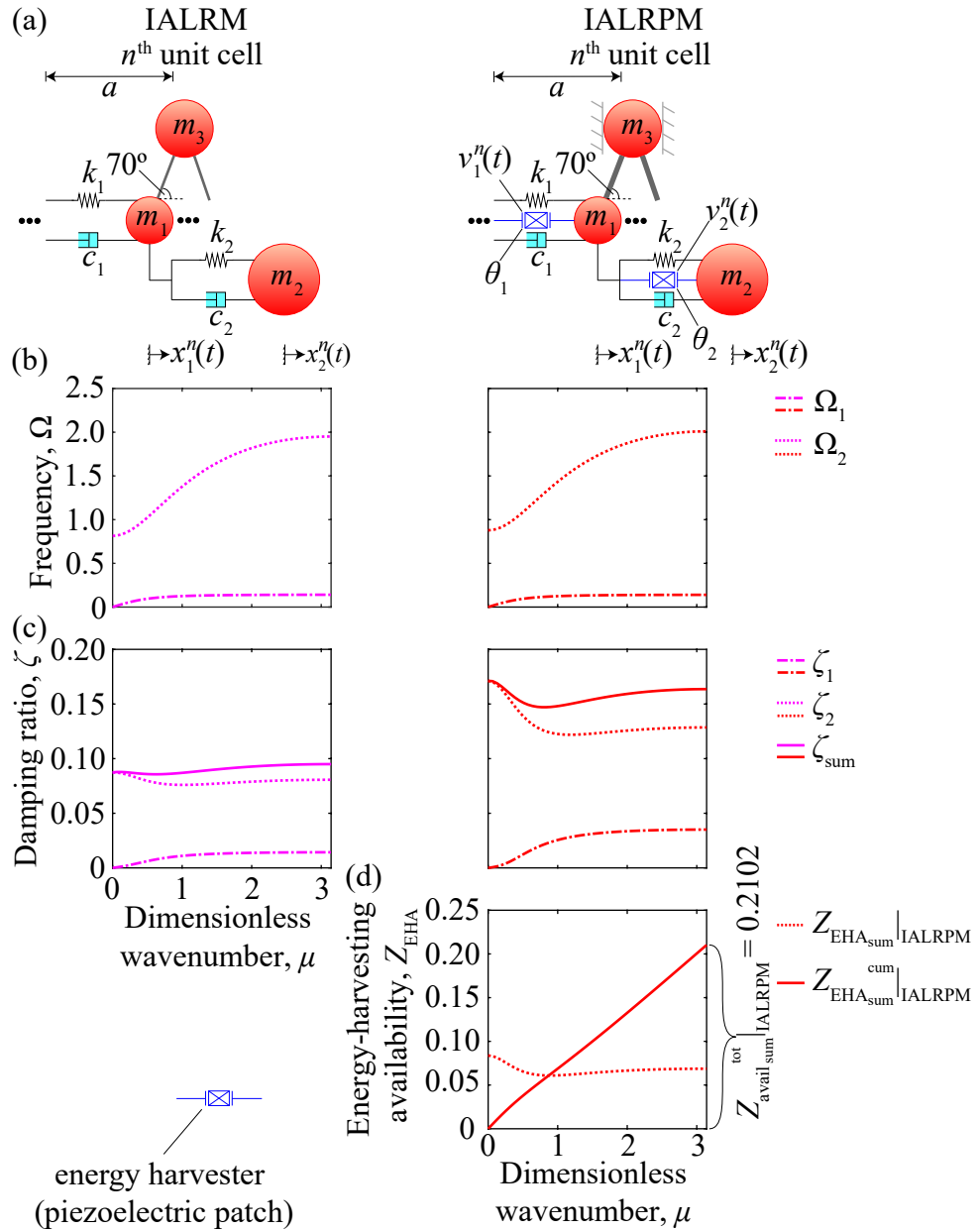


Figure 7.7: (a) Unit-cell schematics, (b) normalized damped-frequency band structures, and (c) damping-ratio diagrams for the inertially amplified locally resonant metamaterial (IALRM) and inertially amplified locally resonant piezoelectric metamaterial (IALRPM), and (d) energy-harvesting availability in the IALRPM relative to the IALRM corresponding to the summation of the two damping-ratio branches ζ_{sum} .

It is observed that ζ_1 overlaps at $\phi = 70^\circ$ and $\phi = 90^\circ$ but ζ_2 and ζ_{sum} are considerably higher at $\phi = 90^\circ$.

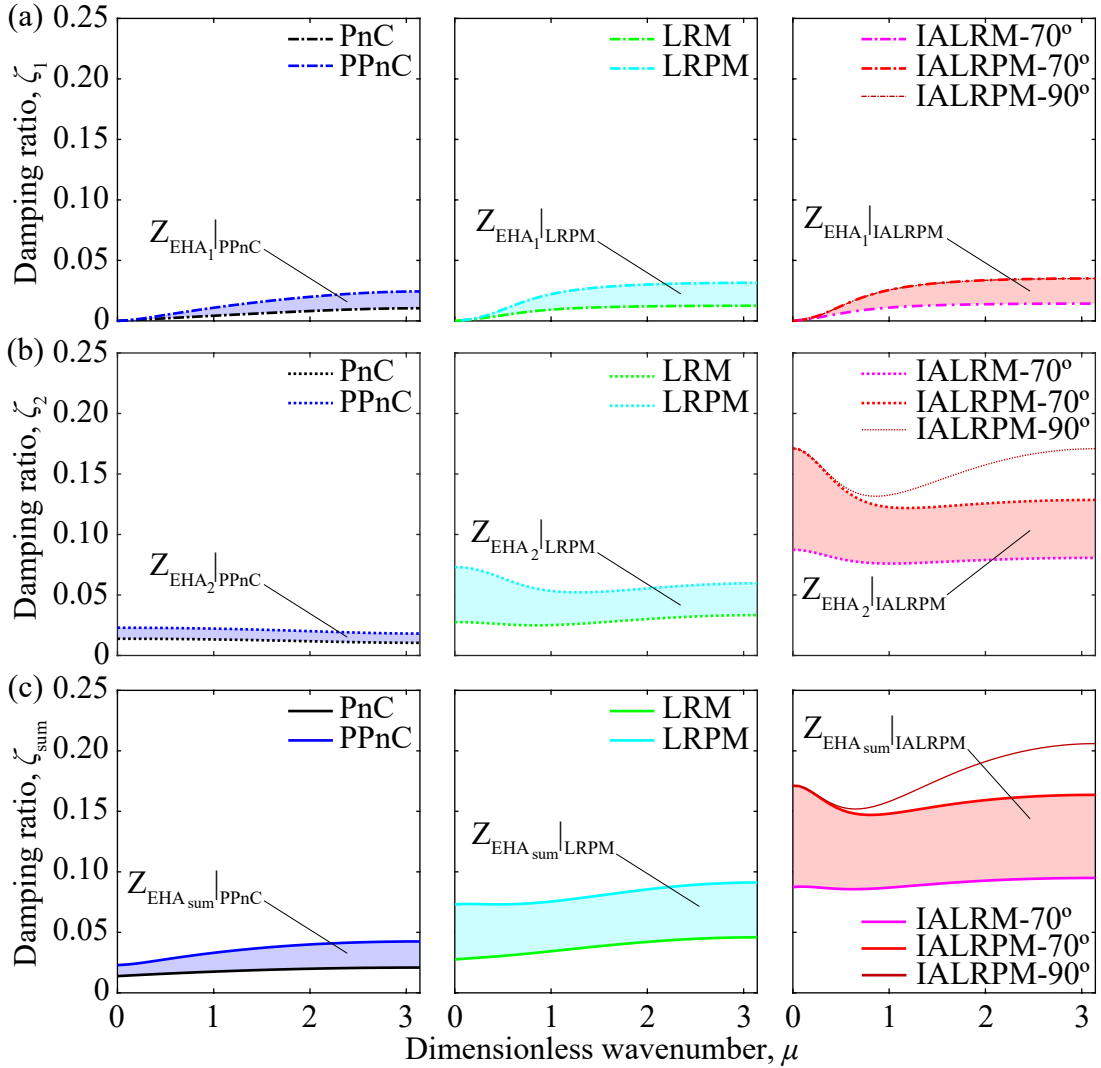


Figure 7.8: Energy-harvesting availability, shown as shaded regions, in the piezoelectric phononic crystal (PPnC), locally resonant piezoelectric metamaterial (LRPM), and inertially amplified locally resonant piezoelectric metamaterial (IALRPM) relative to the phononic crystal (PnC), locally resonant metamaterial (LRM), and inertially amplified locally resonant metamaterial (IALRM), respectively, corresponding to the (a) acoustic damping-ratio branch ζ_1 , (b) optical damping-ratio branch ζ_2 , and (c) summation of the two branches ζ_{sum} .

7.3.4 Metaharvesting: Locally resonant and inertially amplified locally resonant emergent energy-harvesting availability

In the current section, the bottom horizontal arrow, assigned to metaharvesting in the LRPM and IALRPM, in figure 7.2 is addressed via graphical illustrations. Figure 7.9 shows the unit-cell schematics of the PPnC, LRPM, and IALRPM, their non-dimensional damped-frequency band structures, their damping-ratio diagrams, and the quantity $Z_{\text{EHA}_l}^{\text{emerg}} (l = \text{sum})$

for the LRPM and IALRPM. In figure 7.9(c), the LRPM exhibits higher damping ratios compared to the PPnC; and the IALRPM exhibits even higher damping ratios; the increase is remarkable in the optical damping-ratio branch. It is observed that, among the three statically equivalent piezoelectric periodic media, the IALRPM exhibits the highest overall dissipation. Figure 7.9(d) shows an emergence in the energy-harvesting availability in the LRPM and an even higher emergence, i.e., enhanced emergence, in the energy-harvesting availability in the IALRPM. Figure 7.10 illustrates the phenomenon of metaharvesting corresponding to the acoustic damping-ratio branch, optical damping-ratio branch, and the summation of the branches as shaded regions to highlight the contrast between the piezoelectric LR and IA metamaterial. The increase in the size of the shaded regions, $Z_{\text{EHA}}^{\text{emerg}} (l = 1, 2, \text{ and sum})$, while progressing from the LRPM to the IALRPM indicates a significant enhancement in metaharvesting in the IALRPM, which points towards better performance of an electromechanical structure made using an IALRPM.

7.4 Summary and conclusions

The current chapter presents, as an overview, the phenomenon of metadamping, discussed in chapter 6, in an LRM and an IALRM, illustrates the concept of energy-harvesting availability, introduced in 5, in an LRPM and an IALRPM in addition to a PPnC, all of which were introduced in 3, and introduces the phenomenon of metaharvesting in an LRPM and an IALRPM. All the analysis is done at an intrinsic level, i.e., at a material level that is independent of forcing, sizing, and boundary conditions. The aforementioned statements are graphically summarized in figures 7.1 and 7.2. The governing equations for all the periodic media addressed in this chapter are provided and subjected to a Bloch transformation to set up an eigenvalue problem. Using the conventional eigenvalue solution, the non-dimensional damped-frequency band structures and damping-ratio diagrams are produced and shown as a function of the dimensionless wavenumber. The dispersion (frequency band-structure) and, most importantly, the dissipation characteristics are compared for statically equivalent non-piezoelectric and piezoelectric periodic media in adherence to the format depicted in figures 7.1 and 7.2.

Figure 7.11 shows, as a summary, the damping-ratio diagrams of all the non-piezoelectric and piezoelectric materials addressed in this chapter. The figure foundationally illustrates metadamping, energy-harvesting availability, and metaharvesting and presents to the reader a comprehensive summary of the intrinsic energetics framework shown in figures 7.1 and 7.2.

Figure 7.12, for all the periodic media, shows the relation between the non-dimensional damped frequencies, Ω_1 and Ω_2 , with their corresponding damping ratios, ζ_1 and ζ_2 . Figures

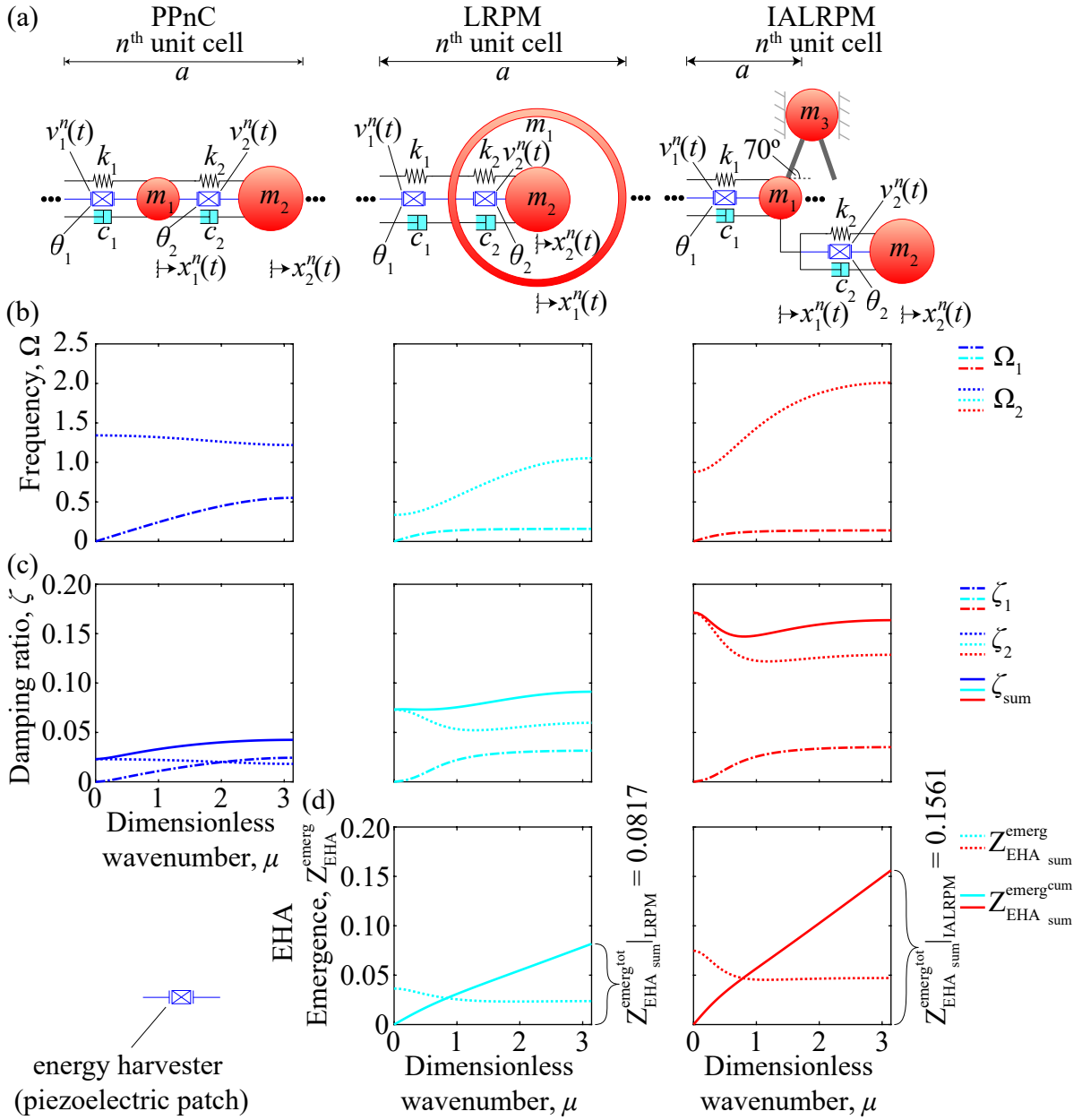


Figure 7.9: (a) Unit-cell schematics, (b) normalized damped-frequency band structures, and (c) damping-ratio diagrams for the statically equivalent piezoelectric phononic crystal (PPnC), locally resonant piezoelectric metamaterial (LRPM), and inertially amplified locally resonant piezoelectric metamaterial (IALRPM), and (d) emergent energy-harvesting availability (EHA)—metaharvesting—in the LRPM and IALRPM relative to the PPnC corresponding to the summation of the two damping-ratio branches ζ_{sum} .

of the this type have recently been used in literature involving the dispersion and dissipation analysis of periodic media. It is observed that the rate of the dash-dot curves corresponding to

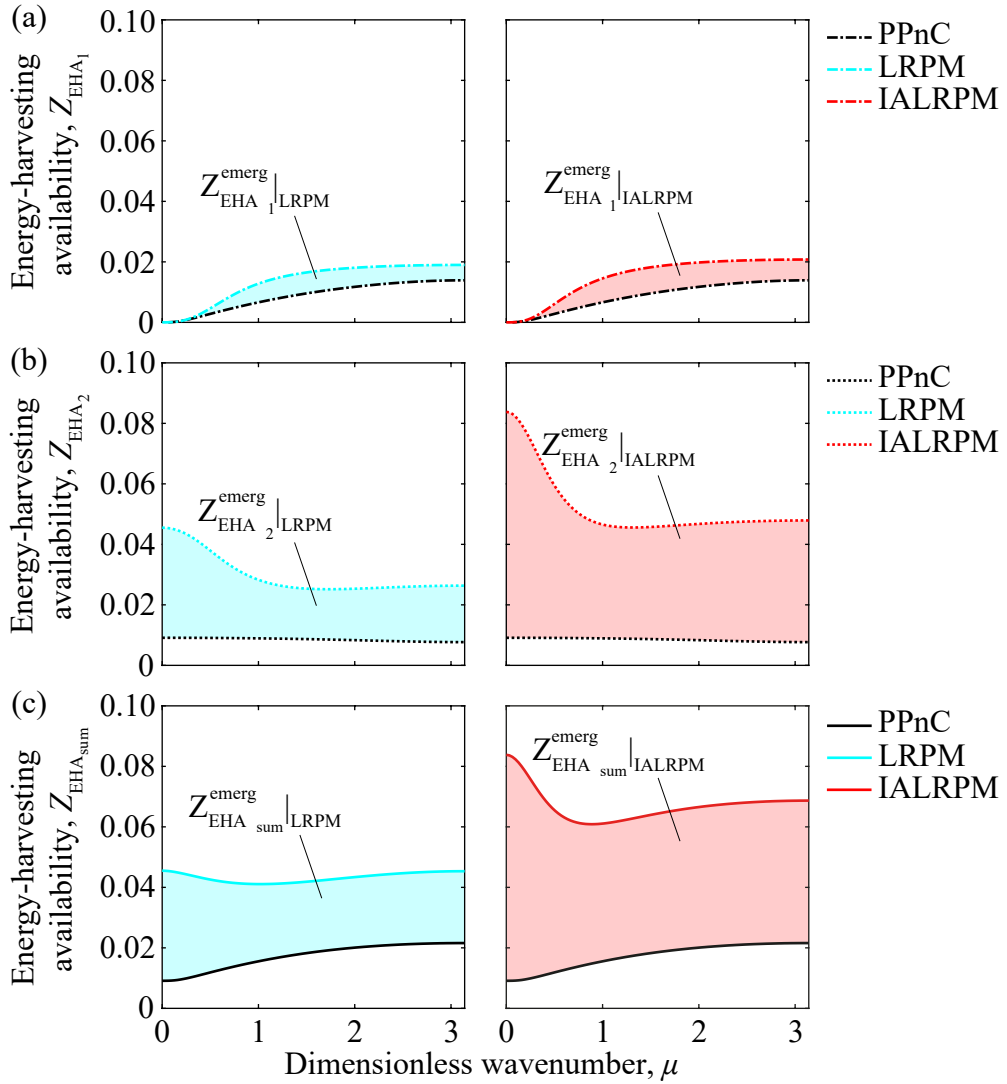


Figure 7.10: Emergent energy-harvesting availability or the phenomenon of metaharvesting, shown as shaded regions, in the locally resonant piezoelectric metamaterial (LRPM) and inertially amplified locally resonant piezoelectric metamaterial (IALRPM) relative to the PPnC corresponding to the (a) acoustic damping-ratio branch ζ_1 , (b) optical damping-ratio branch ζ_2 , and (c) summation of the two branches ζ_{sum} .

the acoustic branch increases and the level of the dotted curves corresponding to the optical branch increases in accordance with the direction of the arrows in figures 7.1 and 7.2.

The results presented in this chapter show that the intrinsic energy-harvesting availability is enhanced by a local-resonance mechanism and even further enhanced by adding an inertial-amplification mechanism. This enhancement is, essentially, an emergence, which is termed as metaharvesting. These findings formulate a pathway towards fundamental design of architected piezoelectric materials with superior energy harvesting capacity. Investigation

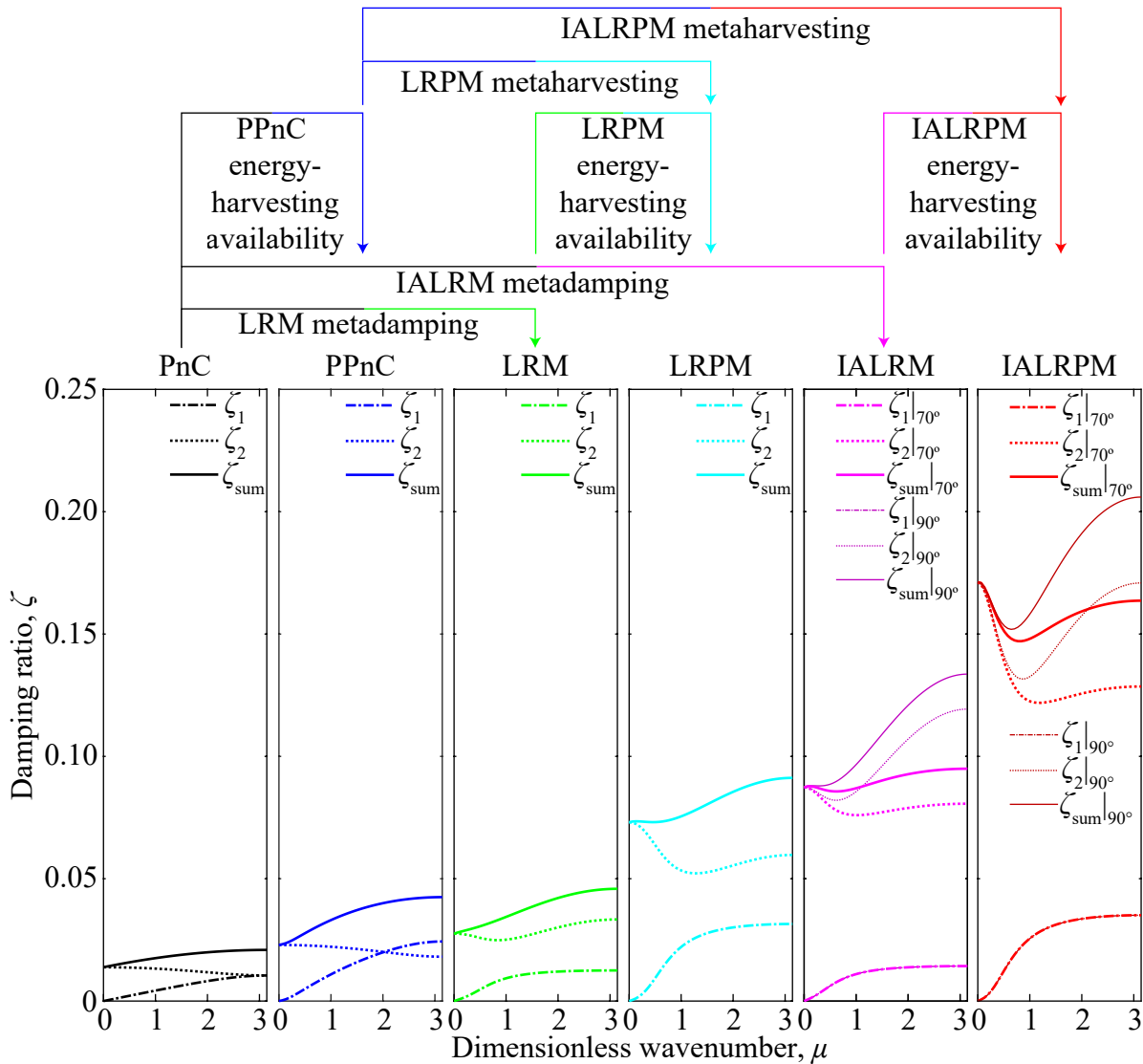


Figure 7.11: Damping-ratio diagrams for the phononic crystal (PnC), piezoelectric phononic crystal (PPnC), locally resonant metamaterial (LRM), locally resonant piezoelectric metamaterial (LRPM), inertially amplified locally resonant metamaterial (IALRM), and inertially amplified locally resonant piezoelectric metamaterial (IALRPM); the figure above depicts the phenomenon of metadamping, the concept of energy-harvesting availability, and the newly introduced phenomenon of metaharvesting as per figures 7.1 and 7.2. Each damping-ratio diagram depicts the acoustic branch (ζ_1), optical branch (ζ_2), and the summation of the two aforementioned branches (ζ_{sum}).

of statically equivalent piezoelectric periodic media, of the types discussed in this chapter, at an intrinsic/material level will facilitate effective performance evaluation, which will result in effective design-based choices to meet and exceed operational requirements and achieve

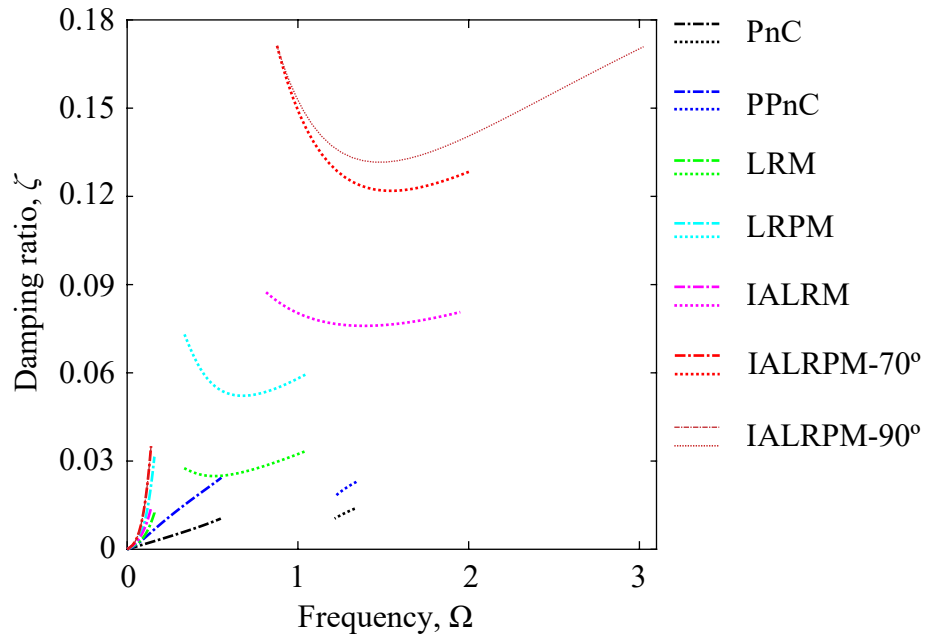


Figure 7.12: Relation between non-dimensional damped frequencies and their corresponding damping ratios for the phononic crystal (PnC), piezoelectric phononic crystal (PPnC), locally resonant metamaterial (LRM), locally resonant piezoelectric metamaterial (LRPM), inertially amplified locally resonant metamaterial (IALRM), and inertially amplified locally resonant piezoelectric metamaterial (IALRPM). The dash-dot lines show the relation for the acoustic branch, and the dotted lines show the relation for the optical branch.

maximum efficiency. The contents of this chapter will potentially form the journal article titled “Metaharvesting: Emergent energy harvesting by piezoelectric metamaterials.”

Chapter 8

Summary and conclusions

8.1 Thesis summary

Chapter 1 presents a preface to this thesis by succinctly providing a review of the technical topics relevant to this thesis, stating the motivation (problem statement), laying out the objectives, and listing the published research outcomes of this thesis.

Chapter 2 further expands on the pertinent technical topics, introduced and briefly discussed in chapter 1, in a brief literature review.

Chapter 3 presents the introductory theoretical framework for the analysis of the propagation of elastic waves through different configurations of linear elastic periodic media under free vibration and with and without energy harvesters by employing a generalized Bloch's theorem for plane waves followed by a state-space transformation to set up an eigenvalue problem. In doing so, the dispersion relations are derived and the mathematical definition of the solution, i.e., the eigenvalues, is given. The chapter serves the purpose of demonstrating that the analytical work presented in chapter 5 can be easily implemented for various types of piezoelectric periodic media, e.g., the types investigated in chapter 3.

Chapter 4 presents the dispersion and dissipation characteristics of a two-dimensional phononic crystal (PnC) and piezoelectric phononic crystal (PPnC) in a Bloch wave-propagation framework to demonstrate that the analytical work presented in chapter 5 is also applicable to two-dimensional cases. For simplicity, only a monoatomic PnC and the corresponding piezoelectric version are considered.

Chapter 5 proposes the new intrinsic concept of energy-harvesting availability by employing suspended monoatomic and diatomic PPnCs. The chapter presents a new formal approach for the characterization of energy-harvesting availability that is fundamentally at the *material* level rather than the structural or device level. Monoatomic and diatomic

PnC with integrated piezoelectric elements are considered and modelled as damped media within a Bloch wave-propagation-analysis framework. The wavenumber-dependent damping ratio—which is a rigorous measure of dissipation capacity—is obtained within the irreducible Brillouin zone (IBZ) and compared directly with that of the same PnC without the piezoelectric elements. The dissipation curves for the latter, the non-piezoelectric medium, give a direct indication of the “raw” dissipation which represents unexploited/lost energy. On the other hand, the difference in the dissipation curves between the two systems—the PnC with piezoelectric elements versus the PnC without piezoelectric elements—provides a formal intrinsic wavenumber-dependent representation of the amount of energy available for harvesting.

Chapter 6 illustrates the phenomena of positive and negative metadamping in an inertially amplified material (IAM) and an inertially amplified locally resonant metamaterial (IALRM) by using a statically equivalent PnC and a statically equivalent locally resonant metamaterial (LRM) as references. All the periodic media are analysed via a generalized Bloch’s theorem and subjected to a state-space transformation in order to obtain an eigenvalue problem. It is also shown that by combining inertial amplification with local resonance, i.e., in the IALRM, and, consequently, coupling the inertially amplified attenuation peak with that of a local-resonance attenuation peak, the unique phenomenon of a trade-off between the temporal- and spatial-attenuation intensities associated with the material properties is observed for a given range of the inertial-amplifier angle, i.e., angle between the rigid links and the central axis of the metamaterial.

Chapter 7 presents an overview of metadamping in an LRM and an IALRM and demonstrates the concept of energy-harvesting availability in a locally resonant piezoelectric metamaterial (LRPM) and an inertially amplified locally resonant piezoelectric metamaterial (IALRPM) and, consequently, an emergence of energy-harvesting availability, i.e., meta-harvesting, in the LRPM and the IALRPM by comparing the quantity to that of statically equivalent PPnC. All the periodic media are analysed via a generalized Bloch’s theorem and subjected to a state-space transformation in order to obtain an eigenvalue problem.

The proposed theory describing the concept of energy-harvesting availability provides a fundamental intrinsic characterization tool for the design and/or selection of piezoelectric energy-harvesting materials from which structure/devices may be formed. The underlying approach for quantifying intrinsic energy-harvesting availability will be useful in formally and generally comparing, categorising, and designing future energy-harvesting phononic materials, including other novel types of phononic crystals and elastic metamaterials.

The traits of enhanced positive and negative metadamping will lead to the effective design of phononic materials with the capability of exhibiting simultaneously high damping and

load-bearing capacities or simultaneously low damping and load-bearing capacities. The trade-off in the spatio-temporal intensities open the way for the design of future phononic materials with tailored spatio-temporal attenuation characteristics and could have significant implications on topological phononics and other contemporary areas in phononic engineering.

The phenomenon of metaharvesting formulates a pathway towards fundamental design of architected piezoelectric materials with superior energy harvesting capacity. Investigation of statically equivalent piezoelectric periodic media, of the types discussed in this chapter, at an intrinsic/material level will facilitate effective performance evaluation, which will result in effective design-based choices to meet and exceed operational requirements and achieve maximum efficiency.

8.2 Directions for future research

The areas of phononic engineering and piezoelectric vibration-energy harvesting (PVEH) using phononic materials are rapidly advancing, which is resulting in innovative and efficient designs with a wide variety of important applications. In terms of potential future works, the following research tasks can be undertaken:

1. Calculate the exact wavenumber-dependent useful dissipative energy available for harvesting in the irreducible Brillouin zone (IBZ).
2. Obtain the dispersion and dissipation characteristics and the quantity mentioned above for a finite discretized version of the piezoelectric periodic media addressed in this work.
3. Look into obtaining numerical solutions, using an appropriate numerical technique, e.g., finite element method (FEM), for finite continuous versions of the piezoelectric periodic media addressed in this work to compare the analytical and numerical results and reduce computational cost and time.
4. Perform optimization studies for the placement of shunted piezoelectric element (patch) in a finite continuous version of the piezoelectric periodic media addressed in this work.

Bibliography

- [1] Priya S and Inman DJ. *Energy Harvesting Technologies*, volume 21. Springer, Salmon Tower Building, New York City, 2009.
- [2] Erturk A and Inman DJ. *Piezoelectric Energy Harvesting*. John Wiley & Sons, Hoboken, New Jersey, 2011.
- [3] Elvin N and Erturk A. *Advances in Energy Harvesting Methods*. Springer Science & Business Media, Berlin, Germany, 2013.
- [4] Anton SR and Sodano HA. A review of power harvesting using piezoelectric materials (2003–2006). *Smart materials and Structures*, **16**(3):R1, 2007.
- [5] Safaei M, Sodano HA, and Anton SR. A review of energy harvesting using piezoelectric materials: state-of-the-art a decade later (2008–2018). *Smart Materials and Structures*, **28**(11):113001, 2019.
- [6] Karaman I, Basaran B, Karaca H, Karsilayan A, and Chumlyakov Y. Energy harvesting using martensite variant reorientation mechanism in a NiTi magnetic shape memory alloy. *Applied Physics Letters*, **90**(17):172505, 2007.
- [7] Aureli M, Prince C, Porfiri M, and Peterson SD. Energy harvesting from base excitation of ionic polymer metal composites in fluid environments. *Smart materials and Structures*, **19**(1):015003, 2009.
- [8] Cellini F, Cha Y, and Porfiri M. Energy harvesting from fluid-induced buckling of ionic polymer metal composites. *Journal of intelligent material systems and structures*, **25**(12):1496–1510, 2014.
- [9] Wang L and Yuan F. Vibration energy harvesting by magnetostrictive material. *Smart Materials and Structures*, **17**(4):045009, 2008.
- [10] Harne RL and Wang K. A review of the recent research on vibration energy harvesting via bistable systems. *Smart materials and structures*, **22**(2):023001, 2013.
- [11] Beeby SP, Tudor MJ, and White N. Energy harvesting vibration sources for microsystems applications. *Measurement science and technology*, **17**(12):R175, 2006.
- [12] Roundy S, Wright PK, and Rabaey JM. Energy scavenging for wireless sensor networks. In *Norwell*, pages 45–47. Springer, 2003.
- [13] Priya S. Advances in energy harvesting using low profile piezoelectric transducers. *Journal of electroceramics*, **19**(1):167–184, 2007.

- [14] Cook-Chennault KA, Thambi N, and Sastry AM. Powering mems portable devices - a review of non-regenerative and regenerative power supply systems with special emphasis on piezoelectric energy harvesting systems. *Smart materials and structures*, **17**(4):043001, 2008.
- [15] Park G and Inman DJ. Structural health monitoring using piezoelectric impedance measurements. *Philosophical Transactions of the Royal Society A: Mathematical, Physical and Engineering Sciences*, **365**(1851):373–392, 2007.
- [16] Park G, Rosing T, Todd MD, Farrar CR, and Hodgkiss W. Energy harvesting for structural health monitoring sensor networks. *Journal of Infrastructure Systems*, **14**(1):64–79, 2008.
- [17] Giurgiutiu V. *Structural Health Monitoring with Piezoelectric Wafer Active Sensors*. Elsevier, Oxford, UK, 2007.
- [18] Amin Karami M and Inman DJ. Powering pacemakers from heartbeat vibrations using linear and nonlinear energy harvesters. *Applied Physics Letters*, **100**(4):042901, 2012.
- [19] Sodano HA, Inman DJ, and Park G. A review of power harvesting from vibration using piezoelectric materials. *Shock and Vibration Digest*, **36**(3):197–206, 2004.
- [20] Erturk A and Inman DJ. A distributed parameter electromechanical model for cantilevered piezoelectric energy harvesters. *Journal of vibration and acoustics*, **130**(4), 2008.
- [21] Erturk A and Inman DJ. An experimentally validated bimorph cantilever model for piezoelectric energy harvesting from base excitations. *Smart materials and structures*, **18**(2):025009, 2009.
- [22] Friswell MI, Ali SF, Bilgen O, Adhikari S, Lees AW, and Litak G. Non-linear piezoelectric vibration energy harvesting from a vertical cantilever beam with tip mass. *Journal of Intelligent Material Systems and Structures*, **23**(13):1505–1521, 2012.
- [23] Hollkamp JJ. Multimodal passive vibration suppression with piezoelectric materials and resonant shunts. *Journal of intelligent material systems and structures*, **5**(1):49–57, 1994.
- [24] Agnes GS. Development of a modal model for simultaneous active and passive piezoelectric vibration suppression. *Journal of Intelligent Material Systems and Structures*, **6**(4):482–487, 1995.
- [25] Bailey T and Hubbard Jr JE. Distributed piezoelectric-polymer active vibration control of a cantilever beam. *Journal of Guidance, Control, and Dynamics*, **8**(5):605–611, 1985.
- [26] Moheimani SR and Fleming AJ. *Piezoelectric transducers for vibration control and damping*, volume 1. Springer, 2006.
- [27] Hagedorn P and Spelsberg-Korspeter G. *Active and passive vibration control of structures*, volume 558. Springer, 2014.

- [28] Wang Y and Inman DJ. A survey of control strategies for simultaneous vibration suppression and energy harvesting via piezoceramics. *Journal of Intelligent Material Systems and Structures*, **23**(18):2021–2037, 2012.
- [29] Deymier PA. *Acoustic Metamaterials and Phononic Crystals*, volume 173. Springer Science & Business Media, Berlin, Germany, 2013.
- [30] Hussein MI, Leamy MJ, and Ruzzene M. Dynamics of phononic materials and structures: Historical origins, recent progress, and future outlook. *Applied Mechanics Reviews*, **66**(4), 2014.
- [31] Phani AS and Hussein MI. *Dynamics of Lattice Materials*. John Wiley & Sons, 2017.
- [32] Mead DJ. Wave propagation and natural modes in periodic systems: I. mono-coupled systems. *Journal of Sound and Vibration*, **40**(1):1–18, 1975.
- [33] Kushwaha MS, Halevi P, Dobrzynski L, and Djafari-Rouhani B. Acoustic band structure of periodic elastic composites. *Physical Review Letters*, **71**(13):2022–2025, 1993.
- [34] Vasseur J, Deymier PA, Chenni B, Djafari-Rouhani B, Dobrzynski L, and Prevost D. Experimental and theoretical evidence for the existence of absolute acoustic band gaps in two-dimensional solid phononic crystals. *Physical Review Letters*, **86**(14):3012, 2001.
- [35] Zhang X and Liu Z. Negative refraction of acoustic waves in two-dimensional phononic crystals. *Applied Physics Letters*, **85**(2):341–343, 2004.
- [36] Phani AS, Woodhouse J, and Fleck NA. Wave propagation in two-dimensional periodic lattices. *Journal of the Acoustical Society of America*, **119**(4):1995–2005, 2006.
- [37] Robillard JF, Matar OB, Vasseur J, Deymier PA, Stippinger M, Hladky-Hennion AC, Pennec Y, and Djafari-Rouhani B. Tunable magnetoelastic phononic crystals. *Applied Physics Letters*, **95**(12):124104, 2009.
- [38] Pennec Y, Vasseur JO, Djafari-Rouhani B, Dobrzyński L, and Deymier PA. Two-dimensional phononic crystals: Examples and applications. *Surface Science Reports*, **65**(8):229–291, 2010.
- [39] Liu Z, Zhang X, Mao Y, Zhu Y, Yang Z, Chan CT, and Sheng P. Locally resonant sonic materials. *science*, **289**(5485):1734–1736, 2000.
- [40] Pennec Y, Djafari-Rouhani B, Larabi H, Vasseur JO, and Hladky-Hennion AC. Low-frequency gaps in a phononic crystal constituted of cylindrical dots deposited on a thin homogeneous plate. *Phys. Rev. B*, **78**(10):104105, 2008.
- [41] Xiao Y, Mace BR, Wen J, and Wen X. Formation and coupling of band gaps in a locally resonant elastic system comprising a string with attached resonators. *Physics Letters A*, **375**(12):1485–1491, 2011.
- [42] Krushynska AO, Kouznetsova VG, and Geers MG. Towards optimal design of locally resonant acoustic metamaterials. *Journal of the Mechanics and Physics of Solids*, **71**:179–196, 2014.

- [43] Kai W, Jiayi Z, Changqi C, Daolin X, and Guilin W. Review of low-frequency elastic wave metamaterials. *Chinese Journal of Theoretical and Applied Mechanics*, **54**:1–17, 2022.
- [44] Brillouin L. *Wave Propagation in Periodic Structures*. Dover Publications, Mineola, New York, 1946.
- [45] Brillouin L. *Wave Propagation and Group Velocity*. Academic Press, Cambridge, Massachusetts, 1960.
- [46] Hussein MI. Theory of damped bloch waves in elastic media. *Physical Review B*, **80**(21):212301, 2009.
- [47] Frazier MJ and Hussein MI. Generalized Bloch’s theorem for viscous metamaterials: Dispersion and effective properties based on frequencies and wavenumbers that are simultaneously complex. *Comptes Rendus Physique*, **17**:565–577, 2016.
- [48] Hussein MI, Patrick I, Banerjee A, and Adhikari S. Metadamping in inertially amplified metamaterials: Trade-off between spatial attenuation and temporal attenuation. *Journal of Sound and Vibration*, page 116977, 2022.
- [49] Sigmund O and Søndergaard Jensen J. Systematic design of phononic band-gap materials and structures by topology optimization. *Philosophical Transactions of the Royal Society of London. Series A: Mathematical, Physical and Engineering Sciences*, **361**(1806):1001–1019, 2003.
- [50] Wang Y, Guo J, and Zhang Z. The deformation induced tunable topology in controlling of band gap characteristics for stepped phononic crystals. *Solid State Communications*, page 114809, 2022.
- [51] Liu Z, Chan CT, and Sheng P. Three-component elastic wave band-gap material. *Physical Review B*, **65**(16):165116, 2002.
- [52] Yilmaz C, Hulbert GM, and Kikuchi N. Phononic band gaps induced by inertial amplification in periodic media. *Physical Review B*, **76**(5):054309, 2007.
- [53] Yilmaz C and Hulbert G. Theory of phononic gaps induced by inertial amplification in finite structures. *Physics Letters A*, **374**(34):3576–3584, 2010.
- [54] Acar G and Yilmaz C. Experimental and numerical evidence for the existence of wide and deep phononic gaps induced by inertial amplification in two-dimensional solid structures. *Journal of Sound and Vibration*, **332**(24):6389–6404, 2013.
- [55] Banerjee A, Adhikari S, and Hussein MI. Inertial amplification band-gap generation by coupling a levered mass with a locally resonant mass. *International Journal of Mechanical Sciences*, **207**:106630, 2021.
- [56] Frandsen NM, Bilal OR, Jensen JS, and Hussein MI. Inertial amplification of continuous structures: Large band gaps from small masses. *Journal of Applied Physics*, **119**(12):124902, 2016.

- [57] Thorp O, Ruzzene M, and Baz A. Attenuation and localization of wave propagation in rods with periodic shunted piezoelectric patches. *Smart Materials and Structures*, **10**(5):979, 2001.
- [58] Hou Z, Wu F, and Liu Y. Phononic crystals containing piezoelectric material. *Solid State Communications*, **130**(11):745–749, 2004.
- [59] Laude V, Wilm M, Benchabane S, and Khelif A. Full band gap for surface acoustic waves in a piezoelectric phononic crystal. *Physical Review E*, **71**(3):036607, 2005.
- [60] Gonella S, To AC, and Liu WK. Interplay between phononic bandgaps and piezoelectric microstructures for energy harvesting. *Journal of the Mechanics and Physics of Solids*, **57**(3):621–633, 2009.
- [61] Rupp CJ, Dunn ML, and Maute K. Switchable phononic wave filtering, guiding, harvesting, and actuating in polarization-patterned piezoelectric solids. *Applied Physics Letters*, **96**(11):111902, 2010.
- [62] Chen Z, Yang Y, Lu Z, and Luo Y. Broadband characteristics of vibration energy harvesting using one-dimensional phononic piezoelectric cantilever beams. *Physica B: Condensed Matter*, **410**:5–12, 2013.
- [63] Park CS, Shin YC, Jo SH, Yoon H, Choi W, Youn BD, and Kim M. Two-dimensional octagonal phononic crystals for highly dense piezoelectric energy harvesting. *Nano Energy*, **57**:327–337, 2019.
- [64] Cao D, Hu W, Gao Y, and Guo X. Vibration and energy harvesting performance of a piezoelectric phononic crystal beam. *Smart Materials and Structures*, **28**(8):085014, 2019.
- [65] Shin YC, Yoon H, Jo SH, Choi W, Park CS, Kim M, and Youn BD. Phononic band gap of a quarter-wave stack for enhanced piezoelectric energy harvesting. *International Journal of Mechanical Sciences*, page 106003, 2020.
- [66] Lee G, Lee D, Park J, Jang Y, Kim M, and Rho J. Piezoelectric energy harvesting using mechanical metamaterials and phononic crystals. *Communications Physics*, **5**(1):1–16, 2022.
- [67] Hu G, Tang L, Liang J, Lan C, and Das R. Acoustic-elastic metamaterials and phononic crystals for energy harvesting: A review. *Smart Materials and Structures*, 2021.
- [68] Chen Z, Guo B, Yang Y, and Cheng C. Metamaterials-based enhanced energy harvesting: A review. *Physica B: Condensed Matter*, **438**:1–8, 2014.
- [69] Shen L, Wu JH, Zhang S, Liu Z, and Li J. Low-frequency vibration energy harvesting using a locally resonant phononic crystal plate with spiral beams. *Modern Physics Letters B*, **29**(01):1450259, 2015.
- [70] Airolidi L and Ruzzene M. Design of tunable acoustic metamaterials through periodic arrays of resonant shunted piezos. *New Journal of Physics*, **13**:113010, 2011.

- [71] Casadei F, Delpero T, Bergamini A, Ermanni P, and Ruzzene M. Piezoelectric resonator arrays for tunable acoustic waveguides and metamaterials. *Journal of Applied Physics*, **112**(6):064902, 2012.
- [72] Sappati KK and Bhadra S. Piezoelectric polymer and paper substrates: A review. *Sensors*, **18**(11):3605, 2018.
- [73] Hu G, Tang L, Banerjee A, and Das R. Metastructure with piezoelectric element for simultaneous vibration suppression and energy harvesting. *Journal of Vibration and Acoustics*, **139**(1), 2017.
- [74] Hu G, Tang L, and Das R. Internally coupled metamaterial beam for simultaneous vibration suppression and low frequency energy harvesting. *Journal of Applied Physics*, **123**(5):055107, 2018.
- [75] Li Y, Baker E, Reissman T, Sun C, and Liu WK. Design of mechanical metamaterials for simultaneous vibration isolation and energy harvesting. *Applied Physics Letters*, **111**(25):251903, 2017.
- [76] Mikoshiba K, Manimala JM, and Sun C. Energy harvesting using an array of multifunctional resonators. *Journal of Intelligent Material Systems and Structures*, **24**(2):168–179, 2013.
- [77] Adhikari S and Banerjee A. Enhanced low-frequency vibration energy harvesting with inertial amplifiers. *Journal of Intelligent Material Systems and Structures*, page 1045389X211032281, 2021.
- [78] Lakes R. High damping composite materials: effect of structural hierarchy. *Journal of composite materials*, **36**(3):287–297, 2002.
- [79] Hussein MI and Frazier MJ. Metadamping: An emergent phenomenon in dissipative metamaterials. *Journal of Sound and Vibration*, **332**(20):4767–4774, 2013.
- [80] Bacquet CL, Al Ba'ba'a H, Frazier MJ, Nouh M, and Hussein MI. Metadamping: dissipation emergence in elastic metamaterials. *Advances in applied mechanics*, **51**:115–164, 2018.
- [81] Aladwani A, Mohammed A, and Nouh M. Tunable dissipation in elastic metamaterials via methodic reconfiguration of inertant mechanical networks. *Meccanica*, **57**(6):1337–1352, 2022.
- [82] Patrick I, Adhikari S, and Hussein MI. Brillouin-zone characterization of piezoelectric material intrinsic energy-harvesting availability. *Smart Materials and Structures*, **30**(8):085022, 2021.
- [83] Williams C and Yates RB. Analysis of a micro-electric generator for microsystems. *sensors and actuators A: Physical*, **52**(1-3):8–11, 1996.
- [84] Roundy S, Wright PK, and Rabaey J. A study of low level vibrations as a power source for wireless sensor nodes. *Computer communications*, **26**(11):1131–1144, 2003.

- [85] Mitcheson PD, Miao P, Stark BH, Yeatman E, Holmes A, and Green T. Mems electrostatic micropower generator for low frequency operation. *Sensors and Actuators A: Physical*, **115**(2-3):523–529, 2004.
- [86] Glynne-Jones P, Tudor MJ, Beeby SP, and White NM. An electromagnetic, vibration-powered generator for intelligent sensor systems. *Sensors and Actuators A: Physical*, **110**(1-3):344–349, 2004.
- [87] Adhikari S, Friswell M, Litak G, and Khodaparast HH. Design and analysis of vibration energy harvesters based on peak response statistics. *Smart Materials and Structures*, **25**(6):065009, 2016.
- [88] Adhikari S, Rastogi A, and Bhattacharya B. Piezoelectric vortex induced vibration energy harvesting in a random flow field. *Smart Materials and Structures*, **29**(3):035034, 2020.
- [89] Adhikari S, Friswell M, , and Inman D. Piezoelectric energy harvesting from broadband random vibrations. *Smart materials and structures*, **18**(11):115005, 2009.
- [90] Feenstra J, Granstrom J, and Sodano H. Energy harvesting through a backpack employing a mechanically amplified piezoelectric stack. *Mechanical Systems and Signal Processing*, **22**(3):721–734, 2008.
- [91] Kim HW, Batra A, Priya S, Uchino K, Markley D, Newnham RE, and Hofmann HF. Energy harvesting using a piezoelectric “cymbal” transducer in dynamic environment. *Japanese journal of applied physics*, **43**(9R):6178, 2004.
- [92] Anton S, Erturk A, and Inman D. Multifunctional self-charging structures using piezoceramics and thin-film batteries. *Smart materials and Structures*, **19**(11):115021, 2010.
- [93] Anton SR, Erturk A, Kong N, Ha DS, and Inman DJ. Self-charging structures using piezoceramics and thin-film batteries. In *Smart Materials, Adaptive Structures and Intelligent Systems*, volume 48975, pages 85–96, 2009.
- [94] Erturk A, Anton S, and Inman D. Piezoelectric energy harvesting from multifunctional wing spars for uavs: Part 1. coupled modeling and preliminary analysis. In *Active and Passive Smart Structures and Integrated Systems 2009*, volume 7288, pages 157–171. SPIE, 2009.
- [95] Anton S, Erturk A, and Inman D. Piezoelectric energy harvesting from multifunctional wing spars for uavs: Part 2. experiments and storage applications. In *Active and Passive Smart Structures and Integrated Systems 2009*, volume 7288, pages 172–183. SPIE, 2009.
- [96] Kushwaha MS, Halevi P, Dobrzynski L, and Djafari-Rouhani B. Acoustic band structure of periodic elastic composites. *Physical review letters*, **71**(13):2022, 1993.
- [97] Sigalas MM and Economou EN. Elastic and acoustic wave band structure. *Journal of sound and vibration*, **158**(2):377–382, 1992.

- [98] Yang S, Page JH, Liu Z, Cowan ML, Chan CT, and Sheng P. Focusing of sound in a 3d phononic crystal. *Physical review letters*, **93**(2):024301, 2004.
- [99] Cummer SA and Schurig D. One path to acoustic cloaking. *New journal of physics*, **9**(3):45, 2007.
- [100] Hussein MI, Biringer S, Bilal OR, and Kucala A. Flow stabilization by subsurface phonons. *Proceedings of the Royal Society A: Mathematical, Physical and Engineering Sciences*, **471**(2177):20140928, 2015.
- [101] Khelif A and Adibi A. Phononic crystals. *Berlin, Germany, Springer*, **10**:978–1, 2015.
- [102] Kohn W, Krumhansl JA, and Lee EH. Variational methods for dispersion relations and elastic properties of composite materials. 1972.
- [103] Lee EH and Yang WH. On waves in composite materials with periodic structure. *SIAM Journal on Applied Mathematics*, **25**(3):492–499, 1973.
- [104] Sun CT, Achenbach JD, and Herrmann G. Time-harmonic waves in a stratified medium propagating in the direction of the layering. 1968.
- [105] Bloch F. Über die quantenmechanik der elektronen in kristallgittern. *Zeitschrift für physik*, **52**(7):555–600, 1929.
- [106] Floquet G. Sur les équations différentielles linéaires à coefficients périodiques. In *Annales scientifiques de l'École normale supérieure*, volume 12, pages 47–88, 1883.
- [107] Smith DR, Padilla WJ, Vier D, Nemat-Nasser SC, and Schultz S. Composite medium with simultaneously negative permeability and permittivity. *Physical review letters*, **84**(18):4184, 2000.
- [108] Christensen J, Kadic M, Kraft O, and Wegener M. Vibrant times for mechanical metamaterials. *Mrs Communications*, **5**(3):453–462, 2015.
- [109] Al Ba'ba'a HB and Nouh M. Mechanics of longitudinal and flexural locally resonant elastic metamaterials using a structural power flow approach. *International Journal of Mechanical Sciences*, **122**:341–354, 2017.
- [110] Bilal OR and Hussein MI. Trampoline metamaterial: Local resonance enhancement by springboards. *Applied Physics Letters*, **103**(11):111901, 2013.
- [111] Wu TT, Huang ZG, Tsai TC, and Wu TC. Evidence of complete band gap and resonances in a plate with periodic stubbed surface. *Applied Physics Letters*, **93**(11):111902, 2008.
- [112] Wang G, Wen X, Wen J, Shao L, and Liu Y. Two-dimensional locally resonant phononic crystals with binary structures. *Physical review letters*, **93**(15):154302, 2004.
- [113] Dwivedi A, Banerjee A, Adhikari S, and Bhattacharya B. Optimal electromechanical bandgaps in piezo-embedded mechanical metamaterials. *International Journal of Mechanics and Materials in Design*, **17**(2):419–439, 2021.

- [114] Dwivedi A, Banerjee A, and Bhattacharya B. Simultaneous energy harvesting and vibration attenuation in piezo-embedded negative stiffness metamaterial. *Journal of Intelligent Material Systems and Structures*, **31**(8):1076–1090, 2020.
- [115] Frazier MJ and Hussein MI. Viscous-to-viscoelastic transition in phononic crystal and metamaterial band structures. *The Journal of the Acoustical Society of America*, **138**(5):3169–3180, 2015.
- [116] Antoniadis I, Chronopoulos D, Spitas V, and Koulocheris D. Hyper-damping properties of a stiff and stable linear oscillator with a negative stiffness element. *Journal of Sound and Vibration*, **346**:37–52, 2015.
- [117] DePauw D, Al Ba'ba'a H, and Nouh M. Metadamping and energy dissipation enhancement via hybrid phononic resonators. *Extreme Mechanics Letters*, **18**:36–44, 2018.
- [118] Al Ba'ba'a H, Lin Z, and Tol S. Metadamping enhancement and tunability via scissor-like electromechanical metamaterials. *Journal of Applied Physics*, **130**(18):184901, 2021.
- [119] Hussein MI and Frazier MJ. Band structure of phononic crystals with general damping. *Journal of Applied Physics*, **108**(9):093506, 2010.
- [120] Meirovitch L. *Principles and Techniques of Vibrations*, volume 1. Prentice Hall, Upper Saddle River, NJ, 1997.
- [121] Craig RR and Kurdila AJ. *Fundamentals of Structural Dynamics*. John Wiley & Sons, Hoboken, New Jersey, 2006.
- [122] Krattiger D, Khajehtourian R, Bacquet CL, and Hussein MI. Anisotropic dissipation in lattice metamaterials. *AIP Advances*, **6**(12):121802, 2016.
- [123] Lv H, Tian X, Wang MY, and Li D. Vibration energy harvesting using a phononic crystal with point defect states. *Applied Physics Letters*, **102**(3):034103, 2013.
- [124] Ma T, Chen Y, Chen H, Zheng Y, Huang G, Wang J, and Du J. Tuning characteristics of a metamaterial beam with lateral-electric-field piezoelectric shuntings. *Journal of Sound and Vibration*, page 115738, 2020.
- [125] Aladwani A and Nouh M. Mechanics of metadamping in flexural dissipative metamaterials: Analysis and design in frequency and time domains. *International Journal of Mechanical Sciences*, **173**:105459, 2020.
- [126] Jin Y, Pennec Y, Bonello B, Honarvar H, Dobrzynski L, Djafari-Rouhani B, and Hussein MI. Physics of surface vibrational resonances: Pillared phononic crystals, metamaterials, and metasurfaces. *Reports on Progress in Physics*, 2021.
- [127] Mukherjee S and Lee EH. Dispersion relations and mode shapes for waves in laminated viscoelastic composites by finite difference methods. *Computers & Structures*, **5**(5-6):279–285, 1975.
- [128] Hussein MI, Frazier MJ, and Abedinnasab MH. Chapter 1: Microdynamics of phononic materials. page 1 – 28, 2013.

Appendix A

Coefficients of non-dimensional equations

A.1 Monoatomic phononic crystal

The coefficients of equation (5.16) are as follows:

$$a_1 = 2\bar{\zeta} \left(4\gamma_2 \sin^2 \frac{\kappa a}{2} + 1 \right) \quad (\text{A.1})$$

$$a_2 = 4\gamma_1 \sin^2 \frac{\kappa a}{2} + 1. \quad (\text{A.2})$$

A.2 Diatomic phononic crystal

The coefficients of equation (5.26) are as follows:

$$a_1 = \frac{1}{\gamma_1} \left(2\bar{\zeta} \left((\gamma_5 + \gamma_7 + 1) \gamma_1 + \gamma_5 + \gamma_6 + \gamma_7 \right) \right), \quad (\text{A.3})$$

$$a_2 = \frac{1}{\gamma_1} \left(16\bar{\zeta}^2 \gamma_5 \gamma_7 \sin^2 \frac{\kappa a}{2} + (4(\gamma_6 + 1) \gamma_5 + 4(\gamma_6 + 1) \gamma_7 + 4\gamma_6) \bar{\zeta}^2 \right. \\ \left. + (1 + \gamma_2 + \gamma_4) \gamma_1 + \gamma_2 + \gamma_3 + \gamma_4 \right), \quad (\text{A.4})$$

$$a_3 = \frac{1}{\gamma_1} \left((8\bar{\zeta} \gamma_7 \gamma_2 + 8\gamma_4 \bar{\zeta} \gamma_5) \sin^2 \frac{\kappa a}{2} + 2\bar{\zeta} \left((\gamma_6 + 1) \gamma_2 \right. \right. \\ \left. \left. + (\gamma_6 + 1) \gamma_4 + (\gamma_3 + 1) \gamma_5 + (\gamma_3 + 1) \gamma_7 + \gamma_6 + \gamma_3 \right) \right), \quad (\text{A.5})$$

$$a_4 = \frac{1}{\gamma_1} \left(4 \sin^2 \frac{\kappa a}{2} \gamma_2 \gamma_4 + (\gamma_3 + 1) \gamma_2 + (\gamma_3 + 1) \gamma_4 + \gamma_3 \right). \quad (\text{A.6})$$

A.3 Monoatomic piezoelectric phononic crystal without inductor

The coefficients of equation (5.34) are as follows:

$$a_1 = \frac{1}{\alpha} \left(2\alpha\bar{\zeta} \left(4\gamma_2 \sin^2 \frac{\kappa a}{2} + 1 \right) + 1 \right), \quad (\text{A.7})$$

$$a_2 = \frac{1}{\alpha} \left(4 \sin^2 \frac{\kappa a}{2} (2\bar{\zeta}\gamma_2 + \alpha\gamma_1) + \alpha (k_{\text{coeff}}^2 + 1) + 2\bar{\zeta} \right), \quad (\text{A.8})$$

$$a_3 = \frac{1}{\alpha} \left(4\gamma_1 \sin^2 \frac{\kappa a}{2} + 1 \right). \quad (\text{A.9})$$

A.4 Monoatomic piezoelectric phononic crystal with inductor

The coefficients of equation (5.43) are as follows:

$$a_1 = \frac{1}{\alpha} \left(2\alpha\bar{\zeta} \left(4\gamma_2 \sin^2 \frac{\kappa a}{2} + 1 \right) + 1 \right), \quad (\text{A.10})$$

$$a_2 = \frac{1}{\alpha\beta} \left(4\beta \sin^2 \frac{\kappa a}{2} (2\bar{\zeta}\gamma_2 + \alpha\gamma_1) + \alpha\beta (k_{\text{coeff}}^2 + 1) + \alpha + 2\bar{\zeta}\beta \right), \quad (\text{A.11})$$

$$a_3 = \frac{1}{\alpha\beta} \left(4 \sin^2 \frac{\kappa a}{2} (2\gamma_2\bar{\zeta}\alpha + \gamma_1\beta) + 2\bar{\zeta}\alpha + \beta \right), \quad (\text{A.12})$$

$$a_4 = \frac{1}{\beta} \left(4\gamma_1 \sin^2 \frac{\kappa a}{2} + 1 \right). \quad (\text{A.13})$$

A.5 Diatomic piezoelectric phononic crystal without inductor

The coefficients of equation (5.58) are as follows:

$$a_1 = \frac{1}{\alpha\gamma_1\gamma_9\gamma_{10}} \left(2\bar{\zeta}\gamma_9\gamma_{10} ((\gamma_1 + 1)\gamma_5 + (\gamma_1 + 1)\gamma_7 + \gamma_6 + \gamma_1)\alpha + \gamma_1(\gamma_{10}\gamma_9 + 1) \right), \quad (\text{A.14})$$

$$\begin{aligned}
a_2 = & \frac{1}{\alpha^2 \gamma_1 \gamma_9 \gamma_{10}} \left(16\alpha^2 \gamma_{10} \gamma_9 \bar{\zeta}^2 \gamma_5 \gamma_7 \sin^2 \frac{\kappa a}{2} + (4\gamma_9 ((\gamma_6 + 1) \gamma_5 \right. \\
& + (\gamma_6 + 1) \gamma_7 + \gamma_6) \bar{\zeta}^2 + ((\gamma_1 + 1) \gamma_2 + (\gamma_1 + 1) \gamma_4 \\
& + k_{\text{coeff}}^2 \gamma_1 + \gamma_3 + \gamma_1) \gamma_9 + \gamma_8^2 k_{\text{coeff}}^2) \gamma_{10} \alpha^2 \\
& + 2\bar{\zeta} (\gamma_{10} \gamma_9 + 1) ((\gamma_1 + 1) \gamma_5 + (\gamma_1 + 1) \gamma_7 + \gamma_6 + \gamma_1) \alpha \\
& \left. + \gamma_1 \right), \tag{A.15}
\end{aligned}$$

$$\begin{aligned}
a_3 = & \frac{1}{\alpha^2 \gamma_1 \gamma_9 \gamma_{10}} \left((((8\alpha \gamma_{10} \gamma_9 \gamma_2 + 16\bar{\zeta} \gamma_5) \alpha + 16\alpha \bar{\zeta} \gamma_{10} \gamma_5 \gamma_9) \bar{\zeta} \gamma_7 \right. \\
& + 8\alpha^2 \gamma_{10} \gamma_9 \bar{\zeta} \gamma_5 \gamma_4) \sin^2 \frac{\kappa a}{2} + 2\bar{\zeta} \gamma_{10} ((\gamma_6 + 1) \gamma_2 \\
& + (\gamma_6 + 1) \gamma_4 + (k_{\text{coeff}}^2 + \gamma_3 + 1) \gamma_5 + (k_{\text{coeff}}^2 + \gamma_3 + 1) \gamma_7 \\
& + \gamma_6 k_{\text{coeff}}^2 + \gamma_3 + \gamma_6) \gamma_9 + \gamma_8^2 k_{\text{coeff}}^2 (\gamma_5 + \gamma_7 + 1)) \alpha^2 \\
& + ((4\gamma_{10} \gamma_9 + 4) ((\gamma_6 + 1) \gamma_5 + (\gamma_6 + 1) \gamma_7 + \gamma_6) \bar{\zeta}^2 \\
& + (((\gamma_1 + 1) \gamma_2 + (\gamma_1 + 1) \gamma_4 + \gamma_3 + \gamma_1) \gamma_9 + \gamma_8^2 k_{\text{coeff}}^2) \gamma_{10} \\
& + (\gamma_1 + 1) \gamma_2 + (\gamma_1 + 1) \gamma_4 + \gamma_1 + \gamma_3 + k_{\text{coeff}}^2 \gamma_1) \alpha \\
& \left. + ((2\gamma_1 + 2) \gamma_5 + (2\gamma_1 + 2) \gamma_7 + 2\gamma_6 + 2\gamma_1) \bar{\zeta} \right), \tag{A.16}
\end{aligned}$$

$$\begin{aligned}
a_4 = & \frac{1}{\alpha^2 \gamma_1 \gamma_9 \gamma_{10}} \left((((8\alpha \gamma_{10} \gamma_9 \gamma_2 + 8\gamma_2 \alpha + 16\bar{\zeta} \gamma_5) \bar{\zeta} \gamma_7 \right. \\
& + ((4\alpha \gamma_{10} \gamma_9 \gamma_2 + 8\bar{\zeta} \gamma_5) \alpha + 8\alpha \bar{\zeta} \gamma_{10} \gamma_5 \gamma_9) \gamma_4) \sin^2 \frac{\kappa a}{2} \\
& + \gamma_{10} (((k_{\text{coeff}}^2 + \gamma_3 + 1) \gamma_2 + (k_{\text{coeff}}^2 + \gamma_3 + 1) \gamma_4 \\
& + \gamma_3 (k_{\text{coeff}}^2 + 1)) \gamma_9 + \gamma_8^2 k_{\text{coeff}}^2 (k_{\text{coeff}}^2 + \gamma_2 + \gamma_4 + 1)) \alpha^2 \\
& + 2\bar{\zeta} (((\gamma_6 + 1) \gamma_2 + (\gamma_6 + 1) \gamma_4 + (\gamma_3 + 1) \gamma_5 \\
& + (\gamma_3 + 1) \gamma_7 + \gamma_6 + \gamma_3) \gamma_9 + \gamma_8^2 k_{\text{coeff}}^2 (\gamma_5 + \gamma_7 + 1)) \gamma_{10} \\
& + (\gamma_6 + 1) \gamma_2 + (\gamma_6 + 1) \gamma_4 + (k_{\text{coeff}}^2 + \gamma_3 + 1) \gamma_5 \\
& + (k_{\text{coeff}}^2 + \gamma_3 + 1) \gamma_7 + \gamma_6 k_{\text{coeff}}^2 + \gamma_3 + \gamma_6) \alpha + ((4\gamma_6 + 4) \gamma_5 \\
& + (4\gamma_6 + 4) \gamma_7 + 4\gamma_6) \bar{\zeta}^2 + (\gamma_1 + 1) \gamma_2 + (\gamma_1 + 1) \gamma_4 \\
& \left. + \gamma_3 + \gamma_1 \right), \tag{A.17}
\end{aligned}$$

$$\begin{aligned}
a_5 = & \frac{1}{\alpha^2 \gamma_1 \gamma_9 \gamma_{10}} \left(8\bar{\zeta} \gamma_7 \gamma_2 + (4\alpha \gamma_{10} \gamma_9 \gamma_2 + 4\gamma_2 \alpha + 8\bar{\zeta} \gamma_5) \gamma_4 \right) \sin^2 \frac{\kappa a}{2} \\
& + (((\gamma_3 + 1) \gamma_2 + (\gamma_3 + 1) \gamma_4 + \gamma_3) \gamma_9 \\
& + \gamma_8^2 k_{\text{coeff}}^2 (1 + \gamma_2 + \gamma_4)) \gamma_{10} + (k_{\text{coeff}}^2 + \gamma_3 + 1) \gamma_2 \\
& + (k_{\text{coeff}}^2 + \gamma_3 + 1) \gamma_4 + \gamma_3 (k_{\text{coeff}}^2 + 1) \alpha \\
& + 2\bar{\zeta} ((\gamma_6 + 1) \gamma_2 + (\gamma_6 + 1) \gamma_4 + (\gamma_3 + 1) \gamma_5 \\
& + (\gamma_3 + 1) \gamma_7 + \gamma_6 + \gamma_3) , \tag{A.18}
\end{aligned}$$

$$a_6 = \frac{1}{\alpha^2 \gamma_1 \gamma_9 \gamma_{10}} \left(4 \sin^2 \frac{\kappa a}{2} \gamma_2 \gamma_4 + (\gamma_3 + 1) \gamma_2 + (\gamma_3 + 1) \gamma_4 + \gamma_3 \right). \tag{A.19}$$

A.6 Diatomic piezoelectric phononic crystal with inductor

The coefficients of equation (5.74) are as follows:

$$a_1 = \frac{1}{\alpha \gamma_1 \gamma_9 \gamma_{10}} \left(2(\bar{\zeta} ((\gamma_5 + \gamma_7 + 1) \gamma_1 + \gamma_5 + \gamma_6 + \gamma_7) \alpha + \frac{\gamma_1}{2}) \gamma_9 \gamma_{10} + \gamma_1 \right), \tag{A.20}$$

$$\begin{aligned}
a_2 = & \frac{1}{\alpha^2 \beta \gamma_1 \gamma_9 \gamma_{10} \gamma_{11}} \left(16 \sin^2 \frac{\kappa a}{2} \alpha^2 \beta \bar{\zeta}^2 \gamma_{10} \gamma_{11} \gamma_5 \gamma_7 \gamma_9 + ((((((4\gamma_6 + 4) \gamma_5 \right. \\
& + (4\gamma_6 + 4) \gamma_7 + 4\gamma_6) \bar{\zeta}^2 + (k_{\text{coeff}}^2 + \gamma_2 + \gamma_4 + 1) \gamma_1 + \gamma_4 \\
& + \gamma_2 + \gamma_3) \gamma_9 + \gamma_8^2 k_{\text{coeff}}^2) \beta + \gamma_1 \gamma_9) \gamma_{10} \alpha^2 \\
& + 2\beta ((\gamma_5 + \gamma_7 + 1) \gamma_1 + \gamma_5 + \gamma_6 + \gamma_7) (\gamma_{10} \gamma_9 + 1) \bar{\zeta} \alpha \\
& \left. + \beta \gamma_1) \gamma_{11} + \alpha^2 \gamma_1 \gamma_{10} \right), \tag{A.21}
\end{aligned}$$

$$\begin{aligned}
a_3 = & \frac{1}{\alpha^2 \beta \gamma_1 \gamma_9 \gamma_{10} \gamma_{11}} (8\beta \gamma_{11} \alpha (\gamma_9 \gamma_{10} (\gamma_2 \gamma_7 + \gamma_4 \gamma_5) \alpha \\
& + 2\gamma_5 \gamma_7 \bar{\zeta} (\gamma_{10} \gamma_9 + 1)) \bar{\zeta} \sin^2 \frac{\kappa a}{2} + 2\gamma_{10} \bar{\zeta} (((k_{\text{coeff}}^2 + \gamma_3 \\
& + 1) \gamma_5 + (k_{\text{coeff}}^2 + \gamma_3 + 1) \gamma_7 + (k_{\text{coeff}}^2 + \gamma_2 + \gamma_4 + 1) \gamma_6 + \gamma_4 \\
& + \gamma_2 + \gamma_3) \gamma_9 + \gamma_8^2 k_{\text{coeff}}^2 (\gamma_5 + \gamma_7 + 1)) \beta + \gamma_9 ((\gamma_5 + \gamma_7 \\
& + 1) \gamma_{11} + \gamma_5 + \gamma_6 + \gamma_7) \gamma_{11} + (\gamma_5 + \gamma_7 + 1) \gamma_1 + \gamma_5 + \gamma_6 \\
& + \gamma_7) \alpha^2 + (((4((\gamma_6 + 1) \gamma_5 + (\gamma_6 + 1) \gamma_7 + \gamma_6) (\gamma_{10} \gamma_9 \\
& + 1) \bar{\zeta}^2 + (((\gamma_4 + \gamma_2 + 1) \gamma_1 + \gamma_4 + \gamma_2 + \gamma_3) \gamma_9 \\
& + \gamma_8^2 k_{\text{coeff}}^2) \gamma_{10} + (k_{\text{coeff}}^2 + \gamma_2 + \gamma_4 + 1) \gamma_1 + \gamma_4 + \gamma_2 + \gamma_3) \beta \\
& + \gamma_1) \gamma_{11} + \gamma_{10} \gamma_1) \alpha + 2\beta ((\gamma_5 + \gamma_7 + 1) \gamma_1 + \gamma_5 + \gamma_6 \\
& + \gamma_7) \gamma_{11} \bar{\zeta}), \tag{A.22}
\end{aligned}$$

$$\begin{aligned}
a_4 = & \frac{1}{\alpha^2 \beta^2 \gamma_1 \gamma_9 \gamma_{10} \gamma_{11}} \left(8\beta \left(\frac{\gamma_4 \gamma_9 \gamma_{10} \alpha^2}{2} \gamma_2 + \bar{\zeta} (\gamma_{10} \gamma_9 + 1) (\gamma_2 \gamma_7 + \gamma_4 \gamma_5) \alpha \right. \right. \\
& + 2\gamma_5 \gamma_7 \bar{\zeta}^2) \gamma_{11} \beta + 2\gamma_5 \gamma_7 \gamma_{10} \alpha^2 \bar{\zeta}^2 (\gamma_{11} \gamma_9 + 1) \sin^2 \frac{\kappa a}{2} \\
& + 2\gamma_{11} \left(\frac{\gamma_{10}}{2} (((k_{\text{coeff}}^2 + \gamma_3 + 1) \gamma_2 + (k_{\text{coeff}}^2 + \gamma_3 + 1) \gamma_4 \right. \\
& + \gamma_3 (k_{\text{coeff}}^2 + 1)) \gamma_9 + \gamma_8^2 k_{\text{coeff}}^2 (k_{\text{coeff}}^2 + \gamma_2 + \gamma_4 + 1)) \alpha^2 \\
& + (((\gamma_3 + 1) \gamma_5 + (\gamma_3 + 1) \gamma_7 + (\gamma_4 + \gamma_2 + 1) \gamma_6 + \gamma_4 + \gamma_2 \\
& + \gamma_3) \gamma_9 + \gamma_8^2 k_{\text{coeff}}^2 (\gamma_5 + \gamma_7 + 1)) \gamma_{10} + (k_{\text{coeff}}^2 + \gamma_3 + 1) \gamma_5 \\
& + (k_{\text{coeff}}^2 + \gamma_3 + 1) \gamma_7 + (k_{\text{coeff}}^2 + \gamma_2 + \gamma_4 + 1) \gamma_6 + \gamma_4 + \gamma_2 \\
& + \gamma_3) \bar{\zeta} \alpha + ((2\gamma_6 + 2) \gamma_5 + (2\gamma_6 + 2) \gamma_7 + 2\gamma_6) \bar{\zeta}^2 \\
& + \left(\frac{\gamma_4}{2} + \frac{\gamma_2}{2} + \frac{1}{2} \right) \gamma_1 + \frac{\gamma_2}{2} + \frac{\gamma_3}{2} + \frac{\gamma_4}{2} \beta^2 \\
& + (\gamma_{10} ((4\gamma_9 ((\gamma_6 + 1) \gamma_5 + (\gamma_6 + 1) \gamma_7 + \gamma_6) \bar{\zeta}^2 + ((\gamma_4 + \gamma_2 \\
& + 1) \gamma_1 + \gamma_4 + \gamma_2 + \gamma_3) \gamma_9 + \gamma_8^2 k_{\text{coeff}}^2) \gamma_{11} + ((4\gamma_6 + 4) \gamma_5 \\
& + (4\gamma_6 + 4) \gamma_7 + 4\gamma_6) \bar{\zeta}^2 + (k_{\text{coeff}}^2 + \gamma_2 + \gamma_4 + 1) \gamma_1 + \gamma_4 + \gamma_2 \\
& + \gamma_3) \alpha + (2(\gamma_1 + 1) \gamma_5 + 2(\gamma_1 + 1) \gamma_7 + 2\gamma_6 + 2\gamma_1) \bar{\zeta} (\gamma_{10} \\
& \left. \left. + \gamma_{11}) \right) \alpha \beta + \alpha^2 \gamma_1 \gamma_{10} \right), \tag{A.23}
\end{aligned}$$

(A.24)

$$\begin{aligned}
a_5 = & \frac{1}{\alpha^2 \beta^2 \gamma_1 \gamma_9 \gamma_{10} \gamma_{11}} \left(8(\gamma_{11} \left(\frac{\gamma_4 \gamma_2}{2} (\gamma_{10} \gamma_9 + 1) \alpha + \bar{\zeta} (\gamma_2 \gamma_7 + \gamma_4 \gamma_5) \right) \beta \right. \\
& + \bar{\zeta} \alpha (\gamma_{10} (\gamma_{11} \gamma_9 + 1) (\gamma_2 \gamma_7 + \gamma_4 \gamma_5) \alpha + 2 \gamma_5 \gamma_7 \bar{\zeta} (\gamma_{10} \\
& + \gamma_{11}))) \beta \sin^2 \frac{\kappa a}{2} + 2 \gamma_{11} \left(\left(\left(\left(\frac{1}{2} + \frac{\gamma_3}{2} \right) \gamma_9 + \frac{k_{\text{coeff}}^2 \gamma_8^2}{2} \right) \gamma_2 \right. \right. \\
& + \left. \left(\left(\frac{1}{2} + \frac{\gamma_3}{2} \right) \gamma_9 + \frac{k_{\text{coeff}}^2 \gamma_8^2}{2} \right) \gamma_4 + \frac{k_{\text{coeff}}^2 \gamma_8^2}{2} + \frac{\gamma_3 \gamma_9}{2} \right) \gamma_{10} \\
& + \left(\frac{1}{2} + \frac{\gamma_3}{2} + \frac{k_{\text{coeff}}^2}{2} \right) \gamma_2 + \frac{1}{2} + \frac{\gamma_3}{2} + \frac{k_{\text{coeff}}^2}{2} \right) \gamma_4 + \frac{\gamma_3}{2} (k_{\text{coeff}}^2 + 1) \alpha \\
& + \bar{\zeta} ((\gamma_6 + 1) \gamma_2 + (\gamma_6 + 1) \gamma_4 + (\gamma_3 + 1) \gamma_5 + (\gamma_3 + 1) \gamma_7 \\
& + \gamma_6 + \gamma_3)) \beta^2 + 2 \alpha (\bar{\zeta} ((\gamma_9 (\gamma_6 + 1) \gamma_2 + \gamma_9 (\gamma_6 + 1) \gamma_4 \\
& + ((\gamma_3 + 1) \gamma_9 + k_{\text{coeff}}^2 \gamma_8^2) \gamma_5 + ((\gamma_3 + 1) \gamma_9 + k_{\text{coeff}}^2 \gamma_8^2) \gamma_7 \\
& + (\gamma_3 + \gamma_6) \gamma_9 + k_{\text{coeff}}^2 \gamma_8^2) \gamma_{11} + (\gamma_6 + 1) \gamma_2 + (\gamma_6 + 1) \gamma_4 \\
& + (k_{\text{coeff}}^2 + \gamma_3 + 1) \gamma_5 + (k_{\text{coeff}}^2 + \gamma_3 + 1) \gamma_7 + \gamma_6 k_{\text{coeff}}^2 + \gamma_6 \\
& + \gamma_3) \gamma_{10} \alpha + \frac{\gamma_{10} + \gamma_{11}}{2} ((4 \gamma_6 + 4) \gamma_5 + (4 \gamma_6 + 4) \gamma_7 \\
& + 4 \gamma_6) \bar{\zeta}^2 + (\gamma_1 + 1) \gamma_2 + (\gamma_1 + 1) \gamma_4 + \gamma_1 + \gamma_3)) \beta \\
& \left. + 2 \bar{\zeta} ((\gamma_1 + 1) \gamma_5 + (\gamma_1 + 1) \gamma_7 + \gamma_6 + \gamma_1) \alpha^2 \gamma_{10} \right), \tag{A.25}
\end{aligned}$$

$$\begin{aligned}
a_6 = & \frac{1}{\alpha^2 \beta^2 \gamma_1 \gamma_9 \gamma_{10} \gamma_{11}} \left((4 \gamma_{10} (\gamma_4 \gamma_2 (\gamma_{11} \gamma_9 + 1) \beta + 4 \gamma_5 \gamma_7 \bar{\zeta}^2) \alpha^2 \right. \\
& + 8 \beta \bar{\zeta} (\gamma_{10} + \gamma_{11}) (\gamma_2 \gamma_7 + \gamma_4 \gamma_5) \alpha \\
& + 4 \beta^2 \gamma_{11} \gamma_2 \gamma_4 \sin^2 \frac{\kappa a}{2} + \gamma_{10} \left(\left(\left(\left(k_{\text{coeff}}^2 \gamma_8^2 + \gamma_3 \gamma_9 \right. \right. \right. \right. \\
& + \gamma_9) \gamma_2 + (k_{\text{coeff}}^2 \gamma_8^2 + \gamma_3 \gamma_9 + \gamma_9) \gamma_4 + k_{\text{coeff}}^2 \gamma_8^2 \\
& + \gamma_3 \gamma_9) \gamma_{11} + (k_{\text{coeff}}^2 + \gamma_3 + 1) \gamma_2 + (k_{\text{coeff}}^2 + \gamma_3 + 1) \gamma_4 \\
& + \gamma_3 (k_{\text{coeff}}^2 + 1) \beta + ((4 \gamma_6 + 4) \gamma_5 + (4 \gamma_7 + 4) \gamma_6 \\
& + 4 \gamma_7) \bar{\zeta}^2 + (\gamma_1 + 1) \gamma_2 + (\gamma_1 + 1) \gamma_4 + \gamma_1 + \gamma_3) \alpha^2 \\
& + 2 \bar{\zeta} ((\gamma_6 + 1) \gamma_2 + (\gamma_6 + 1) \gamma_4 \\
& + (\gamma_5 + \gamma_7 + 1) \gamma_3 + \gamma_5 + \gamma_6 + \gamma_7) (\gamma_{10} + \gamma_{11}) \beta \alpha \\
& \left. + \gamma_{11} \beta^2 ((\gamma_3 + 1) \gamma_2 + (\gamma_3 + 1) \gamma_4 + \gamma_3) \right), \tag{A.26}
\end{aligned}$$

$$\begin{aligned}
a_7 &= \frac{1}{\alpha\beta^2\gamma_1\gamma_9\gamma_{10}\gamma_{11}} \left((8\bar{\xi}(\gamma_2\gamma_7 + \gamma_4\gamma_5)\alpha + 4\beta\gamma_2\gamma_4)\gamma_{10} \right. \\
&\quad + 4\beta\gamma_{11}\gamma_2\gamma_4 \sin^2 \frac{\kappa a}{2} + ((2(\gamma_6 + 1)\gamma_2 \\
&\quad + 2(\gamma_6 + 1)\gamma_4 + 2(\gamma_5 + \gamma_7 + 1)\gamma_3 + 2\gamma_5 \\
&\quad + 2\gamma_6 + 2\gamma_7)\bar{\xi}\alpha + ((\gamma_3 + 1)\gamma_2 + (\gamma_4 + 1)\gamma_3 \\
&\quad + \gamma_4)\beta)\gamma_{10} + ((\gamma_3 + 1)\gamma_2 + (\gamma_4 + 1)\gamma_3 \\
&\quad \left. + \gamma_4)\gamma_{11}\beta \right), \\
a_8 &= \frac{1}{\gamma_1\gamma_9\gamma_{11}\beta^2} \left(4 \sin^2 \frac{\kappa a}{2} \gamma_2\gamma_4 + \gamma_2\gamma_3 + \gamma_4\gamma_3 + \gamma_2 + \gamma_3 + \gamma_4 \right). \tag{A.27}
\end{aligned}$$